Formation, Abundance, and Evolution of Molecular Products in α-Pinene and β-Pinene Secondary Organic Aerosol

Thesis by
Christopher M. Kenseth

In Partial Fulfillment of the Requirements for the
Degree of
Doctor of Philosophy

Caltech

CALIFORNIA INSTITUTE OF TECHNOLOGY
Pasadena, California

2022
Defended May 23, 2022

© 2022

Christopher M. Kenseth
ORCID: 0000-0003-3188-2336

ACKNOWLEDGEMENTS

My time at Caltech has been punctuated by the support of great mentors, colleagues, family, and friends. The work represented in this thesis would not have been remotely possible without their help and guidance. Although nothing I pen could every properly encapsulate the immense appreciation that I hold for the impact they have had on my graduate experience, nor can I thank everyone by name, I would, nonetheless, like to express my sincerest gratitude for making this journey so rewarding.

To my advisors, John Seinfeld, Paul Wennberg, and Brian Stoltz, thank you not only for your mentorship and support but also for giving me the resources, freedom, and trust to pursue my own research interests. It has been a pleasure and a privilege learning from and working with each of you over the past seven years. To Nathan Dalleska, my de facto fourth advisor, thank you for training me on the Xevo and always making the time to talk shop, troubleshoot an instrument, or field countless technical questions. To Rick Flagan, my fourth committee member, thank you for providing valuable external perspective on my work and sharing your extensive knowledge of aerosol instrumentation. I could not have asked for a better group of mentors.

To Yuanlong Huang, thank you for all of the help you have given me over the years. My research would not have been possible without your technical skill, insight, and the generosity of your time. To Team Atmosphere, Nick Hafeman and Samir Rezgui, thank you for your synthetic expertise and the untold hours spent at the bench making compounds to enable my research. To Ran Zhao, thank you for the opportunity to learn from and collaborate with you on two fruitful projects during my first years at Caltech. To John Crounse, thank you for the perennial technical support and many useful discussions about atmospheric chemistry and instrumentation. To Kelvin Bates, thank you for being an incredible academic role model; your work is often the standard against which I judge my own. To Martha Hepworth and Nora

Oshima, thank you for all you do to support our research, our labs, and our communities.

To my friends and colleagues in the Seinfeld, Wennberg, and Stoltz labs, thank you for fostering such supportive and welcoming communities within which to conduct research, for the helpful guidance and discussions, assistance with experiments and instrumentation, and feedback on manuscripts and presentations, and for the camaraderie that has made coming to lab each day so enjoyable and fulfilling. I consider myself extraordinarily fortunate to have been able to work alongside and learn from each of you. To the core members of the Seinfeld lab, past and present, Kelvin Bates, Ran Zhao, Yuanlong Huang, Stephanie Kong, Brigitte Rooney, Sophia Charan, Elyse Pennington, Ben Schulze, Reina Buenconsejo, Ryan Ward, Kat Ball, and Haroula Baliaka, thank you for being such great labmates and friends, for countless crosswords, lab outings, holiday parties, and conference adventures, and, above all, for making the lab feel more like a family. To my friends at Caltech and beyond, thank you for making sure my time in California was spent not just in the lab but also on the baseball/softball field and in the mountains.

To my family, especially my parents and brother, Peter, thank you for your unwavering support, guidance, and love, not only during my time at Caltech but throughout my life. Despite being three thousand miles away, you have always been there, in my corner, when I needed you. Finally to Anya, my fiancée and adventure buddy, thank you for your unceasing support, encouragement, understanding, and love, for keeping me grounded, for bringing Meowshu into our lives, and for being by my side, through thick and thin, since day one of our graduate careers. Although we will spend the next stage of our lives apart as we pursue our academic dreams in Berkeley and Seattle, I cannot wait to see what wonderful adventures this new chapter holds in store. I love you with all my heart, all my soul, and everything in between.

ABSTRACT

The atmospheric oxidation of α-pinene and β-pinene ($C_{10}H_{16}$), emitted in appreciable quantities from forested regions (~85 Tg y^{-1}), contributes significantly to the global burden of secondary organic aerosol (SOA), a substantial component (15–80% by mass) of atmospheric fine particulate matter ($PM_{2.5}$), which exerts large but uncertain effects on climate as well as adverse impacts on air quality and human health. Deciphering the molecular composition, and in turn formation and aging mechanisms, of α-pinene and β-pinene SOA is essential to reducing uncertainty in assessment of their environmental and health impacts. However, molecular characterization of α-pinene and β-pinene SOA is significantly hindered by their chemical complexity. In this work, we constrain the formation, abundance, and evolution of molecular products in SOA derived from ozonolysis and photooxidation of α-pinene and β-pinene using a combination of laboratory experiments, liquid chromatography/electrospray ionization mass spectrometry (LC/ESI-MS), and organic synthesis. Through detailed MS/MS analysis, coupled with ^{13}C isotopic labeling and OH scavenging, we identify a suite of dimeric compounds ($C_{15-19}H_{24-32}O_{5-11}$) formed from synergistic O_3 + OH oxidation of β-pinene (i.e., accretion of O_3- and OH-derived products/intermediates). Informed by these structural analyses, together with ^{18}O isotopic labeling and H/D exchange, we synthesize the first authentic standards of several major dimer esters identified in SOA from ozonolysis of α-pinene and β-pinene and elucidate their formation mechanism from targeted environmental chamber experiments. Additionally, we synthesize a series of pinene-derived carboxylic acid and dimer ester homologues and find that the ESI efficiencies of the dimer esters are 19–36 times higher than that of commercial *cis*-pinonic acid, a common quantification surrogate. Finally, we investigate the aqueous (photo)chemistry (kinetics, products, and mechanisms) of the carboxylic acid and dimer ester homologues at cloudwater-relevant concentrations as a function of pH.

PUBLISHED CONTENT AND CONTRIBUTIONS

(11)   Van Rooy, P.; Tasnia, A.; Barletta, B.; Buenconsejo, R.; Crounse, J. D.; **Kenseth, C. M.**; Meinardi, S.; Murphy, S.; Parker, H.; Schulze, B.; Seinfeld, J. H.; Wennberg, P. O.; Blake, D. R.; Barsanti, K. C. Observations of Volatile Organic Compounds in the Los Angeles Basin during COVID-19. *ACS Earth Space Chem.* **2021**, *5* (11), 3045–3055. DOI: 10.1021/acsearthspacechem.1c00248.
C. M. K. performed research and edited the paper.

(10)   Amanatidis, S.; Huang, Y.; Pushpawela, B.; Schulze, B. C.; **Kenseth, C. M.**; Ward, R. X.; Seinfeld, J. H.; Hering, S. V.; Flagan, R. C. Efficacy of a Portable, Moderate-Resolution, Fast-Scanning Differential Mobility Analyzer for Ambient Aerosol Size Distribution Measurements. *Atmos. Meas. Tech.* **2021**, *14* (6), 4507–4516. DOI: 10.5194/amt-14-4507-2021.
C. M. K. performed research and edited the paper.

(9)   Huang, Y.; **Kenseth, C. M.**; Dalleska, N. F.; Seinfeld, J. H. Coupling Filter-Based Thermal Desorption Chemical Ionization Mass Spectrometry with Liquid Chromatography/Electrospray Ionization Mass Spectrometry for Molecular Analysis of Secondary Organic Aerosol. *Environ. Sci. Technol.* **2020**, *54* (20), 13238–13248. DOI: 10.1021/acs.est.0c01779.
C. M. K. performed research, contributed new reagents, analyzed data, and wrote/edited the paper.

(8)   **Kenseth, C. M.**; Hafeman, N. J.; Huang, Y.; Dalleska, N. F.; Stoltz, B. M.; Seinfeld, J. H. Synthesis of Carboxylic Acid and Dimer Ester Surrogates to Constrain the Abundance and Distribution of Molecular Products in α-Pinene and β-Pinene Secondary Organic Aerosol. *Environ. Sci. Technol.* **2020**, *54* (20), 12829–12839. DOI: 10.1021/acs.est.0c01556.
C. M. K. designed research, performed research, contributed new reagents, analyzed data, and wrote the paper.

(7)   Schulze, B. C.; Charan, S. M.; **Kenseth, C. M.**; Kong, W.; Bates, K. H.; Williams, W.; Metcalf, A. R.; Jonsson, H. H.; Woods, R.; Sorooshian, A.; Flagan, R. C.; Seinfeld, J. H. Characterization of Aerosol Hygroscopicity Over the Northeast Pacific Ocean: Impacts on Prediction of CCN and Stratocumulus Cloud Droplet Number Concentrations. *Earth Space Sci.* **2020**, *7*, e2020EA001098. DOI: 10.1029/2020EA001098.
C. M. K. performed research, analyzed data, and edited the paper.

(6)   **Kenseth, C. M.**; Huang, Y.; Zhao, R.; Dalleska, N. F.; Hethcox, J. C.; Stoltz, B. M.; Seinfeld, J. H. Synergistic O_3 + OH Oxidation Pathway to Extremely Low-Volatility Dimers Revealed in β-Pinene Secondary Organic Aerosol.

Proc. Natl. Acad. Sci. U.S.A. **2018**, *115* (33), 8301–8306. DOI: 10.1073/pnas.1804671115.
C. M. K. designed research, performed research, analyzed data, and wrote the paper.

(5)   Huang, Y.; Barraza, K. M.; **Kenseth, C. M.**; Zhao, R.; Wang, C.; Beauchamp, J. L.; Seinfeld, J. H. Probing the OH Oxidation of Pinonic Acid at the Air-Water Interface Using Field-Induced Droplet Ionization Mass Spectrometry (FIDI-MS). *J. Phys. Chem. A* **2018**, *122* (31), 6445–6456. DOI: 10.1021/acs.jpca.8b05353.
C. M. K. performed research, analyzed data, and wrote/edited the paper.

(4)   Zhao, R.; **Kenseth, C. M.**; Huang, Y.; Dalleska, N. F.; Kuang, X. M.; Chen, J.; Paulson, S. E.; Seinfeld, J. H. Rapid Aqueous-Phase Hydrolysis of Ester Hydroperoxides Arising from Criegee Intermediates and Organic Acids. *J. Phys. Chem. A* **2018**, *122* (23), 5190–5201. DOI: 10.1021/acs.jpca.8b02195.
C. M. K. performed research, analyzed data, and edited the paper.

(3)   Kalashnikova, O. V.; Garay, M. J.; Bates, K. H.; **Kenseth, C. M.**; Kong, W.; Cappa, C. D.; Lyapustin, A.; Jonsson, H. H.; Seidel, F. C.; Xu, F.; Diner, D. J.; Seinfeld, J. H. Photopolarimetric Sensitivity to Black Carbon Content of Wildfire Smoke: Results From the 2016 ImPACT-PM Field Campaign. *J. Geophys. Res. Atmos.* **2018**, *123* (10),5376–5396. DOI: 10.1029/2017JD028032.
C. M. K. performed research, analyzed data, and wrote/edited the paper.

(2)   Huang, Y.; Zhao, R.; Charan, S. M.; **Kenseth, C. M.**; Zhang, X.; Seinfeld, J. H. Unified Theory of Vapor-Wall Mass Transport in Teflon-Walled Environmental Chambers. *Environ. Sci. Technol.* **2018**, *52* (4), 2134–2142. DOI: 10.1021/acs.est.7b05575.
C. M. K. analyzed data and edited the paper.

(1)   Zhao, R.; **Kenseth, C. M.**; Huang, Y.; Dalleska, N. F.; Seinfeld, J. H. Iodometry-Assisted Liquid Chromatography Electrospray Ionization Mass Spectrometry for Analysis of Organic Peroxides: An Application to Atmospheric Secondary Organic Aerosol. *Environ. Sci. Technol.* **2018**, *52* (4), 2108–2117. DOI: 10.1021/acs.est.7b04863.
C. M. K. performed research, analyzed data, and edited the paper.

TABLE OF CONTENTS

LIST OF FIGURES

LIST OF TABLES

LIST OF SCHEMES

LIST OF SPECTRA

Chapter 1

INTRODUCTION

1.1 Background and Motivation

Aerosol particles are ubiquitous in the atmosphere and originate from a wide variety of human and natural sources (e.g., wildfires, desert dust, and fossil fuel combustion). These particles range in size from a few nanometers (smaller than viruses) to tens of micrometers (about the width of human hair) and are broadly grouped into two size modes, those with diameters greater or less than 2.5 μm, referred to as coarse and fine particles, respectively. Fine particulate matter ($PM_{2.5}$) accounts for the vast majority of atmospheric particles by number, as well as a substantial fraction of the total particle surface area and mass.[1]

Aerosol particles exert large but highly uncertain effects on Earth's climate directly, by scattering and absorbing solar radiation, and indirectly, by seeding cloud formation and altering their reflectivity and lifetime;[2] without aerosol particles to serve as cloud condensation nuclei (CCN), there would be many fewer clouds in the atmosphere. Aerosol particles also adversely impact air quality and, by extension, human health. Exposure to ambient $PM_{2.5}$ is associated with increased risk of respiratory and cardiovascular disease and is estimated to cause up to nine million premature deaths per year globally.[3–5]

Aerosol particles are either directly emitted to the atmosphere (primary aerosol), or formed in the atmosphere through oxidation of gaseous emissions (secondary aerosol). Globally, a substantial mass fraction (15–80%) of $PM_{2.5}$ consists of secondary organic aerosol (SOA),[6] formed via the gas-phase oxidation of volatile organic compounds (VOCs) emitted from biogenic and anthropogenic sources. As emissions of biogenic VOCs (~1000 Tg y^{-1})[7] far exceed those from anthropogenic activity (~100 Tg y^{-1}),[1] the biosphere is the dominant source of SOA to the global atmosphere.

The oxidation of monoterpenes ($C_{10}H_{16}$), emitted in large quantities from terrestrial vegetation (~150 Tg y^{-1}),[7] represents a significant and well established source of SOA.[8–11] Deciphering the molecular composition, and in turn formation and aging mechanisms, of monoterpene SOA is essential to reducing uncertainty in assessment of its environmental and health impacts. However, molecular characterization of monoterpene SOA, which generally consists of hundreds or more compounds of diverse classes, is significantly hindered by its chemical complexity.[12]

Electrospray ionization mass spectrometry (ESI-MS), typically coupled with liquid chromatographic (LC) separation, is among the most widely used analytical techniques for identification and quantification of SOA molecular constituents.[12,13] Multifunctional carboxylic acids and high-molecular-weight dimeric compounds, notably those proposed to contain ester linkages, have been identified via ESI-MS methods as significant components of both laboratory-derived and ambient monoterpene SOA,[14,15] and have been implicated as key contributors to particle formation and growth. Due to a lack of authentic standards, however, (*i*) structures of these SOA molecular products are inferred from accurate mass/fragmentation data and, therefore, mechanistic understanding of their formation and aging remains unconstrained and (*ii*) commercial terpenoic acids (e.g., *cis*-pinonic acid) are typically used as surrogates to quantify both monomeric and dimeric SOA constituents, despite the strong dependence of ESI efficiency on molecular structure. In this work, we constrain the formation, abundance, and evolution of carboxylic acids and dimeric compounds identified via LC/ESI-MS in SOA derived from the ozonolysis and photooxidation of α-pinene and β-pinene (Figure 1.1), which together account for >50% of global monoterpene emissions, using a combination of mass spectrometric, chromatographic, and synthetic techniques.

1.2 Organization of Thesis

In Chapter 2, through detailed MS/MS analysis, coupled with ^{13}C isotopic labeling and OH scavenging, we identify a suite of dimeric compounds ($C_{15–19}H_{24–32}O_{5–11}$) formed from concerted $O_3 + OH$ oxidation of β-pinene (i.e., accretion of O_3- and OH-
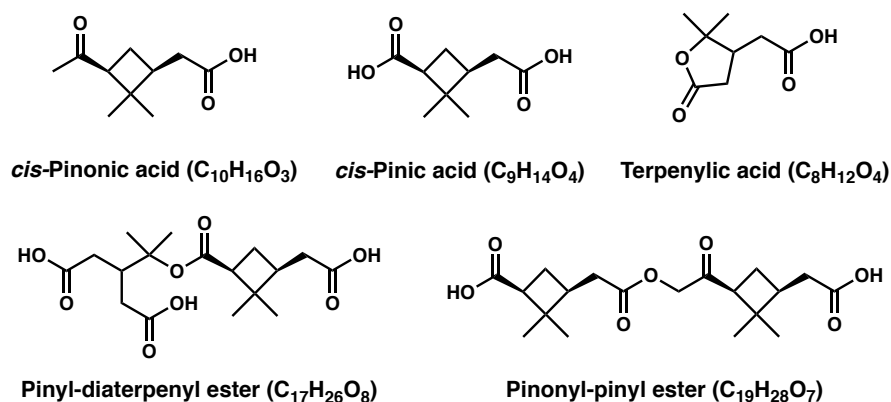
Figure 1.1. Proposed structures of select carboxylic acids and dimer esters identified in α-pinene and β-pinene SOA.

derived products/intermediates). We present evidence for formation of these dimers via both gas- and particle-phase processes, underscoring the complexity of atmospheric accretion chemistry. The production of dimers through synergistic O_3 + OH oxidation represents a potentially significant, heretofore-unidentified source of low-volatility monoterpene SOA, and suggests that the current treatment of SOA formation as a sum of products originating from the isolated oxidation of individual precursors fails to accurately reflect the complexity of oxidation pathways at play in the real atmosphere.

In Chapter 3, we synthesize a series of pinene-derived carboxylic acid and dimer ester homologues. We find that the ESI efficiencies of the dimer esters are 19–36 times higher than that of *cis*-pinonic acid, demonstrating that the mass contribution of dimers to monoterpene SOA has been significantly overestimated in past studies. Using the measured ESI efficiencies of the carboxylic acids and dimer esters as more representative surrogates, we determine that molecular products measurable by LC/ESI-MS account for only ~20% of the mass of SOA formed from ozonolysis of α-pinene and β-pinene. The observed order-of-magnitude difference in ESI efficiency between monomers and dimers demonstrates that the use of

unrepresentative surrogates can lead to substantial systematic errors in quantitative LC/ESI-MS analyses of SOA.

In Chapter 4, we investigate the aqueous (photo)chemistry (kinetics, products, and mechanisms) of the carboxylic acid and dimer ester homologues at cloudwater-relevant concentrations as a function of pH using LC/ESI-MS together with MS/MS analysis and H/D exchange. Characterization of the dark aqueous reactivity, photolysis, and photooxidation of the carboxylic acids and dimer esters, which respectively differ only in the identity of the terminal functional group (i.e., ketone vs. carboxylic acid vs. alcohol), affords key insight into the dependence of aqueous photochemical processing on molecular size/functionality and applicability of aqueous-phase structure-activity relationships (SARs) for monoterpene SOA constituents.

In Chapter 5, informed by the structural analyses presented in Chapter 2, together with ^{18}O isotopic labeling and H/D exchange, we synthesize the first authentic standards of several major dimer esters identified in SOA from ozonolysis of α-pinene and β-pinene and elucidate their formation mechanism from a series of targeted environmental chamber experiments using chemical ionization mass spectrometry (CIMS) and LC/ESI-MS for respective analysis of gas- and particle-phase molecular composition. Identification of the chemistry underlying dimer ester production provides a missing link tying the atmospheric degradation of α-pinene and β-pinene to the observed formation of low-volatility compounds capable of driving particle formation and growth.

Finally, Chapter 6 concludes with a brief summary of the findings presented in the previous five chapters on the formation, identification, quantification, and fate of α-pinene and β-pinene SOA molecular products and discusses directions for future research.

1.3 References

(1) Seinfeld, J. H.; Pandis, S. N. *Atmospheric Chemistry and Physics: From Air Pollution to Climate Change*, 3rd ed.; Wiley: Hoboken, NJ, 2016.

(2) Intergovernmental Panel on Climate Change. *Climate Change 2013: The Physical Science Basis*; Stocker, T. F., Qin, D., Plattner, G. K., Tignor, M., Allen, S. K., Boschung, J., Nauels, A., Xia, Y., Bex, V., Midgley, P. M., Eds.; Cambridge University Press: Cambridge, United Kingdom, 2013.

(3) Pope, C. A.; Ezzati, M.; Dockery, D. W. Fine-Particulate Air Pollution and Life Expectancy in the United States. *N. Engl. J. Med.* **2009**, *360* (4), 376–386. DOI: 10.1056/NEJMsa0805646.

(4) Cohen, A. J.; Brauer, M.; Burnett, R.; Anderson, H. R.; Frostad, J.; Estep, K.; Balakrishnan, K.; Brunekreef, B.; Dandona, L.; Dandona, R.; Feigin, V.; Freedman, G.; Hubbell, B.; Jobling, A.; Kan, H.; Knibbs, L.; Liu, Y.; Martin, R.; Morawska, L.; Pope, C. A.; Shin, H.; Straif, K.; Shaddick, G.; Thomas, M.; van Dingenen, R.; van Donkelaar, A.; Vos, T.; Murray, C. J. L.; Forouzanfar, M. H. Estimates and 25-Year Trends of the Global Burden of Disease Attributable to Ambient Air Pollution: An Analysis of Data from the Global Burden of Diseases Study 2015. *Lancet* **2017**, *389* (10082), 1907–1918. DOI: 10.1016/S0140-6736(17)30505-6.

(5) Burnett, R.; Chen, H.; Szyszkowicz, M.; Fann, N.; Hubbell, B.; Pope, C. A.; Apte, J. S.; Brauer, M.; Cohen, A.; Weichenthal, S.; Coggins, J.; Di, Q.; Brunekreef, B.; Frostad, J.; Lim, S. S.; Kan, H.; Walker, K. D.; Thurston, G. D.; Hayes, R. B.; Lim, C. C.; Turner, M. C.; Jerrett, M.; Krewski, D.; Gapstur, S. M.; Diver, W. R.; Ostro, B.; Goldberg, D.; Crouse, D. L.; Martin, R. V.; Peters, P.; Pinault, L.; Tjepkema, M.; van Donkelaar, A.; Villeneuve, P. J.; Miller, A. B.; Yin, P.; Zhou, M.; Wang, L.; Janssen, N. A. H.; Marra, M.; Atkinson, R. W.; Tsang, H.; Quoc Thach, T.; Cannon, J. B.; Allen, R. T.; Hart, J. E.; Laden, F.; Cesaroni, G.; Forastiere, F.; Weinmayr, G.; Jaensch, A.; Nagel, G.; Concin, H.; Spadaro, J. V. Global Estimates of Mortality Associated with Long-Term Exposure to Outdoor Fine Particulate Matter. *Proc. Natl. Acad. Sci. U.S.A.* **2018**, *115* (38), 9592–9597. DOI: 10.1073/pnas.1803222115.

(6) Jimenez, J. L.; Canagaratna, M. R.; Donahue, N. M.; Prevot, A. S. H.; Zhang, Q.; Kroll, J. H.; DeCarlo, P. F.; Allan, J. D.; Coe, H.; Ng, N. L.; Aiken, A. C.; Docherty, K. S.; Ulbrich, I. M.; Grieshop, A. P.; Robinson, A. L.; Duplissy, J.; Smith, J. D.; Wilson, K. R.; Lanz, V. A.; Hueglin, C.; Sun, Y. L.; Tian, J.; Laaksonen, A.; Raatikainen, T.; Rautiainen, J.; Vaattovaara, P.; Ehn, M.; Kulmala, M.; Tomlinson, J. M.; Collins, D. R.; Cubison, M. J.; E.; Dunlea, J.; Huffman, J. A.; Onasch, T. B.; Alfarra, M. R.; Williams, P. I.; Bower, K.; Kondo, Y.; Schneider, J.; Drewnick, F.;

Borrmann, S.; Weimer, S.; Demerjian, K.; Salcedo, D.; Cottrell, L.; Griffin, R.; Takami, A.; Miyoshi, T.; Hatakeyama, S.; Shimono, A.; Sun, J. Y.; Zhang, Y. M.; Dzepina, K.; Kimmel, J. R.; Sueper, D.; Jayne, J. T.; Herndon, S. C.; Trimborn, A. M.; Williams, L. R.; Wood, E. C.; Middlebrook, A. M.; Kolb, C. E.; Baltensperger, U.; Worsnop, D. R. Evolution of Organic Aerosols in the Atmosphere. *Science* **2009**, *326* (5959), 1525–1529. DOI: 10.1126/science.1180353.

(7)   Guenther, A. B.; Jiang, X.; Heald, C. L.; Sakulyanontvittaya, T.; Duhl, T.; Emmons, L. K.; Wang, X. The Model of Emissions of Gases and Aerosols from Nature Version 2.1 (MEGAN2.1): An Extended and Updated Framework for Modeling Biogenic Emissions. *Geosci. Model Dev.* **2012**, *5* (6), 1471–1492. DOI: 10.5194/gmd-5-1471-2012.

(8)   Hallquist, M.; Wenger, J. C.; Baltensperger, U.; Rudich, Y.; Simpson, D.; Claeys, M.; Dommen, J.; Donahue, N. M.; George, C.; Goldstein, A. H.; Hamilton, J. F.; Herrmann, H.; Hoffmann, T.; Iinuma, Y.; Jang, M.; Jenkin, M. E.; Jimenez, J. L.; Kiendler-Scharr, A.; Maenhaut, W.; McFiggans, G.; Mentel, Th. F.; Monod, A.; Prévôt, A. S. H.; Seinfeld, J. H.; Surratt, J. D.; Szmigielski, R.; Wildt, J. The Formation, Properties and Impact of Secondary Organic Aerosol: Current and Emerging Issues. *Atmos. Chem. Phys.* **2009**, *9* (14), 5155–5236. DOI: 10.5194/acp-9-5155-2009.

(9)   Kanakidou, M.; Seinfeld, J. H.; Pandis, S. N.; Barnes, I.; Dentener, F. J.; Facchini, M. C.; Van Dingenen, R.; Ervens, B.; Nenes, A.; Nielsen, C. J.; Swietlicki, E.; Putaud, J. P.; Balkanski, Y.; Fuzzi, S.; Horth, J.; Moortgat, G. K.; Winterhalter, R.; Myhre, C. E. L.; Tsigaridis, K.; Vignati, E.; Stephanou, E. G.; Wilson, J. Organic Aerosol and Global Climate Modelling: A Review. *Atmos. Chem. Phys.* **2005**, *5* (4), 1053–1123. DOI: 10.5194/acp-5-1053-2005.

(10)   Heald, C. L.; Henze, D. K.; Horowitz, L. W.; Feddema, J.; Lamarque, J.-F.; Guenther, A.; Hess, P. G.; Vitt, F.; Seinfeld, J. H.; Goldstein, A. H.; Fung, I. Predicted Change in Global Secondary Organic Aerosol Concentrations in Response to Future Climate, Emissions, and Land Use Change. *J. Geophys. Res.* **2008**, *113*, D05211. DOI: 10.1029/2007JD009092.

(11)   Zhang, H.; Yee, L. D.; Lee, B. H.; Curtis, M. P.; Worton, D. R.; Isaacman-VanWertz, G.; Offenberg, J. H.; Lewandowski, M.; Kleindienst, T. E.; Beaver, M. R.; Holder, A. L.; Lonneman, W. A.; Docherty, K. S.; Jaoui, M.; Pye, H. O. T.; Hu, W.; Day, D. A.; Campuzano-Jost, P.; Jimenez, J. L.; Guo, H.; Weber, R. J.; de Gouw, J.; Koss, A. R.; Edgerton, E. S.; Brune, W.; Mohr, C.; Lopez-Hilfiker, F. D.; Lutz, A.; Kreisberg, N. M.; Spielman, S. R.; Hering, S. V.; Wilson, K. R.; Thornton, J. A.; Goldstein, A. H. Monoterpenes Are the Largest Source of Summertime Organic Aerosol in the Southeastern United States. *Proc. Natl. Acad. Sci. U.S.A.* **2018**, *115* (9), 2038–2043. DOI: 10.1073/pnas.1717513115.

(12)   Nozière, B.; Kalberer, M.; Claeys, M.; Allan, J.; D'Anna, B.; Decesari, S.; Finessi, E.; Glasius, M.; Grgić, I.; Hamilton, J. F.; Hoffmann, T.; Iinuma, Y.; Jaoui, M.; Kahnt, A.; Kampf, C. J.; Kourtchev, I.; Maenhaut, W.; Marsden, N.; Saarikoski, S.; Schnelle-Kreis, J.; Surratt, J. D.; Szidat, S.; Szmigielski, R.; Wisthaler, A. The Molecular Identification of Organic Compounds in the Atmosphere: State of the Art and Challenges. *Chem. Rev.* **2015**, *115* (10), 3919–3983. DOI: 10.1021/cr5003485.

(13)   Laskin, J.; Laskin, A.; Nizkorodov, S. A. Mass Spectrometry Analysis in Atmospheric Chemistry. *Anal. Chem.* **2018**, *90* (1), 166–189. DOI: 10.1021/acs.analchem.7b04249.

(14)   Kenseth, C. M.; Huang, Y.; Zhao, R.; Dalleska, N. F.; Hethcox, J. C.; Stoltz, B. M.; Seinfeld, J. H. Synergistic O_3 + OH Oxidation Pathway to Extremely Low-Volatility Dimers Revealed in β-Pinene Secondary Organic Aerosol. *Proc. Natl. Acad. Sci. U.S.A.* **2018**, *115* (33), 8301–8306. DOI: 10.1073/pnas.1804671115.

(15)   Kenseth, C. M.; Hafeman, N. J.; Huang, Y.; Dalleska, N. F.; Stoltz, B. M.; Seinfeld, J. H. Synthesis of Carboxylic Acid and Dimer Ester Surrogates to Constrain the Abundance and Distribution of Molecular Products in α-Pinene and β-Pinene Secondary Organic Aerosol. *Environ. Sci. Technol.* **2020**, *54* (20), 12829–12839. DOI: 10.1021/acs.est.0c01566.

Chapter 2

SYNERGISTIC O$_3$ + OH OXIDATION PATHWAY TO EXTREMELY LOW-VOLATILITY DIMERS REVEALED IN β-PINENE SECONDARY ORGANIC AEROSOL

Kenseth, C. M.; Huang, Y.; Zhao, R.; Dalleska, N. F.; Hethcox, J. C.; Stoltz, B. M.; Seinfeld, J. H. Synergistic O$_3$ + OH Oxidation Pathway to Extremely Low-Volatility Dimers Revealed in β-Pinene Secondary Organic Aerosol. *Proc. Natl. Acad. Sci. U.S.A.* **2018**, *115* (33), 8301–8306. DOI: 10.1073/pnas.1804671115.

Abstract

Dimeric compounds contribute significantly to the formation and growth of atmospheric secondary organic aerosol (SOA) derived from monoterpene oxidation. However, the mechanisms of dimer production, in particular the relevance of gas- vs. particle-phase chemistry, remain unclear. Here, through a combination of mass spectrometric, chromatographic, and synthetic techniques, we identify a suite of dimeric compounds (C$_{15-19}$H$_{24-32}$O$_{5-11}$) formed from concerted O$_3$ and OH oxidation of β-pinene (i.e., accretion of O$_3$- and OH-derived products/intermediates). These dimers account for an appreciable fraction (5.9–25.4%) of the β-pinene SOA mass and are designated as extremely low-volatility organic compounds. Certain dimers, characterized as covalent dimer esters, are conclusively shown to form through heterogeneous chemistry, while evidence of dimer production via gas-phase reactions is also presented. The formation of dimers through synergistic O$_3$ + OH oxidation represents a potentially significant, heretofore-unidentified source of low-volatility monoterpene SOA. This reactivity also suggests that the current treatment of SOA formation as a sum of products originating from the isolated oxidation of individual precursors fails to accurately reflect the complexity of oxidation pathways at play in the real atmosphere. Accounting for the role of synergistic oxidation in ambient SOA formation could help to resolve the discrepancy between the measured atmospheric burden of SOA and that predicted by regional air quality and global climate models.

Significance

Secondary organic aerosol (SOA) is ubiquitous in the atmosphere and plays a pivotal role in climate, air quality, and health. Monoterpenes, emitted in large quantities from forested regions, are a dominant source of SOA globally, with dimers having been identified as key contributors to particle formation and growth. Here, we establish the role of concerted oxidation by O_3 and OH as a significant route to dimer formation in SOA generated from β-pinene, the second-most-abundant monoterpene emitted to the atmosphere. Production of this class of dimers is found to occur through both gas- and particle-phase processes. Dimer formation via synergistic O_3 + OH oxidation could represent an appreciable source of "missing" SOA not included in current atmospheric models.

2.1 Introduction

The oxidation of monoterpenes ($C_{10}H_{16}$) represents a substantial and well-established source of atmospheric secondary organic aerosol (SOA),[1,2] which constitutes a dominant mass fraction (15–80%) of fine particulate matter ($PM_{2.5}$)[3] and exerts large but uncertain effects on Earth's radiative balance[4] as well as adverse impacts on regional air quality and human health.[5,6] High-molecular-weight, low-volatility dimeric compounds have been identified as significant components of both ambient[7–11] and laboratory-derived[12–22] monoterpene SOA, and have been implicated as key players in new particle formation and growth,[9–14,23–26] particle viscosity,[27] and cloud condensation nuclei (CCN) activity.[8,24,26]

Accumulating studies of α-pinene SOA indicate that a vast majority of these dimers are formed only through O_3- and not OH-initiated oxidation, despite the apparent monomeric building blocks being present in both oxidative systems.[11–13] Particle-phase reactions of closed-shell monomers [e.g., aldol addition/condensation,[15–18] (peroxy)hemiacetal/acetal formation,[16,21,22] esterification,[7,18–21] and gem-diol formation[16,17]] and gas-phase reactions involving early-stage oxidation products and/or reactive intermediates [e.g., stabilized Criegee intermediates (SCIs), carboxylic acids, and organic peroxy radicals (RO_2)[9–14,23–26]] have been advanced as

possible dimer formation pathways. However, the mechanisms underlying dimer production and the relative importance of gas- vs. particle-phase chemistry remain unresolved.

In this work, we investigate the formation, identity, and abundance of molecular products in SOA derived from the O_3- and OH-initiated oxidation of β-pinene, the second-most-abundant monoterpene emitted to the atmosphere (global emissions estimated at 19 Tg y^{-1}).[28] Through detailed chromatographic and mass spectrometric analysis, coupled with ^{13}C isotopic labeling and OH/SCI scavenging, we identify a reactive pathway to extremely low-volatility dimeric compounds in SOA formed from monoterpene ozonolysis involving reaction of O_3-derived products/intermediates with those generated from oxidation by OH produced in situ via vinyl hydroperoxide (VHP) decomposition. We present evidence for formation of these dimers via both gas- and particle-phase processes, underscoring the complexity of atmospheric accretion chemistry. In establishing that O_3 and OH can act in concert to form nontrivial yields of dimeric SOA constituents, we highlight the potential significance of synergistic oxidation in ambient aerosol formation.

2.2 Results and Discussion

2.2.1 Dimers in β-Pinene SOA

β-Pinene ozonolysis and photooxidation experiments were carried out in the Caltech dual 24 m^3 Teflon Environmental Chambers (CTEC) (*Materials and Methods*). A custom-modified particle-into-liquid sampler (PILS) integrated with ultra-performance liquid chromatography/electrospray ionization quadrupole time-of-flight mass spectrometry operated in negative ion mode [UPLC/(−)ESI-Q-TOF-MS] was used to characterize the time-resolved SOA molecular composition (*Materials and Methods*).[29] Base peak ion (BPI) chromatograms of the O_3- and OH-derived β-pinene SOA are shown in Figure 2.1. The chromatographic fingerprint of the O_3 system displays distinct monomeric and dimeric regions. Conversely, while the identities of the monomers in both systems are similar, dimers measurable by
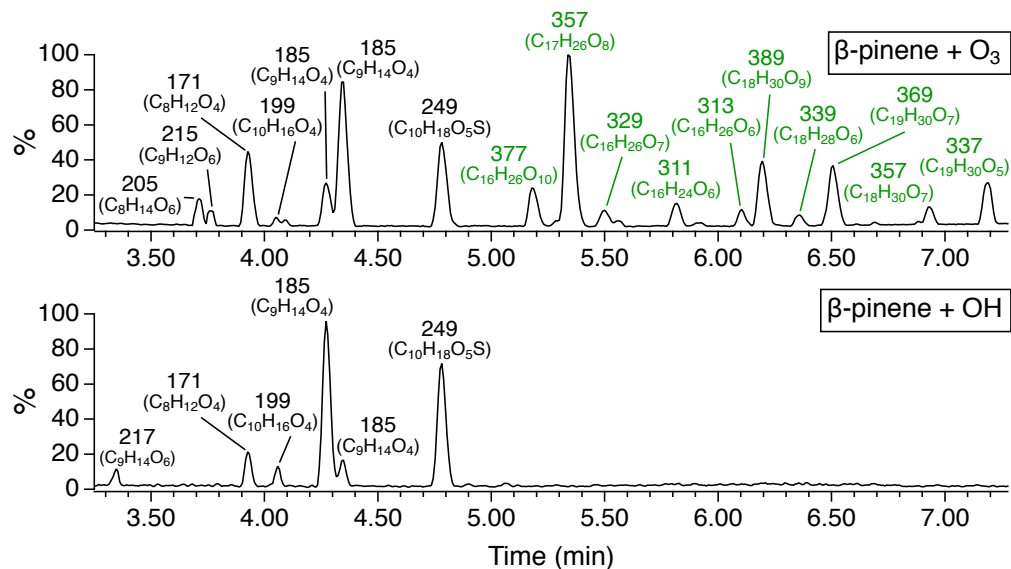
Figure 2.1. UPLC/(−)ESI-Q-TOF-MS BPI chromatograms of SOA produced from the O_3- and OH-initiated oxidation of β-pinene after ~4 h of reaction in the CTEC (*SI Appendix*, Table 2.S1, Exps. 1 and 2). Numbers correspond to nominal *m/z* values of $[M–H]^-$ ions. Molecular formulas ($C_xH_yO_z$) were assigned with mass tolerances of <7 ppm and supported by associated ^{13}C isotope distributions. Chromatograms consist of monomeric (black) and dimeric (green) regions.

PILS + UPLC/(−)ESI-Q-TOF-MS were not formed above the detection limit in the OH system, consistent with previous LC/(−)ESI-MS studies on dimer formation in α-pinene SOA.[11–13] The monomers, on average, exhibit higher O:C ratios than the dimers, suggesting that deoxygenation (e.g., condensation) is operative in dimer formation.[18,21] That the dimers in the O_3-derived SOA elute at retention times (RT) distinct from those of the monomers and are undetected in SOA produced from OH oxidation demonstrates that they are authentic β-pinene SOA products rather than ion-source artifacts (e.g., noncovalent adducts) formed during the (−)ESI process.

The absence of detectable dimers in pinene photooxidation systems has prompted SCIs, specifically reaction of SCIs with first-generation carboxylic acids forming hydroperoxide esters,[11,12,15] to be implicated as potential drivers of monoterpene accretion chemistry. However, we recently demonstrated that dimers identified in α-

pinene SOA using LC/ESI-MS methods do not contain (hydro)peroxide moieties.[30] Further, no clear reduction in dimer abundance was observed for SOA generated from β-pinene ozonolysis when either water vapor or formic acid was introduced as an SCI scavenger (*SI Appendix*, Figure 2.S1). These findings, together with modest SCI yields (15%) measured for α-pinene ozonolysis,[31,32] experimental and theoretical studies showing thermal unimolecular decay to be a dominant SCI loss process,[32–34] and reported increases in dimer concentrations in α-pinene SOA with increasing relative humidity (RH)[11–13] despite the probable role of water vapor as an SCI scavenger, call into question the importance of SCI chemistry in monoterpene dimer production. The lack of peroxide dimers in α-pinene SOA also implies that gas-phase dimers formed via RO_2 self/cross-reactions ($RO_2 + RO_2 \rightarrow ROOR + O_2$)[23–26] do not retain their peroxide character (i.e., undergo chemical transformation/decomposition) following condensation to the particle phase, as previously suggested.[13,20,23]

Although dimers in pinene SOA seem to form only through O_3- and not OH-initiated oxidation, scavenging of OH radicals produced as a byproduct of the hot Criegee VHP channel during α-pinene ozonolysis has been found to suppress the formation of certain dimeric species.[11] To further explore this effect, steady-state β-pinene ozonolysis experiments were conducted in the Caltech Photooxidation Flow Tube (CPOT) in the presence and absence of cyclohexane as an OH scavenger (*Materials and Methods*). UPLC/(−)ESI-Q-TOF-MS was employed to measure the molecular composition of SOA samples collected on Teflon filters and extracted into H_2O (*Materials and Methods*). A group of 23 dimeric compounds, also present in the CTEC experiments, was identified whose formation was significantly inhibited (>65%) by introduction of the OH scavenger; four of the dimers are major peaks in the BPI chromatogram (Figure 2.2). These dimers, with molecular formulas $C_{15–19}H_{24–32}O_{5–11}$ and O:C ratios ranging from 0.26 to 0.61, exhibit saturation mass concentrations (C*) < 3×10^{-4} µg m^{-3} and are designated as extremely low-volatility organic compounds (ELVOC) (Table 2.1). Compounds with accurate masses/molecular formulas corresponding to 20 of the 23 identified dimers have been
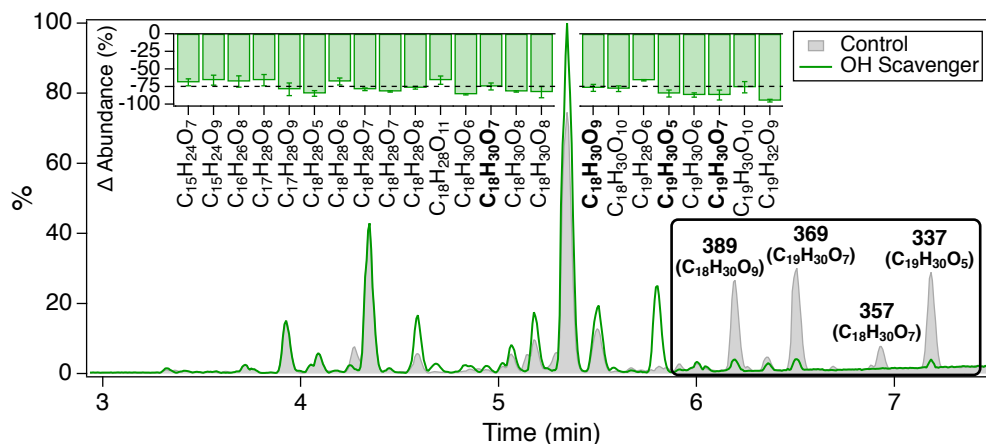
Figure 2.2. UPLC/(−)ESI-Q-TOF-MS BPI chromatograms of SOA produced from the O$_3$-initiated oxidation of β-pinene in the CPOT in the presence and absence of cyclohexane as an OH scavenger (*SI Appendix*, Table 2.S1, Exps. 7 and 8). Numbers correspond to nominal *m/z* values of [M−H]$^-$ ions; molecular formulas are given in parentheses. (*Inset*) Dimers that exhibited a significant decrease in abundance due to cyclohexane addition (Table 2.1), reported as a percent change relative to the control experiment and precise to <10%. Data for Control and OH Scavenger experiments are normalized to the total organic carbon content of the corresponding SOA samples (*SI Appendix*, *2*.S3.4) and are reported as averages of replicates (*n* = 3).

measured in recent monoterpene SOA formation experiments, and 18 such compounds have been observed in ambient SOA samples from forested regions dominated by monoterpene emissions (*SI Appendix*, Table 2.S2). The clear conclusion from these experiments is that formation for this particular collection of dimeric species depends on both O$_3$ and OH oxidation, in either a concurrent or sequential manner.

2.2.2 Dimers from Ozonolysis of ^{13}C-β-Pinene

To determine the point in the O$_3$-initiated dimer formation pathway at which OH radical chemistry occurs (e.g., oxidation of the precursor hydrocarbon, gas-phase reaction with first-generation products, or heterogeneous aging of particle-bound dimers), the exocyclic double bond of β-pinene was exploited. ^{13}C-β-Pinene, labeled at the terminal vinylic carbon, was synthesized from ^{13}C-iodomethane and nopinone via Wittig olefination (Scheme 2.1). Ozonolysis of ^{13}C-β-pinene was carried out in

Table 2.1. Dimers identified in SOA produced from the O$_3$-initiated oxidation of β-pinene that exhibited a significant decrease in abundance (> 65%) due to OH scavenging.

Dimer Type	Observed m/z (–)	RT (min)	Molecular Formula	Error (ppm)	O:C	$\overline{OS}_C$[†]	logC* (µg m^{-3})[‡]	Exchangeable Hydrogens	SOA Mass Fraction (%)[§,¶]
1	323.1860	6.86	C$_{18}$H$_{28}$O$_5$	0.6	0.28	–1.00	–3.9	2	0.04–0.17
	355.1754	6.24	C$_{18}$H$_{28}$O$_7$	–0.8	0.39	–0.78	–7.6	4	0.11–0.36
	419.1525	4.70	C$_{18}$H$_{28}$O$_{11}$	–6.7	0.61	–0.33	–15.2	4	0.02–0.16
	373.1851	5.99	C$_{18}$H$_{30}$O$_8$	–2.9	0.44	–0.78	–9.4	4	0.07–0.23
	405.1764	4.49	C$_{18}$H$_{30}$O$_{10}$	0.7	0.56	–0.56	–13.2	5	0.06–0.62
	351.1828	5.73	C$_{19}$H$_{28}$O$_6$	5.7	0.32	–0.84	–6.1	2	0.10–0.41
	337.2027	7.16	C$_{19}$H$_{30}$O$_5$	3.6	0.26	–1.05	–4.3	2	0.46–2.01
	369.1916	6.48	C$_{19}$H$_{30}$O$_7$	0.8	0.37	–0.84	–7.9	4	2.23–9.24
2	341.1960	6.87	C$_{18}$H$_{30}$O$_6$	–1.2	0.33	–1.00	–5.7	2	0.06–0.24
	357.1919	6.91	C$_{18}$H$_{30}$O$_7$	1.7	0.39	–0.89	–7.6	3	0.39–1.60
	373.1851	5.70	C$_{18}$H$_{30}$O$_8$	–2.9	0.44	–0.78	–9.4	3	0.14–0.47
	389.1814	6.18	C$_{18}$H$_{30}$O$_9$	0.8	0.50	–0.67	–11.3	3	1.88–7.81
	353.1961	6.15	C$_{19}$H$_{30}$O$_6$	–0.8	0.32	–0.95	–6.1	3	0.14–0.60
3	315.1448	5.83	C$_{15}$H$_{24}$O$_7$	1.3	0.47	–0.67	–6.6	3	0.02–0.10
	347.1346	5.19	C$_{15}$H$_{24}$O$_9$	1.2	0.60	–0.40	–10.5	3	0.03–0.25
	375.1653	6.24	C$_{17}$H$_{28}$O$_9$	–0.5	0.53	–0.59	–11.0	3	0.02–0.24
	417.1769	6.76	C$_{19}$H$_{30}$O$_{10}$	1.9	0.53	–0.53	–13.5	2	0.06–0.62
	403.1963	6.28	C$_{19}$H$_{32}$O$_9$	–1.2	0.48	–0.74	–11.6	3	0.07–0.24
4	345.1549	5.36	C$_{16}$H$_{26}$O$_8$	0.1	0.50	–0.63	–8.8	2	0.05–0.50
	359.1714	5.89	C$_{17}$H$_{28}$O$_8$	2.2	0.47	–0.71	–9.1	3	0.32–1.07
	339.1822	6.34	C$_{18}$H$_{28}$O$_6$	4.1	0.33	–0.89	–5.7	2	0.46–1.93
	355.1754	5.27	C$_{18}$H$_{28}$O$_7$	–0.8	0.39	–0.78	–7.6	5	0.51–1.72
	371.1707	5.46	C$_{18}$H$_{28}$O$_8$	0.3	0.44	–0.67	–9.4	3	0.30–1.22

Dimers are grouped into four types based on structure and formation mechanism (see main text).

[†]Average carbon oxidation state ($\overline{OS}_C$ = 2 O:C – H:C).

[‡]Saturation mass concentration (C*). Estimated using empirical model developed by Donahue et al.[35]

[§]Calculated for β-pinene SOA produced from O$_3$-initiated oxidation in the CTEC (*SI Appendix*, Table 2.S1, Exp. 1) after ~4 h of reaction.

[¶]Upper and lower bounds represent mass fraction estimates derived from experimental and computational approaches, respectively. Uncertainties in experimental and computational approaches are estimated to be ± 23% (relative) and a factor of 3, respectively. Details are provided in *SI Appendix, 2.S7*.
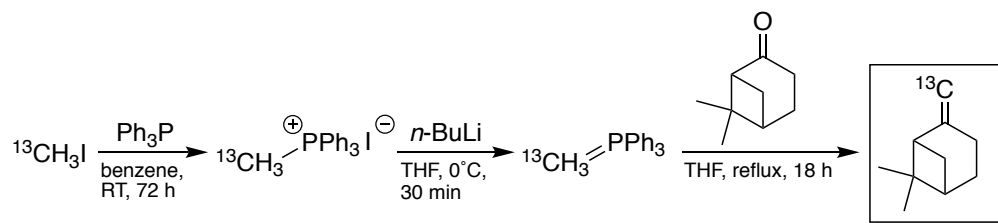
Scheme 2.1. Synthesis of ^{13}C-β-pinene via Wittig olefination (*SI Appendix*, *2*.S5).

the CPOT in the absence of an OH scavenger; SOA samples were collected on Teflon filters and extracted into H_2O. The *m/z* of 18 of the identified dimers (Table 2.1, types 1–3), including the four major BPI peaks, shifted by one mass unit on formation from ^{13}C-β-pinene, indicative of ^{13}C incorporation, while their RT remained unchanged. Recalling that reaction of ^{13}C-β-pinene with O_3 will cleave the ^{13}C label whereas on reaction with OH the label will be retained, the one-unit mass shift suggests that formation of the 18 dimers occurs via reaction, in either the gas or particle phase, of O_3-derived products/intermediates with products/intermediates generated from oxidation of β-pinene by OH produced via VHP decomposition. For those dimers that did not undergo a mass shift (Table 2.1, type 4), the observed dependence of their formation on OH can be rationalized, in addition to the scenarios above, in terms of a photooxidative pathway in which the labeled carbon is eliminated following OH addition to β-pinene[36,37] but prior to reaction with the O_3-derived species.

The steady-state CPOT experiments enabled collection of sufficient quantities of SOA mass for detailed structural analysis via collision-induced dissociation (CID) (*SI Appendix*, 2.S3.5). MS/MS spectra of the ^{13}C-labeled dimers and their ^{12}C isotopologues revealed distinct OH-derived (^{13}C-mass-shifted) and O_3-derived (unshifted) fragmentation patterns (*SI Appendix*, Table 2.S3). A group of eight dimeric compounds (Table 2.1, type 1) was identified with fragmentation patterns and relative peak intensities characteristic of covalent dimer esters, which have been reported to be significant components of monoterpene SOA.[7,10–13,18–21] Specifically, (*i*) the elemental composition of the dimers is given by condensation of the O_3- and

Figure 2.3. Representative (*1*) extracted ion chromatograms (EIC), (*2*) MS spectra, and (*3*) MS/MS spectra, measured by UPLC/(−)ESI-Q-TOF-MS, of dimer esters in SOA produced from the O$_3$-initiated oxidation of β-pinene (Table 2.1, type 1) presumed to form from (*A*) *cis*-pinic acid (C$_9$H$_{14}$O$_4$), (*B*) *cis*-norpinic acid (C$_8$H$_{12}$O$_4$), and (*C*) diaterpenylic acid (C$_8$H$_{14}$O$_5$). MS/MS peaks are colored to denote O$_3$-derived (red) and OH-derived (blue) fragment ions. Numbers in MS/MS spectra correspond to nominal *m/z* values of [M−H]$^-$ fragment ions; ionic formulas [C$_x$H$_y$O$_z$]$^-$ are given in parentheses. *Indicates peaks that underwent a one-unit mass shift on formation from ^{13}C-β-pinene.

OH-derived monomeric product ions ($M_1 + M_2 - M_{H_2O} = M_D$),[7,16] and (*ii*) assuming that the principal fragmentation occurs at the ester linkage, producing carboxyl and alkoxy fragment ions through neutral loss of the alcohol and dehydrated acid moieties, respectively, the carboxyl fragments and associated daughter ions are more intense than the alkoxy fragments and their daughter ions (Figure 2.3),[20,21,38] in line with conventional charge accommodation behavior in (−)ESI-MS. For the remaining 10 dimers (Table 2.1, types 2 and 3), the O_3- and OH-derived fragmentation patterns were not indicative of known accretion chemistry (e.g., formal addition or condensation), and in most instances a reasonable OH-derived (^{13}C-mass-shifted) monomeric building block either could not be identified or failed to account for the observed OH-derived daughter ions (*SI Appendix*, Table 2.S3). The structures of these dimers were not investigated further.

Based on comparison with MS/MS data for commercial standards and/or previously published MS/MS spectra, the O_3-derived monomeric building blocks of the dimer esters are attributed to one of three dicarboxylic acids, each a well-characterized pinene oxidation product that has been implicated in dimer formation: *cis*-pinic acid ($C_9H_{14}O_4$; Figure 2.3*A*), *cis*-norpinic acid ($C_8H_{12}O_4$; Figure 2.3*B*), and diaterpenylic acid ($C_8H_{14}O_5$; Figure 2.3*C*) (*SI Appendix*, 2.S6.1).[7,39] Conversely, the OH-derived monomeric units are characterized by the ionic $[M–H]^-$ formulas $[C_{10}H_{15,17}O_{2-7}]^-$, indicative of OH addition to β-pinene ($C_{10}H_{16}$) followed by varying degrees of O_2 incorporation, isomerization, and bimolecular radical chemistry.[36,37] The daughter ions of the dicarboxylic acid and $[C_{10}H_{15,17}O_{2-7}]^-$ monomeric units are rationalized by successive neutral losses of H_2O (18 Da), CO_2 (44 Da), CH_2O (30 Da), and C_3H_6O (58 Da), all of which are established CID pathways.[40–42] Notably, the loss of $^{13}CH_2O$ (31 Da) from the $[C_{10}H_{15,17}O_{2-7}]^-$ fragment is observed in the MS/MS spectrum of almost every ^{13}C-labeled dimer ester (Figure 2.3 and *SI Appendix*, Table 2.S3), consistent with the expected major addition of OH to β-pinene (83% of total OH reactivity) at the terminal vinylic carbon.[36] Moreover, while the three dicarboxylic acids implicated as O_3-derived precursors were identified as

major products in β-pinene SOA formed from ozonolysis (*SI Appendix*, 2.S6.1), SOA products corresponding to the OH-derived monomeric building blocks (i.e., $C_{10}H_{16}O_{3,7}$ and $C_{10}H_{18}O_{2,4,6}$) were not detected.

To further constrain the structures of the dimer esters, β-pinene SOA filters were extracted into D_2O and analyzed via UPLC/(−)ESI-Q-TOF-MS using D_2O as the polar eluent (*SI Appendix*, 2.S3.6). This approach facilitated deuterium substitution (H → D) of labile hydrogens (e.g., −OH, −OOH, and −COOH) in the SOA constituents while preserving chromatographic separation, enabling quantification of the number of exchangeable hydrogens in the identified dimer molecules based on systematic shifts in *m/z* due to H/D exchange (Table 2.1 and *SI Appendix*, Figure 2.S4). Additionally, using our recently developed iodometry-assisted LC/ESI-MS assay for the molecular-level identification of organic peroxides,[30] it was established that the 23 identified dimers do not contain hydroperoxide (ROOH) or organic peroxide (ROOR) functionalities (*SI Appendix*, 2.S3.7). On the basis of these supporting experiments, the accurate mass (MS) and fragmentation (MS/MS) data, the inferred dicarboxylic acid structures of the O_3-derived monomers, and the prevailing mechanism of β-pinene photooxidation,[36,37] tentative molecular structures and fragmentation pathways for the dimer esters are proposed in *SI Appendix*, Table 2.S4 and Figure 2.S10, respectively (*SI Appendix*, 2.S6.1).

2.2.3 Mechanisms of Dimer Formation

To assess the relative contributions of gas- vs. particle-phase chemistry to the formation of dimers derived from concerted O_3 and OH oxidation, the temporal evolution of individual products in β-pinene SOA formed from ozonolysis in the CTEC was examined. Shown in Figure 2.4 *A–C* are the particle-phase growth profiles of the eight dimer esters (Table 2.1, type 1) overlaid upon those corresponding to the dicarboxylic acid monomers (*cis*-pinic acid, *cis*-norpinic acid, and diaterpenylic acid) that were implicated as precursors based on detailed MS/MS analysis. The strong correlation between the particle-phase abundances of the dimer esters and their
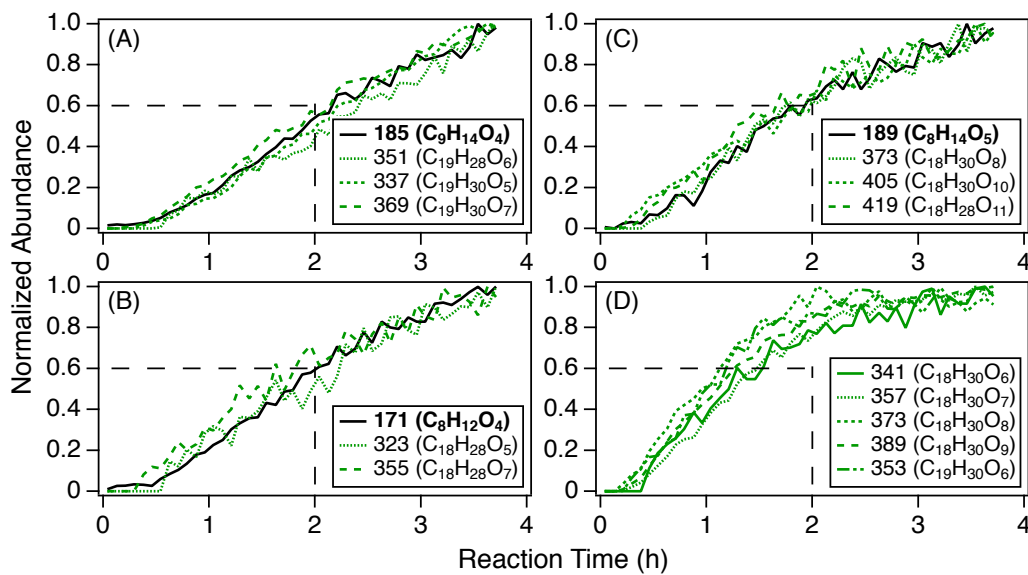
Figure 2.4. Temporal profiles of molecular products in SOA produced from the O₃-initiated oxidation of β-pinene in the CTEC (*SI Appendix*, Table 2.S1, Exp. 1), measured by PILS + UPLC/(−)ESI-Q-TOF-MS. Profiles are plotted as the particle-phase abundance of each species, normalized to the highest abundance observed over 4 h of reaction, as a function of reaction time. Discrete data points (5-min resolution) are presented as lines to aid the eye. Numbers correspond to nominal *m/z* values of [M−H]⁻ ions; molecular formulas are given in parentheses. (*A–C*) Profiles of dimer esters (Table 2.1, type 1) and dicarboxylic acids implicated as precursors based on MS/MS analysis: (*A*) *cis*-pinic acid (*m/z* 185; C₉H₁₄O₄; RT 4.33), (*B*) *cis*-norpinic acid (*m/z* 171; C₈H₁₂O₄; RT 4.06), and (*C*) diaterpenylic acid (*m/z* 189; C₈H₁₄O₅; RT 3.32). (*D*) Profiles of dimers (Table 2.1, type 2) characterized by almost immediate formation and rapid particle-phase growth. Dashed lines (2 h, 0.6 abundance) are drawn to aid in comparison between growth profiles in *A-C* and *D*.

presumed dicarboxylic acid building blocks points toward a mechanism of heterogeneous formation, wherein the semivolatile dicarboxylic acids undergo traditional equilibrium gas-particle partitioning[43] with subsequent reactive uptake of the gas-phase, OH-derived monomers/intermediates on collision with particle surfaces to form ELVOC dimers. A heterogeneous rather than purely particle-phase mechanism is supported by the absence of monomers corresponding to the OH-derived dimer ester precursors in SOA generated from β-pinene ozonolysis. Such heterogeneous/multiphase accretion processes, leading to the production of high-

molecular-weight oligomeric products, have recently been shown to contribute significantly to SOA formation in both biogenic and anthropogenic systems.[44,45]

The growth dynamics of the dimer esters can be contrasted against those shown in Figure 2.4*D* for another group of dimers (Table 2.1, type 2) also produced from coupled O_3 and OH oxidation. These dimers achieve essentially their maximum, steady-state SOA concentrations after ~2 h of reaction, whereas within the same time frame the dimer esters reach only ~60% of their highest measured particle-phase abundances. Prompt formation and rapid particle-phase growth of the dimers in Figure 2.4*D*, at rates faster than those observed for the monomers (Figure 2.4 *A–C*), indicate production via gas-phase reactions of first-generation oxidation products/intermediates followed by irreversible condensation of the resulting ELVOC dimers onto existing aerosol surfaces. As the formation of these dimers was not significantly inhibited by introduction of SCI scavengers (*SI Appendix*, Figure 2.S1), they likely originate from closed-shell/radical species unique to the hot Criegee VHP channel. Although the identified dimers were found not to contain (hydro)peroxide functionalities (*SI Appendix*, 2.S3.7), production of the dimers in Figure 2.4*D* may be explained by gas-phase RO_2 self/cross-reactions[23–26,46] with subsequent particle-phase decomposition leading to nonperoxide species.[13,20] Fast formation of particle-bound dimers during monoterpene ozonolysis has been reported in several recent studies[10–13,20] and, together with their estimated low volatility, has been advanced to explain nucleation and initial growth of monoterpene SOA, both in laboratory studies without seed aerosol and in regions, such as the boreal forest, dominated by biogenic emissions.[47]

As a means of evaluating the hypothesized mechanism of heterogeneous dimer ester formation, β-pinene photooxidation experiments were conducted in the CTEC in the presence of seed aerosol composed of varying mass ratios of ammonium sulfate [$(NH_4)_2SO_4$] and *cis*-pinic acid, the only commercially available pinene-derived dicarboxylic acid (*Materials and Methods*). Consistent with the idea that introducing the O_3-derived dimer ester precursors into the particle phase of the OH system should
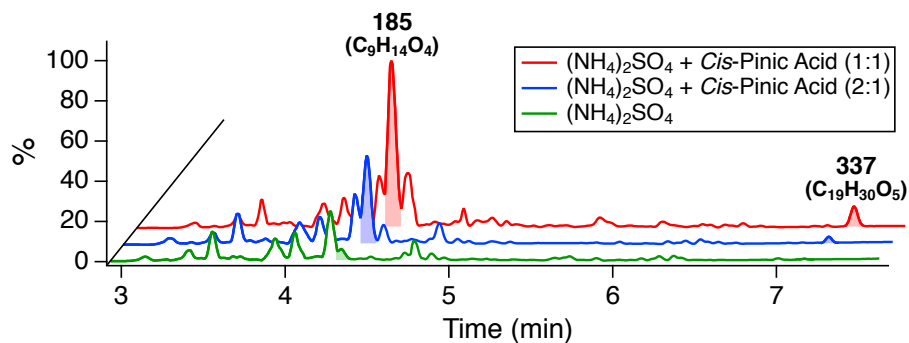
Figure 2.5. UPLC/(−)ESI-Q-TOF-MS BPI chromatograms of SOA produced from the OH-initiated oxidation of β-pinene after ~4 h of reaction in the CTEC (*SI Appendix*, Table 2.S1, Exps. 2–4). Experiments were conducted in the presence of seed aerosol at similar mass loadings but different mass ratios (see legend) of $(NH_4)_2SO_4$ and *cis*-pinic acid ($C_9H_{14}O_4$). Numbers correspond to nominal *m/z* values of [M–H]⁻ ions; molecular formulas are given in parentheses. Shaded peaks correspond to *cis*-pinic acid and the dimer ester at *m/z* 337 ($C_{19}H_{30}O_5$). Chromatograms for each experiment are normalized to the area of the peak at RT 3.93 (*m/z* 171; $C_8H_{12}O_4$).

promote otherwise negligible heterogeneous dimerization, the presence of *cis*-pinic acid in the $(NH_4)_2SO_4$ seed resulted in significant formation, proportional to the mass ratio of *cis*-pinic acid to $(NH_4)_2SO_4$, of the major dimer ester at *m/z* 337 ($C_{19}H_{30}O_5$) (Figure 2.5), corroborating the indirect MS/MS (Figure 2.3*A*) and kinetic (Figure 2.4*A*) evidence for production from particle- bound *cis*-pinic acid. That the dimer ester at *m/z* 337 was not observed in OH-derived β-pinene SOA, with pure $(NH_4)_2SO_4$ seed, collected on a Teflon filter coated with *cis*-pinic acid excludes the possibility of dimer formation via accretion of condensed monomers, either on the filter or during the extraction process (*SI Appendix*, Figure 2.S11). Although the details of the mechanism forming the ester linkage remain unclear, the observed increase in dimer ester abundance at elevated RH (*SI Appendix*, Figure 2.S1) argues against production via conventional esterification (i.e., carboxylic acid + alcohol). Overall, these findings conclusively demonstrate the role of heterogeneous accretion chemistry in monoterpene SOA formation (*SI Appendix*, 2.S6.2).

Surprisingly, these experiments also imply that a simple mass limitation of monomeric precursors in the particle phase is responsible for the absence of dimer esters in β-pinene SOA formed from OH-initiated oxidation. However, increased mass fractions of *cis*-pinic acid in SOA from α-pinene ozonolysis, relative to photooxidation, have been observed in a number of previous studies and have been invoked as a possible explanation for the lack of dimers containing *cis*-pinic acid in α-pinene photooxidation experiments.[7,12,48] Indeed, in this study *cis*-pinic acid was found to comprise a much higher fraction of β-pinene SOA mass when formed from O_3- ($13.4 \pm 3.1\%$) rather than OH-initiated ($1.7 \pm 0.4\%$) oxidation (see *m/z* 185; RT 4.33 in Figure 2.1), while significant but less pronounced disparities in SOA mass fraction between ozonolysis and photooxidation experiments were observed for *cis*-norpinic acid ($1.4 \pm 0.3\%$ vs. $0.24 \pm 0.06\%$) and diaterpenylic acid ($0.71 \pm 0.16\%$ vs. $0.28 \pm 0.06\%$) (*SI Appendix*, 2.S7).

Although also suggested to arise from heterogeneous reaction of particle-phase *cis*-pinic acid (Figure 2.4*A*), neither the prominent dimer ester at *m/z* 369 ($C_{19}H_{30}O_7$) nor the minor dimer ester at *m/z* 351 ($C_{19}H_{28}O_6$) was detected in the photooxidation experiments carried out with *cis*-pinic acid and $(NH_4)_2SO_4$ seed. One plausible explanation for the absence of these dimers is that the high HO_2 concentrations ($\sim 10^{10}$ molecules cm^{-3}) inherent in the use of H_2O_2 as an OH precursor (*SI Appendix*, 2.S1.1) produce an oxidative environment in which the OH-derived RO_2 isomerization and bimolecular reaction channels are vastly different from those operative in the comparatively low-HO_2 ($\sim 10^7$ molecules cm^{-3}) ozonolysis system (*SI Appendix*, 2.S4) that form the $[C_{10}H_{17}O_4]^-$ and $[C_{10}H_{15}O_3]^-$ building blocks of the dimer esters at *m/z* 369 and 351, respectively (*SI Appendix*, Table 2.S3). That $RO_2 + HO_2$ rate coefficients are typically order(s) of magnitude larger than those for $RO_2 + RO_2$ reactions[49] further compounds the disparity between these two RO_2 regimes. Conversely, for the dimer ester at *m/z* 337, although the structure of the $[C_{10}H_{17}O_2]^-$ building block is tentative (*SI Appendix*, Figure 2.S10 and Table 2.S3), theoretical studies indicate that this monomer is able to form under both ozonolysis and

photooxidation conditions from the $C_{10}H_{17}O_3$ hydroxy peroxy radical, produced from OH and subsequent O_2 addition to β-pinene, either via traditional RO_2 + RO_2 chemistry or through an OH-recycling pathway in the reaction with HO_2.[36,50]

2.2.4 Atmospheric Implications

The production of dimeric compounds (Table 2.1, types 1–3) through concerted O_3 and OH oxidation accounts for an appreciable, heretofore-unidentified fraction (5.9–25.4%) of the total mass of β-pinene SOA derived from ozonolysis under the conditions employed in this work (Table 2.1). Although specifically revealed in SOA formation from β-pinene, this reactive pathway represents a potentially significant source of high-molecular-weight ELVOC to the atmosphere that is expected to be broadly applicable to other monoterpenes (*SI Appendix*, 2.S8). Through detailed molecular composition and kinetic analysis, certain dimers are definitively shown to form through heterogeneous processes, while indirect evidence for dimer production via gas-phase routes is also presented. The importance of both gas- and particle-phase reactions to the formation of dimeric SOA constituents demonstrated in the current work underscores the complexity of atmospheric accretion chemistry, as well as the significant shortcomings in scientific understanding that preclude adequate characterization of its impact.

The O_3 + OH reactivity elucidated in β-pinene SOA also highlights the importance of understanding and accounting for the likely role of oxidative synergism in ambient aerosol formation, where SOA precursors are susceptible to concurrent oxidation by O_3 and OH. At present, SOA formation in atmospheric models is treated as an additive combination of products originating from the isolated oxidation of individual precursors (e.g., α-pinene + O_3 or isoprene + OH). In establishing that oxidants can act in concert to produce extremely low-volatility dimers in nontrivial yields, however, this study suggests that the tendency of current atmospheric models to systematically underpredict ambient SOA mass[1] may be due in part to the fact that discrete SOA formation mechanisms, parameterized by laboratory experiments that

typically feature only one oxidant and a single SOA precursor, do not accurately reflect the intricate oxidation pathways at play in the real atmosphere. Revising the chemistry of monoterpene SOA formation in regional air quality and global climate models to account for the role of synergistic oxidation could help to resolve the discrepancy between model predictions and ambient measurements. However, parameterization of this reactivity requires additional work.

2.3   Materials and Methods

β-Pinene ozonolysis and photooxidation experiments were carried out in the CTEC and CPOT at ambient temperature (~295 K) and atmospheric pressure (~1 atm), under dry conditions (<10% RH), in the presence of $(NH_4)_2SO_4$ seed aerosol, and at mixing ratios of NO_x typical of the pristine atmosphere (<0.5 ppb). CTEC experiments were designed to mimic oxidation in ambient air, while those in the CPOT were used to elucidate dimer structures and formation mechanisms. For CTEC experiments with ~4-h duration, β-pinene (~120 ppb) was oxidized by O_3 (~200 ppb) in the absence of an OH scavenger or OH (~2 × 10^6 molecules cm^{-3}). Select photooxidation experiments were performed with mixed $(NH_4)_2SO_4$ and *cis*-pinic acid seed. For steady-state CPOT experiments, oxidation of β-pinene (~150 ppb) by O_3 (~1 ppm) proceeded in the presence and absence of scavengers for both OH (cyclohexane) and SCIs (water vapor and formic acid). In certain CPOT experiments, ^{13}C-β-pinene, synthesized from ^{13}C-iodomethane and nopinone via Wittig olefination (Scheme 2.1), was used. Experimental conditions are reported in *SI Appendix*, Table 2.S1 and described in detail in *SI Appendix*, 2.S1.

β-Pinene mixing ratios were quantified with a gas chromatograph equipped with a flame ionization detector (GC/FID) (*SI Appendix*, 2.S2). Aerosol size distributions and number concentrations were measured with a custom-built scanning mobility particle sizer (SMPS) (*SI Appendix*, 2.S3.1). "Bulk" aerosol chemical composition was quantified with an Aerodyne high- resolution time-of-flight aerosol mass spectrometer (HR-ToF-AMS) (*SI Appendix*, 2.S3.2). The molecular composition of

β-pinene SOA collected by PILS during CTEC experiments (*SI Appendix*, 2.S3.3) and on Teflon filters during steady-state CPOT and select CTEC experiments (*SI Appendix*, 2.S3.4) was characterized off-line by UPLC/(−)ESI-Q-TOF-MS (*SI Appendix*, 2.S3.5). Certain SOA filter samples were analyzed using D_2O in place of H_2O as the extraction solvent/polar eluent (*SI Appendix*, 2.S3.6). Iodometry was coupled to UPLC/ (−)ESI-Q-TOF-MS[30] to identify organic peroxides at the molecular level in β-pinene SOA (*SI Appendix*, 2.S3.7). The Master Chemical Mechanism version 3.2 (MCMv3.2)[51] was used to simulate the concentration profiles of OH, HO_2, and RO_2 during β-pinene ozonolysis in the CTEC, as well as the fractions of β-pinene that react with O_3 vs. OH (*SI Appendix*, 2.S4). Mass fractions of individual organic compounds in β-pinene SOA, along with associated uncertainties, were calculated as described in *SI Appendix*, 2.S7.

2.4 Acknowledgments

2.5   Supporting Information

Table of Contents

2.S1   Secondary Organic Aerosol (SOA) Formation Experiments

Ozonolysis and photooxidation experiments were conducted in the Caltech dual 24 m^3 Teflon Environmental Chambers (CTEC)[52,53] and Caltech Photooxidation Flow Tube (CPOT)[54] at ambient temperature (~295 K) and atmospheric pressure (~1 atm). All experiments were carried out under dry conditions (<10% RH), in the presence of ammonium sulfate [$(NH_4)_2SO_4$] seed aerosol, and at mixing ratios of NO_x typical of the pristine atmosphere (<0.5 ppb). Experimental conditions are reported in Table 2.S1.

2.S1.1 Caltech dual 24 m^3 Teflon Environmental Chambers (CTEC)

Experiments in the CTEC were performed to examine the identity, abundance, and kinetics of molecular products in secondary organic aerosol (SOA) formed from the O_3- and OH-initiated oxidation of β-pinene. Prior to each experiment, the chamber was flushed with dry, purified air for 24 h such that the particle number and volume concentrations were less than 10 cm^{-3} and 0.01 μm^3 cm^{-3}, respectively. β-Pinene (~120 ppb) was added to the chamber by passing dry, purified air at 5 L min^{-1} through a glass cylinder, heated to 50 °C in a water bath, containing a volumetric injection of liquid β-pinene (20 μL, ≥99%, Sigma-Aldrich) for 30 min. Polydisperse seed aerosol (~70 μm^3 cm^{-3}, $\overline{D}_p$ ≈ 95 nm) was generated via atomization of a dilute (0.06 M) aqueous solution of $(NH_4)_2SO_4$ (Macron Fine Chemicals), followed by diffusive drying and neutralization. In select experiments, seed aerosol was produced from dilute aqueous solutions of $(NH_4)_2SO_4$ (0.02 M) and *cis*-pinic acid (Sigma-Aldrich) in 1:1 (~120 μm^3 cm^{-3}, $\overline{D}_p$ ≈ 130 nm) and 2:1 (~140 μm^3 cm^{-3}, $\overline{D}_p$ ≈ 120 nm) mass ratios.

For ozonolysis experiments, O_3 (~200 ppb) was produced via photolysis of O_2 by flowing dry, purified air at 5 L min^{-1} through a custom-built UV O_3 generator for ~40 min. Ozonolysis experiments were conducted in the absence of an OH scavenger, resulting in an initial OH molar yield of 28–44%.[34,55] For photooxidation experiments, H_2O_2 provided the source of OH on photolysis under broadband UV

irradiation (blacklight spectrum centered at 350 nm). H_2O_2 (280 μL, 50% w/w in H_2O, Sigma-Aldrich) was introduced into the chamber from a glass bulb, heated to 40 °C in a water bath, over a 1-h period with a flow of dry, purified air at 5 L min^{-1}, resulting in an initial H_2O_2 mixing ratio of ~4 ppm. At these relatively high mixing ratios of H_2O_2, significant levels of HO_2 are produced via the OH + H_2O_2 reaction, which is favored at the slow chamber photolysis rate of H_2O_2. The steady-state concentrations of OH and HO_2 in these experiments were ~2 × 10^6 and ~1 × 10^{10} molecules cm^{-3}, respectively, as determined in a previous study.[50] The duration of both ozonolysis and photooxidation experiments was ~4 h. Under these conditions, ~70% of the injected β-pinene was consumed in each experiment.

2.S1.2 Caltech Photooxidation Flow Tube (CPOT)

Due to its steady-state operating conditions, the CPOT was utilized to collect sufficient quantities of β-pinene SOA mass for detailed molecular-level composition and structural analysis by offline mass spectrometric and chromatographic techniques. An in-depth description of the CPOT and its standard operating protocol is presented elsewhere.[54] Briefly, the CPOT consists of two 1.2 m × 17 cm i.d. cylindrical quartz tubes, surrounded by an external water jacket and flanged together with clamps and chemically resistant O-rings. Reactants are thoroughly mixed at the inlet to the reactor in a stainless steel static mixer prior to passage through a conical diffuser that serves to expand the mixed flow to the diameter of the cylindrical section while maintaining an idealized laminar profile. A transition cone at the end of the reactor concentrates gas/particle-phase products into a common sampling line that can be split among multiple instruments. Samples extracted at the end of the reactor thus represent so-called cup-mixed averages of the entire reactor cross section. The total flow rate through the CPOT is 12.5 L min^{-1}, giving rise to an average residence time of 3.5 min. The Reynolds number (*Re*) in the cylindrical section of the reactor at this flow rate is ~125, indicating laminar flow (*Re* < 2100).

β-Pinene was introduced into the CPOT by passing dry, purified air at 500 mL min^{-1} through a glass cylinder into which liquid β-pinene (≥99%, Sigma-Aldrich) was continuously injected from a gas-tight volumetric syringe at 0.702 μL h^{-1} using a single syringe infusion pump (11 Plus, Harvard Apparatus), resulting in a steady-state β-pinene mixing ratio of ~150 ppb. Polydisperse seed aerosol (~75 μm^3 cm^{-3}, $\overline{D}_p \approx 85$ nm) was generated via continuous atomization of a dilute (0.01 M) aqueous solution of $(NH_4)_2SO_4$ (Macron Fine Chemicals), followed by diffusive drying and neutralization. A steady-state mixing ratio of O_3 of ~1 ppm was produced via photolysis of O_2 by flowing dry, purified air at 100 mL min^{-1} through a custom-built UV O_3 generator. Ozonolysis experiments were carried out both in the presence and absence of scavengers for OH and stabilized Criegee intermediates (SCIs). Cyclohexane (≥99%, Fisher Scientific) was employed as an OH scavenger (Figure 2.2), while ultra-pure water (18 MΩ, <3 ppb TOC, Millipore Milli-Q) and formic acid (98%, Fluka) were utilized as SCI scavengers (Figure 2.S1). For experiments featuring either cyclohexane or formic acid, steady-state mixing ratios of ~25 and 15 ppm, respectively, were achieved by passing a flow of dry, purified air at 500 mL min^{-1} over the surface of a reservoir of the liquid reagent (i.e., a Stefan tube).[56] For experiments performed under humid conditions, dry, purified air at 15 L min^{-1} was bubbled through a water reservoir to produce a steady-state water vapor mixing ratio in the CPOT of 1% (i.e., 43% RH).

Given recommended k_{OH} values for cyclohexane[57] and β-pinene[58] of 7.2×10^{-12} and 7.89×10^{-11} cm^3 molecules^{-1} s^{-1}, respectively, the OH scavenging efficiency of the added cyclohexane was 93.5%. As rate coefficients for bimolecular reactions of the C_9 β-pinene SCIs are unknown, an estimated $k_{SCI+HCOOH}$ value of 1.7×10^{-12} cm^3 molecules^{-1} s^{-1} for α-pinene[32] was adopted as a surrogate for reaction with both formic acid and the carbonyls/organic acids formed from β-pinene ozonolysis, given that reactions of SCIs with organic acids are far more rapid than reactions with carbonyls.[59] Likewise, k_{SCI+H_2O} and $k_{SCI+(H_2O)_2}$ values of 4.0×10^{-17} and 7.0×10^{-13}

cm^3 molecules^{-1} s^{-1}, respectively, predicted for $(CH_3)_2COO$[60] were adopted for reaction of the C$_9$ β-pinene SCIs with water and the water dimer. Accordingly, assuming complete conversion of β-pinene to reactive carbonyls/organic acids (should clearly be lower) and a water dimer concentration equal to 0.06% that of the monomer,[61] the minimum SCI scavenging efficiencies of the added formic acid and water vapor were 99.1 and 94.5%, respectively.

2.S2 Gas-Phase Measurements

β-Pinene mixing ratios were quantified with an Agilent 6890N gas chromatograph equipped with a flame ionization detector (GC/FID) and operated with an Agilent HP-5 column (30 m × 0.32 mm, 0.25 µm). The GC/FID was calibrated with a commercial β-pinene standard (≥99%, Sigma-Aldrich) over a mixing ratio range from 100 to 200 ppb using a gas-tight volumetric syringe and a mass-controlled dilution flow of N$_2$ into a 100 L Teflon bag. The GC/FID was also calibrated with ppm-level bags (10–20 ppm) prepared via an analogous method and cross-calibrated using Fourier transform infrared spectroscopy (FT-IR) with tabulated absorption cross sections for β-pinene.[65] O$_3$ and NO$_x$ mixing ratios were quantified by a Horiba APOA-360 O$_3$ absorption monitor and a Teledyne T200 NO$_x$ monitor, respectively. The detection limits for O$_3$, NO, and NO$_2$ are 0.5, 0.4, and 0.4 ppb, respectively. Temperature and RH were monitored in the CTEC with a Vaisala HMM211 probe and in the CPOT with an Omega RH-USB sensor.

2.S3 Particle-Phase Measurements

2.S3.1 Scanning Mobility Particle Sizer (SMPS)

Aerosol size distributions and number concentrations for D$_p$ between ~15 and 800 nm were measured with a custom-built scanning mobility particle sizer (SMPS) consisting of a TSI 3081 differential mobility analyzer (DMA) coupled to a TSI 3010 condensation particle counter (CPC). The DMA is operated in a closed-system configuration with a recirculating sheath and excess flow of 2.67 L min^{-1} and an aerosol flow of 0.515 L min^{-1}. The column voltage is scanned from 15 to 9850 V

over a 4-min interval. A more detailed overview of the SMPS operation is provided elsewhere.[53] For β-pinene SOA formation experiments performed in this study, the initial $(NH_4)_2SO_4$ seed volume was ~60–80 µm^3 cm^{-3}, with $\overline{D}_p$ of ~80–100 nm and a size distribution spanning from ~20 to 600 nm. As a result of particle growth driven by gas/particle-phase chemistry and gas-particle partitioning, $\overline{D}_p$ shifted to ~150 nm in steady-state CPOT experiments and to ~230 nm after ~4 h of reaction in CTEC experiments.

Aerosol volume concentrations were calculated assuming homogeneous spherical particles. To enable direct comparison with the concentrations of individual molecular products detected in suspended SOA using offline mass spectrometry, corrections for particle wall loss were neglected. Instead, suspended SOA volume concentrations were derived by applying an exponential fit to the decay of pure $(NH_4)_2SO_4$ seed and subtracting the extrapolated seed volume concentrations from the measured volume concentrations of total suspended aerosol (Figure 2.S2). SOA mass concentrations were calculated assuming an effective density for β-pinene SOA of 1.25 g mL^{-1}.[66–69] Growth profiles of suspended SOA produced from the O$_3$- and OH-initiated oxidation of β-pinene over ~4 h of reaction in the CTEC are shown in Figure 2.S3*A*.

The maximum suspended SOA mass loadings achieved during β-pinene ozonolysis and photooxidation experiments over ~4 h of reaction in the CTEC (Table 2.S1, Exps. 1 and 2) were 35 and 54 µg m^{-3}, respectively (Figure 2.S3*A*). These mass loadings are within a factor of 2 to 10 of ambient organic aerosol (OA) mass concentrations recently measured in forested regions dominated by monoterpene emissions: 1.9–6.8 µg m^{-3} (K-puszta, Hungry; BIOSOL 2006),[70] 4.3 ± 2.3 µg m^{-3} (Sierra Nevada Mountains; BEARPEX 2009),[10] <1–23 µg m^{-3} (SMEAR II Station, Hyytiälä, Finland; HUMPPA-COPEC 2010),[71] 2.9–5.3 µg m^{-3} (SMEAR II Station, Hyytiälä, Finland),[72] and 4.8 µg m^{-3} (Centreville, Alabama; SOAS 2013).[73]

Consequently, the mass loadings of β-pinene SOA generated in this study, and in turn the molecular composition, can be considered relevant to the real atmosphere.

2.S3.2 High-Resolution Time-of-Flight Aerosol Mass Spectrometer (HR-ToF-AMS)

Submicrometer, nonrefractory aerosol chemical composition was quantified with an Aerodyne high-resolution time-of-flight aerosol mass spectrometer (HR-ToF-AMS), providing chemical speciation of sulfate, ammonium, and organic constituents at a frequency of 0.1 Hz. The working principles and modes of operation of the HR-ToF-AMS are described in detail elsewhere.[74] Briefly, submicrometer aerosol (35 nm–1.5 µm) is sampled into the instrument through an aerodynamic lens at a flow rate of ~1.3 mL s^{-1}, producing a collimated particle beam that is directed onto a resistively heated surface where particles undergo vaporization (~600 °C) and electron impact (EI) ionization (70 eV). The resulting ions are detected with a custom-designed Tofwerk HR-ToF-MS configured in V-mode.

Data were analyzed using the SQUIRREL v1.59B and PIKA v1.19B modules for Igor Pro v7.02 (WaveMetrics), and were corrected for gas-phase interferences[75,76] and composition-dependent collection efficiencies.[77] Detection limits for each class of chemical constituents were calculated as three times the standard deviation of blank signals ($3\sigma_{blank}$) measured from high-efficiency particulate arrestance (HEPA) filter samples taken before each experiment. The instrumental ionization efficiency was calibrated using dry, 350 nm ammonium nitrate (NH_4NO_3) particles, generated via atomization of a dilute (0.01 M) aqueous solution of NH_4NO_3 (Macron Fine Chemicals) and size-selected with a DMA. Elemental O:C and H:C ratios, as well as average carbon oxidation states ($\overline{OS}_C$ = 2 O:C − H:C), of β-pinene SOA were calculated using the "Improved-Ambient" elemental analysis method for AMS spectra.[78] After ~4 h of reaction in the CTEC, O:C, H:C, and $\overline{OS}_C$ values for O$_3$-derived β-pinene SOA were found to be 0.38, 1.64, and −0.88, respectively, whereas for OH-derived β-pinene SOA respective values of 0.35, 1.75, and −1.05 were obtained (Figure 2.S3 *B–D*). These results are in good agreement with O:C and H:C

ratios reported in previous laboratory studies for α-pinene SOA generated from ozonolysis (O:C = 0.30–0.43; H:C = 1.47–1.66)[64,78–82] and photooxidation (O:C = 0.36–0.40; H:C = 1.60–1.71).[64,83]

2.S3.3 Particle-Into-Liquid Sampler (PILS)

A custom-modified particle-into-liquid sampler (PILS) was used to collect chamber-generated β-pinene SOA for molecular-level characterization of particle-phase dynamics. A detailed description of the Caltech PILS, which is based on a modification of the original design of Weber et al.,[84] is presented elsewhere.[85] Briefly, chamber aerosol is sampled into the instrument through a 1 μm cut size impactor at a flow rate of 12.5 L min^{-1} and passed successively through individual acid and base denuders and an organic carbon denuder to remove inorganic and organic vapors. A steam flow generated from ultra-pure water (18 MΩ, <3 ppb TOC, Millipore Milli-Q) at 100 °C is adiabatically mixed with the cooler aerosol flow in a condensation chamber, creating a water supersaturation environment in which particles grow sufficiently large (D_p > 1 μm) for collection by inertial impaction onto a quartz plate. Impacted particles are transported to a debubbler by a washing flow (0.15 mL min^{-1}) of ultra-pure water (18 MΩ, <3 ppb TOC, Millipore Milli-Q). The sampled liquid is delivered into vials held on a rotating carousel. Under the current configuration (5-min duty cycle), a total of 48 liquid samples were collected for CTEC experiments with ~4-h duration. Sample vials were stored at −16 °C immediately after collection. The PILS method is particularly suited to the collection of oxygenated, water-soluble organic carbon (WSOC), which typically accounts for a majority of SOA. The overall PILS collection efficiency for β-pinene SOA was estimated to be >85%, based on an empirical correlation of water solubility and the average O:C ratio of the aerosol ensemble derived from HR-ToF-AMS measurement.[29]

2.S3.4 Teflon Filter Samples

β-Pinene SOA from steady-state CPOT and select CTEC experiments was collected on Pall Life Sciences Teflon membrane disc filters (2 μm pore size, 47 mm diameter) at a sampling flow rate of 10 L min^{-1}. Collection periods for CPOT experiments ranged from 15 to 24 h per filter sample, while during CTEC experiments filters were collected for 4 h. A cylindrical diffusion denuder packed with activated charcoal (Sigma-Aldrich) was placed upstream of the sampling apparatus to remove O_3 and gas-phase species, thereby preventing on-filter reactions and further partitioning of compounds from the gas phase to collected particles. The SOA particle loss through the denuder was assumed to be negligible.[86] The mass of SOA collected on each filter was typically 2–3 mg for CPOT experiments and <1 mg for CTEC experiments. Filters were stored at −16 °C immediately after collection.

Filter samples were extracted into 10 mL ultra-pure water (18 MΩ, <3 ppb TOC, Millipore Milli-Q) for 1 h using an orbital shaker at 200 rpm, as extraction via ultrasonic agitation has been shown to cause degradation of α-pinene SOA molecular markers (e.g., *cis*-pinic acid) as well as elevated concentrations of particle-bound peroxides, likely due to formation of OH radicals by acoustic cavitation that react with SOA constituents and combine to form H_2O_2 (49).[87] To account for variations in filter collection and extraction efficiency, the total organic carbon (TOC) content of filter extracts was quantified using an OI-Analytical Aurora 1030W TOC Analyzer. The total carbon (TC) method was employed, wherein all carbon-containing species (i.e., organic and inorganic) are oxidized to CO_2 by sodium persulfate and phosphoric acid at 100 °C and then detected by nondispersive IR spectroscopy. The TC content of blank filter extracts was used for background subtraction. A detection limit of 0.6 ppmC was calculated from the standard deviation of the TC content of the blank filter extracts ($3\sigma_{blank}$). The method was calibrated using standard solutions of potassium hydrogen phthalate (≥99%, Sigma-Aldrich), and the accuracy of the method was verified to within 5% using solutions of *meso-*

erythritol (≥99%, Sigma-Aldrich) and D-sorbitol (≥98%, Sigma-Aldrich) of known concentration.

2.S3.5 Ultra-Performance Liquid Chromatography/Negative Electrospray Ionization Quadrupole Time-of-Flight Mass Spectrometry [UPLC/(−)ESI-Q-TOF-MS]

β-Pinene SOA filter extracts and PILS samples were analyzed by a Waters ACQUITY ultra-performance liquid chromatography (UPLC) I-Class system coupled to a Xevo G2-S quadrupole time-of-flight mass spectrometer (Q-TOF-MS) equipped with an electrospray ionization (ESI) source and operating at a mass resolution (m/Δm) of 20,000–34,000 and a mass accuracy of ≤5 mDa. An ACQUITY BEH C_{18} column (1.7 μm, 2.1 mm × 50 mm) kept at 30 °C was used to separate SOA molecular constituents. The polar (A) and nonpolar (B) eluents were 0.1% v/v formic acid (98%, Fluka) in ultra-pure water (18 MΩ, <3 ppb TOC, Millipore Milli-Q) and 100% acetonitrile (Optima™ LC/MS, Fisher Scientific), respectively. The 12-min eluent program was: (0–2.0 min) 99% A and 1% B; (2.0–10.0 min) linear gradient to 10% A and 90% B; (10.0–10.2 min) 10% A and 90% B; (10.2–10.5 min) linear gradient to 99% A and 1% B; (10.5–12 min) 99% A and 1% B. The total flow rate was 0.3 mL min^{-1} and the injection volume was 10 μL. The sample temperature was 4 °C. Optimized ESI conditions were: 2.0 kV capillary voltage, 40 V sampling cone, 80 V source offset, 120 °C source temperature, 400 °C desolvation temperature, 30 L h^{-1} cone gas flow, and 650 L h^{-1} desolvation gas flow.

Negative (−) ion mass spectra were acquired from *m/z* 40 to 1000, following calibration using sodium formate clusters ($[Na_x(HCOO)_{x+1}]^-$) prepared from formic acid (98%, Fluka) and sodium hydroxide (50% w/w in H_2O, Fisher Scientific). All analytes were detected as pseudomolecular [M−H]$^-$ ions, generated via deprotonation of parent molecules during (−)ESI. The calibrated mass axis was locked to the [M−H]$^-$ ion of a lock spray of leucine enkephalin (≥95%, AnaSpec) at *m/z* 554.2615. MS/MS spectra were collected in tandem with MS measurements (50% duty cycle) via collision-induced dissociation (CID; Ar collision gas) of parent

ions, quadrupole-selected with an isolation width of 3 Da during specified retention time (RT) ranges, using a collision energy ramping program (15−50 V). Instrumental stability (i.e., chromatographic and mass spectral reproducibility) was verified to within 3% using a standard solution of adipic acid (99%, Sigma-Aldrich) and *cis*-pinonic acid (98%, Sigma-Aldrich) run periodically (one standard every 10 samples) during routine analysis. Data were acquired and processed using MassLynx v4.1 software. Molecular formulas ($C_xH_yO_z$) of parent and fragment ions in MS and MS/MS spectra were assigned with mass tolerances of <7 ppm and supported by the associated ^{13}C isotope distributions.

2.S3.6 Hydrogen/Deuterium Exchange (HDX) UPLC/(−)ESI-Q-TOF-MS

β-Pinene SOA filters from steady-state CPOT experiments were extracted into 10 mL D_2O (99.9 atom % D, Sigma-Aldrich) for 1 h with an orbital shaker at 200 rpm and analyzed via UPLC/(−)ESI-Q-TOF-MS using 0.1% v/v formic acid (98%, Fluka) in D_2O as the polar eluent. This approach facilitated deuterium substitution (H→D) of labile hydrogens in the SOA constituents while preserving chromatographic separation, enabling quantification of the number of exchangeable hydrogens in the structures of the identified monomers and dimers based on systematic shifts in *m/z* (Table 2.1). The *m/z* of each SOA constituent shifted by one mass unit for every exchangeable hydrogen present in the molecule in addition to the site deprotonated to form the [M−H]$^-$ ion. For most analytes, H/D exchange proceeded to completion (Figure 2.S4*A* and *C*), indicative of structures containing only fairly acidic and easily exchangeable hydrogens (i.e., −OH, −OOH, and −COOH). However, for certain dimeric compounds, *m/z* 355 ($C_{18}H_{28}O_7$; RT 6.24), *m/z* 373 ($C_{18}H_{30}O_8$; RT 5.99), *m/z* 369 ($C_{19}H_{30}O_7$; RT 6.48), *m/z* 353 ($C_{19}H_{30}O_6$; RT 6.15), and *m/z* 355 ($C_{18}H_{28}O_7$; RT 5.27), only partial H/D exchange was observed (Figure 2.S4*B*), suggesting that the structures of these dimers contain moderately acidic hydrogens, such as α hydrogens adjacent to carbonyls. As pK_a values for aldehyde α hydrogens are typically comparable to those of alcohols (~17) whereas pK_a values of ketone α hydrogens are generally much higher (~20),[88] aldehyde functionalities are assumed to be

responsible for the partial H/D exchange exhibited by the specified dimers. Interestingly, partial H/D exchange of the α hydrogens of β-dicarbonyls, which are significantly more acidic ($pK_a \approx 9-14$) than those of aldehydes,[88] was recently observed via ^{1}H NMR spectroscopy,[89] providing indirect support for the partial H/D exchange hypothesized for aldehyde α hydrogens.

2.S3.7 Iodometry-Assisted UPLC/(–)ESI-Q-TOF-MS

Conventional iodometry was coupled to UPLC/(–)ESI-Q-TOF-MS, as described by Zhao et al.,[30] to identify organic peroxides [i.e., hydroperoxides (ROOH) and organic peroxides (ROOR)] at the molecular level in β-pinene SOA. In the presence of an acid catalyst, I$^-$ selectively reduces organic peroxides to the corresponding alcohol, liberating I$_2$ and subsequently forming I$_3^-$ in solutions of excess I$^-$:

$$R_1OOR_2 + 2\,I^- + 2\,H^+ \longrightarrow R_1OH + R_2OH + I_2$$
$$I_2 + I^- \longrightarrow I_3^-$$
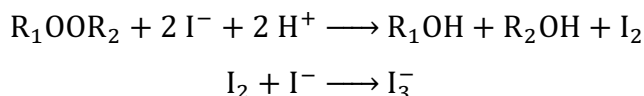
As the iodometric method has been shown to have negligible impact on species that do not possess peroxide functionalities, comparison of treated and control samples via UPLC/(–)ESI-Q-TOF-MS enables identification of peroxide-containing species based on the disappearance of signals corresponding to detected molecular constituents.

Samples were prepared by acidifying an SOA filter extract to pH 2 with formic acid (50% w/w in H$_2$O, Fluka). To an aliquot of the acidified extract, a concentrated aqueous solution of potassium iodide (KI, 99%, Sigma-Aldrich), made fresh daily and purged with N$_2$, was added such that the concentration of I$^-$ was 60 mM. As a control, a second aliquot was diluted to the final volume of the treated sample with ultra-pure water (18 MΩ, <3 ppb TOC, Millipore Milli-Q). In this way, differences between treated and control samples reflected only changes induced by iodometry and not differences due to dilution or acidification. Immediately following dilution

or KI addition, the treated and control samples were purged with N_2 and placed in air-tight vials in the dark for 7 h prior to analysis by UPLC/($-$)ESI-Q-TOF-MS to ensure completion of the iodometric reaction. The iodometric method was validated against a series of H_2O_2 (50% w/w in H_2O, Sigma-Aldrich) solutions of known concentration.

The abundances of the 23 identified dimers (Table 2.1) did not change significantly (<15%) in response to iodometry (Figure 2.S5), indicating that these compounds do not contain ROOH or ROOR functionalities. Although somewhat surprising, given that organic peroxides have been found to account for a significant mass fraction (12–85%) of SOA derived from monoterpene oxidation,[22,90–93] the absence of (hydro)peroxide groups in the dimer structures is not unreasonable. We recently demonstrated using iodometry-assisted UPLC/($-$)ESI-Q-TOF-MS that dimers detected in α-pinene SOA also lack ROOH and ROOR moieties, despite conventional spectrophotometric iodometry suggesting that ~15% of the α-pinene SOA mass is attributable to organic peroxides.[30]

These findings are consistent with the decomposition of particle-bound organic peroxides, likely to smaller peroxides that cannot be detected by UPLC/($-$)ESI-Q-TOF-MS but can contribute to the total peroxide content quantified via spectrophotometric iodometry. The labile nature of organic peroxides in biogenic SOA has been demonstrated in a number of recent studies,[93–95] with reported decomposition timescales on the order of a few hours. Formation of OH radicals[96] and H_2O_2[97,98] from aqueous-phase monoterpene SOA (e.g., filter extracts and PILS samples) has also been observed, indicative of peroxide decomposition or hydrolysis. In addition, decomposition of multifunctional organic peroxides (e.g., peroxyhemiacetals and diacyl peroxides) can lead to nonperoxide species, including carboxylic acids, aldehydes, alcohols, and esters.[13,22]

2.S4   Master Chemical Mechanism (MCM) Simulation

The Master Chemical Mechanism version 3.2 (MCMv3.2)[51,90] was used to predict the time-dependent concentrations of OH, HO$_2$, and RO$_2$ during β-pinene ozonolysis in the CTEC, as well as the fractions of β-pinene that react with O$_3$ vs. OH. The initial conditions for the simulations were those from Exp. 1 in Table 2.S1 (i.e., 123 ppb β-pinene, 200 ppb O$_3$, zero NO$_x$, 295 K, 1 atm, and 5% RH). Three variations of the gas-phase β-pinene ozonolysis mechanism were implemented: (i) MCMv3.2 without modification, (ii) MCMv3.2 revised with the theoretical first-generation ozonolysis branching ratios from Figure 6 in Nguyen, Peeters, and Vereecken[34] (MCMv3.2 + NPV), and (iii) the mechanism from (ii) further modified with the theoretical β-pinene photooxidation mechanism of Vereecken and Peeters[36] (MCMv3.2 + NPV + VP). Key areas in which these theoretical mechanisms, based on quantum chemical calculations and statistical kinetic analysis, deviate from the oxidation schemes currently incorporated in MCMv3.2 are discussed in detail in the corresponding references.

The observed first-order decay of β-pinene is well replicated by each of the three ozonolysis mechanisms; the two modified mechanisms produce slightly better agreement (Figure 2.S6*A*). The simulated concentration profiles of OH and RO$_2$ appear to be fairly insensitive to the gas-phase ozonolysis mechanism employed, yielding concentrations of ~1.5×10^5 and ~2.0×10^{10} molecules cm^{-3}, respectively, after 4 h of reaction (Figure 2.S6*B*). Conversely, HO$_2$ profiles differ moderately between the three oxidation schemes, with concentrations after 4 h ranging from ~1.5 to 3.0×10^7 molecules cm^{-3}. Based on these simulations, OH-initiated oxidation accounts for ~20% of the β-pinene consumption over a 4-h ozonolysis experiment. Assuming typical $k_{RO_2+RO_2}$ and $k_{RO_2+HO_2}$ values of 6.7×10^{-13} and 2.09×10^{-11} cm^3 molecules^{-1} s^{-1}, respectively,[49] the simulated RO$_2$ and HO$_2$ concentration profiles suggest that RO$_2$ + HO$_2$ chemistry is of minor significance to the formation of molecular products in SOA derived from β-pinene ozonolysis in the CTEC.

2.S5   Synthesis of ^{13}C-β-Pinene

Unless otherwise stated, reactions were performed in flame-dried glassware under an Ar or N$_2$ atmosphere using dry, deoxygenated solvents. Solvents were dried by passage through an activated alumina column under Ar. Chemicals and reagents were purchased from Sigma-Aldrich and used as received. Reaction temperatures were controlled by an IKAmag temperature modulator. Thin-layer chromatography (TLC) was performed using E. Merck silica gel 60 F254 precoated plates (0.25 mm) and visualized by UV fluorescence quenching, potassium permanganate staining, or *p*-anisaldehyde staining. Silia*Flash* P60 Academic Silica gel (particle size 0.040–0.063 mm) was used for flash column chromatography. ^{1}H NMR spectra were recorded on a Bruker AVANCE HD 400 MHz NMR spectrometer and are reported in terms of chemical shift relative to residual CHCl$_3$ (δ 7.26 ppm). Data for ^{1}H NMR are reported as follows: chemical shift (δ ppm) (multiplicity, coupling constant, integration). Abbreviations are used as follows: s = singlet, d = doublet, t = triplet, m = multiplet. Reported spectra include minor solvent impurities of ether (δ 3.48, 1.21) and petroleum ether (δ 1.26, 0.86), which do not impact product assignments. High-resolution mass spectra were obtained using a Waters GCT Premier TOF-MS operating in EI ionization mode at a mass resolution (m/Δm) of 7000, interfaced with an Agilent 6890 GC with electronic pressure control and a split-splitless inlet. The GC was equipped with a Phenomenex ZB-5MS column (30 m × 0.25 mm, 0.25 μm) and operated in split mode at a split ratio of 240:1. The TOF-MS was calibrated from *m/z* 40 to 614 using perfluorotributylamine (PFTBA, Sigma-Aldrich) as a mass reference compound. The calibrated mass axis was locked to the (CF$_2$)$_3$CF$_3$$^+$ ion at *m/z* 218.985.

^{13}C-β-Pinene. Triphenylphosphine (4.59 g, 17.5 mmol) was added to a solution of ^{13}C-iodomethane (2.5 g, 17.5 mmol) in benzene (15 mL) and the reaction was stirred for 72 h. The reaction was filtered, washing with benzene, and the filtrate was dried under reduced pressure to provide methyl-^{13}C-triphenylphosphonium iodide in quantitative yield as a white solid. *n*-Butyllithium (2.5 M, 1.7 mL, 4.33 mmol) was

added to a suspension of methyl-^{13}C-triphenylphosphonium iodide (1.86 g, 4.63 mmol) in THF (8 mL) at 0 °C and was stirred for 30 min. Nopinone (0.400 g, 2.89 mmol) was added and the reaction was heated under reflux for 18 h. The reaction was allowed to cool to room temperature (25 °C), diluted with petroleum ether, filtered through celite, and concentrated under reduced pressure. The crude reaction mixture was purified via flash column chromatography, eluting with petroleum ether to provide 0.300 g of ^{13}C-β-pinene as a mixture (1:1) with petroleum ether (Scheme 2.1). Note that due to the volatile nature of the product, the pure material was not fully concentrated. However, the residual petroleum ether affects neither product assignment nor subsequent experiments. ^{1}H NMR (400 MHz, CDCl$_3$) δ 4.85 (d, J = 20.2 Hz, 1 H), 4.33 (d, J = 22.0 Hz, 1 H), 2.66–2.39 (m, 2 H), 2.38–2.15 (m, 2 H), 1.97 (tt, J = 5.8, 3.0 Hz, 1 H), 1.94–1.77 (m, 2 H), 1.42 (d, J = 9.8 Hz, 1 H), 1.24 (s, 3 H), 0.72 (s, 3 H) (Figure 2.S7). High-resolution mass spectra indicate ^{13}C incorporation (Figure 2.S8).

2.S6 Dimer Esters from Synergistic O$_3$ + OH Oxidation

2.S6.1 Structure Elucidation

As discussed in the main text, MS/MS spectra of the ^{13}C-labeled dimers and their ^{12}C isotopologues revealed distinct OH-derived (^{13}C-mass-shifted) and O$_3$-derived (unshifted) fragmentation patterns (Table 2.S3). Detailed analysis of these spectra, constrained by HDX and iodometry-assisted UPLC/(−)ESI-Q-TOF-MS, particle-phase kinetic analysis, and the extant mechanisms of β-pinene ozonolysis and photooxidation, afforded insight into the structures of these dimeric compounds.

The O$_3$-derived fragmentation patterns in the MS/MS spectra (Figure 2.3 and Table 2.S3) of the dimer esters (Table 2.1, type 1) are comparable to those observed for three abundant terpenoic acids identified in β-pinene SOA: m/z 185 (C$_9$H$_{14}$O$_4$; RT 4.33), m/z 171 (C$_8$H$_{12}$O$_4$; RT 4.06), and m/z 189 (C$_8$H$_{14}$O$_5$; RT 3.32). Based on comparison with LC/(−)ESI-MS data reported in the literature,[7,39] these SOA products, and in turn the O$_3$-derived dimer ester precursors, are assigned to three well-

characterized dicarboxylic acids: *cis*-pinic acid ($C_9H_{14}O_4$), *cis*-norpinic acid ($C_8H_{12}O_4$), and diaterpenylic acid ($C_8H_{14}O_5$). In the case of the compound at *m/z* 185, comparison of its chromatographic and mass spectrometric behavior with that of a commercial *cis*-pinic acid standard (Sigma-Aldrich) corroborated the assignment. The extracted ion chromatograms, MS spectra, MS/MS spectra, and proposed fragmentation pathways for the three dicarboxylic acids are presented in Figure 2.S9. It is noted that there are differences between the relative abundances of the MS/MS fragment ions in Figure 2.S9 and those of the O_3-derived fragment ions of the dimer esters shown in Figure 2.3. This feature can be rationalized by a difference in internal energy between the first- and second-generation dicarboxylic acid ions. Namely, the dicarboxylic acid ions produced via CID of dimer ester ions will have higher internal energy and undergo more extensive fragmentation on CID than those formed directly from (−)ESI. The strong correlation between the time-resolved particle-phase abundances of the dimer esters and their presumed dicarboxylic acid building blocks (Figure 2.4 *A–C*) further substantiates these structural assignments.

The OH-derived monomeric units are characterized by the ionic $[M−H]^-$ formulas $[C_{10}H_{15,17}O_{2-7}]^-$, indicative of OH addition to β-pinene ($C_{10}H_{16}$) followed by varying degrees of O_2 incorporation, isomerization, and bimolecular radical chemistry. As iodometry-assisted UPLC/(−)ESI-Q-TOF-MS demonstrated that the dimer esters do not contain ROOH functionalities, formation of OH-derived building blocks is assumed not to proceed via either RO_2 autoxidation (i.e., regenerative RO_2 formation following intramolecular H-shifts)[23,99] or HO_2-mediated reaction channels. Simulations of HO_2 and RO_2 concentrations during β-pinene ozonolysis in the CTEC also suggest that $RO_2 + HO_2$ chemistry is not significant in dimer ester production (*SI Appendix*, 2.S4). Tentative molecular structures for the OH-derived monomers, consistent with observed fragmentation patterns, are formulated based on the theoretical β-pinene photooxidation mechanism of Vereecken and Peeters,[36] which derives from quantum chemical calculations, statistical kinetics, and structure-activity relationships (SARs). A key feature of this mechanism is the predicted

accessibility of ring closure reactions of unsaturated RO and RO_2 radicals, which bring simulated nopinone and acetone yields in line with experimental data. Suggested OH-derived monomeric structures are constrained by the total number of exchangeable hydrogens in the structures of the dimer esters, quantified using HDX UPLC/(−)ESI-Q-TOF-MS, together with the known structures of the inferred O_3-derived dicarboxylic acids. Fragmentation pathways for the dimer esters with proposed OH-derived precursors (Table 2.S4) are presented in Figure 2.S10. These pathways consist of established charge-retention and charge-migration fragmentations (e.g., remote hydrogen rearrangements and pericyclic reactions), and are based on fundamental organic reactivity and ion stability principles.[40,41] While at least two structural isomers are possible for each proposed dimer ester, depending on the position of the ester linkage, only the structure and fragmentations of the most likely isomer are considered.

2.S6.2 Heterogeneous Formation Mechanism

The formation of the major dimer ester at *m/z* 337 ($C_{19}H_{30}O_5$) in β-pinene photooxidation experiments carried out with *cis*-pinic acid and $(NH_4)_2SO_4$ seed (Figure 2.5) corroborates the indirect MS/MS (Figure 2.3*A*) and kinetic (Figure 2.4*A*) evidence for heterogeneous formation via reactive uptake of a gas-phase, OH-derived monomer/intermediate by particle-bound *cis*-pinic acid. A heterogeneous rather than purely particle-phase mechanism is also supported by the absence of stable products corresponding to the OH-derived dimer ester precursors [e.g., *m/z* 169 ($C_{10}H_{18}O_2$) for the dimer ester at *m/z* 337 (Table 2.S3)] in SOA generated from β-pinene ozonolysis. The details of the mechanism forming the ester linkage are presently unclear. However, the observed increase in the abundances of the dimer esters (11–46%) under humid conditions (43% RH) (Figure 2.S1) argues against formation via conventional esterification (i.e., carboxylic acid + alcohol). These findings are in line with a recent theoretical study demonstrating that particle-phase esterification of α-pinene ozonolysis products is thermodynamically unfavorable.[100]

To rule out the possibility of dimer formation through accretion of condensed monomers, either on the filter or during the extraction process, β-pinene SOA from OH-initiated oxidation in the CTEC with pure $(NH_4)_2SO_4$ seed was collected on a Teflon filter uniformly coated with ~0.5 mg of *cis*-pinic acid (Sigma-Aldrich). A clean Teflon filter was also collected in parallel as a control, such that the mass of SOA collected on each filter was approximately equivalent. The filters were stored at room temperature (25 °C) for 48 h following collection, then extracted into 10 mL ultra-pure water (18 MΩ, <3 ppb TOC, Millipore Milli-Q) as described in *SI Appendix*, 2.S3.4. Filter extracts were left at room temperature for 72 h prior to analysis by UPLC/(−)ESI-Q-TOF-MS. As shown in Figure 2.S11, the dimer ester at *m/z* 337 was not observed in either SOA sample, demonstrating that the dimer esters are not artifacts of on-filter or aqueous-phase reactions.

The β-pinene photooxidation experiments performed with *cis*-pinic acid and $(NH_4)_2SO_4$ seed suggest that the hypothesized mechanism of heterogeneous dimer formation requires a sufficient particle-phase concentration of semivolatile dicarboxylic acids, which may be limited in the ambient atmosphere by inefficient gas-particle partitioning. However, recent field measurements of gas-particle partitioning of tracers for biogenic oxidation indicate that the fraction of *cis*-pinic acid residing in the particle phase (F_p) in forested locations is 0.3–0.4 during the day and 0.6–0.8 at night.[73,101] As the saturation mass concentrations (C*) of the dicarboxylic acids identified as dimer ester precursors (*cis*-pinic acid, *cis*-norpinic acid, and diaterpenylic acid) are all on the order of 10 μg m^{-3},[35] the findings for *cis*-pinic acid imply that pinene-derived dicarboxylic acids undergo efficient absorptive equilibrium gas-particle partitioning under ambient conditions and should thus be present in the particle phase in sufficient quantities to facilitate heterogeneous dimer formation.

2.S7 Quantification of SOA Molecular Constituents

Mass concentrations of individual organic compounds in chamber-generated β-pinene SOA collected by PILS and analyzed off-line by UPLC/(−)ESI-Q-TOF-MS were calculated from the following expression:

$$C = \frac{Q_l \cdot \rho_l \cdot DF \cdot R}{Q_s \cdot CE_{PILS} \cdot IE} \tag{2.S1}$$

where C is the particle-phase mass concentration of the compound ($\mu g\ m^{-3}$), Q_s is the aerosol sampling flow rate (12.5 L min^{-1}), Q_l is the rate of the washing flow (0.15 mL min^{-1}), DF is the dilution factor that accounts for water vapor condensation on the PILS impaction plate (assumed to be 1.1),[85] ρ_l is the density of the collected PILS sample (assumed to be the density of the washing flow, 1.0 g mL^{-1}), CE_{PILS} is the overall PILS collection efficiency for β-pinene SOA (estimated to be 0.85),[29] R is the UPLC/(−)ESI-Q-TOF-MS response (i.e., chromatographic peak area) for the compound, and IE is the compound-specific (−)ESI efficiency (ppb^{-1}). From comparison of the resulting particle-phase mass concentrations to the SMPS-derived suspended SOA mass loading, mass fractions of identified molecular products in β-pinene SOA were determined.

2.S7.1 Determination of (−)ESI Efficiency

In the case of small molecules (<1000 Da), such as those analyzed in the current work, the ESI process is described by the ion evaporation model (IEM).[102] Prior separation of analytes from the complex SOA matrix via UPLC precludes potential ion-source artifacts (e.g., signal suppression and noncovalent clustering), ensuring the quantitative nature of the method. As authentic standards were not available, the (−)ESI efficiencies of the three similarly structured dicarboxylic acids implicated as dimer ester precursors (*cis*-pinic acid, *cis*-norpinic acid, and diaterpenylic acid) were quantified using commercially available *cis*-pinic acid (Sigma-Aldrich) as a surrogate. A 5-point calibration curve ($n = 3$) was generated from aqueous solutions

of *cis*-pinic acid spanning a concentration range from 50 to 1000 ng mL^{-1} (ppb); a linear response (R^2 > 0.999) was observed. The detection limit for *cis*-pinic acid, calculated as three times the standard deviation of the blank ($3\sigma_{\text{blank}}$), was found to be 1.2 ppb. The concentrations of the dicarboxylic acids measured in the PILS samples fell well above this threshold, and well within the calibrated linear range of the instrument.

Due to a lack of authentic standards, (−)ESI efficiencies of oligomers in monoterpene SOA are typically quantified using commercially available terpenoic acids as surrogates (e.g., *cis*-pinonic acid and *cis*-pinic acid).[10–12,64,103] The same approach was applied here, using the measured (−)ESI efficiency of *cis*-pinic acid as a proxy for those of the dimeric compounds detected in β-pinene SOA formed from O$_3$-initiated oxidation. The (−)ESI efficiencies of the identified dimers were also estimated theoretically via a linear model (R^2 = 0.83) developed by Kruve et al.[104]:

$$\log RIE = (1.04 \pm 0.34) + (2.23 \pm 0.34) \cdot \alpha - (0.51 \pm 0.04) \cdot WAPS \cdot 10^5$$

$$(2.S2)$$

where log*RIE* is the (−)ESI efficiency relative to benzoic acid on a logarithmic scale (i.e., log*RIE*$_{\text{benzoic acid}}$ = 0), α is the degree of ionization in solution (a function of analyte pK_a and solution pH), and *WAPS* (weighted average positive sigma) is a parameter that quantifies the extent of charge delocalization in anions (i.e., the distribution of charge density across an ionic surface):

$$WAPS = \frac{\int_{\sigma=0}^{\infty} \sigma p(\sigma) \mathrm{d}\sigma}{A \int_{\sigma=0}^{\infty} p(\sigma) \mathrm{d}\sigma}$$

$$(2.S3)$$

where σ is the polarization charge density on the ion surface (e Å^{-2}), $p(\sigma)$ is the probability function of σ, and A is the surface area of the anion (Å^2). The dependence of log*RIE* on α and *WAPS* is in good agreement with current understanding of the

(−)ESI process, as compounds that are more extensively dissociated in the LC mobile phase (higher α) will yield a higher concentration of anions in ESI droplets, while anions with more delocalized charge (lower *WAPS*) will interact more weakly with other molecules/ions in ESI droplets, exhibit lower solvation energy and a lower tendency for ion pairing (i.e., less attraction to polar solvent molecules as well as cations in the droplet interior), and thus partition more readily to and evaporate more easily from ESI droplet surfaces.[104]

The conductor-like screening model for real solvents (COSMO-RS)[105,106] implemented in the Amsterdam Density Functional (ADF 2017.108) molecular modeling suite[107] was used to generate the charge density distributions (i.e., σ profiles) required to derive *WAPS* parameters, as well as calculate analyte pK_a values. Gas-phase molecular and anionic geometries were optimized at the TZP level using the Becke-Perdew (BP) generalized-gradient approximation (GGA) exchange-correlation functional and the scalar zeroth-order regular approximation (ZORA) relativistic Hamiltonian. Default "ADF combi2005" COSMO-RS parameters, which are optimized for ADF calculations, were employed.[107] Representative σ profiles of the [M–H]$^-$ ions of *cis*-pinic acid and the major dimer ester at *m/z* 337 ($C_{19}H_{30}O_5$) are shown in Figure 2.S12. The computed σ profiles, together with anionic surface areas, were used to evaluate *WAPS* parameters. *WAPS* values above 4.5×10^{-5} have been proposed to indicate anions with localized charge.[108]

Aqueous pK_a values for each analyte were calculated from their free energies of dissociation in water (ΔG_{diss}), computed using the COSMO-RS continuum solvation model. Negligible differences in zero-point energy between the neutral and deprotonated forms of each analyte were assumed. Following the approach of Eckert et al. (83), a linear regression of calculated ΔG_{diss} and experimental pK_a values accounted for systematic errors in the method:

$$pK_a = \frac{0.62}{RT\ln(10)}\Delta G_{diss} + 2.10 \qquad (2.S4)$$

Unsurprisingly, the fit parameters in the ADF COSMO-RS implementation (0.62 and 2.10) are quite similar to those reported in Eckert et al.[109] for the continuum model (0.61 and 1.94). To account for the particular acetonitrile-water composition at which each analyte elutes from the LC column (the volume fraction of acetonitrile increases linearly from 12% at RT 3.00 to 62% at RT 7.50), a linear relationship developed by Espinosa et al.[110] was used to estimate analyte pK_a values in acetonitrile-water mixtures ($_s^s pK_a$) of varying composition (0–60% v/v acetonitrile) from the corresponding aqueous pK_a values ($_w^w pK_a$) calculated with COSMO-RS:

$$_s^s pK_a = a_s \, _w^w pK_a + b_s \tag{2.S5}$$

As in the original expression, the IUPAC-recommended notation for pK_a and pH definitions is employed, wherein the solvent in which the properties are measured/calculated and the solvent referred to as the standard state, water (w) or acetonitrile-water (s), are indicated by left-hand superscripts and subscripts, respectively. Both the slope (a_s) and intercept (b_s) are related to differences in specific solvation interactions (e.g., hydrogen bonding) between water and the acetonitrile-water mixtures, and depend on the solute compound class. The intercept (b_s) is also related to differences in solvent basicities and dielectric constants. For specific values of a_s and b_s used in this study, see Equations 2 and 3 and Tables 4 and 5 in the original paper.

The pH of five acetonitrile-water mixtures ranging from 1 to 70% v/v acetonitrile were measured potentiometrically ($n = 3$) using a VWR Scientific 8015 pH meter, calibrated with certified aqueous buffers (pH 4.00 and 7.00, Fisher Scientific). Linear regression of the measured pH values as a function of the acetonitrile volume fraction ($R^2 > 0.995$) enabled calculation of the pH of the LC mobile phase at any point during the 12-min eluent program. The pH values obtained from this approach refer to water as the standard state ($_w^s pH$). To convert from $_w^s pH$ to $_s^s pH$ (i.e., pH values that refer to

the acetonitrile-water mixtures as the standard state), a conversion parameter (δ) derived by Espinosa et al.[110] was applied:

$$_s^s pH = {}_w^s pH + \delta \qquad (2.S6)$$

The δ term includes both the primary medium effect and the difference between the liquid-junction potentials of the electrode system in water and the acetonitrile-water mixtures. Specific values of δ used in this work were calculated from Equation 10 in the original paper. Given the estimated analyte $_s^s pK_a$ and mobile phase $_s^s pH$ values, the degree of ionization of each analyte (α) in the particular acetonitrile-water mobile phase at which it elutes from the LC column was calculated:

$$\alpha = \frac{10^{-_s^s pK_a}}{10^{-_s^s pK_a} + 10^{-_s^s pH}} \qquad (2.S7)$$

RIE values were determined for the five dimer esters with proposed molecular structures (Table 2.S4), as well as for *cis*-pinic acid. For compounds with multiple sites for deprotonation (e.g., *cis*-pinic acid), *RIE* values were derived independently for each possible monoanion and the results were summed to give an aggregate *RIE*. *RIE* values were normalized to that of *cis*-pinic acid, and scaled by the measured *cis*-pinic acid (−)ESI efficiency. In this way, absolute (−)ESI efficiencies for the five dimer esters were ascertained. For the dimers with unknown molecular structures, (−)ESI efficiencies were approximated by those of the dimer esters with the most similar $\overline{OS}_C$ values (Table 2.1).

Due to fundamental differences in the (−)ESI behavior of monomers and oligomers, namely that larger molecules produce anions with more delocalized charge (lower *WAPS*), the theoretical (−)ESI efficiencies of the dimer esters are roughly an order of magnitude higher than that of *cis*-pinic acid (Table 2.S4). These findings suggest that the mass contribution of oligomers to monoterpene SOA is

significantly overestimated in studies that use commercially available terpenoic acids as surrogates to quantify oligomeric (−)ESI efficiencies.[10–12,64,103] Indeed, dimers formed from coupled O_3 and OH oxidation (Table 2.1, types 1–3) are found to account for 25.4% of the total mass of β-pinene SOA formed after ~4 h of ozonolysis in the CTEC (Table 2.S1, Exp. 1) when quantified using the measured (−)ESI efficiency of *cis*-pinic acid, whereas theoretical estimation of the (−)ESI efficiencies of the dimers via the model of Kruve et al.[104] leads to a mass fraction of only 5.9% for dimers produced via concerted O_3 and OH chemistry. The treatment of oligomeric (−)ESI efficiencies in monoterpene SOA formation experiments, and its potential role as a source systematic bias, will be explored in detail in a forthcoming study on the abundance of oligomeric products in SOA derived from the O_3-initiated oxidation of α- and β-pinene.

2.S7.2 Uncertainty Analysis

Uncertainty in the PILS method (δ_{PILS}) arises mainly from variation in the collected liquid volume due to the existence of air bubbles, and has been estimated to be less than ± 11%.[29] Uncertainty associated with the chromatographic and mass spectral reproducibility of the UPLC/(−)ESI-Q-TOF-MS (δ_{UPLC}) was determined to be less than ± 3% by performing replicate injections of a standard solution of adipic acid (99%, Sigma-Aldrich) and *cis*-pinonic acid (98%, Sigma-Aldrich). Uncertainty in the measured (−)ESI efficiency of *cis*-pinic acid ($\delta_{(-)ESI}$) was found to be small, less than ± 1%. An uncertainty of ± 20% is assumed for SMPS-derived suspended SOA mass loadings (δ_{SMPS}).[111] For molecular products in β-pinene SOA quantified using *cis*-pinic acid, propagation of these individual uncertainties yields a total estimated relative uncertainty in the reported SOA mass fractions (δ_{total}) of ± 23%:

$$\delta_{total} = \sqrt{\delta_{PILS}^2 + \delta_{UPLC}^2 + \delta_{(-)ESI}^2 + \delta_{SMPS}^2}$$

$$\delta_{total} = \sqrt{(0.11)^2 + (0.03)^2 + (0.01)^2 + (0.20)^2} = 0.23 \qquad (2.S8)$$

For the mass fractions of dimeric compounds in O_3-derived β-pinene SOA quantified via the model of Kruve et al.,[104] the most considerable contribution to the associated uncertainty arises from the error in the logRIE estimates. The root-mean-square deviation (RMSD) for the model validation set, a measure of the average disagreement between measured and predicted logRIE values, is taken as approximation of this error:

$$\text{RMSD} = \sqrt{\frac{\Sigma(\log RIE_\text{p} - \log RIE_\text{m})^2}{n}} \qquad (2.\text{S9})$$

where logRIE_p and logRIE_m are the predicted and measured (–)ESI efficiencies relative to benzoic acid on a logarithmic scale, respectively, and n is the number of compounds in the model validation set. The stated RMSD for the validation set is 0.48 log units,[104] which translates to an estimated uncertainty in the reported SOA mass fractions of a factor of 3.

2.S8 General Applicability of O_3 + OH Oxidation to Monoterpene SOA Formation

Although specifically revealed in SOA formation from β-pinene, the production of dimers through concerted O_3 and OH oxidation is expected to be broadly applicable to other monoterpenes, most notably α-pinene. While the endocyclic double bond of α-pinene rules out the isotopic labeling approach that was used with β-pinene to directly probe this chemistry, several dimeric compounds with the accurate masses/molecular formulas corresponding to dimers demonstrated to derive from coupled O_3 and OH oxidation of β-pinene (Table 2.1, types 1–3) were measured by PILS + UPLC/(–)ESI-Q-TOF-MS in SOA produced from α-pinene ozonolysis (Table 2.S5); two of the dimers, m/z 337 ($C_{19}H_{30}O_5$) and m/z 369 ($C_{19}H_{30}O_7$), are major peaks in the BPI chromatogram. These dimers were detected at either the same or similar RT (less than ± 0.18 min) to those of their β-pinene counterparts, and with analogous MS/MS spectra. The formation of these dimers was also significantly suppressed (>60%) by introduction of cyclohexane as an OH scavenger. These

findings indirectly confirm that dimer production via synergistic O_3 + OH oxidation is operative in the α-pinene ozonolysis system. However, due to the structural isomerism of α- and β-pinene (i.e., endocyclic vs. exocyclic double bond), the scope of the O_3 + OH reactivity in the α-pinene system is likely underestimated by the limited number of equivalent/identical dimeric compounds formed via ozonolysis of α- and β-pinene reported in Table 2.S5.

2.S9 Figures 2.S1–2.S12
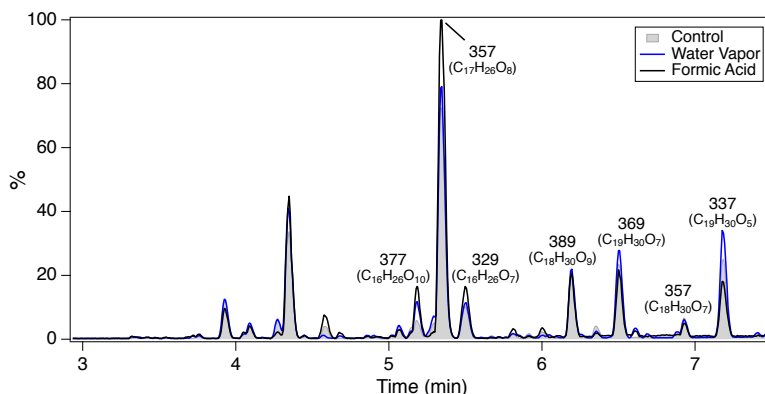
Figure 2.S1. UPLC/(−)ESI-Q-TOF-MS BPI chromatograms of SOA produced from the O_3-initiated oxidation of β-pinene in the CPOT (Table 2.S1, Exps. 7, 9, and 10) in the presence and absence of water vapor and formic acid as SCI scavengers (*SI Appendix*, 2.S1.2). Numbers correspond to nominal *m/z* values of $[M-H]^-$ ions; molecular formulas are given in parentheses. Chromatograms for Control, Water Vapor, and Formic Acid experiments are normalized to the TOC content of the corresponding SOA samples (*SI Appendix*, 2.S3.4) and are reported as averages of replicates ($n = 3$).
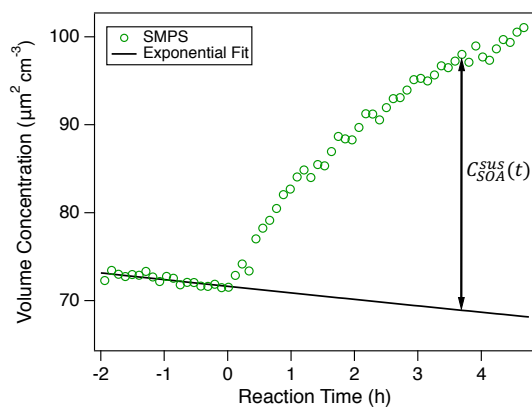
Figure 2.S2. Determination of SMPS-derived suspended SOA volume concentrations, $C_{SOA}^{sus}(t)$. An exponential fit was applied to the decay of pure $(NH_4)_2SO_4$ seed ($t < 0$). The extrapolated seed volume concentrations ($t > 0$) were subtracted from the volume concentrations of total suspended aerosol measured by the SMPS. Data shown are for Exp. 1 in Table 2.S1.
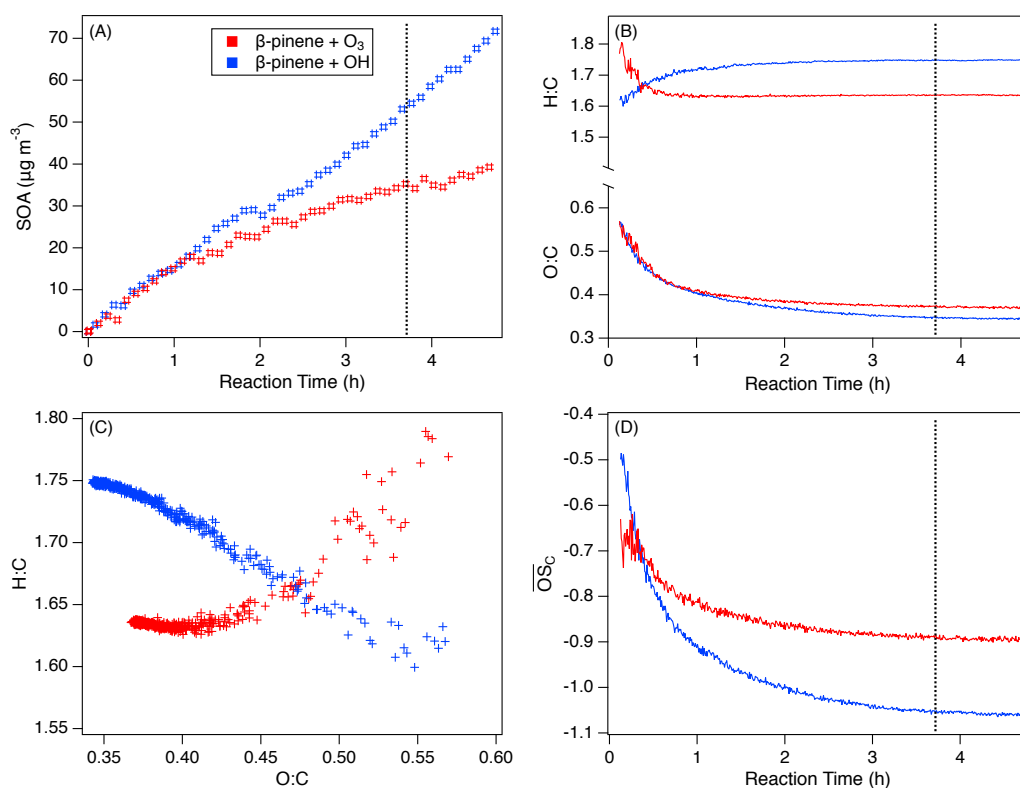
Figure 2.S3. "Bulk" properties of SOA produced from the O_3- and OH-initiated oxidation of β-pinene over ~4 h of reaction in the CTEC (Table 2.S1, Exps. 1 and 2). (*A*) SMPS-derived suspended SOA mass concentrations (*SI Appendix*, 2.S3.1). (*B*) AMS-derived elemental O:C and H:C ratios (*SI Appendix*, 2.S3.2). (*C*) van Krevelen diagram. (*D*) AMS-derived average carbon oxidation states ($\overline{OS}_C = 2\,O{:}C - H{:}C$). Dashed lines denote time point for which BPI chromatograms are presented in Figure 2.1, SOA mass fractions are calculated in Table 2.1, and O:C, H:C, and $\overline{OS}_C$ values are reported in *SI Appendix*, 2.S3.2.
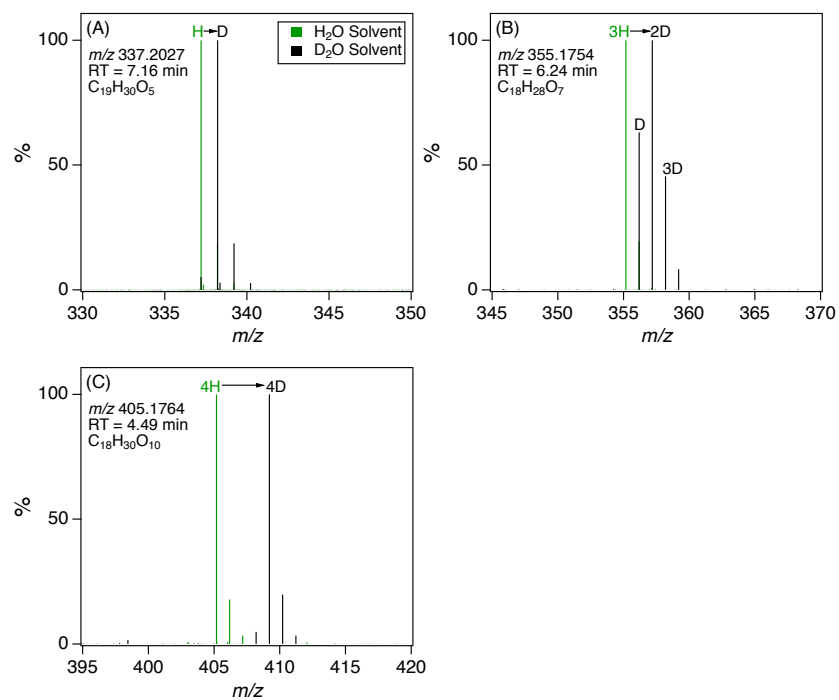
Figure 2.S4. Shift in *m/z* of representative dimers in β-pinene SOA, measured by UPLC/(–)ESI-Q-TOF-MS, due to H/D exchange of labile hydrogens (e.g., –OH, –OOH, and –COOH) when D$_2$O is used in place of H$_2$O as the solvent/polar eluent. The *m/z* shifts by one mass unit for every exchangeable hydrogen present in the molecule in addition to the site deprotonated to form the [M−H]$^-$ ion. The partial H/D exchange exemplified in *B* is attributed to structures containing moderately acidic α hydrogens (*SI Appendix*, 2.S3.6).
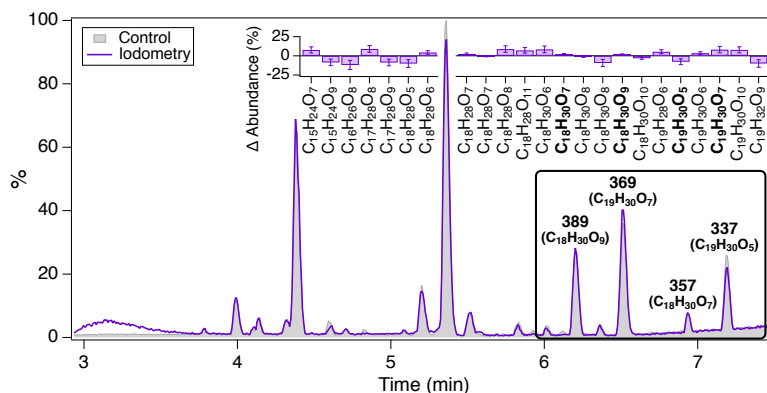
Figure 2.S5. UPLC/(−)ESI-Q-TOF-MS BPI chromatograms of SOA produced from the O_3-initiated oxidation of β-pinene in the CPOT (Table 2.S1, Exp. 7); comparison between iodometry and control samples (*SI Appendix*, 2.S3.7). Numbers correspond to nominal *m/z* values of [M−H]⁻ ions; molecular formulas are given in parentheses. (*Inset*) Effect of iodometry on the abundance of dimers whose formation was significantly inhibited (>65%) by OH scavenging (Table 2.1), reported as a percent change relative to the control sample and precise to <6%. Data for Control and Iodometry samples are reported as averages of replicates (*n* = 3).
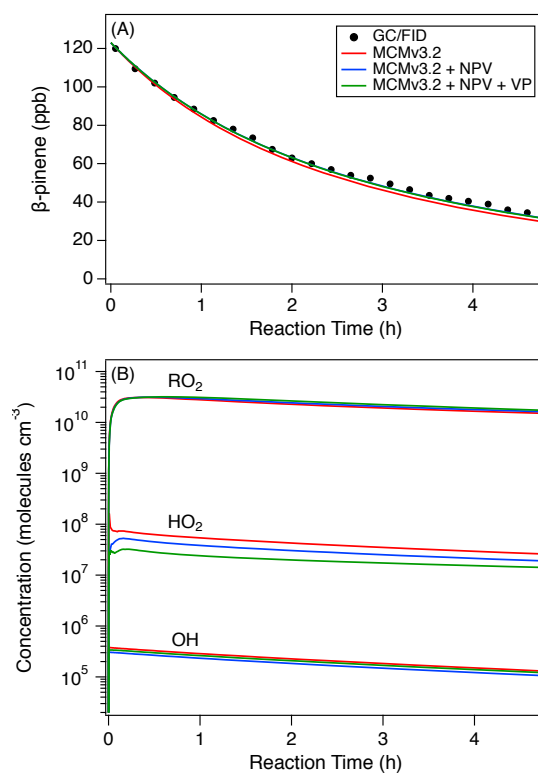
Figure 2.S6. MCMv3.2 simulations of the gas-phase ozonolysis of β-pinene in the CTEC under initial conditions of 123 ppb β-pinene, 200 ppb O_3, zero NO_x, 295 K, 1 atm, and 5% RH (Table 2.S1, Exp. 1). Three variations of the β-pinene ozonolysis mechanism were implemented (*SI Appendix*, 2.S4). (*A*) First-order decay of β-pinene, measured by GC/FID and modeled. (*B*) Simulated concentration profiles of OH, HO_2, and RO_2.
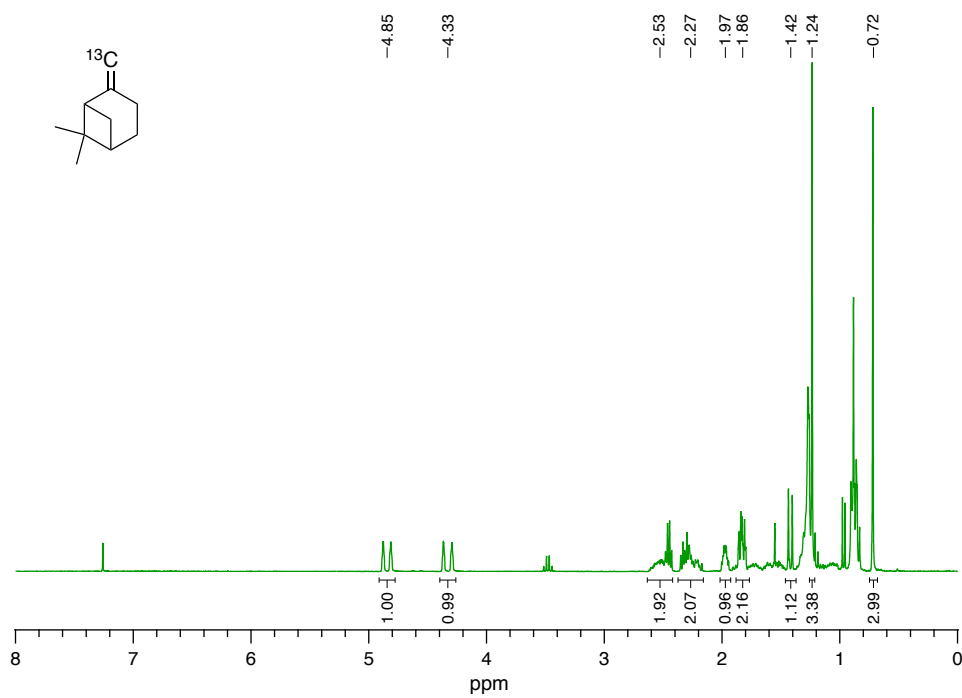
Figure 2.S7. ^{1}H NMR spectrum (300 MHz, CDCl$_3$) of ^{13}C-β-pinene.
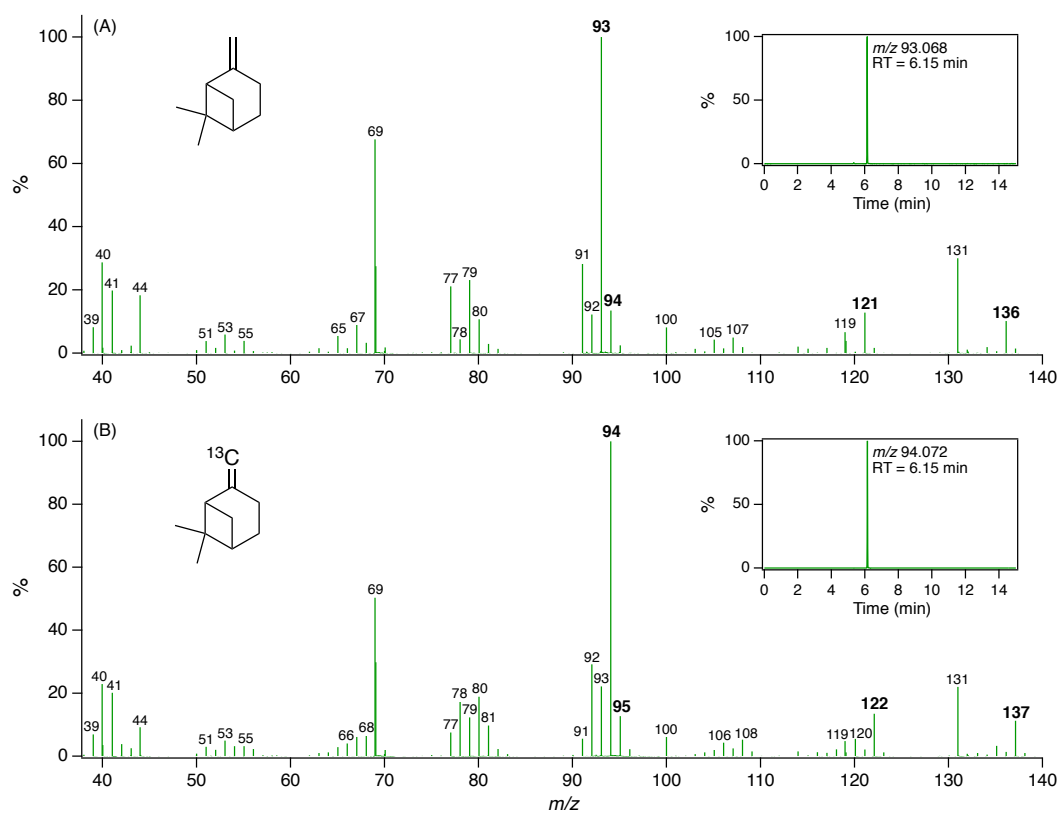
Figure 2.S8. GC/EI-MS spectra of (*A*) commercial β-pinene and (*B*) ^{13}C-β-pinene. (*Insets*) BPI chromatograms of *A* and *B*.
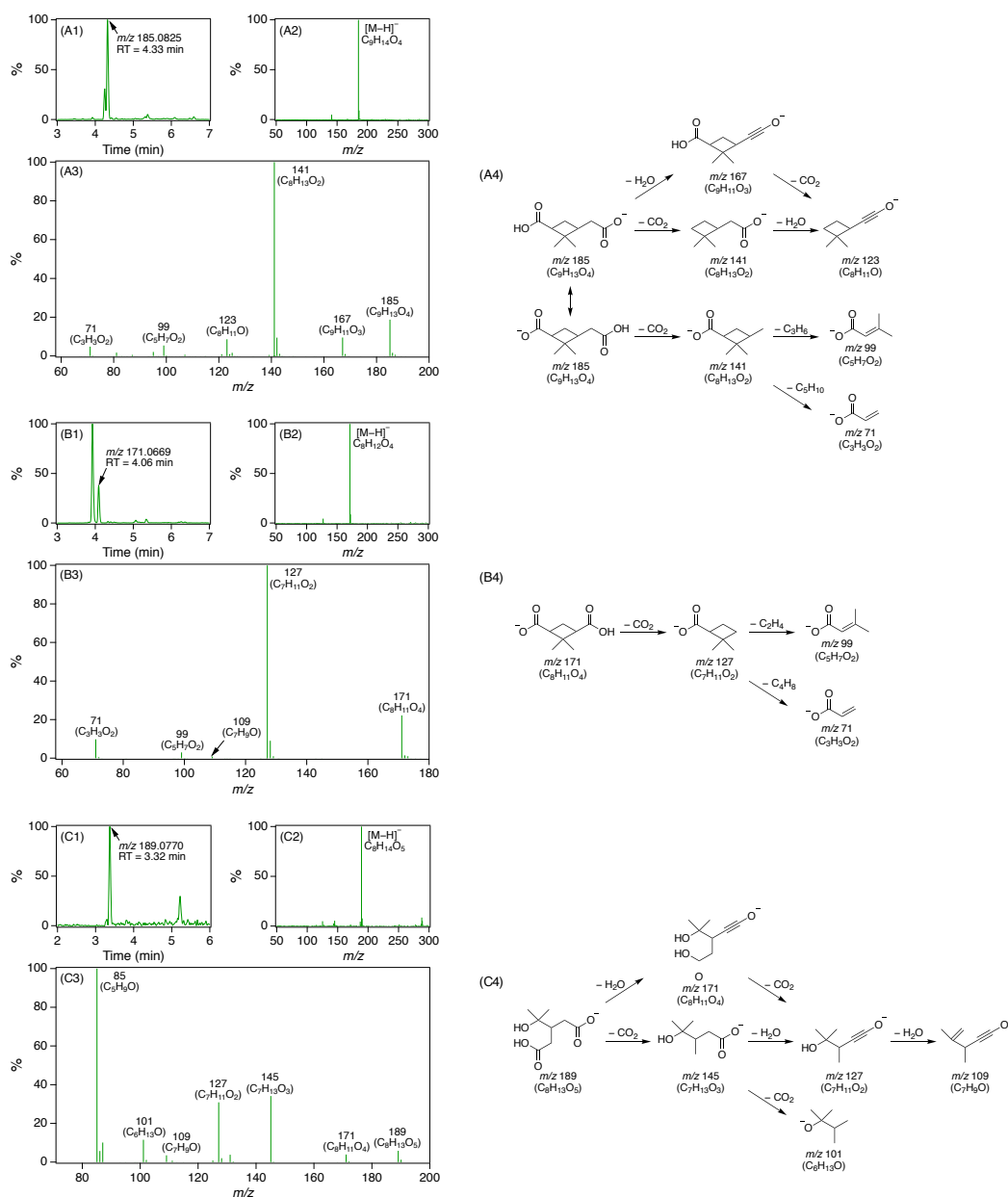
Figure 2.S9. (*1*) Extracted ion chromatograms, (*2*) MS spectra, and (*3*) MS/MS spectra, measured by UPLC/(−)ESI-Q-TOF-MS, along with (*4*) proposed fragmentation pathways, for dicarboxylic acids in β-pinene SOA assigned to (*A*) *cis*-pinic acid ($C_9H_{14}O_4$), (*B*) *cis*-norpinic acid ($C_8H_{12}O_4$), and (*C*) diaterpenylic acid ($C_8H_{14}O_5$). Numbers in MS/MS spectra and fragmentation pathways correspond to nominal *m/z* values of [M−H]⁻ fragment ions; ionic formulas $[C_xH_yO_z]^-$ are given in parentheses.
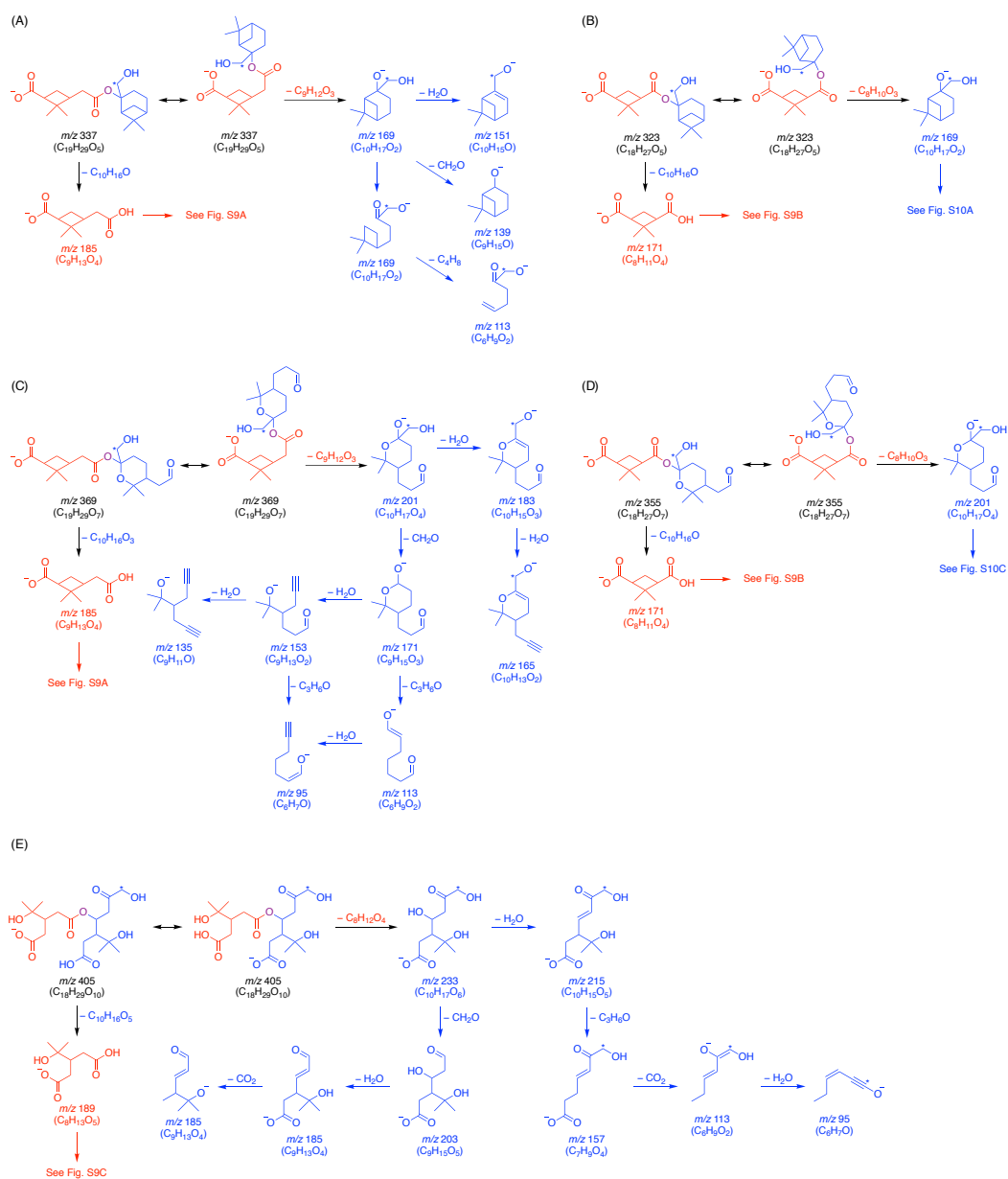
Figure 2.S10. Proposed fragmentation pathways for dimer esters (Table 2.S4) formed from concerted O$_3$ and OH oxidation of β-pinene. Structures are colored to denote O$_3$-derived (red) and OH-derived (blue) monomeric units. Numbers correspond to nominal *m/z* values of [M−H]$^-$ fragment ions; ionic formulas [C$_x$H$_y$O$_z$]$^-$ are given in parentheses. *Indicates position of ^{13}C label on formation from ^{13}C-β-pinene.
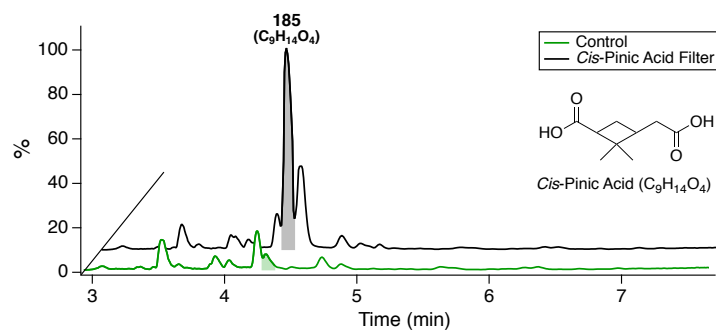
Figure 2.S11. UPLC/(−)ESI-Q-TOF-MS BPI chromatograms of SOA produced from the OH-initiated oxidation of β-pinene in the presence of pure $(NH_4)_2SO_4$ seed after ~4 h of reaction in the CTEC (Table 2.S1, Exp. 5). SOA was collected on either a clean Teflon filter (Control) or a Teflon filter coated with *cis*-pinic acid ($C_9H_{14}O_4$). Filters were collected in parallel such that the mass of SOA on each filter was approximately equivalent (*SI Appendix*, 2.S6.2). Shaded peaks correspond to *cis*-pinic acid.
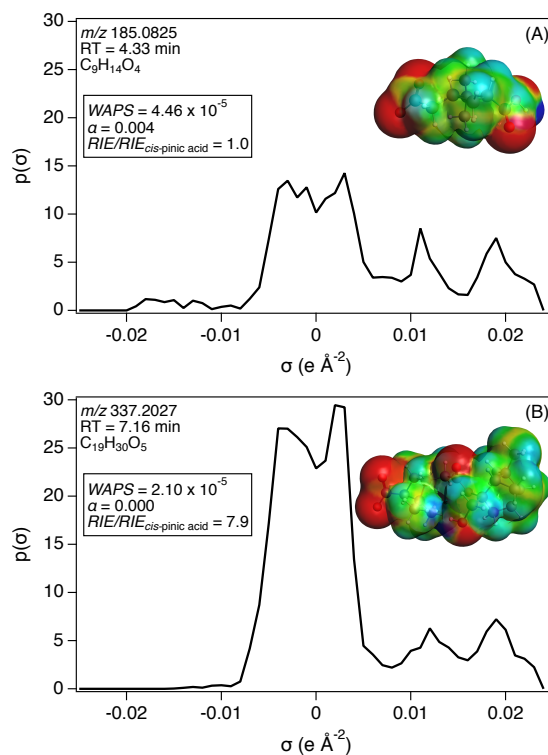
Figure 2.S12. COSMO-RS σ profiles of the [M−H]⁻ ions of (*A*) *cis*-pinic acid (C$_9$H$_{14}$O$_4$) and (*B*) the dimer ester at *m/z* 337 (C$_{19}$H$_{30}$O$_5$). Each σ profile contains 90 segments, 0.0089 e Å^{-2} wide; positive σ values correspond to surface segments with negative charge. (*Insets*) COSMO surface charge density superposed on the ball-and-stick structure for each anion; red represents positive charge density (underlying molecular charge is negative), blue represents negative charge density (underlying molecular charge is positive). The calculated weighted average positive sigma (*WAPS*), degree of ionization in solution (α), and relative (−)ESI efficiency normalized to that of *cis*-pinic acid (*RIE/RIE$_{cis}$*-pinic acid) are also reported for each compound.

2.S10 Tables 2.S1–2.S5

Table 2.S1. Summary of experimental conditions.

Reactor	Exp.	VOC	$[VOC]_0$ (ppb)	$[O_3]_0$ (ppb)[†]	Oxidant	Seed Aerosol[‡]	Initial Seed Volume ($\mu m^3\ cm^{-3}$)	OH/SCI Scavenger	T_0 (K)	RH_0 (%)
Caltech 24 m³ Environmental Chamber (CTEC)	1	β-pinene	123	~200	O_3	$(NH_4)_2SO_4$	72	–	295 ± 2	<5
	2	β-pinene	117	~3	OH	$(NH_4)_2SO_4$	66	–	295 ± 2	<5
	3	β-pinene	124	~3	OH	$(NH_4)_2SO_4$ + Cis-Pinic Acid (1:1)	122	–	295 ± 2	<5
	4	β-pinene	132	~3	OH	$(NH_4)_2SO_4$ + Cis-Pinic Acid (2:1)	143	–	295 ± 2	<5
	5	β-pinene	127	~3	OH	$(NH_4)_2SO_4$	74	–	295 ± 2	<5
	6	α-pinene	124	~200	O_3	$(NH_4)_2SO_4$	86	–	295 ± 2	<5
Caltech Photooxidation Flow Tube (CPOT)	7	β-pinene	147	~980	O_3	$(NH_4)_2SO_4$	77	–	295 ± 2	<10
	8	β-pinene	149	~990	O_3	$(NH_4)_2SO_4$	74	Cyclohexane (25 ppm)	295 ± 2	<10
	9	β-pinene	143	~1010	O_3	$(NH_4)_2SO_4$	81	Formic Acid (15 ppm)	295 ± 2	<10
	10	β-pinene	146	~970	O_3	$(NH_4)_2SO_4$	73	Water Vapor (1%)	295 ± 2	43 ± 1
	11	^{13}C-β-pinene	152	~990	O_3	$(NH_4)_2SO_4$	79	–	295 ± 2	<10

[†]H_2O_2 interference artificially increases O_3 absorption monitor readout by ~2–3 ppb in photooxidation experiments.
[‡]Seed aerosol was dried and neutralized in all experiments.

Table 2.S2. Laboratory and field observations of compounds with accurate masses/molecular formulas corresponding to the dimers identified in SOA produced from the O$_3$-initiated oxidation of β-pinene whose formation was significantly inhibited (>65%) by OH scavenging.

Dimer Type	Observed m/z (−)	RT (min)	Molecular Formula	Reported Observations	
				Laboratory	Field
1	323.1860	6.86	$C_{18}H_{28}O_5$	1,5	2
	355.1754	6.24	$C_{18}H_{28}O_7$	3,5,8,9,10	2,9,11
	419.1525	4.70	$C_{18}H_{28}O_{11}$	5	–
	373.1851	5.99	$C_{18}H_{30}O_8$	5	11
	405.1764	4.49	$C_{18}H_{30}O_{10}$	5,9,10	–
	351.1828	5.73	$C_{19}H_{28}O_6$	1,5,10	11
	337.2027	7.16	$C_{19}H_{30}O_5$	1,4,5,6,7,9,10	2,9
	369.1916	6.48	$C_{19}H_{30}O_7$	3,5,7,9,10	2,9,11
2	341.1960	6.87	$C_{18}H_{30}O_6$	–	11
	357.1919	6.91	$C_{18}H_{30}O_7$	–	2
	373.1851	5.70	$C_{18}H_{30}O_8$	5	11
	389.1814	6.18	$C_{18}H_{30}O_9$	5	11
	353.1961	6.15	$C_{19}H_{30}O_6$	5,9,10	9,11
3	315.1448	5.83	$C_{15}H_{24}O_7$	5,9,10	9
	347.1346	5.19	$C_{15}H_{24}O_9$	–	–
	375.1653	6.24	$C_{17}H_{28}O_9$	5,6	11
	417.1769	6.76	$C_{19}H_{30}O_{10}$	5	–
	403.1963	6.28	$C_{19}H_{32}O_9$	5	–
4	345.1549	5.36	$C_{16}H_{26}O_8$	5	11
	359.1714	5.89	$C_{17}H_{28}O_8$	5,9,10	11
	339.1822	6.34	$C_{18}H_{28}O_6$	3,5,9,10	2,11
	355.1754	5.27	$C_{18}H_{28}O_7$	3,5,8,9,10	2,9,11
	371.1707	5.46	$C_{18}H_{28}O_8$	3,5,9,10	9,11

(1) Tolocka et al.[17] (7) Kourtchev et al.[48]
(2) Wozniak et al.[62] (8) Zhang et al.[13]
(3) Müller et al.[21] (9) Kristensen et al.[11]
(4) Gao et al.[19] (10) Kristensen et al.[64]
(5) Putman et al.[63] (11) Mohr et al.[9]
(6) Witkowski and Gierczak[15]

Table 2.S3. MS/MS fragmentation patterns of dimers identified in SOA produced from the O_3-initiated oxidation of β-pinene whose m/z shifted by one mass unit on formation from ^{13}C-β-pinene.
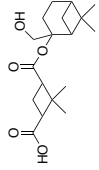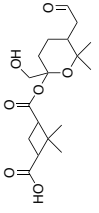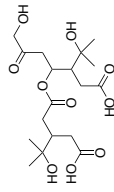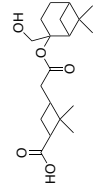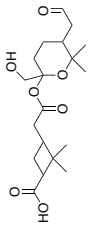
Dimer Type	Observed m/z (−)	RT (min)	Molecular Formula	Major MS/MS Fragment Ions†
	323.1860	6.86	$C_{18}H_{28}O_5$	171($C_8H_{11}O_4$), 127($C_7H_{11}O_2$), 99($C_5H_7O_2$), 71($C_3H_3O_2$) 169*($C_{10}H_{17}O_2$), 151*($C_{10}H_{15}O$), 139($C_9H_{15}O$), 113*($C_6H_9O_2$)
	355.1754	6.24	$C_{18}H_{28}O_7$	325($C_{17}H_{25}O_6$) 171($C_8H_{11}O_4$), 127($C_7H_{11}O_2$), 99($C_5H_7O_2$), 71($C_3H_3O_2$) 201*($C_{10}H_{17}O_4$), 183*($C_{10}H_{15}O_3$), 171($C_9H_{15}O_3$), 153($C_9H_{13}O_2$), 135($C_9H_{11}O$), 113($C_6H_9O_2$), 95(C_6H_7O)
	419.1525	4.70	$C_{18}H_{28}O_{11}$	343($C_{16}H_{23}O_8$) 189($C_8H_{13}O_5$), 171($C_8H_{11}O_4$), 145($C_7H_{13}O_3$), 127($C_7H_{11}O_2$), 109(C_7H_9O), 85(C_5H_9O) 247*($C_{10}H_{15}O_7$), 203($C_9H_{15}O_5$), 185($C_9H_{13}O_5$), 171($C_8H_{11}O_4$), 141($C_8H_{13}O_2$), 75*($C_2H_3O_3$)
1	373.1851	5.99	$C_{18}H_{30}O_8$	343($C_{17}H_{27}O_7$), 325($C_{17}H_{25}O_6$), 299($C_{16}H_{27}O_5$), 281($C_{16}H_{25}O_4$) 189($C_8H_{13}O_5$), 171($C_8H_{11}O_4$), 145($C_7H_{13}O_3$), 127($C_7H_{11}O_2$), 109(C_7H_9O), 85(C_5H_9O) 171($C_9H_{15}O_3$), 135($C_9H_{11}O$), 113($C_6H_9O_2$), 95(C_6H_7O)
	405.1764	4.49	$C_{18}H_{30}O_{10}$	189($C_8H_{13}O_5$), 171($C_8H_{11}O_4$), 145($C_7H_{13}O_3$), 127($C_7H_{11}O_2$), 109(C_7H_9O), 85(C_5H_9O) 233*($C_{10}H_{17}O_6$), 215*($C_{10}H_{15}O_5$), 203($C_9H_{15}O_5$), 185($C_9H_{13}O_4$), 157*($C_7H_9O_4$), 141($C_8H_{13}O_2$), 113*($C_6H_9O_2$), 95*(C_6H_7O)
	351.1828	5.73	$C_{19}H_{28}O_6$	185($C_9H_{13}O_4$), 167($C_9H_{11}O_3$), 141($C_8H_{13}O_2$), 123($C_8H_{11}O$), 99($C_5H_7O_2$), 71($C_3H_3O_2$) 183*($C_{10}H_{15}O_3$), 165*($C_{10}H_{13}O_2$), 153($C_9H_{13}O_2$), 135($C_9H_{11}O$)
	337.2027	7.16	$C_{19}H_{30}O_5$	185($C_9H_{13}O_4$), 167($C_9H_{11}O_3$), 141($C_8H_{13}O_2$), 123($C_8H_{11}O$), 99($C_5H_7O_2$), 71($C_3H_3O_2$) 169*($C_{10}H_{17}O_2$), 151*($C_{10}H_{15}O$), 139($C_9H_{15}O$), 113*($C_6H_9O_2$)
	369.1916	6.48	$C_{19}H_{30}O_7$	339($C_{18}H_{27}O_6$), 321($C_{18}H_{25}O_5$) 185($C_9H_{13}O_4$), 167($C_9H_{11}O_3$), 141($C_8H_{13}O_2$), 123($C_8H_{11}O$), 99($C_5H_7O_2$), 71($C_3H_3O_2$) 201*($C_{10}H_{17}O_4$), 183*($C_{10}H_{15}O_3$), 171($C_9H_{15}O_3$), 153($C_9H_{13}O_2$), 135($C_9H_{11}O$), 113($C_6H_9O_2$), 95(C_6H_7O)

67

Cmpd	m/z	RT	Formula	Fragment ions
	341.1960	6.87	$C_{18}H_{30}O_6$	$311(C_{17}H_{27}O_5)$, $253(C_{14}H_{21}O_4)$
				$157(C_8H_{13}O_3)$, $139(C_8H_{11}O_2)$
				$183^*(C_{10}H_{15}O_3)$, $171(C_9H_{15}O_3)$, $165^*(C_{10}H_{13}O_2)$, $125^*(C_7H_9O_2)$, $113(C_6H_9O_2)$ $107^*(C_7H_7O)$, $95(C_6H_7O)$, $73^*(C_3H_5O_2)$
	357.1919	6.91	$C_{18}H_{30}O_7$	$311(C_{17}H_{27}O_5)$, $255^*(C_{14}H_{23}O_4)$
				$189(C_8H_{13}O_5)$, $173(C_7H_9O_5)$, $171(C_8H_{11}O_4)$, $145(C_7H_{13}O_3)$, $130(C_5H_6O_4)$, $127(C_7H_{11}O_2)$, $101(C_6H_{13}O)$, $85(C_5H_9O)$
				$169^*(C_{10}H_{17}O_2)$, $151^*(C_{10}H_{15}O)$, $139^*(C_9H_{15}O)$, $117^*(C_5H_9O_3)$, $99^*(C_5H_7O_2)$, $71^*(C_4H_7O)$
2	373.1851	5.70	$C_{18}H_{30}O_8$	$343(C_{17}H_{27}O_7)$
				$189(C_8H_{13}O_5)$, $171(C_8H_{11}O_4)$, $145(C_7H_{13}O_3)$, $131(C_5H_7O_4)$, $127(C_7H_{11}O_2)$, $109(C_7H_9O)$, $87(C_4H_7O_2)$
				$185(C_9H_{13}O_4)$, $167(C_9H_{11}O_3)$, $141(C_8H_{13}O_2)$, $123(C_8H_{11}O)$
	389.1814	6.18	$C_{18}H_{30}O_9$	$189(C_8H_{13}O_5)$, $173(C_7H_9O_5)$, $171(C_8H_{11}O_4)$, $145(C_7H_{13}O_3)$, $130(C_5H_6O_4)$, $127(C_7H_{11}O_2)$, $101(C_6H_{13}O)$, $85(C_5H_9O)$
				$171(C_9H_{15}O_3)$, $165^*(C_{10}H_{13}O_2)$, $125^*(C_7H_9O_2)$, $117^*(C_5H_9O_3)$, $107^*(C_7H_7O)$, $99^*(C_5H_7O_2)$, $95(C_6H_7O_2)$, $71^*(C_4H_7O)$
	353.1961	6.15	$C_{19}H_{30}O_6$	$185(C_9H_{13}O_4)$, $167(C_9H_{11}O_3)$, $141(C_8H_{13}O_2)$, $123(C_8H_{11}O)$, $99(C_5H_7O_2)$, $71(C_3H_3O_2)$
				$185^*(C_{10}H_{17}O_3)$, $183^*(C_{10}H_{15}O_3)$, $155^*(C_9H_{15}O_2)$, $153^*(C_9H_{13}O_2)$, $85^*(C_4H_5O_2)$, $73^*(C_3H_5O_2)$
	315.1448	5.83	$C_{15}H_{24}O_7$	$145(C_5H_5O_5)$, $101(C_4H_5O_3)$, $83(C_4H_3O_2)$, $57(C_3H_5O)$
				$169^*(C_{10}H_{17}O_2)$, $151^*(C_{10}H_{15}O)$, $139(C_9H_{15}O)$
	347.1346	5.19	$C_{15}H_{24}O_9$	$189(C_8H_{13}O_5)$, $171(C_8H_{11}O_4)$, $145(C_7H_{13}O_3)$, $127(C_7H_{11}O_2)$, $109(C_7H_9O)$, $85(C_5H_9O)$
				$125^*(C_7H_9O_2)$, $107^*(C_7H_7O)$, $101(C_4H_5O_3)$, $83(C_4H_3O_2)$, $57(C_3H_5O)$
3	375.1653	6.24	$C_{17}H_{28}O_9$	$175(C_7H_{11}O_5)$, $173(C_7H_9O_5)$, $157(C_7H_9O_4)$, $129(C_6H_9O_3)$, $117(C_4H_5O_4)$, $99(C_4H_3O_3)$, $85(C_5H_9O)$, $73(C_3H_5O_2)$
				$171(C_9H_{15}O_3)$, $165^*(C_{10}H_{13}O_2)$, $135^*(C_9H_{11}O)$, $125^*(C_7H_9O_2)$, $113(C_6H_9O_2)$ 107^* (C_7H_7O), $95(C_6H_7O)$
	417.1769	6.76	$C_{19}H_{30}O_{10}$	$189(C_8H_{13}O_5)$, $173(C_7H_9O_5)$, $171(C_8H_{11}O_4)$, $145(C_7H_{13}O_3)$, $130(C_5H_6O_4)$, $127(C_7H_{11}O_2)$, $101(C_6H_{13}O)$, $85(C_5H_9O)$
				$171(C_9H_{15}O_3)$, $165^*(C_{10}H_{13}O_2)$, $125^*(C_7H_9O_2)$, $107^*(C_7H_7O)$, $95(C_6H_7O)$
	403.1963	6.28	$C_{19}H_{32}O_9$	$203(C_9H_{15}O_5)$, $185(C_9H_{13}O_4)$, $159(C_8H_{15}O_3)$, $141(C_8H_{13}O_2)$, $123(C_8H_{11}O)$, $115(C_7H_{15}O)$, $99(C_6H_{11}O)$
				$171(C_9H_{15}O_3)$, $125^*(C_7H_9O_2)$, $113^*(C_6H_9O_2)$ $107^*(C_7H_7O)$, $95^*(C_6H_7O)$, $85^*(C_5H_9O)$

†Nominal m/z values are colored to denote O_3-derived (red) and OH-derived (blue) fragment ions. Ionic formulas $[C_xH_yO_z]^-$ are given in parentheses.
*Indicates peaks that underwent a one-unit mass shift on formation from ^{13}C-β-pinene.

Table 2.S4. COSMO-RS theoretical parameters for proposed molecular structures of dimer esters (Table 2.1, type 1) formed from concerted O_3 and OH oxidation of β-pinene, and for *cis*-pinic acid.

Observed m/z (−)	RT (min)	Molecular Formula	Exchangeable Hydrogens	WAPS (× 10^5)[†]	α[‡]	RIE/ RIE_cis-pinic acid[§]	Proposed Molecular Structure
323.1860	6.86	$C_{18}H_{28}O_5$	2	2.18	0.005	7.3	
355.1754	6.24	$C_{18}H_{28}O_7$	4	2.35	0.018	6.4	
405.1764	4.49	$C_{18}H_{30}O_{10}$	5	2.18 2.17	0.099 0.055	21.5	
337.2027	7.16	$C_{19}H_{30}O_5$	2	2.10	0.001	7.9	
369.1916	6.48	$C_{19}H_{30}O_7$	4	2.25	0.045	8.3	
185.0825	4.33	$C_9H_{14}O_4$	2	4.47 4.46	0.004 0.008	1.0	

[†]Weighted average positive sigma.
[‡]Degree of ionization in solution.
[§]Relative (−)ESI efficiency normalized to that of *cis*-pinic acid.

Table 2.S5. Dimers identified in SOA produced from the O_3-initiated oxidation of α-pinene (Table 2.S1, Exp. 6) with the same accurate masses/molecular formulas, similar RT, and analogous MS/MS spectra to those in β-pinene SOA demonstrated to derive from concerted O_3 and OH oxidation.

Dimer Type	Observed m/z (−)	RT (min)		Molecular Formula	Error (ppm)
		α-Pinene	β-Pinene		
	323.1860	6.93	6.86	$C_{18}H_{28}O_5$	0.6
	323.1860	6.68	6.86	$C_{18}H_{28}O_5$	0.6
1	337.2027	7.31	7.16	$C_{19}H_{30}O_5$	3.6
	369.1916	6.48	6.48	$C_{19}H_{30}O_7$	0.8
	357.1919	6.91	6.91	$C_{18}H_{30}O_7$	1.7
	357.1919	6.77	6.91	$C_{18}H_{30}O_7$	1.7
2	389.1814	6.02	6.18	$C_{18}H_{30}O_9$	0.8
	353.1961	6.31	6.15	$C_{19}H_{30}O_6$	−0.8

2.6 References

(1) Hallquist, M.; Wenger, J. C.; Baltensperger, U.; Rudich, Y.; Simpson, D.; Claeys, M.; Dommen, J.; Donahue, N. M.; George, C.; Goldstein, A. H.; Hamilton, J. F.; Herrmann, H.; Hoffmann, T.; Iinuma, Y.; Jang, M.; Jenkin, M. E.; Jimenez, J. L.; Kiendler-Scharr, A.; Maenhaut, W.; McFiggans, G.; Mentel, Th. F.; Monod, A.; Prévôt, A. S. H.; Seinfeld, J. H.; Surratt, J. D.; Szmigielski, R.; Wildt, J. The Formation, Properties and Impact of Secondary Organic Aerosol: Current and Emerging Issues. *Atmos. Chem. Phys.* **2009**, *9* (14), 5155–5236. DOI: 10.5194/acp-9-5155-2009.

(2) Kanakidou, M.; Seinfeld, J. H.; Pandis, S. N.; Barnes, I.; Dentener, F. J.; Facchini, M. C.; Van Dingenen, R.; Ervens, B.; Nenes, A.; Nielsen, C. J.; Swietlicki, E.; Putaud, J. P.; Balkanski, Y.; Fuzzi, S.; Horth, J.; Moortgat, G. K.; Winterhalter, R.; Myhre, C. E. L.; Tsigaridis, K.; Vignati, E.; Stephanou, E. G.; Wilson, J. Organic Aerosol and Global Climate Modelling: A Review. *Atmos. Chem. Phys.* **2005**, *5* (4), 1053–1123. DOI: 10.5194/acp-5-1053-2005.

(3) Jimenez, J. L.; Canagaratna, M. R.; Donahue, N. M.; Prevot, A. S. H.; Zhang, Q.; Kroll, J. H.; DeCarlo, P. F.; Allan, J. D.; Coe, H.; Ng, N. L.; Aiken, A. C.; Docherty, K. S.; Ulbrich, I. M.; Grieshop, A. P.; Robinson, A. L.; Duplissy, J.; Smith, J. D.; Wilson, K. R.; Lanz, V. A.; Hueglin, C.; Sun, Y. L.; Tian, J.; Laaksonen, A.; Raatikainen, T.; Rautiainen, J.; Vaattovaara, P.; Ehn, M.; Kulmala, M.; Tomlinson, J. M.; Collins, D. R.; Cubison, M. J.; E.; Dunlea, J.; Huffman, J. A.; Onasch, T. B.; Alfarra, M. R.; Williams, P. I.; Bower, K.; Kondo, Y.; Schneider, J.; Drewnick, F.; Borrmann, S.; Weimer, S.; Demerjian, K.; Salcedo, D.; Cottrell, L.; Griffin, R.; Takami, A.; Miyoshi, T.; Hatakeyama, S.; Shimono, A.; Sun, J. Y.; Zhang, Y. M.; Dzepina, K.; Kimmel, J. R.; Sueper, D.; Jayne, J. T.; Herndon, S. C.; Trimborn, A. M.; Williams, L. R.; Wood, E. C.; Middlebrook, A. M.; Kolb, C. E.; Baltensperger, U.; Worsnop, D. R. Evolution of Organic Aerosols in the Atmosphere. *Science* **2009**, *326* (5959), 1525–1529. DOI: 10.1126/science.1180353.

(4) Intergovernmental Panel on Climate Change. *Climate Change 2013: The Physical Science Basis*; Stocker, T. F., Qin, D., Plattner, G. K., Tignor, M., Allen, S. K., Boschung, J., Nauels, A., Xia, Y., Bex, V., Midgley, P. M., Eds.; Cambridge University Press: Cambridge, United Kingdom, 2013.

(5) Pope, C. A.; Ezzati, M.; Dockery, D. W. Fine-Particulate Air Pollution and Life Expectancy in the United States. *N. Engl. J. Med.* **2009**, *360* (4), 376–386. DOI: 10.1056/NEJMsa0805646.

(6) Cohen, A. J.; Brauer, M.; Burnett, R.; Anderson, H. R.; Frostad, J.; Estep, K.; Balakrishnan, K.; Brunekreef, B.; Dandona, L.; Dandona, R.; Feigin, V.; Freedman, G.; Hubbell, B.; Jobling, A.; Kan, H.; Knibbs, L.; Liu, Y.; Martin, R.; Morawska, L.; Pope, C. A.; Shin, H.; Straif, K.; Shaddick, G.;

Thomas, M.; van Dingenen, R.; van Donkelaar, A.; Vos, T.; Murray, C. J. L.; Forouzanfar, M. H. Estimates and 25-Year Trends of the Global Burden of Disease Attributable to Ambient Air Pollution: An Analysis of Data from the Global Burden of Diseases Study 2015. *Lancet* **2017**, *389* (10082), 1907–1918. DOI: 10.1016/S0140-6736(17)30505-6.

(7)   Yasmeen, F.; Vermeylen, R.; Szmigielski, R.; Iinuma, Y.; Böge, O.; Herrmann, H.; Maenhaut, W.; Claeys, M. Terpenylic Acid and Related Compounds: Precursors for Dimers in Secondary Organic Aerosol from the Ozonolysis of α- and β-Pinene. *Atmos. Chem. Phys.* **2010**, *10* (19), 9383–9392. DOI: 10.5194/acp-10-9383-2010.

(8)   Kourtchev, I.; Giorio, C.; Manninen, A.; Wilson, E.; Mahon, B.; Aalto, J.; Kajos, M.; Venables, D.; Ruuskanen, T.; Levula, J.; Loponen, M.; Connors, S.; Harris, N.; Zhao, D.; Kiendler-Scharr, A.; Mentel, T.; Rudich, Y.; Hallquist, M.; Doussin, J.-F.; Maenhaut, W.; Bäck, J.; Petäjä, T.; Wenger, J.; Kulmala, M.; Kalberer, M. Enhanced Volatile Organic Compounds Emissions and Organic Aerosol Mass Increase the Oligomer Content of Atmospheric Aerosols. *Sci Rep* **2016**, *6* (1), 35038. DOI: 10.1038/srep35038.

(9)   Mohr, C.; Lopez-Hilfiker, F. D.; Yli-Juuti, T.; Heitto, A.; Lutz, A.; Hallquist, M.; D'Ambro, E. L.; Rissanen, M. P.; Hao, L.; Schobesberger, S.; Kulmala, M.; Mauldin, R. L.; Makkonen, U.; Sipilä, M.; Petäjä, T.; Thornton, J. A. Ambient Observations of Dimers from Terpene Oxidation in the Gas Phase: Implications for New Particle Formation and Growth. *Geophys. Res. Lett.* **2017**, *44* (6), 2958–2966. DOI: 10.1002/2017GL072718.

(10)   Kristensen, K.; Enggrob, K. L.; King, S. M.; Worton, D. R.; Platt, S. M.; Mortensen, R.; Rosenoern, T.; Surratt, J. D.; Bilde, M.; Goldstein, A. H.; Glasius, M. Formation and Occurrence of Dimer Esters of Pinene Oxidation Products in Atmospheric Aerosols. *Atmos. Chem. Phys.* **2013**, *13* (7), 3763–3776. DOI: 10.5194/acp-13-3763-2013.

(11)   Kristensen, K.; Watne, Å. K.; Hammes, J.; Lutz, A.; Petäjä, T.; Hallquist, M.; Bilde, M.; Glasius, M. High-Molecular Weight Dimer Esters Are Major Products in Aerosols from α-Pinene Ozonolysis and the Boreal Forest. *Environ. Sci. Technol. Lett.* **2016**, *3* (8), 280–285. DOI: 10.1021/acs.estlett.6b00152.

(12)   Kristensen, K.; Cui, T.; Zhang, H.; Gold, A.; Glasius, M.; Surratt, J. D. Dimers in α-Pinene Secondary Organic Aerosol: Effect of Hydroxyl Radical, Ozone, Relative Humidity and Aerosol Acidity. *Atmos. Chem. Phys.* **2014**, *14* (8), 4201–4218. DOI: 10.5194/acp-14-4201-2014.

(13)   Zhang, X.; McVay, R. C.; Huang, D. D.; Dalleska, N. F.; Aumont, B.; Flagan, R. C.; Seinfeld, J. H. Formation and Evolution of Molecular

Products in α-Pinene Secondary Organic Aerosol. *Proc. Natl. Acad. Sci. U.S.A.* **2015**, *112* (46), 14168–14173. DOI: 10.1073/pnas.1517742112.

(14) Zhao, Y.; Wingen, L. M.; Perraud, V.; Greaves, J.; Finlayson-Pitts, B. J. Role of the Reaction of Stabilized Criegee Intermediates with Peroxy Radicals in Particle Formation and Growth in Air. *Phys. Chem. Chem. Phys.* **2015**, *17* (19), 12500–12514. DOI: 10.1039/C5CP01171J.

(15) Witkowski, B.; Gierczak, T. Early Stage Composition of SOA Produced by α-Pinene/Ozone Reaction: α-Acyloxyhydroperoxy Aldehydes and Acidic Dimers. *Atmos. Environ.* **2014**, *95*, 59–70. DOI: 10.1016/j.atmosenv.2014.06.018.

(16) Hall, W. A.; Johnston, M. V. Oligomer Formation Pathways in Secondary Organic Aerosol from MS and MS/MS Measurements with High Mass Accuracy and Resolving Power. *J. Am. Soc. Mass Spectrom.* **2012**, *23* (6), 1097–1108. DOI: 10.1007/s13361-012-0362-6.

(17) Tolocka, M. P.; Jang, M.; Ginter, J. M.; Cox, F. J.; Kamens, R. M.; Johnston, M. V. Formation of Oligomers in Secondary Organic Aerosol. *Environ. Sci. Technol.* **2004**, *38* (5), 1428–1434. DOI: 10.1021/es035030r.

(18) Reinhardt, A.; Emmenegger, C.; Gerrits, B.; Panse, C.; Dommen, J.; Baltensperger, U.; Zenobi, R.; Kalberer, M. Ultrahigh Mass Resolution and Accurate Mass Measurements as a Tool To Characterize Oligomers in Secondary Organic Aerosols. *Anal. Chem.* **2007**, *79* (11), 4074–4082. DOI: 10.1021/ac062425v.

(19) Gao, Y.; Hall, W. A.; Johnston, M. V. Molecular Composition of Monoterpene Secondary Organic Aerosol at Low Mass Loading. *Environ. Sci. Technol.* **2010**, *44* (20), 7897–7902. DOI: 10.1021/es101861k.

(20) Müller, L.; Reinnig, M.-C.; Warnke, J.; Hoffmann, Th. Unambiguous Identification of Esters as Oligomers in Secondary Organic Aerosol Formed from Cyclohexene and Cyclohexene/α-Pinene Ozonolysis. *Atmos. Chem. Phys.* **2008**, *8* (5), 1423–1433. DOI: 10.5194/acp-8-1423-2008.

(21) Müller, L.; Reinnig, M.-C.; Hayen, H.; Hoffmann, T. Characterization of Oligomeric Compounds in Secondary Organic Aerosol Using Liquid Chromatography Coupled to Electrospray Ionization Fourier Transform Ion Cyclotron Resonance Mass Spectrometry. *Rapid Commun. Mass Spectrom.* **2009**, *23* (7), 971–979. DOI: 10.1002/rcm.3957.

(22) Docherty, K. S.; Wu, W.; Lim, Y. B.; Ziemann, P. J. Contributions of Organic Peroxides to Secondary Aerosol Formed from Reactions of Monoterpenes with O_3. *Environ. Sci. Technol.* **2005**, *39* (11), 4049–4059. DOI: 10.1021/es050228s.

(23) Ehn, M.; Thornton, J. A.; Kleist, E.; Sipilä, M.; Junninen, H.; Pullinen, I.; Springer, M.; Rubach, F.; Tillmann, R.; Lee, B.; Lopez-Hilfiker, F.; Andres,

S.; Acir, I.-H.; Rissanen, M.; Jokinen, T.; Schobesberger, S.; Kangasluoma, J.; Kontkanen, J.; Nieminen, T.; Kurtén, T.; Nielsen, L. B.; Jørgensen, S.; Kjaergaard, H. G.; Canagaratna, M.; Maso, M. D.; Berndt, T.; Petäjä, T.; Wahner, A.; Kerminen, V.-M.; Kulmala, M.; Worsnop, D. R.; Wildt, J.; Mentel, T. F. A Large Source of Low-Volatility Secondary Organic Aerosol. *Nature* **2014**, *506* (7489), 476–479. DOI: 10.1038/nature13032.

(24)   Jokinen, T.; Berndt, T.; Makkonen, R.; Kerminen, V.-M.; Junninen, H.; Paasonen, P.; Stratmann, F.; Herrmann, H.; Guenther, A. B.; Worsnop, D. R.; Kulmala, M.; Ehn, M.; Sipilä, M. Production of Extremely Low Volatile Organic Compounds from Biogenic Emissions: Measured Yields and Atmospheric Implications. *Proc. Natl. Acad. Sci. U.S.A.* **2015**, *112* (23), 7123–7128. DOI: 10.1073/pnas.1423977112.

(25)   Kirkby, J.; Duplissy, J.; Sengupta, K.; Frege, C.; Gordon, H.; Williamson, C.; Heinritzi, M.; Simon, M.; Yan, C.; Almeida, J.; Tröstl, J.; Nieminen, T.; Ortega, I. K.; Wagner, R.; Adamov, A.; Amorim, A.; Bernhammer, A.-K.; Bianchi, F.; Breitenlechner, M.; Brilke, S.; Chen, X.; Craven, J.; Dias, A.; Ehrhart, S.; Flagan, R. C.; Franchin, A.; Fuchs, C.; Guida, R.; Hakala, J.; Hoyle, C. R.; Jokinen, T.; Junninen, H.; Kangasluoma, J.; Kim, J.; Krapf, M.; Kürten, A.; Laaksonen, A.; Lehtipalo, K.; Makhmutov, V.; Mathot, S.; Molteni, U.; Onnela, A.; Peräkylä, O.; Piel, F.; Petäjä, T.; Praplan, A. P.; Pringle, K.; Rap, A.; Richards, N. A. D.; Riipinen, I.; Rissanen, M. P.; Rondo, L.; Sarnela, N.; Schobesberger, S.; Scott, C. E.; Seinfeld, J. H.; Sipilä, M.; Steiner, G.; Stozhkov, Y.; Stratmann, F.; Tomé, A.; Virtanen, A.; Vogel, A. L.; Wagner, A. C.; Wagner, P. E.; Weingartner, E.; Wimmer, D.; Winkler, P. M.; Ye, P.; Zhang, X.; Hansel, A.; Dommen, J.; Donahue, N. M.; Worsnop, D. R.; Baltensperger, U.; Kulmala, M.; Carslaw, K. S.; Curtius, J. Ion-Induced Nucleation of Pure Biogenic Particles. *Nature* **2016**, *533* (7604), 521–526. DOI: 10.1038/nature17953.

(26)   Tröstl, J.; Chuang, W. K.; Gordon, H.; Heinritzi, M.; Yan, C.; Molteni, U.; Ahlm, L.; Frege, C.; Bianchi, F.; Wagner, R.; Simon, M.; Lehtipalo, K.; Williamson, C.; Craven, J. S.; Duplissy, J.; Adamov, A.; Almeida, J.; Bernhammer, A.-K.; Breitenlechner, M.; Brilke, S.; Dias, A.; Ehrhart, S.; Flagan, R. C.; Franchin, A.; Fuchs, C.; Guida, R.; Gysel, M.; Hansel, A.; Hoyle, C. R.; Jokinen, T.; Junninen, H.; Kangasluoma, J.; Keskinen, H.; Kim, J.; Krapf, M.; Kürten, A.; Laaksonen, A.; Lawler, M.; Leiminger, M.; Mathot, S.; Möhler, O.; Nieminen, T.; Onnela, A.; Petäjä, T.; Piel, F. M.; Miettinen, P.; Rissanen, M. P.; Rondo, L.; Sarnela, N.; Schobesberger, S.; Sengupta, K.; Sipilä, M.; Smith, J. N.; Steiner, G.; Tomè, A.; Virtanen, A.; Wagner, A. C.; Weingartner, E.; Wimmer, D.; Winkler, P. M.; Ye, P.; Carslaw, K. S.; Curtius, J.; Dommen, J.; Kirkby, J.; Kulmala, M.; Riipinen, I.; Worsnop, D. R.; Donahue, N. M.; Baltensperger, U. The Role of Low-Volatility Organic Compounds in Initial Particle Growth in the Atmosphere. *Nature* **2016**, *533* (7604), 527–531. DOI: 10.1038/nature18271.

(27)   Kidd, C.; Perraud, V.; Wingen, L. M.; Finlayson-Pitts, B. J. Integrating Phase and Composition of Secondary Organic Aerosol from the Ozonolysis of α-Pinene. *Proc. Natl. Acad. Sci. U.S.A.* **2014**, *111* (21), 7552–7557. DOI: 10.1073/pnas.1322558111.

(28)   Guenther, A. B.; Jiang, X.; Heald, C. L.; Sakulyanontvittaya, T.; Duhl, T.; Emmons, L. K.; Wang, X. The Model of Emissions of Gases and Aerosols from Nature Version 2.1 (MEGAN2.1): An Extended and Updated Framework for Modeling Biogenic Emissions. *Geosci. Model Dev.* **2012**, *5* (6), 1471–1492. DOI: 10.5194/gmd-5-1471-2012.

(29)   Zhang, X.; Dalleska, N. F.; Huang, D. D.; Bates, K. H.; Sorooshian, A.; Flagan, R. C.; Seinfeld, J. H. Time-Resolved Molecular Characterization of Organic Aerosols by PILS + UPLC/ESI-Q-TOFMS. *Atmos. Environ.* **2016**, *130*, 180–189. DOI: 10.1016/j.atmosenv.2015.08.049.

(30)   Zhao, R.; Kenseth, C. M.; Huang, Y.; Dalleska, N. F.; Seinfeld, J. H. Iodometry-Assisted Liquid Chromatography Electrospray Ionization Mass Spectrometry for Analysis of Organic Peroxides: An Application to Atmospheric Secondary Organic Aerosol. *Environ. Sci. Technol.* **2018**, *52* (4), 2108–2117. DOI: 10.1021/acs.est.7b04863.

(31)   Donahue, N. M.; Drozd, G. T.; Epstein, S. A.; Presto, A. A.; Kroll, J. H. Adventures in Ozoneland: Down the Rabbit-Hole. *Phys. Chem. Chem. Phys.* **2011**, *13* (23), 10848. DOI: 10.1039/c0cp02564j.

(32)   Sipilä, M.; Jokinen, T.; Berndt, T.; Richters, S.; Makkonen, R.; Donahue, N. M.; Mauldin III, R. L.; Kurtén, T.; Paasonen, P.; Sarnela, N.; Ehn, M.; Junninen, H.; Rissanen, M. P.; Thornton, J.; Stratmann, F.; Herrmann, H.; Worsnop, D. R.; Kulmala, M.; Kerminen, V.-M.; Petäjä, T. Reactivity of Stabilized Criegee Intermediates (SCIs) from Isoprene and Monoterpene Ozonolysis toward SO_2 and Organic Acids. *Atmos. Chem. Phys.* **2014**, *14* (22), 12143–12153. DOI: 10.5194/acp-14-12143-2014.

(33)   Drozd, G. T.; Kurtén, T.; Donahue, N. M.; Lester, M. I. Unimolecular Decay of the Dimethyl-Substituted Criegee Intermediate in Alkene Ozonolysis: Decay Time Scales and the Importance of Tunneling. *J. Phys. Chem. A* **2017**, *121* (32), 6036–6045. DOI: 10.1021/acs.jpca.7b05495.

(34)   Nguyen, T. L.; Peeters, J.; Vereecken, L. Theoretical Study of the Gas-Phase Ozonolysis of β-Pinene ($C_{10}H_{16}$). *Phys. Chem. Chem. Phys.* **2009**, *11* (27), 5643. DOI: 10.1039/b822984h.

(35)   Donahue, N. M.; Epstein, S. A.; Pandis, S. N.; Robinson, A. L. A Two-Dimensional Volatility Basis Set: 1. Organic-Aerosol Mixing Thermodynamics. *Atmos. Chem. Phys.* **2011**, *11* (7), 3303–3318. DOI: 10.5194/acp-11-3303-2011.

(36)   Vereecken, L.; Peeters, J. A Theoretical Study of the OH-Initiated Gas-Phase Oxidation Mechanism of β-Pinene ($C_{10}H_{16}$): First Generation

Products. *Phys. Chem. Chem. Phys.* **2012**, *14* (11), 3802. DOI: 10.1039/c2cp23711c.

(37)   Kaminski, M.; Fuchs, H.; Acir, I.-H.; Bohn, B.; Brauers, T.; Dorn, H.-P.; Häseler, R.; Hofzumahaus, A.; Li, X.; Lutz, A.; Nehr, S.; Rohrer, F.; Tillmann, R.; Vereecken, L.; Wegener, R.; Wahner, A. Investigation of the β-Pinene Photooxidation by OH in the Atmosphere Simulation Chamber SAPHIR. *Atmos. Chem. Phys.* **2017**, *17* (11), 6631–6650. DOI: 10.5194/acp-17-6631-2017.

(38)   Reinnig, M.-C.; Müller, L.; Warnke, J.; Hoffmann, T. Characterization of Selected Organic Compound Classes in Secondary Organic Aerosol from Biogenic VOCs by HPLC/MS^n. *Anal Bioanal Chem* **2008**, *391* (1), 171–182. DOI: 10.1007/s00216-008-1964-5.

(39)   Yasmeen, F.; Vermeylen, R.; Maurin, N.; Perraudin, E.; Doussin, J.-F.; Claeys, M. Characterisation of Tracers for Aging of α-Pinene Secondary Organic Aerosol Using Liquid Chromatography/Negative Ion Electrospray Ionisation Mass Spectrometry. *Environ. Chem.* **2012**, *9* (3), 236–246. DOI: 10.1071/EN11148.

(40)   Grossert, J. S.; Fancy, P. D.; White, R. L. Fragmentation Pathways of Negative Ions Produced by Electrospray Ionization of Acyclic Dicarboxylic Acids and Derivatives. *Can. J. Chem.* **2005**, *83* (11), 1878–1890. DOI: 10.1139/V05-214.

(41)   Demarque, D. P.; Crotti, A. E. M.; Vessecchi, R.; Lopes, J. L. C.; Lopes, N. P. Fragmentation Reactions Using Electrospray Ionization Mass Spectrometry: An Important Tool for the Structural Elucidation and Characterization of Synthetic and Natural Products. *Nat. Prod. Rep.* **2016**, *33* (3), 432–455. DOI: 10.1039/C5NP00073D.

(42)   Kingston, D. G. I.; Hobrock, B. W.; Bursey, M. M.; Bursey, J. T. Intramolecular Hydrogen Transfer in Mass Spectra. III. Rearrangements Involving the Loss of Small Neutral Molecules. *Chem. Rev.* **1975**, *75* (6), 693–730. DOI: 10.1021/cr60298a002.

(43)   Pankow, J. F. An Absorption Model of Gas/Particle Partitioning of Organic Compounds in the Atmosphere. *Atmos. Environ.* **1994**, *28* (2), 185–188. DOI: 10.1016/1352-2310(94)90093-0.

(44)   Shiraiwa, M.; Yee, L. D.; Schilling, K. A.; Loza, C. L.; Craven, J. S.; Zuend, A.; Ziemann, P. J.; Seinfeld, J. H. Size Distribution Dynamics Reveal Particle-Phase Chemistry in Organic Aerosol Formation. *Proc. Natl. Acad. Sci. U.S.A.* **2013**, *110* (29), 11746–11750. DOI: 10.1073/pnas.1307501110.

(45)   Barsanti, K. C.; Kroll, J. H.; Thornton, J. A. Formation of Low-Volatility Organic Compounds in the Atmosphere: Recent Advancements and Insights. *J. Phys. Chem. Lett.* **2017**, *8* (7), 1503–1511. DOI: 10.1021/acs.jpclett.6b02969.

(46)   Berndt, T.; Scholz, W.; Mentler, B.; Fischer, L.; Herrmann, H.; Kulmala, M.; Hansel, A. Accretion Product Formation from Self- and Cross-Reactions of RO_2 Radicals in the Atmosphere. *Angew. Chem. Int. Ed.* **2018**, *57* (14), 3820–3824. DOI: 10.1002/anie.201710989.

(47)   Glasius, M.; Goldstein, A. H. Recent Discoveries and Future Challenges in Atmospheric Organic Chemistry. *Environ. Sci. Technol.* **2016**, *50* (6), 2754–2764. DOI: 10.1021/acs.est.5b05105.

(48)   Kourtchev, I.; Doussin, J.-F.; Giorio, C.; Mahon, B.; Wilson, E. M.; Maurin, N.; Pangui, E.; Venables, D. S.; Wenger, J. C.; Kalberer, M. Molecular Composition of Fresh and Aged Secondary Organic Aerosol from a Mixture of Biogenic Volatile Compounds: A High-Resolution Mass Spectrometry Study. *Atmos. Chem. Phys.* **2015**, *15* (10), 5683–5695. DOI: 10.5194/acp-15-5683-2015.

(49)   Orlando, J. J.; Tyndall, G. S. Laboratory Studies of Organic Peroxy Radical Chemistry: An Overview with Emphasis on Recent Issues of Atmospheric Significance. *Chem. Soc. Rev.* **2012**, *41* (19), 6294. DOI: 10.1039/c2cs35166h.

(50)   Eddingsaas, N. C.; Loza, C. L.; Yee, L. D.; Seinfeld, J. H.; Wennberg, P. O. α-Pinene Photooxidation under Controlled Chemical Conditions – Part 1: Gas-Phase Composition in Low- and High-NO_x Environments. *Atmos. Chem. Phys.* **2012**, *12* (14), 6489–6504. DOI: 10.5194/acp-12-6489-2012.

(51)   Saunders, S. M.; Jenkin, M. E.; Derwent, R. G.; Pilling, M. J. Protocol for the Development of the Master Chemical Mechanism, MCM v3 (Part A): Tropospheric Degradation of Non-Aromatic Volatile Organic Compounds. *Atmos. Chem. Phys.* **2003**, *3* (1), 161–180. DOI: 10.5194/acp-3-161-2003.

(52)   Schwantes, R. H.; McVay, R. C.; Zhang, X.; Coggon, M. M.; Lignell, H.; Flagan, R. C.; Wennberg, P. O.; Seinfeld, J. H. Science of the Environmental Chamber. In *Advances in Atmospheric Chemistry*; Barker, J. R., Steiner, A. L., Wallington, T. J., Eds.; World Scientific: Singapore, 2017; pp 1–93. DOI: 10.1142/9789813147355_0001.

(53)   Loza, C. L.; Craven, J. S.; Yee, L. D.; Coggon, M. M.; Schwantes, R. H.; Shiraiwa, M.; Zhang, X.; Schilling, K. A.; Ng, N. L.; Canagaratna, M. R.; Ziemann, P. J.; Flagan, R. C.; Seinfeld, J. H. Secondary Organic Aerosol Yields of 12-Carbon Alkanes. *Atmos. Chem. Phys.* **2014**, *14* (3), 1423–1439. DOI: 10.5194/acp-14-1423-2014.

(54)   Huang, Y.; Coggon, M. M.; Zhao, R.; Lignell, H.; Bauer, M. U.; Flagan, R. C.; Seinfeld, J. H. The Caltech Photooxidation Flow Tube Reactor: Design, Fluid Dynamics and Characterization. *Atmos. Meas. Tech.* **2017**, *10* (3), 839–867. DOI: 10.5194/amt-10-839-2017.

(55) Ma, Y.; Marston, G. Multifunctional Acid Formation from the Gas-Phase Ozonolysis of β-Pinene. *Phys. Chem. Chem. Phys.* **2008**, *10* (40), 6115. DOI: 10.1039/b807863g.

(56) Bird, R. B.; Stewart, W. E.; Lightfoot, E. N. *Transport Phenomena*, 2nd ed.; Wiley: New York, NY, 2007.

(57) Keywood, M. D.; Kroll, J. H.; Varutbangkul, V.; Bahreini, R.; Flagan, R. C.; Seinfeld, J. H. Secondary Organic Aerosol Formation from Cyclohexene Ozonolysis: Effect of OH Scavenger and the Role of Radical Chemistry. *Environ. Sci. Technol.* **2004**, *38* (12), 3343–3350. DOI: 10.1021/es049725j.

(58) Seinfeld, J. H.; Pandis, S. N. *Atmospheric Chemistry and Physics: From Air Pollution to Climate Change*, 3rd ed.; Wiley: Hoboken, NJ, 2016.

(59) Taatjes, C. A. Criegee Intermediates: What Direct Production and Detection Can Teach Us About Reactions of Carbonyl Oxides. *Annu. Rev. Phys. Chem.* **2017**, *68* (1), 183–207. DOI: 10.1146/annurev-physchem-052516-050739.

(60) Anglada, J. M.; Solé, A. Impact of the Water Dimer on the Atmospheric Reactivity of Carbonyl Oxides. *Phys. Chem. Chem. Phys.* **2016**, *18* (26), 17698–17712. DOI: 10.1039/C6CP02531E.

(61) Shillings, A. J. L.; Ball, S. M.; Barber, M. J.; Tennyson, J.; Jones, R. L. An Upper Limit for Water Dimer Absorption in the 750 nm Spectral Region and a Revised Water Line List. *Atmos. Chem. Phys.* **2011**, *11* (9), 4273–4287. DOI: 10.5194/acp-11-4273-2011.

(62) Wozniak, A. S.; Bauer, J. E.; Sleighter, R. L.; Dickhut, R. M.; Hatcher, P. G. Technical Note: Molecular Characterization of Aerosol-Derived Water Soluble Organic Carbon Using Ultrahigh Resolution Electrospray Ionization Fourier Transform Ion Cyclotron Resonance Mass Spectrometry. *Atmos. Chem. Phys.* **2008**, *8* (17), 5099–5111. DOI: 10.5194/acp-8-5099-2008.

(63) Putman, A. L.; Offenberg, J. H.; Fisseha, R.; Kundu, S.; Rahn, T. A.; Mazzoleni, L. R. Ultrahigh-Resolution FT-ICR Mass Spectrometry Characterization of α-Pinene Ozonolysis SOA. *Atmos. Environ.* **2012**, *46*, 164–172. DOI: 10.1016/j.atmosenv.2011.10.003.

(64) Kristensen, K.; Jensen, L. N.; Glasius, M.; Bilde, M. The Effect of Sub-Zero Temperature on the Formation and Composition of Secondary Organic Aerosol from Ozonolysis of Alpha-Pinene. *Environ. Sci.: Processes Impacts* **2017**, *19* (10), 1220–1234. DOI: 10.1039/C7EM00231A.

(65) Sharpe, S. W.; Sams, R. L.; Johnson, T. J. The PNNL Quantitative IR Database for Infrared Remote Sensing and Hyperspectral Imaging. In *Applied Imagery Pattern Recognition Workshop, 2002. Proceedings.*; IEEE

Comput. Soc: Washington, DC, USA, 2002; pp 45–48. DOI: 10.1109/AIPR.2002.1182253.

(66) Bahreini, R.; Keywood, M. D.; Ng, N. L.; Varutbangkul, V.; Gao, S.; Flagan, R. C.; Seinfeld, J. H.; Worsnop, D. R.; Jimenez, J. L. Measurements of Secondary Organic Aerosol from Oxidation of Cycloalkenes, Terpenes, and *m*-Xylene Using an Aerodyne Aerosol Mass Spectrometer. *Environ. Sci. Technol.* **2005**, *39* (15), 5674–5688. DOI: 10.1021/es048061a.

(67) Malloy, Q. G. J.; Nakao, S.; Qi, L.; Austin, R.; Stothers, C.; Hagino, H.; Cocker, D. R. Real-Time Aerosol Density Determination Utilizing a Modified Scanning Mobility Particle Sizer—Aerosol Particle Mass Analyzer System. *Aerosol Sci. Technol.* **2009**, *43* (7), 673–678. DOI: 10.1080/02786820902832960.

(68) Shilling, J. E.; Chen, Q.; King, S. M.; Rosenoern, T.; Kroll, J. H.; Worsnop, D. R.; DeCarlo, P. F.; Aiken, A. C.; Sueper, D.; Jimenez, J. L.; Martin, S. T. Loading-Dependent Elemental Composition of α-Pinene SOA Particles. *Atmos. Chem. Phys.* **2009**, *9* (3), 771–782. DOI: 10.5194/acp-9-771-2009.

(69) Saathoff, H.; Naumann, K.-H.; Möhler, O.; Jonsson, Å. M.; Hallquist, M.; Kiendler-Scharr, A.; Mentel, Th. F.; Tillmann, R.; Schurath, U. Temperature Dependence of Yields of Secondary Organic Aerosols from the Ozonolysis of α-Pinene and Limonene. *Atmos. Chem. Phys.* **2009**, *9* (5), 1551–1577. DOI: 10.5194/acp-9-1551-2009.

(70) Kourtchev, I.; Copolovici, L.; Claeys, M.; Maenhaut, W. Characterization of Atmospheric Aerosols at a Forested Site in Central Europe. *Environ. Sci. Technol.* **2009**, *43* (13), 4665–4671. DOI: 10.1021/es803055w.

(71) Vogel, A. L.; Äijälä, M.; Corrigan, A. L.; Junninen, H.; Ehn, M.; Petäjä, T.; Worsnop, D. R.; Kulmala, M.; Russell, L. M.; Williams, J.; Hoffmann, T. In Situ Submicron Organic Aerosol Characterization at a Boreal Forest Research Station during HUMPPA-COPEC 2010 Using Soft and Hard Ionization Mass Spectrometry. *Atmos. Chem. Phys.* **2013**, *13* (21), 10933–10950. DOI: 10.5194/acp-13-10933-2013.

(72) Vestenius, M.; Hellén, H.; Levula, J.; Kuronen, P.; Helminen, K. J.; Nieminen, T.; Kulmala, M.; Hakola, H. Acidic Reaction Products of Monoterpenes and Sesquiterpenes in Atmospheric Fine Particles in a Boreal Forest. *Atmos. Chem. Phys.* **2014**, *14* (15), 7883–7893. DOI: 10.5194/acp-14-7883-2014.

(73) Isaacman-VanWertz, G.; Yee, L. D.; Kreisberg, N. M.; Wernis, R.; Moss, J. A.; Hering, S. V.; de Sá, S. S.; Martin, S. T.; Alexander, M. L.; Palm, B. B.; Hu, W.; Campuzano-Jost, P.; Day, D. A.; Jimenez, J. L.; Riva, M.; Surratt, J. D.; Viegas, J.; Manzi, A.; Edgerton, E.; Baumann, K.; Souza, R.; Artaxo, P.; Goldstein, A. H. Ambient Gas-Particle Partitioning of Tracers

for Biogenic Oxidation. *Environ. Sci. Technol.* **2016**, *50* (18), 9952–9962. DOI: 10.1021/acs.est.6b01674.

(74)   DeCarlo, P. F.; Kimmel, J. R.; Trimborn, A.; Northway, M. J.; Jayne, J. T.; Aiken, A. C.; Gonin, M.; Fuhrer, K.; Horvath, T.; Docherty, K. S.; Worsnop, D. R.; Jimenez, J. L. Field-Deployable, High-Resolution, Time-of-Flight Aerosol Mass Spectrometer. *Anal. Chem.* **2006**, *78* (24), 8281–8289. DOI: 10.1021/ac061249n.

(75)   Allan, J. D.; Delia, A. E.; Coe, H.; Bower, K. N.; Alfarra, M. R.; Jimenez, J. L.; Middlebrook, A. M.; Drewnick, F.; Onasch, T. B.; Canagaratna, M. R.; Jayne, J. T.; Worsnop, D. R. A Generalised Method for the Extraction of Chemically Resolved Mass Spectra from Aerodyne Aerosol Mass Spectrometer Data. *J. of Aerosol Sci.* **2004**, *35* (7), 909–922. DOI: 10.1016/j.jaerosci.2004.02.007.

(76)   Aiken, A. C.; DeCarlo, P. F.; Kroll, J. H.; Worsnop, D. R.; Huffman, J. A.; Docherty, K. S.; Ulbrich, I. M.; Mohr, C.; Kimmel, J. R.; Sueper, D.; Sun, Y.; Zhang, Q.; Trimborn, A.; Northway, M.; Ziemann, P. J.; Canagaratna, M. R.; Onasch, T. B.; Alfarra, M. R.; Prevot, A. S. H.; Dommen, J.; Duplissy, J.; Metzger, A.; Baltensperger, U.; Jimenez, J. L. O/C and OM/OC Ratios of Primary, Secondary, and Ambient Organic Aerosols with High-Resolution Time-of-Flight Aerosol Mass Spectrometry. *Environ. Sci. Technol.* **2008**, *42* (12), 4478–4485. DOI: 10.1021/es703009q.

(77)   Middlebrook, A. M.; Bahreini, R.; Jimenez, J. L.; Canagaratna, M. R. Evaluation of Composition-Dependent Collection Efficiencies for the Aerodyne Aerosol Mass Spectrometer Using Field Data. *Aerosol Sci. Technol.* **2012**, *46* (3), 258–271. DOI: 10.1080/02786826.2011.620041.

(78)   Canagaratna, M. R.; Jimenez, J. L.; Kroll, J. H.; Chen, Q.; Kessler, S. H.; Massoli, P.; Hildebrandt Ruiz, L.; Fortner, E.; Williams, L. R.; Wilson, K. R.; Surratt, J. D.; Donahue, N. M.; Jayne, J. T.; Worsnop, D. R. Elemental Ratio Measurements of Organic Compounds Using Aerosol Mass Spectrometry: Characterization, Improved Calibration, and Implications. *Atmos. Chem. Phys.* **2015**, *15* (1), 253–272. DOI: 10.5194/acp-15-253-2015.

(79)   Chhabra, P. S.; Flagan, R. C.; Seinfeld, J. H. Elemental Analysis of Chamber Organic Aerosol Using an Aerodyne High-Resolution Aerosol Mass Spectrometer. *Atmos. Chem. Phys.* **2010**, *10* (9), 4111–4131. DOI: 10.5194/acp-10-4111-2010.

(80)   Chen, Q.; Liu, Y.; Donahue, N. M.; Shilling, J. E.; Martin, S. T. Particle-Phase Chemistry of Secondary Organic Material: Modeled Compared to Measured O:C and H:C Elemental Ratios Provide Constraints. *Environ. Sci. Technol.* **2011**, *45* (11), 4763–4770. DOI: 10.1021/es104398s.

(81)   Donahue, N. M.; Henry, K. M.; Mentel, T. F.; Kiendler-Scharr, A.; Spindler, C.; Bohn, B.; Brauers, T.; Dorn, H. P.; Fuchs, H.; Tillmann, R.; Wahner, A.; Saathoff, H.; Naumann, K.-H.; Mohler, O.; Leisner, T.; Muller, L.; Reinnig, M.-C.; Hoffmann, T.; Salo, K.; Hallquist, M.; Frosch, M.; Bilde, M.; Tritscher, T.; Barmet, P.; Praplan, A. P.; DeCarlo, P. F.; Dommen, J.; Prevot, A. S. H.; Baltensperger, U. Aging of Biogenic Secondary Organic Aerosol via Gas-Phase OH Radical Reactions. *Proc. Natl. Acad. Sci. U.S.A.* **2012**, *109* (34), 13503–13508. DOI: 10.1073/pnas.1115186109.

(82)   Nakao, S.; Tang, P.; Tang, X.; Clark, C. H.; Qi, L.; Seo, E.; Asa-Awuku, A.; Cocker, D. Density and Elemental Ratios of Secondary Organic Aerosol: Application of a Density Prediction Method. *Atmos. Environ.* **2013**, *68*, 273–277. DOI: 10.1016/j.atmosenv.2012.11.006.

(83)   Chhabra, P. S.; Ng, N. L.; Canagaratna, M. R.; Corrigan, A. L.; Russell, L. M.; Worsnop, D. R.; Flagan, R. C.; Seinfeld, J. H. Elemental Composition and Oxidation of Chamber Organic Aerosol. *Atmos. Chem. Phys.* **2011**, *11* (17), 8827–8845. DOI: 10.5194/acp-11-8827-2011.

(84)   Weber, R. J.; Orsini, D.; Daun, Y.; Lee, Y.-N.; Klotz, P. J.; Brechtel, F. A Particle-into-Liquid Collector for Rapid Measurement of Aerosol Bulk Chemical Composition. *Aerosol Sci. Technol.* **2001**, *35* (3), 718–727. DOI: 10.1080/02786820152546761.

(85)   Sorooshian, A.; Brechtel, F. J.; Ma, Y.; Weber, R. J.; Corless, A.; Flagan, R. C.; Seinfeld, J. H. Modeling and Characterization of a Particle-into-Liquid Sampler (PILS). *Aerosol Sci. Technol.* **2006**, *40* (6), 396–409. DOI: 10.1080/02786820600632282.

(86)   Mikuška, P.; Večeřa, Z.; Bartošíková, A.; Maenhaut, W. Annular Diffusion Denuder for Simultaneous Removal of Gaseous Organic Compounds and Air Oxidants during Sampling of Carbonaceous Aerosols. *Anal. Chim. Acta* **2012**, *714*, 68–75. DOI: 10.1016/j.aca.2011.11.054.

(87)   Mutzel, A.; Rodigast, M.; Iinuma, Y.; Böge, O.; Herrmann, H. An Improved Method for the Quantification of SOA Bound Peroxides. *Atmos. Environ.* **2013**, *67*, 365–369. DOI: 10.1016/j.atmosenv.2012.11.012.

(88)   *CRC Handbook of Chemistry and Physics*, 92nd ed.; Haynes, W., Lide, D., Eds.; CRC Press: Boca Raton, FL, 2010.

(89)   Nichols, M. A.; Waner, M. J. Kinetic and Mechanistic Studies of the Deuterium Exchange in Classical Keto−Enol Tautomeric Equilibrium Reactions. *J. Chem. Educ.* **2010**, *87* (9), 952–955. DOI: 10.1021/ed100292r.

(90)   Jenkin, M. E. Modelling the Formation and Composition of Secondary Organic Aerosol from α- and β-Pinene Ozonolysis Using MCM v3. *Atmos. Chem. Phys.* **2004**, *4* (7), 1741–1757. DOI: 10.5194/acp-4-1741-2004.

(91)   Mertes, P.; Pfaffenberger, L.; Dommen, J.; Kalberer, M.; Baltensperger, U. Development of a Sensitive Long Path Absorption Photometer to Quantify Peroxides in Aerosol Particles (Peroxide-LOPAP). *Atmos. Meas. Tech.* **2012**, *5* (10), 2339–2348. DOI: 10.5194/amt-5-2339-2012.

(92)   Epstein, S. A.; Blair, S. L.; Nizkorodov, S. A. Direct Photolysis of α-Pinene Ozonolysis Secondary Organic Aerosol: Effect on Particle Mass and Peroxide Content. *Environ. Sci. Technol.* **2014**, *48* (19), 11251–11258. DOI: 10.1021/es502350u.

(93)   Li, H.; Chen, Z.; Huang, L.; Huang, D. Organic Peroxides' Gas-Particle Partitioning and Rapid Heterogeneous Decomposition on Secondary Organic Aerosol. *Atmos. Chem. Phys.* **2016**, *16* (3), 1837–1848. DOI: 10.5194/acp-16-1837-2016.

(94)   Krapf, M.; El Haddad, I.; Bruns, E. A.; Molteni, U.; Daellenbach, K. R.; Prévôt, A. S. H.; Baltensperger, U.; Dommen, J. Labile Peroxides in Secondary Organic Aerosol. *Chem* **2016**, *1* (4), 603–616. DOI: 10.1016/j.chempr.2016.09.007.

(95)   Riva, M.; Budisulistiorini, S. H.; Zhang, Z.; Gold, A.; Thornton, J. A.; Turpin, B. J.; Surratt, J. D. Multiphase Reactivity of Gaseous Hydroperoxide Oligomers Produced from Isoprene Ozonolysis in the Presence of Acidified Aerosols. *Atmos. Environ.* **2017**, *152*, 314–322. DOI: 10.1016/j.atmosenv.2016.12.040.

(96)   Tong, H.; Arangio, A. M.; Lakey, P. S. J.; Berkemeier, T.; Liu, F.; Kampf, C. J.; Brune, W. H.; Pöschl, U.; Shiraiwa, M. Hydroxyl Radicals from Secondary Organic Aerosol Decomposition in Water. *Atmos. Chem. Phys.* **2016**, *16* (3), 1761–1771. DOI: 10.5194/acp-16-1761-2016.

(97)   Wang, Y.; Kim, H.; Paulson, S. E. Hydrogen Peroxide Generation from α- and β-Pinene and Toluene Secondary Organic Aerosols. *Atmos. Environ.* **2011**, *45* (18), 3149–3156. DOI: 10.1016/j.atmosenv.2011.02.060.

(98)   Badali, K. M.; Zhou, S.; Aljawhary, D.; Antiñolo, M.; Chen, W. J.; Lok, A.; Mungall, E.; Wong, J. P. S.; Zhao, R.; Abbatt, J. P. D. Formation of Hydroxyl Radicals from Photolysis of Secondary Organic Aerosol Material. *Atmos. Chem. Phys.* **2015**, *15* (14), 7831–7840. DOI: 10.5194/acp-15-7831-2015.

(99)   Crounse, J. D.; Nielsen, L. B.; Jørgensen, S.; Kjaergaard, H. G.; Wennberg, P. O. Autoxidation of Organic Compounds in the Atmosphere. *J. Phys. Chem. Lett.* **2013**, *4* (20), 3513–3520. DOI: 10.1021/jz4019207.

(100)   DePalma, J. W.; Horan, A. J.; Hall IV, W. A.; Johnston, M. V. Thermodynamics of Oligomer Formation: Implications for Secondary Organic Aerosol Formation and Reactivity. *Phys. Chem. Chem. Phys.* **2013**, *15* (18), 6935. DOI: 10.1039/c3cp44586k.

(101) Yatavelli, R. L. N.; Stark, H.; Thompson, S. L.; Kimmel, J. R.; Cubison, M. J.; Day, D. A.; Campuzano-Jost, P.; Palm, B. B.; Hodzic, A.; Thornton, J. A.; Jayne, J. T.; Worsnop, D. R.; Jimenez, J. L. Semicontinuous Measurements of Gas–Particle Partitioning of Organic Acids in a Ponderosa Pine Forest Using a MOVI-HRToF-CIMS. *Atmos. Chem. Phys.* **2014**, *14* (3), 1527–1546. DOI: 10.5194/acp-14-1527-2014.

(102) Konermann, L.; Ahadi, E.; Rodriguez, A. D.; Vahidi, S. Unraveling the Mechanism of Electrospray Ionization. *Anal. Chem.* **2013**, *85* (1), 2–9. DOI: 10.1021/ac302789c.

(103) Sato, K.; Jia, T.; Tanabe, K.; Morino, Y.; Kajii, Y.; Imamura, T. Terpenylic Acid and Nine-Carbon Multifunctional Compounds Formed during the Aging of β-Pinene Ozonolysis Secondary Organic Aerosol. *Atmos. Environ.* **2016**, *130*, 127–135. DOI: 10.1016/j.atmosenv.2015.08.047.

(104) Kruve, A.; Kaupmees, K.; Liigand, J.; Leito, I. Negative Electrospray Ionization via Deprotonation: Predicting the Ionization Efficiency. *Anal. Chem.* **2014**, *86* (10), 4822–4830. DOI: 10.1021/ac404066v.

(105) Klamt, A. Conductor-like Screening Model for Real Solvents: A New Approach to the Quantitative Calculation of Solvation Phenomena. *J. Phys. Chem.* **1995**, *99* (7), 2224–2235. DOI: 10.1021/j100007a062.

(106) Klamt, A. *COSMO-RS: From Quantum Chemistry to Fluid Phase Thermodynamics and Drug Design*; Elsevier: Amsterdam, Netherlands, 2005.

(107) Pye, C. C.; Ziegler, T.; van Lenthe, E.; Louwen, J. N. An Implementation of the Conductor-Like Screening Model of Solvation within the Amsterdam Density Functional Package — Part II. COSMO for Real Solvents. *Can. J. Chem.* **2009**, *87* (7), 790–797. DOI: 10.1139/V09-008.

(108) Kaupmees, K.; Kaljurand, I.; Leito, I. Influence of Water Content on the Acidities in Acetonitrile. Quantifying Charge Delocalization in Anions. *J. Phys. Chem. A* **2010**, *114* (43), 11788–11793. DOI: 10.1021/jp105670t.

(109) Eckert, F.; Diedenhofen, M.; Klamt, A. Towards a First Principles Prediction of pK_a: COSMO-RS and the Cluster-Continuum Approach. *Mol. Phys.* **2010**, *108* (3–4), 229–241. DOI: 10.1080/00268970903313667.

(110) Espinosa, S.; Bosch, E.; Rosés, M. Retention of Ionizable Compounds in High-Performance Liquid Chromatography: 14. Acid-Base p*K* Values in Acetonitrile-Water Mobile Phase. *J. Chromatogr. A* **2002**, *964* (1–2), 55–66. DOI: 10.1016/S0021-9673(02)00558-7.

(111) Ryerson, T. B.; Andrews, A. E.; Angevine, W. M.; Bates, T. S.; Brock, C. A.; Cairns, B.; Cohen, R. C.; Cooper, O. R.; de Gouw, J. A.; Fehsenfeld, F. C.; Ferrare, R. A.; Fischer, M. L.; Flagan, R. C.; Goldstein, A. H.; Hair, J. W.; Hardesty, R. M.; Hostetler, C. A.; Jimenez, J. L.; Langford, A. O.;

McCauley, E.; McKeen, S. A.; Molina, L. T.; Nenes, A.; Oltmans, S. J.; Parrish, D. D.; Pederson, J. R.; Pierce, R. B.; Prather, K.; Quinn, P. K.; Seinfeld, J. H.; Senff, C. J.; Sorooshian, A.; Stutz, J.; Surratt, J. D.; Trainer, M.; Volkamer, R.; Williams, E. J.; Wofsy, S. C. The 2010 California Research at the Nexus of Air Quality and Climate Change (CalNex) Field Study. *J. Geophys. Res. Atmos.* **2013**, *118* (11), 5830–5866. DOI: 10.1002/jgrd.50331.

Chapter 3

SYNTHESIS OF CARBOXYLIC ACID AND DIMER ESTER SURROGATES TO CONSTRAIN THE ABUNDANCE AND DISTRIBUTION OF MOLECULAR PRODUCTS IN α-PINENE AND β-PINENE SECONDARY ORGANIC AEROSOL

Abstract

Liquid chromatography/negative electrospray ionization mass spectrometry [LC/(–)ESI-MS] is routinely employed to characterize the identity and abundance of molecular products in secondary organic aerosol (SOA) derived from monoterpene oxidation. Due to a lack of authentic standards, however, commercial terpenoic acids (e.g., *cis*-pinonic acid) are typically used as surrogates to quantify both monomeric and dimeric SOA constituents. Here, we synthesize a series of enantiopure, pinene-derived carboxylic acid and dimer ester homologues. We find that the (–)ESI efficiencies of the dimer esters are 19–36 times higher than that of *cis*-pinonic acid, demonstrating that the mass contribution of dimers to monoterpene SOA has been significantly overestimated in past studies. Using the measured (–)ESI efficiencies of the carboxylic acids and dimer esters as more representative surrogates, we determine that molecular products measurable by LC/(–)ESI-MS account for only 21.8 ± 2.6% and 18.9 ± 3.2% of the mass of SOA formed from ozonolysis of α-pinene and β-pinene, respectively. The 28–36 identified monomers ($C_{7–10}H_{10–18}O_{3–6}$) constitute 15.6–20.5% of total SOA mass, whereas only 1.3–3.3% of the SOA mass is attributable to the 46–62 identified dimers ($C_{15–19}H_{24–32}O_{4–11}$). The distribution of identified α-pinene and β-pinene SOA molecular products is examined as a function of carbon number (n_C), average carbon oxidation state ($\overline{OS_C}$), and volatility (C^*). The

observed order-of-magnitude difference in (−)ESI efficiency between monomers and dimers is expected to be broadly applicable to other biogenic and anthropogenic SOA systems analyzed via (−) or (+) LC/ESI-MS under various LC conditions, and demonstrates that the use of unrepresentative surrogates can lead to substantial systematic errors in quantitative LC/ESI-MS analyses of SOA.

3.1 Introduction

Secondary organic aerosol (SOA) comprises a substantial mass fraction (15–80%) of atmospheric fine particulate matter (PM$_{2.5}$),[1] and plays a pivotal role in climate,[2] air quality, and health.[3,4] Monoterpenes (C$_{10}$H$_{16}$), emitted in large quantities from terrestrial vegetation (~150 Tg y^{-1}),[5] represent a dominant source of SOA globally.[6–9] Deciphering the molecular composition, and in turn formation mechanisms, of monoterpene SOA is essential to reducing uncertainty in assessment of its environmental and health impacts. However, molecular characterization of monoterpene SOA is significantly hindered by its chemical complexity.[10]

Electrospray ionization mass spectrometry (ESI-MS), typically coupled with liquid chromatographic (LC) separation, is among the most widely used analytical techniques for identification and quantification of SOA molecular constituents.[10,11] Multifunctional carboxylic acids and dimer esters have been identified via ESI-MS methods as significant components of both laboratory-derived[12–37] and ambient[16–18,24,26,27,29,38] monoterpene SOA, reportedly accounting for as much as 58% of chamber-generated SOA mass from α-pinene ozonolysis.[31] Due to a lack of authentic standards, the abundances of molecular products in monoterpene SOA are (*i*) represented as (mass-weighted) fractions of the total ion signal/chromatographic peak area[20–22,37] or (*ii*) quantified using commercially available terpenoic acids (e.g., *cis*-pinonic acid) as surrogates.[23,25,27–33] However, given the strong dependence of ESI efficiency on molecular structure,[39–42] these approaches could lead to inaccurate apportionment of monoterpene SOA mass.

In this work, we synthesize a series of enantiopure, pinene-derived carboxylic acid and dimer ester homologues to determine the effect of molecular size and functionality on the ESI efficiency of monoterpene SOA constituents. Using the measured ESI efficiencies of the carboxylic acids and dimer esters as more representative proxies for those of like-structured monomers and dimers, respectively, we quantify the abundances of the most extensive suite of molecular products identified to date in SOA derived from ozonolysis of α-pinene and β-pinene, which together account for over 50% of global monoterpene emissions.[5]

3.2 Experimental

3.2.1 Synthesis of Carboxylic Acids and Dimer Esters

(+)-*cis*-Pinonic acid (**1**), (+)-*cis*-pinic acid (**2**), and (+)-*cis*-pinolic acid (**3**) were prepared according to modified literature procedures[43,44] from commercial (+)-α-pinene (98%, 89% ee, Sigma-Aldrich) in 56–88% yield (Scheme 3.1). Dimer esters **4–6** were synthesized as single stereoisomers in 38–59% yield from alcohol **3a** via Steglich esterification followed by Pd/C-catalyzed hydrogenolysis (Scheme 3.1). Experimental procedures, characterization data, and NMR and IR spectra for carboxylic acids **1–3,** dimer esters **4–6**, and all synthetic intermediates are provided in the Supporting Information (SI).

3.2.2 SOA Formation Experiments

α-Pinene and β-pinene ozonolysis experiments were carried out in the Caltech dual 24 m^3 Teflon Environmental Chambers (CTEC).[45] Experimental conditions are reported in Table 3.1 and time series of reactants/products for a representative experiment are shown in Figure 3.S1. Prior to each experiment, the chamber was flushed with dry, purified air for 24 h such that the particle number and volume concentrations were less than 10 cm^{-3} and 0.01 μm^3 cm^{-3}, respectively. α-Pinene or β-pinene (~100 ppb) was added to the chamber by passing dry, purified air through a glass cylinder, warmed to 50 °C with electrical heat tape, containing a volumetric injection (15.5 μL) of liquid (+)-α-pinene (≥99%, Sigma-Aldrich) or (−)-β-pinene
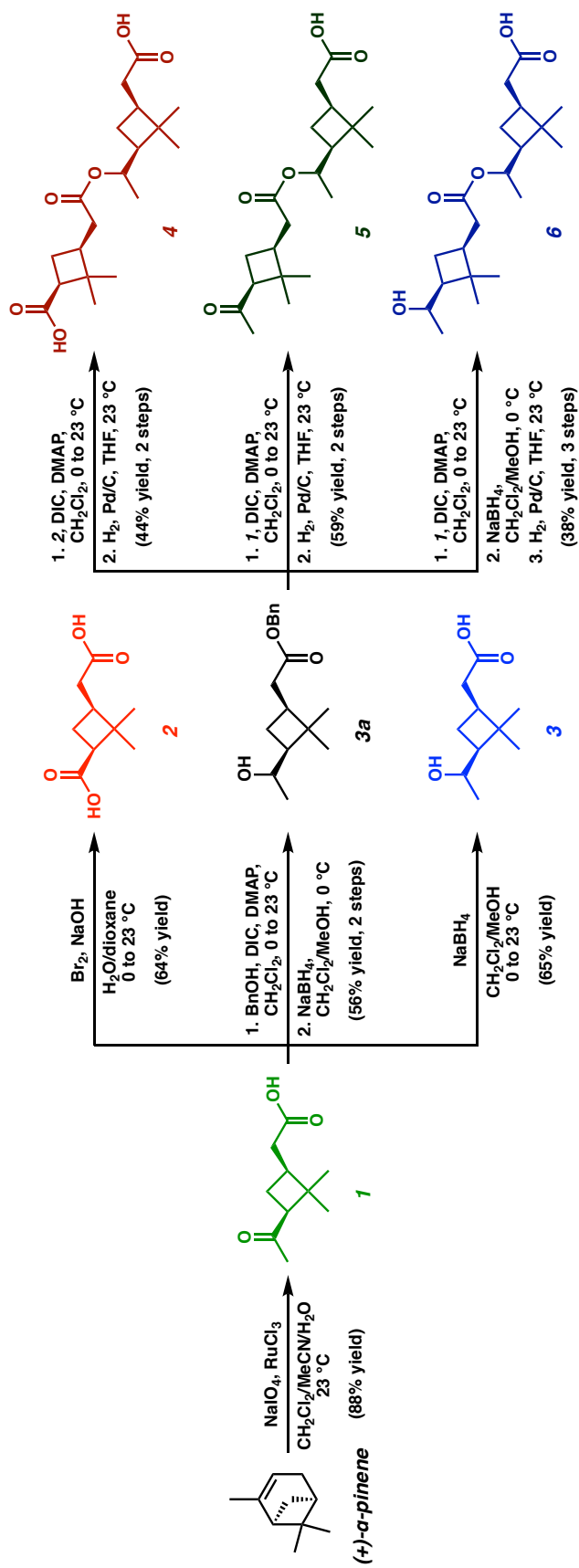
Scheme 3.1. Synthesis of carboxylic acids **1–3** and dimer esters **4–6** from commercially available (+)-α-pinene. In cases where epimers were generated via reduction of ketones with NaBH₄ (i.e., compounds **3**, **3a**, and **6**), only the major epimer was isolated but the relative stereochemistry remains unassigned.

Table 3.1. Initial conditions and SOA properties for α-pinene and β-pinene ozonolysis experiments in the CTEC.[a,b]

VOC	Exp.	$[VOC]_0$ (ppb)	$[O_3]_0$ (ppb)	$[(NH_4)_2SO_4]_0$ ($\mu m^3\,cm^{-3}$)	$[SOA]$ ($\mu g\,m^{-3}$)[c]	Bulk O:C[c]	Bulk $\overline{OS}_C$[c,d]	SOA Mass Fraction (%)[c,e]		
								Monomer	Dimer	Total
α-Pinene	1–4	104 ± 5	150	86–223	232 ± 26	0.41 ± 0.01	−0.87 ± 0.02	20.5 ± 2.5	1.3 ± 0.1	21.8 ± 2.6
β-Pinene	5–9	95 ± 2	150	137–283	78 ± 14	0.36 ± 0.01	−0.92 ± 0.02	15.6 ± 2.7	3.3 ± 0.6	18.9 ± 3.2

[a] ~5-h duration; T_0 = 295 ± 2 K; P = 1 atm; RH < 5%; $[NO_x]_0$ < 0.5 ppb; no OH scavenger.
[b] Data are reported as averages (1σ) of replicate experiments for α-pinene (n = 4) and β-pinene (n = 5).
[c] Calculated for suspended SOA after ~5 h of ozonolysis (see Figure 3.1).
[d] Average carbon oxidation state ($\overline{OS}_C$ = 2 O:C − H:C).
[e] Method uncertainty is estimated to be ±23% (relative). See Experimental for details.

(≥99%, Sigma-Aldrich). Polydisperse seed aerosol (~90–280 $\mu m^3\ cm^{-3}$, $\overline{D}_p \approx 144 \pm 17$ nm) was generated via atomization of a dilute (0.06 M) aqueous solution of $(NH_4)_2SO_4$ (Macron Fine Chemicals), followed by diffusive drying and neutralization. O_3 (~150 ppb) was produced by flowing dry, purified air through a custom-built UV O_3 generator. Ozonolysis experiments were conducted in the absence of an OH scavenger, resulting in initial OH molar yields for α-pinene and β-pinene of 77–89%[46,47] and 28–44%,[48,49] respectively. Under these conditions, ~97% of α-pinene and ~58% of β-pinene was consumed over ~5 h of reaction in the CTEC.

3.2.3   Gas-Phase Instrumentation

α-Pinene and β-pinene mixing ratios were quantified with an Agilent 6890N gas chromatograph equipped with a flame ionization detector (GC/FID) and operated with an Agilent HP-5 column (30 m × 0.32 mm, 0.25 μm). The GC/FID was calibrated as described in Kenseth et al.[34] α-Pinene and β-pinene decay curves over ~5 h of ozonolysis in the CTEC are shown in Figure 3.1A. O_3 and NO_x mixing ratios were quantified by a Horiba APOA-360 O_3 monitor and a Teledyne T200 NO_x analyzer, respectively. Temperature and relative humidity (RH) were monitored with a Vaisala HMM211 probe.

3.2.4   Particle-Phase Instrumentation

Scanning Mobility Particle Sizer (SMPS). Aerosol size distributions and number concentrations ($D_p \approx 15$–800 nm) were measured with a custom-built SMPS consisting of a TSI 3081 differential mobility analyzer (DMA) coupled to a TSI 3010 condensation particle counter (CPC). Details of the SMPS operation are provided elsewhere.[34,50] Suspended SOA volume concentrations were derived using the approach of Kenseth et al.,[34] and were not corrected for particle wall loss to enable direct comparison with the concentrations of individual molecular products detected in suspended SOA using off-line mass spectrometry. SOA mass concentrations were calculated assuming an effective density of 1.25 g mL^{-1} for α-pinene and β-pinene
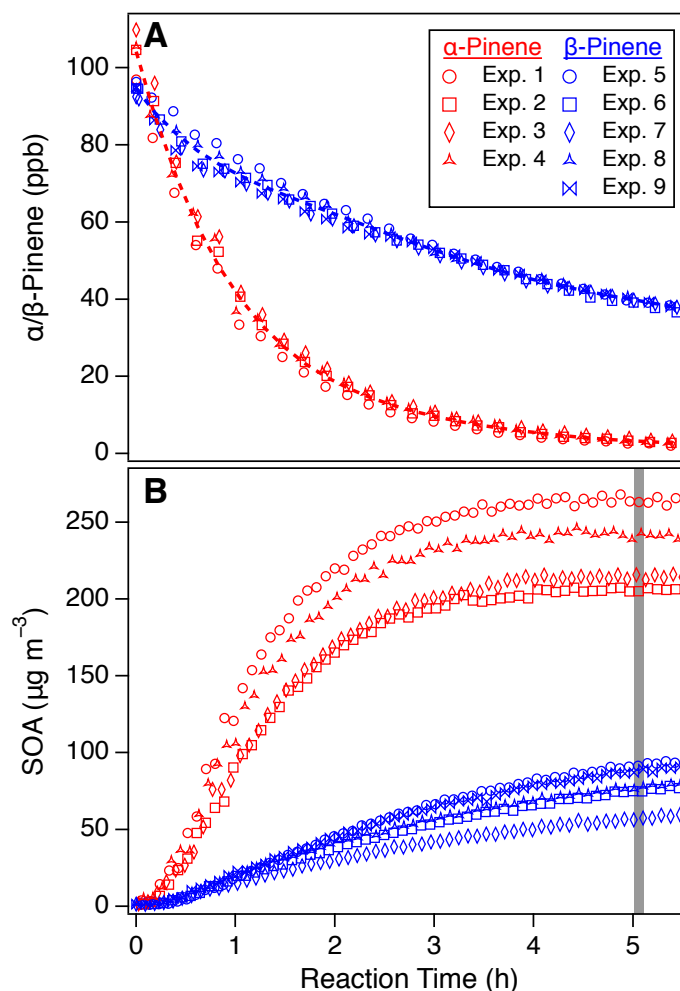
Figure 3.1. (A) GC/FID-derived decay curves and (B) SMPS-derived suspended SOA growth profiles for α-pinene and β-pinene ozonolysis experiments in the CTEC. Experimental conditions are reported in Table 3.S1. Gray bar denotes 5-min interval for which SOA mass fractions and properties were calculated in each experiment.

SOA.[51–54] Growth profiles of suspended SOA produced from ozonolysis of α-pinene and β-pinene over ~5 h of reaction in the CTEC are shown in Figure 3.1B.

High-Resolution Time-of-Flight Aerosol Mass Spectrometer (HR-ToF-AMS). Submicrometer, nonrefractory aerosol chemical composition was quantified with an Aerodyne HR-ToF-AMS[55] configured in V-mode. Detection limits and instrumental

ionization efficiencies for each class of speciated constituents (i.e., sulfate, ammonium, and organics) were determined following the methods in Kenseth et al.[34] Data were analyzed using the SQUIRREL v1.61 and PIKA v1.21 modules for Igor Pro v7.08 (WaveMetrics), and were corrected for gas-phase interferences[56,57] and composition-dependent collection efficiencies.[58] Elemental O:C and H:C ratios, as well as average carbon oxidation states ($\overline{OS}_C$ = 2 O:C – H:C), were calculated using the "Improved-Ambient" elemental analysis method for AMS spectra.[59] Average O:C and $\overline{OS}_C$ values for α-pinene and β-pinene SOA after ~5 h of ozonolysis in the CTEC are reported in Table 3.1. These values are in good agreement with O:C and H:C ratios previously reported for laboratory-derived SOA formed from α-pinene ozonolysis (O:C = 0.30–0.43; H:C = 1.47–1.66).[30,59–63]

Particle-Into-Liquid Sampler (PILS). A custom-modified PILS was used to collect chamber-generated α-pinene and β-pinene SOA for off-line, molecular-level characterization. A detailed description of the Caltech PILS is presented elsewhere.[34,64] Briefly, sampled aerosol (1-μm cut size, 12.5 L min^{-1} flow rate) is passed through successive acid, base, and organic carbon denuders into a condensation chamber where particles grow sufficiently large (D_p > 1 μm) for collection by inertial impaction via adiabatic mixing with steam generated from ultra-pure water (18.2 MΩ cm, <3 ppb TOC, Millipore Milli-Q). Impacted particles are transported to a debubbler by a washing flow (0.15 mL min^{-1}) of ultra-pure water, and the sampled liquid is delivered into vials (5-min duty cycle) held on a rotating carousel. Sample vials were stored at −16 °C immediately after collection. The overall PILS collection efficiency for α-pinene and β-pinene SOA was estimated to be >85%, based on an empirical correlation of water solubility and the AMS-derived bulk O:C ratio of the SOA.[65]

Ultra-Performance Liquid Chromatography/Negative Electrospray Ionization Quadrupole Time-of-Flight Mass Spectrometry [UPLC/(–)ESI-Q-TOF-MS]. α-Pinene and β-pinene SOA PILS samples were analyzed by a Waters ACQUITY

UPLC I-Class system coupled to a Xevo G2-S Q-TOF-MS equipped with an ESI source and operated in (−) ion mode. An ACQUITY BEH C$_{18}$ column (1.7 μm, 2.1 mm × 50 mm) fitted with an ACQUITY BEH C$_{18}$ VanGaurd pre-column (1.7 μm, 2.1 mm × 5 mm) was used to separate SOA molecular constituents. Instrument specifications, acquisition parameters (e.g., gradient-elution and MS/MS methods), and calibration procedures are detailed in Kenseth et al.[34] Note that due to the addition of the guard column, retention times (t_R) of SOA molecular products are shifted by +0.11–0.15 min compared to those reported in Kenseth et al.[34] All analytes were detected as [M–H]$^-$ ions, generated via deprotonation of parent molecules during (−)ESI. Instrument stability (i.e., chromatographic and mass spectral reproducibility) was verified to within 4% using an equimolar (1.00 μM) aqueous solution of carboxylic acids **1–3** and dimer esters **4–6**, run twice every 10 samples during routine analysis. Data were acquired and processed using MassLynx v4.1 software. Molecular formulas (C$_x$H$_y$O$_z$) of [M–H]$^-$ ions were assigned with mass tolerances of <7 ppm and supported by the associated ^{13}C isotope distributions.

3.2.5 Quantification of SOA Molecular Products

Mass concentrations of individual organic compounds in chamber-generated α-pinene and β-pinene SOA collected by PILS and analyzed off-line by UPLC/(−)ESI-Q-TOF-MS were calculated from the following expression:

$$C = \frac{Q_l \cdot DF \cdot R \cdot M}{Q_s \cdot CE_{PILS} \cdot IE} \tag{3.1}$$

where C is the particle-phase mass concentration of the compound (μg m^{-3}), Q_s is the aerosol sampling flow rate (12.5 L min^{-1}), Q_l is the rate of the washing flow (0.15 mL min^{-1}), DF is the dilution factor that accounts for water vapor condensation on the PILS impaction plate (assumed to be 1.1),[64] CE_{PILS} is the overall PILS collection efficiency for α-pinene and β-pinene SOA (estimated to be 0.85),[65] R is the UPLC/(−)ESI-Q-TOF-MS response for the compound [i.e., extracted ion

chromatogram (EIC) peak area], M is the molecular weight of the compound (g mol^{-1}), and IE is the compound-specific (−)ESI efficiency (μM^{-1}). Prior separation of analytes from the complex SOA matrix via UPLC precludes potential ion-source artifacts (e.g., signal suppression and noncovalent clustering), ensuring the quantitative nature of the method. From comparison of the resulting particle-phase mass concentrations to the SMPS-derived suspended SOA mass loading, mass fractions of identified molecular products in α-pinene and β-pinene SOA were determined.

Due to a lack of authentic standards, (−)ESI efficiencies of monomers and dimers identified in α-pinene and β-pinene SOA were quantified using those measured for carboxylic acids **1–3** and dimer esters **4–6** as surrogates. Weighted (1/X), linear (R^2 > 0.998) calibration curves were generated from triplicate measurements of equimolar aqueous solutions of carboxylic acids **1–3** and dimer esters **4–6** spanning a concentration range from 0.200 to 5.00 µM (Figure 3.2); all surrogates were fully water soluble at 5.00 µM (295 K, 1 atm). Limits of quantitation (LOQ), calculated as ten times the standard deviation of the blank ($10\sigma_{blank}$), were found to range from 1.8–2.7 nM for dimer esters **4–6** to 8.1–39 nM for carboxylic acids **1–3** and are reported in Table 3.S2, along with limits of detection (LOD, $3\sigma_{blank}$) and (−)ESI efficiencies (μM^{-1}). The concentration of every monomer and dimer measured in the PILS samples fell above the LOQ and within the calibrated linear range of the corresponding surrogate.

Uncertainty Analysis. Uncertainty in the PILS method (δ_{PILS}) arises mainly from variation in the collected liquid volume due to imperfect debubbling, and has been estimated to be less than ±11%.[65] Uncertainty associated with the chromatographic and mass spectral reproducibility of the UPLC/(−)ESI-Q-TOF-MS (δ_{UPLC}) was determined to be less than ±4% (see above). Uncertainty in the concentrations of the calibration standards for carboxylic acids **1–3** and dimer esters **4–6** due to the precision of the analytical balance and Class A volumetric glassware (δ_{CalStd}) was

calculated to be less than ±1%. Uncertainty in the measured (–)ESI efficiencies of carboxylic acids **1–3** and dimer esters **4–6** ($\delta_{(-)ESI}$) was found to be less than ±1%. An uncertainty of ±20% is assumed for SMPS-derived suspended SOA mass loadings (δ_{SMPS}).[66] Propagation of these individual uncertainties yields a total estimated relative uncertainty in the reported SOA mass fractions (δ_{total}) of ±23%:

$$\delta_{total} = \sqrt{\delta_{PILS}^2 + \delta_{UPLC}^2 + \delta_{CalStd}^2 + \delta_{(-)ESI}^2 + \delta_{SMPS}^2} = 0.23 \qquad (3.2)$$

Note, however, that this method uncertainty is not explicitly quoted in the following sections. Rather, all data are reported as averages of replicate experiments for α-pinene ($n = 4$) and β-pinene ($n = 5$) together with their standard deviations (1σ).

3.3 Results and Discussion

3.3.1 (–)ESI Efficiencies of Carboxylic Acids and Dimer Esters

Equimolar aqueous solutions of carboxylic acids **1–3** and dimer esters **4–6** were analyzed by UPLC/(–)ESI-Q-TOF-MS; a representative base peak ion (BPI) chromatogram and weighted (1/X) calibration curves are shown in Figure 3.2. Contrary to the assumptions of previous LC/(–)ESI-MS studies that monoterpene oxidation products exhibit comparable (–)ESI efficiencies due to the presence of similar structures/functional groups,[20–22] the (–)ESI efficiencies of carboxylic acids **1–3** varied by almost a factor of six despite differing only in the identity of the terminal functional group (i.e., ketone vs. carboxylic acid vs. alcohol). More strikingly, the (–)ESI efficiencies of dimer esters **4–6** were found to be 19–36 times higher than that of commercially available *cis*-pinonic acid (**1**). These findings conclusively demonstrate that as a result of fundamental differences in ionizing behavior, the mass contribution of dimers (and to a lesser extent dicarboxylic acids) to monoterpene SOA has been significantly overestimated in past studies.[20–23,25,27–33]
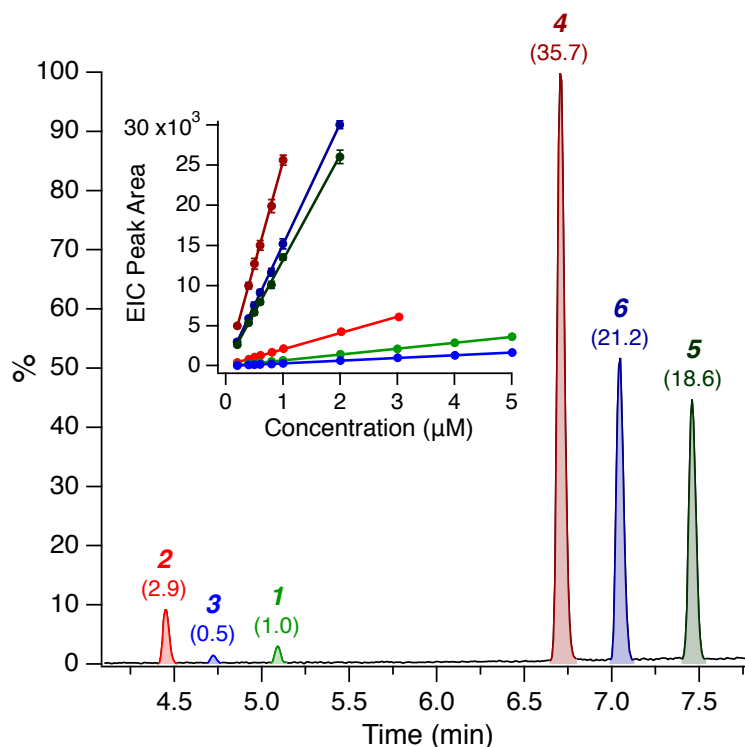
Figure 3.2. UPLC/(−)ESI-Q-TOF-MS BPI chromatogram of an equimolar (1.00 μM) aqueous solution of carboxylic acids **1−3** and dimer esters **4−6**. (−)ESI efficiencies, normalized to that of *cis*-pinonic acid (**1**), are given in parentheses. (Inset) Weighted (1/X), linear ($R^2 > 0.998$) calibration curves, generated from triplicate measurements (1σ) of equimolar aqueous solutions of carboxylic acids **1–3** and dimer esters **4–6** spanning a concentration range from 0.200 to 5.00 μM.

The observed trends in (−)ESI efficiency for carboxylic acids **1–3** and dimer esters **4–6** are consistent with the current understanding of the (−)ESI process, which for molecules <1000 Da is described by the ion evaporation model (IEM).[39] To first order, (−)ESI efficiency depends on (*i*) the degree of ionization in solution, a function of analyte acidity (pK_a) and the number of potentially ionizable (carboxyl) groups, and (*ii*) the ease of ion evaporation from the ESI droplet, which relates to the extent of ion charge delocalization and increases with molecular size (i.e., larger molecules produce ions with more delocalized charge).[41,42] Mechanistically, compounds that are more extensively dissociated in solution will yield a higher concentration of anions in ESI droplets, while anions with more delocalized charge will more readily

partition to and evaporate from ESI droplet surfaces due to lower solvation energy and a lower tendency for ion pairing (i.e., weaker interaction with solvent molecules and cations in the droplet interior).[41] For LC/(−)ESI-MS analysis of SOA molecular constituents, therefore, (−)ESI efficiencies will scale with pK_a [(−)ESI$_{strong\_acid}$ > (−)ESI$_{weak\_acid}$], the number of sites available for deprotonation [(−)ESI$_{diacid}$ ≳ 2(−)ESI$_{monoacid}$], and (most strongly) molecular weight [(−)ESI$_{dimer}$ ≳ 10(−)ESI$_{monomer}$]. Notably, the (−)ESI efficiencies estimated in our recent study for dimer esters in β-pinene SOA[34] by adapting the linear model of Kruve et al.,[41] which contains only the degree of solution ionization and anion charge delocalization as input parameters, effectively captured the order-of-magnitude difference in (−)ESI efficiency between monomers and dimers.

In addition to analyte properties, (−)ESI efficiency has been found to depend on the solvent composition of the ESI droplet.[42] Given the varying acetonitrile-water content of the gradient UPLC method (12–62% acetonitrile over t_R 3.00–7.50 min), the influence of eluent composition on the (−)ESI efficiencies of carboxylic acids **1–3** and dimer esters **4–6** was evaluated for an equimolar (1.00 µM) aqueous solution via isocratic UPLC/(−)ESI-Q-TOF-MS across a range of acetonitrile volume fractions (10–60%) (Figure 3.S2). Compared to those obtained with the gradient method, the (−)ESI efficiencies of carboxylic acids **1–3** and dimer esters **4–6** changed by only 20–50% over the respective ranges of acetonitrile content within which monomers (10–30%) and dimers (40–60%) in α-pinene and β-pinene SOA elute during gradient UPLC. In contrast, the (−)ESI efficiencies of carboxylic acids **1–3** at 60% acetonitrile were found to be 1.6–1.9 times higher than those from the gradient method. As molecular structure determines the solvent composition at which an analyte elutes from the LC column, the distinct (−)ESI behavior of monomers and dimers in LC/(−)ESI-MS, and the resultant overestimation of dimeric SOA mass fractions in past studies,[20,23,25,27–33] thus stems from both a direct (analyte properties)

and lesser indirect (ESI droplet composition) dependence of (−)ESI efficiency on molecular structure.

3.3.2 Abundance of Molecular Products in α-Pinene and β-Pinene SOA

Replicate α-pinene ($n = 4$) and β-pinene ($n = 5$) ozonolysis experiments were carried out in the CTEC (Figure 3.1, Table 3.1). PILS + UPLC/(−)ESI-Q-TOF-MS was used to characterize the SOA molecular composition (5-min average) after ~5 h of reaction; representative BPI chromatograms are shown in Figure 3.S3. A total of 36 monomers ($C_{7-10}H_{10-18}O_{3-6}$) and 46 dimers ($C_{15-19}H_{24-30}O_{4-10}$) were identified in α-pinene SOA, while 28 monomers ($C_{7-10}H_{10-18}O_{3-6}$) and 62 dimers ($C_{15-19}H_{24-32}O_{5-11}$) were identified in β-pinene SOA (Table 3.S3). Many of these compounds are isomers that elute at unique t_R. The monomers, in general, exhibit higher O:C ratios (0.30–0.75) than the dimers (0.22–0.63), suggesting that deoxygenation (e.g., condensation) is involved in dimer formation.[12,14,34] That the dimers elute at t_R distinct from those of the monomers demonstrates that they are authentic, covalently bound SOA products and not ion-source artifacts formed during the (−)ESI process.

Using the measured (−)ESI efficiencies of carboxylic acids **1−3** and dimer esters **4−6** as surrogates for those of like-structured (i.e., mono vs. polycarboxylic) monomers and dimers, respectively (Table 3.S3), identified molecular products were determined to account for $21.8 \pm 2.6\%$ and $18.9 \pm 3.2\%$ of α-pinene and β-pinene SOA mass, respectively. Notably, the dimers comprised only a small fraction (1.3–3.3%) of total SOA mass, whereas the mass contribution of the monomers was appreciable (15.6–20.5%) (Table 3.1). Based on comparison with authentic standards and/or previously reported LC/(−)ESI-MS data,[17,34] *cis*-pinic acid ($C_9H_{14}O_4$; t_R 4.45 min) and terpenylic acid ($C_8H_{12}O_4$; t_R 4.07 min) were identified as the most abundant monomers, with respective mass fractions of $3.9 \pm 0.6\%$ and $3.4 \pm 0.6\%$ in α-pinene SOA and $3.3 \pm 0.6\%$ and $3.3 \pm 0.6\%$ in β-pinene SOA. Similarly, pinyl-diaterpenyl ester ($C_{17}H_{26}O_8$; t_R 5.43 min) was found to be the most abundant dimer, constituting $0.2 \pm 0.02\%$ and $0.6 \pm 0.1\%$ of α-pinene and β-pinene SOA mass, respectively. Mass

fractions and proposed molecular structures of the most abundant seven monomers and eight dimers identified in SOA from ozonolysis of α-pinene and β-pinene, representing 13.8–15.5% of total SOA mass, are listed in Table 3.S4, while mass fractions and physicochemical properties of all identified molecular products are presented in Table 3.S3.

Comparison of the monomeric and dimeric SOA mass fractions derived in this work to those reported in two recent, comprehensive LC/(−)ESI-MS analyses of chamber-generated SOA from α-pinene ozonolysis[30,31] reveals significant discrepancies (Table 3.2). Encouragingly, however, adjustment of the mass fraction estimates in these studies based on the relative (−)ESI efficiencies of carboxylic acids **1−3** and dimer esters **4−6** (details provided in SI, Section 3.S1) brings the three sets of mass fractions into general agreement and suggests that carboxyl-containing products constitute ~20–30% of the mass of chamber-generated SOA formed from α-pinene ozonolysis at 293–298 K and ~1 atm, under dry (<5% RH), low-NO_x (<1 ppb) conditions, and in the absence of an OH scavenger (Table 3.2). These findings are consistent with recent measurements of organic acids in laboratory-derived α-pinene SOA made with a filter inlet for gases and aerosol coupled to an acetate chemical ionization mass spectrometer (FIGAERO-CIMS).[67] Additionally, an average empirical relationship between the fraction of OA mass composed of organic acids (f_{acid}) and the fraction of AMS OA signal at m/z 44 (f_{44}) was recently developed based on acetate/O_2^- CIMS measurements of particle-phase organic acids and AMS data from three field campaigns in forested regions with significant monoterpene emissions [$f_{acid} = (2.50 \pm 0.19) f_{44}$].[68] Using the SOA mass fractions of total carboxyl-containing species detected by PILS + UPLC/(−)ESI-Q-TOF-MS and AMS data in this work, similar relationships were derived for chamber-generated SOA from ozonolysis of α-pinene [$f_{acid} = (2.54 \pm 0.22) f_{44}$] and β-pinene [$f_{acid} = (1.91 \pm 0.28) f_{44}$], further suggesting that a simple scaling of AMS f_{44} by a factor of ~2–2.5 can provide a reasonable estimate of the mass contribution of organic acids to OA with appreciable monoterpene SOA influence.

Table 3.2. Mass fractions of molecular products in SOA from α-pinene ozonolysis quantified via LC/(−)ESI-MS.[a]

Reference	$[\alpha\text{-P}]_0$ (ppb)	$[O_3]_0$ (ppb)	$[(NH_4)_2SO_4]_0$ (μm^3 cm^{-3})	[SOA] (μg m^{-3})	Bulk O:C	Bulk $\overline{OS}_C$	SOA Mass Fraction (%)[c,d]			
							cis-Pinic Acid	Monomer	Dimer	Total
Zhang et al. (2015)[31]	154	200	73	120	0.45	−0.72	21.0 [5.3]	39.2 [26.0] (9)	6.5 [2.6] (13)	45.7 [28.6]
Kristensen et al. (2017)[30]	50	200	–	60	0.40	−0.85	4.5	20.5 (16)	8.6 [1.1] (30)	29.1 [21.6]
This Work[b]	104 ± 5	150	86–223	232 ± 26	0.41 ± 0.01	−0.87 ± 0.02	3.9 ± 0.6	20.5 ± 2.5 (36)	1.3 ± 0.1 (46)	21.8 ± 2.6

[a]Experiments in each study were carried out in batch-mode Teflon environmental chambers at 293–298 K and ~1 atm, under dry (<5% RH), low-NO$_x$ (<1 ppb) conditions, and in the absence of an OH scavenger.
[b]See Table 3.1 for details.
[c]Bracketed values represent adjusted mass fraction estimates based on (−)ESI efficiencies derived in this work. Details are provided in SI, Section 3.S1.
[d]Numbers of identified monomers and dimers are given in parentheses.

The use of carboxylic acids **1–3** and dimer esters **4–6** as surrogates to quantify the respective mass fractions of monomers and dimers identified in α-pinene and β-pinene SOA represents a significant analytical improvement compared to previous LC/(−)ESI-MS studies.[20–23,25,27–33] Due to the lack of structural information for the majority of identified carboxyl-containing species, however, and the dependence of (−)ESI efficiency on the number of ionizable carboxyl groups, the SOA mass fractions of monomers and dimers with unknown structures, respectively quantified using carboxylic acid **1** and dimer ester **6** as defaults (Table 3.S3), are likely overestimated for those that possess two or more carboxyl groups. Likewise, SOA mass fractions for molecular products with proposed structures containing three or more carboxyl groups [e.g., pinyl-diaterpenyl ester[17] and 3-methyl-1,2,3-butanetricarboxylic acid (MBTCA)[19]], calculated using carboxylic acid **2** or dimer ester **4** (Table 3.S3), are expected to constitute overestimates. Together, these structural limitations imply that molecular products measureable by LC/(−)ESI-MS may account for an even smaller fraction of α-pinene and β-pinene SOA mass than reported here, particularly dimeric compounds given the dominant mass contribution of pinyl-diaterpenyl ester.

3.3.3 Distribution of Molecular Products in α-Pinene and β-Pinene SOA

Mass fractions of identified molecular products in SOA derived from ozonolysis of α-pinene and β-pinene are shown in Figure 3.3 as a function of carbon number (n_C). For $C_{7–9}$ compounds, as well as total monomers ($C_{7–10}$), statistically similar SOA mass fractions for α-pinene and β-pinene were obtained. Conversely, the fraction of SOA mass attributable to C_{10} species was considerably larger in the α-pinene system, in line with established gas-phase ozonolysis mechanisms (i.e., the carbon backbone of endocyclic α-pinene is retained on ozonolysis whereas the terminal vinylic carbon of exocyclic β-pinene is cleaved).[48,49,69]

With the exception of C_{19} compounds, identified dimers ($C_{15–18}$) accounted for significantly larger fractions of β-pinene SOA mass, resulting in roughly a three-fold
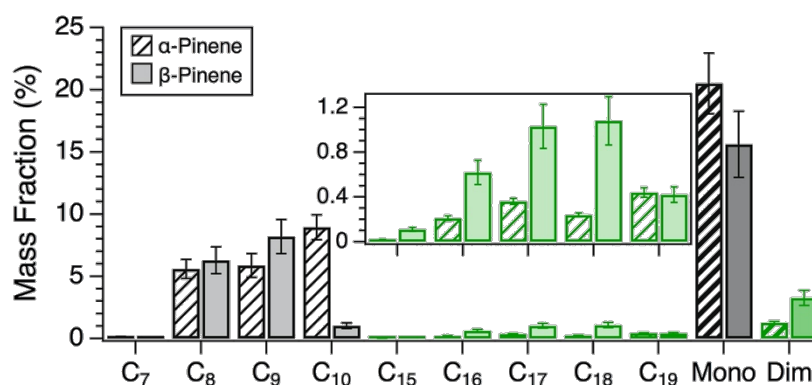
Figure 3.3. Mass fractions of molecular products identified in α-pinene and β-pinene SOA as a function of carbon number (n_C), calculated for suspended SOA after ~5 h of ozonolysis in the CTEC (see Figure 3.1) and reported as averages (1σ) of replicate experiments for α-pinene ($n = 4$) and β-pinene ($n = 5$).

difference in total dimeric mass fraction between SOA produced from ozonolysis of α-pinene (1.3 ± 0.1%) and β-pinene (3.3 ± 0.6%). In part, this difference is explained by the much higher suspended SOA mass loadings formed in the α-pinene system (Figure 3.1, Table 3.1), due to the faster rate at which ozonolysis proceeds for α-pinene ($k_{\alpha p+O_3}= 8.4 \times 10^{-17}$ cm³ molecules⁻¹ s⁻¹) as compared to β-pinene ($k_{\beta p+O_3}= 1.5 \times 10^{-17}$ cm³ molecules⁻¹ s⁻¹).[70] At higher SOA loadings, equilibrium partitioning of semivolatile monomers becomes an increasingly dominant source of SOA mass, minimizing the mass contribution of (extremely) low-volatility dimers, which provide the main SOA source at low loading via irreversible condensation.[31,71] Even so, based on mass yields of total dimers identified in α-pinene (0.48 ± 0.01%) and β-pinene (0.80 ± 0.04%) SOA after ~5 h of reaction ($m_{total\_dimer}/m_{pinene\_reacted}$), ozonolysis of β-pinene appears to be more efficient at producing dimeric compounds measureable by PILS + UPLC/(−)ESI-Q-TOF-MS. However, the mechanisms underlying dimer formation in these systems remain unresolved.[34]

3.3.4 Physicochemical Properties of Molecular Products in α-Pinene and β-Pinene SOA

Shown in Figure 3.4 are the molecular products identified in α-pinene and β-pinene SOA mapped onto the average carbon oxidation state vs. carbon number ($\overline{OS}_C$-n_C) space, as well as in mass defect plots. Note that in these frameworks, isomers are represented collectively as single data points. In terms of saturation mass concentration (C*), monomers (C_{7-10}) are classified as intermediate-volatility (IVOC; $300 < C^* < 3 \times 10^6$ μg m^{-3}), semivolatile (SVOC; $0.3 < C^* < 300$ μg m^{-3}), or low-volatility organic compounds (LVOC; $3 \times 10^{-4} < C^* < 0.3$ μg m^{-3}), whereas all dimers (C_{15-19}) are designated as extremely low-volatility organic compounds (ELVOC; $C^* < 3 \times 10^{-4}$ μg m^{-3}).[72] The molecular formulas of a number of these compounds are common to both α-pinene and β-pinene SOA and can largely be grouped into homologous series of monomers ($C_8H_{12}O_{4-6}$, $C_8H_{14}O_{4-6}$, and $C_9H_{14}O_{3-5}$) and dimers ($C_{16}H_{26}O_{6-10}$, $C_{17}H_{26}O_{5-9}$, $C_{18}H_{28}O_{4-11}$, and $C_{19}H_{30}O_{5-10}$). Distinct homologous series for α-pinene ($C_{10}H_{14}O_{4-6}$, $C_{10}H_{16}O_{3-6}$, $C_{18}H_{26}O_{6-8}$, and $C_{19}H_{28}O_{5-9}$) and β-pinene ($C_{17}H_{28}O_{5-10}$ and $C_{18}H_{30}O_{6-10}$) were also observed.

The mass-weighted $\overline{OS}_C$ of the identified molecular products in α-pinene (-0.62 ± 0.07) and β-pinene (-0.57 ± 0.10) SOA are significantly higher than the corresponding AMS-derived bulk $\overline{OS}_C$ values (Figure 3.4, Table 3.1), indicating that the SOA mass undetected by PILS + UPLC/(−)ESI-Q-TOF-MS (~80%) is less oxygenated, on average, than the identified carboxyl-containing species. The comparatively reduced nature of the unidentified SOA mass implies that particle-phase chemistry involving the loss of oxygen, particularly from highly oxygenated organic molecules (HOMs)[73] that have been implicated as important contributors to monoterpene SOA,[71,74–76] is operative in modulating the $\overline{OS}_C$ of α-pinene and β-pinene SOA molecular constituents. For example, decomposition of multifunctional organic (hydro)peroxides (e.g., peroxyhemiacetals and diacyl peroxides) in biogenic SOA, on time scales of hours or less, has been demonstrated in a number of recent
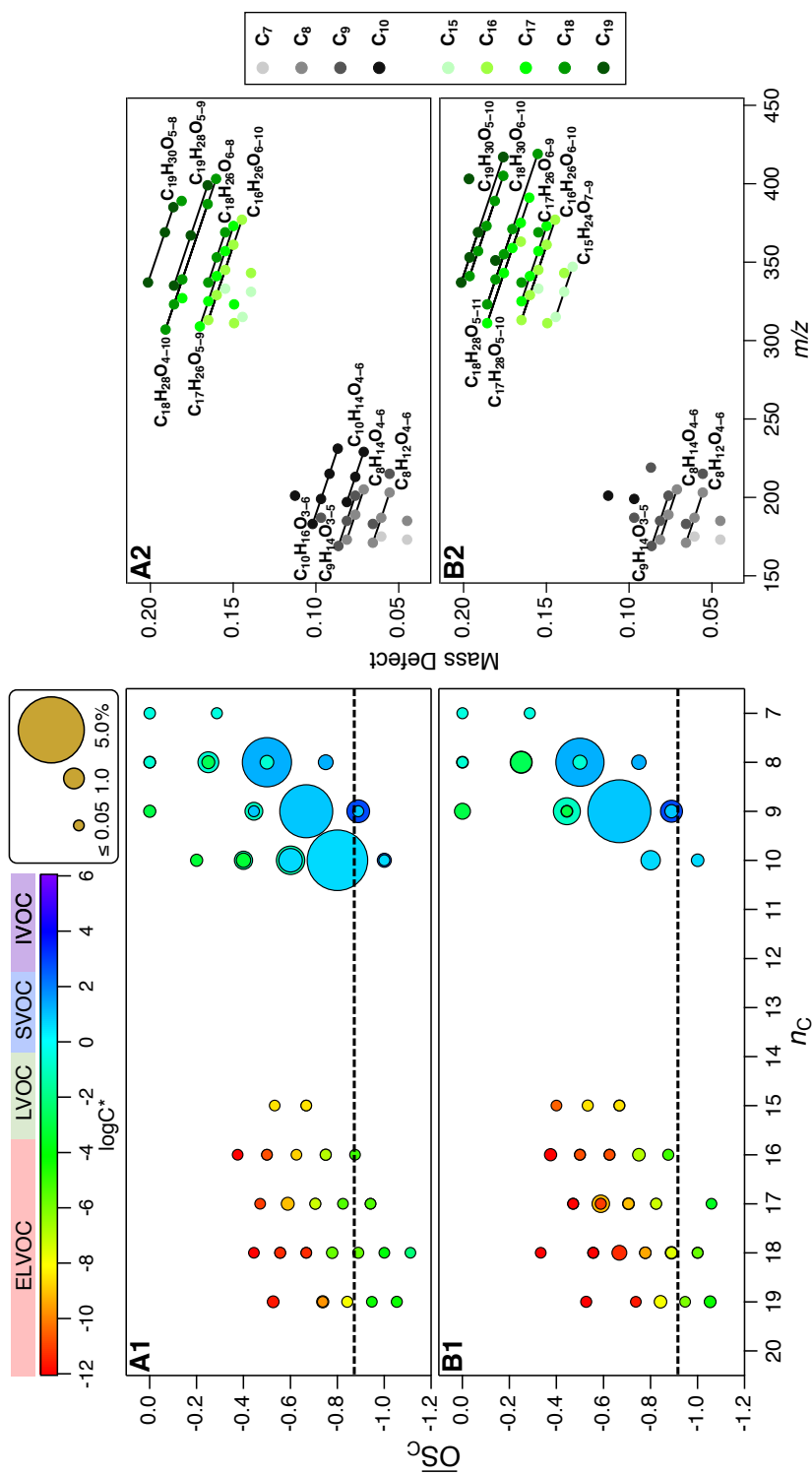
Figure 3.4. Molecular products identified in SOA produced from ozonolysis of (A) α-pinene and (B) β-pinene mapped onto (1) the $\overline{OS}_C$-n_C space and (2) mass defect plots. Markers in (1) and (2) represent all isomers identified for a given molecular formula (Table S3). Marker size in (1) denotes total isomer mass fraction and dashed lines represent AMS-derived bulk $\overline{OS}_C$ values (Table 1), both calculated for suspended SOA after ~5 h of ozonolysis in the CTEC (see Figure 1) and reported as averages of replicate experiments for α-pinene ($n = 4$) and β-pinene ($n = 5$). logC* values were estimated using the empirical model of Donahue et al.[72]

studies[35,77–80] and can lead to nonperoxide species (e.g., carboxylic acids, aldehydes, and esters) with decreased oxygen content.[31,81,82]

In addition, despite being routinely measured in the gas phase,[71,74,76,83,84] C_{20} compounds were not detected in SOA from α-pinene ozonolysis, consistent with several recent LC/(−)ESI-MS studies.[14,24–31,35] This implies that C_{20} dimers, likely formed via gas-phase self/cross-reactions of organic peroxy radicals (RO$_2$ + RO$_2$ → ROOR + O$_2$), undergo chemical transformation/decomposition following condensation to the particle phase, as previously suggested.[13,31,71] The decomposition of ROOR is in line with results from our recently developed iodometry-assisted LC/(−)ESI-MS assay, which found that only one compound identified in SOA from α-pinene ozonolysis ($C_8H_{14}O_6$) contained (hydro)peroxide moieties.[35] That said, the lack of detection by LC/(−)ESI-MS could also indicate that C_{20} compounds formed from α-pinene ozonolysis simply do not contain carboxyl groups.

3.4 Atmospheric Implications

Due to the inherent chemical complexity of SOA and resultant lack of authentic standards required for calibration, quantification of SOA molecular products via LC/ESI-MS is subject to the use of surrogates and proceeds under the assumption that compounds with similar structures/functionalities exhibit comparable ESI efficiencies. For α-pinene and β-pinene SOA, this has led to extensive use of commercial terpenoic acids (e.g., *cis*-pinonic acid) as surrogates for quantifying both monomeric and dimeric SOA constituents. However, in establishing that the (−)ESI efficiencies of dimer esters **4–6** are at least an order of magnitude higher than those of carboxylic acids **1–3**, which in turn differ by almost a factor of six, this study demonstrates that the use of unrepresentative surrogates can lead to substantial, previously unrecognized systematic errors in quantitative LC/ESI-MS analyses of SOA, particularly with respect to quantification of high-molecular-weight compounds using low-molecular-weight proxies. Although specifically elucidated via LC/(−)ESI-MS of pinene-derived carboxylic acids and dimer esters, the observed

order-of-magnitude difference in (–)ESI efficiency between monomers and dimers is consistent with the general mechanistic understanding of the ESI process and is expected to be equally applicable to other biogenic and anthropogenic SOA systems analyzed via either (–) or (+) LC/ESI-MS under various LC conditions (e.g., organic solvent content, buffer concentration, and pH).[42]

The failure of past LC/(–)ESI-MS studies to account for the distinct (–)ESI behavior of monomers and dimers, and the consequent overestimation of dimeric (and polycarboxylic) SOA mass fractions (Table 3.2), has led carboxyl-containing compounds to be regarded as dominant constituents of α-pinene and β-pinene SOA; a reasonable supposition given that the carboxyl moiety represents an approximate endpoint in carbon oxidation state and its incorporation leads to a ~1000-fold reduction in vapor pressure relative to the parent compound.[67] However, constrained by the (–)ESI efficiencies of carboxylic acids **1−3** and dimer esters **4−6**, the 82–90 carboxyl-containing compounds identified in this work (Table 3.S3), as well as those in previous LC/(–)ESI-MS studies (Table 3.2), are found to account for only ~20–30% of the mass of chamber-generated SOA from ozonolysis of α-pinene or β-pinene. In particular, the 46–62 identified ELVOC dimers, although still expected to play a critical role in new particle formation and growth (i.e., at low SOA loading), are determined to make only a minor contribution (~1–3%) to total α-pinene and β-pinene SOA mass. A substantial fraction (~70–80%) of α-pinene and β-pinene SOA mass remains undetected by LC/(–)ESI-MS methods. Based on comparison of AMS-derived bulk $\overline{OS}_C$ and mass-weighted molecular $\overline{OS}_C$ values, this unspeciated mass appears to be less oxygenated, on average, than identified carboxyl-containing species. However, elucidation of the molecular composition of the outstanding SOA mass (i.e., carbon closure) will require the concerted application and proper calibration of mass spectrometric techniques sensitive to other compound classes.

3.5 Acknowledgements

We thank John Crounse and Paul Wennberg for useful discussions. UPLC/(−)ESI-Q-TOF-MS was performed in the Caltech Environmental Analysis Center (EAC). This work was supported by National Science Foundation Grants AGS-1523500, CHE-1800511, and CHE-1905340. The EAC is supported by the Linde Center and Beckman Institute at Caltech.

3.6 Supporting Information

Table of Contents

3.S1 Adjustment of Mass Fractions in Published LC/(−)ESI-MS Studies of SOA from α-Pinene Ozonolysis

Zhang et al. (2015).[31] For the mass fractions of identified monomers and dimers reported in Zhang et al.,[31] Fig. 3 ($MF_{reported}$), calculated using compound-specific, computationally derived (−)ESI efficiencies normalized to that of *cis*-pinonic acid (RIE; Zhang et al.,[31] *SI Appendix*, Table S2),[a] adjusted mass fractions ($MF_{adjusted}$) were obtained as follows:

$$MF_{adjusted} = MF_{reported} \cdot \frac{RIE}{\left(\frac{(-)ESI_{surrogate}}{(-)ESI_{cis-pinonic}} \right)} \qquad (3.S1)$$

---

[a]For *RIE* estimates, "molecules that have two or more equivalent sites for deprotonation (e.g., dicarboxylic acids) were not taken into account" (Zhang et al.,[31] *SI Appendix*, S3.2.2), leading to systematic underprediction of *RIE* for polycarboxylic monomers and dimers, given the dependence of (−)ESI efficiency on the number of ionizable carboxyl groups.

where the bracketed term is the measured (−)ESI efficiency of the most representative surrogate (carboxylic acid **1–3** or dimer ester **4–6**) normalized to that of *cis*-pinonic acid (Figure 3.2). The calculation for *cis*-pinic acid ($C_9H_{14}O_4$) is shown as an example: $5.3\% = 21\% \cdot \frac{0.73}{2.91}$.

Kristensen et al. (2017).[30] Mass fractions of identified monomers reported in Kristensen et al.,[30] Table 3S were quantified using representative surrogates [i.e., *cis*-pinonic acid, *cis*-pinic acid, pimelic acid, terpenylic acid, diaterpenylic acid acetate (DTAA), and 3-methyl-1,2,3-butanetricarboxylic acid (MBTCA)] and, therefore, were not adjusted. For the mass fractions of identified dimers reported in Kristensen et al.,[30] Table 4S ($MF_{reported}$), calculated using "an average standard calibration curve of *cis*-pinic acid and DTAA" given that "most of the suggested molecular structures for the identified dimer esters have moieties resembling *cis*-pinic acid and DTAA,"[85] adjusted mass fractions ($MF_{adjusted}$) were obtained as follows:

$$MF_{\text{adjusted}} = MF_{\text{reported}} \cdot \frac{(-)ESI_{cis-\text{pinic}}}{(-)ESI_{\text{dimer}}} \qquad (3.\text{S2})$$
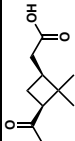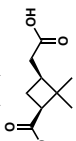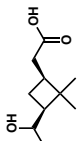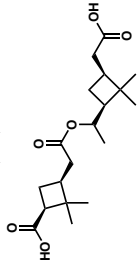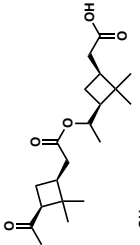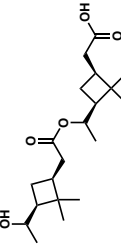
where $(-)ESI_{cis\text{-pinic}}$ is the measured (−)ESI efficiency of *cis*-pinic acid (Table 3.S2; assumes *cis*-pinic acid and DTAA have similar (−)ESI efficiencies as both are pinene-derived dicarboxylic acids) and $(-)ESI_{\text{dimer}}$ is the measured (−)ESI efficiency of the most representative surrogate dimer (dimer ester **4–6**; Table 3.S2). The calculation for pinonyl-pinyl ester ($C_{19}H_{28}O_7$) is shown as an example: $0.08\% = 0.94\% \cdot \frac{2076\ \mu M^{-1}}{25418\ \mu M^{-1}}$.

3.S2   Tables 3.S1–3.S4

Table 3.S1. Initial conditions and SOA properties for α-pinene and β-pinene ozonolysis experiments in the CTEC.[a]

VOC	Exp.	[VOC]₀ (ppb)	[O₃]₀ (ppb)	[(NH₄)₂SO₄]₀ ($\mu m^3\ cm^{-3}$)	[SOA] ($\mu g\ m^{-3}$)[b]	Bulk O:C[b]	Bulk $\overline{OS}_C$[b,c]	SOA Mass Fraction (%)[b,d] Monomer	Dimer	Total
α-Pinene	1	97	150	86	264	0.41	-0.88	20.4	1.2	21.6
	2	105	150	213	207	0.42	-0.86	22.0	1.3	23.3
	3	110	150	203	215	0.42	-0.86	21.9	1.3	23.2
	4	106	150	223	243	0.40	-0.89	17.7	1.1	18.8
β-Pinene	5	96	150	137	93	0.38	-0.90	14.2	2.6	16.8
	6	95	150	192	75	0.38	-0.90	18.0	3.5	21.5
	7	93	150	243	57	0.35	-0.92	18.4	4.1	22.4
	8	95	150	283	77	0.36	-0.93	15.3	3.4	18.8
	9	95	150	211	87	0.35	-0.94	12.0	2.7	14.8

[a] ~5-h duration; T_0 = 295 ± 2 K; P = 1 atm; RH < 5%; $[NO_x]_0$ < 0.5 ppb; no OH scavenger.
[b] Calculated for suspended SOA after ~5 h of ozonolysis (see Figure 3.1).
[c] Average carbon oxidation state ($\overline{OS}_C$ = 2 O:C – H:C).
[d] Method uncertainty is estimated to be ±23% (relative). See Experimental for details.

Table 3.S2. UPLC/(−)ESI-Q-TOF-MS analytical figures of merit for carboxylic acids **1–3** and dimer esters **4–6**.[a]

Compound	Observed m/z (−)	Molecular Formula	t_R (min)	Molecular Structure	(−)ESI Efficiency (μM^{-1})	Concentration Range (μM)	LOD (nM)[b]	LOQ (nM)[c]
1	183.1024	$C_{10}H_{16}O_3$	5.09		713 ± 7	0.200–5.00	7.2	24
2	185.0815	$C_9H_{14}O_4$	4.45		2076 ± 17	0.200–5.00	2.4	8.1
3	185.1179	$C_{10}H_{18}O_3$	4.72		328 ± 4	0.200–3.00	12	39
4	353.1967	$C_{19}H_{30}O_6$	6.71		25418 ± 237	0.200–1.00	0.53	1.8
5	351.2178	$C_{20}H_{32}O_5$	7.46		13235 ± 209	0.200–2.00	0.80	2.7
6	353.2332	$C_{20}H_{34}O_5$	7.05		15079 ± 172	0.200–2.00	0.60	2.0

[a]Weighted (1/X), linear ($R^2 > 0.998$) calibration curves were generated from triplicate measurements of equimolar aqueous solutions of carboxylic acids **1–3** and dimer esters **4–6**. Intercepts of calibration curves were not statistically different from zero.
[b]Limit of detection (LOD); calculated as three times the standard deviation of the blank ($3\sigma_{blank}$).
[c]Limit of quantitation (LOQ); calculated as ten times the standard deviation of the blank ($10\sigma_{blank}$).

Table 3.S3. Molecular products identified in SOA produced from ozonolysis of α-pinene and β-pinene.

Carbon Number	Observed m/z (–)	Molecular Formula	Error (ppm)	O:C	$\overline{OS}_C$ [a]	logC* (μg m^{-3}) [b]	t_R (min)	(–)ESI Surrogate [c]	SOA Mass Fraction (%) [d,e] α-Pinene	β-Pinene
C$_7$	173.0456	$C_7H_{10}O_5$	3.5	0.71	0.00	-0.5	2.21	2	0.07 ± 0.01	0.03 ± 0.01
	175.0616	$C_7H_{12}O_5$	5.7	0.71	-0.29	-0.5	2.46	2	0.05 ± 0.04	0.05 ± 0.005
C$_8$	185.0451	$C_8H_{10}O_5$	0.5	0.63	0.00	-0.7	3.84	2	0.07 ± 0.01	0.04 ± 0.01
	171.0669	$C_8H_{12}O_4$	7.0	0.50	-0.50	1.2	4.07	1†‡§¶	3.36 ± 0.59	3.27 ± 0.63
							4.20	2†‡¶	0.17 ± 0.02	0.15 ± 0.03
	187.0615	$C_8H_{12}O_5$	4.8	0.63	-0.25	-0.7	3.48	1	0.20 ± 0.03	0.36 ± 0.07
							3.91	1	0.35 ± 0.02	0.34 ± 0.06
							2.86	1	0.40 ± 0.09	0.34 ± 0.06
	203.0554	$C_8H_{12}O_6$	-1.0	0.75	0.00	-2.7	3.86	2‡	0.11 ± 0.01	0.07 ± 0.02
							3.59	2‡	0.03 ± 0.002	0.04 ± 0.01
	173.0826	$C_8H_{14}O_4$	6.9	0.50	-0.75	1.2	3.67	1	0.40 ± 0.07	0.37 ± 0.06
	189.0770	$C_8H_{14}O_5$	3.7	0.63	-0.50	-0.7	3.49	2‡§¶	0.06 ± 0.04	0.18 ± 0.04
							5.31	1	0.23 ± 0.02	0.16 ± 0.04
	205.0722	$C_8H_{14}O_6$	4.9	0.75	-0.25	-2.7	3.83	2	0.22 ± 0.03	0.97 ± 0.12
C$_9$	183.0668	$C_9H_{12}O_4$	6.0	0.44	-0.44	0.9	4.10	1	0.04 ± 0.02	0.12 ± 0.02
	215.0564	$C_9H_{12}O_6$	3.7	0.67	0.00	-3.0	3.86	2	0.10 ± 0.01	0.38 ± 0.07
							3.59	2	0.06 ± 0.01	0.10 ± 0.02
	169.0872	$C_9H_{14}O_3$	4.1	0.33	-0.89	2.8	4.71	1§	1.10 ± 0.13	1.06 ± 0.21
	185.0825	$C_9H_{14}O_4$	5.9	0.44	-0.67	0.9	4.45	2†‡§¶*	3.86 ± 0.59	3.30 ± 0.56
							4.39	1†¶	–	1.45 ± 0.25
	201.0762	$C_9H_{14}O_5$	-0.5	0.56	-0.44	-1.0	3.65	1	0.52 ± 0.05	1.21 ± 0.20
							4.20	1	–	0.29 ± 0.05
							4.31	1	0.15 ± 0.02	–
	187.0972	$C_9H_{16}O_4$	1.1	0.44	-0.89	0.9	5.16	2	0.04 ± 0.004	0.16 ± 0.02
							4.00	2	–	0.08 ± 0.01
	219.0879	$C_9H_{16}O_6$	4.6	0.67	-0.44	-3.0	4.14	2	–	0.04 ± 0.01

m/z	Formula					RT	n		
197.0801	$C_{10}H_{14}O_4$	−6.6	0.40	−0.60	0.6	3.93	1	0.52 ± 0.24	—
						4.49	1§	0.66 ± 0.29	—
213.0767	$C_{10}H_{14}O_5$	1.9	0.50	−0.40	−1.3	3.89	1	0.19 ± 0.12	—
						4.13	1	0.49 ± 0.05	—
229.0720	$C_{10}H_{14}O_6$	3.5	0.60	−0.20	−3.2	4.35	2	0.14 ± 0.02	—
183.1030	$C_{10}H_{16}O_3$	4.9	0.30	−1.00	2.4	5.09	1†,§,*	0.32 ± 0.05	—
199.0979	$C_{10}H_{16}O_4$	4.5	0.40	−0.80	0.6	4.16	1†,§	3.66 ± 0.69	0.75 ± 0.13
						4.30	1‡	0.91 ± 0.16	0.08 ± 0.03
215.0917	$C_{10}H_{16}O_5$	−0.9	0.50	−0.60	−1.3	4.43	1	0.45 ± 0.03	
						5.03	1	1.19 ± 0.17	—
231.0872	$C_{10}H_{16}O_6$	1.3	0.60	−0.40	−3.2	4.61	2†,‡,§	0.10 ± 0.01	—
						4.23	2†,‡	0.13 ± 0.01	—
						5.29	2†,‡	0.13 ± 0.01	—
201.1127	$C_{10}H_{18}O_4$	0.0	0.40	−1.00	0.6	5.63	1	0.05 ± 0.01	0.20 ± 0.08
C_{10}									
315.1448	$C_{15}H_{24}O_7$	1.3	0.47	−0.67	−6.6	5.34	6	0.01 ± 0.002	0.02 ± 0.01
						5.95	6	–	0.01 ± 0.002
331.1404	$C_{15}H_{24}O_8$	3.3	0.53	−0.53	−8.5	5.67	6	<0.01	0.03 ± 0.005
						5.52	6	<0.01	0.01 ± 0.002
347.1346	$C_{15}H_{24}O_9$	1.2	0.60	−0.40	−10.5	5.32	6	–	0.02 ± 0.003
333.1551	$C_{15}H_{26}O_8$	0.6	0.53	−0.67	−8.5	5.98	6	<0.01	0.03 ± 0.003
C_{15}									
311.1503	$C_{16}H_{24}O_6$	2.6	0.38	−0.75	−5.1	5.93	6	0.06 ± 0.01	0.09 ± 0.02
343.1386	$C_{16}H_{24}O_8$	−2.0	0.50	−0.50	−8.8	5.42	4†,§	0.01 ± 0.001	0.02 ± 0.003
						5.33	4†,§	<0.01	0.02 ± 0.003
						5.16	4†	0.01 ± 0.002	0.02 ± 0.005
313.1661	$C_{16}H_{26}O_6$	3.2	0.38	−0.88	−5.1	6.23	6§	0.02 ± 0.002	0.06 ± 0.01
329.1607	$C_{16}H_{26}O_7$	2.1	0.44	−0.75	−6.9	5.59	6	0.04 ± 0.004	0.14 ± 0.03
						5.27	6	0.01 ± 0.001	0.02 ± 0.005
						5.10	6	<0.01	0.01 ± 0.003
345.1549	$C_{16}H_{26}O_8$	0.0	0.50	−0.63	−8.8	5.48	6	–	0.03 ± 0.01
						4.89	6	0.01 ± 0.001	0.02 ± 0.004
						5.68	6	0.01 ± 0.001	–
C_{16}									

m/z	Formula						n		
361.1512	$C_{16}H_{26}O_9$	3.6	0.56	-0.50	-10.7	5.17	6	–	0.01 ± 0.003
						4.94	6	0.01 ± 0.001	0.02 ± 0.005
377.1455	$C_{16}H_{26}O_{10}$	1.9	0.63	-0.38	-12.7	5.60	6	0.01 ± 0.002	–
363.1640	$C_{16}H_{28}O_9$	-4.1	0.56	-0.63	-10.7	5.27	6	0.02 ± 0.003	0.15 ± 0.02
						5.01	6	–	0.01 ± 0.002
323.1509	$C_{17}H_{24}O_6$	4.3	0.35	-0.71	-5.4	6.05	6	0.01 ± 0.001	–
						6.29	6	<0.01	–
309.1699	$C_{17}H_{26}O_5$	-1.0	0.29	-0.94	-3.6	5.90	6§	0.02 ± 0.002	–
325.1672	$C_{17}H_{26}O_6$	6.5	0.35	-0.82	-5.4	5.87	4§	–	0.02 ± 0.005
						5.76	4§	0.01 ± 0.002	–
						6.14	4§	0.01 ± 0.001	–
341.1607	$C_{17}H_{26}O_7$	2.1	0.41	-0.71	-7.2	5.80	6	0.06 ± 0.005	0.11 ± 0.02
						6.46	6	–	0.02 ± 0.004
357.1555	$C_{17}H_{26}O_8$	1.7	0.47	-0.59	-9.1	5.43	4†‡§	0.22 ± 0.02	0.59 ± 0.12
						5.24	4†	–	0.06 ± 0.01
373.1485	$C_{17}H_{26}O_9$	-3.8	0.53	-0.47	-11.0	4.90	6	–	0.03 ± 0.004
						5.36	6	0.01 ± 0.001	0.01 ± 0.002
311.1859	$C_{17}H_{28}O_5$	0.3	0.29	-1.06	-3.6	7.13	6	–	0.01 ± 0.01
327.1808	$C_{17}H_{28}O_6$	0.0	0.35	-0.94	-5.4	6.05	6	0.01 ± 0.001	–
343.1761	$C_{17}H_{28}O_7$	1.2	0.41	-0.82	-7.2	5.76	6	–	0.03 ± 0.005
						5.90	6	–	0.02 ± 0.004
						6.09	6	–	0.01 ± 0.001
359.1714	$C_{17}H_{28}O_8$	2.2	0.47	-0.71	-9.1	6.02	6	–	0.05 ± 0.01
375.1653	$C_{17}H_{28}O_9$	-0.5	0.53	-0.59	-11.0	4.78	6	–	0.03 ± 0.01
						6.34	6	–	0.01 ± 0.003
391.1599	$C_{17}H_{28}O_{10}$	-1.3	0.59	-0.47	-13.0	5.40	6	–	0.03 ± 0.005
337.1634	$C_{18}H_{26}O_6$	-5.0	0.33	-0.78	-5.7	6.32	6	0.07 ± 0.01	0.02 ± 0.005
353.1604	$C_{18}H_{26}O_7$	1.1	0.39	-0.67	-7.6	5.88	6	0.02 ± 0.002	–
369.1554	$C_{18}H_{26}O_8$	1.4	0.44	-0.56	-9.4	5.16	6	0.01 ± 0.001	0.02 ± 0.004
						5.36	6	–	0.02 ± 0.002
307.1893	$C_{18}H_{28}O_4$	-5.2	0.22	-1.11	-2.2	6.65	6	0.01 ± 0.002	–

Group label: C_{17}

323.1860	$C_{18}H_{28}O_5$	0.6	0.28	−1.00	−3.9	6.22	6	—	0.04 ± 0.01
						6.99	6¶	—	0.01 ± 0.004
339.1822	$C_{18}H_{28}O_6$	4.1	0.33	−0.89	−5.7	6.83	6	0.01 ± 0.001	0.13 ± 0.02
						6.72	6	—	0.06 ± 0.01
						6.45	6	—	—
355.1754	$C_{18}H_{28}O_7$	−0.8	0.39	−0.78	−7.6	5.86	6	0.03 ± 0.002	0.08 ± 0.02
						5.38	6	—	0.01 ± 0.004
						6.37	6¶	—	0.06 ± 0.01
371.1707	$C_{18}H_{28}O_8$	0.3	0.44	−0.67	−9.4	5.58	6	—	—
387.1651	$C_{18}H_{28}O_9$	−1.0	0.50	−0.56	−11.3	5.55	6	0.06 ± 0.003	—
403.1601	$C_{18}H_{28}O_{10}$	−0.7	0.56	−0.44	−13.2	6.09	6	0.01 ± 0.001	—
419.1525	$C_{18}H_{28}O_{11}$	−6.7	0.61	−0.33	−15.2	4.80	6	—	0.01 ± 0.003
341.1960	$C_{18}H_{30}O_6$	−1.2	0.33	−1.00	−5.7	7.01	6	—	0.02 ± 0.004
357.1919	$C_{18}H_{30}O_7$	1.7	0.39	−0.89	−7.6	7.04	6	—	0.07 ± 0.02
						6.79	6	—	0.02 ± 0.003
373.1851	$C_{18}H_{30}O_8$	−2.9	0.44	−0.78	−9.4	5.82	6	—	0.03 ± 0.005
						5.00	6	—	0.03 ± 0.01
						6.09	6	—	0.01 ± 0.002
389.1814	$C_{18}H_{30}O_9$	0.5	0.50	−0.67	−11.3	6.29	6	—	0.40 ± 0.08
						6.13	4¶	0.02 ± 0.002	—
405.1764	$C_{18}H_{30}O_{10}$	0.7	0.56	−0.56	−13.2	4.61	4¶	—	0.03 ± 0.005
335.1862	$C_{19}H_{28}O_5$	1.2	0.26	−0.95	−4.3	7.12	6	0.02 ± 0.002	—
351.1828	$C_{19}H_{28}O_6$	5.7	0.32	−0.84	−6.1	5.87	6	—	0.02 ± 0.004
367.1766	$C_{19}H_{28}O_7$	2.5	0.37	−0.74	−7.9	6.10	4‡§	0.12 ± 0.01	—
						6.00	4‡	0.04 ± 0.004	—
399.1663	$C_{19}H_{28}O_9$	2.0	0.47	−0.53	−11.6	5.86	6	0.07 ± 0.005	—
						5.99	6	0.06 ± 0.01	—
337.2027	$C_{19}H_{30}O_5$	3.6	0.26	−1.05	−4.3	7.31	6¶	—	0.11 ± 0.02
						7.54	6	—	0.01 ± 0.001
						6.07	6	0.05 ± 0.005	—
						7.48	6	0.01 ± 0.001	—
353.1961	$C_{19}H_{30}O_6$	−0.8	0.32	−0.95	−6.1	6.28	6	—	0.02 ± 0.005

C_{18}

C_{19}

m/z	Formula	C*[b]	OS_C[a]			n		
369.1916	$C_{19}H_{30}O_7$	0.8	0.37	−7.9	6.62	6[¶]	0.02 ± 0.005	0.12 ± 0.02
					6.72	6	–	0.07 ± 0.02
385.1873	$C_{19}H_{30}O_8$	2.9	0.42	−9.7	5.96	6	0.02 ± 0.003	–
					6.14	6	0.01 ± 0.001	–
417.1769	$C_{19}H_{30}O_{10}$	1.9	0.53	−13.5	5.48	6	0.01 ± 0.003	–
403.1963	$C_{19}H_{32}O_9$	−1.2	0.47	−11.6	6.88	6	–	0.04 ± 0.01
					6.40	6	–	0.01 ± 0.003
				TOTAL MONOMER			20.51 ± 2.45	15.60 ± 2.65
				TOTAL DIMER			1.27 ± 0.11	3.26 ± 0.60
				TOTAL			21.78 ± 2.55	18.86 ± 3.19
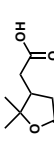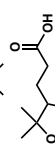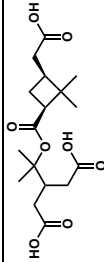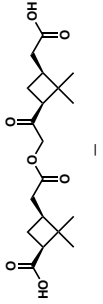
[a] Average carbon oxidation state ($\overline{OS}_C = 2\,O{:}C - H{:}C$).
[b] Saturation mass concentration (C*). Estimated using the empirical model of Donahue et al.[72]
[c] Assigned based on comparison with * authentic standards and/or LC/(−)ESI-MS data from †Yasmeen et al. (2010),[17] ‡Yasmeen et al. (2012),[19] §Zhang et al. (2015),[31] and ¶Kenseth et al. (2018).[34] Structures containing (hydro)peroxide functionalities were not considered.[34,35] Absent structural information, carboxylic acid **1** and dimer ester **6** were used, unless $O{:}C > 0.65$ or $\overline{OS}_C > -0.25$.
[d] Calculated for suspended SOA after ~5 h of ozonolysis (see Figure 3.1) and reported as averages of replicate experiments for α-pinene (n = 4) and β-pinene (n = 5) together with standard deviations (1σ).
[e] Method uncertainty is estimated to be ±23% (relative). See Experimental for details.
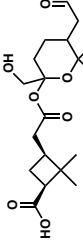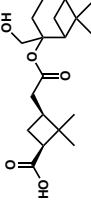
Table 3.S4. Major monomers and dimers identified in SOA produced from ozonolysis of α-pinene and β-pinene.[a]

Observed m/z (–)	Molecular Formula	t_R (min)	Compound Assignment[b]	Proposed Molecular Structure[b]	SOA Mass Fraction[c,d] (%)	
					α-Pinene	β-Pinene
185.0825	$C_9H_{14}O_4$	4.45	cis-Pinic acid[†,‡,§,‖,*]		3.86 ± 0.59	3.30 ± 0.56
171.0669	$C_8H_{12}O_4$	4.07	Terpenylic acid[†,‡,§]		3.36 ± 0.59	3.27 ± 0.63
199.0979	$C_{10}H_{16}O_4$	4.16	10-hydroxypinonic acid[‡,§]		3.66 ± 0.69	0.75 ± 0.13
185.0825	$C_9H_{14}O_4$	4.39	Homoterpenylic acid[†]		–	1.45 ± 0.25
215.0917	$C_{10}H_{16}O_5$	5.03	–	–	1.19 ± 0.17	–
169.0872	$C_9H_{14}O_3$	4.71	cis-Pinalic acid[§]		1.10 ± 0.13	1.06 ± 0.21
199.0979	$C_{10}H_{16}O_4$	4.30	8-hydroxypinonic acid[‡]		0.91 ± 0.16	N/A
197.0801	$C_{10}H_{14}O_4$	4.49	Oxopinonic acid[§]		0.66 ± 0.29	–
201.0762	$C_9H_{14}O_5$	3.65	–	–	N/A	1.21 ± 0.20
205.0722	$C_8H_{14}O_6$	3.83	–	–	N/A	0.97 ± 0.12
357.1555	$C_{17}H_{26}O_8$	5.43	Pinyl-diaterpenyl ester[†,‡,§]		0.22 ± 0.02	0.59 ± 0.12
367.1766	$C_{19}H_{28}O_7$	6.10	Pinonyl-pinyl ester[‡,§]		0.12 ± 0.01	–
337.1634	$C_{18}H_{26}O_6$	6.32	–	–	0.07 ± 0.01	N/A
399.1663	$C_{19}H_{28}O_9$	5.86	–	–	0.07 ± 0.005	–

m/z	Formula	RT			
387.1651	$C_{18}H_{28}O_9$	5.55	—	0.06 ± 0.003	—
399.1663	$C_{19}H_{28}O_9$	5.99	—	0.06 ± 0.01	—
337.2027	$C_{19}H_{30}O_5$	6.07	—	0.05 ± 0.005	—
389.1814	$C_{18}H_{30}O_9$	6.29	—	—	0.40 ± 0.08
377.1455	$C_{16}H_{26}O_{10}$	5.27	—	N/A	0.15 ± 0.02
329.1607	$C_{16}H_{26}O_7$	5.59	—	N/A	0.14 ± 0.03
339.1822	$C_{18}H_{28}O_6$	6.72	—	—	0.13 ± 0.02
369.1916	$C_{19}H_{30}O_7$	6.62	—¶	N/A	0.12 ± 0.02
337.2027	$C_{19}H_{30}O_5$	7.31	—¶	—	0.11 ± 0.02
311.1503	$C_{16}H_{24}O_6$	5.93	—	—	0.09 ± 0.02
				0.06 ± 0.01	0.09 ± 0.02
TOTAL MONOMER				14.73 ± 2.02	12.01 ± 2.05
TOTAL DIMER				0.72 ± 0.07	1.74 ± 0.31
TOTAL				15.45 ± 2.08	13.75 ± 2.33

[a] Monomer mass fraction >0.65%. Dimer mass fraction >0.05% for α-pinene and >0.09% for β-pinene. N/A denotes below threshold.
[b] Based on comparison with *authentic standards and/or LC/(−)ESI-MS data from †Yasmeen et al. (2010),[17] ‡Yasmeen et al. (2012),[19] §Zhang et al. (2015),[31] and ¶Kenseth et al. (2018).[34]
[c] Calculated for suspended SOA after ~5 h of ozonolysis (see Figure 3.1) and reported as averages of replicate experiments for α-pinene (n = 4) and β-pinene (n = 5) together with standard deviations (1σ).
[d] Method uncertainty is estimated to be ±23% (relative). See Experimental for details.

3.S3 Figures 3.S1–3.S3
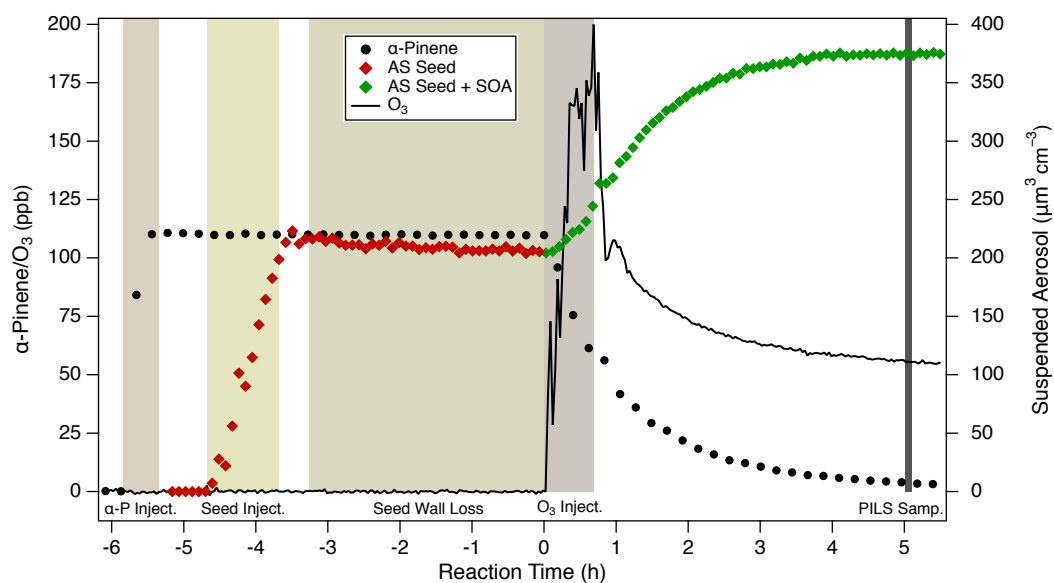
Figure 3.S1. Time series of GC/FID-derived α-pinene mixing ratios, O_3 mixing ratios, and SMPS-derived suspended aerosol volume concentrations for a representative α-pinene ozonolysis experiment in the CTEC (Table 3.S1, Exp. 3). Shading denotes sequential periods of α-pinene injection (30 min), $(NH_4)_2SO_4$ (AS) seed injection (1 h), AS seed wall loss (3.25 h), O_3 injection (42 min), and PILS sample collection (5 min).
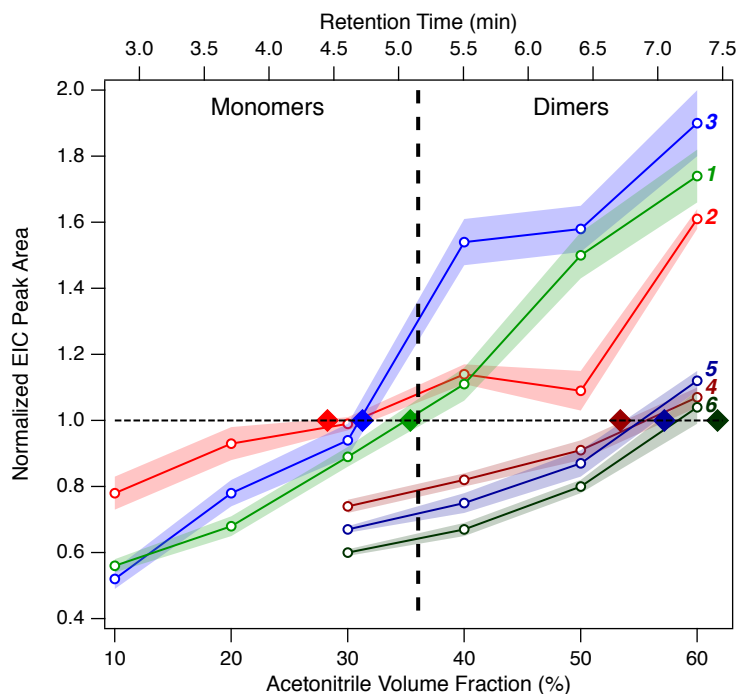
Figure 3.S2. Influence of eluent composition on the (−)ESI efficiencies of carboxylic acids **1–3** and dimer esters **4–6**, evaluated for an equimolar (1.00 µM) aqueous solution via isocratic UPLC/(−)ESI-Q-TOF-MS; all other acquisition parameters [e.g., total flow rate, injection volume, and (−)ESI conditions] were unchanged. Profiles for each compound are plotted as the average (1σ) EIC peak area of triplicate measurements, normalized to the EIC peak area from the gradient method, as a function of isocratic acetonitrile volume fraction. Vertical dashed line separates ranges of acetonitrile content within which monomers (10–38%) and dimers (34–63%) in α-pinene and β-pinene SOA elute during gradient UPLC, while diamonds denote acetonitrile volume fractions at which carboxylic acids **1–3** and dimer esters **4–6** elute during gradient UPLC. Retention times in the gradient method (t_R 2.81–7.30 min) corresponding to the given acetonitrile volume fractions (10–60%) are also shown.
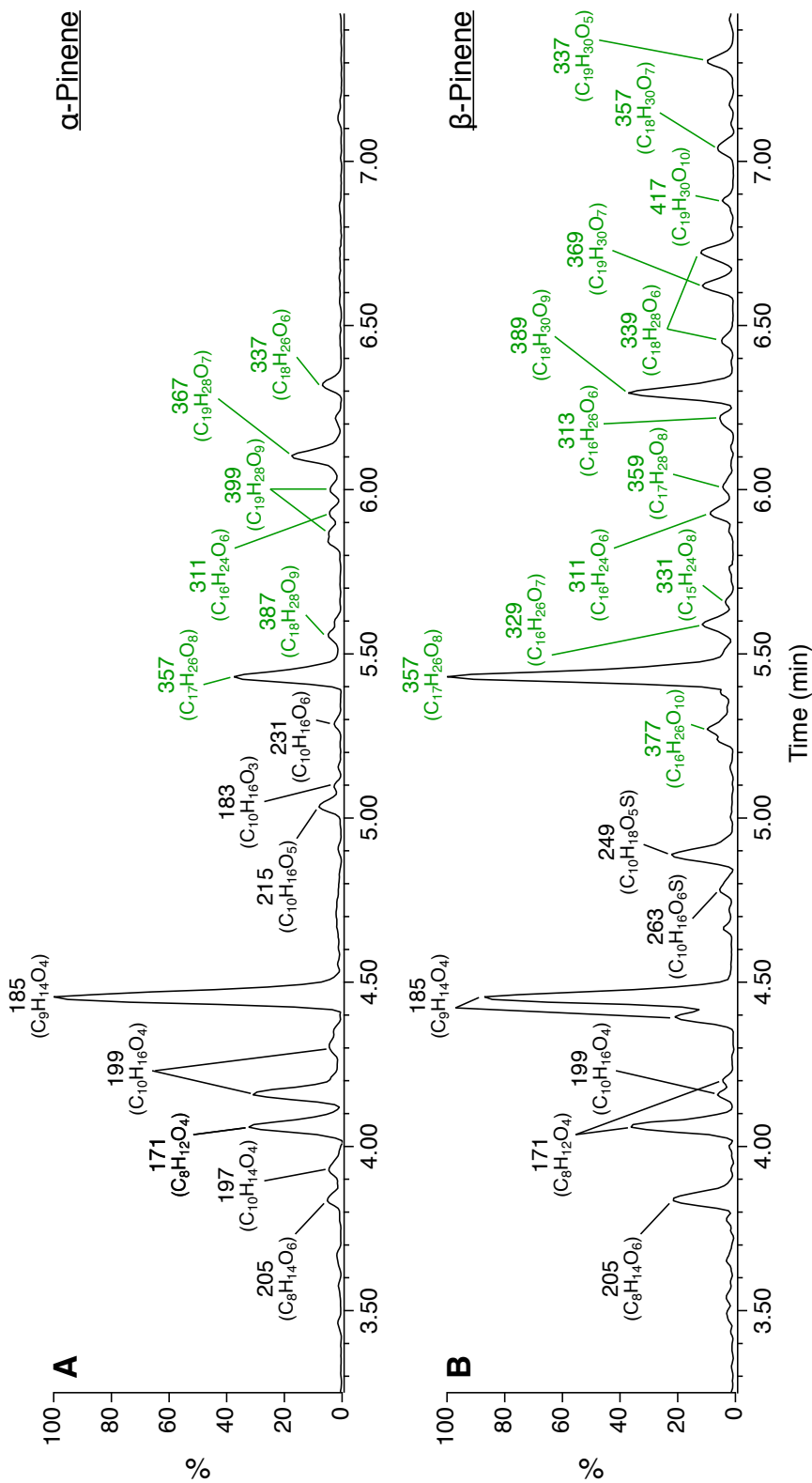
Figure 3.S3. Representative UPLC/(−)ESI-Q-TOF-MS BPI chromatograms of SOA produced from ozonolysis of (A) α-pinene and (B) β-pinene after ~5 h of reaction in the CTEC (see Figure 3.1). Numbers correspond to nominal m/z values of $[M–H]^-$ ions. Molecular formulas ($C_xH_yO_z$) were assigned with mass tolerances of <7 ppm and supported by associated ^{13}C isotope distributions. Chromatograms consist of monomeric (black) and dimeric (green) regions.

3.S4   Synthetic Procedures and Characterization Data

General Information

Unless otherwise stated, reactions were performed in flame-dried glassware under ambient conditions using dry, deoxygenated solvents. Solvents were dried by passage through an activated alumina column under argon. Reagents were purchased from commercial sources and used as received. Reaction temperatures were controlled by an IKAmag temperature modulator. Thin-layer chromatography (TLC) was performed using E. Merck silica gel 60 F254 pre-coated plates (250 µm) and visualized by UV fluorescence quenching, potassium permanganate staining, or *p*-anisaldehyde staining. Silicycle Silia*Flash* P60 Academic Silica gel (particle size 40–63 µm) was used for flash chromatography. Preparative HPLC was performed using an Agilent 1200 HPLC system equipped with an ACE C_{18} column (5 µm, 21.2 mm × 250 mm). ^1H and ^{13}C NMR spectra were recorded on a Varian Inova 500 (500 and 125 MHz, respectively) spectrometer and are reported in terms of chemical shift relative to $CHCl_3$ (δ 7.26 and 77.16 ppm, respectively). Data for ^1H NMR are reported as follows: chemical shift (δ ppm) (multiplicity, coupling constant, integration). Abbreviations are used as follows: s = singlet, d = doublet, t = triplet, q = quartet, m = multiplet. IR spectra were obtained from thin films deposited on NaCl plates using a Perkin Elmer Spectrum BXII spectrometer and are reported in frequency of absorption (cm^{-1}). Optical rotations were measured with a Jasco P-2000 polarimeter operating on the sodium D-line (589 nm) using a 100 mm path-length cell. High resolution mass spectra (HRMS) were acquired using a Waters ACQUITY UPLC I-Class system coupled to a Xevo G2-S ESI-Q-TOF-MS (see Experimental).
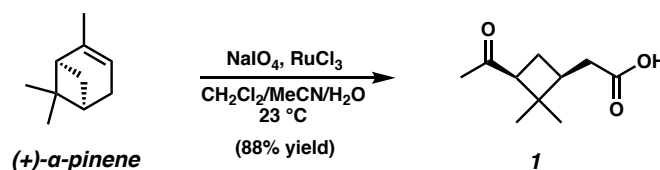
2-((1S,3S)-3-acetyl-2,2-dimethylcyclobutyl)acetic acid ((+)-*cis*-pinonic acid, 1)

(+)-*cis*-Pinonic acid (**1**) was prepared according to a modified literature procedure[1] from commercial (+)-α-pinene (98%, 89% ee, Sigma-Aldrich). To a stirred solution of (+)-α-pinene (5.00 mL, 31.5 mmol, 1.0 equiv) in CH_2Cl_2/MeCN/H_2O (2:2:3, 260 mL) at 23 °C was added $NaIO_4$ (26.8 g, 125.3 mmol, 4.0 equiv) followed by catalytic $RuCl_3$ hydrate (240 mg). After 24 h, TLC indicated complete conversion of the starting material and the mixture was diluted with Et_2O (200 mL). The layers were separated and the aqueous layer was extracted with Et_2O (3 × 150 mL). The combined organic phases were filtered through celite and concentrated. The crude residue was dissolved in Et_2O (100 mL) and extracted with 10% aqueous Na_2CO_3 (3 × 150 mL). The aqueous phases were combined, acidified to pH 1 with concentrated H_2SO_4, and extracted with Et_2O (3 × 150 mL). The combined organic phases were washed with brine, dried over $MgSO_4$, and concentrated. The crude product was purified by flash chromatography (40% EtOAc/hexanes) to afford the title compound as a white solid (5.13 g, 27.8 mmol, 88% yield). $[\alpha]_D^{25}$ = +81.4° (*c* 1.0, $CHCl_3$); ^{1}H NMR (500 MHz, $CDCl_3$) δ 2.89 (dd, *J* = 10.2, 7.6 Hz, 1H), 2.42 – 2.26 (m, 3H), 2.05 (s, 3H), 2.03 – 1.91 (m, 2H), 1.33 (s, 3H), 0.88 (s, 3H); ^{13}C NMR (125 MHz, $CDCl_3$) δ 207.8, 179.1, 54.3, 43.4, 37.8, 35.0, 30.3, 30.3, 23.1, 17.5; IR (thin film, NaCl) 2959, 1731, 1708, 1184, 956 cm^{-1}; HRMS (ESI-TOF) *m/z* calc'd for [M–H]$^-$ $C_{10}H_{15}O_3$ = 183.1021, found 183.1024. All physical and spectral data were in good accordance with previously reported values.[43,86,87]
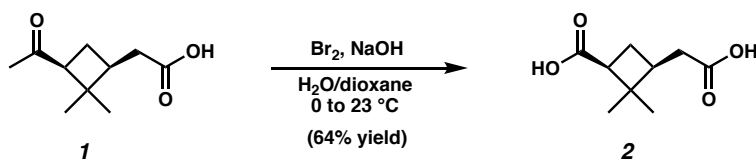
(1*S*,3*S*)-3-(carboxymethyl)-2,2-dimethylcyclobutane-1-carboxylic acid ((+)-*cis*-pinic acid, 2)

(+)-*cis*-Pinic acid (**2**) was prepared according to a modified literature procedure.[1] To a stirred solution of (+)-*cis*-pinonic acid (**1**) (2.50 g, 13.6 mmol, 1.0 equiv) in H_2O/dioxane (1:5, 200 mL) at 0 °C was added dropwise an aqueous solution of NaOBr, prepared via addition of Br_2 (2.30 mL, 44.9 mmol, 3.3 equiv) to a solution of NaOH (7.05 g, 176.3 mmol, 13.0 equiv) in H_2O (68 mL) at 0 °C. The mixture was stirred for 16 h and gradually allowed to warm to 23 °C, at which point TLC indicated complete consumption of **1**. The mixture was washed with CH_2Cl_2 (3 × 100 mL) and 40% aqueous $NaHSO_3$ (63 mL) was added. The aqueous phase was acidified to pH 1 with concentrated HCl and extracted with Et_2O (3 × 150 mL). The combined organic phases were washed with brine, dried over $MgSO_4$, and concentrated. The crude product was purified by flash chromatography (40% EtOAc/hexanes) followed by preparative HPLC [H_2O/MeCN; 40.0 mL min^{-1}; λ = 220 nm; (0–8.0 min) 82% H_2O, (8.0–10.0 min) 100% MeCN; 450 μL injection; t_R = 3.02 min] to afford the title compound as a white solid (1.61 g, 8.65 mmol, 64% yield). $[\alpha]_D^{25}$ = +4.6° (*c* 1.0, CHCl$_3$); ^{1}H NMR (500 MHz, CDCl$_3$) δ 2.78 (dd, *J* = 10.3, 7.8 Hz, 1H), 2.44 – 2.30 (m, 3H), 2.16 – 2.09 (m, 1H), 1.97 – 1.89 (m, 1H), 1.24 (s, 3H), 1.01 (s, 3H); ^{13}C NMR (125 MHz, CDCl$_3$) δ 179.4, 179.1, 46.2, 43.1, 38.1, 35.3, 30.0, 24.4, 17.7; IR (thin film, NaCl) 2959, 1703, 1422, 1248, 937 cm^{-1}; HRMS (ESI-TOF) *m/z* calc'd for [M–H]$^-$ $C_9H_{13}O_4$ = 185.0814, found 185.0815. All physical and spectral data were in good accordance with previously reported values.[43,87]
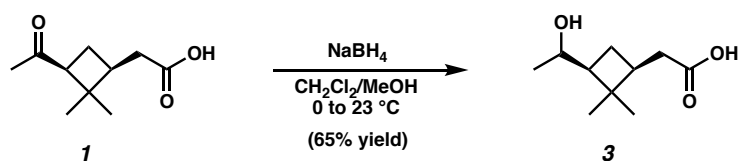
2-((1*S*,3*S*)-3-(1-hydroxyethyl)-2,2-dimethylcyclobutyl)acetic   acid   ((+)-*cis*-pinolic acid, 3)

To a stirred solution of (+)-*cis*-pinonic acid (**1**) (2.00 g, 10.9 mmol, 1.0 equiv) in CH$_2$Cl$_2$/MeOH (4:1, 109 mL) at 0 °C was added NaBH$_4$ (2.46 g, 65.0 mmol, 6.0 equiv) in one portion. The resulting suspension was stirred for 10 h and gradually allowed to warm to 23 °C, at which point TLC indicated complete consumption of **1**. The reaction mixture was cooled to 0 °C, quenched by slow addition of saturated aqueous NH$_4$Cl, and diluted with Et$_2$O (100 mL) and H$_2$O (100 mL). The layers were separated and the aqueous layer was extracted with Et$_2$O (3 × 100 mL). The combined organic phases were washed with brine, dried over MgSO$_4$, and concentrated to provide the crude product in quantitative yield as a mixture of epimers (^{1}H NMR shows epimers form in 2:1 ratio). The crude product was purified by flash chromatography (40% EtOAc/hexanes) to afford the major epimer as a white solid (1.32 g, 7.09 mmol, 65% yield). [α]$_D^{25}$ = −28.7° (*c* 1.0, CHCl$_3$); ^{1}H NMR (500 MHz, CDCl$_3$) δ 3.73 (dq, *J* = 10.0, 6.2 Hz, 1H), 2.41 – 2.32 (m, 1H), 2.27 – 2.16 (m, 2H), 2.07 – 1.98 (m, 1H), 1.78 (dt, *J* = 8.0, 10.2 Hz, 1H), 1.24 – 1.17 (m, 1H), 1.15 (s, 3H), 1.06 (d, *J* = 6.2 Hz, 3H), 1.03 (s, 3H); ^{13}C NMR (125 MHz, CDCl$_3$) δ 179.0, 69.4, 50.4, 40.0, 37.8, 35.0, 31.0, 26.6, 21.3, 16.9; IR (thin film, NaCl) 3304, 2962, 1684, 1255, 1169, 668 cm^{-1}; HRMS (ESI-TOF) *m/z* calc'd for [M−H]$^-$ C$_{10}$H$_{17}$O$_3$ = 185.1178, found 185.1179. All physical and spectral data were in good accordance with previously reported values.[44]
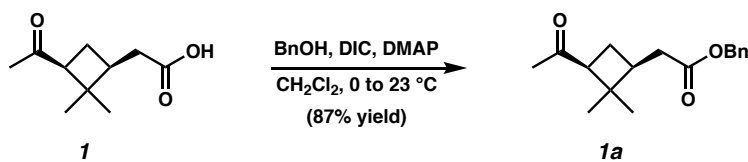
benzyl 2-((1*S*,3*S*)-3-acetyl-2,2-dimethylcyclobutyl)acetate (1a)

To a stirred solution of (+)-*cis*-pinonic acid (**1**) (3.00 g, 16.3 mmol, 1.0 equiv), benzyl alcohol (5.08 mL, 48.9 mmol, 3.0 equiv), and DMAP (199 mg, 1.63 mmol, 0.10 equiv) in CH_2Cl_2 (33 mL) at 0 °C was added DIC (2.55 mL, 16.3 mmol, 1.0 equiv) dropwise. The mixture was stirred for 24 h and gradually allowed to warm to 23 °C, at which point TLC indicated complete consumption of **1**. The solution was diluted with Et_2O (100 mL) and H_2O (100 mL). The layers were separated and the aqueous layer was extracted with Et_2O (3 × 50 mL). The combined organic phases were washed with brine, dried over $MgSO_4$, and concentrated. The crude product was purified by flash chromatography (30% Et_2O/hexanes) to afford the title compound as a colorless oil (3.89 g, 14.2 mmol, 87% yield). $[\alpha]_D^{25}$ +44.8° (*c* 1.0, CHCl$_3$); ^{1}H NMR (500 MHz, CDCl$_3$) δ 7.38 – 7.27 (m, 5H), 5.08 (s, 2H), 2.85 (dd, *J* = 10.2, 7.5 Hz, 1H), 2.42 – 2.26 (m, 3H), 2.02 (s, 3H), 2.00 – 1.94 (m, 1H), 1.93 – 1.86 (m, 1H), 1.28 (s, 3H), 0.84 (s, 3H); ^{13}C NMR (125 MHz, CDCl$_3$) δ 207.5, 172.6, 135.9, 128.6, 128.3, 128.3, 66.2, 54.2 43.3, 38.0, 35.2, 30.2, 30.2, 23.0, 17.3; IR (thin film, NaCl) 2954, 1733, 1704, 1164, 977, 751, 699 cm^{-1}; HRMS (ESI-TOF) *m/z* calc'd for [M+Na]$^+$ C$_{17}$H$_{22}$O$_3$Na = 297.1467, found 297.1476.
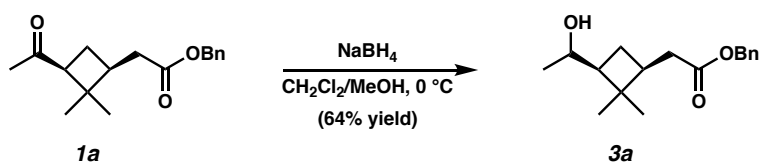
benzyl 2-((1*S*,3*S*)-3-(1-hydroxyethyl)-2,2-dimethylcyclobutyl)acetate (3a)

To a stirred solution of benzyl ester **1a** (2.00 g, 7.29 mmol, 1.0 equiv) in CH$_2$Cl$_2$/MeOH (4:1, 73 mL) at 0 °C was added NaBH$_4$ (827 mg, 21.9 mmol, 3.0 equiv) in one portion. The resulting suspension was stirred at 0 °C for 10 min, at which time TLC indicated complete consumption of **1a**. The mixture was quenched by slow addition of saturated aqueous NH$_4$Cl, then diluted with Et$_2$O (100 mL) and H$_2$O (100 mL). The layers were separated and the aqueous layer was extracted with Et$_2$O (3 × 100 mL). The combined organic phases were washed with brine, dried over MgSO$_4$, and concentrated to provide the crude product as a mixture of epimers. The crude product was purified by flash chromatography (40% Et$_2$O/hexanes) to afford the major epimer as a colorless oil (1.28 g, 4.63 mmol, 64% yield). $[\alpha]_D^{25}$ −23.8° (*c* 1.0, CHCl$_3$); ^{1}H NMR (500 MHz, CDCl$_3$) δ 7.39 – 7.29 (m, 5H), 5.09 (s, 2H), 3.69 (dq, *J* = 10.0, 6.2 Hz, 1H), 2.41 – 2.33 (m, 1H), 2.28 – 2.17 (m, 2H), 2.00 – 1.93 (m, 1H), 1.75 (dt, *J* = 8.0, 10.2 Hz, 1H), 1.16 (m, 1H), 1.11 (s, 3H), 1.04 (d, *J* = 6.2 Hz, 3H), 1.00 (s, 3H); ^{13}C NMR (125 MHz, CDCl$_3$) δ 173.0, 136.0, 128.6, 128.3, 128.2, 69.2, 66.2, 50.3, 39.9, 37.9, 35.3, 30.9, 26.6, 21.3, 16.8; IR (thin film, NaCl) 3425, 2960, 1734, 1456, 1164, 750, 698 cm^{-1}; HRMS (ESI-TOF) *m/z* calc'd for [M+Na]$^+$ C$_{17}$H$_{24}$O$_3$Na = 299.1623, found 299.1616.

Note: Deviation from the procedure described above by allowing the reaction to warm to room temperature and stir for prolonged periods of time (i.e., 10 h) was found to result in formation of significant quantities of the methyl ester of 3a, which is extremely difficult to separate from 3a.
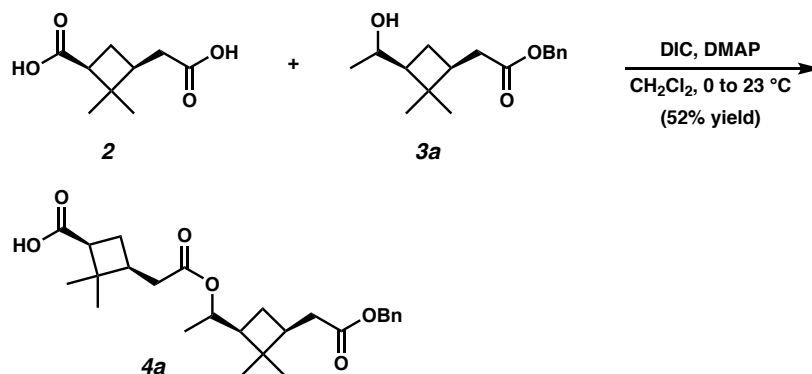
(1*S*,3*S*)-3-(2-(1-(((1*S*,3*S*)-3-(2-(benzyloxy)-2-oxoethyl)-2,2-dimethylcyclobutyl)ethoxy)-2-oxoethyl)-2,2-dimethylcyclobutane-1-carboxylic acid (4a)

To a stirred solution of alcohol **3a** (100 mg, 0.362 mmol, 1.00 equiv), (+)-*cis*-pinic acid (**2**) (101 mg, 0.543 mmol, 1.5 equiv), and DMAP (4.4 mg, 0.0362 mmol, 0.10 equiv) in CH$_2$Cl$_2$ (3.6 mL) at 0 °C was added DIC (85 μL, 0.543 mmol, 1.5 equiv) dropwise. The mixture was stirred for 24 h and gradually allowed to warm to 23 °C, at which point TLC indicated complete consumption of **3a**. The solution was diluted with Et$_2$O (20 mL) and H$_2$O (20 mL). The layers were separated and the aqueous layer was extracted with Et$_2$O (3 × 20 mL). The combined organic phases were washed with brine, dried over MgSO$_4$, and concentrated. The crude product was purified by flash chromatography (30–40% Et$_2$O/hexanes) to afford the title compound as a colorless oil (83 mg, 0.187 mmol, 52% yield). $[\alpha]_D^{25} = -11.3°$ (*c* 1.0, CHCl$_3$); ^{1}H NMR (500 MHz, CDCl$_3$) δ 7.38 – 7.27 (m, 5H), 5.08 (s, 2H), 4.76 (dq, *J* = 10.2, 6.1 Hz, 1H), 2.78 (dd, *J* = 10.3, 7.8 Hz, 1H), 2.41 – 2.29 (m, 3H), 2.28 – 2.18 (m, 3H), 2.14–2.08 (m, 1H), 2.06 – 1.95 (m, 2H), 1.89 (dt, *J* = 11.2, 10.3 Hz, 1H), 1.25 (s, 3H), 1.22 (m, 1H), 1.06 (s, 3H), 1.04 (d, *J* = 6.2 Hz, 3H), 1.00 (s, 3H), 0.86 (s, 3H); ^{13}C NMR (125 MHz, CDCl$_3$) δ 178.8, 172.9, 172.2, 136.0, 128.6, 128.4, 128.3, 71.8, 66.3, 47.0, 46.1, 43.0, 39.9, 38.4, 38.1, 35.9, 35.2, 30.5, 30.1, 26.5, 24.5, 17.7, 17.7, 16.9; IR (thin film, NaCl) 2958, 1731, 1456, 1170, 1067, 750, 697 cm^{-1}; HRMS (ESI-TOF) *m/z* calc'd for [M–H]$^-$ C$_{26}$H$_{35}$O$_6$ = 443.2434, found 443.2442.
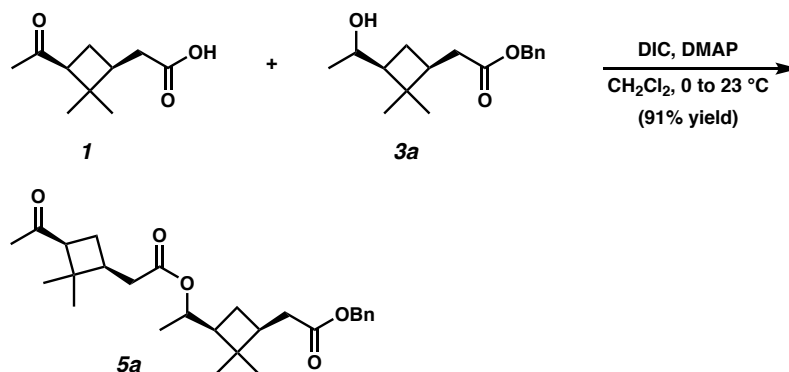
benzyl 2-((1*S*,3*S*)-3-(1-(2-((1*S*,3*S*)-3-acetyl-2,2-dimethylcyclobutyl)acetoxy) ethyl)-2,2-dimethylcyclobutyl)acetate (5a)

To a stirred solution of alcohol **3a** (1.00 g, 3.62 mmol, 1.0 equiv), (+)-*cis*-pinonic acid (**1**) (1.33 g, 7.24 mmol, 2.0 equiv), and DMAP (44 mg, 0.362 mmol, 0.10 equiv) in CH_2Cl_2 (36 mL) at 0 °C was added DIC (1.14 mL, 7.24 mmol, 2.0 equiv) dropwise. The mixture was stirred for 24 h and gradually allowed to warm to 23 °C, at which point TLC indicated complete consumption of **3a**. The solution was diluted with Et_2O (100 mL) and H_2O (100 mL). The layers were separated and the aqueous layer was extracted with Et_2O (3 × 100 mL). The combined organic phases were washed with brine, dried over $MgSO_4$, and concentrated. The crude product was purified by flash chromatography (30% Et_2O/hexanes) to afford the title compound as a colorless oil (1.46 g, 3.31 mmol, 91% yield). $[\alpha]_D^{25}$ +22.4° (*c* 1.0, CHCl$_3$); ^{1}H NMR (500 MHz, CDCl$_3$) δ 7.38 – 7.27 (m, 5H), 5.06 (s, 2H), 4.74 (dq, *J* = 10.2, 6.1 Hz, 1H), 2.85 (dd, *J* = 10.0, 7.7 Hz, 1H), 2.38 – 2.29 (m, 2H), 2.28 – 2.19 (m, 3H), 2.16 (dd, *J* = 15.4, 7.7 Hz, 1H), 2.02 (s, 3H), 2.00 – 1.87 (m, 4H), 1.30 (s, 3H), 1.22 (m, 1H), 1.04 (s, 3H), 1.02 (d, *J* = 6.2 Hz, 3H), 0.84 (s, 6H); ^{13}C NMR (125 MHz, CDCl$_3$) δ 207.5, 172.8, 172.2, 136.0, 128.6, 128.3, 128.3, 71.7, 66.2, 54.2, 47.0, 43.3, 39.8, 38.1, 38.0, 35.6, 35.2, 30.4, 30.3, 30.2, 26.4, 23.1, 17.6, 17.4, 16.8; IR (thin film, NaCl) 2956, 1731, 1706, 1455, 1369, 1167, 698 cm^{-1}; HRMS (ESI-TOF) *m/z* calc'd for [M+Na]$^+$ $C_{27}H_{38}O_5Na$ = 465.2617, found 465.2611.
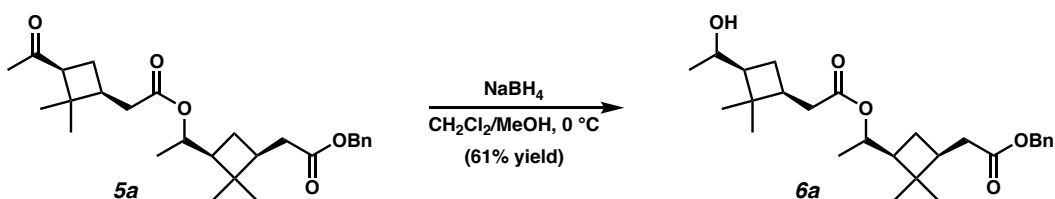
benzyl 2-((1*S*,3*S*)-3-(1-(2-((1*S*,3*S*)-3-(1-hydroxyethyl)-2,2-dimethylcyclobutyl)acetoxy)ethyl)-2,2-dimethylcyclobutyl)acetate (6a)

To a stirred solution of benzyl ester **5a** (400 mg, 0.904 mmol, 1.0 equiv) in CH$_2$Cl$_2$/MeOH (4:1, 9.0 mL) at 0 °C was added NaBH$_4$ (103 mg, 2.72 mmol, 3.0 equiv) in one portion. The resulting suspension was stirred at 0 °C for 10 min, at which time TLC indicated complete consumption of **5a**. The mixture was quenched by slow addition of saturated aqueous NH$_4$Cl, then diluted with Et$_2$O (100 mL) and H$_2$O (100 mL). The layers were separated and the aqueous layer was extracted with Et$_2$O (3 × 100 mL). The combined organic phases were washed with brine, dried over MgSO$_4$, and concentrated to provide the crude product as a mixture of epimers. The crude product was purified by flash chromatography (40% Et$_2$O/hexanes) to afford the major epimer as a colorless oil (245 mg, 0.551 mmol, 61% yield). [α]$_D^{25}$ −22.1° (*c* 1.0, CHCl$_3$); ^{1}H NMR (500 MHz, CDCl$_3$) δ 7.38 – 7.27 (m, 5H), 5.07 (s, 2H), 4.74 (dq, *J* = 10.2, 6.1 Hz, 1H), 3.68 (dq, *J* = 10.0, 6.2 Hz, 1H), 2.41 – 2.05 (m, 6H), 2.04 – 1.91 (m, 3H), 1.73 (dt, *J* = 8.0, 10.2 Hz, 1H), 1.21 (m, 1H), 1.13 (s, 3H), 1.12 (m, *J* = 10.4 Hz, 1H), 1.05 (s, 3H), 1.03 (d, *J* = 6.1 Hz, 3H), 1.02 (d, *J* = 6.2 Hz, 3H), 1.00 (s, 3H), 0.85 (s, 3H); ^{13}C NMR (125 MHz, CDCl$_3$) δ 172.9, 172.6, 136.0, 128.6, 128.3, 128.3, 71.5, 69.2, 66.2, 50.3, 47.0, 39.9, 39.9, 38.1, 38.1, 35.8, 35.2, 31.1, 30.4, 26.7, 26.5, 21.3, 17.7, 16.9, 16.8; IR (thin film, NaCl) 3504, 2958, 1732, 1456, 1367, 1187, 1166, 750, 698 cm^{-1}; HRMS (ESI-TOF) *m/z* calc'd for [M+Na]$^+$ C$_{27}$H$_{40}$O$_5$Na = 467.2773, found 467.2773.
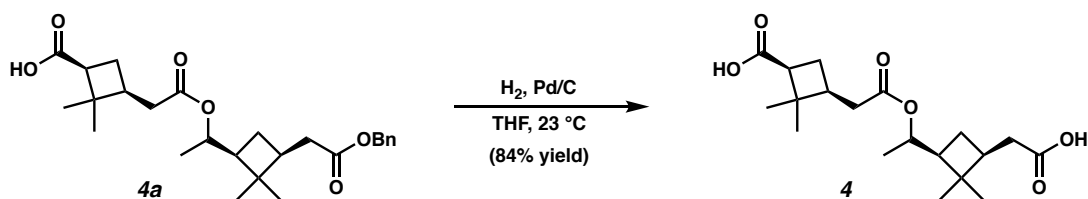
(1*S*,3*S*)-3-(2-(1-((1*S*,3*S*)-3-(carboxymethyl)-2,2-dimethylcyclobutyl)ethoxy)-2-oxoethyl)-2,2-dimethylcyclobutane-1-carboxylic acid (4)

In a 2-necked round bottom flask equipped with a 3-way valve at 23 °C, benzyl ester **4a** (100 mg, 0.225 mmol, 1.0 equiv) was dissolved in THF (2.3 mL) and to this solution was added Pd/C (10% w/w, 25 mg). The flask was evacuated and backfilled with N$_2$ (3×), then purged and backfilled with H$_2$ (3×). The suspension was stirred for 2 h under H$_2$ (1 atm, balloon), at which point TLC indicated complete consumption of **4a**. The flask was evacuated and backfilled with N$_2$ (3×), then the suspension was diluted with EtOAc (20 mL), filtered through celite, and concentrated. The crude product was purified by flash chromatography (50% EtOAc/hexanes) to afford the title compound as a white solid (67 mg, 0.189 mmol, 84% yield). $[\alpha]_D^{25} = -11.4°$ (*c* 1.0, CHCl$_3$); ^{1}H NMR (500 MHz, CDCl$_3$) δ 4.76 (dq, *J* = 10.2, 6.1 Hz, 1H), 2.77 (dd, *J* = 10.3, 7.8 Hz, 1H), 2.41 – 2.29 (m, 3H), 2.28 – 2.18 (m, 3H), 2.15 – 1.94 (m, 3H), 1.88 (dt, *J* = 11.0, 10.3 Hz, 1H), 1.24 (s, 3H), 1.22 (m, 1H), 1.09 (s, 3H), 1.04 (d, *J* = 6.1 Hz, 3H), 0.99 (s, 3H), 0.87 (s, 3H); ^{13}C NMR (125 MHz, CDCl$_3$) δ 179.8, 179.2, 172.3, 71.8, 47.1, 46.2, 43.1, 39.9, 38.5, 37.8, 35.9, 35.0, 30.5, 30.1, 26.5, 24.5, 17.7, 17.7, 16.9 ; IR (thin film, NaCl) 2957, 1704, 1247, 1211, 958, 739 cm^{-1}; HRMS (ESI-TOF) *m/z* calc'd for [M–H]$^-$ C$_{19}$H$_{29}$O$_6$ = 353.1964, found 353.1967.
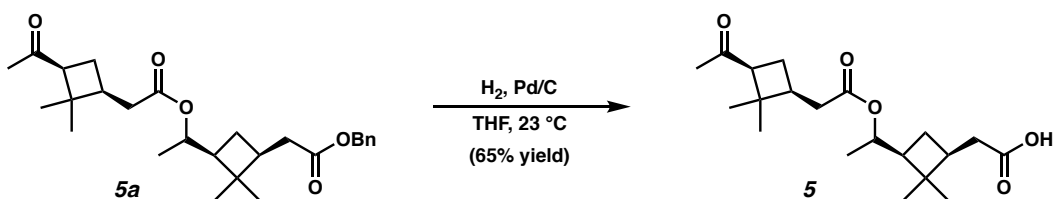
2-((1*S*,3*S*)-3-(1-(2-((1*S*,3*S*)-3-acetyl-2,2-dimethylcyclobutyl)acetoxy)ethyl)-2,2-dimethylcyclobutyl)acetic acid (5)

In a 2-necked round bottom flask equipped with a 3-way valve at 23 °C, benzyl ester **5a** (400 mg, 0.904 mmol, 1.0 equiv) was dissolved in THF (9.1 mL) and to this solution was added Pd/C (10%, 100 mg). The flask was evacuated and backfilled with N$_2$ (3×), then purged and backfilled with H$_2$ (3×). The suspension was stirred for 2 h under H$_2$ (1 atm, balloon), at which point TLC indicated complete consumption of **5a**. The flask was evacuated and backfilled with N$_2$ (3×), then the suspension was diluted with EtOAc (50 mL), filtered through celite, and concentrated. The crude product was purified by flash chromatography (40% EtOAc/hexanes) to afford the title compound as a white solid (206 mg, 0.585 mmol, 65% yield). [α]$_D^{25}$ +29.4°(*c* 1.0, CHCl$_3$); ^{1}H NMR (500 MHz, CDCl$_3$) δ 4.74 (dq, *J* = 10.2, 6.1 Hz, 1H), 2.85 (dd, *J* = 10.0, 7.8 Hz, 1H), 2.37 – 2.09 (m, 6H), 2.08 – 1.83 (m, 7H), 1.29 (s, 3H), 1.22 (m, 1H), 1.06 (s, 3H), 1.01 (d, *J* = 6.1 Hz, 3H), 0.84 (s, 3H), 0.82 (s, 3H); ^{13}C NMR (125 MHz, CDCl$_3$) δ 207.9, 179.1, 172.3, 71.7, 54.3, 47.0, 43.4, 39.9, 38.1, 37.8, 35.6, 34.9, 30.5, 30.3, 30.2, 26.4, 23.2, 17.6, 17.4, 16.8; IR (thin film, NaCl) 2956, 1728, 1706, 1369, 1180, 959, 867 cm^{-1}; HRMS (ESI-TOF) *m/z* calc'd for [M−H]$^-$ C$_{20}$H$_{31}$O$_5$ = 351.2171, found 351.2178.
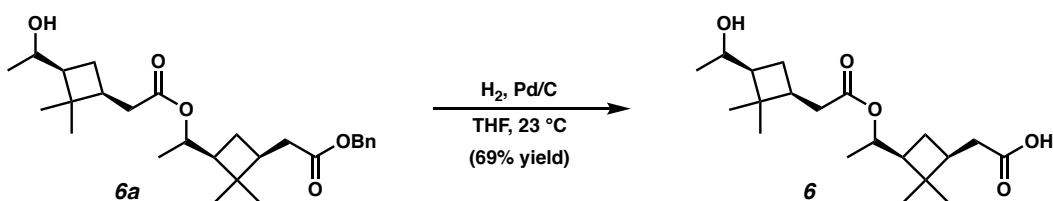
2-((1*S*,3*S*)-3-(1-(2-((1*S*,3*S*)-3-(1-hydroxyethyl)-2,2-dimethylcyclobutyl)acetoxy)ethyl)-2,2-dimethylcyclobutyl)acetic acid (6)

In a 2-necked round bottom flask equipped with a 3-way valve, benzyl ester **6a** (100 mg, 0.225 mmol, 1.0 equiv) was dissolved in THF (2.3 mL) and to this solution was added Pd/C (10% w/w, 25 mg). The flask was evacuated and backfilled with N_2 (3×), then purged and backfilled with H_2 (3×). The suspension was stirred for 2 h under H_2 (1 atm, balloon), at which point TLC indicated complete consumption of **6a**. The flask was evacuated and backfilled with N_2 (3×), then the suspension was diluted with EtOAc (20 mL), filtered through celite, and concentrated. The crude product was purified by flash chromatography (50% EtOAc/hexanes) to afford the title compound as a white solid (55 mg, 0.156 mmol, 69% yield). $[\alpha]_D^{25}$ −17.8° (*c* 1.0, CHCl$_3$); ^{1}H NMR (500 MHz, CDCl$_3$) δ 4.74 (dq, *J* = 10.1, 6.1 Hz, 1H), 3.69 (dq, *J* = 10.0, 6.2 Hz, 1H), 2.39 – 1.92 (m, 9H), 1.74 (dt, *J* = 8.0, 10.2 Hz, 1H), 1.21 (m, 1H), 1.14 (m, *J* = 10.4 Hz, 1H), 1.12 (s, 3H), 1.08 (s, 3H), 1.03 (d, *J* = 6.1 Hz, 3H), 1.02 (d, *J* = 6.2 Hz, 3H), 0.99 (s, 3H), 0.86 (s, 3H); ^{13}C NMR (125 MHz, CDCl$_3$) δ 178.6, 172.7, 71.6, 69.4, 50.2, 47.1, 39.9, 39.9, 38.1, 37.9, 35.8, 35.0, 31.0, 30.5, 26.7, 26.5, 21.2, 17.7, 16.9, 16.8; IR (thin film, NaCl) 3441, 2959, 1709, 1451, 1368, 1191, 874, 736, 668 cm^{-1}; HRMS (ESI-TOF) *m/z* calc'd for [M–H]$^-$ C$_{20}$H$_{33}$O$_5$ = 353.2328, found 353.2332.

3.S5 NMR and IR Spectra

^{1}H NMR (500 MHz, CDCl$_3$) of compound **1**.
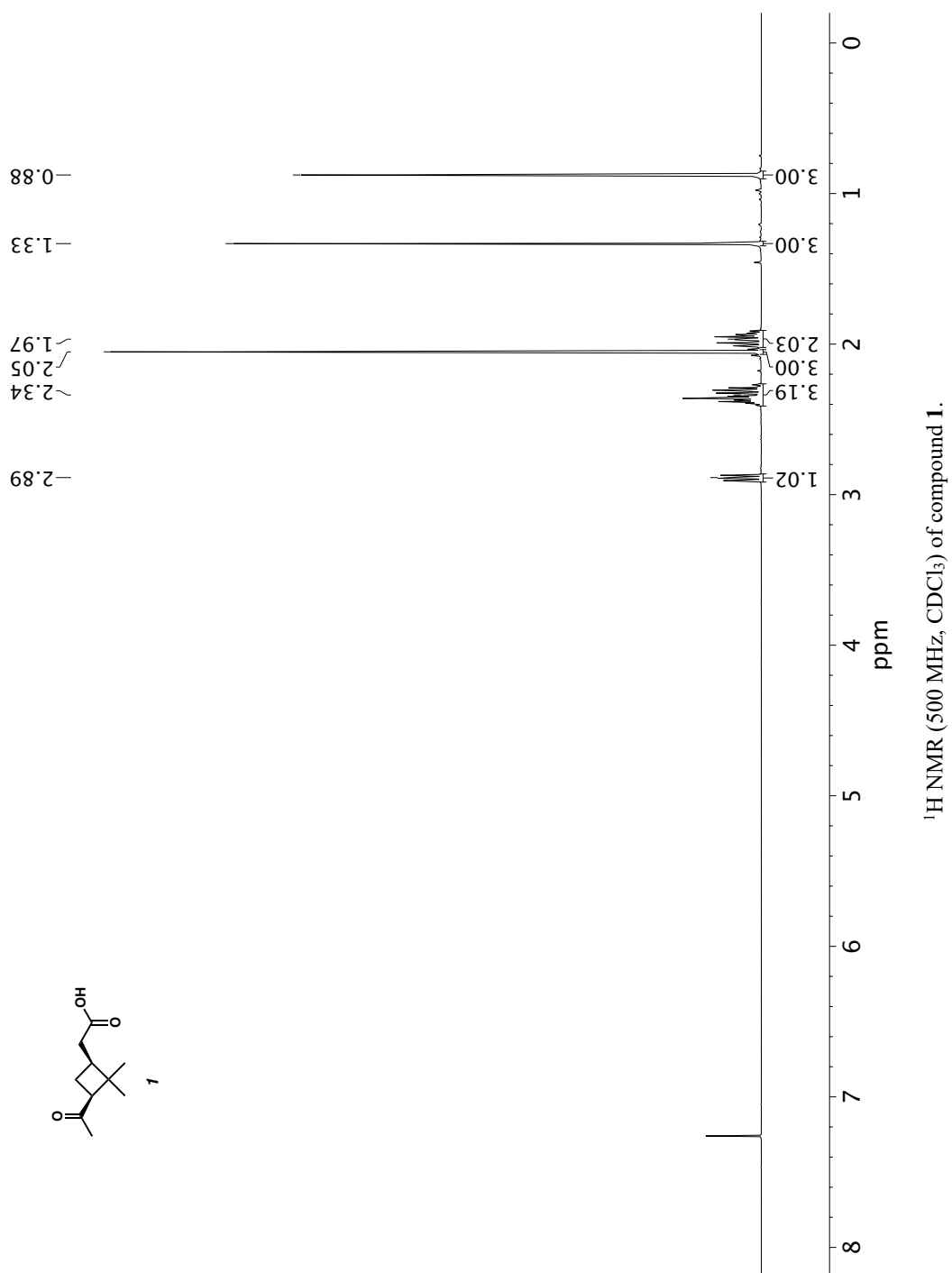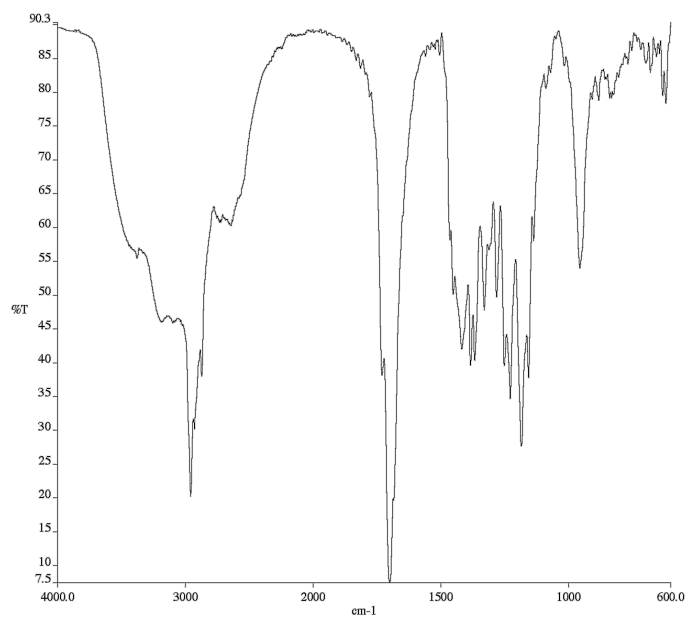
Infrared spectrum (thin film, NaCl) of compound **1**.

^{13}C NMR (125 MHz, CDCl$_3$) of compound **1**.

^{1}H NMR (500 MHz, CDCl$_3$) of compound **2**.
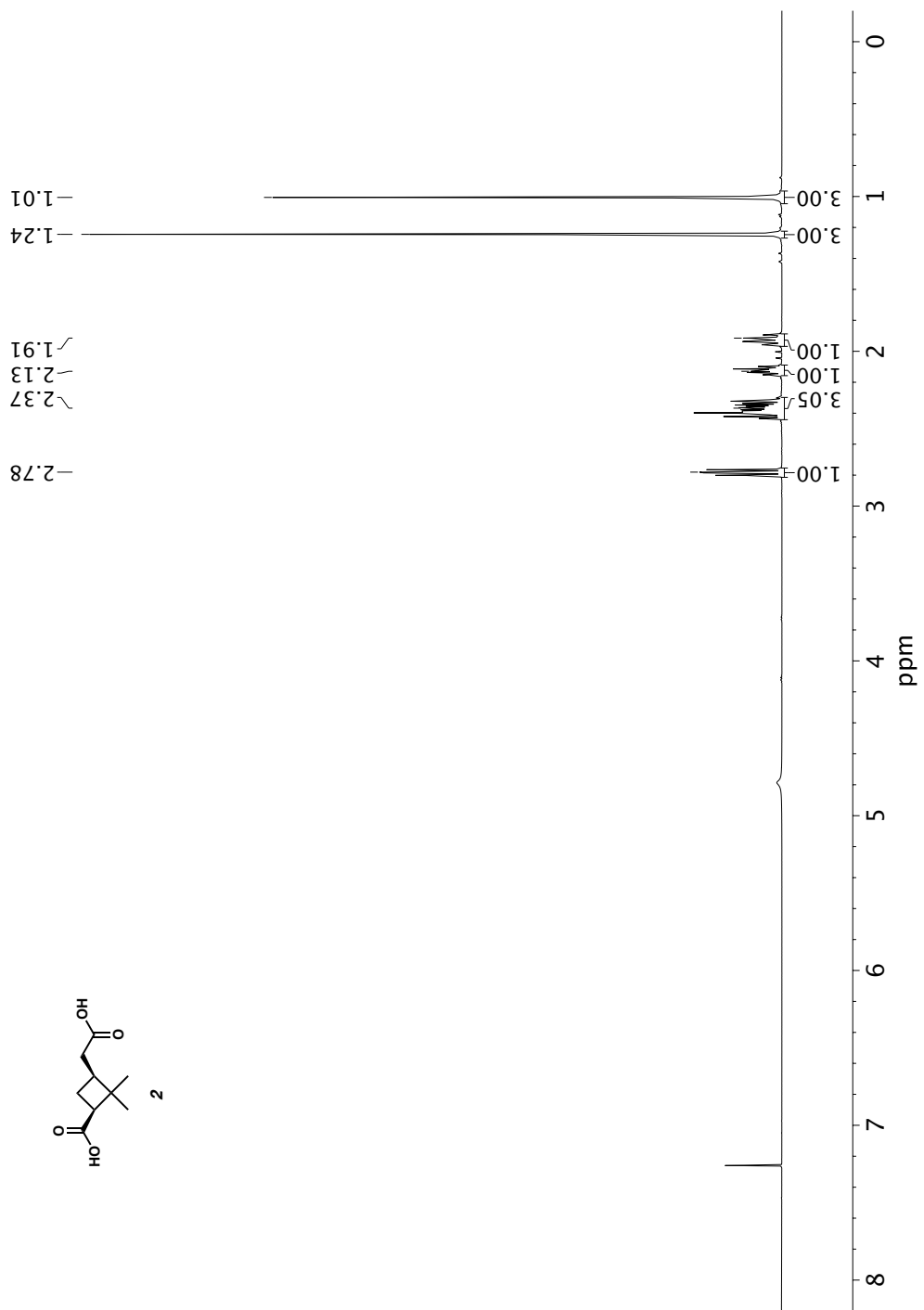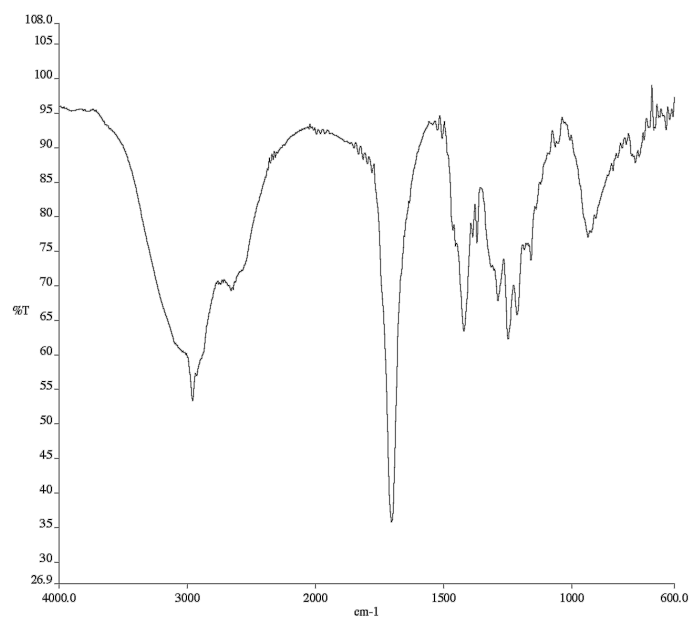
Infrared spectrum (thin film, NaCl) of compound **2**.

^{13}C NMR (125 MHz, CDCl$_3$) of compound **2**.

^{1}H NMR (500 MHz, CDCl$_3$) of compound **3**.
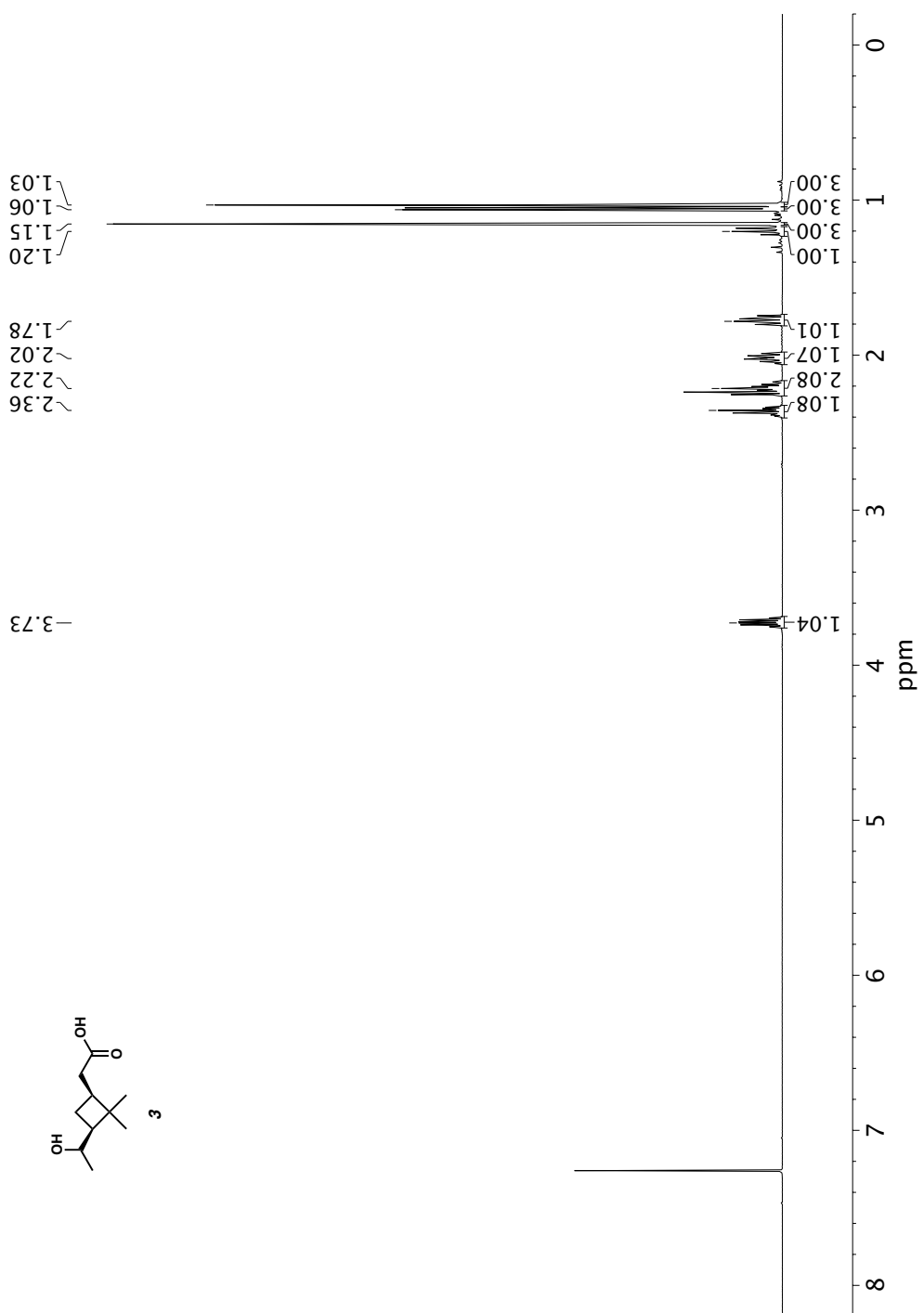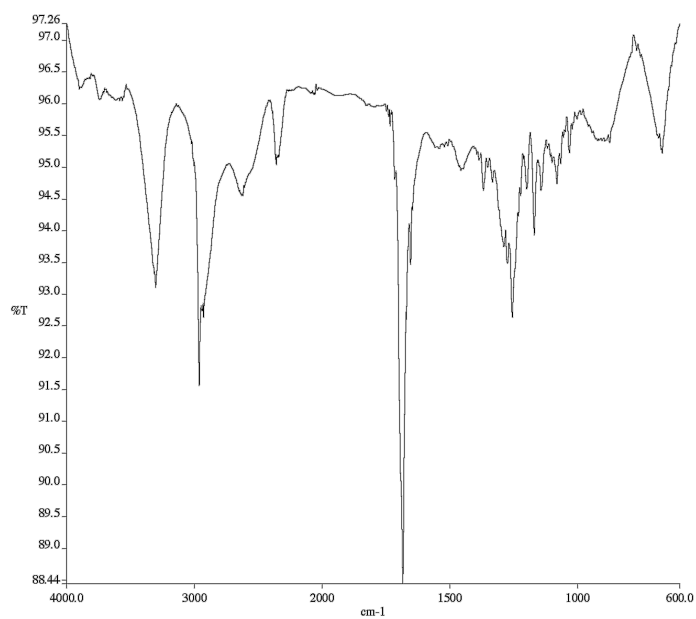
Infrared spectrum (thin film, NaCl) of compound **3**.

^{13}C NMR (125 MHz, CDCl$_3$) of compound **3**.

^{1}H NMR (500 MHz, CDCl$_3$) of compound **1a**.
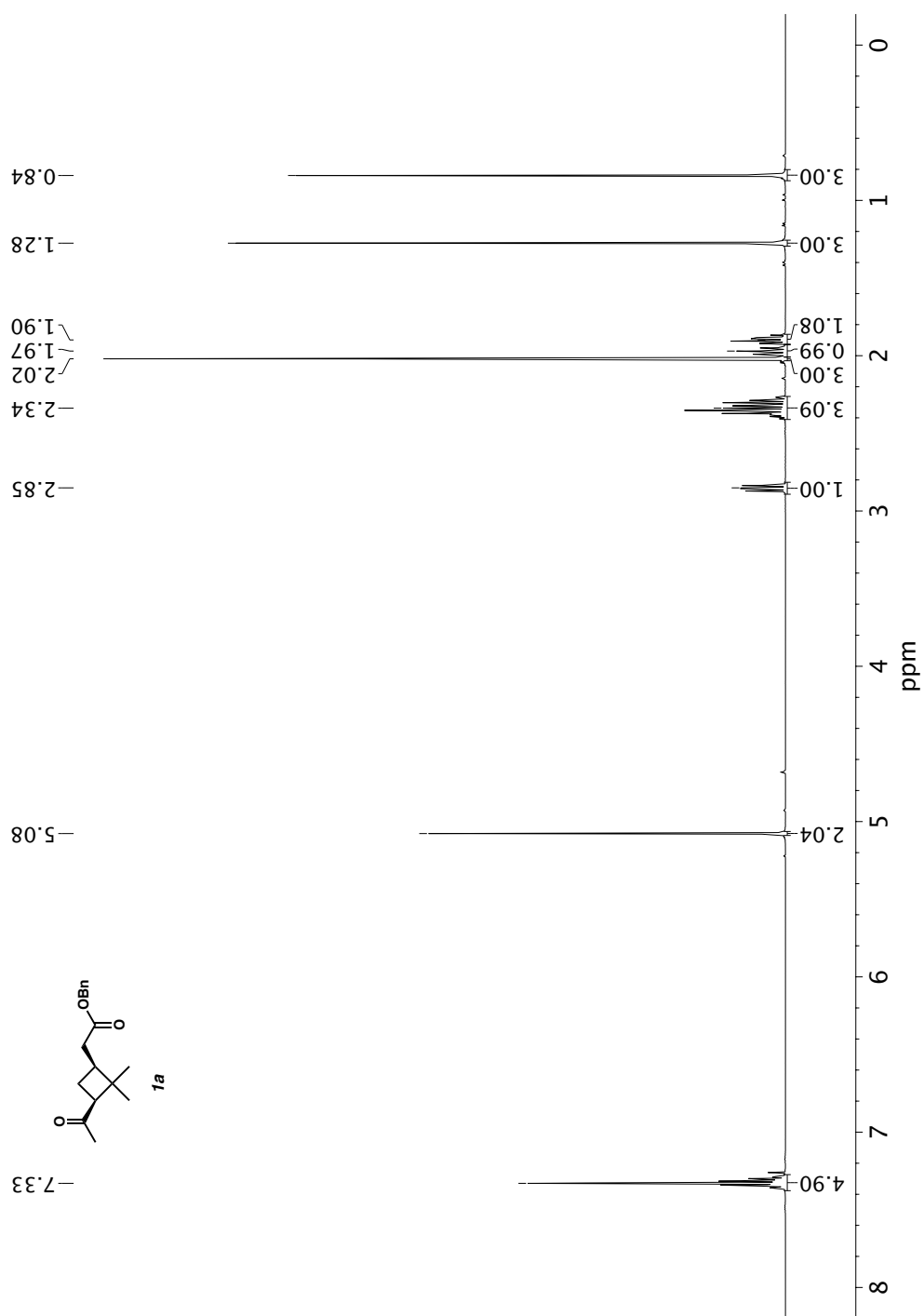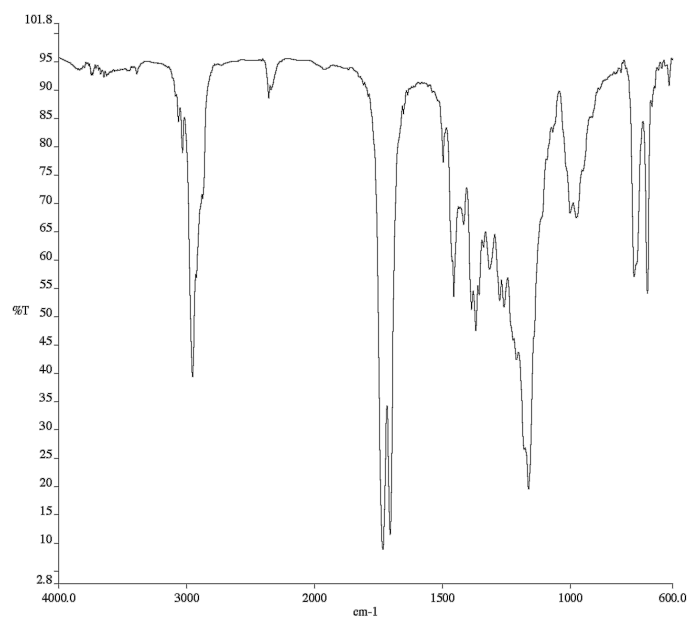
Infrared spectrum (thin film, NaCl) of compound **1a**.

^{13}C NMR (125 MHz, CDCl$_3$) of compound **1a**.

^{1}H NMR (500 MHz, CDCl$_3$) of compound **3a**.
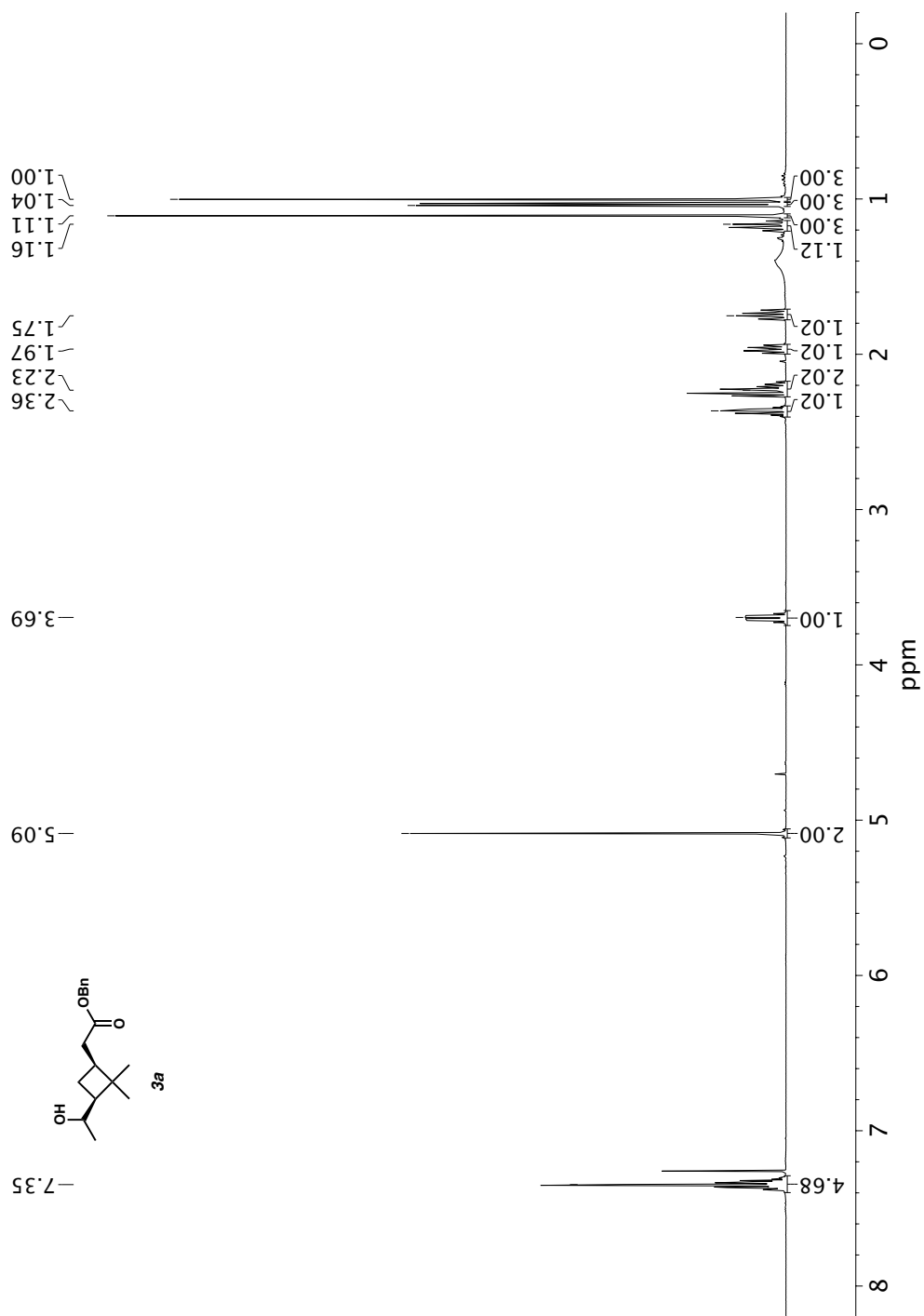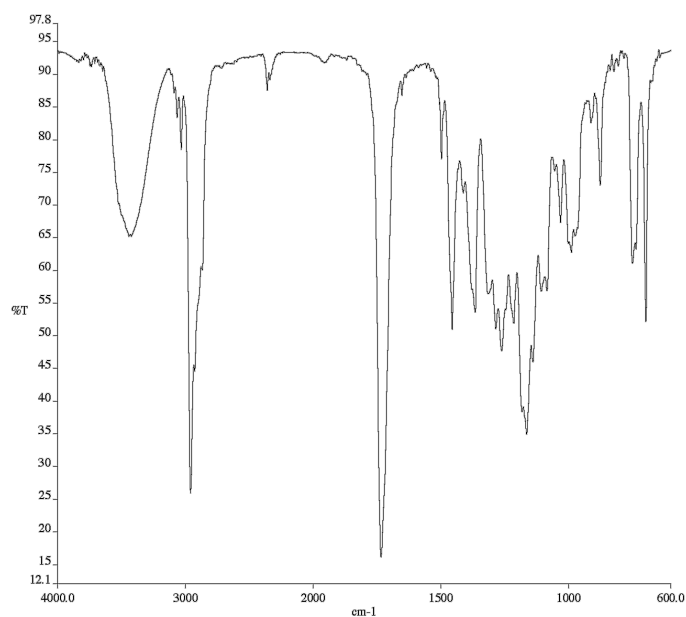
Infrared spectrum (thin film, NaCl) of compound **3a**.

^{13}C NMR (125 MHz, CDCl$_3$) of compound **3a**.

^{1}H NMR (500 MHz, CDCl$_3$) of compound **4a**.
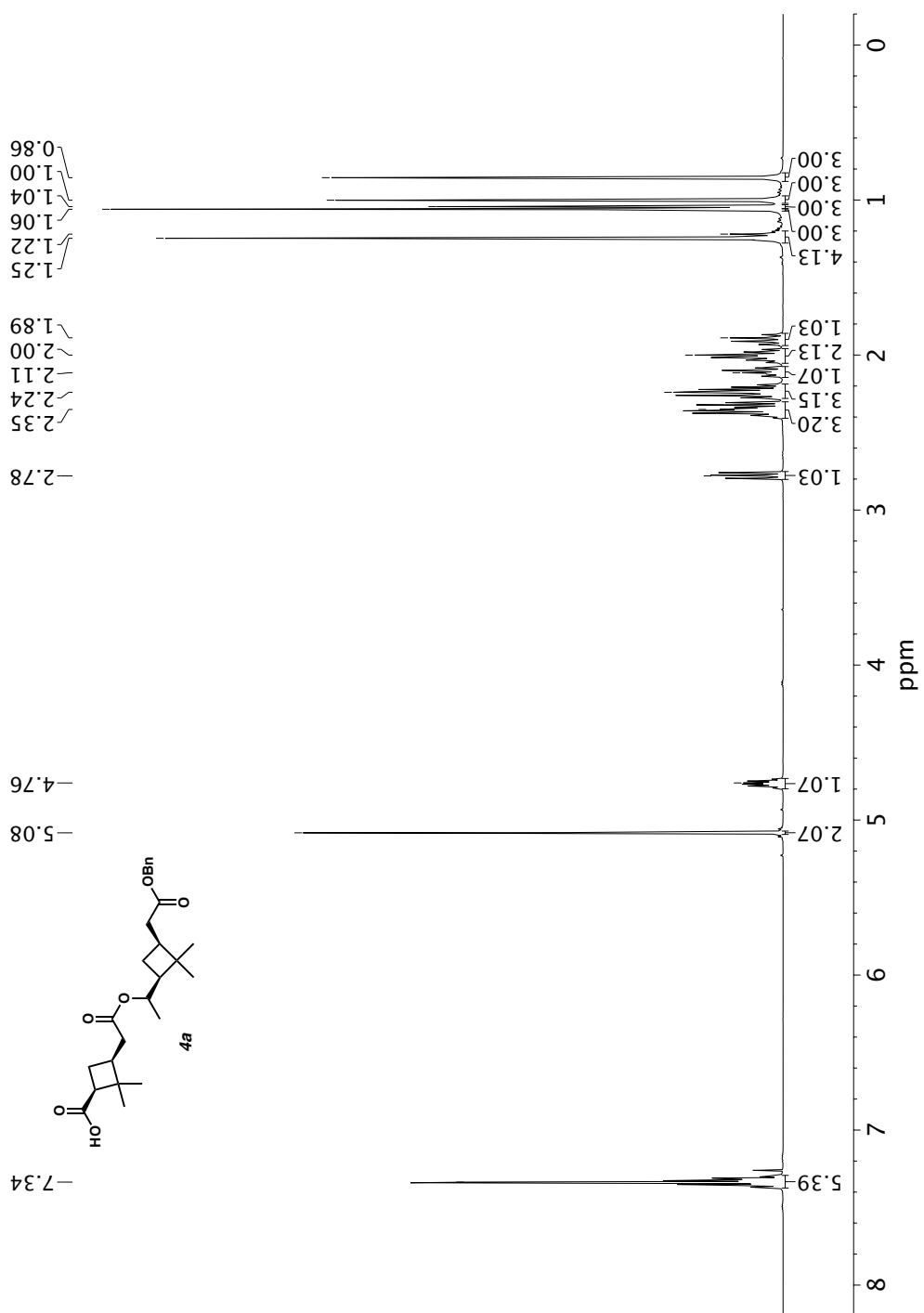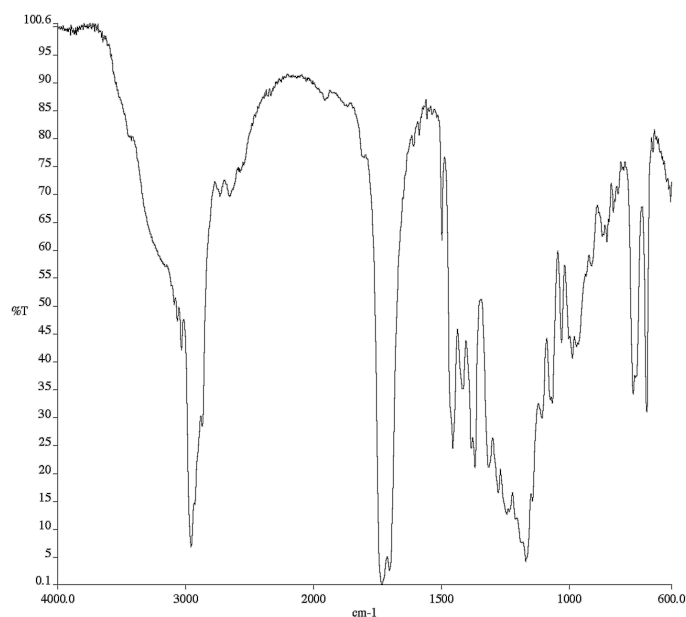
Infrared spectrum (thin film, NaCl) of compound **4a**.

^{13}C NMR (125 MHz, CDCl$_3$) of compound **4a**.

^{1}H NMR (500 MHz, CDCl$_3$) of compound **5a**.
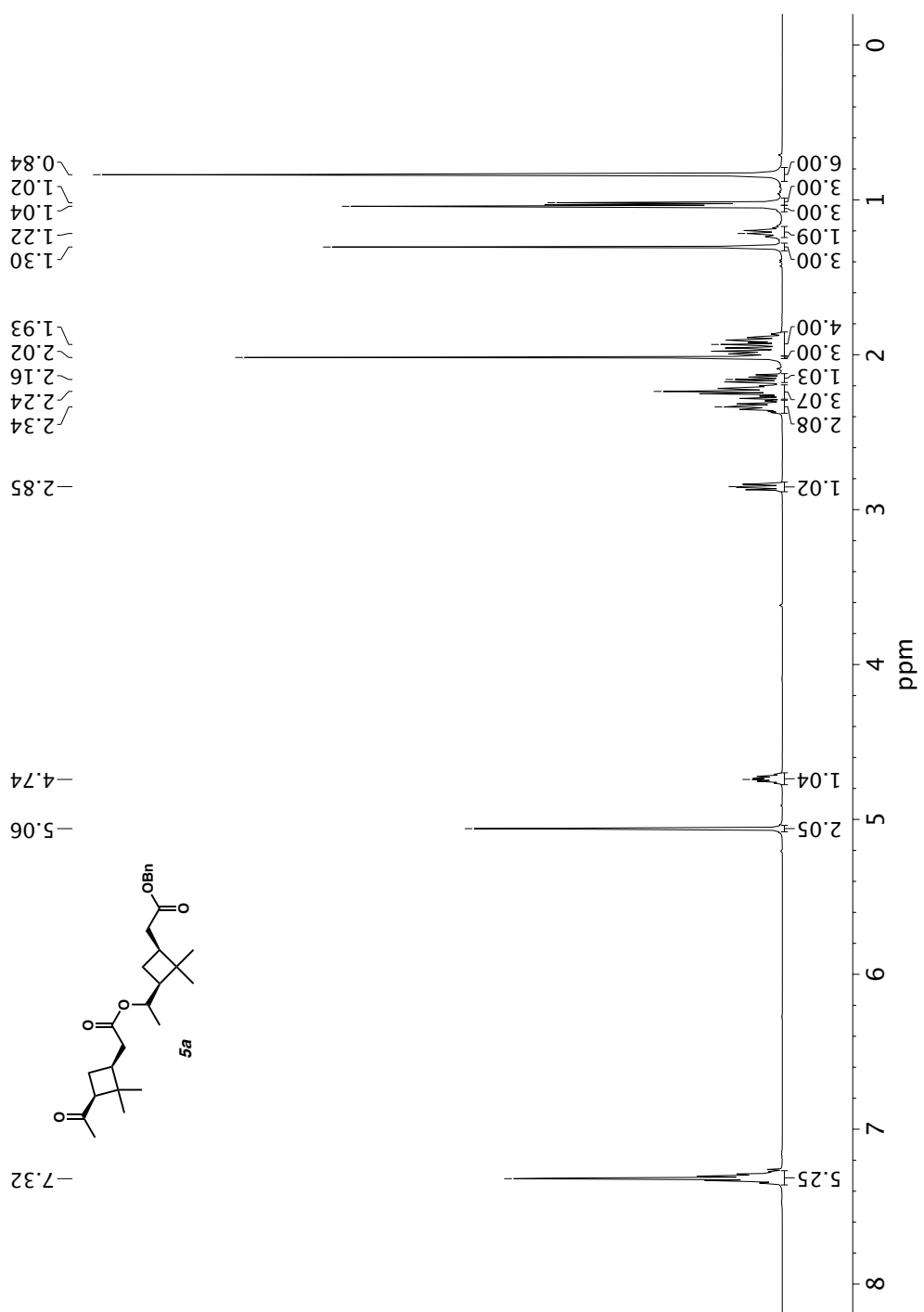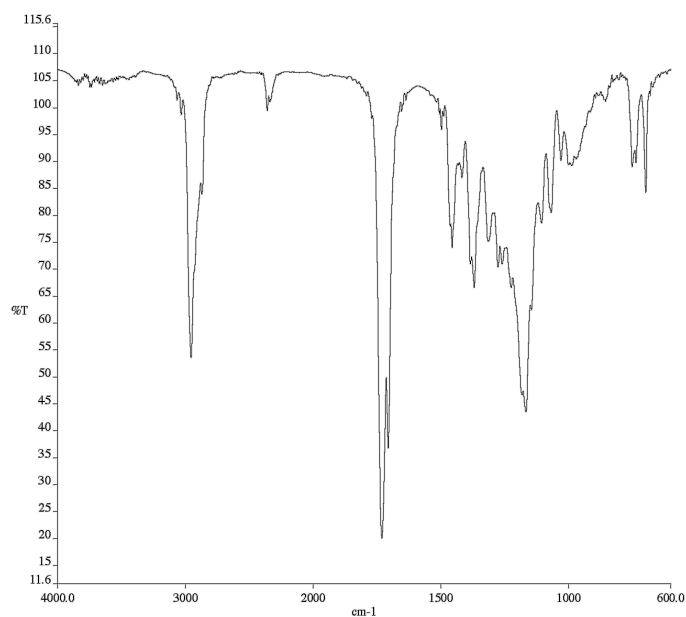
Infrared spectrum (thin film, NaCl) of compound **5a**.

^{13}C NMR (125 MHz, CDCl$_3$) of compound **5a**.

0.85
1.00
1.02
1.03
1.05
1.12
1.13
1.21

1.73
1.97
2.23

3.68

4.74

5.07

7.33

^{1}H NMR (500 MHz, CDCl$_3$) of compound **6a**.

ppm

3.00
3.00
3.00
3.00
3.00
4.17
1.00

1.02
3.14
6.45

1.06

1.06

2.07

5.40

Infrared spectrum (thin film, NaCl) of compound **6a**.

^{13}C NMR (125 MHz, CDCl$_3$) of compound **6a**.

^{1}H NMR (500 MHz, CDCl$_3$) of compound **4**.
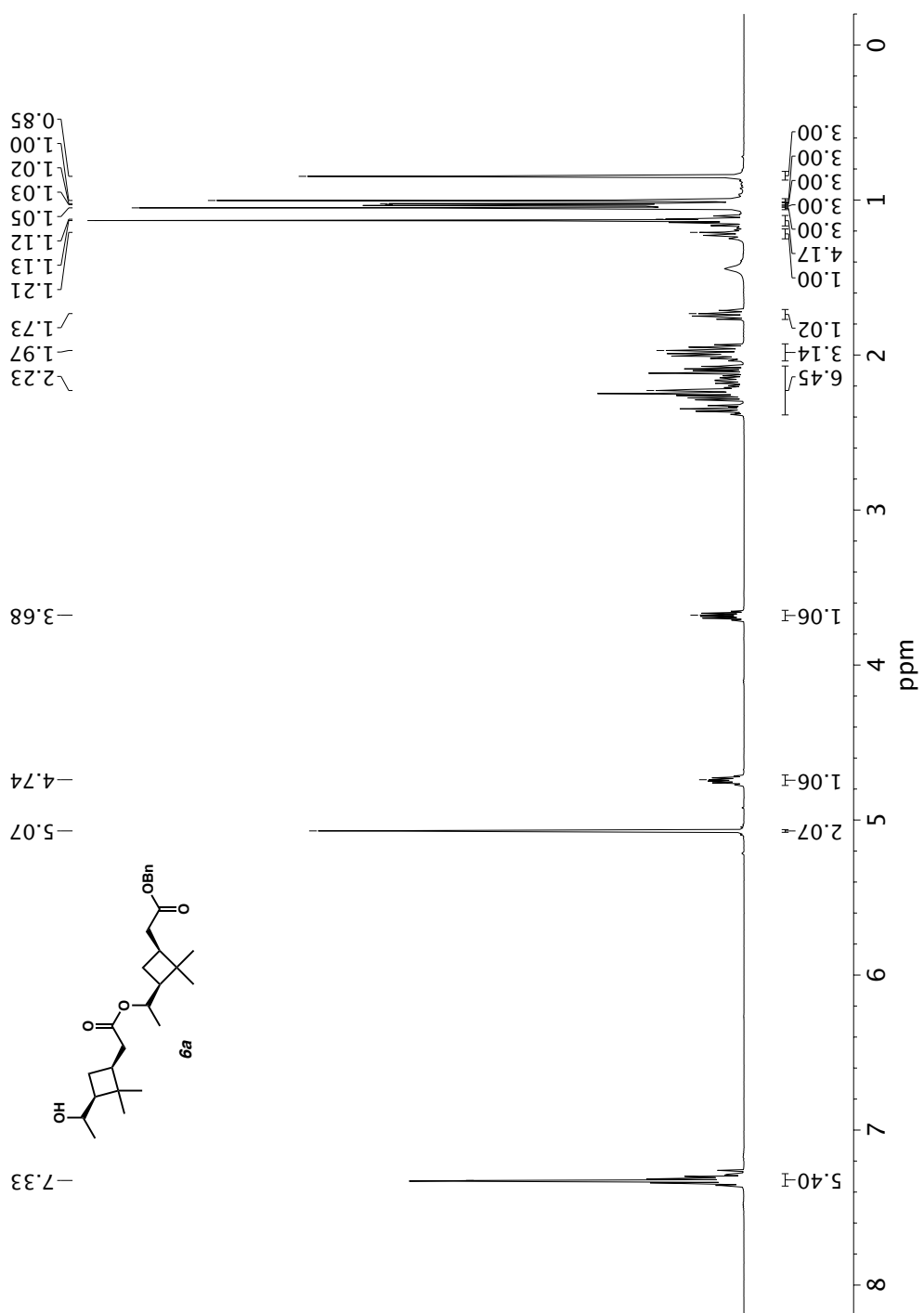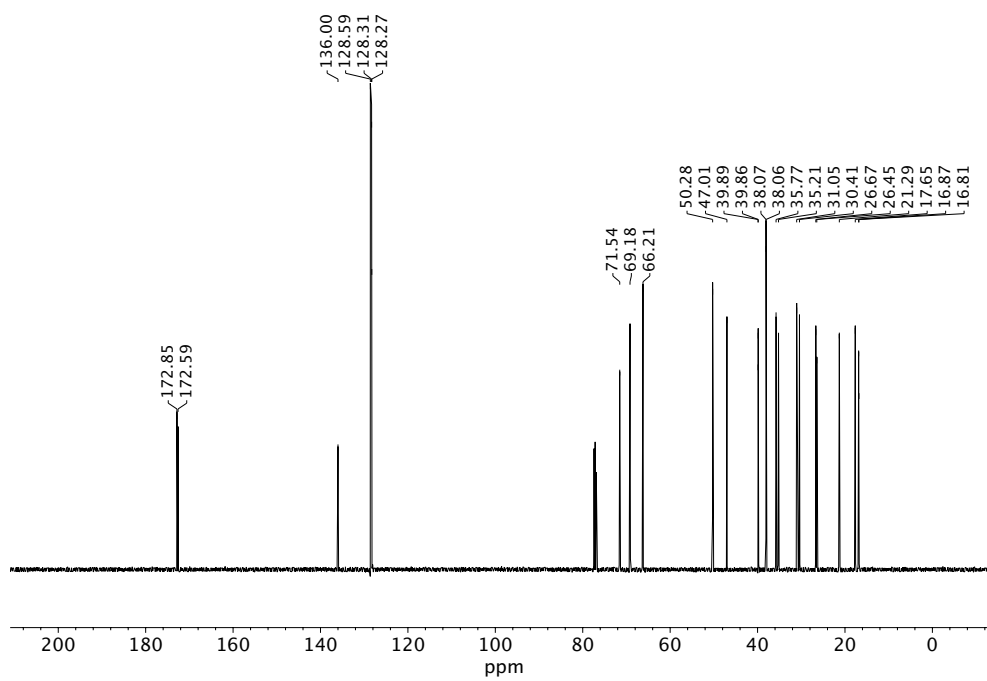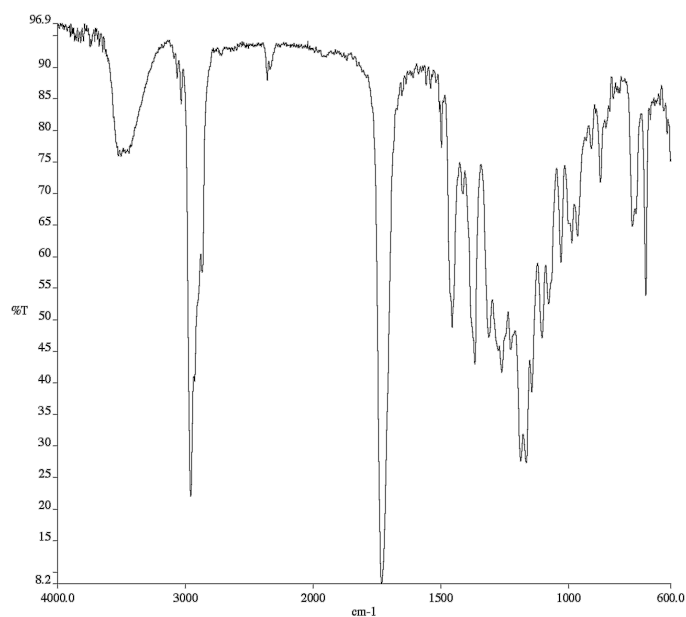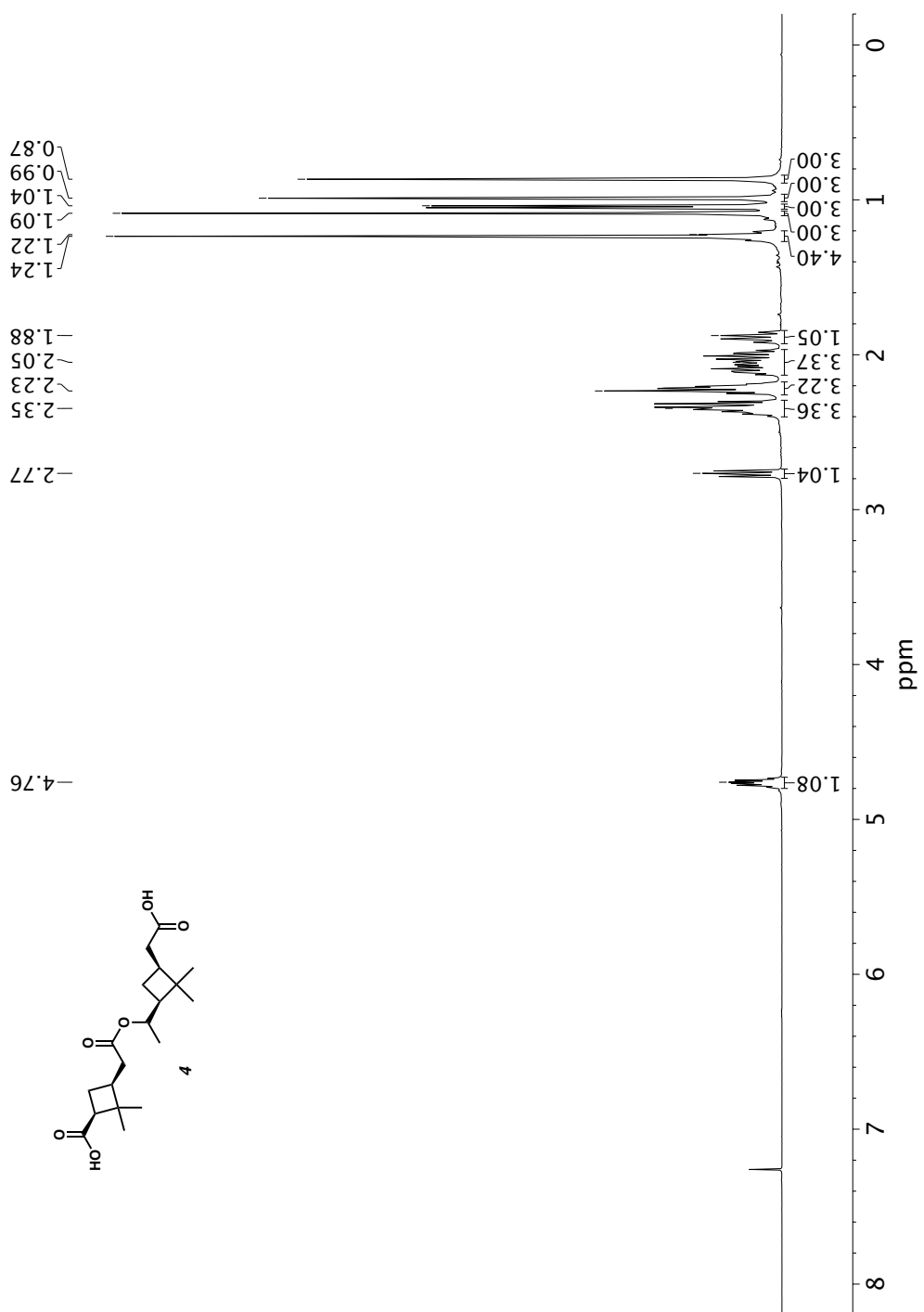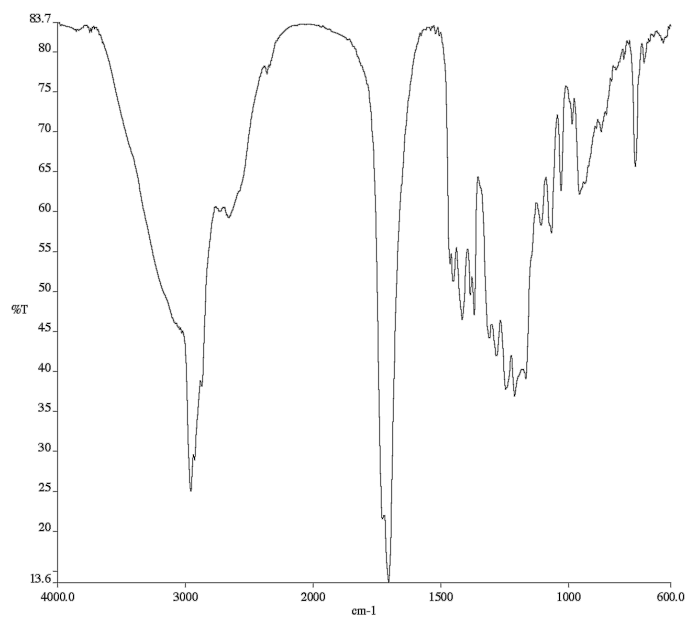
Infrared spectrum (thin film, NaCl) of compound **4**.

^{13}C NMR (125 MHz, CDCl$_3$) of compound **4**.

^{1}H NMR (500 MHz, CDCl$_3$) of compound **5**.
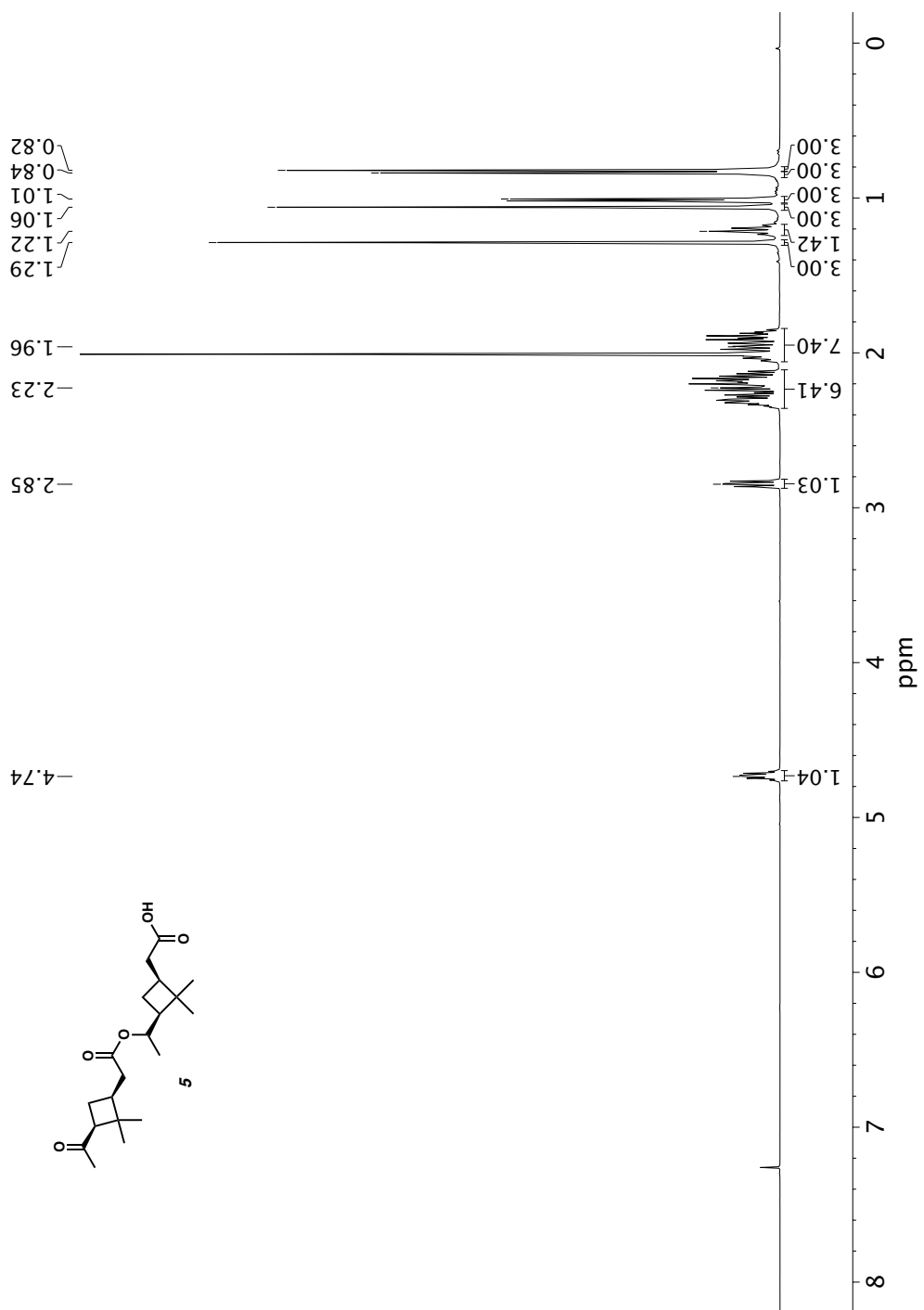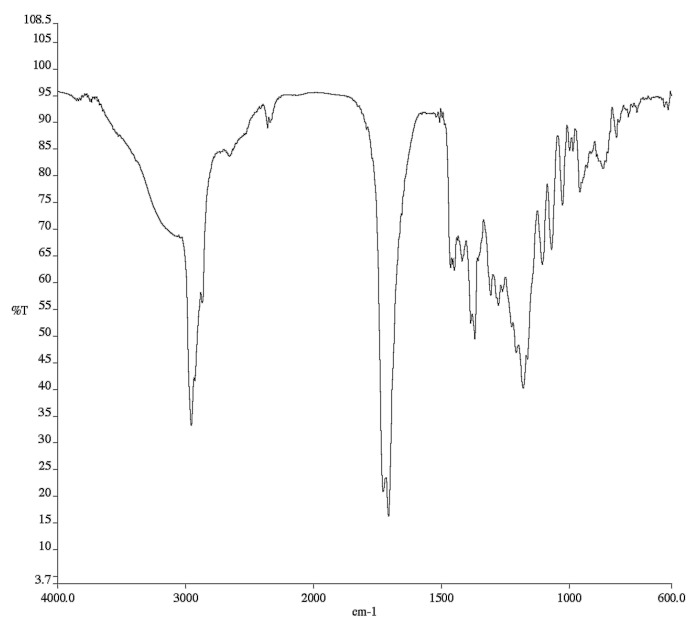
Infrared spectrum (thin film, NaCl) of compound **5**.

^{13}C NMR (125 MHz, CDCl$_3$) of compound **5**.

^{1}H NMR (500 MHz, CDCl$_3$) of compound **6**.
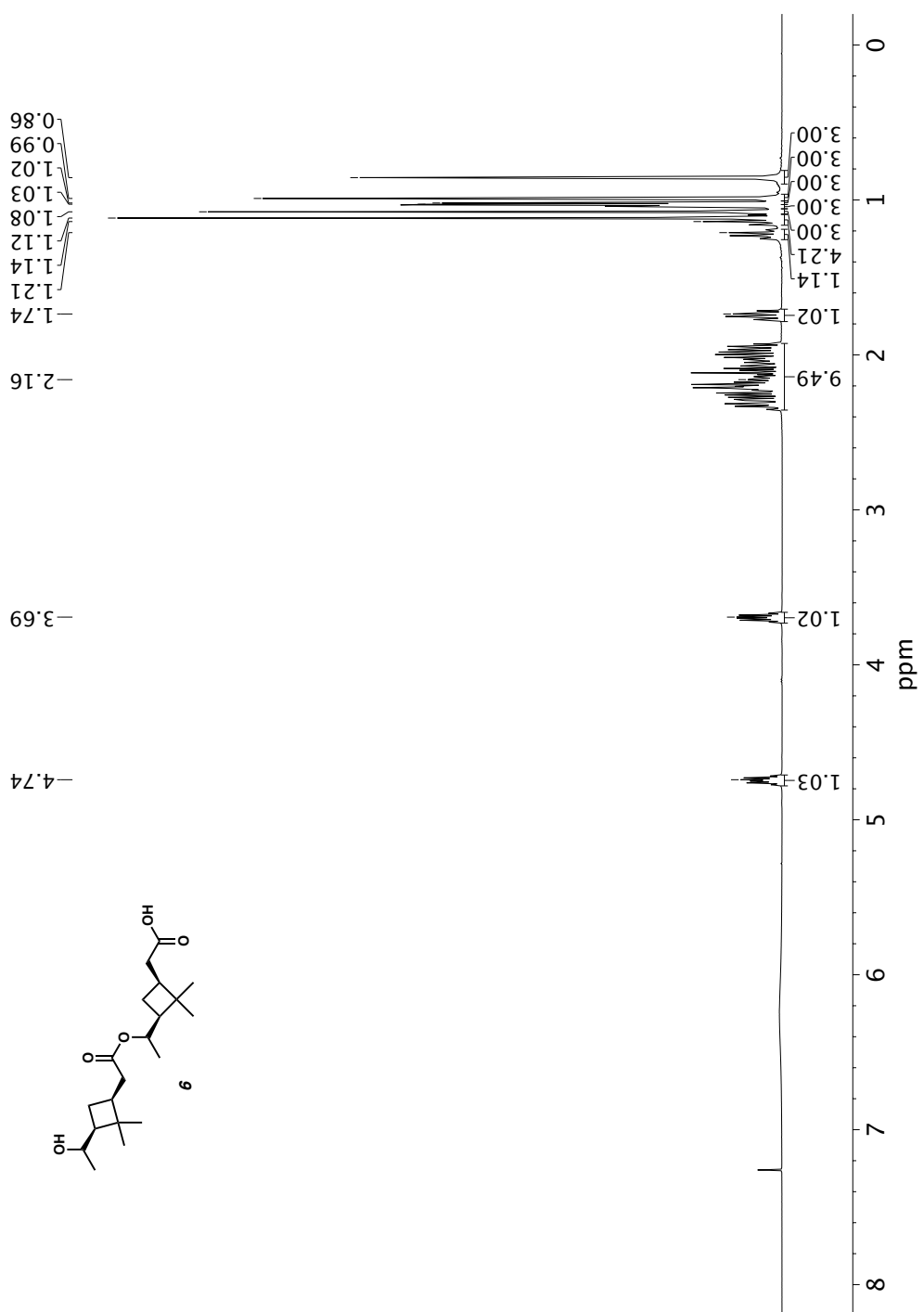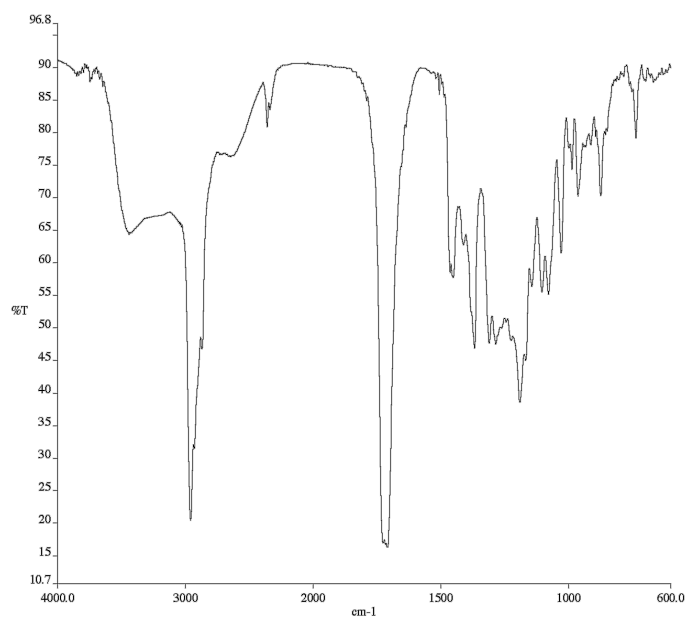
Infrared spectrum (thin film, NaCl) of compound **6**.
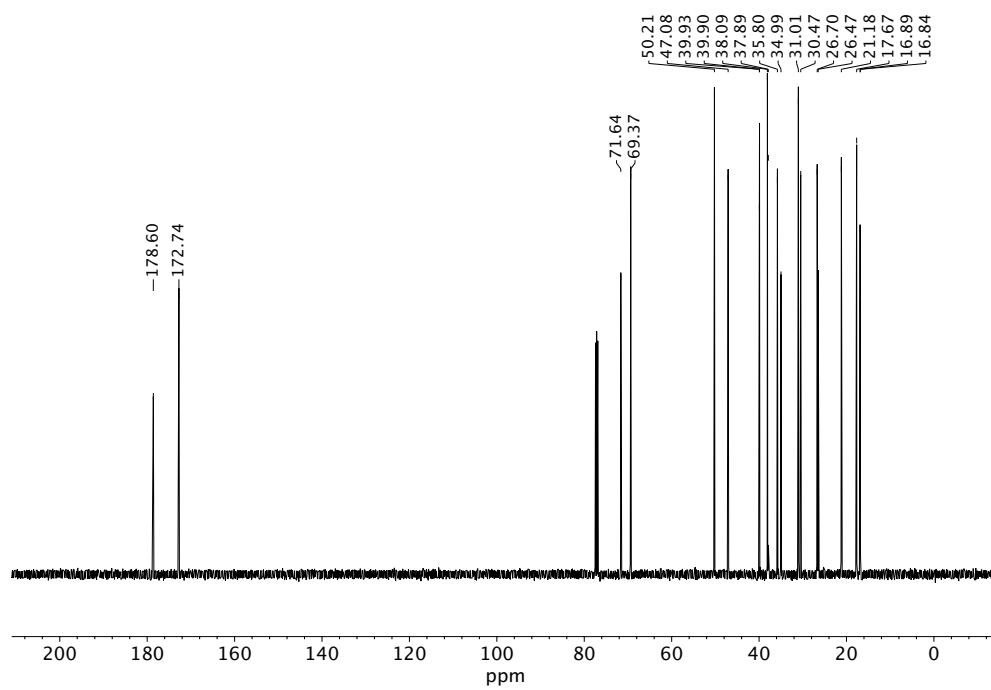
^{13}C NMR (125 MHz, CDCl$_3$) of compound **6**.

3.7 References

(1) Jimenez, J. L.; Canagaratna, M. R.; Donahue, N. M.; Prevot, A. S. H.; Zhang, Q.; Kroll, J. H.; DeCarlo, P. F.; Allan, J. D.; Coe, H.; Ng, N. L.; Aiken, A. C.; Docherty, K. S.; Ulbrich, I. M.; Grieshop, A. P.; Robinson, A. L.; Duplissy, J.; Smith, J. D.; Wilson, K. R.; Lanz, V. A.; Hueglin, C.; Sun, Y. L.; Tian, J.; Laaksonen, A.; Raatikainen, T.; Rautiainen, J.; Vaattovaara, P.; Ehn, M.; Kulmala, M.; Tomlinson, J. M.; Collins, D. R.; Cubison, M. J.; E.; Dunlea, J.; Huffman, J. A.; Onasch, T. B.; Alfarra, M. R.; Williams, P. I.; Bower, K.; Kondo, Y.; Schneider, J.; Drewnick, F.; Borrmann, S.; Weimer, S.; Demerjian, K.; Salcedo, D.; Cottrell, L.; Griffin, R.; Takami, A.; Miyoshi, T.; Hatakeyama, S.; Shimono, A.; Sun, J. Y.; Zhang, Y. M.; Dzepina, K.; Kimmel, J. R.; Sueper, D.; Jayne, J. T.; Herndon, S. C.; Trimborn, A. M.; Williams, L. R.; Wood, E. C.; Middlebrook, A. M.; Kolb, C. E.; Baltensperger, U.; Worsnop, D. R. Evolution of Organic Aerosols in the Atmosphere. *Science* **2009**, *326* (5959), 1525–1529. DOI: 10.1126/science.1180353.

(2) Intergovernmental Panel on Climate Change. *Climate Change 2013: The Physical Science Basis*; Stocker, T. F., Qin, D., Plattner, G. K., Tignor, M., Allen, S. K., Boschung, J., Nauels, A., Xia, Y., Bex, V., Midgley, P. M., Eds.; Cambridge University Press: Cambridge, United Kingdom, 2013.

(3) Pope, C. A.; Ezzati, M.; Dockery, D. W. Fine-Particulate Air Pollution and Life Expectancy in the United States. *N. Engl. J. Med.* **2009**, *360* (4), 376–386. DOI: 10.1056/NEJMsa0805646.

(4) Cohen, A. J.; Brauer, M.; Burnett, R.; Anderson, H. R.; Frostad, J.; Estep, K.; Balakrishnan, K.; Brunekreef, B.; Dandona, L.; Dandona, R.; Feigin, V.; Freedman, G.; Hubbell, B.; Jobling, A.; Kan, H.; Knibbs, L.; Liu, Y.; Martin, R.; Morawska, L.; Pope, C. A.; Shin, H.; Straif, K.; Shaddick, G.; Thomas, M.; van Dingenen, R.; van Donkelaar, A.; Vos, T.; Murray, C. J. L.; Forouzanfar, M. H. Estimates and 25-Year Trends of the Global Burden of Disease Attributable to Ambient Air Pollution: An Analysis of Data from the Global Burden of Diseases Study 2015. *Lancet* **2017**, *389* (10082), 1907–1918. DOI: 10.1016/S0140-6736(17)30505-6.

(5) Guenther, A. B.; Jiang, X.; Heald, C. L.; Sakulyanontvittaya, T.; Duhl, T.; Emmons, L. K.; Wang, X. The Model of Emissions of Gases and Aerosols from Nature Version 2.1 (MEGAN2.1): An Extended and Updated Framework for Modeling Biogenic Emissions. *Geosci. Model Dev.* **2012**, *5* (6), 1471–1492. DOI: 10.5194/gmd-5-1471-2012.

(6) Hallquist, M.; Wenger, J. C.; Baltensperger, U.; Rudich, Y.; Simpson, D.; Claeys, M.; Dommen, J.; Donahue, N. M.; George, C.; Goldstein, A. H.; Hamilton, J. F.; Herrmann, H.; Hoffmann, T.; Iinuma, Y.; Jang, M.; Jenkin, M. E.; Jimenez, J. L.; Kiendler-Scharr, A.; Maenhaut, W.; McFiggans, G.; Mentel, Th. F.; Monod, A.; Prévôt, A. S. H.; Seinfeld, J. H.; Surratt, J. D.;

Szmigielski, R.; Wildt, J. The Formation, Properties and Impact of Secondary Organic Aerosol: Current and Emerging Issues. *Atmos. Chem. Phys.* **2009**, *9* (14), 5155–5236. DOI: 10.5194/acp-9-5155-2009.

(7)   Kanakidou, M.; Seinfeld, J. H.; Pandis, S. N.; Barnes, I.; Dentener, F. J.; Facchini, M. C.; Van Dingenen, R.; Ervens, B.; Nenes, A.; Nielsen, C. J.; Swietlicki, E.; Putaud, J. P.; Balkanski, Y.; Fuzzi, S.; Horth, J.; Moortgat, G. K.; Winterhalter, R.; Myhre, C. E. L.; Tsigaridis, K.; Vignati, E.; Stephanou, E. G.; Wilson, J. Organic Aerosol and Global Climate Modelling: A Review. *Atmos. Chem. Phys.* **2005**, *5* (4), 1053–1123. DOI: 10.5194/acp-5-1053-2005.

(8)   Heald, C. L.; Henze, D. K.; Horowitz, L. W.; Feddema, J.; Lamarque, J.-F.; Guenther, A.; Hess, P. G.; Vitt, F.; Seinfeld, J. H.; Goldstein, A. H.; Fung, I. Predicted Change in Global Secondary Organic Aerosol Concentrations in Response to Future Climate, Emissions, and Land Use Change. *J. Geophys. Res.* **2008**, *113* D05211. DOI: 10.1029/2007JD009092.

(9)   Zhang, H.; Yee, L. D.; Lee, B. H.; Curtis, M. P.; Worton, D. R.; Isaacman-VanWertz, G.; Offenberg, J. H.; Lewandowski, M.; Kleindienst, T. E.; Beaver, M. R.; Holder, A. L.; Lonneman, W. A.; Docherty, K. S.; Jaoui, M.; Pye, H. O. T.; Hu, W.; Day, D. A.; Campuzano-Jost, P.; Jimenez, J. L.; Guo, H.; Weber, R. J.; de Gouw, J.; Koss, A. R.; Edgerton, E. S.; Brune, W.; Mohr, C.; Lopez-Hilfiker, F. D.; Lutz, A.; Kreisberg, N. M.; Spielman, S. R.; Hering, S. V.; Wilson, K. R.; Thornton, J. A.; Goldstein, A. H. Monoterpenes Are the Largest Source of Summertime Organic Aerosol in the Southeastern United States. *Proc. Natl. Acad. Sci. U.S.A.* **2018**, *115* (9), 2038–2043. DOI: 10.1073/pnas.1717513115.

(10)   Nozière, B.; Kalberer, M.; Claeys, M.; Allan, J.; D'Anna, B.; Decesari, S.; Finessi, E.; Glasius, M.; Grgić, I.; Hamilton, J. F.; Hoffmann, T.; Iinuma, Y.; Jaoui, M.; Kahnt, A.; Kampf, C. J.; Kourtchev, I.; Maenhaut, W.; Marsden, N.; Saarikoski, S.; Schnelle-Kreis, J.; Surratt, J. D.; Szidat, S.; Szmigielski, R.; Wisthaler, A. The Molecular Identification of Organic Compounds in the Atmosphere: State of the Art and Challenges. *Chem. Rev.* **2015**, *115* (10), 3919–3983. DOI: 10.1021/cr5003485.

(11)   Laskin, J.; Laskin, A.; Nizkorodov, S. A. Mass Spectrometry Analysis in Atmospheric Chemistry. *Anal. Chem.* **2018**, *90* (1), 166–189. DOI: 10.1021/acs.analchem.7b04249.

(12)   Reinhardt, A.; Emmenegger, C.; Gerrits, B.; Panse, C.; Dommen, J.; Baltensperger, U.; Zenobi, R.; Kalberer, M. Ultrahigh Mass Resolution and Accurate Mass Measurements as a Tool To Characterize Oligomers in Secondary Organic Aerosols. *Anal. Chem.* **2007**, *79* (11), 4074–4082. DOI: 10.1021/ac062425v.

(13)   Müller, L.; Reinnig, M.-C.; Warnke, J.; Hoffmann, Th. Unambiguous Identification of Esters as Oligomers in Secondary Organic Aerosol Formed from Cyclohexene and Cyclohexene/α-Pinene Ozonolysis. *Atmos. Chem. Phys.* **2008**, *8* (5), 1423–1433. DOI: 10.5194/acp-8-1423-2008.

(14)   Müller, L.; Reinnig, M.-C.; Hayen, H.; Hoffmann, T. Characterization of Oligomeric Compounds in Secondary Organic Aerosol Using Liquid Chromatography Coupled to Electrospray Ionization Fourier Transform Ion Cyclotron Resonance Mass Spectrometry. *Rapid Commun. Mass Spectrom.* **2009**, *23* (7), 971–979. DOI: 10.1002/rcm.3957.

(15)   Camredon, M.; Hamilton, J. F.; Alam, M. S.; Wyche, K. P.; Carr, T.; White, I. R.; Monks, P. S.; Rickard, A. R.; Bloss, W. J. Distribution of Gaseous and Particulate Organic Composition during Dark α-Pinene Ozonolysis. *Atmos. Chem. Phys.* **2010**, *10* (6), 2893–2917. DOI: 10.5194/acp-10-2893-2010.

(16)   Claeys, M.; Iinuma, Y.; Szmigielski, R.; Surratt, J. D.; Blockhuys, F.; Van Alsenoy, C.; Böge, O.; Sierau, B.; Gómez-González, Y.; Vermeylen, R.; Van der Veken, P.; Shahgholi, M.; Chan, A. W. H.; Herrmann, H.; Seinfeld, J. H.; Maenhaut, W. Terpenylic Acid and Related Compounds from the Oxidation of α-Pinene: Implications for New Particle Formation and Growth above Forests. *Environ. Sci. Technol.* **2009**, *43* (18), 6976–6982. DOI: 10.1021/es9007596.

(17)   Yasmeen, F.; Vermeylen, R.; Szmigielski, R.; Iinuma, Y.; Böge, O.; Herrmann, H.; Maenhaut, W.; Claeys, M. Terpenylic Acid and Related Compounds: Precursors for Dimers in Secondary Organic Aerosol from the Ozonolysis of α- and β-Pinene. *Atmos. Chem. Phys.* **2010**, *10* (19), 9383–9392. DOI: 10.5194/acp-10-9383-2010.

(18)   Yasmeen, F.; Szmigielski, R.; Vermeylen, R.; Gómez-González, Y.; Surratt, J. D.; Chan, A. W. H.; Seinfeld, J. H.; Maenhaut, W.; Claeys, M. Mass Spectrometric Characterization of Isomeric Terpenoic Acids from the Oxidation of α-Pinene, β-Pinene, *d*-Limonene, and Δ^3-Carene in Fine Forest Aerosol. *J. Mass Spectrom.* **2011**, *46* (4), 425–442. DOI: 10.1002/jms.1911.

(19)   Yasmeen, F.; Vermeylen, R.; Maurin, N.; Perraudin, E.; Doussin, J.-F.; Claeys, M. Characterisation of Tracers for Aging of α-Pinene Secondary Organic Aerosol Using Liquid Chromatography/Negative Ion Electrospray Ionisation Mass Spectrometry. *Environ. Chem.* **2012**, *9* (3), 236–246. DOI: 10.1071/EN11148.

(20)   Gao, Y.; Hall, W. A.; Johnston, M. V. Molecular Composition of Monoterpene Secondary Organic Aerosol at Low Mass Loading. *Environ. Sci. Technol.* **2010**, *44* (20), 7897–7902. DOI: 10.1021/es101861k.

(21)   Hall, W. A.; Johnston, M. V. Oligomer Content of α-Pinene Secondary Organic Aerosol. *Aerosol Sci. Technol.* **2011**, *45* (1), 37–45. DOI: 10.1080/02786826.2010.517580.

(22) Putman, A. L.; Offenberg, J. H.; Fisseha, R.; Kundu, S.; Rahn, T. A.; Mazzoleni, L. R. Ultrahigh-Resolution FT-ICR Mass Spectrometry Characterization of α-Pinene Ozonolysis SOA. *Atmos. Environ.* **2012**, *46*, 164–172. DOI: 10.1016/j.atmosenv.2011.10.003.

(23) Witkowski, B.; Gierczak, T. Early Stage Composition of SOA Produced by α-Pinene/Ozone Reaction: α-Acyloxyhydroperoxy Aldehydes and Acidic Dimers. *Atmos. Environ.* **2014**, *95*, 59–70. DOI: 10.1016/j.atmosenv.2014.06.018.

(24) Kourtchev, I.; Fuller, S. J.; Giorio, C.; Healy, R. M.; Wilson, E.; O&apos;Connor, I.; Wenger, J. C.; McLeod, M.; Aalto, J.; Ruuskanen, T. M.; Maenhaut, W.; Jones, R.; Venables, D. S.; Sodeau, J. R.; Kulmala, M.; Kalberer, M. Molecular Composition of Biogenic Secondary Organic Aerosols Using Ultrahigh-Resolution Mass Spectrometry: Comparing Laboratory and Field Studies. *Atmos. Chem. Phys.* **2014**, *14* (4), 2155–2167. DOI: 10.5194/acp-14-2155-2014.

(25) Kourtchev, I.; Doussin, J.-F.; Giorio, C.; Mahon, B.; Wilson, E. M.; Maurin, N.; Pangui, E.; Venables, D. S.; Wenger, J. C.; Kalberer, M. Molecular Composition of Fresh and Aged Secondary Organic Aerosol from a Mixture of Biogenic Volatile Compounds: A High-Resolution Mass Spectrometry Study. *Atmos. Chem. Phys.* **2015**, *15* (10), 5683–5695. DOI: 10.5194/acp-15-5683-2015.

(26) Kourtchev, I.; Giorio, C.; Manninen, A.; Wilson, E.; Mahon, B.; Aalto, J.; Kajos, M.; Venables, D.; Ruuskanen, T.; Levula, J.; Loponen, M.; Connors, S.; Harris, N.; Zhao, D.; Kiendler-Scharr, A.; Mentel, T.; Rudich, Y.; Hallquist, M.; Doussin, J.-F.; Maenhaut, W.; Bäck, J.; Petäjä, T.; Wenger, J.; Kulmala, M.; Kalberer, M. Enhanced Volatile Organic Compounds Emissions and Organic Aerosol Mass Increase the Oligomer Content of Atmospheric Aerosols. *Sci. Rep.* **2016**, *6* (1), 35038. DOI: 10.1038/srep35038.

(27) Kristensen, K.; Enggrob, K. L.; King, S. M.; Worton, D. R.; Platt, S. M.; Mortensen, R.; Rosenoern, T.; Surratt, J. D.; Bilde, M.; Goldstein, A. H.; Glasius, M. Formation and Occurrence of Dimer Esters of Pinene Oxidation Products in Atmospheric Aerosols. *Atmos. Chem. Phys.* **2013**, *13* (7), 3763–3776. DOI: 10.5194/acp-13-3763-2013.

(28) Kristensen, K.; Cui, T.; Zhang, H.; Gold, A.; Glasius, M.; Surratt, J. D. Dimers in α-Pinene Secondary Organic Aerosol: Effect of Hydroxyl Radical, Ozone, Relative Humidity and Aerosol Acidity. *Atmos. Chem. Phys.* **2014**, *14* (8), 4201–4218. DOI: 10.5194/acp-14-4201-2014.

(29) Kristensen, K.; Watne, Å. K.; Hammes, J.; Lutz, A.; Petäjä, T.; Hallquist, M.; Bilde, M.; Glasius, M. High-Molecular Weight Dimer Esters Are Major Products in Aerosols from α-Pinene Ozonolysis and the Boreal Forest.

Environ. Sci. Technol. Lett. **2016**, *3* (8), 280–285. DOI: 10.1021/acs.estlett.6b00152.

(30) Kristensen, K.; Jensen, L. N.; Glasius, M.; Bilde, M. The Effect of Sub-Zero Temperature on the Formation and Composition of Secondary Organic Aerosol from Ozonolysis of Alpha-Pinene. *Environ. Sci.: Processes Impacts* **2017**, *19* (10), 1220–1234. DOI: 10.1039/C7EM00231A.

(31) Zhang, X.; McVay, R. C.; Huang, D. D.; Dalleska, N. F.; Aumont, B.; Flagan, R. C.; Seinfeld, J. H. Formation and Evolution of Molecular Products in α-Pinene Secondary Organic Aerosol. *Proc. Natl. Acad. Sci. U.S.A.* **2015**, *112* (46), 14168–14173. DOI: 10.1073/pnas.1517742112.

(32) Sato, K.; Jia, T.; Tanabe, K.; Morino, Y.; Kajii, Y.; Imamura, T. Terpenylic Acid and Nine-Carbon Multifunctional Compounds Formed during the Aging of β-Pinene Ozonolysis Secondary Organic Aerosol. *Atmos. Environ.* **2016**, *130*, 127–135. DOI: 10.1016/j.atmosenv.2015.08.047.

(33) Mutzel, A.; Rodigast, M.; Iinuma, Y.; Böge, O.; Herrmann, H. Monoterpene SOA – Contribution of First-Generation Oxidation Products to Formation and Chemical Composition. *Atmos. Environ.* **2016**, *130,* 136–144. DOI: 10.1016/j.atmosenv.2015.10.080.

(34) Kenseth, C. M.; Huang, Y.; Zhao, R.; Dalleska, N. F.; Hethcox, J. C.; Stoltz, B. M.; Seinfeld, J. H. Synergistic O_3 + OH Oxidation Pathway to Extremely Low-Volatility Dimers Revealed in β-Pinene Secondary Organic Aerosol. *Proc. Natl. Acad. Sci. U.S.A.* **2018**, *115* (33), 8301–8306. DOI: 10.1073/pnas.1804671115.

(35) Zhao, R.; Kenseth, C. M.; Huang, Y.; Dalleska, N. F.; Seinfeld, J. H. Iodometry-Assisted Liquid Chromatography Electrospray Ionization Mass Spectrometry for Analysis of Organic Peroxides: An Application to Atmospheric Secondary Organic Aerosol. *Environ. Sci. Technol.* **2018**, *52* (4), 2108–2117. DOI: 10.1021/acs.est.7b04863.

(36) Kahnt, A.; Vermeylen, R.; Iinuma, Y.; Safi Shalamzari, M.; Maenhaut, W.; Claeys, M. High-Molecular-Weight Esters in α-Pinene Ozonolysis Secondary Organic Aerosol: Structural Characterization and Mechanistic Proposal for Their Formation from Highly Oxygenated Molecules. *Atmos. Chem. Phys.* **2018**, *18* (11), 8453–8467. DOI: 10.5194/acp-18-8453-2018.

(37) Sato, K.; Fujitani, Y.; Inomata, S.; Morino, Y.; Tanabe, K.; Ramasamy, S.; Hikida, T.; Shimono, A.; Takami, A.; Fushimi, A.; Kondo, Y.; Imamura, T.; Tanimoto, H.; Sugata, S. Studying Volatility from Composition, Dilution, and Heating Measurements of Secondary Organic Aerosols Formed during α-Pinene Ozonolysis. *Atmos. Chem. Phys.* **2018**, *18* (8), 5455–5466. DOI: 10.5194/acp-18-5455-2018.

(38) Wozniak, A. S.; Bauer, J. E.; Sleighter, R. L.; Dickhut, R. M.; Hatcher, P. G. Technical Note: Molecular Characterization of Aerosol-Derived Water

Soluble Organic Carbon Using Ultrahigh Resolution Electrospray Ionization Fourier Transform Ion Cyclotron Resonance Mass Spectrometry. *Atmos. Chem. Phys.* **2008**, *8* (17), 5099–5111. DOI: 10.5194/acp-8-5099-2008.

(39)　Konermann, L.; Ahadi, E.; Rodriguez, A. D.; Vahidi, S. Unraveling the Mechanism of Electrospray Ionization. *Anal. Chem.* **2013**, *85* (1), 2–9. DOI: 10.1021/ac302789c.

(40)　Oss, M.; Kruve, A.; Herodes, K.; Leito, I. Electrospray Ionization Efficiency Scale of Organic Compounds. *Anal. Chem.* **2010**, *82* (7), 2865–2872. DOI: 10.1021/ac902856t.

(41)　Kruve, A.; Kaupmees, K.; Liigand, J.; Leito, I. Negative Electrospray Ionization via Deprotonation: Predicting the Ionization Efficiency. *Anal. Chem.* **2014**, *86* (10), 4822–4830. DOI: 10.1021/ac404066v.

(42)　Kruve, A.; Kaupmees, K. Predicting ESI/MS Signal Change for Anions in Different Solvents. *Anal. Chem.* **2017**, *89* (9), 5079–5086. DOI: 10.1021/acs.analchem.7b00595.

(43)　Moglioni, A. G.; García-Expósito, E.; Aguado, G. P.; Parella, T.; Branchadell, V.; Moltrasio, G. Y.; Ortuño, R. M. Divergent Routes to Chiral Cyclobutane Synthons from (−)-α-Pinene and Their Use in the Stereoselective Synthesis of Dehydro Amino Acids. *J. Org. Chem.* **2000**, *65* (13), 3934–3940. DOI: 10.1021/jo991773c.

(44)　Hergueta, A. R.; López, C.; Fernández, F.; Caamaño, O.; Blanco, J. M. Synthesis of Two Enantiomerically Pure Precursors of Cyclobutane Carbocyclic Nucleosides. *Tetrahedron: Asymmetry* **2003**, *14* (23), 3773–3778. DOI: 10.1016/j.tetasy.2003.09.033.

(45)　Schwantes, R. H.; McVay, R. C.; Zhang, X.; Coggon, M. M.; Lignell, H.; Flagan, R. C.; Wennberg, P. O.; Seinfeld, J. H. Science of the Environmental Chamber. In *Advances in Atmospheric Chemistry*; Barker, J. R., Steiner, A. L., Wallington, T. J., Eds.; World Scientific: Singapore, 2017; pp 1–93. DOI: 10.1142/9789813147355_0001.

(46)　Aschmann, S. M.; Arey, J.; Atkinson, R. OH Radical Formation from the Gas-Phase Reactions of O_3 with a Series of Terpenes. *Atmos. Environ.* **2002**, *36* (27), 4347–4355. DOI: 10.1016/S1352-2310(02)00355-2.

(47)　Presto, A. A.; Donahue, N. M. Ozonolysis Fragment Quenching by Nitrate Formation: The Pressure Dependence of Prompt OH Radical Formation. *J. Phys. Chem. A* **2004**, *108* (42), 9096–9104. DOI: 10.1021/jp047162s.

(48)　Ma, Y.; Marston, G. Multifunctional Acid Formation from the Gas-Phase Ozonolysis of β-Pinene. *Phys. Chem. Chem. Phys.* **2008**, *10* (40), 6115. DOI: 10.1039/b807863g.

(49) Nguyen, T. L.; Peeters, J.; Vereecken, L. Theoretical Study of the Gas-Phase Ozonolysis of β-Pinene ($C_{10}H_{16}$). *Phys. Chem. Chem. Phys.* **2009**, *11* (27), 5643. DOI: 10.1039/b822984h.

(50) Schwantes, R. H.; Charan, S. M.; Bates, K. H.; Huang, Y.; Nguyen, T. B.; Mai, H.; Kong, W.; Flagan, R. C.; Seinfeld, J. H. Low-Volatility Compounds Contribute Significantly to Isoprene Secondary Organic Aerosol (SOA) under High-NO_x Conditions. *Atmos. Chem. Phys.* **2019**, *19* (11), 7255–7278. DOI: 10.5194/acp-19-7255-2019.

(51) Bahreini, R.; Keywood, M. D.; Ng, N. L.; Varutbangkul, V.; Gao, S.; Flagan, R. C.; Seinfeld, J. H.; Worsnop, D. R.; Jimenez, J. L. Measurements of Secondary Organic Aerosol from Oxidation of Cycloalkenes, Terpenes, and *m*-Xylene Using an Aerodyne Aerosol Mass Spectrometer. *Environ. Sci. Technol.* **2005**, *39* (15), 5674–5688. DOI: 10.1021/es048061a.

(52) Malloy, Q. G. J.; Nakao, S.; Qi, L.; Austin, R.; Stothers, C.; Hagino, H.; Cocker, D. R. Real-Time Aerosol Density Determination Utilizing a Modified Scanning Mobility Particle Sizer—Aerosol Particle Mass Analyzer System. *Aerosol Sci. Technol.* **2009**, *43* (7), 673–678. DOI: 10.1080/02786820902832960.

(53) Shilling, J. E.; Chen, Q.; King, S. M.; Rosenoern, T.; Kroll, J. H.; Worsnop, D. R.; DeCarlo, P. F.; Aiken, A. C.; Sueper, D.; Jimenez, J. L.; Martin, S. T. Loading-Dependent Elemental Composition of α-Pinene SOA Particles. *Atmos. Chem. Phys.* **2009**, *9* (3), 771–782. DOI: 10.5194/acp-9-771-2009.

(54) Saathoff, H.; Naumann, K.-H.; Möhler, O.; Jonsson, Å. M.; Hallquist, M.; Kiendler-Scharr, A.; Mentel, Th. F.; Tillmann, R.; Schurath, U. Temperature Dependence of Yields of Secondary Organic Aerosols from the Ozonolysis of α-Pinene and Limonene. *Atmos. Chem. Phys.* **2009**, *9* (5), 1551–1577. DOI: 10.5194/acp-9-1551-2009.

(55) DeCarlo, P. F.; Kimmel, J. R.; Trimborn, A.; Northway, M. J.; Jayne, J. T.; Aiken, A. C.; Gonin, M.; Fuhrer, K.; Horvath, T.; Docherty, K. S.; Worsnop, D. R.; Jimenez, J. L. Field-Deployable, High-Resolution, Time-of-Flight Aerosol Mass Spectrometer. *Anal. Chem.* **2006**, *78* (24), 8281–8289. DOI: 10.1021/ac061249n.

(56) Allan, J. D.; Delia, A. E.; Coe, H.; Bower, K. N.; Alfarra, M. R.; Jimenez, J. L.; Middlebrook, A. M.; Drewnick, F.; Onasch, T. B.; Canagaratna, M. R.; Jayne, J. T.; Worsnop, D. R. A Generalised Method for the Extraction of Chemically Resolved Mass Spectra from Aerodyne Aerosol Mass Spectrometer Data. *J. Aerosol Sci.* **2004**, *35* (7), 909–922. DOI: 10.1016/j.jaerosci.2004.02.007.

(57) Aiken, A. C.; DeCarlo, P. F.; Kroll, J. H.; Worsnop, D. R.; Huffman, J. A.; Docherty, K. S.; Ulbrich, I. M.; Mohr, C.; Kimmel, J. R.; Sueper, D.; Sun, Y.; Zhang, Q.; Trimborn, A.; Northway, M.; Ziemann, P. J.; Canagaratna,

M. R.; Onasch, T. B.; Alfarra, M. R.; Prevot, A. S. H.; Dommen, J.; Duplissy, J.; Metzger, A.; Baltensperger, U.; Jimenez, J. L. O/C and OM/OC Ratios of Primary, Secondary, and Ambient Organic Aerosols with High-Resolution Time-of-Flight Aerosol Mass Spectrometry. *Environ. Sci. Technol.* **2008**, *42* (12), 4478–4485. DOI: 10.1021/es703009q.

(58) Middlebrook, A. M.; Bahreini, R.; Jimenez, J. L.; Canagaratna, M. R. Evaluation of Composition-Dependent Collection Efficiencies for the Aerodyne Aerosol Mass Spectrometer Using Field Data. *Aerosol Sci. Technol.* **2012**, *46* (3), 258–271. DOI: 10.1080/02786826.2011.620041.

(59) Canagaratna, M. R.; Jimenez, J. L.; Kroll, J. H.; Chen, Q.; Kessler, S. H.; Massoli, P.; Hildebrandt Ruiz, L.; Fortner, E.; Williams, L. R.; Wilson, K. R.; Surratt, J. D.; Donahue, N. M.; Jayne, J. T.; Worsnop, D. R. Elemental Ratio Measurements of Organic Compounds Using Aerosol Mass Spectrometry: Characterization, Improved Calibration, and Implications. *Atmos. Chem. Phys.* **2015**, *15* (1), 253–272. DOI: 10.5194/acp-15-253-2015.

(60) Chhabra, P. S.; Flagan, R. C.; Seinfeld, J. H. Elemental Analysis of Chamber Organic Aerosol Using an Aerodyne High-Resolution Aerosol Mass Spectrometer. *Atmos. Chem. Phys.* **2010**, *10* (9), 4111–4131. DOI: 10.5194/acp-10-4111-2010.

(61) Chen, Q.; Liu, Y.; Donahue, N. M.; Shilling, J. E.; Martin, S. T. Particle-Phase Chemistry of Secondary Organic Material: Modeled Compared to Measured O:C and H:C Elemental Ratios Provide Constraints. *Environ. Sci. Technol.* **2011**, *45* (11), 4763–4770. DOI: 10.1021/es104398s.

(62) Donahue, N. M.; Henry, K. M.; Mentel, T. F.; Kiendler-Scharr, A.; Spindler, C.; Bohn, B.; Brauers, T.; Dorn, H. P.; Fuchs, H.; Tillmann, R.; Wahner, A.; Saathoff, H.; Naumann, K.-H.; Mohler, O.; Leisner, T.; Muller, L.; Reinnig, M.-C.; Hoffmann, T.; Salo, K.; Hallquist, M.; Frosch, M.; Bilde, M.; Tritscher, T.; Barmet, P.; Praplan, A. P.; DeCarlo, P. F.; Dommen, J.; Prevot, A. S. H.; Baltensperger, U. Aging of Biogenic Secondary Organic Aerosol via Gas-Phase OH Radical Reactions. *Proc. Natl. Acad. Sci. U.S.A.* **2012**, *109* (34), 13503–13508. DOI: 10.1073/pnas.1115186109.

(63) Nakao, S.; Tang, P.; Tang, X.; Clark, C. H.; Qi, L.; Seo, E.; Asa-Awuku, A.; Cocker, D. Density and Elemental Ratios of Secondary Organic Aerosol: Application of a Density Prediction Method. *Atmos. Environ.* **2013**, *68*, 273–277. DOI: 10.1016/j.atmosenv.2012.11.006.

(64) Sorooshian, A.; Brechtel, F. J.; Ma, Y.; Weber, R. J.; Corless, A.; Flagan, R. C.; Seinfeld, J. H. Modeling and Characterization of a Particle-into-Liquid Sampler (PILS). *Aerosol Sci. Technol.* **2006**, *40* (6), 396–409. DOI: 10.1080/02786820600632282.

(65) Zhang, X.; Dalleska, N. F.; Huang, D. D.; Bates, K. H.; Sorooshian, A.; Flagan, R. C.; Seinfeld, J. H. Time-Resolved Molecular Characterization of Organic Aerosols by PILS + UPLC/ESI-Q-TOFMS. *Atmos. Environ.* **2016**, *130*, 180–189. DOI: 10.1016/j.atmosenv.2015.08.049.

(66) Ryerson, T. B.; Andrews, A. E.; Angevine, W. M.; Bates, T. S.; Brock, C. A.; Cairns, B.; Cohen, R. C.; Cooper, O. R.; de Gouw, J. A.; Fehsenfeld, F. C.; Ferrare, R. A.; Fischer, M. L.; Flagan, R. C.; Goldstein, A. H.; Hair, J. W.; Hardesty, R. M.; Hostetler, C. A.; Jimenez, J. L.; Langford, A. O.; McCauley, E.; McKeen, S. A.; Molina, L. T.; Nenes, A.; Oltmans, S. J.; Parrish, D. D.; Pederson, J. R.; Pierce, R. B.; Prather, K.; Quinn, P. K.; Seinfeld, J. H.; Senff, C. J.; Sorooshian, A.; Stutz, J.; Surratt, J. D.; Trainer, M.; Volkamer, R.; Williams, E. J.; Wofsy, S. C. The 2010 California Research at the Nexus of Air Quality and Climate Change (CalNex) Field Study. *J. Geophys. Res. Atmos.* **2013**, *118* (11), 5830–5866. DOI: 10.1002/jgrd.50331.

(67) Lopez-Hilfiker, F. D.; Mohr, C.; Ehn, M.; Rubach, F.; Kleist, E.; Wildt, J.; Mentel, Th. F.; Carrasquillo, A. J.; Daumit, K. E.; Hunter, J. F.; Kroll, J. H.; Worsnop, D. R.; Thornton, J. A. Phase Partitioning and Volatility of Secondary Organic Aerosol Components Formed from α-Pinene Ozonolysis and OH Oxidation: The Importance of Accretion Products and Other Low Volatility Compounds. *Atmos. Chem. Phys.* **2015**, *15* (14), 7765–7776. DOI: 10.5194/acp-15-7765-2015.

(68) Yatavelli, R. L. N.; Mohr, C.; Stark, H.; Day, D. A.; Thompson, S. L.; Lopez-Hilfiker, F. D.; Campuzano-Jost, P.; Palm, B. B.; Vogel, A. L.; Hoffmann, T.; Heikkinen, L.; Äijälä, M.; Ng, N. L.; Kimmel, J. R.; Canagaratna, M. R.; Ehn, M.; Junninen, H.; Cubison, M. J.; Petäjä, T.; Kulmala, M.; Jayne, J. T.; Worsnop, D. R.; Jimenez, J. L. Estimating the Contribution of Organic Acids to Northern Hemispheric Continental Organic Aerosol. *Geophys. Res. Lett.* **2015**, *42* (14), 6084–6090. DOI: 10.1002/2015GL064650.

(69) Ma, Y.; Russell, A. T.; Marston, G. Mechanisms for the Formation of Secondary Organic Aerosol Components from the Gas-Phase Ozonolysis of α-Pinene. *Phys. Chem. Chem. Phys.* **2008**, *10* (29), 4294. DOI: 10.1039/b803283a.

(70) Atkinson, R.; Arey, J. Atmospheric Degradation of Volatile Organic Compounds. *Chem. Rev.* **2003**, *103* (12), 4605–4638. DOI: 10.1021/cr0206420.

(71) Ehn, M.; Thornton, J. A.; Kleist, E.; Sipilä, M.; Junninen, H.; Pullinen, I.; Springer, M.; Rubach, F.; Tillmann, R.; Lee, B.; Lopez-Hilfiker, F.; Andres, S.; Acir, I.-H.; Rissanen, M.; Jokinen, T.; Schobesberger, S.; Kangasluoma, J.; Kontkanen, J.; Nieminen, T.; Kurtén, T.; Nielsen, L. B.; Jørgensen, S.; Kjaergaard, H. G.; Canagaratna, M.; Maso, M. D.; Berndt, T.; Petäjä, T.;

Wahner, A.; Kerminen, V.-M.; Kulmala, M.; Worsnop, D. R.; Wildt, J.; Mentel, T. F. A Large Source of Low-Volatility Secondary Organic Aerosol. *Nature* **2014**, *506* (7489), 476–479. DOI: 10.1038/nature13032.

(72)   Donahue, N. M.; Epstein, S. A.; Pandis, S. N.; Robinson, A. L. A Two-Dimensional Volatility Basis Set: 1. Organic-Aerosol Mixing Thermodynamics. *Atmos. Chem. Phys.* **2011**, *11* (7), 3303–3318. DOI: 10.5194/acp-11-3303-2011.

(73)   Bianchi, F.; Kurtén, T.; Riva, M.; Mohr, C.; Rissanen, M. P.; Roldin, P.; Berndt, T.; Crounse, J. D.; Wennberg, P. O.; Mentel, T. F.; Wildt, J.; Junninen, H.; Jokinen, T.; Kulmala, M.; Worsnop, D. R.; Thornton, J. A.; Donahue, N.; Kjaergaard, H. G.; Ehn, M. Highly Oxygenated Organic Molecules (HOM) from Gas-Phase Autoxidation Involving Peroxy Radicals: A Key Contributor to Atmospheric Aerosol. *Chem. Rev.* **2019**, *119* (6), 3472–3509. DOI: 10.1021/acs.chemrev.8b00395.

(74)   Jokinen, T.; Berndt, T.; Makkonen, R.; Kerminen, V.-M.; Junninen, H.; Paasonen, P.; Stratmann, F.; Herrmann, H.; Guenther, A. B.; Worsnop, D. R.; Kulmala, M.; Ehn, M.; Sipilä, M. Production of Extremely Low Volatile Organic Compounds from Biogenic Emissions: Measured Yields and Atmospheric Implications. *Proc. Natl. Acad. Sci. U.S.A.* **2015**, *112* (23), 7123–7128. DOI: 10.1073/pnas.1423977112.

(75)   Zhang, X.; Lambe, A. T.; Upshur, M. A.; Brooks, W. A.; Gray Bé, A.; Thomson, R. J.; Geiger, F. M.; Surratt, J. D.; Zhang, Z.; Gold, A.; Graf, S.; Cubison, M. J.; Groessl, M.; Jayne, J. T.; Worsnop, D. R.; Canagaratna, M. R. Highly Oxygenated Multifunctional Compounds in α-Pinene Secondary Organic Aerosol. *Environ. Sci. Technol.* **2017**, *51* (11), 5932–5940. DOI: 10.1021/acs.est.6b06588.

(76)   Zhao, Y.; Thornton, J. A.; Pye, H. O. T. Quantitative Constraints on Autoxidation and Dimer Formation from Direct Probing of Monoterpene-Derived Peroxy Radical Chemistry. *Proc. Natl. Acad. Sci. U.S.A.* **2018**, *115* (48), 12142–12147. DOI: 10.1073/pnas.1812147115.

(77)   Li, H.; Chen, Z.; Huang, L.; Huang, D. Organic Peroxides' Gas-Particle Partitioning and Rapid Heterogeneous Decomposition on Secondary Organic Aerosol. *Atmos. Chem. Phys.* **2016**, *16* (3), 1837–1848. DOI: 10.5194/acp-16-1837-2016.

(78)   Krapf, M.; El Haddad, I.; Bruns, E. A.; Molteni, U.; Daellenbach, K. R.; Prévôt, A. S. H.; Baltensperger, U.; Dommen, J. Labile Peroxides in Secondary Organic Aerosol. *Chem* **2016**, *1* (4), 603–616. DOI: 10.1016/j.chempr.2016.09.007.

(79)   Riva, M.; Budisulistiorini, S. H.; Zhang, Z.; Gold, A.; Thornton, J. A.; Turpin, B. J.; Surratt, J. D. Multiphase Reactivity of Gaseous Hydroperoxide Oligomers Produced from Isoprene Ozonolysis in the

Presence of Acidified Aerosols. *Atmos. Environ.* **2017**, *152*, 314–322. DOI: 10.1016/j.atmosenv.2016.12.040.

(80)   Zhao, R.; Kenseth, C. M.; Huang, Y.; Dalleska, N. F.; Kuang, X. M.; Chen, J.; Paulson, S. E.; Seinfeld, J. H. Rapid Aqueous-Phase Hydrolysis of Ester Hydroperoxides Arising from Criegee Intermediates and Organic Acids. *J. Phys. Chem. A* **2018**, *122* (23), 5190–5201. DOI: 10.1021/acs.jpca.8b02195.

(81)   Docherty, K. S.; Wu, W.; Lim, Y. B.; Ziemann, P. J. Contributions of Organic Peroxides to Secondary Aerosol Formed from Reactions of Monoterpenes with O_3. *Environ. Sci. Technol.* **2005**, *39* (11), 4049–4059. DOI: 10.1021/es050228s.

(82)   Claflin, M. S.; Krechmer, J. E.; Hu, W.; Jimenez, J. L.; Ziemann, P. J. Functional Group Composition of Secondary Organic Aerosol Formed from Ozonolysis of α-Pinene Under High VOC and Autoxidation Conditions. *ACS Earth Space Chem.* **2018**, *2* (11), 1196–1210. DOI: 10.1021/acsearthspacechem.8b00117.

(83)   Li, X.; Chee, S.; Hao, J.; Abbatt, J. P. D.; Jiang, J.; Smith, J. N. Relative Humidity Effect on the Formation of Highly Oxidized Molecules and New Particles during Monoterpene Oxidation. *Atmos. Chem. Phys.* **2019**, *19* (3), 1555–1570. DOI: 10.5194/acp-19-1555-2019.

(84)   Berndt, T.; Mentler, B.; Scholz, W.; Fischer, L.; Herrmann, H.; Kulmala, M.; Hansel, A. Accretion Product Formation from Ozonolysis and OH Radical Reaction of α-Pinene: Mechanistic Insight and the Influence of Isoprene and Ethylene. *Environ. Sci. Technol.* **2018**, *52* (19), 11069–11077. DOI: 10.1021/acs.est.8b02210.

(85)   Kristensen, K. Department of Chemistry, Aarhus University, Aarhus, Denmark. Personal communication, 2017.

(86)   Fernández, F.; López, C.; Hergueta, A. R. Synthesis of a Precursor of Cyclobutane Carbocyclic Nucleosides from α-Pinene. *Tetrahedron* **1995**, *51* (37), 10317–10322. DOI: 10.1016/0040-4020(95)00600-D.

(87)   Kołodziejczyk, A.; Pyrcz, P.; Pobudkowska, A.; Błaziak, K.; Szmigielski, R. Physicochemical Properties of Pinic, Pinonic, Norpinic, and Norpinonic Acids as Relevant α-Pinene Oxidation Products. *J. Phys. Chem. B* **2019**, *123* (39), 8261–8267. DOI: 10.1021/acs.jpcb.9b05211.

C h a p t e r   4

ATMOSPHERIC AQUEOUS CHEMISTRY OF PINENE-DERIVED CARBOXYLIC ACIDS AND DIMER ESTERS

Kenseth, C. M.; Seinfeld, J. H. Atmospheric Aqueous Chemistry of Pinene-Derived Carboxylic Acids and Dimer Esters. *Environ. Sci. Technol.* In preparation.

C h a p t e r   5

ELUCIDATION OF THE STRUCTURES AND FORMATION MECHANISM OF DIMER ESTERS IN α-PINENE AND β-PINENE SECONDARY ORGANIC AEROSOL

C h a p t e r 6

CONCLUSIONS

Forthcoming.

IODOMETRY-ASSISTED LIQUID CHROMATOGRAPHY ELECTROSPRAY IONIZATION MASS SPECTROMETRY FOR ANALYSIS OF ORGANIC PEROXIDES: AN APPLICATION TO ATMOSPHERIC SECONDARY ORGANIC AEROSOL

Zhao, R.; Kenseth, C. M.; Huang, Y.; Dalleska, N. F.; Seinfeld, J. H. Iodometry-Assisted Liquid Chromatography Electrospray Ionization Mass Spectrometry for Analysis of Organic Peroxides: An Application to Atmospheric Secondary Organic Aerosol. *Environ. Sci. Technol.* **2018**, *52* (4), 2108–2117. DOI: 10.1021/acs.est.7b04863.

Iodometry-Assisted Liquid Chromatography Electrospray Ionization Mass Spectrometry for Analysis of Organic Peroxides: An Application to Atmospheric Secondary Organic Aerosol

Ran Zhao,*[†] Christopher M. Kenseth,[†] Yuanlong Huang,[‡] Nathan F. Dalleska,[§] and John H. Seinfeld[†,‖]

[†]Division of Chemistry and Chemical Engineering, California Institute of Technology, Pasadena, California 91125, United States
[‡]Division of Geological and Planetary Sciences, California Institute of Technology, Pasadena, California 91125, United States
[§]Environmental Analysis Center, California Institute of Technology, Pasadena, California 91125, United States
[‖]Division of Engineering and Applied Science, California Institute of Technology, Pasadena, California 91125, United States

S Supporting Information

ABSTRACT: Organic peroxides comprise a significant fraction of atmospheric secondary organic aerosol (SOA). Detection and quantification of particle-phase organic peroxides are highly challenging, and current efforts rely significantly on filter extraction and offline mass spectrometry (MS). Here, a novel technique, iodometry-assisted liquid chromatography electrospray ionization mass spectrometry (iodometry-assisted LC-ESI-MS), is developed and evaluated with a class of atmospherically relevant organic peroxides, α-acyloxyalkyl hydroperoxides, synthesized via liquid ozonolysis. Iodometry-assisted LC-ESI-MS unambiguously distinguishes organic peroxides, compensating for the lack of functional group information that can be obtained with MS. This technique can be versatile for a wide spectrum of environmental analytical applications for which a molecular-level identification of organic peroxide is required. Here, iodometry-assisted LC-ESI-MS is applied to the water-soluble organic carbon (WSOC) of α-pinene SOA. Unexpectedly, a limited number of detectable compounds in WSOC appear to be organic peroxides, despite the fact that spectroscopy-based iodometry indicates 15% of WSOC mass is associated with organic peroxides. This observation would be consistent with decomposition of multifunctional organic peroxides to small peroxides that can be quantified by spectroscopy-based iodometry but not by LC-ESI-MS. Overall, this study raises concerns regarding filter extraction-based studies, showing that assignment of organic peroxides solely on the basis of MS signatures can be misleading.
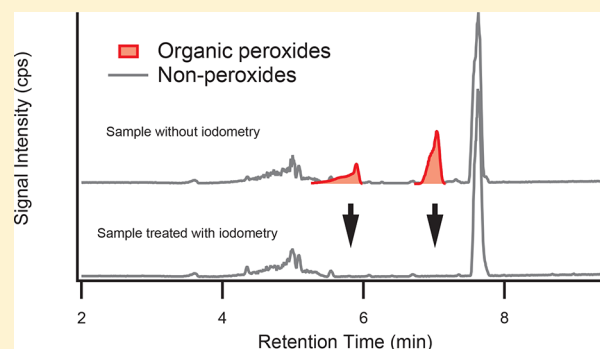
INTRODUCTION

Organic peroxides are ubiquitous in the atmospheric environment, participating in the oxidation of SO_2 to form acid rain,[1] serving as a reservoir for atmospheric oxidants,[2] and potentially contributing to the adverse health effects of air pollution.[3] Recent studies have revealed a critical role that organic peroxides play in the formation of secondary organic aerosol (SOA), submicrometer particulate matter that forms in the atmosphere via condensation of oxidation products of volatile organic compounds (VOCs).[4] Despite the prominent role that SOA plays in air quality and the global climate, our understanding of the reaction mechanisms and products of VOC oxidation remains incomplete. In particular, the identity and chemistry of organic peroxides represent important missing aspects.

On a global scale, biogenic monoterpenes ($C_{10}H_{16}$) are important precursors to SOA. Estimated global SOA production from mono- and sesquiterpenes varies from 14 to 246 Tg/year.[5,6] α-Pinene is the dominant monoterpene by mass[7] and is readily oxidized in the atmosphere by the major oxidants, O_3 and the OH radical. It has been established that SOA arising from α-pinene contains a substantial amount of total organic peroxides.[8,9] Quantification of organic peroxides in SOA extracts has been successful using spectroscopic techniques, such as iodometry.[8,10−12] Iodometry proceeds as $R_1OOR_2 + 2I^- + 2H^+ \rightarrow R_1OH + R_2OH + I_2$, followed by $I_2 + I^- \rightarrow I_3^-$,[13] where R_1 and R_2 represent any alkyl group or H. With acid catalysis, I^- reduces an organic peroxide molecule to the corresponding alcohols, liberating I_2 that subsequently forms I_3^- in an excess of I^-. The characteristic absorption of I_3^- reaches a peak at 350 nm and can be measured by ultraviolet−

visible (UV−vis) spectrometry. As I⁻ reacts with essentially all types of organic peroxides,[14] iodometry determines the total organic peroxide content. Molecular-level identification of particle-phase organic peroxides is more challenging, because of the chemical complexity of SOA components, a lack of authentic organic peroxide chemical standards, and their chemical instability. A number of recent studies have reported decomposition of SOA organic peroxides in the particle phase[12,15] and the aqueous phase.[16]

Recent application of liquid chromatography electrospray ionization mass spectrometry (LC-ESI-MS) to extracted SOA components has significantly advanced our understanding of particle-phase organic compounds, including both monomers and dimers,[17−29] a number of which have been proposed to be organic peroxides. In particular, it is proposed that the stabilized Criegee intermediate (SCI) formed during ozonolysis can react with organic acids and form a class of hydroperoxy dimer esters, α-acyloxyalkyl hydroperoxides (αAAHPs).[15,17,18,30,31] The importance of α-AAHPs in the ambient atmosphere remains unclear, but a ≤16% contribution by mass to laboratory-generated SOA has been reported.[17] Additionally, gas-phase measurements using chemical ionization mass spectrometry have detected highly oxidized multifunctional organic compounds (HOMs), which bear multiple hydroperoxy functional groups and arise from repeated intramolecular hydrogen-abstraction reactions.[32,33] HOMs exhibit extremely low volatility, and their presence in the particle phase has been reported.[34−37] These studies have highlighted novel SOA formation pathways in which organic peroxides play a pivotal role. Determination of such organic peroxides at the molecular level is critical and is the only means of revealing the underlying mechanisms of formation of SOA.

Although ESI-MS is a versatile technique for a wide spectrum of organic compounds,[38,39] unambiguous identification of organic peroxides using MS-based techniques is challenging, given that MS provides limited information about functional groups. A number of studies have used ESI-MS to detect synthesized organic peroxides, including peracids,[40,41] alkylhydroperoxides,[42] peroxy esters,[29] diacyl peroxides,[43] and αAAHPs.[44] Despite the capability of ESI-MS for organic peroxide detection, detection of organic peroxide is highly sensitive to specific conditions employed in each ESI-MS instrument.

The primary objective of this study is to develop and demonstrate the applicability of a novel technique, iodometry-assisted LC-ESI-MS, to unambiguously distinguish organic peroxides present in a complex chemical matrix. The method is evaluated with αAAHPs synthesized via liquid-phase ozonolysis. For the first time, iodometry is employed not only to determine the total peroxide content but also to provide molecularly resolved information by coupling to LC-ESI-MS. We have applied iodometry-assisted LC-ESI-MS to investigate organic peroxides present in the water-soluble fraction of α-pinene SOA. Measurements of water-soluble organic carbon (WSOC) in SOA can be performed using filter extraction and/or the particle-into-liquid sampler (PILS).[45] WSOC has gained attention as a proxy for the oxygenated fraction of SOA[46] that can dissolve in cloudwater and undergo multiphase chemistry.[47−49]

■ EXPERIMENTAL SECTION

Chemicals. All chemicals were used without further purification. The following chemicals were purchased from

Sigma-Aldrich: adipic acid (99%), α-pinene (>99%), benzoyl-peroxide (Luperox, 75%), cis-pinonic acid (98%), D-sorbitol (>98%), hydrogen peroxide (H₂O₂, 50% in water), lauroyl peroxide (Luperox, 97%), leucine enkephalin [>95%, high-performance liquid chromatography (HPLC) grade], meso-erythritol (>99%), pinic acid (custom-synthesized), potassium hydrogen phthalate (>99.95%), potassium iodide (KI, 99%), and tert-butyl hydroperoxide (Luperox, 50% in water). Chemicals were also purcahsed from other sources: acetonitrile (EMD), ammonium sulfate [(NH₄)₂SO₄, Mallinckrodt Chemicals], formic acid (Fluka, HPLC grade, 50% in water), glacial acetic acid (Macron Fine Chemicals), and methylhydroper-oxide (synthesized).

SOA Generation and Collection. SOA was generated in the steady state Caltech photooxidation flow tube (CPOT) reactor,[50] details of which are given in section S1 of the Supporting Information. Briefly, α-pinene (175 ppb) and O₃ (1 ppm) reacted in the CPOT to generate SOA at room temperature without light or nitrogen oxides. No OH scavenger was added; therefore, α-pinene is oxidized primarily by O₃ with a contribution from the OH radical generated during ozonolysis. The total rate of gas flow through the CPOT was 12.5 L/min, giving rise to an average residence time of 3.5 min. Polydisperse (NH₄)₂SO₄ seed aerosol was generated by aerosolizing an aqueous solution (0.01 M) with a custom-built atomizer, followed by using a diffuser dryer and a neutralizer. The relative humidity (RH) in the CPOT was approximately 10%.

Approximately 10 L/min of flow from the CPOT was introduced through a Teflon filter (Pall Life Sciences, 47 mm diameter and 2 μm pore size) to collect SOA samples. A diffuser packed with activated charcoal was employed before the filter to remove O₃ and gas-phase species to prevent continuous on-filter reactions and further partitioning of gas-phase species to the collected particles. One filter sample was collected per experiment, with collection times of 15−18 h. The mass of collected particle samples was typically 1−2 mg. Filters were frozen at −16 °C immediately after collection. Note that we employed collection times longer than those in previous studies (0.6−4 h)[8,11,51,52] to overcome the detection limits of offline analyses and to maximize detection of compounds by LC-ESI-MS.

Synthesis of α-Acyloxyalkyl Hydroperoxides (αAAHPs). Two αAAHP species were synthesized as surrogates for multifunctional organic peroxides.[17,30,31] They were synthesized via liquid-phase ozonolysis with a method modified from a previous study.[44] Briefly, α-pinene (50 mM) and an organic acid (10 mM) were dissolved in acetonitrile. A 5 mL aliquot of this solution was bubbled with an air stream containing roughly 100 ppm of O₃ at a flow rate of 120 sccm for 5 min. The ozonolysis solution was immersed in an ice bath throughout the synthesis and storage to minimize decomposition.

The proposed pathway for formation of αAAHPs, as well as their structures, is shown in Figure 1. Briefly, α-pinene reacts with O₃ to form a primary ozonide that decomposes to form two possible Criegee intermediates. Upon interaction with the surrounding solvent molecules, stabilized Criegee intermediates (SCIs) are formed. The SCI reacts with the excess of the organic acid added to the solution, forming an αAAHP species with two possible structural isomers. Two organic acids, pinonic acid and adipic acid, were chosen in this work to synthesize two different αAAHPs. Pinonic acid was selected for
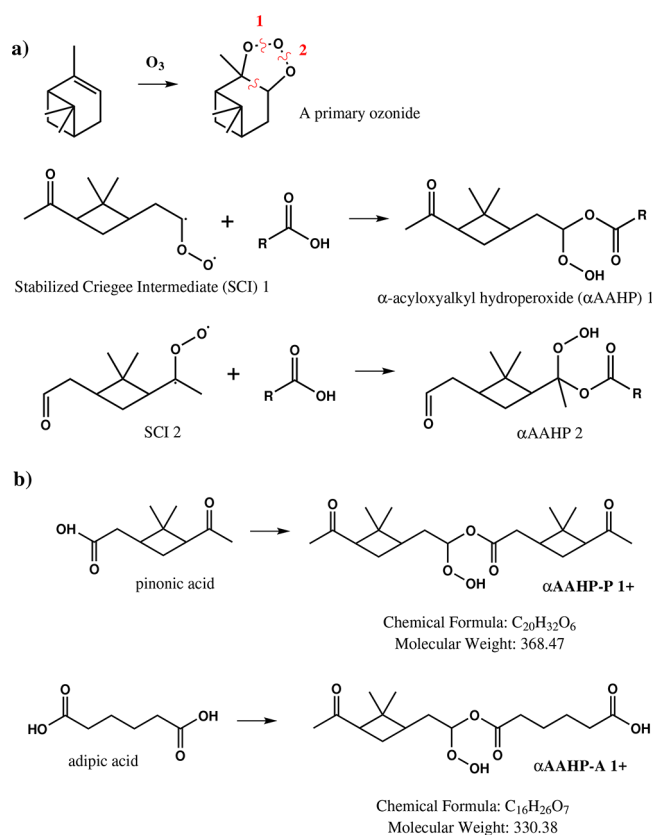
Figure 1. Schematic of the mechanism underlying the synthesis of the αAAHP species. Reactions in panel (a) illustrate the general reaction between a stabilized Criegee intermediate (SCI) and an organic acid, giving rise to αAAHP with two possible structural isomers. Reactions in panel (b) show the specific cases employed in this work to synthesize αAAHP-P and αAAHP-A. Only one structural isomer is shown for each of them.

its relevance in α-pinene oxidation. Adipic acid, being a diacid, contains an additional carboxylic acid functional group for which αAAHP-A is more easily detected by ESI$^-$-MS. These two species are hereafter termed αAAHP-P and αAAHP-A, respectively.

Offline Chemical Analyses. The frozen filter samples were thawed and extracted in 10 mL of Milli-Q water (18.2 mΩ) by being mechanically shaken before in-depth chemical analyses were performed. Sonication was avoided to prevent potential artifacts.[10]

Total Organic Carbon (TOC). The total organic carbon (TOC) content of the SOA extracts was quantified using a TOC analyzer (OI Analytical model 1030W). The total carbon (TC) method was employed, wherein all the carbon-containing species (i.e., both organic and inorganic) are oxidized to CO_2 by sodium persulfate with phosphoric acid at 100 °C, with the CO_2 detected by nondispersive infrared detection. The TC content measured in a blank filter extract was subtracted as the background. The limit of detection is 0.6 ppm of C, determined as 3σ + the mean of the filter blank. The method was calibrated using potassium hydrogen phthalate, and the accuracy of the method was 5%, tested by measuring *meso*-erythritol and D-sorbitol solutions at known concentrations.

Iodometry. Formic acid or acetic acid was added to an aliquot of a WSOC sample to adjust the solution pH to 2 or 3, respectively. To this solution was added a concentrated potassium iodide (KI) aqueous solution, made fresh daily and

purged with N_2 gas, such that the concentration of I$^-$ in the solution was 60 mM. Immediately after the addition of KI, the solution was gently purged with N_2 and placed in an airtight vial in the dark for 1 h before the UV−vis measurement was conducted with a spectrophotometer (Shimadzu, UV-1601). The method was calibrated prior to each experiment against a set of H_2O_2 solutions, standardized with the molar absorptivity of H_2O_2 at 254 nm. The calibration accounts for the reaction of I$^-$ with dissolved O_2 and confirms the linearity of the method. The detection limit of the current method is 1.5 μM H_2O_2 equivalent, determined as 3σ of the water blank.

Iodometry-Assisted LC-ESI-MS. The instrument and methods employed for the LC-ESI-MS analysis have been described previously.[22,23] Briefly, the instrument consists of a Waters ACQUITY UPLC I-Class system, coupled to a quadrupole time-of-flight mass spectrometer (Xevo G2-S QToF). LC separation was performed on an ACQUITY BEH C_{18} column (2.1 mm × 50 mm) held at 30 °C. The total flow rate was 0.3 mL min^{-1}, and the injection volume was 10 μL. LC uses two eluents: A [0.1% (v/v) formic acid in water] and B (100% acetonitrile). The gradient was programmed as follows: 100% A from 0 to 2.0 min, 10% A and 90% B from 2.0 to 10.2 min, and 100% A from 10.2 to 12 min. ESI settings were as follows: capillary voltage, 2.0 kV; sampling cone voltage, 40 V; source offset, 80 V; source temperature, 120 °C; desolvation temperature, 400 °C; cone gas, 30 L h^{-1}; desolvation gas, 650 L h^{-1}. Leucine enkephalin was employed as the lock mass for accurate mass determination. The method stability is within 5%, as determined by frequent consistency tests. The positive (LC-ESI$^+$-MS) and negative (LC-ESI$^-$-MS) modes were used under the same settings, and data were acquired and processed with MassLynx version 4.1.

For a number of samples, the iodometry method described above was applied prior to the LC-ESI-MS measurement. Formic acid was used to adjust the solution pH to 2. To ensure the completion of iodometry, the iodometry solutions were allowed to react for 5−7 h before the LC-ESI-MS measurement was conducted. As iodometry selectively reacts away organic peroxides, it is hypothesized that organic peroxide compounds can be elucidated by a comparison of iodometry-treated samples and nontreated samples. Four different conditions were examined to explore the effects of formic acid and iodide on WSOC: with neither formic acid nor KI (condition I), with formic acid (condition II), with KI (condition III), and with both formic acid and KI (condition IV). These four conditions maintain the same dilution ratio but with variable reagents added.

■ RESULTS AND DISCUSSION

Detection of Organic Peroxides. The LC-ESI-MS method separated and detected the two synthesized αAAHP species. Base peak intensity (BPI) chromatograms of an aqueous solution containing both αAAHPs are shown in [Figure 2](#).

LC-ESI$^-$-MS detected αAAHP-A as its deprotonated form ([M − H]$^-$) due to the additional carboxylic acid functional group in the molecule ([Figure 2](#)a). Without a carboxylic acid functional group, αAAHP-P is not detected as the deprotonated form. Instead, a peak with a nominal mass of 183 Da appears at the retention time (t_R) corresponding to αAAHP-P, and its elemental composition is identical to that of the deprotonated pinonic acid ($C_{10}H_{15}O_3$). We propose that this peak is not pinonic acid, but instead a fragment of αAAHP-P because the t_R
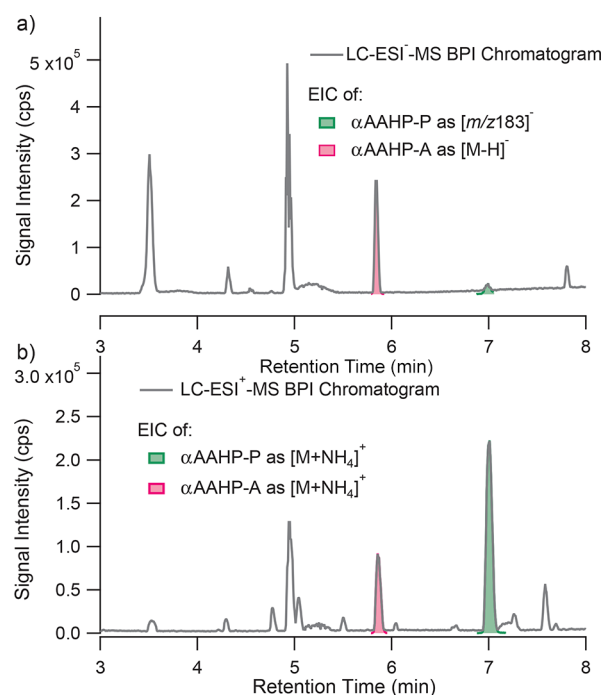
Figure 2. Base peak intensity (BPI) chromatogram of an aqueous solution containing αAAHP-P and αAAHP-A detected by (a) LC-ESI⁻-MS and (b) LC-ESI⁺-MS. Colored areas represent the extracted ion chromatograms (EICs) of these two αAAHP species.

of pinonic acid is 4.7 min. In addition, as we will discuss next, this m/z 183 fragment disappears when iodometry is applied, while pinonic acid does not. This observation gives rise to an important implication for the detection of SOA components, as a fraction of organic acids commonly observed by LC-ESI⁻-MS may have been fragments of αAAHP or other high-molecular weight compounds. LC-ESI⁺-MS has detected the αAAHP species predominantly as their ammonium clusters ([M + NH₄]⁺) but also as their sodium clusters ([M + Na]⁺). Note that the BPI chromatogram presents only the most intensive peak at each t_R.

To provide general guidance for future applications of ESI-MS in organic peroxide detection, we have also carefully evaluated the detection of organic peroxides using direct-infusion ESI-MS, which bypasses the LC component and directly injects the sample solution into the ESI-MS instrument (section S2 of the Supporting Information). Two commercially available organic peroxides, benzoyl peroxide and lauroryl peroxide, were chosen as representatives for ROOR species, while the synthesized αAAHP species were employed as those for multifunctional ROOH species. As expected, αAAHP-P is not detected by ESI⁻-MS as it does not contain any carboxylic functional group. ESI⁻-MS detects αAAHP-A as its [M − H]⁻ and [2M − H]⁻ forms. ESI⁺-MS detects all the four organic peroxides as their sodium clusters, as opposed to LC-ESI⁺-MS, in which ammonium clusters dominate. As sodium formate is introduced into the infusion system regularly for calibration, there can be a potential source of Na⁺ in the system. On the other hand, the amount of Na⁺ co-eluting with analytes during LC-ESI-MS is likely much smaller. Our results show that the difference in the ionization environment can likely change the mode of detection of organic peroxides. In future studies, the detectability of organic peroxides should be examined before any assumptions are made about their detection.

Characterization of Iodometry and the Total Peroxide Contents of α-Pinene SOA. Prior to application of iodometry to LC-ESI-MS, spectroscopy-based iodometry was performed to determine the total organic peroxide content of the WSOC samples. We performed measurements for five replicate filters. The H_2O_2 equivalent concentration of total organic peroxide ranged from 14 to 30 μM. Because the amount of SOA collected on each filter and the extraction efficiency vary, the measured total peroxide concentration of each filter extract was normalized to the measured TOC concentration.

The total peroxide content is commonly reported as molar yield (moles of organic peroxide per SOA mass) and mass yield (mass of organic peroxide per mass of SOA). Obtaining these values requires the average organic matter to organic carbon ratio (OM/OC) of SOA components and the average molecular weight of organic peroxides. Here, we assume the average OM/OC to be equivalent to that of pinic acid (i.e., 1.7), which is one of the most abundant compounds in α-pinene SOA,[7] while the average molecular weight of 300 g mol⁻¹ for organic peroxides was adapted from previous studies.[8,52] With these assumptions, an average molar yield of $(4.8 \pm 1.2) \times 10^{-10}$ mol μg^{-1} and an average mass yield of $15 \pm 3.7\%$ were obtained from this study. As discussed with details in section S3.1 of the Supporting Information, this mass yield is lower but comparable to those reported in the literature.[8,11,51−55]

To improve our understanding of the current iodometry method, we have investigated the reaction kinetics of the iodometry reaction by monitoring the solution absorbance at 350 nm. We performed this experiment on WSOC as well as a number of individual peroxide solutions, including H_2O_2, tert-butyl hydroperoxide, and methyl hydroperoxide. The detailed results are presented in section S3.2 of the Supporting Information and Figure S3. Our results show that iodometry proceeds with different organic peroxides at different rates, with H_2O_2 reacting with iodide the most rapidly. The reaction with WSOC may not have reached completion after 1 h, at which point the UV measurement was taken in the current and a number of past studies,[8,10] giving rise to a potential underestimation of the total organic peroxide content (see section S.2 of the Supporting Information).

Iodometry-Assisted LC-ESI-MS. *Iodometry Performed on Non-Peroxide Species.* Iodometry was first performed on an aqueous solution containing each of three nonperoxide organic acids at 5 μM: adipic acid, pinonic acid, and pinic acid. These three organic acids can be readily detected by LC-ESI⁻-MS. An aliquot treated with iodometry (condition IV described in the Experimental Section) was compared with a control (condition II), and the BPI chromatograms are shown in section S4 of the Supporting Information. The peak intensities of the three organic acids treated with and without iodometry are essentially identical, confirming that iodide does not react with non-peroxide compounds. Another important observation is that the t_R of the three organic acids is not affected by iodometry. For the iodometry-treated sample, a large peak of iodide (127 Da) emerges at the beginning of the chromatogram ($t_R < 2$ min) but is directed to waste.

Iodometry Performed on αAAHP Species. Iodometry was performed on an acetonitrile solution containing both of the synthesized αAAHP species. Acetonitrile is used here to minimize hydrolysis of αAAHPs and to ensure that the spectral changes are induced by only iodometry. The solution was
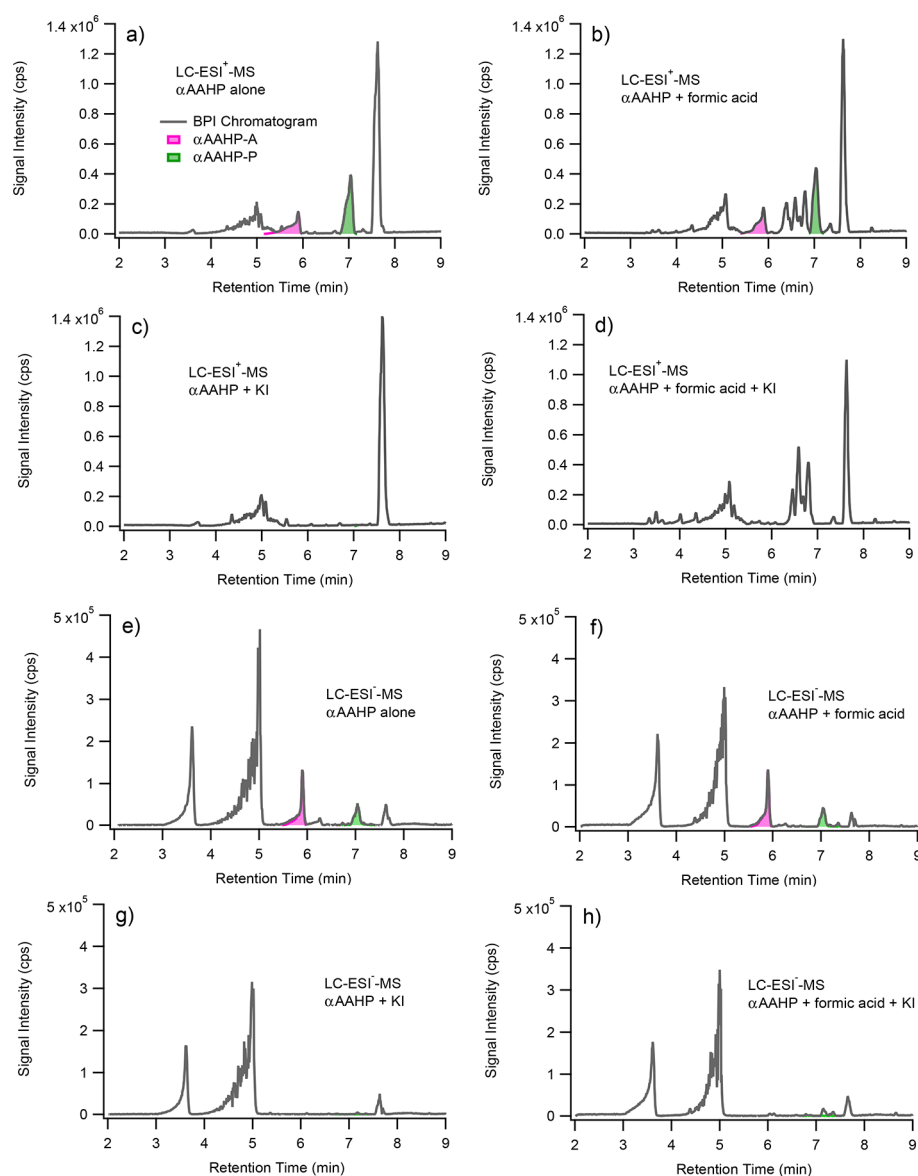
Figure 3. Results of iodometry performed on a mixture of synthesized αAAHP-P and αAAHP-A dissolved in acetonitrile. Results of LC-ESI$^+$-MS and LC-ESI$^-$-MS are presented in panels (a−d) and (e−h), respectively.

allowed to react for 2 h before LC-ESI-MS measurement. To the best of our knowledge, this is the first investigation of the iodometry reaction at the molecular level; therefore, detailed results are presented in Figure 3. Panels (a−d) of Figure 3 show the results obtained with LC-ESI$^+$-MS. When formic acid was added to the solution, several additional peaks appeared on the chromatogram, but the αAAHP peaks were unaffected (Figure 3b). When KI was added to the solution, either with or without formic acid, only the αAAHP peaks disappeared (Figure 3c,d). The excess of organic acid added to the solution for the synthesis likely made the solution sufficiently acidic, and iodometry proceeds without additional formic acid. A similar observation was obtained using LC-ESI$^-$-MS (Figure 3e−h). In particular, the *m/z* 183 peak at a t_R of 7 min disappears with iodometry, confirming that it is likely a fragment of αAAHP-P and unrelated to pinonic acid. These results illustrate that iodometry selectively reacts away organic peroxides with a negligible impact on non-peroxide species.

Effect of Iodometry on the SOA Extract. *Negative Mode (LC-ESI$^-$-MS).* Analysis of α-pinene SOA components using LC-ESI$^-$-MS has been reported in a number of studies, including our previous work.[17,18,20,22,26−28,56] The chromatogram and mass spectra recorded in this work are provided in section S5 of the Supporting Information. The BPI chromatogram obtained in this study (Figure S5a) reproduces well those of our previous study, confirming the reproducibility of the LC-ESI-MS method. Figure S5b shows the reconstructed mass spectrum, defined to be the sum of all mass spectra at t_R values from 2 to 9 min with a peak height of $\geq 2 \times 10^3$ counts per second (cps). The mass spectrum demonstrates a bimodal form, attributed to monomers and dimers in WSOC.[28,57,58] In Table S2, we provide a list of major peaks detected in this work. We did not conduct a detailed structural analysis, as this has already been done in a number of other studies.[17,23,35,59] Instead, we have annotated peaks that have been previously proposed as candidates of organic peroxides.
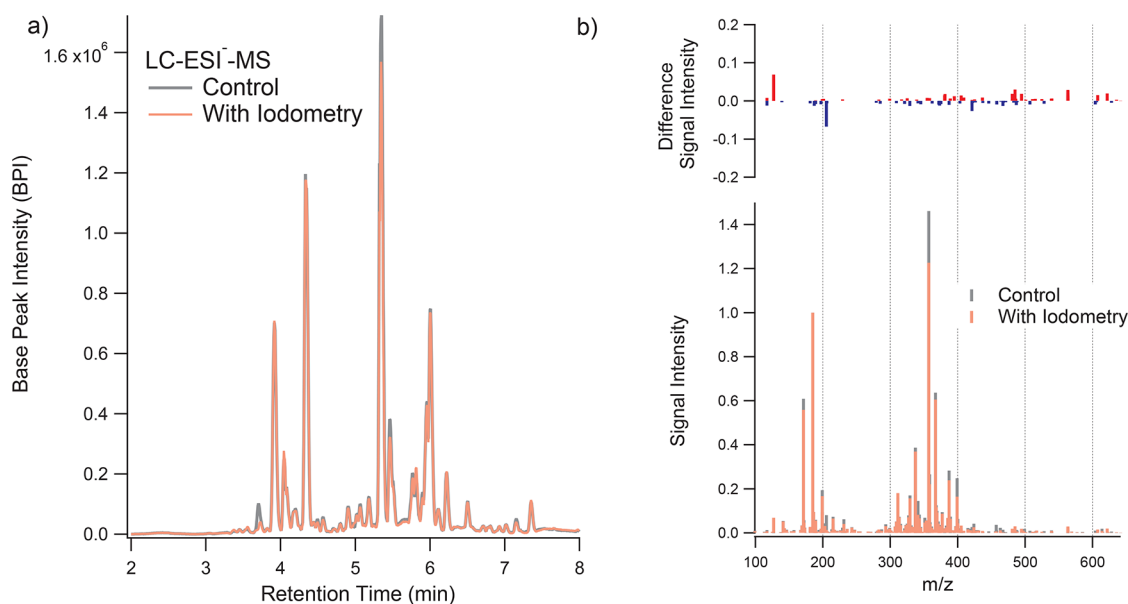
Figure 4. Comparison of a sample treated with and without iodometry, measured by LC-ESI⁻-MS. Comparison of the base peak intensity (BPI) chromatograms is shown in panel (a). The reconstructed mass spectra are shown in the bottom part of panel (b), where the peak intensities have been normalized to that of pinic acid ($[C_9H_{14}O_4 - H]^-$ at 185.08 Da). The top part of panel (b) shows a difference mass spectrum showing peaks that are depleted by >70% and those newly introduced by iodometry. Each BPI chromatogram and mass spectrum shown here is the average of triplicate measurements. The control sample refers to condition II described in the Experimental Section, while the iodometry sample refers to condition IV.
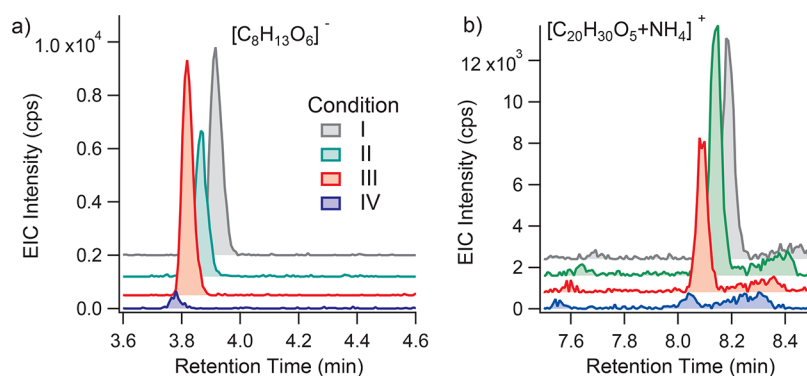
Figure 5. Extracted ion chromatogram (EIC) of two organic peroxide candidates: (a) $[C_8H_{13}O_6]^-$ from LC-ESI⁻-MS and (b) $[C_{20}H_{30}O_5 + NH_4]^+$ from LC-ESI⁺-MS. From top to bottom, the four traces represent iodometry conditions I−IV, respectively (see the Experimental Section).

We performed a comparison of samples treated with and without iodometry, and the results for LC-ESI⁻-MS are shown in Figure 4, focusing on the comparison between the sample treated with only formic acid (condition II) and that treated with both formic acid and KI (condition IV), as this comparison excludes any mass spectral changes induced by formic acid alone and best reflects changes induced by iodometry.

Iodometry did not induce significant changes in the BPI chromatograms or reconstructed mass spectra. The top panel of Figure 4b shows the difference mass spectrum between the control and iodometry samples. Given that the reactivity of αAAHP species has been exhibited (Figure 3), any organic peroxides present in the WSOC of α-pinene SOA should be depleted by the time of measurement. Therefore, only peaks that exhibit a significant change, i.e., either depleted by >70% or newly introduced by iodometry, are shown in the difference mass spectrum.

The only major peak that is depleted by iodometry and showed consistency between different filter samples is that of the deprotonated form of $C_8H_{14}O_6$ (205.071 Da, t_R of 3.71 min). The effect of iodometry on other major peaks is discussed in section S5 of the Supporting Information. The decay of $C_8H_{14}O_6$ on the BPI chromatogram can be observed (Figure 4a). The EICs of this compound are presented in Figure 5a, showing that $C_8H_{14}O_6$ is depleted only when both formic acid and KI are present. As the WSOC does not contain an excess of organic acids, compared to the synthesized αAAHPs in which an organic acid is added in excess for synthesis, it seems that additional formic acid is necessary for the iodometry reaction to proceed. We have attempted to perform MS² measurements on $C_8H_{14}O_6$, but the signal intensities of its fragments were too low to obtain structural information. $C_8H_{14}O_6$ has been observed previously and has been tentatively defined as an unknown carboxylic acid.[17] Results from this study suggest that this compound contains a peroxide functional group. Given the high oxygen/carbon ratio
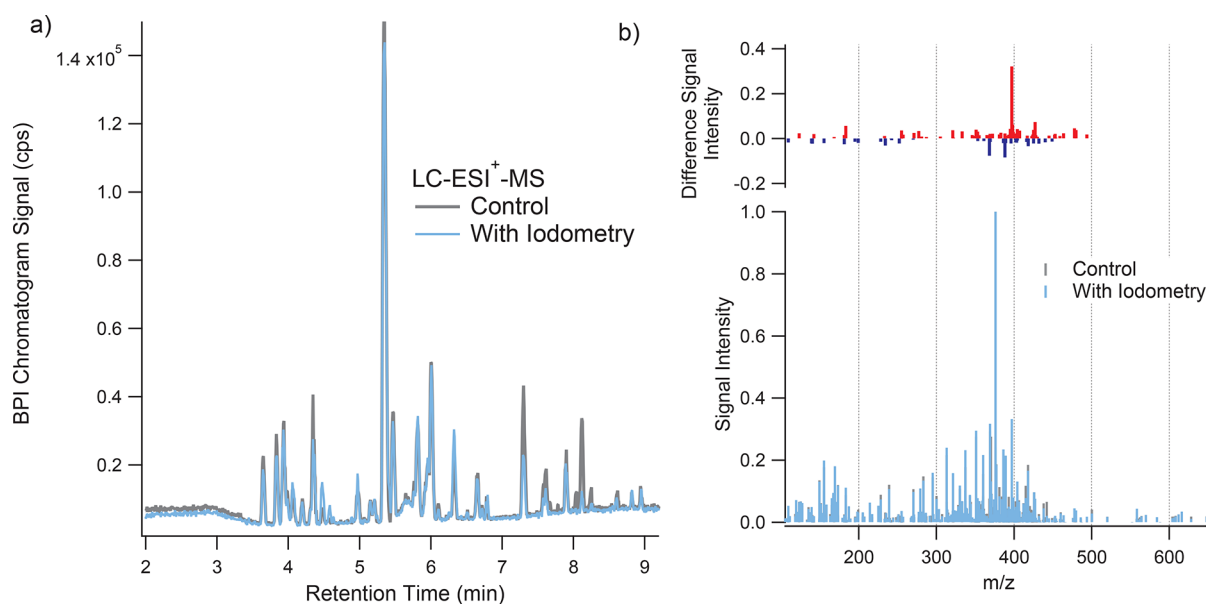
Figure 6. Comparison of a sample treated with and without iodometry, measured by LC-ESI$^+$-MS. Comparison of the base peak intensity (BPI) chromatograms is shown in panel (a). The reconstructed mass spectra are shown in the bottom part of panel (b), where the peak intensities have been normalized to that of pinyl-diaterpenyl ester ($[C_{17}H_{26}O_8 + Na]^+$ at 376.20 Da). The top part of panel (b) is a difference mass spectrum showing peaks that are depleted by >70% and those newly introduced by iodometry. Each BPI chromatogram and mass spectrum shown here is the average of triplicate measurements. The control sample refers to condition II described in the Experimental Section, while the iodometry sample refers to condition IV.

(O/C) of this compound, $C_8H_{14}O_6$ can potentially be a HOM species arising from intramolecular hydrogen abstraction (see Introduction). Alternatively, it can also be a compound similar to 3-methyl-1,2,3-butanetricarboxylic acid (MBTCA, $C_8H_{12}O_6$; t_R = 3.73 min), a well-established organic tracer for α-pinene SOA.[60−62]

Positive Mode (LC-ESI$^+$-MS). Driven by the abundance of organic acids, the use of ESI$^-$ has prevailed in molecular analyses of α-pinene SOA components. Only a few studies have employed ESI$^+$.[24,35,37,56,59,63] The BPI chromatogram recorded by LC-ESI$^+$-MS and its reconstructed mass spectrum are shown in panels (a) and (c) of Figure S5, respectively. A number of major compounds are detected in positive and negative modes, while some can be detected only by the positive mode, as clusters of H$^+$, Na$^+$, and NH$_4^+$. Because the polarity of ESI detection does not affect the chromatographic t_R, we have made peak assignments for the positive mode by comparison with peaks detected in the negative mode, and major compounds are listed in Table S3.

Comparison of a sample treated with and without iodometry is shown in Figure 6 in the same manner as in Figure 4. The only noticeable change on the BPI chromatograms is that two major peaks, appearing at t_R values of 7.3 and 8.1 min, disappear when iodometry is applied. Judging solely on the basis of the comparison of conditions II and IV, which is the case for Figure 6, these two peaks appear to be organic peroxides. However, a detailed investigation of these peaks under all four conditions, presented in section S6.1 of the Supporting Information, indicates that the addition of formic acid has introduced artifacts, and these two peaks are unlikely to be peroxides. Among all the peaks with a peak height of ≥2000 cps, five appear to be candidates for organic peroxides: $[C_8H_{10}O_3 + H]^+$ (155.07 Da), $[C_{10}H_{16}O_5 + NH_4]^+$ (234.13.34 Da), $[C_{10}H_{18}O_6 + NH_4]^+$ (252.15 Da), $[C_{20}H_{30}O_5 + NH_4]^+$ (368.24 Da), and $[C_{19}H_{30}O_7 + NH_4]^+$ (388.23 Da). The EICs

of $[C_{20}H_{30}O_5 + NH_4]^+$ under condition I−IV are shown in Figure 5b, while those of the others are presented in section S6.2 of the Supporting Information. $[C_8H_{10}O_3 + H]^+$ and $[C_{10}H_{16}O_5 + NH_4]^+$ are detected as multiple peaks, and not all of them appear to be organic peroxides. This observation demonstrates the ability of iodometry-assisted LC-ESI-MS to resolve organic peroxides from non-peroxide isomers. The consistency of these observed trends has been confirmed with a separate filter sample. All five candidates for organic peroxides are detected as minor peaks and do not belong to the group of the 50 largest peaks summarized in Table S3. Their peak areas are 2−5% of that of pinyl-diaterpenyl ester, which is the largest peak detected by LC-ESI$^+$-MS. The effect of iodometry on other major peaks is presented in section S5 of the Supporting Information.

Explanations for the Absence of Organic Peroxides in WSOC. The absence of organic peroxides among the major products was unexpected, as α-pinene SOA has been believed to contain a high organic peroxide content.[9,64] In fact, our conventional iodometry measurement using UV−vis detected a total organic peroxide content comparable to that found in previous studies (Table S1). Many of the proposed organic peroxides from previous studies[17,18,23,59] are detected in this work with the corresponding elemental compositions (Table S2). However, none of these compounds decayed in response to the iodometry treatment. We have altered a number of experimental and instrumental conditions that can potentially affect iodometry and the detection of organic peroxides, including the temperature of the iodometry reaction and the ESI settings. Detailed results of these experiments are presented in section S7 of the Supporting Information. However, varying these factors did not explain the absence of major organic peroxide peaks.

The current LC-ESI-MS method is not quantitative, as determination of electrospray ionization efficiency for com-

pounds without definite structural information is difficult; therefore, the peak area of a compound does not directly reflect its concentration in the WSOC sample. With a computational approach, our previous study[23] has found that the ionization efficiencies of the dimer esters are 3−10 times higher than those of the monomeric compounds. Currently, we cannot rule out the possibility that LC-ESI-MS fails to detect certain organic peroxide species due to inefficient ionization. In particular, the major peaks detected by the current method include very few HOM compounds that typically exhibit O/C ratios of >0.7. It is likely that our method and/or instrument is less optimized toward HOMs than those of a number of previous studies.[34,35,37]

Alternatively, decomposition of organic peroxides may play an important role in filter extraction-based techniques. Decomposition can occur at different stages of the experiment. Highly labile organic peroxides may decompose in suspended particles before they can be collected.[12,15,23,52] Decomposition may also occur on the filter, with longer collection times leading to a loss of organic peroxide.[52] In future applications, the filter collection duration can be shortened from that in the current work (15−18 h) to minimize decomposition and evaporation. Finally, decomposition may occur after the SOA component is extracted to condensed phases, forming the OH radical[16] and H_2O_2.[53,55,65] Small and polar peroxides, such as H_2O_2, can contribute to the total peroxide content measured by the conventional, spectroscopy-based iodometry but cannot be detected by our LC-ESI-MS method, which is optimized for monomeric and dimeric oxidation products of α-pinene.

■ ENVIRONMENTAL IMPLICATIONS

With an emerging awareness of the role that organic peroxides play in SOA formation and the consequent health effects, identification of particle-phase organic peroxides has become a priority in atmospheric chemistry research. Employing advanced MS techniques, many recent studies have reported detection of particle-phase organic peroxides. However, structural assignment with MS is often based only on exact mass and/or fragmentation patterns, supported by feasible formation mechanisms, leaving room for potential misassignment due to a lack of structural information about functional groups. In this work, we have developed a novel technique, iodometry-assisted LC-ESI-MS, to unambiguously identify organic peroxides present in extracted SOA components at the molecular level.

Because of a lack of commercially available organic peroxides, characterization of our method was performed with synthesized α-acyloxyalkyl hydroperoxides (αAAHPs). Detection of αAAHPs was successful, but our results reveal concerns regarding the use of ESI-MS for the detection of organic peroxides. In particular, even with the same ESI-MS instrument, a difference in the ionization mode was observed between direct infusion and LC-ESI-MS, likely due to different ionization conditions. In future studies, the utility of LC-ESI-MS for organic peroxide identification should be thoroughly characterized.

The utility of iodometry-assisted LC-ESI-MS has been demonstrated with αAAHPs. Iodometry selectively reacts away organic peroxides with negligible interference with non-peroxide species. While iodometry-assisted LC-ESI-MS was applied in this work to study one specific issue related to atmospheric particulate matter, the versatility of this technique makes it applicable to a wide range of environmental applications that require the determination of organic peroxides at the molecular level.

Iodometry-assisted LC-ESI-MS was applied to the water-soluble organic carbon (WSOC) of α-pinene SOA collected from a flow tube reactor, following a standard sample collection procedure. Unexpectedly, only a limited number of detectable compounds, $C_8H_{14}O_6$ from the negative mode and five minor peaks from the positive mode, appeared to be organic peroxides. This observation is inconsistent with conventional, spectroscopy-based iodometry, which suggests that the average mass yield of organic peroxides is 15% in this system. We propose that the multifunctional organic peroxides may have decomposed to smaller peroxides that cannot be detected with the current LC-ESI-MS technique. Future studies should investigate the stability and decomposition mechanisms of organic peroxides on filters and in extraction solutions. Although this work focused only on the decay of organic peroxides during iodometry, an interesting direction would be the investigation of the corresponding alcohols arising from iodometry. Unlike organic peroxides, functionalized alcohols and polyols are commercially available, which may lead to new avenues for quantifying organic peroxides.

Our results raise significant concerns about all filter extraction-based studies of atmospheric SOA, showing that labile organic peroxides can be lost either during sample collection or after extraction. The use of MS prevails in the field of atmospheric chemistry, and the versatility of LC-ESI-MS has been proven by many studies. However, previously unrecognized considerations are required for the interpretation of MS data, particularly for the assignment of organic peroxides.

■ ASSOCIATED CONTENT

ⓢ Supporting Information

The Supporting Information is available free of charge on the ACS Publications website at DOI: 10.1021/acs.est.7b04863.

> Additional information about the generation and collection of SOA (section S1), detection of organic peroxides with direct-infusion ESI-MS (section S2), a comparison of the total organic peroxide content obtained in this work to those from previous studies and a detailed characterization of the iodometry method (section S3), results from iodometry performed on non-peroxide species (section S4), chromatograms and lists of major compounds detected by LC-ESI-MS (section S5), additional information about the analyses of iodometry-assisted LC-ESI-MS (section S6), and additional examination of various instrumental conditions for iodometry-assisted LC-ESI-MS (section S7) (PDF)

■ AUTHOR INFORMATION

Corresponding Author
*E-mail: rzhao@caltech.edu. Phone: +1 626-395-8928.

ORCID ⓞ
Ran Zhao: 0000-0002-1096-7632
Christopher M. Kenseth: 0000-0003-3188-2336
John H. Seinfeld: 0000-0003-1344-4068

Notes
The authors declare no competing financial interest.

■ REFERENCES

(1) Sakugawa, H.; Kaplan, I. R.; Tsai, W.; Cohen, Y. Atmospheric hydrogen peroxide. *Environ. Sci. Technol.* **1990**, *24*, 1452−1462.

(2) Pandis, S. N.; Seinfeld, J. H. Sensitivity analysis of a chemical mechanism for aqueous-phase atmospheric chemistry. *J. Geophys. Res.* **1989**, *94*, 1105−1126.

(3) Tao, F.; Gonzalez-Flecha, B.; Kobzik, L. Reactive oxygen species in pulmonary inflammation by ambient particulates. *Free Radical Biol. Med.* **2003**, *35*, 327−340.

(4) Seinfeld, J. H.; Pandis, S. N. *Atmospheric Chemistry and Physics: From Air Pollution to Climate Change*, 3rd ed.; John Wiley & Sons: Hoboken, NJ, 2016.

(5) Pye, H. O. T.; Chan, A. W. H.; Barkley, M. P.; Seinfeld, J. H. Global modeling of organic aerosol: the importance of reactive nitrogen (NO_x and NO_3). *Atmos. Chem. Phys.* **2010**, *10*, 11261−11276.

(6) Spracklen, D. V.; Jimenez, J. L.; Carslaw, K. S.; Worsnop, D. R.; Evans, M. J.; Mann, G. W.; Zhang, Q.; Canagaratna, M. R.; Allan, J.; Coe, H.; McFiggans, G.; Rap, A.; Forster, P. Aerosol mass spectrometer constraint on the global secondary organic aerosol budget. *Atmos. Chem. Phys.* **2011**, *11*, 12109−12136.

(7) Kanakidou, M.; et al. Organic aerosol and global climate modelling: a review. *Atmos. Chem. Phys.* **2005**, *5*, 1053−1123.

(8) Docherty, K. S.; Wu, W.; Lim, Y. B.; Ziemann, P. J. Contributions of organic peroxides to secondary aerosol formed from reactions of monoterpenes with O_3. *Environ. Sci. Technol.* **2005**, *39*, 4049−4059.

(9) Bonn, B.; von Kuhlmann, R.; Lawrence, M. G. High contribution of biogenic hydroperoxides to secondary organic aerosol formation. *Geophys. Res. Lett.* **2004**, *31*, L10108.

(10) Mutzel, A.; Rodigast, M.; Iinuma, Y.; Böge, O.; Herrmann, H. An improved method for the quantification of SOA bound peroxides. *Atmos. Environ.* **2013**, *67*, 365−369.

(11) Mertes, P.; Pfaffenberger, L.; Dommen, J.; Kalberer, M.; Baltensperger, U. Development of a sensitive long path absorption photometer to quantify peroxides in aerosol particles (Peroxide-LOPAP). *Atmos. Meas. Tech.* **2012**, *5*, 2339−2348.

(12) Krapf, M.; El Haddad, I.; Bruns, E. A.; Molteni, U.; Daellenbach, K. R.; Prévôt, A. S.; Baltensperger, U.; Dommen, J. Labile Peroxides in Secondary Organic Aerosol. *Chem.* **2016**, *1*, 603−616.

(13) Bloomfield, M. The spectrophotometric determination of hydroperoxide and peroxide in a lipid pharmaceutical product by flow injection analysis. *Analyst* **1999**, *124*, 1865−1871.

(14) Banerjee, D. K.; Budke, C. C. Spectrophotometric determination of traces of peroxides in organic solvents. *Anal. Chem.* **1964**, *36*, 792−796.

(15) Riva, M.; Budisulistiorini, S. H.; Zhang, Z.; Gold, A.; Thornton, J. A.; Turpin, B. J.; Surratt, J. D. Multiphase reactivity of gaseous hydroperoxide oligomers produced from isoprene ozonolysis in the presence of acidified aerosols. *Atmos. Environ.* **2017**, *152*, 314−322.

(16) Tong, H.; Arangio, A. M.; Lakey, P. S. J.; Berkemeier, T.; Liu, F.; Kampf, C. J.; Brune, W. H.; Pöschl, U.; Shiraiwa, M. Hydroxyl radicals from secondary organic aerosol decomposition in water. *Atmos. Chem. Phys.* **2016**, *16*, 1761−1771.

(17) Kristensen, K.; Watne, a. K.; Hammes, J.; Lutz, A.; Petäjä, T.; Hallquist, M.; Bilde, M.; Glasius, M. High-molecular weight dimer esters are major products in aerosols from α-pinene ozonolysis and the boreal forest. *Environ. Sci. Technol. Lett.* **2016**, *3*, 280−285.

(18) Kristensen, K.; Cui, T.; Zhang, H.; Gold, A.; Glasius, M.; Surratt, J. D. Dimers in α-pinene secondary organic aerosol: effect of hydroxyl radical, ozone, relative humidity and aerosol acidity. *Atmos. Chem. Phys.* **2014**, *14*, 4201−4218.

(19) Kristensen, K.; Enggrob, K. L.; King, S. M.; Worton, D. R.; Platt, S. M.; Mortensen, R.; Rosenoern, T.; Surratt, J. D.; Bilde, M.; Goldstein, A. H.; Glasius, M. Formation and occurrence of dimer esters of pinene oxidation products in atmospheric aerosols. *Atmos. Chem. Phys.* **2013**, *13*, 3763−3776.

(20) Yasmeen, F.; Vermeylen, R.; Szmigielski, R.; Iinuma, Y.; Böge, O.; Herrmann, H.; Maenhaut, W.; Claeys, M. Terpenylic acid and related compounds: precursors for dimers in secondary organic aerosol from the ozonolysis of α-and β-pinene. *Atmos. Chem. Phys.* **2010**, *10*, 9383−9392.

(21) Yasmeen, F.; Vermeylen, R.; Maurin, N.; Perraudin, E.; Doussin, J.-F.; Claeys, M. Characterisation of tracers for aging of α-pinene secondary organic aerosol using liquid chromatography/negative ion electrospray ionisation mass spectrometry. *Environ. Chem.* **2012**, *9*, 236−246.

(22) Zhang, X.; Dalleska, N. F.; Huang, D. D.; Bates, K. H.; Sorooshian, A.; Flagan, R. C.; Seinfeld, J. H. Time-resolved molecular characterization of organic aerosols by PILS+ UPLC/ESI-Q-TOFMS. *Atmos. Environ.* **2016**, *130*, 180−189.

(23) Zhang, X.; McVay, R. C.; Huang, D. D.; Dalleska, N. F.; Aumont, B.; Flagan, R. C.; Seinfeld, J. H. Formation and evolution of molecular products in α-pinene secondary organic aerosol. *Proc. Natl. Acad. Sci. U. S. A.* **2015**, *112*, 14168−14173.

(24) Witkowski, B.; Gierczak, T. Early stage composition of SOA produced by α-pinene/ozone reaction: α-Acyloxyhydroperoxy aldehydes and acidic dimers. *Atmos. Environ.* **2014**, *95*, 59−70.

(25) Hall, W. A., VI; Johnston, M. V. Oligomer content of α-pinene secondary organic aerosol. *Aerosol Sci. Technol.* **2011**, *45*, 37−45.

(26) Müller, L.; Reinnig, M.-C.; Warnke, J.; Hoffmann, T. Unambiguous identification of esters as oligomers in secondary organic aerosol formed from cyclohexene and cyclohexene/α-pinene ozonolysis. *Atmos. Chem. Phys.* **2008**, *8*, 1423−1433.

(27) Müller, L.; Reinnig, M.-C.; Hayen, H.; Hoffmann, T. Characterization of oligomeric compounds in secondary organic aerosol using liquid chromatography coupled to electrospray ionization Fourier transform ion cyclotron resonance mass spectrometry. *Rapid Commun. Mass Spectrom.* **2009**, *23*, 971−979.

(28) Kourtchev, I.; Doussin, J.-F.; Giorio, C.; Mahon, B.; Wilson, E. M.; Maurin, N.; Pangui, E.; Venables, D. S.; Wenger, J. C.; Kalberer, M. Molecular composition of fresh and aged secondary organic aerosol from a mixture of biogenic volatile compounds: a high-resolution mass spectrometry study. *Atmos. Chem. Phys.* **2015**, *15*, 5683−5695.

(29) Reinnig, M.-C.; Müller, L.; Warnke, J.; Hoffmann, T. Characterization of selected organic compound classes in secondary organic aerosol from biogenic VOCs by HPLC/MS^n. *Anal. Bioanal. Chem.* **2008**, *391*, 171−182.

(30) Mochida, M.; Katrib, Y.; Jayne, J. T.; Worsnop, D. R.; Martin, S. T. The relative importance of competing pathways for the formation of high-molecular-weight peroxides in the ozonolysis of organic aerosol particles. *Atmos. Chem. Phys.* **2006**, *6*, 4851−4866.

(31) Enami, S.; Colussi, A. J. Efficient scavenging of Criegee intermediates on water by surface-active cis-pinonic acid. *Phys. Chem. Chem. Phys.* **2017**, *19*, 17044−17051.

(32) Ehn, M.; Thornton, J. A.; Kleist, E.; Sipilä, M.; Junninen, H.; Pullinen, I.; Springer, M.; Rubach, F.; Tillmann, R.; Lee, B.; others.; et al. A large source of low-volatility secondary organic aerosol. *Nature* **2014**, *506*, 476−479.

(33) Crounse, J. D.; Nielsen, L. C.; Jørgensen, S.; Kjaergaard, H. G.; Wennberg, P. O. Autoxidation of organic compounds in the atmosphere. *J. Phys. Chem. Lett.* **2013**, *4*, 3513−3520.

(34) Mutzel, A.; Poulain, L.; Berndt, T.; Iinuma, Y.; Rodigast, M.; Böge, O.; Richters, S.; Spindler, G.; Sipilä, M.; Jokinen, T.; Kulmala, M.; Herrmann, H. Highly Oxidized Multifunctional Organic

Compounds Observed in Tropospheric Particles: A Field and Laboratory Study. *Environ. Sci. Technol.* **2015**, *49*, 7754−7761.

(35) Zhang, X.; et al. Highly oxygenated multifunctional compounds in α-pinene secondary organic aerosoll. *Environ. Sci. Technol.* **2017**, *51*, 5932−5940.

(36) Lee, B. H.; et al. Highly functionalized organic nitrates in the southeast United States: Contribution to secondary organic aerosol and reactive nitrogen budgets. *Proc. Natl. Acad. Sci. U. S. A.* **2016**, *113*, 1516−1521.

(37) Tu, P.; Hall, W. A.; Johnston, M. V. Characterization of highly oxidized molecules in fresh and aged biogenic secondary organic aerosol. *Anal. Chem.* **2016**, *88*, 4495−4501.

(38) Oss, M.; Kruve, A.; Herodes, K.; Leito, I. Electrospray ionization efficiency scale of organic compounds. *Anal. Chem.* **2010**, *82*, 2865−2872.

(39) Cech, N. B.; Enke, C. G. Practical implications of some recent studies in electrospray ionization fundamentals. *Mass Spectrom. Rev.* **2001**, *20*, 362−387.

(40) Steimer, S. S.; Kourtchev, I.; Kalberer, M. Mass spectrometry characterization of peroxycarboxylic acids as proxies for reactive oxygen species and highly oxygenated molecules in atmospheric aerosols. *Anal. Chem.* **2017**, *89*, 2873−2879.

(41) Ferdousi, B. N.; Islam, M. M.; Okajima, T.; Ohsaka, T. Electrochemical, HPLC and electrospray ionization mass spectroscopic analyses of peroxycitric acid coexisting with citric acid and hydrogen peroxide in aqueous solution. *Talanta* **2008**, *74*, 1355−1362.

(42) Nilsson, J.; Carlberg, J.; Abrahamsson, P.; Hulthe, G.; Persson, B.-A.; Karlberg, A.-T. Evaluation of ionization techniques for mass spectrometric detection of contact allergenic hydroperoxides formed by autoxidation of fragrance terpenes. *Rapid Commun. Mass Spectrom.* **2008**, *22*, 3593−3598.

(43) Yin, H.; Hachey, D. L.; Porter, N. A. Structural analysis of diacyl peroxides by electrospray tandem mass spectrometry with ammonium acetate: bond homolysis of peroxide-ammonium and peroxide-proton adducts. *Rapid Commun. Mass Spectrom.* **2000**, *14*, 1248−1254.

(44) Witkowski, B.; Gierczak, T. Analysis of α-acyloxyhydroperoxy aldehydes with electrospray ionization-tandem mass spectrometry (ESI-MS(n)). *J. Mass Spectrom.* **2013**, *48*, 79−88.

(45) Weber, R. J.; Orsini, D.; Daun, Y.; Lee, Y.-N.; Klotz, P. J.; Brechtel, F. A particle-into-liquid collector for rapid measurement of aerosol bulk chemical composition. *Aerosol Sci. Technol.* **2001**, *35*, 718−727.

(46) Kondo, Y.; Miyazaki, Y.; Takegawa, N.; Miyakawa, T.; Weber, R. J.; Jimenez, J. L.; Zhang, Q.; Worsnop, D. R. Oxygenated and water-soluble organic aerosols in Tokyo. *J. Geophys. Res.* **2007**, *112*, D01203 DOI: 10.1029/2006JD007056.

(47) Lee, A. K. Y.; Hayden, K. L.; Herckes, P.; Leaitch, W. R.; Liggio, J.; Macdonald, A. M.; Abbatt, J. P. D. Characterization of aerosol and cloud water at a mountain site during WACS 2010: secondary organic aerosol formation through oxidative cloud processing. *Atmos. Chem. Phys.* **2012**, *12*, 7103−7116.

(48) Herckes, P.; Valsaraj, K. T.; Collett, J. L., Jr A review of observations of organic matter in fogs and clouds: Origin, processing and fate. *Atmos. Res.* **2013**, *132−133*, 434−449.

(49) Blando, J. D.; Turpin, B. J. Secondary organic aerosol formation in cloud and fog droplets: a literature evaluation of plausibility. *Atmos. Environ.* **2000**, *34*, 1623−1632.

(50) Huang, Y.; Coggon, M. M.; Zhao, R.; Lignell, H.; Bauer, M. U.; Flagan, R. C.; Seinfeld, J. H. The Caltech Photooxidation Flow Tube reactor: design, fluid dynamics and characterization. *Atmos. Meas. Tech.* **2017**, *10*, 839−867.

(51) Epstein, S. A.; Blair, S. L.; Nizkorodov, S. A. Direct photolysis of α-pinene ozonolysis secondary organic aerosol: effect on particle mass and peroxide content. *Environ. Sci. Technol.* **2014**, *48*, 11251−11258.

(52) Li, H.; Chen, Z.; Huang, L.; Huang, D. Organic peroxides' gas-particle partitioning and rapid heterogeneous decomposition on secondary organic aerosol. *Atmos. Chem. Phys.* **2016**, *16*, 1837−1848.

(53) Badali, K. M.; Zhou, S.; Aljawhary, D.; Antiñolo, M.; Chen, W. J.; Lok, A.; Mungall, E.; Wong, J. P. S.; Zhao, R.; Abbatt, J. P. D.

Formation of hydroxyl radicals from photolysis of secondary organic aerosol material. *Atmos. Chem. Phys.* **2015**, *15*, 7831−7840.

(54) Chen, X.; Hopke, P. K. Secondary organic aerosol from α-pinene ozonolysis in dynamic chamber system. *Indoor Air* **2009**, *19*, 335−345.

(55) Wang, Y.; Kim, H.; Paulson, S. E. Hydrogen peroxide generation from α- and β-pinene and toluene secondary organic aerosols. *Atmos. Environ.* **2011**, *45*, 3149−3156.

(56) Gao, Y.; Hall, W. H.; Johnston, M. Molecular composition of monoterpene secondary organic aerosol at low mass loading. *Environ. Sci. Technol.* **2010**, *44*, 7897−7902.

(57) Aljawhary, D.; Lee, A. K. Y.; Abbatt, J. P. D. High-resolution chemical ionization mass spectrometry (ToF-CIMS): application to study SOA composition and processing. *Atmos. Meas. Tech.* **2013**, *6*, 3211−3224.

(58) Zhao, R.; Aljawhary, D.; Lee, A. K. Y.; Abbatt, J. P. D. Rapid aqueous-phase photooxidation of dimers in the α-pinene secondary organic aerosol. *Environ. Sci. Technol. Lett.* **2017**, *4*, 205−210.

(59) Venkatachari, P.; Hopke, P. K. Characterization of products formed in the reaction of ozone with α-pinene: case for organic peroxides. *J. Environ. Monit.* **2008**, *10*, 966−974.

(60) Szmigielski, R.; Surratt, J. D.; Gómez-González, Y.; Van der Veken, P.; Kourtchev, I.; Vermeylen, R.; Blockhuys, F.; Jaoui, M.; Kleindienst, T. E.; Lewandowski, M.; Offenberg, J. H.; Edney, E. O.; Seinfeld, J. H.; Maenhaut, W.; Claeys, M. 3-methyl-1,2,3-butane-tricarboxylic acid: An atmospheric tracer for terpene secondary organic aerosol. *Geophys. Res. Lett.* **2007**, *34*, L24811.

(61) Müller, L.; Reinnig, M.-C.; Naumann, K. H.; Saathoff, H.; Mentel, T. F.; Donahue, N. M.; Hoffmann, T. Formation of 3-methyl-1,2,3-butanetricarboxylic acid via gas phase oxidation of pinonic acid - a mass spectrometric study of SOA aging. *Atmos. Chem. Phys.* **2012**, *12*, 1483−1496.

(62) Aljawhary, D.; Zhao, R.; Lee, A. K.; Wang, C.; Abbatt, J. P. Kinetics, mechanism and secondary organic aerosol yield of aqueous phase photo-oxidation of α-pinene oxidation products. *J. Phys. Chem. A* **2016**, *120*, 1395−1407.

(63) Gao, S.; Keywood, M.; Ng, N. L.; Surratt, J.; Varutbangkul, V.; Bahreini, R.; Flagan, R. C.; Seinfeld, J. H. Low-molecular-weight and oligomeric components in secondary organic aerosol from the ozonolysis of cycloalkenes and α-pinene. *J. Phys. Chem. A* **2004**, *108*, 10147−10164.

(64) Jenkin, M. E. Modelling the formation and composition of secondary organic aerosol from α- and β-pinene ozonolysis using MCM v3. *Atmos. Chem. Phys.* **2004**, *4*, 1741−1757.

(65) Arellanes, C.; Paulson, S. E.; Fine, P. M.; Sioutas, C. Exceeding of Henry's law by hydrogen peroxide associated with urban aerosols. *Environ. Sci. Technol.* **2006**, *40*, 4859−4866.

A p p e n d i x   B

RAPID AQUEOUS-PHASE HYDROLYSIS OF ESTER HYDROPEROXIDES ARISING FROM CRIEGEE INTERMEDIATES AND ORGANIC ACIDS

Rapid Aqueous-Phase Hydrolysis of Ester Hydroperoxides Arising from Criegee Intermediates and Organic Acids

Ran Zhao,*,†,‡ Christopher M. Kenseth,† Yuanlong Huang,¶ Nathan F. Dalleska,§ Xiaobi M. Kuang,‖ Jierou Chen,‖ Suzanne E. Paulson,‖ and John H. Seinfeld†,⊥

†Devision of Chemistry and Chemical Engineering, California Institute of Technology, Pasadena, California 91125, United States

¶Division of Geological and Planetary Sciences, California Institute of Technology, Pasadena, California 91125, United States

§Environmental Analysis Center, California Institute of Technology, Pasadena, California 91125, United States

‖Department of Atmospheric and Oceanic Sciences, University of California—Los Angeles, Los Angeles, California 90095, United States

⊥Division of Engineering and Applied Science, California Institute of Technology, Pasadena, California 91125, United States

ABSTRACT: Stabilized Criegee intermediates react with organic acids in the gas phase and at the air–water interface to form a class of ester hydroperoxides, α-acyloxyalkyl hydroperoxides (αAAHPs). A number of recent studies have proposed the importance of αAAHPs to the formation and growth of secondary organic aerosol (SOA). The chemistry of αAAHPs has not been investigated due to a lack of commercially available chemical standards. In this work, the behavior of αAAHPs in condensed phases is investigated for the first time. Experiments were performed with two synthesized αAAHP species. αAAHPs decomposed rapidly in the aqueous phase, with the rate highly dependent on the solvent, temperature, solution pH, and other compounds present in the solution. The measured 1st-order decomposition rate coefficient varied between 10^{-3} and 10^{-5} s^{-1} under the conditions examined in this work. Elucidation of the reaction mechanism is complicated by byproducts arising from the synthetic procedure, but observations are consistent with a base-catalyzed hydrolysis of αAAHPs. The rapid hydrolysis of αAAHPs observed in this work implies their short lifetimes in ambient cloud and fog waters. Decomposition of αAAHPs likely gives rise to smaller peroxides, such as H_2O_2. The loss of αAAHPs is also relevant to filter extraction, which is commonly practiced in laboratory experiments, potentially explaining contradictory results reported in the existing literature regarding the importance of αAAHPs in SOA.
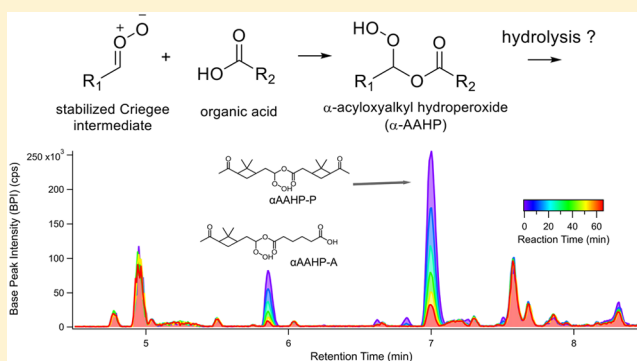
INTRODUCTION

Alkenes (e.g., isoprene and monoterpenes) comprise over half of the total volatile organic compounds (VOCs) emitted to Earth's atmosphere.[1] Owing to the reactivity of the C=C bond toward O_3, ozonolysis is a major sink of alkenes. Ozonolysis converts alkenes into oxygenated products that exhibit lower vapor pressures and contribute to the formation of secondary organic aerosol (SOA), a class of suspended organic particulate matter that affects air quality and global climate.[2] As shown in the generalized reaction scheme of alkene ozonolysis (Figure 1), O_3 first adds across the C=C bond, giving rise to a primary ozonide, which decomposes to a carbonyl compound and an excited carbonyl oxide referred to as the Criegee intermediate.[3] The Criegee intermediate is presented as a zwitterion in Figure 1, as it is the most stable configuration,[4] but it is also commonly referred to as a biradical in the literature. The Criegee intermediate can either undergo unimolecular decomposition or be stabilized upon collision with air (i.e., N_2 and O_2). The stabilized Criegee intermediate (SCI) can react bimolecularly with a wide spectrum of molecules collectively known as Criegee scavengers, among which organic acids are particularly efficient.[4,5] The reaction between the C_1 SCI and formic acid proceeds nearly at the collision limit,[6] with a rate coefficient larger than that of SCI + H_2O by 3 to 4 orders of magnitude.[7−9] The product arising from the SCI + organic acid reaction is an ester hydroperoxide, α-acyloxyalkyl hydroperoxide (αAAHP, Figure 1).[10] A number of studies have proposed that αAAHPs can contribute to SOA mass due to their low volatility, and alternatively, they can react further with another SCI to form compounds with even lower volatilities.[6,11]

Monoterpenes comprise a major fraction of global biogenic VOC emissions,[1] and the reaction products of monoterpene SCIs are of great importance to atmospheric chemistry. Recent studies have observed high molecular weight αAAHPs that are
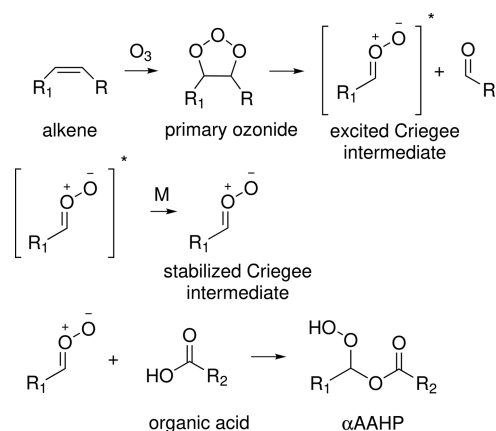
Figure 1. Schematic of the general atmospheric formation mechanism of α-acyloxyalkyl hydroperoxide (αAAHP).

likely attributable to the gas-phase reaction of monoterpene SCIs with organic acids.[12−15] Kristensen et al.[14] have proposed that αAAHPs are a major fraction of monoterpene SOA. The reaction of monoterpene SCIs with organic acids can also occur at the air−water interface, such as the surface of cloud droplets and aqueous aerosol. In particular, computational studies have shown that SCIs with hydrophobic substituents are relatively unreactive with water, allowing for reaction with other species, such as acids.[16−18] Recent experimental studies have provided supporting observations, showing that SCIs from monoterpenes and sesquiterpenes give rise to αAAHPs at the air−water interface.[19,20] While these studies suggest the importance of αAAHPs arising from monoterpenes, contradictory results have also been reported. A few studies have found that αAAHPs comprised only a minor fraction of α-pinene SOA extracted in organic or aqueous solvents.[21,22] Such contradictory results reflect the fact that the chemistry of αAAHPs has not been

investigated in a systematic manner. Unrecognized reactions of αAAHPs are likely occurring in SOA and/or after sample collection.

Multifunctional organic peroxides, such as αAAHPs, comprise a highly complex, unresolved fraction of SOA. These organic peroxide species serve as reservoirs of important oxidants (e.g., the OH radical) and represent a class of reactive oxygen species (ROS), which are linked to adverse health effects of airborne particulate matter.[23,24] Despite their environmental significance, the chemistry of such multifunctional organic peroxides is poorly understood due to their complexity, lack of commercially available standards, and chemical instability. In particular, recent studies have demonstrated the labile nature of particle-bound organic peroxides.[25−27] Other studies have observed formation of H_2O_2 and the OH radical from the water extract of SOA, implying decomposition of larger organic peroxides.[28−30] In this work, two αAAHP species arising from the α-pinene SCIs are synthesized, and their condensed-phase chemistry is investigated for the first time. A specific objective is to understand the behavior of αAAHPs in the aqueous phase, which reflects their fate in cloudwater, aqueous aerosol, and aqueous solvents after extraction. We also attempt to determine the reaction mechanism of the decomposition of αAAHPs, with a particular interest in the extent to which they produce H_2O_2.

■ EXPERIMENTAL SECTION

Liquid Chromatography Electrospray Ionization Mass Spectrometry (LC-ESI-MS). An LC-ESI-MS technique is used here as the primary analytical method to characterize the synthesized αAAHPs and to monitor their decomposition. The same technique has been employed in a number of our previous studies.[21,31,32] A Waters ACQUITY UPLC I-Class system was coupled to a quadrupole time-of-flight MS (Xevo G2-S QToF). LC separation was performed on an AQUITY
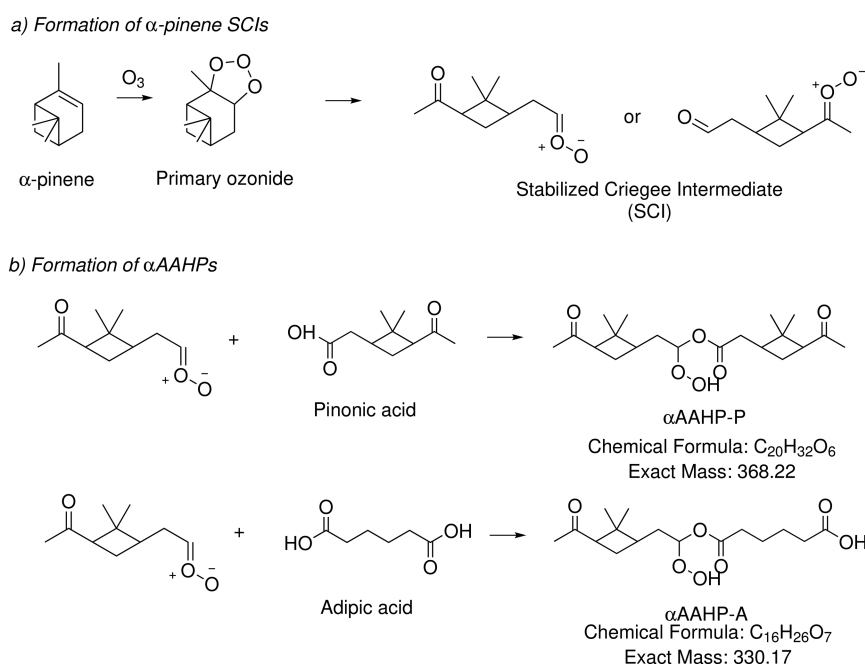
Figure 2. Synthetic pathways and possible structures of αAAHP-P and αAAHP-A. Simplified schematics for (a) the formation of α-pinene SCIs and (b) the formation of αAAHPs are shown. Ozonolysis of α-pinene gives rise to two possible SCIs, which subsequently form two αAAHP structural isomers upon reaction with an organic acid. For simplicity, only the αAAHPs arising from one SCI are shown in part b.

BEH C_{18} column (1.7 μm, 2.1 × 50 mm), with the column temperature controlled at 30 °C. The injection volume was set at 10 μL, and the flow rate was 0.3 mL min^{-1}. The mobile phase gradient and ESI settings in this study are identical to those in Zhao et al.[21] and will not be discussed with further details here. Leucine enkephalin was employed as the lock mass for accurate mass determination. LC-ESI-MS was operated in both the positive (ESI(+)) and the negative (ESI(−)) modes. Generally, ESI(+) detects oxygenated compounds as ion clusters with Na$^+$, NH$_4^+$, or K$^+$, while ESI(−) detects compounds containing acidic protons in their deprotonated forms (i.e., as [M − H]$^-$). In this study, the instrument was operated primarily with ESI(+) as it detects both of the synthesized αAAHPs. ESI(−) was also employed to characterize αAAHPs and to elucidate the reaction mechanisms. Data were acquired and processed with MassLynx v.4.1 software. The reproducibility in the detected peak areas is within 5%, as determined by frequent consistency tests.

Synthesis of αAAHPs. Unless noted otherwise, all chemicals were purchased from Sigma-Aldrich without further purification. The synthetic procedure, adapted and modified from that of Witkowski and Gierczak,[33] is based on a liquid-phase ozonolysis of α-pinene. The SCIs generated from liquid-phase ozonolysis are forced to form αAAHPs in the presence of an excess amount of an organic acid. The chemical mechanisms behind the synthesis are shown in Figure 2. The synthetic procedure has been described elsewhere.[21] Briefly, α-pinene (50 mM) and an individual organic acid (10 mM) were dissolved in acetonitrile (EMD Millipore). A gentle stream of air (120 sccm) containing approximately 100 ppm of O$_3$ (generated from a custom-built O$_3$ generator) was bubbled through the acetonitrile solution. Synthesis of αAAHPs was carried out in an ice bath, and the solutions were stored in a freezer maintained at −16 °C. Two organic acids were selected to synthesize two different αAAHPs. Pinonic acid was selected for its relevance to monoterpene oxidation and its reactivity with SCIs.[14,19] Adipic acid was selected as representative of diacids. The two synthesized αAAHPs are herein referred to as αAAHP-P, and αAAHP-A, respectively (Figure 2). A synthetic control was also prepared by following the same synthetic procedures, except that no organic acid was added to force the formation of αAAHPs. The synthesized αAAHPs were not further purified due to their chemical instability; therefore, the solutions likely contain byproducts of liquid-phase α-pinene ozonolysis, e.g., through acid-catalyzed tautomerization of SCIs.[34]

Characterization of the Synthesized αAAHPs. The identity of the synthesized αAAHPs was first confirmed with the LC-ESI-MS technique. The synthetic control, αAAHP-A, and αAAHP-P were individually diluted by a factor of 50 to water acidified to pH 2 with H$_2$SO$_4$. The purpose of adding H$_2$SO$_4$ was to minimize decomposition of αAAHPs, which simplifies their characterization. As will be demonstrated in Results and Discussion, the decomposition of αAAHPs is found to be slow under acidic conditions. The diluted solutions were measured with LC-ESI-MS with both ESI(−) and ESI(+).

Iodometry was employed to confirm the peroxide functionality of αAAHPs. Iodometry is a method that selectively reduces organic peroxides into the corresponding alcohols.[35,36] It has been traditionally employed with UV−vis spectrometry to quantify the total peroxide content in a sample.[37,38] Our previous work has established a method to couple iodometry to LC-ESI-MS for a molecular-level analysis of organic peroxide;

this method has been named iodometry-assisted LC-ESI-MS.[21] In the present work, both of the synthesized αAAHPs were first mixed and diluted by a factor of 50 in an aqueous solution, preacidified to pH 2 with H$_2$SO$_4$. In this case, acidifying the solution supplies the acid needed for iodometry. The solution was then divided into two aliquots. Potassium iodide (KI, 60 mM) was added to one aliquot to initiate iodometry, while no KI was added to the other aliquot as a control. Both aliquots were kept in the dark at room temperature. LC-ESI-MS measurement with ESI(+) was performed approximately 30 min after the addition of KI.

Hydrolysis of αAAHPs in Condensed Phases. The two αAAHPs were mixed and diluted simultaneously by a factor of 50 in an aqueous solution contained in a plastic LC-ESI-MS sample vial. The emphasis of the current work was placed on hydrolysis in the aqueous phase, but experiments were also performed in methanol and acetonitrile to explore the solvent effects. The sample vial was placed in a temperature-controlled sample holder, and the αAAHP signals were tracked over time using LC-ESI-MS. The temperature in the sample holder was adjusted to 7, 15, 25, and 35 °C to explore the temperature effect. The sample vials and aqueous solutions were preconditioned at the set temperatures before αAAHPs were added. The pH of the αAAHP solution at the default dilution ratio was 4.4 (monitored with a Thermo Scientific pH meter). Its acidity is likely due to the presence of residual pinonic acid and adipic acid used in the synthesis. To investigate the effect of solution pH on the decomposition of αAAHPs, experiments were also conducted in solutions with pH values either adjusted with H$_2$SO$_4$/NaOH or buffered with potassium hydrogen phthalate (KHP) (Baker Chemical Co.).

In the ambient atmosphere, αAAHPs are likely present in aqueous phases with highly complex chemical compositions, including numerous organic and inorganic compounds. To account for any matrix effect, we have also performed αAAHP hydrolysis experiments in an aqueous extract of SOA, generated from the reaction of O$_3$ and α-pinene in the Caltech PhotoOxidation flow Tube (CPOT) reactor.[39] The details of SOA generation, extraction, and characterization are provided in our previous work.[21] Briefly, α-pinene (175 ppb) and O$_3$ (1 ppm) were mixed in the CPOT in the absence of light, NO$_x$, and OH scavengers. The experiments were performed at room temperature and under dry conditions (RH < 10%). The average residence time in the CPOT was 3.5 min. Ammonium sulfate ((NH$_4$)$_2$SO$_4$) (Mallinckrodt Chemicals) seed aerosol was injected to assist formation of SOA and to minimize vapor-wall interactions. SOA generated in the CPOT was collected on a Teflon filter over 16 h. The filter was extracted to water by being mechanically shaken for 10 min, immediately before the hydrolysis experiments.

The pH of the SOA extract with diluted αAAHPs was measured to be 4.2. The (NH$_4$)$_2$SO$_4$ concentration, arising from the (NH$_4$)$_2$SO$_4$ seed aerosol, was approximately 200 μM, semiquantitatively determined by comparing the peak area of HSO$_4^-$ observed by LC-ESI-MS to those from standard solutions of (NH$_4$)$_2$SO$_4$. The total organic carbon (TOC) in the water extract of SOA was measured to be 31 ppm carbon (ppmC) using a TOC analyzer (OI Analytical, Aurora model 1030w). The accuracy of the TOC instrument was within 5%.

High Performance Liquid Chromatography with Fluorescence Detection (HPLC-Fluorescence). The formation of H$_2$O$_2$ from αAAHPs was monitored with a HPLC-fluorescence instrument (Shimadzu RF-10AXL) located at the
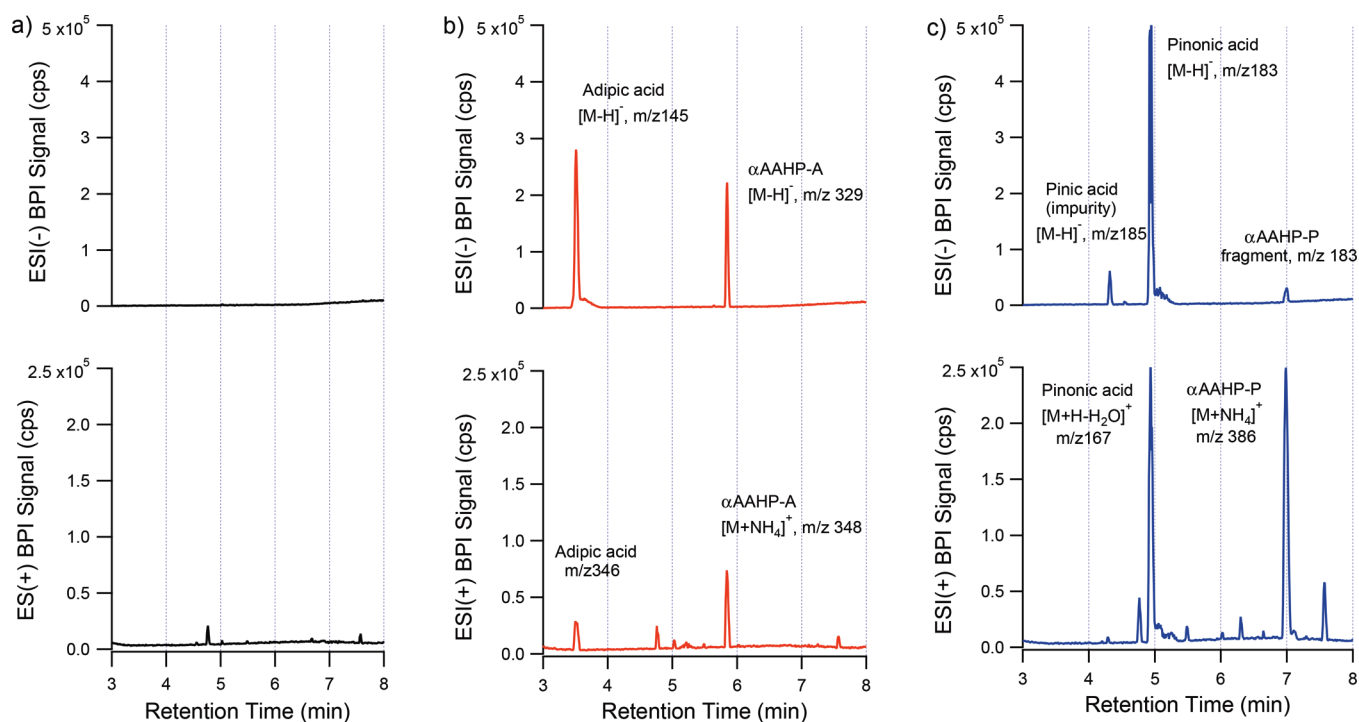
Figure 3. LC-ESI-MS BPI chromatograms of (a) the synthetic control, (b) αAAHP-A, and (c) αAAHP-P. The top panels show the results obtained with ESI(−) and the bottom panels show those obtained with ESI(+).

University of California—Los Angeles.[30,40−43] The technique is based on an LC separation of H_2O_2 and organic peroxides on a C_{18} reversed-phase column (GL Science Inc., 5 μm, 4.6 × 250 mm), followed by a postcolumn addition of a fluorescent reagent consisted of horseradish peroxidase (HRP) and p-hydroxyphenyl acetic acid (PHOPAA). With the catalytic assistance of HRP, PHOPAA selectively reacts with H_2O_2 and organic peroxides to form a fluorescent dimer, which was detected with a fluorescent detector. The excitation and emission wavelengths were set at 320 and 400 nm, respectively. The LC separation is based on an isocratic method with a 100% aqueous mobile phase containing 1 mM of H_2SO_4 (Fisher, 0.1 N, reagent grade) and 0.1 mM of ethylenediaminetetraacetic acid (EDTA) at a total flow rate of 0.6 mL min^{-1}. The length of the LC method was 10 min. The current LC method is optimized for the detection of H_2O_2 and polar organic peroxides. A pulse of acetonitrile (200 μL) was injected 3 min after the sample injection to facilitate the elution of less polar organic peroxides. The synthesized αAAHPs did not elute from the column and were not detected.

For the hydrolysis experiments, αAAHP-A or αAAHP-P was diluted by a factor of 250 in water and stored in the dark at room temperature. Aliquots (20 μL) of the experimental solution were injected into the HPLC-fluorescence instrument to monitor the formation of H_2O_2. The method was calibrated against standard H_2O_2 solutions, produced by diluting a commercial H_2O_2 solution (50% in water). The detection limit of the method was 10 nM. We have also performed control experiments in which the synthesized αAAHPs were diluted to the same ratio but in acetonitrile instead of water.

RESULTS AND DISCUSSION

Characterization of the Synthesized αAAHPs. Figure 3 shows the base peak intensity (BPI) chromatograms of the synthetic control, αAAHP-A, and αAAHP-P obtained with LC-

ESI-MS. BPI chromatograms display the most intense peak at each given retention time (RT). Neither ESI(−) nor ESI(+) has detected any major compounds in the synthetic control (Figure 3a). αAAHPs are detected by both ESI(−) and ESI(+) (Figure 3, parts b and c), and the agreement between the detected and exact masses (Figure 2) is within ±10 ppm.

αAAHP-A emerges at RT = 5.8 min and is detected as [M − H]$^-$ (m/z 329) and [2M − H]$^-$ (m/z 659) by ESI(−). Along with αAAHP-A, residual adipic acid was also detected by ESI(−) at RT = 3.4 min, primarily as [M − H]$^-$ (m/z 145). ESI(+) detects αAAHP-A primarily as [M + NH$_4$]$^+$ (m/z 348), but also as [M + Na]$^+$ (m/z 353) and [M + K]$^+$ (m/z 369). Small organic acids, such as adipic acid, are not efficiently detected as [M + Na]$^+$ or [M + NH$_4$]$^+$. In fact, adipic acid is detected by ESI(+) primarily at m/z 346, which corresponds to a complex with iron ([Fe^{3+}·(M$^-$)$_2$]$^-$). Iron is likely present at the ESI source or the injection system. We have confirmed that the isotope profile of this peak agrees with that of iron and that the peak area of m/z 346 is proportional to the adipic acid concentration. αAAHP-P (RT = 7 min) does not have any carboxylic groups and is not detected as [M − H]$^-$ by ESI(−), but instead as a fragment at m/z 183. The precursor of αAAHP-P, pinonic acid, is detected primarily as [M − H]$^-$ (m/z 183) by ESI(−) at RT = 4.9 min. Similar to the case of αAAHP-A, αAAHP-P is detected by ESI(+) primarily as [M + NH$_4$]$^+$ (m/z 386), but also as [M + Na]$^+$ (m/z 391) and [M + K]$^+$ (m/z 407). ESI(+) detects pinonic acid primarily in a dehydrated form, [M + H − H$_2$O]$^+$ (m/z 167), but also as the iron complex ([Fe^{3+}·(M$^-$)$_2$]$^-$) at m/z 422, similar to the case of adipic acid. Besides the peaks of αAAHPs and their precursor organic acids, ESI(+) has detected a number of minor peaks likely attributable to byproducts arising from the current synthetic procedure. These byproducts do not contain acidic functionalities, as they are not detected by ESI(−).

Figure 4 compares the ESI(+) BPI chromatograms of a mixture of the two αAAHPs treated with and without
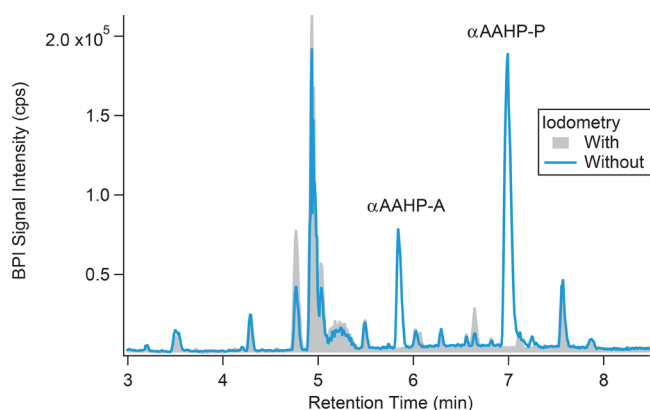
Figure 4. Characterization of the synthesized αAAHPs with iodometry-assisted LC-ESI-MS. ESI(+) BPI chromatograms of an aqueous solution treated with and without iodometry are compared.

iodometry. The only major difference between the two BPI chromatograms is a complete attenuation of αAAHP peaks, confirming that they are organic peroxides. Iodometry induced negligible effects on the peaks of synthetic byproducts, indicating that most of these byproducts are nonperoxide species.

Overall, it is confirmed that the synthesized αAAHPs are organic peroxides with the accurate masses and elemental compositions shown in Figure 2. However, we cannot distinguish structural isomers of αAAHPs with the current techniques. As shown in Figure 2a, α-pinene gives rise to two different SCIs, each leading to a distinct αAAHP structural isomer upon reaction with pinonic acid or adipic acid. The characterization also reveals that the αAAHP solutions contain numerous synthetic byproducts. The dominant byproducts are the residual precursor organic acids: adipic acid and pinonic acid. Their concentrations are determined to be approximately 200 μM in the synthetic solution diluted by a factor of 50. Although the majority of byproducts detected by LC-ESI-MS are nonperoxide species, there are likely undetected peroxide

species. As will be discussed shortly, the HPLC-fluorescent technique detected a high initial background of H_2O_2, which is too polar to be retained by the LC method used in LC-ESI-MS. The presence of byproducts does not significantly affect the kinetic investigation of αAAHP decomposition but complicates the interpretation of the reaction mechanisms and will be discussed.

Decay of αAAHPs Signals in Condensed Phases. Figure 5 shows the ESI(+) BPI chromatograms recorded during an example experiment conducted in the aqueous phase at 25 °C with uncontrolled pH (4.4). The chromatograms are color-coded by the time at which each sample is injected to LC-ESI-MS, with that of the first sample defined as time 0. Both of the αAAHP species exhibit rapid decay, while the intensities of other nonperoxide peaks exhibit minimal changes during 1 h of reaction time. The inset of Figure 5 shows the 1st-order kinetic plots of the two αAAHPs recorded for the same experiment. The linearity of the plots indicates that the reaction is first-order. As discussed in the previous section, αAAHPs are detected by ESI(+) in multiple forms, including $[M + NH_4]^+$, $[M + Na]^+$, and $[M + K]^+$. Each of these three peaks exhibits decay at a very similar rate, and so only the dominant peak $[M + NH_4]^+$ is used for the kinetic analysis. We also conducted an experiment with pimelic acid added to the solution as an internal standard and monitored the signals of αAAHP-A and pimelic acid using ESI(−). The αAAHP-A decay rates with and without the internal standard differed by 8%, which is within the experimental uncertainties; the relative standard deviation of the hydrolysis rate at 25 °C is approximately 15%. As such, all the results discussed here are from experiments without an internal standard.

The effect of solvent on the decay rate of αAAHPs was investigated by performing the experiment at the same dilution ratio and temperature (25 °C), but in methanol and acetonitrile, which are the most commonly employed solvents for filter extraction and analysis. The decay profiles of αAAHP-P in the three solvents are shown in Figure 6. The decay rates of αAAHPs increase in the order of acetonitrile < methanol < water. The results for αAAHP-A exhibit the same trend and are not shown. The 1st-order decay rate coefficients (k^I) of αAAHPs and their corresponding e-folding lifetimes (τ_{avg}) in the three solvents are summarized in Table 1. The trend that
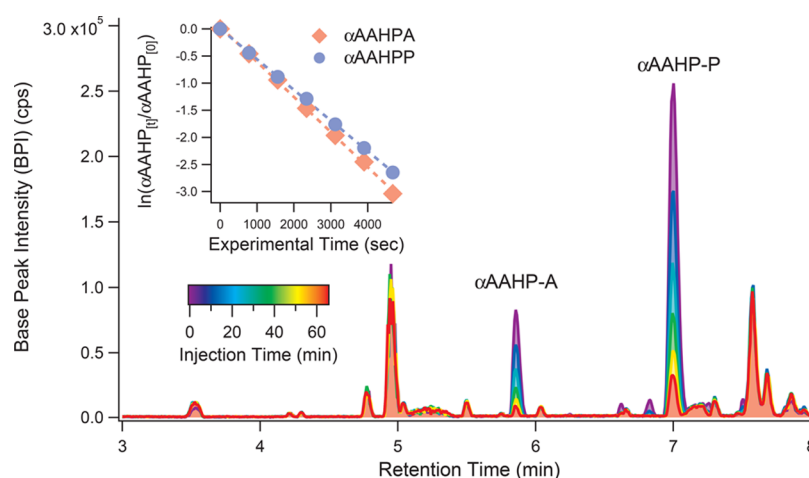
Figure 5. ESI(+) BPI chromatograms recorded in an example experiment at 25 °C with uncontrolled pH (4.4). Chromatograms are color-coded by the time each sample is injected to LC-ESI-MS. Time at which the first sample is injected is defined as time 0. The inset presents the 1st-order kinetic plots of the αAAHPs signal from the same experiment.
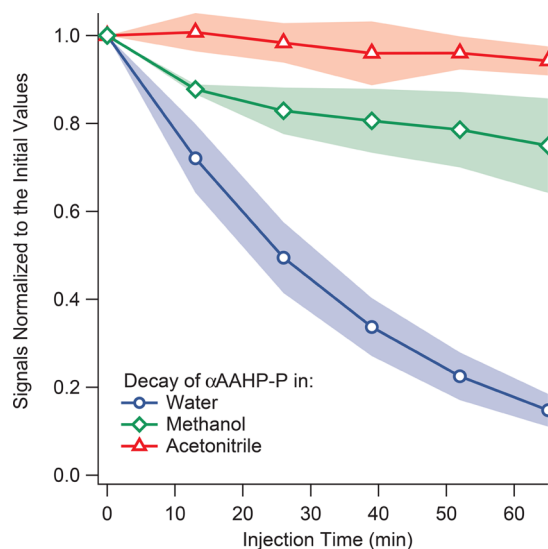
Figure 6. Decay of αAAHP-P in acetonitrile, methanol, and water. Experiments were performed at 25 °C with uncontrolled solution pH. The results represent the average of three replicates, with the error shading indicating one standard deviation.

αAAHPs are more reactive in polar and protic solvents is consistent with hydrolysis. We also note that when αAAHPs are stored in acetonitrile in a freezer maintained at −16 °C, their signals exhibit a slow decay of approximately 25% over the course of two weeks, indicating that they are highly stable under this condition.

Temperature Effects. The decomposition rates of αAAHPs appear to be highly temperature-dependent. The temperature dependences of the two αAAHPs are shown in Figure 7a, in the format of an Arrhenius plot (i.e., $\ln(k^I)$ vs $1/T$). The k^I and τ_{avg} values at each temperature are summarized in Table 1. Decomposition of both αAAHPs is accelerated at higher temperatures, with their τ_{avg} values decreasing by roughly an order of magnitude from 7 to 35 °C. The slope of the Arrhenius plot is equivalent to $-E_a/R$, where E_a is the activation energy, and R is the gas constant. In this manner, the E_a values for αAAHP-A and αAAHP-P are obtained to be 62.6 ± 4.2 and 60.7 ± 6.7 kJ mol^{-1}, respectively. The uncertainty is obtained from that of the slope. These E_a values are comparable to but larger than those of simple alkyl esters, indicating that hydrolysis of αAAHPs is more sensitive to temperature than that of simple alkyl esters. For instance, E_a values for ethyl formate and diethyl ester are 37.4 and 44.9 kJ mol^{-1}, respectively.[44]

Effects of Solution pH. The effect of solution pH on the decomposition rate of αAAHPs is shown in Figure 7b. All of these experiments were performed at 25 °C. Decomposition of αAAHPs is highly pH dependent, proceeding more rapidly in basic solutions. The solid markers on Figure 7b represent those experiments in which the solution pH was adjusted with either H$_2$SO$_4$ or NaOH. These $\log_{10}(k^I)$ values exhibit a linear relationship with solution pH, indicating that the rate coefficients are proportional to the concentration of OH$^-$ from pH 3.5 to 5.1. This is within the typical pH range for ambient cloud and fog waters.[45] The highest solution pH examined here is 5.1, as we found that the decomposition rate was too fast to be quantified by the current LC-ESI-MS method at higher pH values.

If organic acids are generated during decomposition of αAAHPs, the solution pH can be potentially altered during the course of an experiment. To account for this possibility, we also performed experiments in buffered solutions, and the results are shown in Figure 7b. The pH-dependence is similar in buffered and pH-adjusted solutions, indicated by the identical slopes between the two data series. However, the data of the buffered solutions is shifted up from those of the pH-adjusted solution, indicating more rapid decomposition of αAAHPs in buffers.

Matrix Effect. The faster decay of αAAHPs in buffers is likely the result of a matrix effect, which has also been observed in hydrolysis of other organic compounds.[44] The buffer solutions employed in the current work are generated by mixing KHP and NaOH. The KHP concentration ranges from 0.07 M (pH 5.0 buffer) and 0.1 M (pH 4.1 buffer), and that of NaOH ranges between 0.002 M (pH 5.0 buffer) and 0.03 M (pH 4.1 buffer). To explore the potential effect of Na$^+$ on hydrolysis of αAAHP, we performed a separate control experiment in which the decomposition of αAAHPs was monitored in an aqueous solution containing 0.015 M of Na$_2$SO$_4$. This experiment confirmed that Na$^+$ and SO$_4^{2-}$ at this concentration do not accelerate the decomposition of αAAHPs. As such, KHP present in the buffers is likely responsible. Although KHP at the mM-level concentration is not atmospherically relevant, the fact that KHP accelerated αAAHP decomposition suggests that dissolved organic compounds in cloudwater may also be able to accelerate the decomposition of αAAHPs.

In the atmosphere, particle-phase αAAHPs are likely introduced into cloud and fog waters when the αAAHP-bearing particle is activated into a droplet, a process referred to as nucleation scavenging.[46] As such, in real cloudwater, αAAHPs are present with many other chemical components. The ideal way to investigate matrix effects of other cloudwater

Table 1. Summary of 1st-Order Decay Rates (k^I) and Corresponding e-Folding Lifetimes (τ_{avg}) of αAAHPs under a Variety of Experimental Conditions

			αAAHP-A		αAAHP-P	
solvent	T (°C)	pH[a]	k^I (s^{-1})[b]	τ_{avg} (min)	k^I (s^{-1})[b]	τ_{avg} (min)
acetonitrile	25	N.A.	$(1.4 \pm 0.8) \times 10^{-5}$	1200	$(1.3 \pm 0.8) \times 10^{-5}$	1200
methanol	25	N.A.	$(8.9 \pm 0.3) \times 10^{-5}$	190	$(8.8 \pm 0.2) \times 10^{-5}$	190
SOA	25	4.2	$(6.9 \pm 0.6) \times 10^{-4}$	24	$(7.0 \pm 0.4) \times 10^{-4}$	24
water	25	4.4	$(5.8 \pm 1.0) \times 10^{-4}$	29	$(4.9 \pm 0.7) \times 10^{-4}$	34
water	7	4.4	$(1.3 \pm 0.2) \times 10^{-4}$	110	$(1.4 \pm 0.1) \times 10^{-4}$	110
water	15	4.4	$(2.3 \pm 0.3) \times 10^{-4}$	72	$(2.0 \pm 0.3) \times 10^{-4}$	83
water	35	4.4	$(1.6 \pm 0.4) \times 10^{-3}$	11	$(1.4 \pm 0.4) \times 10^{-3}$	12

[a]Solution pH was uncontrolled in the listed experiments. [b]Uncertainties associated with k^I are the standard deviation of three replicates.
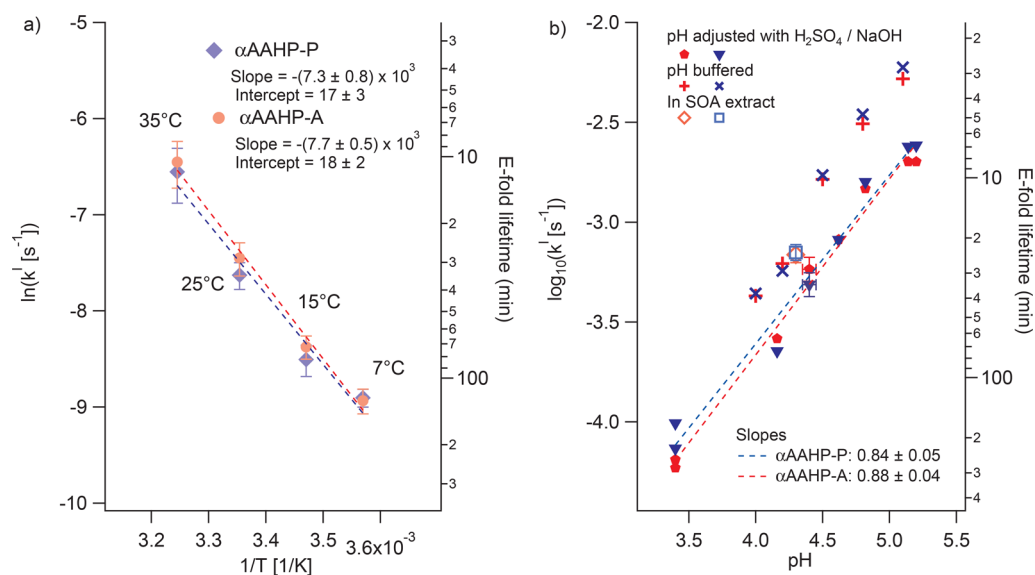
Figure 7. Temperature effect on the 1st-order decay rate of αAAHP (k^I), shown in part a as an Arrhenius plot (i.e., as $\ln(k^I)$ vs $1/T$). These experiments were performed with the solution pH uncontrolled ($\sim$4.4). The effects of pH and solution matrix on k^I (in the $\log_{10}$ scale) are shown in part b. All of these experiments were performed at 25 °C. Red markers denote αAAHP-A, while blue markers represent αAAHP-P. For both parts a and b, the corresponding e-folding lifetimes are shown on the right axis. The uncertainty bars, where applicable, represent one standard deviation obtained from triplicate experiments.
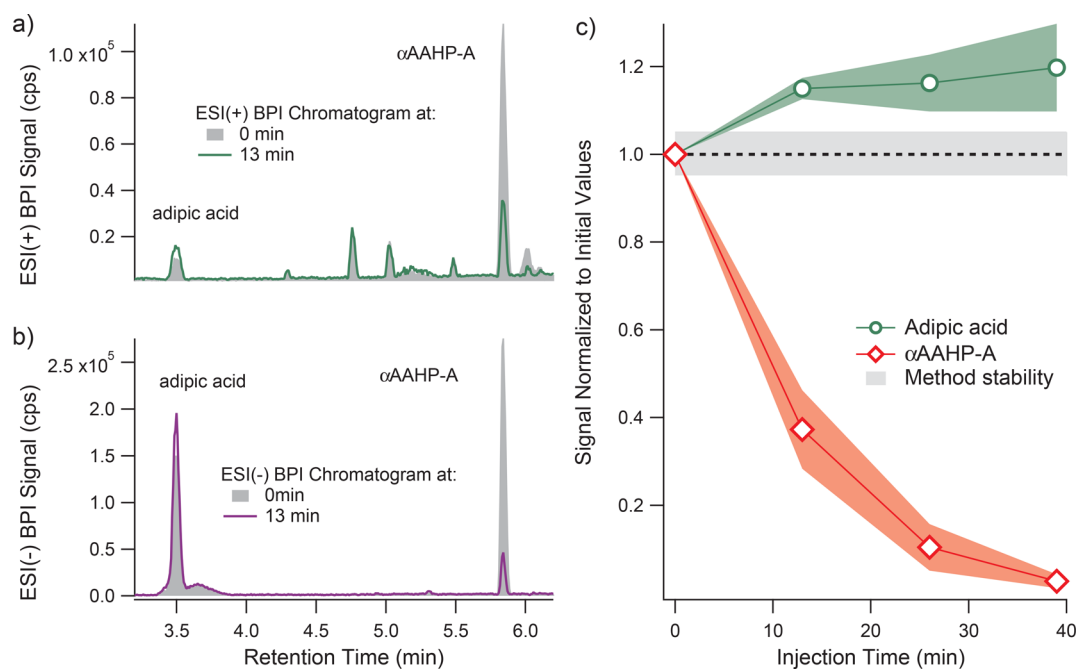
Figure 8. Change of signals in αAAHP-A hydrolysis experiment at 35 °C. The BPI chromatograms obtained with ESI(+) (a) and ESI($-$) (b) at 0 and 13 min injection time are compared. The growth of the adipic acid signal and the decay of αAAHP-A signal as a function of injection time, measured with ESI(+), are shown in part c. Signals are normalized to the values obtained for the first injection, and the uncertainties correspond to the standard deviation of triplicate. The dashed line and the shaded area around it represent the stability ($\pm$5%) of the LC-ESI-MS method.

components is to use authentic cloudwater samples.[47,48] In the absence of such samples, we have taken a matrix-matching approach by extracting α-pinene SOA components and $(NH_4)_2SO_4$ into water to create an atmospherically relevant sample matrix. In the SOA extract, the k^I values were determined to be $(6.9 \pm 0.6) \times 10^{-4}$ and $(7.0 \pm 0.4) \times 10^{-4}$ for αAAHP-A and αAAHP-P, respectively. These values are significantly higher than those in water with the same pH (pH 4.2). The corresponding k^I values in pH 4.2 water are 3.2 $\times$

10^{-4} and 3.6×10^{-4}, calculated with the pH-dependent curves shown in Figure 7b. Our results indicate that the presence of SOA compounds has doubled the decomposition rate of αAAHPs. Note that the hydrolysis experiment in the SOA extract was repeated in triplicate, and the uncertainty bars are shown in Figure 7b as a reference for the uncertainty range of this matrix-matching experiment.

As discussed in Experimental Section, the synthesized solutions contain organic acids and other byproducts. To
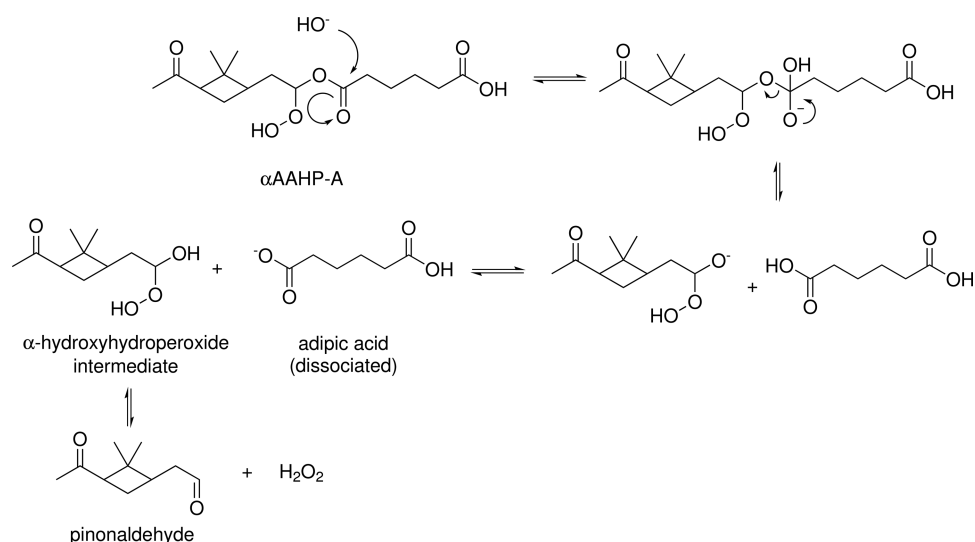
Figure 9. Base-catalyzed hydrolysis of αAAHP. The case of αAAHP-A is shown.

address the potential effect of the synthetic byproducts on the decomposition rate of αAAHPs, we performed an experiment with the αAAHPs diluted by an extra factor of two from the default dilution ratio (i.e., a dilution factor of 100 instead of 50) to reduce the concentration of byproducts. The k^I values obtained at these two dilution ratios agree to within 7%. As hydrolysis, a 1st-order reaction, should not be affected by dilution alone, these results indicate that the effect of organic acids and synthetic byproducts on αAAHP decomposition is relatively small under the current experimental conditions.

The TOC concentration of the SOA water extract was measured to be 31 ppmC. Such a level of TOC is typically observed in polluted fog and cloudwater samples, such as those from Fresno, California, and Jeju Island, Korea.[46] We did not further perform a systematic investigation of the effect of each individual organic species on the hydrolysis rate of αAAHPs; it is an interesting direction for future studies.

Proposed Mechanism of αAAHP Decomposition. *Base-Catalyzed Hydrolysis.* We have attempted to derive the reaction mechanism of αAAHP decomposition by monitoring the growth of product peaks using LC-ESI-MS. However, as shown in Figure 5, none of the peaks exhibits significant changes in intensity besides those of the decaying αAAHPs. The only peaks that exhibit minor, yet consistent growth are those attributable to the precursor organic acids, i.e., adipic acid and pinonic acid. Tracking the growth of these peaks is complicated by the fact that high concentrations of these organic acids are present in the solution as byproducts of the αAAHP synthesis prior to the hydrolysis experiments. Growth of the organic acid peaks is most clearly observed when the decomposition of αAAHPs is more rapid, i.e., in experiments with high temperature or high solution pH. Parts a and b of Figure 8 show the BPI chromatograms of an αAAHP-A solution during a hydrolysis experiment at 35 °C; the growth of adipic acid is confirmed with both ESI(+) and ESI(−). The growing signal of adipic acid and the decaying signal of αAAHP-A during hydrolysis experiments at 35 °C are shown in Figure 8c. Signals are normalized to those at time = 0 (the first injection) for comparison. The growth of adipic acid is highly variable, but an average growth of 19 ± 9% is observed when αAAHP-A is nearly depleted. This magnitude of growth is larger than the method stability of the LC-ESI-MS (±5%).

Production of pinonic acid from αAAHP-P is also observed, but to a less significant extent: 10 ± 3%. Such a small amount of pinonic acid production is close to the method stability. Our results highlight the importance of further purifying the synthesized αAAHPs in future studies, so that large residual acid signals do not mask signal growth due to αAAHP decomposition.

The observed pH-dependence and formation of organic acids are consistent with a base-catalyzed hydrolysis of αAAHPs, as shown by the case of αAAHP-A in Figure 9. The reaction proceeds via a nucleophilic addition of OH⁻ to the ester, yielding adipic acid and an α-hydroxyhydroperoxide (αHHP) intermediate that is in equilibrium with the corresponding aldehyde, pinonaldehyde, and H_2O_2.[49,50] The formation of H_2O_2 is qualitatively confirmed with the HPLC-fluorescence technique, with the results shown in Figure 10. As mentioned in Experimental, the synthesized solutions were diluted by a factor of 250 in water before the HPLC-fluorescence measurement. A high initial background of H_2O_2, 3.1 μM from αAAHP-A and 2.5 μM from αAAHP-P, is found in the
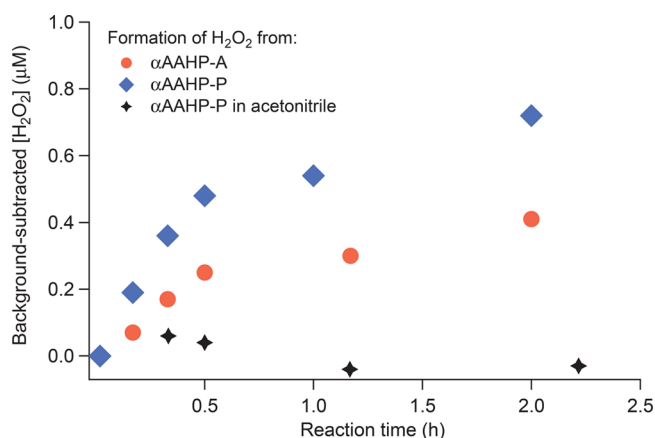
Figure 10. Production of H_2O_2 from αAAHPs diluted in water, measured using HPLC-fluorescence. The samples contain a high background of H_2O_2 from synthesis, which has been subtracted. The black trace shows the result of a control experiment, where αAAHP-P is dissolved in acetonitrile instead of water.

a) Acid anhydride formation
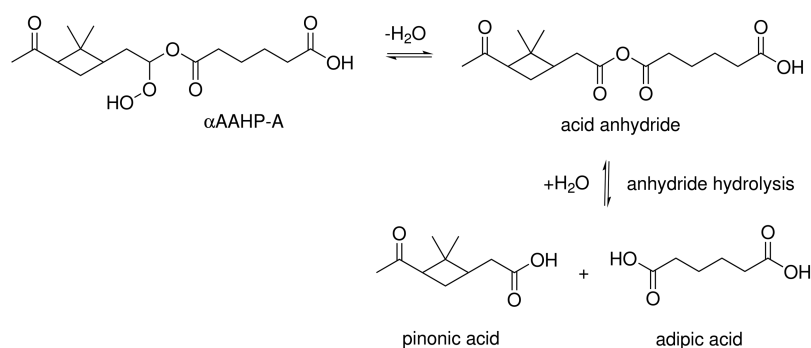
b) Cyclization and the Korcek mechanism
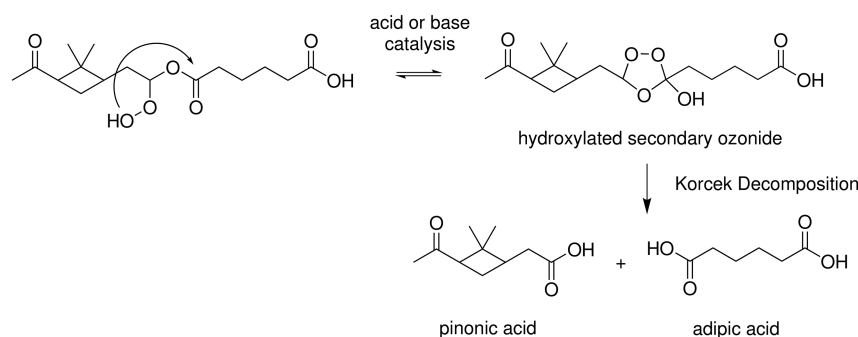
Figure 11. Other potential decomposition mechanisms of αAAHPs: (a) acid anhydride formation and (b) the Korcek mechanism. The cases for αAAHP-A are shown.

diluted aqueous solutions. We conducted a control experiment, in which αAAHP-P is diluted in acetonitrile instead of water. A similar initial H_2O_2 concentration (2.9 μM) is measured, but no further production of H_2O_2 is observed over the course of 2 h (Figure 10). The control experiment indicates that the initial H_2O_2 likely arises from the synthesis, and is not due to a rapid production upon dilution in water. The initial background has been subtracted from the results presented in Figure 10. When either αAAHP-A or αAAHP-P is diluted in water, a steady production of H_2O_2 is observed. While αAAHPs are depleted in approximately 1 h (as shown by the LC-ESI-MS results), the production of H_2O_2 continues over a much longer time. The HPLC-fluorescence results are consistent with the proposed mechanism (Figure 9), where αAAHPs are first converted into an αHHP intermediate, which likely generates H_2O_2 over a longer time scale. However, due to the impure nature of the synthesized solution, we cannot rule out the possibility that synthetic byproducts can also give rise to H_2O_2.

The observed base-catalyzed hydrolysis of αAAHPs is unique to aqueous-phase reactions. In fact, gas-phase decomposition of organic peroxides is often acid-catalyzed. Computational studies have shown that organic acids (e.g., formic acid) can form prereaction complexes with organic peroxides in the gas phase and reduce the energy barriers associated with their decomposition.[51,52] Conversely, in the aqueous phase, hydrolysis of αAAHPs is initiated via nucleophilic addition of OH^- to the ester functional group (Figure 9) The dependence of aqueous-phase decomposition on acid−base chemistry thus differentiates aqueous-phase mechanisms from their gas-phase counterparts.

Base-catalyzed hydrolysis in the aqueous phase has also been reported for a related class of organic hydroperoxides, αHHPs.

In particular, the hydrolysis rates of hydroxymethyl hydroperoxide (HMP) and bis(hydroxymethyl) peroxide (BHMP) exhibit a linear relationship with the concentration of HO^- from pH 4 to 6.[53,54] This observation is similar to the case of αAAHPs observed in the current work. In general, hydrolysis reactions can be catalyzed by either acid or base.[44] We did not observe any signs of acid-catalyzed hydrolysis within the pH range studied here (pH 3.5 to 5.1), nor did we perform experiments under highly acidic conditions. However, acid-catalyzed hydrolysis of HMP and BHMP was observed in solutions with pH 1.5 or lower.[54] It will be of interest for future studies to investigate potential acid-catalyzed hydrolysis of αAAHPs in highly acidic solutions.

Other Potential Reaction Mechanisms. Besides the base-catalyzed hydrolysis mechanism, a number of other potential mechanisms have been proposed in previous work. The first mechanism is acid anhydride formation via loss of water from αAAHPs (Figure 11a). Studies of gas-phase ozonolysis of ethene in the presence of formic acid have observed the formation of formic acid anhydride, which likely arises from this reaction pathway.[7,55] A computational study[52] has shown that the presence of a third molecule, e.g., an organic acid, serves as the carrier of hydrogen and can efficiently lower the energy barrier of this reaction pathway. As shown in Figure 11a, the acid anhydride arising from αAAHP-A should undergo hydrolysis in the aqueous phase and give rise to pinonic acid and adipic acid. However, pinonic acid, which would have appeared at RT = 4.9 min, is not observed in the αAAHP-A hydrolysis experiments (Figure 8, parts a and b). Our results indicate that the acid anhydride pathway is unlikely a major reaction mechanism.

The second reaction pathway considered here involves a cyclization reaction followed by decomposition, a route known as the Korcek mechanism.[56] The Korcek mechanism is particularly relevant to γ-ketohydroperoxides, forming a five-membered cyclic peroxide intermediate, which subsequently decomposes to a carbonyl compound and an organic acid.[57] In particular, Mutzel et al.[38] have proposed that the Korcek mechanism can be responsible for the loss of highly oxidized organic compounds present in SOA. As shown in Figure 11b, the cyclization of αAAHPs represents a special case of the Korcek mechanism, giving rise to a hydroxylated secondary ozonide intermediate. Information on the decomposition pathway of this hydroxylated secondary ozonide intermediate is limited.[58] In the case of αAAHP-A, the Korcek mechanism likely results in two organic acids, pinonic acid and adipic acid for the case of αAAHP-A. As already discussed for the acid anhydride pathway, production of pinonic acid is not observed in the current work, indicating that the Korcek mechanism is likely a minor reaction pathway.

CONCLUSION AND ENVIRONMENTAL IMPLICATIONS

A growing body of work suggests the importance of the reactions between stabilized Criegee intermediates (SCIs) and organic acids in the atmosphere.[5,6,14,18,20] The atmospheric fate of the resulting products, α-acyloxyalkyl hydroperoxides (αAAHPs), needs to be understood for in order to properly assess the environmental importance of SCI + organic acid chemistry. The current study presents the first systematic investigation of the behavior of αAAHPs in the condensed phase. Given a lack of commercially available standards, two αAAHPs were synthesized via liquid-phase ozonolysis of α-pinene. The most significant finding of the current work is a rapid decomposition of αAAHPs in the aqueous phase. The reaction rate is highly dependent on temperature and solution pH, with the observed e-folding lifetimes of αAAHPs ranging from 10 min (at 35 °C or pH 5) to over 100 min (at 7 °C or pH 3.5).

The observations have significant implications for the fate of αAAHPs in the atmosphere. It is now widely accepted that atmospheric aqueous phases, including cloud, fog, and aerosol liquid water, are important reaction media for organic compounds.[59−61] Highly functionalized organic compounds, such as αAAHPs arising from α-pinene ozonolysis, can be introduced into cloud and fog waters through nucleation scavenging. The pH of ambient cloud and fog waters varies between 2 and 7, depending on the chemical composition and the size of the droplets.[45] Larger droplets tend to be less acidic, as they are enriched in species arising from mineral dust and sea salt. Our study shows that base-catalyzed hydrolysis is likely the dominant decomposition pathway of αAAHPs in the cloud-water-relevant pH range. The rapid decay observed in this study implies that αAAHPs can be lost promptly when exposed to cloud and fog with pH values larger than 5. The stability of αAAHPs in aerosol liquid water is dependent on several competing factors and is difficult to predict. The pH values of aerosol liquid water tend to be lower, typically ranging between −1 and +3.[62] While we did not investigate the behavior of αAAHPs under such acidic conditions, studies on other types of organic hydroperoxide indicate that acid-catalyzed hydrolysis may become dominant in highly acidic solutions.[54] Aerosol liquid water also tends to contain a much higher concentration of organic compounds.[63,64] Observations from the current work

show an acceleration of the αAAHP decomposition by dissolved organic compounds generated from α-pinene ozonolysis. The total organic carbon concentration used in the current work is 31 ppmC, equivalent to that in cloud and fog waters from polluted regions. However, extrapolation of the current results to highly complex ambient aerosol liquid water is difficult.

Rapid decomposition of αAAHPs can also occur in laboratory experiments when filter samples are extracted in aqueous or organic solvents. Such loss can potentially explain contradictory results reported in the existing literature regarding the importance of αAAHPs in SOA.[21,22] On the basis of the kinetic results obtained in this work, key suggestions can be made for future laboratory experiments targeting αAAHPs. Currently, the majority of chemical analyses of SOA components are based on filter collection, extraction, and off-line analyses. Our results suggest that the use of aprotic solvents, such as acetonitrile, can significantly reduce the decomposition of αAAHPs after extraction. If the use of aqueous solvents is unavoidable, the solution should be acidified and stored under lower temperatures to minimize αAAHP decomposition.

The reaction mechanism and the products arising from αAAHP decomposition are also of particular interest in atmospheric chemistry. The observed production of organic acids and H_2O_2 in this work is consistent with a base-catalyzed hydrolysis reaction of αAAHPs. The production of H_2O_2 is particularly important, given that H_2O_2 is a reactive oxygen species and is likely linked to adverse health effects of particulate matter pollution.[23] Formation of H_2O_2 in extracted SOA components has been previously observed and has been attributed to decomposition of larger organic peroxides.[28,30,40] αAAHP may represent one such H_2O_2 source. However, the interpretation of the reaction mechanism in the current work is significantly hindered by the presence of organic acids and synthetic byproducts that cannot be easily separated. Currently, we cannot rule out the possibility that H_2O_2 arises from compounds other than αAAHPs. Our results should be confirmed by future studies using pure αAAHP standards. A remaining question for the reaction mechanism of αAAHPs is the cause of their chemical instability. The water extract of α-pinene SOA contains a large number of nonperoxide dimer esters[31,65,66] that are much more stable than αAAHPs and do not exhibit a noticeable decay over a period of days. The hydroperoxide functional group likely introduces the observed chemical lability to αAAHPs, and base-catalyzed hydrolysis alone may not fully explain their rapid decomposition.

Finally, the two αAAHP species studied in this work exhibit similar dependence on all of the experimental conditions examined, implying that a generalized description for the reactivity of αAAHPs may be feasible. The current work focuses on two specific αAAHPs arising from α-pinene SCIs, which does not cover the diversity of SCI-derived organic species in the ambient atmosphere. Future studies should be extended to a wider spectrum of αAAHPs, including those arising from isoprene and other major alkenes.

AUTHOR INFORMATION

Corresponding Author
*(R.Z.) E-mail: rzhao@caltech.edu. Telephone: +1 626-395-8928.

ORCID ●

Ran Zhao: 0000-0002-1096-7632

Christopher M. Kenseth: 0000-0003-3188-2336

Suzanne E. Paulson: 0000-0003-0855-7615

John H. Seinfeld: 0000-0003-1344-4068

Present Address

‡Department of Chemistry, University of Alberta, Edmonton, AB, Canada T6G 2G2

Notes

The authors declare no competing financial interest.

■ REFERENCES

(1) Guenther, A.; Hewitt, C. N.; Erickson, D.; Fall, R.; Geron, C.; Graedel, T.; Harley, P.; Klinger, L.; Lerdau, M.; Mckay, W. A.; et al. A global model of natural volatile organic compound emissions. *J. Geophys. Res.* **1995**, *100*, 8873−8892.

(2) Seinfeld, J. H.; Pandis, S. N. *Atmospheric Chemistry and Physics: From Air Pollution to Climate Change*, 3rd ed.; John Wiley & Sons: Hoboken, NJ, 2016.

(3) Criegee, R. Mechanism of ozonolysis. *Angew. Chem., Int. Ed. Engl.* **1975**, *14*, 745−752.

(4) Osborn, D. L.; Taatjes, C. A. The physical chemistry of Criegee intermediates in the gas phase. *Int. Rev. Phys. Chem.* **2015**, *34*, 309−360.

(5) Taatjes, C. A.; Shallcross, D. E.; Percival, C. J. Research frontiers in the chemistry of Criegee intermediates and tropospheric ozonolysis. *Phys. Chem. Chem. Phys.* **2014**, *16*, 1704−1718.

(6) Welz, O.; Eskola, A. J.; Sheps, L.; Rotavera, B.; Savee, J. D.; Scheer, A. M.; Osborn, D. L.; Lowe, D.; Murray Booth, A.; Xiao, P.; et al. Rate coefficients of C1 and C2 Criegee intermediate reactions with formic and acetic acid near the collision limit: direct kinetics measurements and atmospheric implications. *Angew. Chem., Int. Ed.* **2014**, *53*, 4547−4550.

(7) Neeb, P.; Horie, O.; Moortgat, G. K. Gas-phase ozonolysis of ethene in the presence of hydroxylic compounds. *Int. J. Chem. Kinet.* **1996**, *28*, 721−730.

(8) Tobias, H. J.; Ziemann, P. J. Kinetics of the gas-phase reactions of alcohols, aldehydes, carboxylic acids, and water with the C13 stabilized Criegee intermediate formed from ozonolysis of 1-tetradecene. *J. Phys. Chem. A* **2001**, *105*, 6129−6135.

(9) Stone, D.; Blitz, M.; Daubney, L.; Howes, N. U.; Seakins, P. Kinetics of CH_2OO reactions with SO_2, NO_2, NO, H_2O and CH_3CHO as a function of pressure. *Phys. Chem. Chem. Phys.* **2014**, *16*, 1139−1149.

(10) Mochida, M.; Katrib, Y.; Jayne, J. T.; Worsnop, D. R.; Martin, S. T. The relative importance of competing pathways for the formation of high-molecular-weight peroxides in the ozonolysis of organic aerosol particles. *Atmos. Chem. Phys.* **2006**, *6*, 4851−4866.

(11) Sakamoto, Y.; Inomata, S.; Hirokawa, J. Oligomerization reaction of the criegee intermediate leads to secondary organic aerosol formation in ethylene ozonolysis. *J. Phys. Chem. A* **2013**, *117*, 12912−12921.

(12) Kristensen, K.; Enggrob, K. L.; King, S. M.; Worton, D. R.; Platt, S. M.; Mortensen, R.; Rosenoern, T.; Surratt, J. D.; Bilde, M.; Goldstein, A. H.; et al. Formation and occurrence of dimer esters of pinene oxidation products in atmospheric aerosols. *Atmos. Chem. Phys.* **2013**, *13*, 3763−3776.

(13) Kristensen, K.; Cui, T.; Zhang, H.; Gold, A.; Glasius, M.; Surratt, J. D. Dimers in α-pinene secondary organic aerosol: effect of hydroxyl radical, ozone, relative humidity and aerosol acidity. *Atmos. Chem. Phys.* **2014**, *14*, 4201−4218.

(14) Kristensen, K.; Watne, A. K.; Hammes, J.; Lutz, A.; Petäjä, T.; Hallquist, M.; Bilde, M.; Glasius, M. High-molecular weight dimer esters are major products in aerosols from α-pinene ozonolysis and the boreal forest. *Environ. Sci. Technol. Lett.* **2016**, *3*, 280−285.

(15) Kristensen, K.; Jensen, L.; Glasius, M.; Bilde, M. The effect of sub-zero temperature on the formation and composition of secondary organic aerosol from ozonolysis of α-pinene. *Environ. Sci. Processes Impacts* **2017**, *19*, 1220−1234.

(16) Zhu, C.; Kumar, M.; Zhong, J.; Li, L.; Francisco, J. S.; Zeng, X. C. New mechanistic pathways for Criegee−water chemistry at the air/water interface. *J. Am. Chem. Soc.* **2016**, *138*, 11164−11169.

(17) Zhong, J.; Kumar, M.; Zhu, C. Q.; Francisco, J. S.; Zeng, X. C. Surprising stability of larger Criegee intermediates on aqueous interfaces. *Angew. Chem., Int. Ed.* **2017**, *56*, 7740−7744.

(18) Kumar, M.; Zhong, J.; Zeng, X. C.; Francisco, J. S. Reaction of Criegee intermediate with nitric acid at the air−water interface. *J. Am. Chem. Soc.* **2018**, *140*, 4913−4921.

(19) Enami, S.; Colussi, A. J. Efficient scavenging of Criegee intermediates on water by surface-active cis-pinonic acid. *Phys. Chem. Chem. Phys.* **2017**, *19*, 17044−17051.

(20) Enami, S.; Colussi, A. J. Criegee chemistry on aqueous organic surfaces. *J. Phys. Chem. Lett.* **2017**, *8*, 1615−1623.

(21) Zhao, R.; Kenseth, C. M.; Huang, Y.; Dalleska, N. F.; Seinfeld, J. H. Iodometry-assisted liquid chromatography electrospray ionization mass spectrometry for analysis of organic peroxides - an application to atmospheric secondary organic aerosol. *Environ. Sci. Technol.* **2018**, *52*, 2108−2117.

(22) Witkowski, B.; Gierczak, T. Early stage composition of SOA produced by α-pinene/ozone reaction: α-Acyloxyhydroperoxy aldehydes and acidic dimers. *Atmos. Environ.* **2014**, *95*, 59−70.

(23) Tao, F.; Gonzalez-Flecha, B.; Kobzik, L. Reactive oxygen species in pulmonary inflammation by ambient particulates. *Free Radical Biol. Med.* **2003**, *35*, 327−340.

(24) Shiraiwa, M.; Ueda, K.; Pozzer, A.; Lammel, G.; Kampf, C. J.; Fushimi, A.; Enami, S.; Arangio, A. M.; Fröhlich-Nowoisky, J.; Fujitani, Y.; et al. Aerosol health effects from molecular to global scales. *Environ. Sci. Technol.* **2017**, *51*, 13545−13567.

(25) Krapf, M.; El Haddad, I.; Bruns, E. A.; Molteni, U.; Daellenbach, K. R.; Prévôt, A. S.; Baltensperger, U.; Dommen, J. Labile peroxides in secondary organic aerosol. *Chem.* **2016**, *1*, 603−616.

(26) Li, H.; Chen, Z.; Huang, L.; Huang, D. Organic peroxides' gas-particle partitioning and rapid heterogeneous decomposition on secondary organic aerosol. *Atmos. Chem. Phys.* **2016**, *16*, 1837−1848.

(27) Riva, M.; Budisulistiorini, S. H.; Zhang, Z.; Gold, A.; Thornton, J. A.; Turpin, B. J.; Surratt, J. D. Multiphase reactivity of gaseous hydroperoxide oligomers produced from isoprene ozonolysis in the presence of acidified aerosols. *Atmos. Environ.* **2017**, *152*, 314−322.

(28) Badali, K. M.; Zhou, S.; Aljawhary, D.; Antiñolo, M.; Chen, W. J.; Lok, A.; Mungall, E.; Wong, J. P. S.; Zhao, R.; Abbatt, J. P. D. Formation of hydroxyl radicals from photolysis of secondary organic aerosol material. *Atmos. Chem. Phys.* **2015**, *15*, 7831−7840.

(29) Tong, H.; Arangio, A. M.; Lakey, P. S. J.; Berkemeier, T.; Liu, F.; Kampf, C. J.; Brune, W. H.; Pöschl, U.; Shiraiwa, M. Hydroxyl radicals from secondary organic aerosol decomposition in water. *Atmos. Chem. Phys.* **2016**, *16*, 1761−1771.

(30) Arellanes, C.; Paulson, S. E.; Fine, P. M.; Sioutas, C. Exceeding of Henry's law by hydrogen peroxide associated with urban aerosols. *Environ. Sci. Technol.* **2006**, *40*, 4859−4866.

(31) Zhang, X.; McVay, R. C.; Huang, D. D.; Dalleska, N. F.; Aumont, B.; Flagan, R. C.; Seinfeld, J. H. Formation and evolution of molecular products in α-pinene secondary organic aerosol. *Proc. Natl. Acad. Sci. U. S. A.* **2015**, *112*, 14168−14173.

(32) Zhang, X.; Dalleska, N. F.; Huang, D. D.; Bates, K. H.; Sorooshian, A.; Flagan, R. C.; Seinfeld, J. H. Time-resolved molecular characterization of organic aerosols by PILS+ UPLC/ESI-Q-TOFMS. *Atmos. Environ.* **2016**, *130*, 180−189.

(33) Witkowski, B.; Gierczak, T. Analysis of α-acyloxyhydroperoxy aldehydes with electrospray ionization-tandem mass spectrometry (ESI-MS(n)). *J. Mass Spectrom.* **2013**, *48*, 79−88.

(34) Kumar, M.; Busch, D. H.; Subramaniam, B.; Thompson, W. H. Barrierless tautomerization of Criegee intermediates via acid catalysis. *Phys. Chem. Chem. Phys.* **2014**, *16*, 22968−22973.

(35) Banerjee, D. K.; Budke, C. C. Spectrophotometric determination of traces of peroxides in organic solvents. *Anal. Chem.* **1964**, *36*, 792−796.

(36) Bloomfield, M. The spectrophotometric determination of hydroperoxide and peroxide in a lipid pharmaceutical product by flow injection analysis. *Analyst* **1999**, *124*, 1865−1871.

(37) Docherty, K. S.; Wu, W.; Lim, Y. B.; Ziemann, P. J. Contributions of organic peroxides to secondary aerosol formed from reactions of monoterpenes with O_3. *Environ. Sci. Technol.* **2005**, *39*, 4049−4059.

(38) Mutzel, A.; Poulain, L.; Berndt, T.; Iinuma, Y.; Rodigast, M.; Böge, O.; Richters, S.; Spindler, G.; Sipilä, M.; Jokinen, T.; et al. Highly oxidized multifunctional organic compounds observed in tropospheric particles: a field and laboratory study. *Environ. Sci. Technol.* **2015**, *49*, 7754−7761.

(39) Huang, Y.; Coggon, M. M.; Zhao, R.; Lignell, H.; Bauer, M. U.; Flagan, R. C.; Seinfeld, J. H. The Caltech Photooxidation Flow Tube reactor: design, fluid dynamics and characterization. *Atmos. Meas. Tech.* **2017**, *10*, 839−867.

(40) Wang, Y.; Kim, H.; Paulson, S. E. Hydrogen peroxide generation from α- and β-pinene and toluene secondary organic aerosols. *Atmos. Environ.* **2011**, *45*, 3149−3156.

(41) Wang, Y.; Arellanes, C.; Paulson, S. E. Hydrogen peroxide associated with ambient fine-mode, diesel, and biodiesel aerosol particles in Southern California. *Aerosol Sci. Technol.* **2012**, *46*, 394−402.

(42) Hasson, A. S.; Orzechowska, G.; Paulson, S. E. Production of stabilized Criegee intermediates and peroxides in the gas phase ozonolysis of alkenes: 1. Ethene, trans-2-butene, and 2,3-dimethyl-2-butene. *J. Geophys. Res. Atmos.* **2001**, *106*, 34131−34142.

(43) Hasson, A. S.; Ho, A. W.; Kuwata, K. T.; Paulson, S. E. Production of stabilized Criegee intermediates and peroxides in the gas phase ozonolysis of alkenes: 2. Asymmetric and biogenic alkenes. *J. Geophys. Res. Atmos.* **2001**, *106*, 34143−34153.

(44) Mabey, W.; Mill, T. Critical review of hydrolysis of organic compounds in water under environmental conditions. *J. Phys. Chem. Ref. Data* **1978**, *7*, 383−415.

(45) Collett, J. L.; Bator, A.; Rao, X.; Demoz, B. B. Acidity variations across the cloud drop size spectrum and their influence on rates of atmospheric sulfate production. *Geophys. Res. Lett.* **1994**, *21*, 2393−2396.

(46) Herckes, P.; Valsaraj, K. T.; Collett, J. L., Jr A review of observations of organic matter in fogs and clouds: origin, processing and fate. *Atmos. Res.* **2013**, *132-133*, 434−449.

(47) Boris, A. J.; Desyaterik, Y.; Collett, J. L. How do components of real cloud water affect aqueous pyruvate oxidation? *Atmos. Res.* **2014**, *143*, 95−106.

(48) Lee, A. K. Y.; Herckes, P.; Leaitch, W. R.; Macdonald, A. M.; Abbatt, J. P. D. Aqueous OH oxidation of ambient organic aerosol and cloud water organics: Formation of highly oxidized products. *Geophys. Res. Lett.* **2011**, *38*, GL047439.

(49) Zhao, R.; Lee, A. K. Y.; Abbatt, J. P. D. Investigation of aqueous-phase photooxidation of glyoxal and methylglyoxal by aerosol chemical ionization mass spectrometry: observation of hydroxyhydroperoxide formation. *J. Phys. Chem. A* **2012**, *116*, 6253−6263.

(50) Zhao, R.; Lee, A. K. Y.; Soong, R.; Simpson, A. J.; Abbatt, J. P. D. Formation of aqueous-phase α-hydroxyhydroperoxides (α-HHP): potential atmospheric impacts. *Atmos. Chem. Phys.* **2013**, *13*, 5857−5872.

(51) Kumar, M.; Busch, D. H.; Subramaniam, B.; Thompson, W. H. Role of tunable acid catalysis in decomposition of α-hydroxyalkyl hydroperoxides and mechanistic implications for tropospheric chemistry. *J. Phys. Chem. A* **2014**, *118*, 9701−9711.

(52) Aplincourt, P.; Ruiz-López, M. F. Theoretical study of formic acid anhydride formation from carbonyl oxide in the atmosphere. *J. Phys. Chem. A* **2000**, *104*, 380−388.

(53) Zhou, X.; Lee, Y. N. Aqueous solubility and reaction kinetics of hydroxymethyl hydroperoxide. *J. Phys. Chem.* **1992**, *96*, 265−272.

(54) Marklund, S.; et al. Simultaneous determination of bis (hydroxymethyl)-peroxide (BHMP), hydroxymethylhydroperoxide (HMP), and H_2O_2 with titanium (IV)-equilibria between peroxides and stabilities of HMP and BHMP at physiological conditions. *Acta Chem. Scand.* **1971**, *25*, 3517.

(55) Neeb, P.; Horie, O.; Moortgat, G. K. The nature of the transitory product in the gas-phase ozonolysis of ethene. *Chem. Phys. Lett.* **1995**, *246*, 150−156.

(56) Jensen, R. K.; Korcek, S.; Mahoney, L. R.; Zinbo, M. Liquid-phase autoxidation of organic compounds at elevated temperatures. 2. Kinetics and mechanisms of the formation of cleavage products in n-hexadecane autoxidation. *J. Am. Chem. Soc.* **1981**, *103*, 1742−1749.

(57) Jalan, A.; Alecu, I. M.; Meana-Pañeda, R.; Aguilera-Iparraguirre, J.; Yang, K. R.; Merchant, S. S.; Truhlar, D. G.; Green, W. H. New pathways for formation of acids and carbonyl products in low-temperature oxidation: the Korcek decomposition of γ-ketohydroperoxides. *J. Am. Chem. Soc.* **2013**, *135*, 11100−11114.

(58) Moshammer, K.; Jasper, A. W.; Popolan-Vaida, D. M.; Lucassen, A.; Dievart, P.; Selim, H.; Eskola, A. J.; Taatjes, C. A.; Leone, S. R.; Sarathy, S. M.; et al. Detection and identification of the keto-hydroperoxide ($HOOCH_2OCHO$) and other intermediates during low-temperature oxidation of dimethyl ether. *J. Phys. Chem. A* **2015**, *119*, 7361−7374.

(59) Ervens, B. Modeling the processing of aerosol and trace gases in clouds and fogs. *Chem. Rev.* **2015**, *115*, 4157−4198.

(60) McNeill, V. F. Aqueous organic chemistry in the atmosphere: sources and chemical processing of organic aerosols. *Environ. Sci. Technol.* **2015**, *49*, 1237−1244.

(61) Zhao, R.; Lee, A. K. Y.; Wang, C.; Wania, F.; Wong, J. P. S.; Zhou, S.; Abbatt, J. P. D. The Role of Water in Organic Aerosol Multiphase Chemistry: Focus on Partitioning and Reactivity. *Advances in Atmospheric Chemistry* **2017**, 95−184.

(62) Murphy, J. G.; Gregoire, P. K.; Tevlin, A. G.; Wentworth, G. R.; Ellis, R. A.; Markovic, M. Z.; VandenBoer, T. C. Observational constraints on particle acidity using measurements and modelling of particles and gases. *Faraday Discuss.* **2017**, *200*, 379−395.

(63) Arakaki, T.; Anastasio, C.; Kuroki, Y.; Nakajima, H.; Okada, K.; Kotani, Y.; Handa, D.; Azechi, S.; Kimura, T.; Tsuhako, A.; et al. A general scavenging rate constant for reaction of hydroxyl radical with organic carbon in atmospheric waters. *Environ. Sci. Technol.* **2013**, *47*, 8196−8203.

(64) Volkamer, R.; Ziemann, P. J.; Molina, M. J. Secondary organic aerosol formation from acetylene (C_2H_2): seed effect on SOA yields due to organic photochemistry in the aerosol aqueous phase. *Atmos. Chem. Phys.* **2009**, *9*, 1907−1928.

(65) Yasmeen, F.; Vermeylen, R.; Szmigielski, R.; Iinuma, Y.; Böge, O.; Herrmann, H.; Maenhaut, W.; Claeys, M. Terpenylic acid and related compounds: precursors for dimers in secondary organic aerosol from the ozonolysis of α-and β-pinene. *Atmos. Chem. Phys.* **2010**, *10*, 9383−9392.

(66) Müller, L.; Reinnig, M.-C.; Warnke, J.; Hoffmann, T. Unambiguous identification of esters as oligomers in secondary organic aerosol formed from cyclohexene and cyclohexene/α-pinene ozonolysis. *Atmos. Chem. Phys.* **2008**, *8*, 1423−1433.

COUPLING FILTER-BASED THERMAL DESORPTION CHEMICAL IONIZATION MASS SPECTROMETRY WITH LIQUID CHROMATOGRAPHY/ELECTROSPRAY IONIZATION MASS SPECTROMETRY FOR MOLECULAR ANALYSIS OF SECONDARY ORGANIC AEROSOL

Coupling Filter-Based Thermal Desorption Chemical Ionization Mass Spectrometry with Liquid Chromatography/Electrospray Ionization Mass Spectrometry for Molecular Analysis of Secondary Organic Aerosol

Yuanlong Huang, Christopher M. Kenseth, Nathan F. Dalleska, and John H. Seinfeld*

ACCESS | Metrics & More | Article Recommendations | Supporting Information

ABSTRACT: Filter-based thermal desorption (F-TD) techniques, such as the filter inlet for gases and aerosols, are widely employed to investigate the molecular composition and physicochemical properties of secondary organic aerosol (SOA). Here, we introduce an enhanced capability of F-TD through the combination of a customized F-TD inlet with chemical ionization mass spectrometry (CIMS) and ultraperformance liquid chromatography/electrospray ionization mass spectrometry (UPLC/ESI-MS). The utility of F-TD/CIMS + UPLC/ESI-MS is demonstrated by application to α-pinene ozonolysis SOA for which increased filter aerosol mass loading is shown to slow the evaporation rates of deposited compounds. Evidence for oligomer decomposition producing multimode F-TD/CIMS thermograms is provided by the measurement of the mass fraction remaining of monomeric and dimeric α-pinene oxidation products on the filter via UPLC/ESI-MS. In situ evaporation of aerosol particles suggests that α-pinene-derived hydroperoxides are thermally labile; thus, analysis of particle-phase (hydro)peroxides via F-TD may not be appropriate. A synthesized pinene-derived dimer ester ($C_{20}H_{32}O_5$) is found to be thermally stable up to 200 °C, whereas particle-phase dimers ($C_{19}H_{30}O_5$) are observed to form during F-TD analysis via thermally induced condensation of synthesized pinene-derived alcohols and diacids. The complementary F-TD/CIMS + UPLC/ESI-MS method offers previously inaccessible insight into the molecular composition and thermal desorption behavior of SOA that both clarifies and expands on analysis via traditional F-TD techniques.
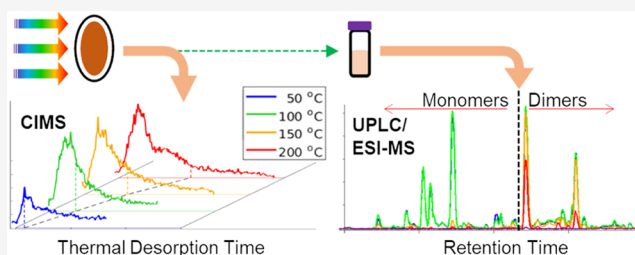
INTRODUCTION

Analysis of secondary organic aerosol (SOA) formation includes consideration of gas-phase chemistry, multiphase transport,[1] particle-phase state (or viscosity),[2] and particle-phase reactions (e.g., oligomerization). No single instrument exists that can interrogate all these processes. A significant challenge to the molecular-level detection of SOA constituents is the fact that aerosol particles comprise only a small amount of mass, yet generally contain an extensive array of diverse compounds. Moveover, the nature of SOA generally requires pretreatment (e.g., thermal desorption, extraction, charging, etc.) before the analysis of particle physicochemical properties.

Heat-induced evaporation of particles, as a pretreatment process, has long been employed to investigate aerosol volatility, as well as particle-phase composition.[3−5] Two common particle-evaporation techniques include (1) detection of the vapors coming off the particles (e.g., with a mass spectrometer[6−8]) and (2) removing the vapors with adsorptive materials (e.g., with a thermodenuder[9,10]) to determine the mass fraction remaining (MFR) in the particle phase after evaporation. These two approaches can provide complementary understanding of SOA chemical properties if one can simultaneously analyze both the vapors from the particles as well as the mass remaining in the particles.

To address the minute amount of single-particle mass, particles are routinely collected on filters or impactors[11,12] and analysis is focused on the concentrated material. A recently developed technique, the filter inlet for gases and aerosols (FIGAERO),[13] is now widely employed to investigate SOA composition. The details of FIGAERO operation, which leverages filter-based evaporation to detect both gas- and particle-phase components in a semicontinuous mode, are described extensively elsewhere.[14−17]

Application of filter-based evaporation of aerosol-phase compounds upon heating has significantly advanced the analysis of SOA composition across a wide range of molecular volatilities. Nevertheless, some intrinsic properties of this

method introduce uncertainties into the data analysis. First, the temperature at which the chemical ionization mass spectrometer (CIMS) detects the maximum ion signal during thermal desorption (so-called T_{max}) for a pure compound can differ as a function of the analyte matrix (i.e., pure compound vs SOA sample).[13] This results because (1) (semi)solid particle phase states determined by aerosol composition may retard the evaporation,[17] (2) increasing the aerosol mass loading on the filter[18] may limit interlayer particle-phase diffusion, and (3) the complexity of SOA may induce stronger noncovalent H-bonding between the compound of interest and other SOA constituents as compared to those of the pure compound.[19] Second, temperature ramping to separate particle-phase components based on molecular volatility can lead to thermal decomposition of larger molecules or oligomerization in the condensed phase with poorly constrained transformation rates.[20,21] Third, owing to the relatively large surface area of filters in F-TD, evaporated molecules can interact with the filter (e.g., adsorption and desorption) before entering the CIMS. Schobesberger et al.[5] developed a comprehensive model framework to explain observed thermograms (CIMS signal vs temperature) for different compounds that incorporates the effect of the filter itself and is based on temperature-dependent reversible oligomerization between monomers and oligomers and irreversible thermal decomposition.

Owing to these issues associated with thermal-induced evaporation of aerosols, interpretation of data derived from thermal desorption measurements and direct comparison between studies are difficult. Alternatively, another widely used, comparatively mild, method to pretreat aerosol samples is extraction followed by electrospray ionization (ESI), often coupled with liquid chromatography (LC). It is noted, however, that the extraction efficiency of the condensed-phase compound depends on the polarity of the solvent.[22] Furthermore, ESI efficiencies have been shown to depend strongly on molecular structures.[23]

Here, we introduce and demonstrate a complementary capability of filter-based thermal desorption (F-TD) by combining a customized inlet system, the key feature of FIGAERO, with CIMS and offline ultraperformance liquid chromatography/electrospray ionization mass spectrometry (UPLC/ESI-MS). The F-TD inlet processes the filter sample with a conventional procedure (ramp to a temperature setpoint and hold) from which one obtains thermograms of evaporating species via CIMS, while UPLC/ESI-MS provides complementary information about the components remaining on the filter after evaporation under a range of temperatures. The combination of F-TD/CIMS + UPLC/ESI-MS enables a more comprehensive analysis of aerosol molecular composition and volatility than that afforded by traditional thermal desorption techniques. With F-TD/CIMS + UPLC/ESI-MS, we seek to (1) provide direct evidence for the role of thermal decomposition in producing multimode thermograms, (2) demonstrate that the amount of aerosol mass deposited on the filter affects the performance of thermal desorption in terms of both evaporation fluxes and the MFR in the particle phase, and (3) explore the thermal stability and reactivity of typical aerosol oxidation products.

■ EXPERIMENTAL SECTION

Filter-Based Thermal Desorption System. A custom F-TD inlet system was developed for the Caltech CIMS.[24] The basic operating principles of the F-TD inlet follow those of the FIGAERO.[13] The F-TD inlet scheme and a detailed comparison with the FIGAERO can be found in the Supporting Information (Section I and Figure S1A). Evaluation of the performance of the F-TD system is described in Supporting Information, Section II. Briefly, the F-TD inlet comprises three parts: a N_2 flow control system, heating system, and filter holder. The main N_2 flow is set at 2 LPM by a mass flow controller (Horiba, SEC-4400MC), while a critical orifice extracts 200 ccm N_2 from a bypass flow open to the room air; together, these flows maintain the pressure in the ion−molecule reaction (IMR) chamber at 26.6 Torr. The heating tube of 8 in. length and 3/8 in. OD stainless steel is surrounded by ultrahigh temperature heating tape (Omega, STH051-020). The heating process involves a ramping controller (Watlow, F4SH-CKA0-01RG) and two K-type thermocouple probes (PerfectPrime) that monitor the temperature: probe 1 (TL0260) is positioned above the filter and provides the feedback to the ramping controller, while probe 2 (TL0700) is twined with the heating tape. The probes are connected to an Arduino board (UNO Rev3), and real-time data are recorded by a customized program in MATLAB (R2010) through a serial cable. The stainless steel filter holder is customized for 25 mm diameter filters with a hole for probe 1. A stainless steel porous disc pretreated by FluoroPel (Cytonix, 801A) is used to support the filter. The essential difference between the F-TD inlet and that of FIGAERO is the pressure to which the filter is exposed: 26.6 Torr versus ambient pressure. The pressure of the F-TD, however, is still much higher than the vapor pressure of typical SOA oxidation products, thus having limited impact on their evaporation behavior compared to that in the FIGAERO (see explanation in Supporting Information, Section I). Vapor wall loss is also minimized during transportation from the filter to the IMR immediately below.

CF_3O^--CIMS. The quadrupole CIMS (nominal m/z) uses CF_3O^- as the reagent ion, which has high selectivity for multifunctional compounds and hydroperoxides (ROOH).[24] CF_3O^- is generated by exposing a flow of 10 ppmv CF_3OOCF_3 in N_2 to a radioactive ^{210}Po source. In the IMR chamber, which is maintained at 26.6 Torr, the analytes M can be ionized through clustering (M·CF_3O^-), F^- transfer (HF·M − H^-), or proton transfer (M − H^-) channels. The quadrupole MS was operated in a scanning mode (m/z 50−400), with a scan rate of ∼1.5 s. Details concerning the design and characterization of CF_3O^--CIMS can be found elsewhere.[25,26]

Filter Sample Collection and Pretreatment. Analysis of α-pinene ozonolysis SOA, an extensively investigated system in the steady-state Caltech photo-oxidation flow tube reactor (CPOT)[27] consisting predominantly of monomers ($C_{7−10}$) and dimers ($C_{14−20}$), was used to evaluate the methodology. A continuous flow of α-pinene (Airgas, 20 ppm in N_2) at 75 ccm was mixed with 5 LPM purified air (generated by Parker 75-62NA), yielding a steady-state α-pinene concentration of ∼300 ppb with an average CPOT residence time of 10 min. O_3 was maintained at a mixing ratio of 1 ppm by adjusting the flow rate of purified air through an ozone generator (AnalytikJena, 97-0067-01). The high concentrations of α-pinene and O_3 in CPOT were used to generate sufficient SOA mass for further analysis. Neither seed aerosol nor OH scavenger was used. Relative humidity was <1% and temperature was maintained at 25 ± 0.2 °C. The CPOT outlet flow was pulled through an activated charcoal denuder that efficiently removed gas-phase
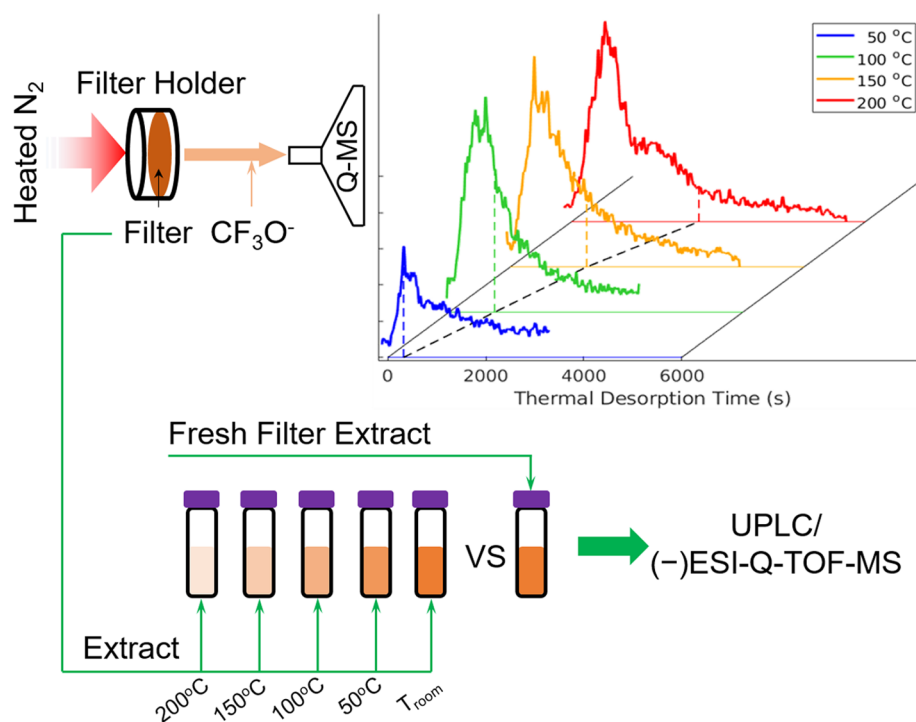
Figure 1. Filter-based thermal desorption experimental protocol. Filter samples are first thermally desorbed via the F-TD inlet system for CF_3O^--CIMS. Filters are then extracted with H_2O at room temperature into vials that are subsequently delivered to UPLC/($-$)ESI-Q-TOF-MS. Heated N_2 is ramped to different temperatures at 10 °C min^{-1} and held for 50 min to allow sufficient evaporation. Temporal profiles of thermal desorption of compound(s) at the same nominal m/z as pinic acid (HF·$C_9H_{13}O_4^-$, m/z 205) are shown as an example. Curve colors correspond to thermal desorption with temperature setpoints of 50 (blue), 100 (green), 150 (orange), and 200 (red) °C. Dashed vertical lines indicate the time at which the temperature setpoint has been reached. The black dashed line tracks the temperature setpoints for different desorptions.

organic components and O_3 before collection on Teflon filters (TF 1000, 1 μm pore size, Pall Corp.). The CPOT experimental setup is shown in Figure S4.

To evaluate the extent to which the amount of aerosol mass on the filter might bias the data analysis, filters were collected for either ~30 or ~300 min, corresponding to estimated organic aerosol mass depositions of ~1 and ~10 μg cm^{-2}, respectively (assuming an effective SOA density of 1.2 g cm^{-3} and an effective filter collection radius of 1 cm). Given an average particle diameter of 80 nm and a filter solidity of 0.1,[5] it is estimated that ~1 and 10 particle layers were present on the filters, respectively. Filters were stored at -16 °C immediately after collection until analysis.

Before sample treatment, each filter was cut into six identical slices. One of the six slices was set aside as a standard, while the other five were placed sequentially on a supporting mesh disc for F-TD/CIMS. In the thermal desorption process, the temperature of the N_2 flow above the filter was ramped at 10 °C min^{-1} (the typical working condition of FIGAERO-ToF-CIMS[5]) to maximum setpoints of 25, 50, 100, 150, and 200 °C; the 25 °C case corresponds to isothermal evaporation with dry N_2 at room temperature. After the temperature setpoint was achieved, the system was held at the setpoint for 50 min. Figure 1 diagrams the thermal desorption and extraction protocol and provides an example of the temporal profiles of thermal desorption for compounds at the same nominal m/z as pinic acid (HF·$C_9H_{13}O_4^-$, m/z 205), a well-characterized α-pinene oxidation product, for filters with 300 min sample collection. Table S1 provides an overview of the treatment applied to each filter sample.

UPLC/($-$)ESI-Q-TOF-MS. Following thermal desorption, each filter, along with the standard, was extracted in 1 mL of ultrapure water (18 MΩ, <3 ppb TOC, Millipore Milli-Q) with a mini vortexer (VMR) for 1 h at room temperature. The extracts were then delivered to the ultraperformance liquid chromatography/negative electrospray ionization quadrupole time-of-flight mass spectrometer (UPLC/($-$)ESI-Q-TOF-MS, hereafter UPLC/ESI-MS) for analysis of the remaining components on the filters.[28,29] Briefly, filter extracts were separated by a Waters ACQUITY UPLC I-Class system equipped with an ACQUITY BEH C_{18} column (1.7 μm, 2.1 mm × 50 mm) fitted with an ACQUITY BEH C_{18} VanGaurd precolumn (1.7 μm, 2.1 mm × 5 mm) at 30 °C. Samples were injected with a 10 μL volume, and the total flow rate through the column was 0.3 mL min^{-1}. Eluate was ionized by ESI in the negative ion ($-$) mode and sent to a Xevo G2-S Q-TOF-MS where ions are detected as [M $-$ H]$^-$. The mass resolution ($m/\Delta m$) is 20,000−34,000 with a mass accuracy of <5 mDa. Molecular formulas ($C_xH_yO_z$) were assigned with errors of <7 ppm. Details of the gradient-elution method, instrument working conditions and acquisition parameters, calibration protocol, and data analysis can be found elsewhere.[28,29] Note that as a result of the guard column, the SOA molecular products elute at later retention times (+0.11−0.15 min) than previously reported.[28−30]

Direct Evaporation of Particles. The design of the filter holder provides the flexibility to quickly transition between different applications. For example, the hole for probe 1 is suitable for a standard 1/4″ critical orifice, which can be used for direct sampling of aerosols in the absence of the porous disc (Figure S1B). In this setup, the temperature-ramped N_2

flow mixes with the aerosol flow and evaporates the condensed-phase compounds immediately before the IMR chamber. The temperature of the N_2 flow at the mixing point has been verified to have a linear relationship with the temperature of the heating tube, so only probe 2 is necessary. The mixing and evaporating time is on the order of 0.1 s; thus, only a portion of the condensed organic matter evaporates before the particles exit the F-TD inlet (i.e., the compounds in the gas and particle phases have not reached equilibrium during this period[4]). The change of CIMS signal S thus follows eq 1:

$$S = (E(T) - D(T)) \times \tau + I \tag{1}$$

where $E(T)$ and $D(T)$ are the temperature-dependent particle evaporation and thermal decomposition rates, τ is the residence time in the heating region, and I is the initial CIMS signal without heating. This setup is used to evaluate the thermal stability of particle-phase compounds (e.g., ROOH). As higher temperatures promote faster evaporation from the particle phase ($E \propto T$), one would expect that the CIMS signal of a thermally stable compound analyzed in this way should always increase as temperature increases (i.e., $E > D$ or $D = 0$). Accordingly, a decreasing signal as a function of increasing temperature will serve as an indication that a compound has undergone thermal decomposition at high temperatures, since the decomposition rate must exceed the evaporation rate (i.e., $E < D$).

Data Analysis. The thermal desorption profile for a given compound deposited on a filter reflects its gas-phase concentration (mass volume^{-1}) determined by the evaporation flux (mass time^{-1}) and the carrier gas flow rate (volume time^{-1}) in CIMS. The integrated mass evaporated from the filter sample (N_{evap}) and the remaining mass on the filter (N_{remain}) are complementary:

$$N_{tot} - N_{remain} = N_{evap} = \int_0^t J(t')dt' = (\dot{T})^{-1} \int_{T_0}^{T_s} J(T')$$
$$dT' + \int_{t(T_s)}^t J(t')dt' \tag{2}$$

where $J(t')$ and $J(T')$ represent the evaporation flux (mass time^{-1}) as a function of time or temperature, T' is the linear heating rate (°C s^{-1}), and T_0 and T_s are the initial temperature and setpoint, respectively. The first term on the right-hand side (RHS) of eq 2 is the integral of flux during the temperature ramping period (i.e., the conventional thermogram), and the second term represents the integral of flux when temperature is held constant at the setpoint. Figure 1 shows the temporal profile of the evaporation flux during ramping and holding periods.

The flux, $J(t')$ or $J(T')$, coming off the filter is proportional to the product of the sample vapor pressure (which increases as temperature increases) and the available surface area of the sample (which decreases with time).[31] Thus, the evaporation flux of a specific compound during thermal desorption exhibits a maximum value at a corresponding temperature, T_{max}. In addition to vapor pressure and available surface area, the thermal desorption profile of a compound also depends on the rate of reversible oligomerization and the rate of thermal decomposition of oligomers.[5] The thermal desorption profile, therefore, is not a simple curve that can be analytically represented. We fit the first term of the RHS of eq 2 to a Gaussian distribution using the simplified fitting procedure of

Lopez-Hilfiker et al.,[13] which shows good agreement ($R^2 > 0.9$). Note that the raw CIMS data have been corrected by the background signal (i.e., the signal of a blank filter subjected to the temperature ramp).

For desorption driven only by a temperature ramp, if the thermal desorption profile arises solely from authentic compounds and not desorption artifacts (e.g., decomposition), then the MFR of those compounds on the filter should be 50% at T_{max}. The equation for this behavior has the form of a complementary error function: $f(T) = \text{erfc}\left(\frac{T - T_{mid}}{\sigma_r}\right) = 1 - N_{evap}$, where T_{mid} corresponds to the temperature at which the MFR is 50%, and σ_r relates to the width of the desorption peak (an indicator of isomers, which could broaden the peak and thus increase σ_r). Note that although a sigmoidal curve is usually applied to fit the MFR of aerosol-phase components derived from thermodenuder measurements,[32] we choose the error function to be consistent with the Gaussian fitting of the thermogram.

Since the filters were held at the temperature setpoint for 50 min after the temperature ramp (the second term on the RHS of eq 2), the MFR on the filter at the end of the thermal desorption will be lower than that derived by considering only the integral of the Gaussian distribution (the first term on the RHS of eq 2). Thus, for the desorption profiles presented here, T_{mid} must be $< T_{max}$ when the profile is only a result of the authentic compounds. If $T_{mid} \geq T_{max}$, the desorption profile could result from thermal decomposition, which can be further constrained with the UPLC/ESI-MS data. See Figure S5 for clarification.

Owing to the inability of techniques that measure the evaporation flux during thermal desorption events to discriminate between signals due to authentic compounds versus artifacts of thermal decomposition, it is not possible to calculate the MFR of individual compounds from thermal desorption profiles based on CIMS signals. As such, in this study, the MFR is calculated from UPLC/ESI-MS data by taking the ratio of compound mass on the treated filters to that on the standard filter. As a result, the MFR reported in this study includes both the residual compound mass in the aerosol phase as well as that which may have been adsorbed on the filter surface. This is in contrast to Schobesberger et al.'s work,[5] which distinguished the mass in the aerosol phase from that on the filter. This approach to calculating MFR also differs from that presented in D'Ambro et al.,[17] which defines the signal fraction remaining (SFR) as the ratio of integrated thermograms prior to and following an isothermal evaporation period. The concept of SFR thus includes the contribution of the second peak in the thermogram, which is understood to be due to the thermal decomposition of oligomers.

■ RESULTS AND DISCUSSION

F-TD of α-pinene ozonolysis SOA yields two sets of complementary data: the evaporation flux monitored by CIMS and the residual filter components detected by UPLC/ESI-MS. The following discussion starts from the thermal desorption of SOA filter samples, proceeds to analysis of the remaining mass on the filter, and concludes with insights afforded from the combination of these two data sets. The evaporation of aerosol introduced directly into the F-TD/CIMS provides additional information on the thermal stability of aerosol-phase compounds.
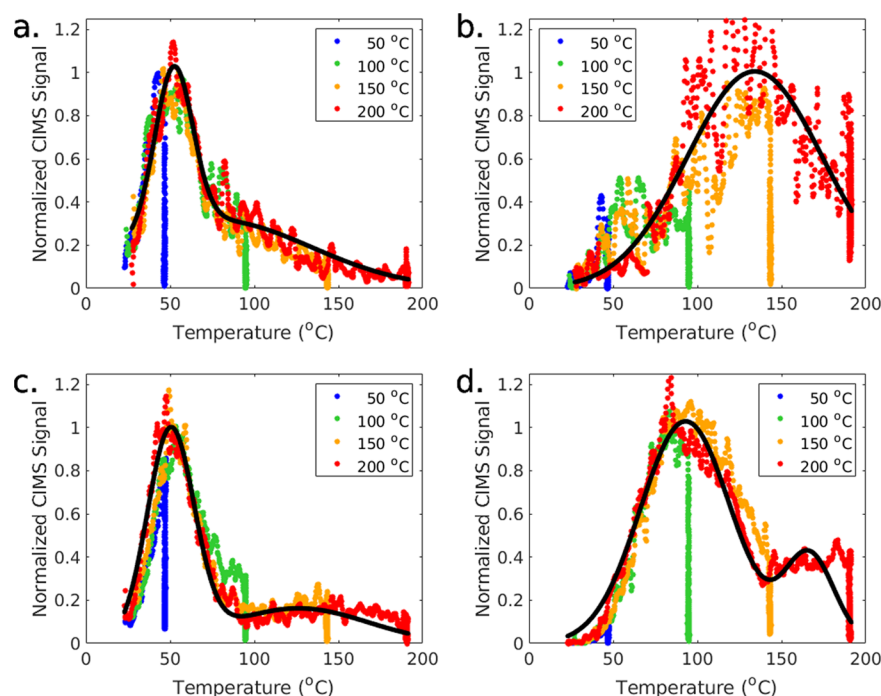
Figure 2. Thermograms of compounds with the same nominal m/z as pinonic acid (HF·$C_{10}H_{15}O_3^-$, m/z 203, panels (a) and (c) for 30 and 300 min filter collections, respectively) and pinyl-diaterpenyl ester (HF·$C_{17}H_{25}O_8^-$, m/z 377, panels (b) and (d) for 30 and 300 min filter collections, respectively). Black lines are double-Gaussian fitting curves applied to the 200 °C thermogram. The four data sets (blue, green, orange, and red) correspond to the different temperature setpoints (50, 100, 150, and 200 °C) to which the filters were ramped and then held for 50 min.

Thermal Desorption of α-Pinene Ozonolysis SOA. The room temperature (25 °C) thermal desorption scenario is analogous to isothermal evaporation. The decreasing desorption profile of compounds with a nominal m/z of 203, assumed to correspond almost exclusively to pinonic acid (HF·$C_{10}H_{15}O_3^-$) upon isothermal evaporation, is shown in Figure S6 for filter samples collected for 30 and 300 min. Although the evaporation fluxes of the 30 and 300 min filter samples show similar trends, the absolute fluxes do not scale by a factor of 0.1 (the ratio of aerosol mass loading for the 30 and 300 min collections, assuming that the evaporation flux from single particles do not interact). This suggests that the aerosol mass loading on the filter affects the evaporation rate. D'Ambro et al.[17] observed an initial rapid decrease in flux followed by slow decay during isothermal evaporation of semivolatile organic compounds from fresh α-pinene SOA. Such behavior could be a result of the slow diffusion of vapor molecules within multiparticle layers, a process that increases in importance at high aerosol mass loading.

Figure 2 shows the thermograms of compounds with the same nominal m/z as pinonic acid (HF·$C_{10}H_{15}O_3^-$, m/z 203) and pinyl-diaterpenyl ester (HF·$C_{17}H_{25}O_8^-$, m/z 377), two well-characterized α-pinene oxidation products,[30] for 30 and 300 min filter collection durations. Thermograms at four temperature setpoints (50, 100, 150, and 200 °C) are overlaid, illustrating that the thermal desorption behavior of compounds on a filter sample is independent of the temperature setpoint. A double-Gaussian function fits the raw thermogram data well ($R^2 > 0.9$). The first peak in the thermogram corresponds to the compound that is initially present in the SOA, while the second peak arises from the thermal decomposition of oligomers. From this fitting, the first peak in the thermogram can be compared and verified against the MFR on the filter, as explained in Data Analysis.

The compounds shown in Figure 2 represent α-pinene-derived monomers (a and c) and dimers (b and d), respectively. For the monomers, a distinctive narrow peak (T_{max}) exists at ~50 °C for both 30 and 300 min filter samples. This value exceeds that obtained from pure pinonic acid (<32 °C),[33] which can be explained by enhanced noncovalent H-bonding between pinonic acid and the SOA matrix as well as by the presence of isomeric/isobaric oxidation products.[5] Particle phase state could also affect the value of T_{max}, since α-pinene SOA can be semisolid under the dry conditions[34] employed in this work (25 °C, <1% RH), which may retard the rate of evaporation. The second peak of the monomer thermogram is indicative of thermal decomposition of oligomers at high temperatures. The shape of the second peak in Figure 2a is the same as those observed by Lopez-Hilfiker et al.[33] Note that the second peaks of Figure 2a,c exhibit different behavior, with the 300 min filter sample having a higher peak temperature (100 vs 130 °C). Figure S7 shows thermograms for compounds with the same nominal m/z as pinic acid (HF·$C_9H_{13}O_4^-$, m/z 205), norpinic acid (HF·$C_8H_{11}O_4^-$, m/z 191), HO-pinonic acid (HF·$C_{10}H_{15}O_4^-$, m/z 219), and diaterpenylic acid (HF·$C_8H_{13}O_5^-$, m/z 209) for 30 and 300 min filter samples. No apparent dependence of the T_{max} values of all monomers in 30 and 300 min filter samples (Table S2) on the filter aerosol mass loading was observed. This is consistent with the work of Huang et al.,[18] which reported a trend of increasing T_{max} as a function of aerosol mass loading that plateaued when the aerosol mass loading increased to >~1 $\mu g\ cm^{-2}$, the regime in which the current filter samples lie ($\geq 1\ \mu g\ cm^{-2}$). Moreover, for all monomers, the second peak occurs at a higher temperature for the 300 min filter samples.

For the dimer shown in Figure 2b,d, at lower aerosol mass loadings, the thermogram exhibits a wide single peak at ~140
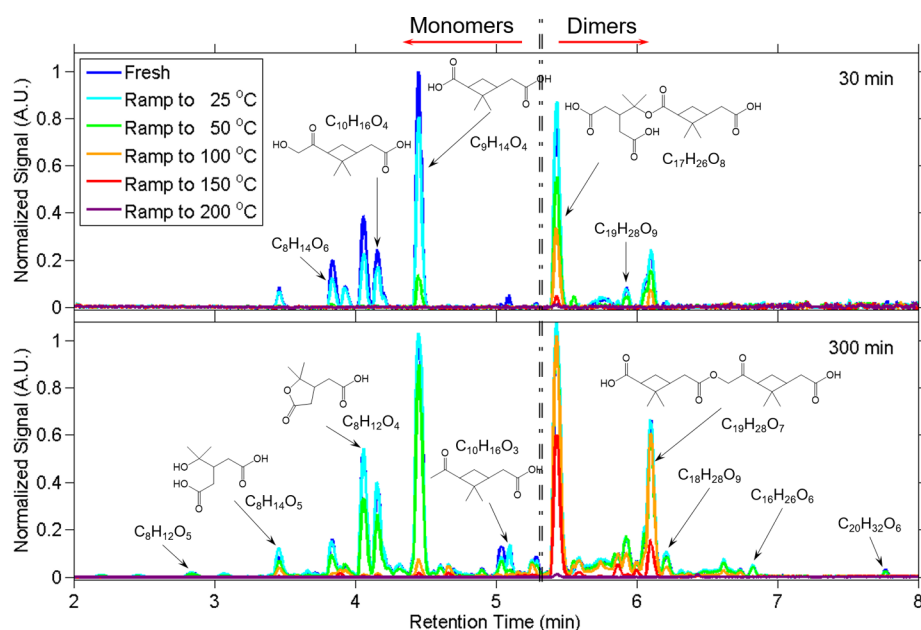
Figure 3. UPLC/(−)ESI-Q-TOF-MS BPI chromatograms of SOA formed from α-pinene ozonolysis in the CPOT, collected on Teflon filters for 30 (upper) and 300 min (lower). Molecular formulas and/or proposed structures for the dominant peaks are shown. Chromatogram colors correspond to the temperature setpoints at which the filters were thermally desorbed by the F-TD system prior to extraction. The chromatogram is roughly divided into monomer and dimer regimes based on identified molecular formulas and retention time.
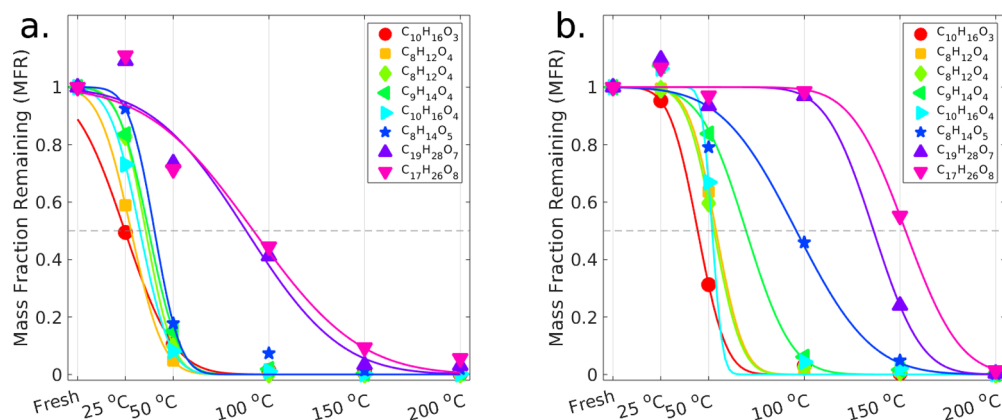
Figure 4. MFR of eight compounds identified in SOA from α-pinene ozonolysis and assigned to well-characterized oxidation products (pinonic acid $C_{10}H_{16}O_3$, terpenylic (solid square) and norpinic (solid diamond) acids $C_8H_{12}O_4$, pinic acid $C_9H_{14}O_4$, HO-pinonic acid $C_{10}H_{16}O_4$, diaterpenylic acid $C_8H_{14}O_5$, pinonyl-pinyl ester $C_{19}H_{28}O_7$, and pinyl-diaterpenyl ester $C_{17}H_{26}O_8$) as a function of the temperature setpoints at which filters were thermally desorbed by the F-TD system before extraction for (a) 30 and (b) 300 min filter collections. Data points are fitted by the complementary error function $f(T) = \mathrm{erfc}\left(\dfrac{T - T_{\mathrm{mid}}}{\sigma_{\mathrm{r}}}\right)$ (see Data Analysis for details).

°C, whereas for higher mass loadings, a bimodal thermogram is observed. Similar to the monomers, the first peak at 95 °C in Figure 2d is assigned to the evaporation of the authentic dimer (with the same nominal m/z as pinyl-diaterpenyl ester), whereas the second peak at 165 °C is attributed to the thermal decompositon of oligomers with m/z greater than the dimers observed. The broad single peak in Figure 2b is thought to be due solely to thermal decompsotion and, like the monomers, occurs at a lower temperature (140 °C) in the 30 min filter samples. We hypothesize that the difference in temperature of the second peak between the 30 and 300 min samples for both monomers and dimers is a result of larger absolute amounts of oligomers being deposited on the filter at higher aerosol mass loadings and undergoing decomposition at higher temperatures.

Remaining Fraction on Filters. Figure 3 shows the UPLC base peak ion (BPI) chromatograms of six filter samples: a fresh filter that is used as a reference and five filters that have undergone thermal desorption in the F-TD system. The molecular formulas and proposed structures of dominant compounds are marked. The chromatograms of 30 and 300 min filter samples before any treatment have similar product distributions, indicating that the mass fractions of these species are independent of collection time. However, given the dependence of ESI efficiency on molecular structure, namely, that the ESI efficiencies of dimers are at least an order of magnitude higher than those of monomers, the peak areas of the detected compounds are not proportional to their relative abundances on the filter.[23] The chromatogram can be roughly divided into two regions based on retention time (t_R) and thus

molecular size: most of the peaks at t_R< 5.4 min with cold colors (blue and green) correspond to monomer acids, while those eluted later with warm colors (orange and red) are dimer acids. Whereas most of the monomers on the filter have fully evaporated at higher temperature setpoints (≥100 °C), the persistence of dimer peaks (e.g., pinyl-diaterpenyl ester and pinonyl-pinyl ester) up to temperature setpoints of 150 °C suggests that SOA monomers and dimers evaporate at different rates upon heating. For some of the dimers, over 50% of the collected filter mass remains for the 300 min filter sample at 150 °C. Furthermore, the appreciable MFR values derived from UPLC/ESI-MS demonstrate that the sharp decrease in normalized signal to <0.05 during the 50 min desorption at the temperature setpoint (Figure 2) is not a result of the particle-phase compounds having been fully desorbed but rather is likely due to the particle morphology having been modified upon heating, thereby limiting further evaporation.

For the system studied here, 53 main products were identified from the UPLC/ESI-MS data (Table S3). Figure 4 shows the MFR (i.e., chromatographic peak area normalized by that of the fresh filter samples) of eight prominent monomeric and dimeric α-pinene oxidation products, previously characterized by LC/ESI-MS,[35,36] as a function of temperature setpoint for the 30 and 300 min filter samples. Interestingly, for both 30 and 300 min filter samples, isothermal evaporation at room temperature resulted in an MFR for dimers statistically greater than 1, while the MFR of monomers decreased in accord with their volatility. This behavior points to an additional source of dimers on the filter. Since isothermal evaporation is carried out with pure N_2 in a dark environment (i.e., oxidant- and photolysis-free), the likely source of dimers on the filter appears to be reversible oligomerization,[5] forming dimers either via decomposition of oligomers or accretion of monomers. Owing to their lower volatility, dimers produced through either oligomer decomposition or monomer accretion will accumulate on the filter, while monomers formed from oligomer decomposition will evaporate based on their volatility.[5]

T_{mid} (dashed horizontal line in Figure 4a,b) is smaller than T_{max} (e.g., Figure 2) for all of the monomers in 30 min filter samples. This behavior verifies that the first peak in the thermogram arises from direct evaporation of monomers initially present in the aerosol. Generally, T_{mid} is higher for 300 min filter samples than for 30 min filter samples, confirming the effect of aerosol mass loading on the compound evaporation rates.[18] Table S2 summarizes T_{max} and T_{mid} for six compounds in this study.

$C_8H_{12}O_4$ isomers assigned to terpenylic and norpinic acid exhibit virtually the same MFR decay profile for the 300 min sample (Figure 4b) The thermogram for compounds with the same nominal m/z as terpenylic and norpinic acid (HF· $C_8H_{11}O_4^-$, m/z 191) also has a narrow first peak (Figure S7), suggesting that monomer isomers do not cover a wide range of saturation vapor pressure. The narrow thermogram and similar MFR profiles indicate that despite the notable structural dissimilarities between terpenylic and norpinic acids, the thermal behavior of the isomers is similar. However, additional measurements are needed to confirm the generality of this observation. The large σ_r of the two dimers in the 30 min filter sample (illustrated in Figure 4a by the shallow slope of the fit) is consistent with the observed broad Gaussian distribution in their thermograms (Figure 2), further suggesting that thermal

decomposition of oligomers could be an important source of dimers upon heating.

At large aerosol mass loadings, a high fraction of dimers remains on the filter at high temperatures, with 50 min at 200 °C required for full evaporation. Below 200 °C, the dimer MFR is higher for all temperatures at higher mass loadings. This has been suggested to be the result of an artifact: multiparticle layers on the filter due to long collection time limit the vapor diffusion between layers.[18,37] The effect of high mass loading on the volatility of filter samples is also exemplified by the compound $C_8H_{14}O_5$ (the same molecular formula as diaterpenylic acid), which has a T_{mid} of ∼100 °C for the 300 °C sam ple, well exceeding the T_{mid} of ∼40 °C for the 30 min sample and T_{max} of ∼50 °C in its thermogram (Figure S7). Since the width of the thermogram is large, the profile of $C_8H_{14}O_5$ could be a result of oligomer dissociation at high aerosol mass loadings.

Thermal Stability of SOA Molecular Products. Thermal decomposition of monomers, dimers, and oligomers, particularly those with labile functionalities (e.g., organic (hydro)-peroxides), occurs in thermal-induced desorption of SOA.[13,20,38,39]

Monomers. We first use the direct evaporation of aerosol-phase components to evaluate the thermal stability of compounds expected to contain ROOH moities.[40,41] The CF_3O^--CIMS has been shown to have high sensitivity to ROOH via reagent ion clustering (ROOH·CF_3O^-).[24,25] Figure S8 shows the thermograms of two classes of α-pinene ozonolysis products with distinct desorption behaviors (i.e., increasing vs decreasing signal intensity with increasing desorption temperature). The signal of the nominal m/z assigned to pinonic acid, a relatively volatile species, increases by ∼25% at 200 versus 25 °C, while the signals attributed to pinic acid and OH-pinonic acid at 200 °C are a factor of 2−3 higher than those at 25 °C. In contrast, the signals previously assigned to ROOH species[30,41] decrease at 200 °C to 30−50% of their intensities at 25 °C. Generally, higher temperatures prompt faster evaporation flux from particles; thus, the signals should monotonically increase as temperature increases. Since the ionization efficiency is not a function of temperature (i.e., the kinetics in the IMR are already in the collision-limited regime[42]), the increasing signal upon heating is due to accelerated evaporation ($E > D$) or transformation from other species through chemical reactions (e.g., thermal decomposition of oligomers), whereas the decreasing trend is a result of thermal instability at high temperatures ($E < D$). For example, Pagonis and Ziemann[43] reported that the particle-phase chemistry of hydroperoxycarbonls can eliminate the −OOH group. Note that gas-phase species, including O_3, were not removed before introducing aerosols to the heating region, which could lead to artifacts via oxidation at high temperatures.[44] We also cannot exclude the possibility of ROOH decomposition on the metal surface at high temperatures as a possible artifact, since the inside surface of IMR was not coated with an inert material (e.g., Teflon). Particle-phase peroxides are known to be labile,[45] making detection challenging. The thermal instability of compounds expected to contain ROOH demonstrated here through direct evaporation of α-pinene SOA suggests that F-TD may not be the best method to study condensed-phase peroxides.[29]

Dimers. Since α-pinene-derived oligomers (carbon number > 20) are not detected by either F-TD/CIMS or UPLC/ESI-MS, we evaluated two possible mechanistic hypotheses
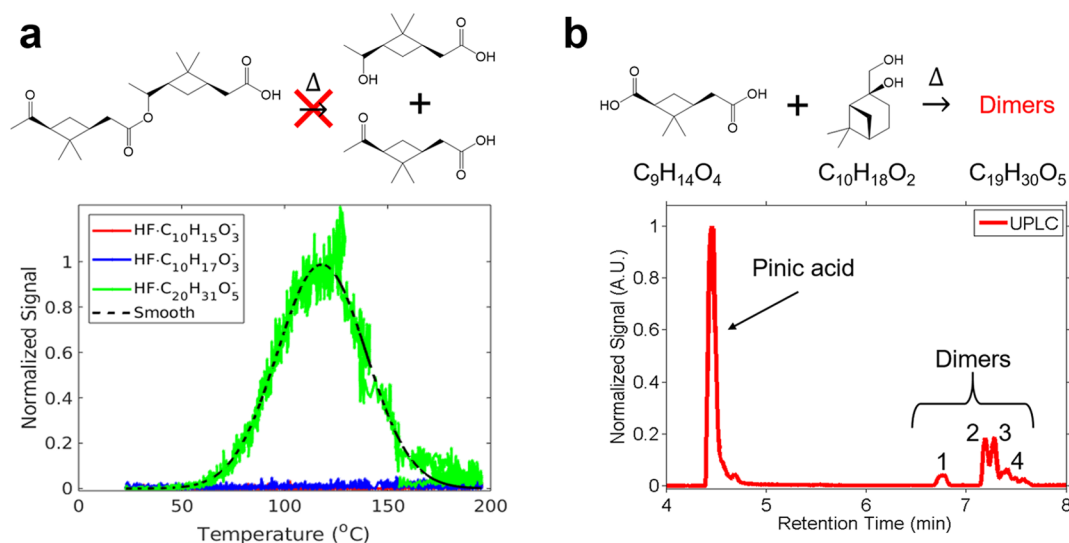
Figure 5. (a) Thermogram of a synthesized pinene-derived ester (HF·$C_{20}H_{31}O_5^-$, m/z 371). The absence of signals at the same nominal m/z as monomeric decomposition products, pinonic acid (HF·$C_{10}H_{15}O_3^-$, m/z 203) or pinolic acid (HF·$C_{10}H_{17}O_3^-$, m/z 205) during the temperature ramp suggests that the ester is stable at high temperatures, consistent with the conclusion by Claflin and Ziemann.[39] (b) UPLC/(−)ESI-Q-TOF-MS BPI chromatogram of a mixture of enantiopure *cis*-pinic acid ($C_9H_{14}O_4$) and β-pinene diol ($C_{10}H_{18}O_2$) after heating at 100 °C in the F-TD inlet. The appearance of four distinct dimer peaks ($C_{19}H_{30}O_5$) demonstrates that heating has induced condensation of *cis*-pinic acid and β-pinene diol.

concerning the fate of dimers to explain the observed modes in the monomer and dimer thermograms: (1) thermal decomposition of dimers at high temperatures and (2) heat-induced accretion of monomers.

F-TD was performed on a synthesized pinene-derived dimer ester standard (Figure 5a; see Kenseth et al.[23] for synthesis and characterization details) that was dissolved in ethanol and deposited on a filter by a microsyringe. CIMS signals corresponding to the monomeric decomposition products (i.e., pinonic acid and pinolic acid) of the dimer via cleavage of the ester bond were not observed under standard thermal desorption conditions. This conclusion agrees with that of Claflin and Ziemann[39] that esters are stable at high temperatures.

The possible formation of dimers from monomers upon heating was also explored, since, as indicated by the higher MFR values at higher mass loadings (see the Remaining Fraction on Filters section), the morphology and/or composition of the particles changes upon heating-induced evaporation and may increase the probability of condensed-phase reactions. To carry out this test, equimolar (~35 μmol) masses of enantiopure *cis*-pinic acid (see Kenseth et al.[23] for synthesis and characterization details) and enantiopure β-pinene diol (synthesis and characterization details available on request) were ground and deposited on a filter, instead of dissolving the compounds in ethanol and depositing the solution. Since the thermograms of observed dimers in α-pinene SOA exhibit a T_{max} of ~100 °C (Figure 2, the F-TD was maintained at 100 °C until complete desorption of the sample was achieved. Instead of sending the resulting hot and highly concentrated vapors to the CIMS, a Teflon filter was placed ~0.5 m downstream to capture nucleated particles formed due to the steep temperature gradient; the filter was then extracted and delivered to the UPLC/ESI-MS. The UPLC BPI chromatogram is shown in Figure 5b. In contrast to the result of Zhao et al.[21] that mixed organic acids displayed no oligomer formation on heating, four distinct dimer peaks with

the formula $C_{19}H_{30}O_5$ (i.e., the formal condensation product of *cis*-pinic acid ($C_9H_{14}O_4$) and β-pinene diol ($C_{10}H_{18}O_2$)) are observed. The absence of observable dimer formation in a control experiment in which an equimolar (~1.0 mM) aqueous solution of the two monomers was directly subjected to UPLC/ESI-MS demonstrates that these monomers undergo thermally induced condensation reactions (e.g., esterification) during F-TD analysis rather than on the filter or in solution at 25 °C. This experiment indicates that at high temperatures, if monomers remain, dimer formation via thermal accretion chemistry is possible. This situation is most likely to occur under high aerosol mass loadings and (semi)solid particle phase state or when temperature increases rapidly (e.g., a step increase of the temperature in a thermodenuder), where the limitation of monomer evaporation increases the likelihood of accretion reactions. Note that the particle-phase reaction could also occur over time in the absence of oxidants even at room temperature.[46,47]

Atmospheric Implications. Filter-based thermal desorption is widely used to analyze SOA molecular constituents. We show here that aerosol mass loadings higher than typically collected for filter-based thermal desorption can lead to significantly different characteristics of the thermal desorption profile, likely an artifact arising from diffusion limitations of vapor molecules between the multiple particle layers deposited on the filter. This situation can be viewed as analogous to that in which a (semi)solid particle phase state limits vapor diffusion within particles. The condensation of acid and alcohol monomers to form dimers (likely ester dimers) upon fast heating provides direct evidence that unexpected, thermally driven particle-phase chemistry could bias the analysis of the thermogram.

Simultaneous examination of both gas- and particle-phase components provides direct evidence that the second peak at higher temperatures in the thermograms of monomers is a result of thermal decomposition of oligomers. Although it is not possible to resolve those oligomers that contribute to the

second peak in the thermogram with the current technique, we have demonstrated that the first peak of the thermogram arises from the evaporation of pure compounds through combination with UPLC/ESI-MS, which resolves the remaining compounds on the filter. The UPLC/ESI-MS is able to isolate isomers, further verifying that the multimode thermogram of a monomer is not a result of isomers with distinct volatility but arises from the thermal decomposition of oligomers.

With the direct evaporation of aerosol samples, we demonstrate that particle-phase compounds assigned to ROOH, a highly labile species, undergo decomposition as temperature increases; however, the decomposition trends as a function of temperature are compound-dependent. In contrast, a synthesized pinene-derived dimer ester, a representative surrogate of dimers present in α-pinene ozonolysis SOA, exhibits thermal stability at high temperatures. Thus, thermal desorption works well for thermally stable condensed-phase compounds but is not an appropriate method to quantitatively resolve labile particle-phase species.

Thermally induced evaporation of SOA separates the condensed-phase components based on their volatility, a process for which heat-accelerated condensed-phase reactions (e.g., oligomerization and decomposition) are highly likely. Interpretation of evaporation flux of possible isomers or dissociation of oligomers can be constrained from the remaining components on the filter. Using the dry α-pinene ozonolysis nucleation system, we demonstrate that the complementary F-TD/CIMS + UPLC/ESI-MS method of detecting SOA components at the molecular level provides important insights into SOA formation.

ASSOCIATED CONTENT

ⓢ Supporting Information

The Supporting Information is available free of charge at https://pubs.acs.org/doi/10.1021/acs.est.0c01779.

Section I, filter-based thermal desorption system; Section II, performance of F-TD; Section III, sample generation; Section IV, data analysis; Section V, isothermal evaporation; Section VI, thermograms; Section VII, identified main compounds from UPLC/ESI-MS; and Section VIII, decomposition of hydroperoxides (PDF)

AUTHOR INFORMATION

Corresponding Author

John H. Seinfeld − *Division of Chemistry and Chemical Engineering and Division of Engineering and Applied Science, California Institute of Technology, Pasadena, California 91125, United States;* ⓘ orcid.org/0000-0003-1344-4068; Phone: +1 626 395 4635; Email: seinfeld@caltech.edu; Fax: +1 626 568 8743

Authors

Yuanlong Huang − *Division of Geological and Planetary Sciences, California Institute of Technology, Pasadena, California 91125, United States;* ⓘ orcid.org/0000-0002-6726-8904

Christopher M. Kenseth − *Division of Chemistry and Chemical Engineering, California Institute of Technology, Pasadena, California 91125, United States;* ⓘ orcid.org/0000-0003-3188-2336

Nathan F. Dalleska − *Division of Geological and Planetary Sciences, California Institute of Technology, Pasadena, California 91125, United States*

Complete contact information is available at:
https://pubs.acs.org/10.1021/acs.est.0c01779

Notes
The authors declare no competing financial interest.

REFERENCES

(1) George, I. J.; Abbatt, J. P. D. Heterogeneous oxidation of atmospheric aerosol particles by gas-phase radicals. *Nat. Chem.* **2010**, *2*, 713.

(2) Reid, J. P.; Bertram, A. K.; Topping, D. O.; Laskin, A.; Martin, S. T.; Petters, M. D.; Pope, F. D.; Rovelli, G. The viscosity of atmospherically relevant organic particles. *Nat. Commun.* **2018**, *9*, 956.

(3) Chow, J. C.; Yu, J. Z.; Watson, J. G.; Ho, S. S. H.; Bohannan, T. L.; Hays, M. D.; Fung, K. K. The application of thermal methods for determining chemical composition of carbonaceous aerosols: A review. *J. Environ. Sci. Health A* **2007**, *42*, 1521−1541.

(4) Cappa, C. D. A model of aerosol evaporation kinetics in a thermodenuder. *Atmos. Meas. Technol.* **2010**, *3*, 579−592.

(5) Schobesberger, S.; D'Ambro, E. L.; Lopez-Hilfiker, F. D.; Mohr, C.; Thornton, J. A. A model framework to retrieve thermodynamic and kinetic properties of organic aerosol from composition-resolved thermal desorption measurements. *Atmos. Chem. Phys.* **2018**, *18*, 14757−14785.

(6) Hearn, J. D.; Smith, G. D. A chemical ionization mass spectrometry method for the online analysis of organic aerosols. *Anal. Chem.* **2004**, *76*, 2820−2826.

(7) Smith, J. N.; Moore, K. F.; McMurry, P. H.; Eisele, F. L. Atmospheric measurements of sub-20 nm diameter particle chemical composition by thermal desorption chemical ionization mass spectrometry. *Aerosol Sci. Technol.* **2004**, *38*, 100−110.

(8) DeCarlo, P. F.; Kimmel, J. R.; Trimborn, A.; Northway, M. J.; Jayne, J. T.; Aiken, A. C.; Gonin, M.; Fuhrer, K.; Horvath, T.; Docherty, K. S.; Worsnop, D. R.; Jimenez, J. L. Field-deployable, high-resolution, time-of-flight aerosol mass spectrometer. *Anal. Chem.* **2006**, *78*, 8281−8289.

(9) Huffman, J. A.; Ziemann, P. J.; Jayne, J. T.; Worsnop, D. R.; Jimenez, J. L. Development and characterization of a fast-stepping/scanning thermodenuder for chemically-resolved aerosol volatility measurements. *Aerosol Sci. Technol.* **2008**, *42*, 395−407.

(10) Cappa, C. D.; Wilson, K. R. Evolution of organic aerosol mass spectra upon heating: implications for OA phase and partitioning behavior. *Atmos. Chem. Phys.* **2011**, *11*, 1895−1911.

(11) Tobias, H. J.; Ziemann, P. J. Compound identification in organic aerosols using temperature-programmed thermal desorption particle beam mass spectrometry. *Anal. Chem.* **1999**, *71*, 3428−3435.

(12) Yatavelli, R. L. N.; Thornton, J. A. Particulate organic matter detection using a micro-orifice volatilization impactor coupled to a chemical ionization mass spectrometer (MOVI-CIMS). *Aerosol Sci. Technol.* **2010**, *44*, 61−74.

(13) Lopez-Hilfiker, F. D.; Mohr, C.; Ehn, M.; Rubach, F.; Kleist, E.; Wildt, J.; Mentel, T. F.; Lutz, A.; Hallquist, M.; Worsnop, D.; Thornton, J. A. A novel method for online analysis of gas and particle composition: description and evaluation of a filter inlet for gases and aerosols (FIGAERO). *Atmos. Meas. Tech.* **2014**, *7*, 983−1001.

(14) Williams, B. J.; Goldstein, A. H.; Kreisberg, N. M.; Hering, S. V. In situ measurements of gas/particle-phase transitions for atmospheric semivolatile organic compounds. *Proc. Natl. Acad. Sci. U. S. A.* **2010**, *107*, 6676−6681.

(15) Isaacman, G.; Kreisberg, N. M.; Yee, L. D.; Worton, D. R.; Chan, A. W. H.; Moss, J. A.; Hering, S. V.; Goldstein, A. H. Online derivatization for hourly measurements of gas- and particle-phase semi-volatile oxygenated organic compounds by thermal desorption aerosol gas chromatography (SV-TAG). *Atmos. Meas. Tech.* **2014**, *7*, 4417−4429.

(16) Yatavelli, R. L. N.; Stark, H.; Thompson, S. L.; Kimmel, J. R.; Cubison, M. J.; Day, D. A.; Campuzano-Jost, P.; Palm, B. B.; Hodzic, A.; Thornton, J. A.; Jayne, J. T.; Worsnop, D. R.; Jimenez, J. L. Semicontinuous measurements of gas-particle partitioning of organic acids in a ponderosa pine forest using a MOVI-HRToF-CIMS. *Atmos. Chem. Phys.* **2014**, *14*, 1527−1546.

(17) D'Ambro, E. L.; Schobesberger, S.; Zaveri, R. A.; Shilling, J. E.; Lee, B. H.; Lopez-Hilfiker, F. D.; Mohr, C.; Thornton, J. A. Isothermal evaporation of α-pinene ozonolysis SOA: volatility, phase state, and oligomeric composition. *ACS Earth Space Chem.* **2018**, *2*, 1058−1067.

(18) Huang, W.; Saathoff, H.; Pajunoja, A.; Shen, X.; Naumann, K.-H.; Wagner, R.; Virtanen, A.; Leisner, T.; Mohr, C. α-Pinene secondary organic aerosol at low temperature: chemical composition and implications for particle viscosity. *Atmos. Chem. Phys.* **2018**, *18*, 2883−2898.

(19) Steiner, T. The hydrogen bond in the solid state. *Angew. Chem., Int. Ed.* **2002**, *41*, 48−76.

(20) Stark, H.; Yatavelli, R. L. N.; Thompson, S. L.; Kang, H.; Krechmer, J. E.; Kimmel, J. R.; Palm, B. B.; Hu, W.; Hayes, P. L.; Day, D. A.; Campuzano-Jost, P.; Canagaratna, M. R.; Jayne, J. T.; Worsnop, D. R.; Jimenez, J. L. Impact of thermal decomposition on thermal desorption instruments: advantage of thermogram analysis for quantifying volatility distributions of organic species. *Environ. Sci. Technol.* **2017**, *51*, 8491−8500.

(21) Zhao, Z.; Yang, X.; Lee, J.; Tolentino, R.; Mayorga, R.; Zhang, W.; Zhang, H. Diverse Reactions in Highly Functionalized Organic Aerosols during Thermal Desorption. *ACS Earth Space Chem.* **2020**, *4*, 283−296.

(22) Willoughby, A. S.; Wozniak, A. S.; Hatcher, P. G. A molecular-level approach for characterizing water-insoluble components of ambient organic aerosol particulates using ultrahigh-resolution mass spectrometry. *Atmos. Chem. Phys.* **2014**, *14*, 10299−10314.

(23) Kenseth, C. M.; Hafeman, N. J.; Huang, Y.; Dalleska, N. F.; Stoltz, B. M.; Seinfeld, J. H. Synthesis of carboxylic acid and dimer ester surrogates to constrain the abundance and distribution of molecular products in α -pinene and β-pinene secondary organic aerosol. *Environ. Sci. Technol.* DOI: 10.1021/acs.est.0c01566.

(24) Crounse, J. D.; McKinney, K. A.; Kwan, A. J.; Wennberg, P. O. Measurement of gas-phase hydroperoxides by chemical ionization mass spectrometry. *Anal. Chem.* **2006**, *78*, 6726−6732.

(25) St. Clair, J. M.; McCabe, D. C.; Crounse, J. D.; Steiner, U.; Wennberg, P. O. Chemical ionization tandem mass spectrometer for the in situ measurement of methyl hydrogen peroxide. *Rev. Sci. Instrum.* **2010**, *81*, 094102.

(26) Paulot, F.; Crounse, J. D.; Kjaergaard, H. G.; Kurten, A.; St. Clair, J. M.; Seinfeld, J. H.; Wennberg, P. O. Unexpected epoxide formation in the gas-phase photooxidation of isoprene. *Science* **2009**, *325*, 730−733.

(27) Huang, Y.; Coggon, M. M.; Zhao, R.; Lignell, H.; Bauer, M. U.; Flagan, R. C.; Seinfeld, J. H. The Caltech photooxidation flow tube reactor: design, fluid dynamics and characterization. *Atmos. Meas. Tech.* **2017**, *10*, 839−867.

(28) Kenseth, C. M.; Huang, Y.; Zhao, R.; Dalleska, N. F.; Hethcox, J. C.; Stoltz, B. M.; Seinfeld, J. H. Synergistic O3 + OH oxidation pathway to extremely low-volatility dimers revealed in β-pinene secondary organic aerosol. *Proc. Natl. Acad. Sci. U. S. A.* **2018**, *115*, 8301−8306.

(29) Zhao, R.; Kenseth, C. M.; Huang, Y.; Dalleska, N. F.; Seinfeld, J. H. Iodometry-assisted liquid chromatography electrospray ionization mass spectrometry for analysis of organic peroxides: an application to atmospheric secondary organic aerosol. *Environ. Sci. Technol.* **2018**, *52*, 2108−2117.

(30) Zhang, X.; McVay, R. C.; Huang, D. D.; Dalleska, N. F.; Aumont, B.; Flagan, R. C.; Seinfeld, J. H. Formation and evolution of molecular products in α-pinene secondary organic aerosol. *Proc. Natl. Acad. Sci. U. S. A.* **2015**, *112*, 14168−14173.

(31) Cappa, C. D.; Lovejoy, E. R.; Ravishankara, A. R. Determination of evaporation rates and vapor pressures of very low volatility compounds: a study of the C4-C10 and C12 dicarboxylic acids. *J. Phys. Chem. A* **2007**, *111*, 3099−3109.

(32) Emanuelsson, E. U.; Watne, Å. K.; Lutz, A.; Ljungström, E.; Hallquist, M. Influence of humidity, temperature, and radicals on the formation and thermal properties of secondary organic aerosol (SOA) from ozonolysis of β-pinene. *J. Phys. Chem. A* **2013**, *117*, 10346−10358.

(33) Lopez-Hilfiker, F. D.; Mohr, C.; Ehn, M.; Rubach, F.; Kleist, E.; Wildt, J.; Mentel, T. F.; Carrasquillo, A. J.; Daumit, K. E.; Hunter, J. F.; Kroll, J. H.; Worsnop, D. R.; Thornton, J. A. Phase partitioning and volatility of secondary organic aerosol components formed from α-pinene ozonolysis and OH oxidation: the importance of accretion products and other low volatility compounds. *Atmos. Chem. Phys.* **2015**, *15*, 7765−7776.

(34) Liu, P.; Li, Y. J.; Wang, Y.; Gilles, M. K.; Zaveri, R. A.; Bertram, A. K.; Martin, S. T. Lability of secondary organic particulate matter. *Proc. Natl. Acad. Sci. U. S. A.* **2016**, *113*, 12643−12648.

(35) Yasmeen, F.; Vermeylen, R.; Szmigielski, R.; Iinuma, Y.; Böge, O.; Herrmann, H.; Maenhaut, W.; Claeys, M. Terpenylic acid and related compounds: precursors for dimers in secondary organic aerosol from the ozonolysis of α- and β-pinene. *Atmos. Chem. Phys.* **2010**, *10*, 9383−9392.

(36) Yasmeen, F.; Vermeylen, R.; Maurin, N.; Perraudin, E.; Doussin, J.-F.; Claeys, M. Characterisation of tracers for aging of α-pinene secondary organic aerosol using liquid chromatography/negative ion electrospray ionisation mass spectrometry. *Environ. Chem.* **2012**, *9*, 236−246.

(37) Kolesar, K. R.; Chen, C.; Johnson, D.; Cappa, C. D. The influences of mass loading and rapid dilution of secondary organic aerosol on particle volatility. *Atmos. Chem. Phys.* **2015**, *15*, 9327−9343.

(38) Hall, W. A., IV; Johnston, M. V. The thermal-stability of oligomers in alpha-pinene secondary organic aerosol. *Aerosol Sci. Technol.* **2012**, *46*, 983−989.

(39) Claflin, M. S.; Ziemann, P. J. Thermal desorption behavior of hemiacetal, acetal, ether, and ester oligomers. *Aerosol Sci. Technol.* **2019**, *53*, 473−484.

(40) Docherty, K. S.; Wu, W.; Lim, Y. B.; Ziemann, P. J. Contributions of organic peroxides to secondary aerosol formed from reactions of monoterpenes with O3. *Environ. Sci. Technol.* **2005**, *39*, 4049−4059.

(41) Eddingsaas, N. C.; Loza, C. L.; Yee, L. D.; Seinfeld, J. H.; Wennberg, P. O. α-pinene photooxidation under controlled chemical conditions - Part 1: Gas-phase composition in low- and high-NOx environments. *Atmos. Chem. Phys.* **2012**, *12*, 6489−6504.

(42) Lopez-Hilfiker, F. D.; Iyer, S.; Mohr, C.; Lee, B. H.; D'Ambro, E. L.; Kurtén, T.; Thornton, J. A. Constraining the sensitivity of iodide adduct chemical ionization mass spectrometry to multifunctional organic molecules using the collision limit and thermodynamic stability of iodide ion adducts. *Atmos. Meas. Technol.* **2016**, *9*, 1505−1512.

(43) Pagonis, D.; Ziemann, P. J. Chemistry of hydroperoxycarbonyls in secondary organic aerosol. *Aerosol Sci. Technol.* **2018**, *52*, 1178−1193.

(44) Batakliev, T.; Georgiev, V.; Anachkov, M.; Rakovsky, S. Ozone decomposition. *Interdiscip. Toxicol.* **2014**, *7*, 47−59.

(45) Krapf, M.; El Haddad, I.; Bruns, E. A.; Molteni, U.; Daellenbach, K. R.; Prévôt, A. S. H.; Baltensperger, U.; Dommen, J.

Labile Peroxides in Secondary Organic Aerosol. *Chem* **2016**, *1*, 603−616.

(46) Tritscher, T.; Dommen, J.; DeCarlo, P. F.; Gysel, M.; Barmet, P. B.; Praplan, A. P.; Weingartner, E.; Prévôt, A. S. H.; Riipinen, I.; Donahue, N. M.; Baltensperger, U. Volatility and hygroscopicity of aging secondary organic aerosol in a smog chamber. *Atmos. Chem. Phys.* **2011**, *11*, 11477−11496.

(47) Donahue, N. M.; Henry, K. M.; Mentel, T. F.; Kiendler-Scharr, A.; Spindler, C.; Bohn, B.; Brauers, T.; Dorn, H. P.; Fuchs, H.; Tillmann, R.; Wahner, A.; Saathoff, H.; Naumann, K.-H.; Möhler, O.; Leisner, T.; Müller, L.; Reinnig, M.-C.; Hoffmann, T.; Salo, K.; Hallquist, M.; Frosch, M.; Bilde, M.; Tritscher, T.; Barmet, P.; Praplan, A. P.; DeCarlo, P. F.; Dommen, J.; Prévôt, A. S. H.; Baltensperger, U. Aging of biogenic secondary organic aerosol via gas-phase OH radical reactions. *Proc. Natl. Acad. Sci. U. S. A.* **2012**, *109*, 13503−13508.

A p p e n d i x   D

PROBING THE OH OXIDATION OF PINONIC ACID AT THE AIR-WATER INTERFACE USING FIELD-INDUCED DROPLET IONIZATION MASS SPECTROMETRY (FIDI-MS)

Probing the OH Oxidation of Pinonic Acid at the Air−Water Interface Using Field-Induced Droplet Ionization Mass Spectrometry (FIDI-MS)

Yuanlong Huang,[†,∥] Kevin M. Barraza,[‡,∥] Christopher M. Kenseth,[‡] Ran Zhao,[‡,⊥] Chen Wang,[¶] J. L. Beauchamp,[‡] and John H. Seinfeld*[,‡,§]

[†]Division of Geological and Planetary Sciences, California Institute of Technology, Pasadena, California 91125, United States

[‡]Division of Chemistry and Chemical Engineering, California Institute of Technology, Pasadena, California 91125, United States

[¶]Department of Chemistry and Department of Physical and Environmental Sciences, University of Toronto, Toronto, Ontario M1C 1A4, Canada

[§]Division of Engineering and Applied Science, California Institute of Technology, Pasadena, California 91125, United States

S *Supporting Information*

ABSTRACT: Gas and aqueous phases are essential media for atmospheric chemistry and aerosol formation. Numerous studies have focused on aqueous-phase reactions as well as coupled gas/aqueous-phase mass transport and reaction. Few studies have directly addressed processes occurring at the air−water interface, especially involving surface-active compounds. We report here the application of field-induced droplet ionization mass spectrometry (FIDI-MS) to chemical reactions occurring at the atmospheric air−water interface. We determine the air−water interfacial OH radical reaction rate constants for sodium dodecyl sulfate (SDS), a common surfactant, and pinonic acid (PA), a surface-active species and proxy for biogenic atmospheric oxidation products, as 2.87×10^{-8} and 9.38×10^{-8} cm^2 molec^{-1} s^{-1}, respectively. In support of the experimental data, a comprehensive gas-surface-aqueous multiphase transport and reaction model of general applicability to atmospheric interfacial processes is developed. Through application of the model, PA is shown to be oxidized exclusively at the air−water interface of droplets with a diameter of 5 μm under typical ambient OH levels. In the absence of interfacial reaction, aqueous- rather than gas-phase oxidation is the major PA sink. We demonstrate the critical importance of air−water interfacial chemistry in determining the fate of surface-active species.
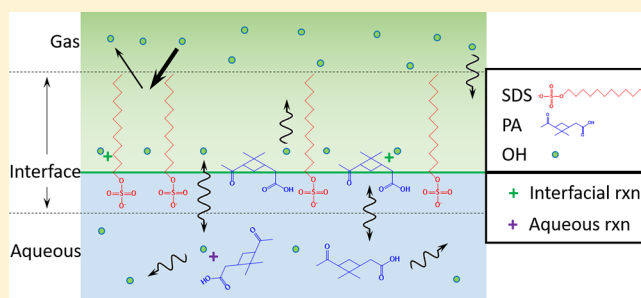
INTRODUCTION

The hydroxyl radical (OH) is the fundamental oxidant in the atmosphere. In addition to reaction with gas-phase molecules (e.g., volatile organic compounds), OH reaction can modify the physicochemical properties (e.g., surface tension, hygroscopicity, composition, etc.) of airborne particles through heterogeneous chemistry.[1] Heterogeneous OH-initiated oxidation of particles can be confined to the interface due to the particle bulk properties, such as high viscosity.[2] The air−water interface is ubiquitous in the atmosphere owing to the high surface-to-volume ratio of cloud and fog droplets. Moreover, heterogeneous reaction at the air−water interface can be facilitated if the air−water interface lowers the reaction energy barrier.[3] In addition, organic molecules at the air−water interface may have preferred orientation as a result of hydrogen bonding involving substituent groups;[4] thus, the reaction mechanisms at the air−water interface can differ from those of gas- and aqueous-phase reactions.[5−11] Studies of the air−water interfacial oxidation of organic compounds have been focused on the effects of substitutions,[12] unsaturation,[13,14] and chain length[15] on reaction kinetics and mechanisms.

Pinonic acid (PA) is a major oxidation product of α-pinene, one of the most abundant biogenic volatile organic compounds emitted to the atmosphere (global emissions estimated at 66.1 Tg/y).[16] Studies have focused on gas- and aqueous-phase oxidation of PA by OH.[17,18] Upon oxidation by OH, PA has been shown to have a high potential to form the secondary organic aerosols (SOA).[19,20] With a saturation vapor pressure of $\sim 7 \times 10^{-5}$ Pa at 296 K,[21] PA partitions between the gas and particle phases. Given its high Henry's law constant of $\sim 2 \times 10^7$ M atm^{-1},[22] PA tends to reside in the aqueous phase under cloudy and foggy conditions, or in the presence of aerosol liquid water. Although PA has been shown to be a highly surface-active species in the atmosphere,[23] limited studies have been directed to its behavior at the air−water interface.[8,24] Enami and Sakamoto[24] showed that PA resides at the air−water interface and observed peroxyl radicals and hydroperoxides at the early stage of exposure of PA solution droplets to OH. Though OH oxidation of PA at the air−water interface

is rapid, kinetic data of the interfacial reaction have been lacking. Lai et al.[25] estimated the atmospheric lifetime of PA as 2.1−3.3 days under environmentally relevant humidity conditions based on heterogeneous OH oxidation of PA film as opposed to an actual air−water interface. Given its high surface activity and tendency to partition to the aqueous phase, investigation of mechanisms and kinetics of interfacial oxidation of PA by OH under atmospheric conditions is addressed here.

We employ field-induced droplet ionization mass spectrometry (FIDI-MS) to investigate the OH oxidation of pinonic acid at the air−water interface.[26,27] FIDI-MS is differentiated from other mass spectrometric techniques by the ability to perform online detection of chemical species at the air−water interface via a surface-selective sampling mechanism, for which the ionization process has been studied extensively. The FIDI sampling apparatus produces millimeter-sized water droplets containing analytes at concentrations relevant to the ambient atmosphere (i.e., clouds, fog, and aerosol liquid water). Because of the specificity of sampling, FIDI-MS has been employed to monitor the adsorption and heterogeneous chemistry of organic compounds at the air−water interface of both atmospherically[28−30] and biologically[31−33] relevant systems. The controllable time scale for reaction in FIDI-MS makes it possible to track the kinetics of interfacial reactions over many half-lives and multiple generations of oxidation.

Through study of the OH oxidation of PA at the air−water interface with FIDI-MS, we seek to elucidate the mechanistic details of its surface reaction. To interpret the kinetic data, we develop a gas-surface-aqueous multiphase transport and reaction model that describes the heterogeneous OH oxidation of PA and constrains the surface reaction rate constant of PA + OH at the air−water interface. For the first time, the interplay between chemistry, diffusion, and phase-partitioning occurring at a droplet's air−water interface is investigated. We demonstrate that under typical ambient OH levels ($\sim 10^6$ molecules cm^{-3}), the majority of the multiphase PA oxidation occurs on the surface of water droplets representative of cloud/fogwater. In short, the present study addresses the importance of interfacial oxidation for surface-active atmospheric species.

■ METHODS

Experimental Setup. A schematic diagram of the FIDI-MS setup is depicted in Figure 1; a detailed description of the FIDI-MS method is presented elsewhere.[26,27] Briefly, an aqueous droplet of $\sim$2 mm diameter ($\sim$4 μL volume) is suspended on the end of a stainless steel capillary held
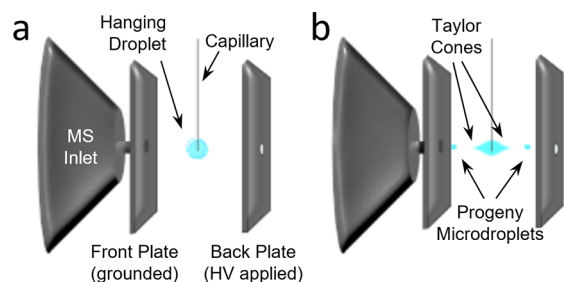
Figure 1. Schematic of FIDI-MS for oxidation studies, as viewed from the side. (a) A droplet hanging between two parallel plate electrodes. (b) A snapshot of the elongated droplet when the pulsed voltage is employed to the plate electrodes.

equidistant between two parallel plate electrodes separated by 6.3 mm (Figure 1a). Droplets are formed from analyte solutions fed through the capillary using a motorized syringe pump. The parallel plates are mounted on a translation stage to allow alignment of an aperture in the electrically grounded front plate with the atmospheric pressure inlet of an LTQ-XL mass spectrometer (Thermo-Fischer, Waltham, MA) that is open to ambient lab air. Following droplet formation, a period of 60 s is allowed for diffusion of surface-active species to achieve equilibrium coverage at the air−water interface. The sampling of the hanging droplet proceeds by applying a high voltage pulse (3−5 kV, 100 ms duration, variable polarity) to the back plate electrode and to the capillary at half the magnitude supplied to the back plate, establishing a homogeneous electric field. The electric field induces an aligned dipole that stretches the suspended droplet until dual Taylor cones are formed at opposite ends, ejecting charged submicrometer progeny droplets of opposite polarity toward the appropriately biased electrodes (Figure 1b). Progeny droplets of a specific polarity pass through the aperture in the grounded front plate and enter the inlet of the mass spectrometer, resulting in the detection of gas-phase ions. As FIDI sampling causes significant perturbation to the droplet, a fresh droplet is generated for each measurement. In many respects, the FIDI process is similar to that of electrospray ionization (ESI), except that sampling occurs only from the sheared electrical double layer at the droplet surface. In this study, a negative voltage was applied to the back plate and capillary to detect deprotonated [M−H]$^-$ ions.

A dielectric barrier discharge source (DBDS) was used to generated hydroxyl radicals. The DBDS consists of a 38 mm borosilicate tube (6.45 mm O.D., 3.91 mm I.D.) with a tungsten rod (1.02 mm diameter) inner electrode and a conductive silver epoxy outer electrode. A bubbler provides water-saturated helium through the DBDS with flow monitored by a Type πMFC digital mass flow controller (model PFC-50, MKS Instruments). A high voltage AC power supply (Trek PM04015, Trek, Inc.) biases the inner electrode during experiments, while the outer electrode remains grounded. The operational conditions of the DBDS are as follows: 12 kVpp (peak-to-peak AC voltage) bias, 1 kHz sine waveform, 1.414 mA current, and 1000 cm^3 min^{-1} He/H$_2$O flow. The proposed mechanism of OH generation proceeds either directly via an electron capture reaction with water (e$^-$+H$_2$O $\rightarrow$ H$^-$+OH), or through a two-step process (e$^-$+H$_2$O $\rightarrow$ H$_2$O++2e$^-$ and H$_2$O$^+$+H$_2$O $\rightarrow$ H$_3$O$^+$+OH).[34] No H, O, or HO$_2$ is anticipated to form in the DBDS. The characterization of gas-phase OH concentration will be discussed subsequently.

Ultrapure water (18 MΩ, < 3 ppb TOC, Millipore Milli-Q) and HPLC-grade methanol (J.T.Baker) were used as solvents. Aqueous stock solutions of *cis*-pinonic acid (PA, 98%, Sigma-Aldrich) and sodium dodecyl sulfate (SDS, 98%, Fischer Scientific) were prepared at concentrations of 5 and 2 mM, respectively, and diluted as needed. Settings for FIDI-MS were optimized for deprotonated *cis*-pinonic acid [PA−H]$^-$ using a 20 μM solution of PA in 99.2:0.8 methanol:water (v/v%).

To study the interfacial OH + PA reaction mechanism, an aqueous PA droplet with an average bulk concentration of 50 μM is exposed to OH from the DBDS for varying reaction times, at which concentration, based on its equilibrium constant, $\sim$19% of PA is estimated to remain on the surface of the droplet with a radius of 1 mm. Droplets of 20 μM SDS
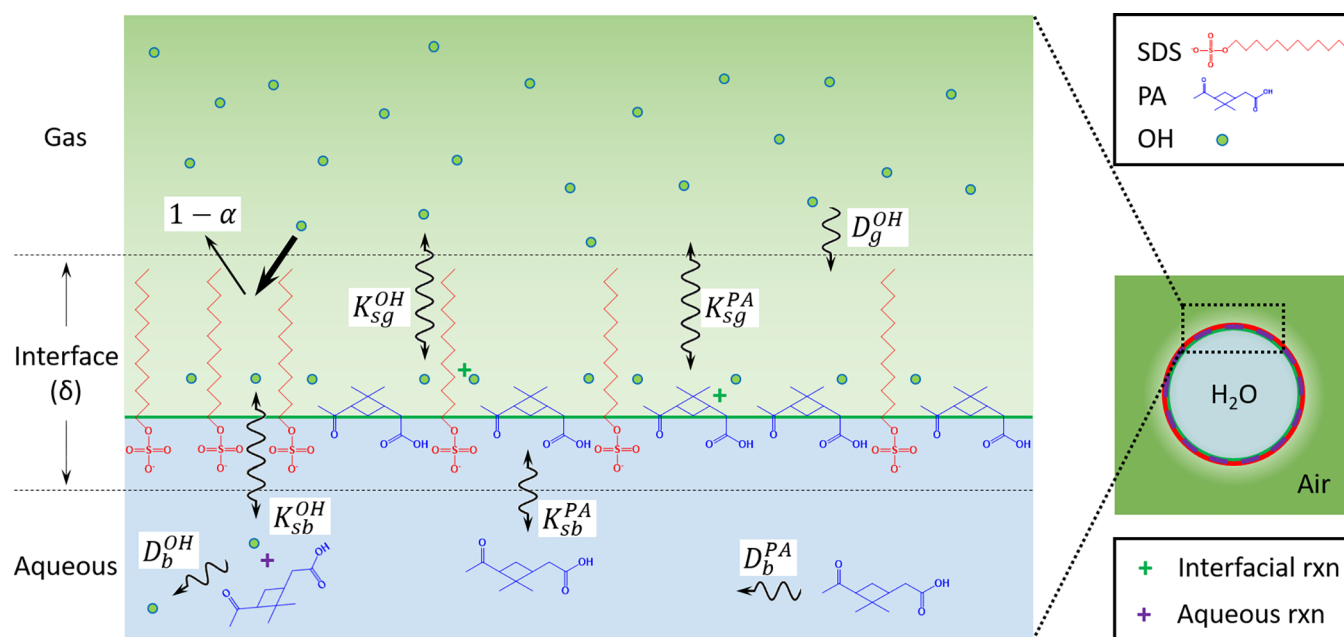
Figure 2. Multiphase transport and reaction model for OH reaction with sodium dodecyl sulfate (SDS) and pinonic acid (PA) at the air–water interface. Key parameters of corresponding processes are labeled and explanation can be found in SI.I and Table 1.

Table 1. Parameters and Reaction Rate Constants Used in This Work

symbol	parameter	value
α_s^i	surface accommodation coefficient for species i	1
δ	interface thickness (m)	6.9×10^{-10} (ref 37)
D_g^{OH}	gas-phase OH diffusivity (m^2 s^{-1})	2.67×10^{-5}
D_b^{OH}	aqueous-phase OH diffusivity (m^2 s^{-1})	2.30×10^{-9} (ref 75)
D_b^{PA}	aqueous-phase PA diffusivity (m^2 s^{-1})	1×10^{-10}
K_{sg}^{OH}	surface-gas adsorption equilibrium constant of OH (m)	6.07×10^{-6} (ref 37)
K_{sb}^{OH}	surface-bulk adsorption equilibrium constant of OH (m)	5.52×10^{-9} (ref 37)
K_{sg}^{PA}	surface-gas adsorption equilibrium constant of PA (m)	9.62×10^4
K_{sb}^{PA}	surface-bulk adsorption equilibrium constant of PA (m)	2.01×10^{-4}
$k_{bulk}^{OH + PA}$	bulk reaction rate constant of OH + PA (M^{-1} s^{-1})	3.30×10^9 (ref 20)
$k_{surf}^{OH + SDS}$	surface reaction rate constant of OH + SDS (cm^2 molec^{-1} s^{-1})	2.87×10^{-8} (see below)[a]
$k_{surf}^{OH + PA}$	surface reaction rate constant of OH + PA (cm^2 molec^{-1} s^{-1})	9.38×10^{-8} (see below)[a]

[a]These values are from fitting of the experimental data. Refer to Results and Discussion for details.

were exposed to the OH source for different durations to characterize the gas-phase OH concentration. To constrain the surface reaction rate constant for OH + PA, a mixture of PA and SDS solution is diluted to 50 and 20 μM, respectively. Under each reaction condition, 5 droplets were repeated and averaged to overcome drop-to-drop variation.

Diffusion-Reaction Interfacial Model. We present the development of a diffusion-reaction model designed to describe the air–water interfacial reaction on a droplet between gas-phase OH and a surface-active component, PA in this study. In addition to its surface reaction with OH, PA can evaporate into the gas phase, diffuse into the bulk droplet and undergo bulk oxidation if dissolved OH is present. Sodium dodecyl sulfate (SDS) is used as a reference compound that, in contrast to PA, given its high molecular weight and long alkyl chain, undergoes only surface reaction (i.e., no evaporation and no diffusion into the bulk). Moreover, SDS oxidation products are easy to characterize at early time scales as SDS undergoes sequential oxygenation with negligible fragmentation. As such, by measuring the rate of decay of SDS on the surface, one can infer the gas-phase OH concentration and, in turn, calculate

the surface reaction rate constant with OH for the surface active species. The model accounts for each of these transport and reaction processes explicitly, for both PA and SDS, in order to extract the surface reaction rate of PA + OH from the experimental data.

The physical system to which this model is applied is depicted in Figure 2; additional details of the model are discussed in Supporting Information SI.I. The following reactions describe the transport and reaction processes:

$$OH\,(gs) \rightleftharpoons OH\,(s) \tag{R1}$$

$$PA\,(gs) \rightleftharpoons PA\,(s) \tag{R2}$$

$$PA_p\,(gs) \rightleftharpoons PA_p\,(s) \tag{R3}$$

$$OH\,(s) + SDS\,(s) \rightarrow SDS_{p1}\,(s) \xrightarrow{OH\,(s)} SDS_{p2}\,(s)$$
$$\xrightarrow{OH\,(s)} SDS_{p3}\,(s) \xrightarrow{OH(s)} \ldots \tag{R4}$$
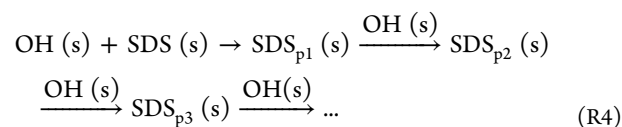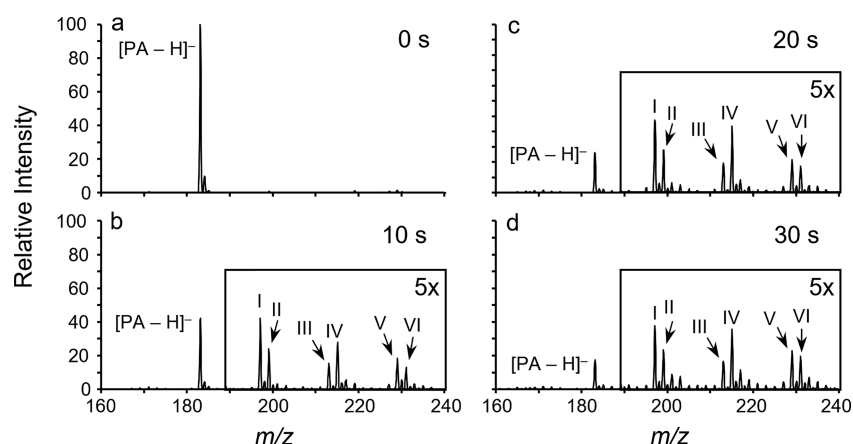
Figure 3. Pinonic acid (PA) oxidation at the air–water interface by gas-phase OH detected by FIDI-MS OH exposure. (a) 0 s; (b) 10 s; (c) 20 s; (d) 30 s. m/z of identified products are as follows: I = 197, II = 199, III = 213, IV = 215, V = 229, and VI = 231. Mass spectra are reported as averages of replicate samples (N = 5). The peak intensities in panels b, c, and d have been normalized with respect to the peak intensity of $[PA-H]^-$ in panel a.

$$OH\ (s) + PA\ (s) \rightarrow PA_p\ (s) \tag{R5}$$

$$OH\ (s) \rightleftharpoons OH\ (b) \tag{R6}$$

$$PA\ (s) \rightleftharpoons PA\ (b) \tag{R7}$$

$$PA_p\ (s) \rightleftharpoons PA_p\ (b) \tag{R8}$$

$$OH\ (b) + PA\ (b) \rightarrow PA_p\ (b) \tag{R9}$$
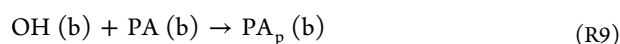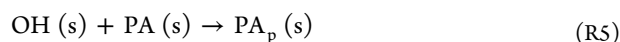
where s refers to the surface, b represents the bulk aqueous phase, and gs denotes the gas phase within one molecular mean free path above the surface. Note that gs is distinct from g, the bulk gas phase sufficiently far from the surface. Differences in concentrations between gs and g is described in SI.I.

Reactions R1, R2, and R3 correspond to the surface adsorption and desorption of OH, PA, and PA products (PA_p), respectively. Reactions R4 and R5 are the surface reaction of SDS + OH and PA + OH. Reactions R6, R7, and R8 represent surface to bulk droplet transport. Reaction R9 represents the bulk aqueous-phase reaction of PA + OH. The forward and reverse reaction rate constants for reactions R1–R3 and reactions R6–R8 follow the multiphase transport theory in Pöschl et al.[35] and are explicitly discussed in SI.I. The bulk aqueous-phase rate constant of PA + OH in R9 is adopted from Aljawhary et al.[20] Reactions R4 and R5 are the key processes on which we focus here. Values of key parameters are summarized in Table 1.

The gas-phase OH concentration sufficiently far from the droplet surface is assumed to be constant, based on the assumption that the OH concentration from the DBDS is constant. Close to the droplet, however, a concentration gradient exists that depends on the OH uptake coefficient (γ_{gs}). During the reaction period, the droplet size is assumed to be constant (i.e., no water evaporation occurs). However, evaporation of surface-active PA is considered (R2). The Langmuir adsorption model (monolayer) is used to calculate the initial surface coverage of PA given the bulk concentration of the PA solution from which the droplet is formed (see SI.II). When PA and SDS coexist in the droplet, we assume that PA and SDS do not interact, that the surface coverages of PA and SDS are equivalent (i.e., $\theta_{0,PA} = \theta_{0,SDS} = 1$), and that the surface coverage is homogeneous. An implicit assumption

is the absence of reaction between PA, SDS, and their products.

OH surface reactions are assumed to follow Langmuir–Hinshelwood kinetics;[35,36] that is, OH first adsorbs to the organic surface (reaction R1) and then reacts interfacially with PA and SDS (reaction R4 and R5). This assumption is consistent with the experimental data, as will be discussed subsequently. The adsorption property of OH is following Vácha et al.[37] Adsorbed OH can also diffuse into the droplet (reaction R6) and react with PA in the bulk aqueous phase (reaction R9).[38] The oxidation products of SDS + OH are assumed to stay in the interface because even after several generations of oxidation, the long alkyl chain remains largely intact (i.e., functionalization predominates). The SDS oxidation products are assumed to continue to react with adsorbed OH at different rates (reaction R4). For simplicity, the first-generation oxidation products of the PA + OH reactions at the interface (reaction R5) and in the bulk (reaction R9) are represented as single lumped products, PA_p (s) and PA_p (b). PA_p (s) and PA_p (b) are assumed to have equivalent compositions and properties, even though their formation rates and mechanisms may differ. Depletion of the PA (s) by reaction with OH is replenished by aqueous-phase diffusion of PA_p (b) toward the surface (reaction R7). Equilibrium partitioning of PA and PA_p between the gas phase, the surface, and the aqueous phase was estimated using the quantum chemical program COSMOtherm based on density functional theory calculations (see SI.III for details).[39,40] The predicted surface/water and surface/air equilibrium constants for PA and proposed products of the interfacial reaction of PA + OH (see Results and Discussion) are listed in Table S1. The predicted equilibrium constants for the PA oxidation products span several orders of magnitude. For simplicity, the lumped PA oxidation product PA_p is assumed to have the same equilibrium constants as PA. Subsequent reactions of the lumped PA products, PA_p, with OH are also represented in the model.

■ RESULTS AND DISCUSSION

OH Oxidation of Pinonic Acid Droplet. As a compound of intermediate volatility,[40] we first examine the extent to which PA evaporates from the droplet. Both experimental and simulation results (SI.IV) suggest that changes in PA
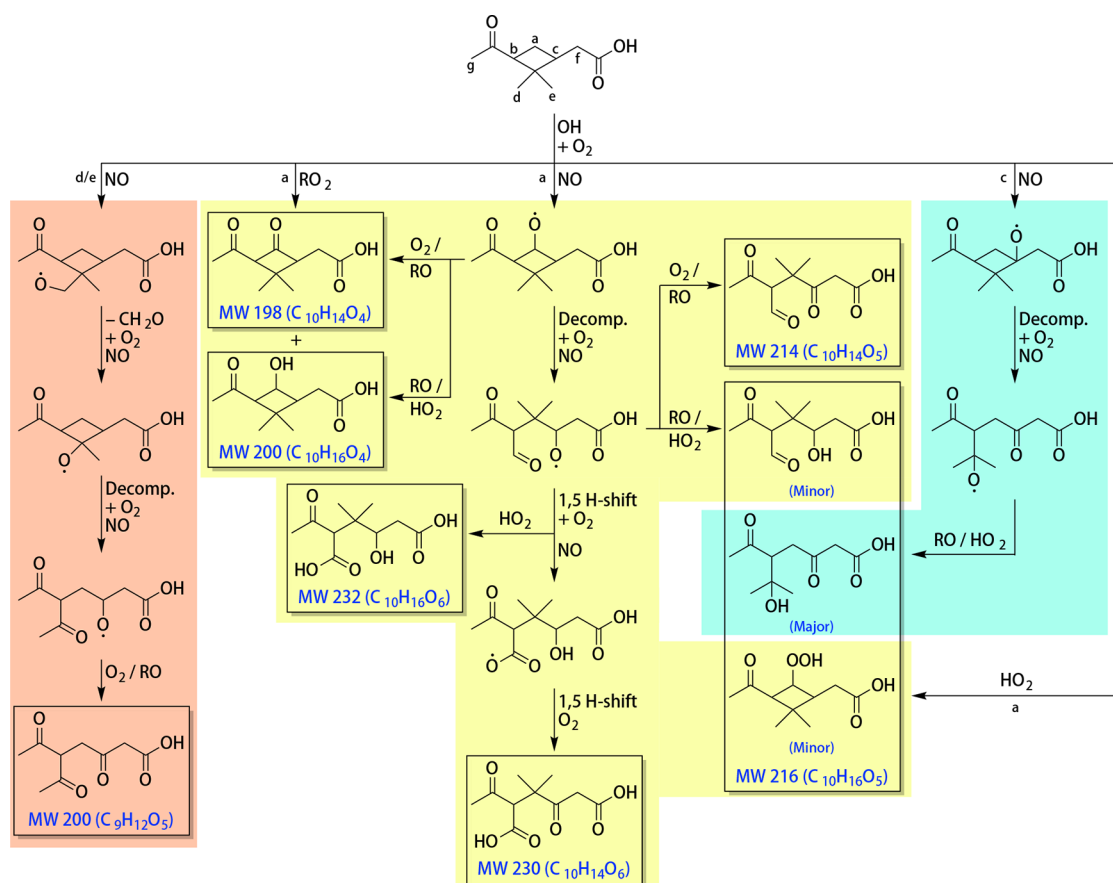
Figure 4. Mechanism of OH-initiated oxidation of PA under NO-dominant conditions.

concentration due to evaporation within the experimental time scale of 100 s are negligible. Figure 3 depicts the mass spectra of a PA droplet, in 10 s intervals, over a 30 s OH exposure. A series of six major oxidation products, at m/z 197 (I), 199 (II), 213 (III), 215 (IV), 229 (V), and 231 (VI) are identified. Because FIDI-MS provides only unit-mass resolution, each peak likely represents the combination of several isomers and isobars. As a first approximation, $[PA-H]^- + 14$ is assumed to represent the addition of one carbonyl ($>C=O$), $[PA-H]^- + 16$ the addition of one hydroxyl ($-OH$), $[PA-H]^- + 30$ the addition of one carboxylic acid ($-C(=O)OH$) or one hydroxyl and one carbonyl, and $[M-H]^- + 32$ the addition of two hydroxyls or one hydroperoxyl ($-OOH$).

As shown in Figure 4, the initial H-abstraction by OH from PA can occur at 7 possible sites (a–g). Quantum chemical calculations suggest that in gas-phase OH oxidation, H-abstraction occurs most likely on carbon f.[17,41] However, results of structure activity relationships (SAR) for OH oxidation in the aqueous-phase indicate that carbons a and c are preferred positions.[18] At the air−water interface, molecular dynamics simulations[23] suggest that PA molecules are oriented such that the hydrophilic functional groups ($-C(=O)OH$ and $> C=O$) are embedded in the droplet, while the hydrophobic cyclobutyl ring is exposed on the droplet surface (see Figure 2), making carbons a−c the most vulnerable to OH attack. Following the initial H-abstraction (Figure 4), the resulting alkyl radical combines exclusively with O_2 at the air−water interface to form a peroxyl radical (RO_2), which may undergo the same competitive reaction channels as those in the gas phase.[42] The three dominant gas-phase bimolecular

reactions are $RO_2 + RO_2$ ($k_{RO2} \sim 10^{-14}-10^{-12}$ cm^3 molec^{-1} s^{-1}), $RO_2 + NO$ ($k_{NO} = 7-10 \times 10^{-12}$ cm^3 molec^{-1} s^{-1}), and $RO_2 + HO_2$ ($k_{HO_2} = 5-20 \times 10^{-12}$ cm^3 molec^{-1} s^{-1}).[42,43] Note that the aqueous-phase $RO_2 + RO_2$ and $RO_2 + HO_2$ reactions have similar rate constants (10^9 M^{-1} s^{-1} $\sim 1.7 \times 10^{-12}$ molecule^{-1} cm^3 s^{-1})[44,45] as those in the gas-phase. Assuming NO and HO_2 have similar air−water interfacial adsorptive and reactive properties, and given that the FIDI source is exposed to the ambient atmosphere and typical daily average NO mixing ratio in the Los Angeles area is ~1 ppb ($10^{11}-10^{12}$ molecules cm^{-3})[46,47] and indoor HO_2 mixing ratio <10 ppt ($\sim 10^9$ molecules cm^{-3}),[48] it is expected that reaction with NO is the dominant fate of PA peroxyl radicals at the air−water interface, with a small fraction of $RO_2 + RO_2$ and $RO_2 + HO_2$ reactions (Figure 4). Reaction of $RO_2 + NO$ yields alkoxy radicals (RO) that undergo decomposition, isomerization, or reaction with O_2.[49]

To aid in identification of the compounds that contribute to the six major mass spectral peaks detected by FIDI-MS, collision-induced dissociation (CID) was employed for detailed analysis of molecular structure. The MS/MS fragmentation patterns of the six parent ions are shown in Figure S5. The daughter ions in each MS/MS spectrum can be explained by neutral losses of H_2O, CO_2, C_3H_6O, and $C_6H_{10}O$[50] (Figure S5). Certain neutral losses are characteristic to specific functional groups; for example, carboxylic acid ions exhibit losses of 18 u (H_2O) and 44 u (CO_2).[51] All structures proposed in Figure 4 are consistent with the observed MS/MS spectra. The peak at m/z 197 can be explained by a $C_{10}H_{14}O_4$ species derived from the RO_2 formed by H-abstraction from
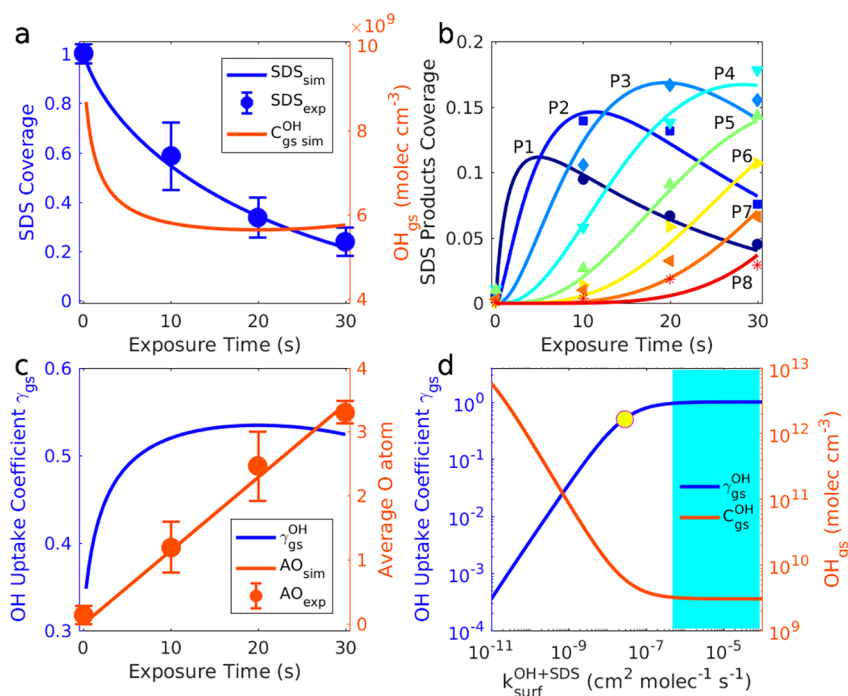
Figure 5. Experimental and fitted results of the OH oxidation of the SDS droplet. (a) Temporal profiles of SDS coverage (blue dots, measured values averaged by 5 repeats; blue line, fitting result) and the modeling gas-phase OH concentration above the surface (orange line). (b) Temporal profiles of 8 generations of SDS + OH products (lines are fitting results and dots are experimental results). (c) Temporal profiles of predicted OH uptake coefficient (blue line) and the average number of oxygen atoms incorporated into SDS via OH oxidation (orange dots, measured values averaged by 5 repeats; orange line, fitting result). (d) Calculated OH uptake coefficient and the gas-phase OH concentration above the surface as a function of the optimally fitted surface reaction rate constant for SDS + OH system. Yellow dot represents the value adopted in this study and cyan background marks the gas-phase diffusion limit regime for the determination of $k_{surf}^{OH + SDS}$.

carbon a via successive reactions with NO and O₂ or through Russell disproportionation.[52] The compound at m/z 199 can also form through the Russell mechanism. The RO formed through OH-attack on a carbon can undergo ring-opening processes via scission of either the a−b or a−c bonds (for simplification, Figure 4 depicts only the cleavage of the a−c bond), yielding a new alkyl radical, which after reacting with O₂ and NO forms another RO. This intermediate RO can undergo a 1,5 H-shift to form the species at m/z 229 and m/z 231, react with O₂ to yield m/z 213, or react with RO to yield what is believed to be a minor product at m/z 215. H-abstraction from carbons b or c leads to the formation of a RO, which will decompose, react with O₂ and NO, and ultimately yield a tertiary RO. The resulting tertiary alcohol at m/z 215 shown in Figure 4 is expected to be the major isobaric contributor at this m/z, given its agreement with the major fragments observed in the MS/MS spectrum.

The aqueous-phase pH can affect the reaction mechanism as well as the reaction rate.[18] Given pK_a = 4.82,[53] the pH in the bulk droplet of PA solution at equilibrium with the surface is at most 5.2, and the ratio of deprotonated PA to PA is ∼2.2 (assuming the surface and the bulk are decoupled). Deprotonated PA has an additional reaction pathway in the aqueous phase (i.e., electron transfer).[54] However, the undissociated PA is expected to dominate at the surface.[55] Thus, Figure 4 only illustrates the mechanism of undissociated PA reacted with OH at the air−water interface.

The kinetic behavior of PA and its 6 oxidation products is shown in Figure S6. The relative rates of appearance of each product are consistent with the PA reaction pathways proposed on the basis of MS/MS analysis. While I and II

are both the lowest mass products, the considerably slower rate of appearance of II suggests that this product is formed by a slower and/or more complex mechanism. Figure 4 proposes a fragmentation product (H-abstraction from carbons d or e) as one of the possible structures of II, whereas I is suggested to be predominantly due to functionalization. The highest mass species (V and VI) are characterized by the highest level of oxidation. The kinetic behavior of V and VI indicates a net balance between formation and degradation pathways for these species, suggesting that as the O/C ratio increases, the interfacial OH + PA oxidation system exhibits a propensity to shift from functionalization to fragmentation products.

Characterization of Gas-Phase OH Concentration. To study the kinetics of interfacial OH oxidation of PA, a sufficient constraint on the gas-phase OH concentration is necessary. By monitoring the heterogeneous OH oxidation of surfactant (i.e., SDS in this study) and assuming that the surfactant remains exclusively on the surface, one can infer the gas-phase OH concentration. As stated in the section Diffusion-Reaction Interfacial Model, it is necessary to incorporate all possible processes (i.e., adsorption and reaction on the surface, as well as diffusion in the bulk droplet) into a unified model, from which the gas-phase OH concentration can be inferred.

Assuming an effective cross-section area of 30 Å² for SDS[56] and that the SDS resides solely at the surface, a monolayer of SDS is formed on the surface of a droplet with a radius of 1 mm. Mass spectra of the interfacial OH oxidation of SDS are shown in Figure S7, and the measured decay of SDS is shown in Figure 5a. Due to the linear alkyl chain, the successive increases of m/z 14 and 16 indicate that alcohols and carbonyls are the most likely products via RO₂/RO chemistry in the SDS
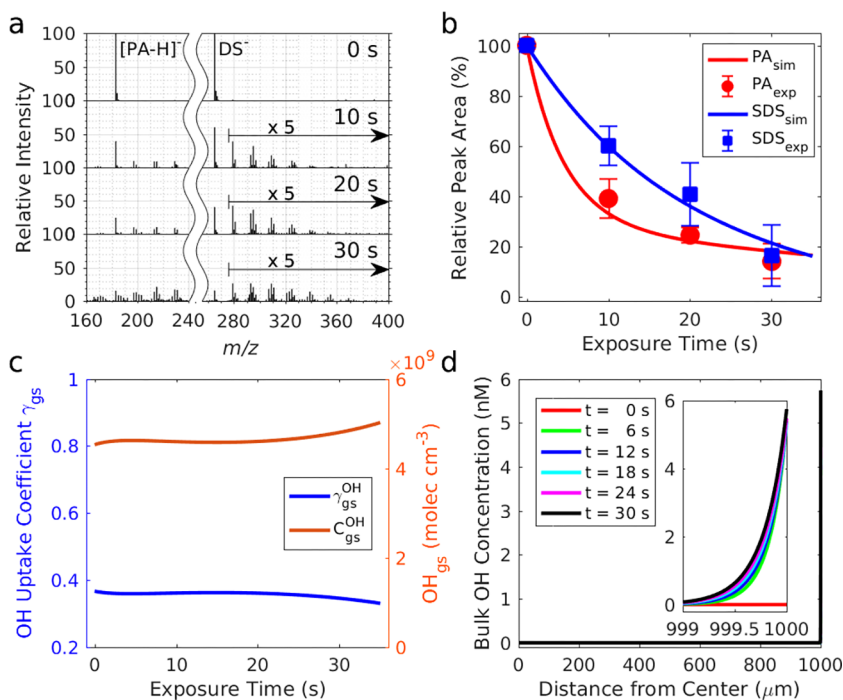
Figure 6. Experimental and simulation results of the OH oxidation of the mixture of PA and SDS droplet. (a) Mass spectra of the sampling under different OH exposure (left is the PA regime and right is the SDS regime). (b) Temporal profiles of the surface coverage of PA and SDS. Dots represent experimental measurements (averaged by 5 repeats) and lines represent simulated results. (c) Predicted temporal profiles of the OH uptake coefficient and the gas-phase OH concentration. (d) Simulated bulk aqueous-phase OH distribution at different exposure time. Inset panel is the zoom-in near the surface regime.

+ OH reaction. However, other functionalities (e.g., carboxylic acids (m/z+30)) are possible. Instead of assigning specific formula to each m/z peak, the products can be clustered into groups; that is, peaks at m/z [DS]$^-$+14 and [DS]$^-$+16 are grouped into the products that contain one oxygen atom, while products at m/z [DS]$^-$+28, [DS]$^-$+30, and [DS]$^-$+32 are those with two oxygen atoms. Figure 5b presents the temporal profiles of 8 generations of identified SDS + OH oxidation products. Assuming that SDS incorporates one oxygen after reacting with one OH, by defining the average oxygen atom as the signal-intensity-weighted sum of the oxygen content in the identified oxidation products (m/z 265−400), the experimental results indicate that ~10 s is required for OH to react with the entire monolayer of SDS (Figure 5c). The near-linear relationship in Figure 5c suggests Langmuir−Hinshelwood kinetics govern the air−water system, since if OH were to react with the interfacial molecules upon collision (Eley−Rideal mechanism), the rate of oxygen atom incorporation would increase as the reaction progresses given that more reactive C−H bonds are formed (e.g., those adjacent to a carbonyl group).

By fitting the experimental data in Figure 5a−c, we seek to estimate the gas-phase OH concentration, as well as the surface reaction rate constants for both SDS and SDS products. The best-fit gas-phase OH mixing ratio is found to be ~698 ppb. The experimental distribution patterns of the eight oxidation generations and the decay curve of SDS determine the reaction rate constants of SDS$_p$ + OH to relative that of SDS + OH (i.e., $k_{surf}^{OH + SDS}$). All generations are found to react faster with OH than SDS. Nonetheless, without any constraint on the surface concentration of OH, the optimally fitted $k_{surf}^{OH + SDS}$ values span from 10^{-11} to 10^{-4} cm^2 molec^{-1} s^{-1}, within which range, $k_{surf}^{OH + SDS}\theta_{OH}$ (Figure S8a) is nearly constant, suggesting that the decay of SDS is a quasi-first-order reaction (~0.0516

s^{-1}). Figure 5d shows the estimated average OH uptake coefficient γ_{gs} and the gas-phase OH concentration above the surface C_{gs}^{OH} as functions of the optimally fitted $k_{surf}^{OH + SDS}$. In the regime where $k_{surf}^{OH + SDS} > 10^{-7}$ cm^2 molec^{-1} s^{-1}, both γ_{gs} and C_{gs}^{OH} remain constant, which is a result of the fast surface reaction rate causing gas-phase diffusion of OH to the surface to become the rate-limiting step in this system. γ_{gs} of OH onto thin organic film is typically ≥0.1 [1] and the gas-phase diffusion limit is unlikely in the FIDI experiment because the DBDS aims directly at the droplet. Adopting a median value $\gamma_{gs} = 0.5$, we find the average values $C_{gs}^{OH} \approx 6 \times 10^9$ molecules cm^{-3}, $k_{surf}^{OH + SDS} \approx 2.87 \times 10^{-8}$ cm^2 molec^{-1} s^{-1}, and $\theta_{OH} \approx 10^{-9}$. Figure 5a,c show the calculated temporal profiles of C_{gs}^{OH} and γ_{gs}.

The simulation suggests that in the absence of bulk reaction consuming aqueous-phase OH, OH radicals can diffuse to the center of the droplet and reach ~1 nM after 30 s (Figure S8b), indicating that the bulk droplet serves as a significant sink of OH in the OH + SDS interfacial reaction system. The high gas-phase OH concentration above the surface gives ~10^{11} molecules cm^{-3} s OH exposure in the FIDI system, corresponding to ~1 day exposure under typical atmospheric conditions (assuming ambient OH concentration of 1×10^6 molecules cm^{-3}). The air-interface-water properties of OH employed in the model and the best-fit surface reaction rate constant of SDS + OH are summarized in Table 1.

Kinetics of Interfacial OH Oxidation of Pinonic Acid. PA partitions between the droplet surface and bulk. Because of diffusion to the bulk of both PA and PA oxidation products, one can not use the same strategy as employed for OH + SDS to determine the surface reaction rate constant. As discussed above, the products of PA + OH are complex, and it is impossible to track the fractions of all the PA products that

diffuse into the bulk. By adding a reference compound to the system, such as a surfactant that undergoes only surface reaction, we can better constrain the OH concentration on the surface and determine the surface reaction rate constant for OH + PA. The resulting mass spectra under different exposure times are shown in Figure 6a. The decay of both PA and SDS is shown in Figure 6b. The apparent decay rate of PA exceeds that of SDS, which is indicative of the relative reactivity of PA. One cannot, however, rule out the possibility that bulk aqueous-phase transport and oxidation can affect the decay rate.

By fitting to the data points in Figure 6b, where the surface reaction rate constants for both SDS and SDS products are known, the bulk gas-phase OH concentration is estimated as ~678 ppb, consistent with the value evaluated for SDS + OH experiments, demonstrating the reproducibility of DBDS employed for air–water interfacial oxidation studies. The surface reaction rate constant of PA + OH is determined to be 9.38×10^{-8} cm^2 molec^{-1} s^{-1}, ~3 times of that of SDS + OH. The fitted surface rate constant of PA + OH is not sensitive to the surface coverage of PA and SDS. The gas-phase OH concentration above the surface is ~5×10^9 molecules cm^{-3} and the OH uptake coefficient is ~0.35 (Figure 6c).

The calculated average oxygen atom incorporation into SDS products fits the experimental data (Figure S9a) as well. The simulated bulk aqueous-phase OH distribution (Figure 6d) predicts that OH is confined to the surface region (within a distance of ~1 μm). The heterogeneous nature of the reactions can be quantified by utilizing the concept of a reacto-diffusive length L_{OH}:[35]

$$L_{OH} = \sqrt{\frac{\mathcal{D}_b^{OH}}{k_b^{OH+PA} C_b^{PA}}} \qquad (1)$$

where $\mathcal{D}_b^{OH}$ is the bulk diffusion coefficient of OH (2.3×10^{-9} m^2 s^{-1}), k_b^{OH+PA} is the bulk reaction rate constant of PA + OH (3.3×10^9 M^{-1} s^{-1}),[20] and C_b^{PA} is the bulk concentration of PA (~$(1-19\%) \times 50$ μM). In this system, $L_{OH} \approx 0.6$ μm, consistent with the prediction of the simulation (Figure 6d). To replenish its consumption by OH in the subsurface region, a continuous diffusive flux of PA from the bulk aqueous phase has to be established (Figure S9b). Though the surface reaction rate constant of PA + OH is faster than that of SDS + OH, the simulated decay curves of PA and SDS cross after 30 s exposure to OH, since at that point replenishment of PA from the bulk competes with the surface reaction rate.

In summary, to determine the air–water interfacial reaction rate constant of a surface-active species, one has to account for simultaneous aqueous-phase diffusion and reaction. For a system with high bulk OH reactivity ($k_b^{II} C_b$, where k_b^{II} is a second-order aqueous-phase reaction rate constant and C_b is the bulk aqueous-phase concentration of the surface-active species), the heterogeneous reaction is enhanced, since the penetration of OH into the droplet bulk is confined to the subsurface region. If the bulk reaction rate is smaller than that on the surface, a slower "apparent" decay rate of the surface coverage can be expected due to the replenishment from bulk diffusion.

Atmospheric Implications. In the atmosphere in which cloud and fog droplets or aerosol water are present, for species with high Henry's law constants, a large fraction will partition to the aqueous phase, where aqueous phase chemistry can be significant.[57−59] The Henry's law constant relates the gas and

bulk aqueous phases and is routinely adopted in the cloud or aqueous aerosol chemistry models.[60,61] However, by accounting for the surface activity, the fraction that partitions in the gas phase, on the surface, and in the bulk aqueous phase may be quite different. The fraction partitioning on the surface of the droplet, F_{surf}, can be estimated by

$$F_{surf} = \frac{\frac{3w_L}{\overline{R}_P}}{\frac{1}{K_{sg}} + \frac{w_L}{K_{sb}} + \frac{3w_L}{\overline{R}_P}} \qquad (2)$$

where K_{sg} and K_{sb} are the surface/gas phase and surface/bulk aqueous phase equilibrium constants, respectively. The ratio $\frac{K_{sg}}{K_{sb}}$ can be viewed as the effective Henry's law constant. w_L is the liquid water mixing ratio in the air and $\overline{R}_P$ is the volume-weighted average radius of the droplets. For PA in the present study, Figure S1 indicates that the smaller the droplet, the higher the fraction of PA that resides on the surface.

If the sole source of OH is from the gas phase (thus ignoring possible aqueous-phase photolysis reactions[20,22]), multiphase OH oxidation can be divided into sequential processes: gas-phase reaction, gas-surface adsorption/desorption, surface reaction, surface-bulk aqueous transport, and bulk aqueous phase reaction. Given reaction rate constants in the gas phase, on the surface, and in the aqueous phase, the following questions concerning oxidation of a surface-active species arise: What is the rate-limiting step in ambient OH multiphase oxidation? Is the gas-surface-bulk system always at equilibrium? What is the major sink of surface-active species?

The FIDI studies simulate processes occurring within 1 min with an equivalent OH exposure of 1 day under typical ambient conditions. Within a relatively short period, interfacial transport is the rate-limiting step under extremely high OH levels (Figure 6d). For ambient OH levels, the conclusion that OH oxidation of PA occurs predominately at the air–water interface may not be directly extrapolated to typical environmental conditions. To clarify this point, we apply the derived rate constant of PA + OH in a case study simulation of the ambient OH oxidation of PA in cloud and fog droplets.

We assume an air parcel with a typical liquid water mixing ratio $w_L = 3 \times 10^{-7}$,[49] equivalent to ~0.6 cm^{-3} droplets of 100 μm diameter or ~5×10^3 cm^{-3} droplets of 5 μm diameter (Figure S10a), and an overall PA concentration of 0.5 nmol m^{-3} (~100 ng m^{-3}).[62,63] The gas-phase OH concentration is assumed constant, 1×10^6 molecules cm^{-3}. The multiphase reactions are studied in two ambient cloud droplet sizes,[49,64] i.e., 5 and 100 μm. The reaction of PA + OH occurs in the gas phase,[17] on the surface, and in the bulk aqueous phase[20] with rate constants of 1.125×10^{-11} molec^{-1} cm^3 s^{-1}, 9.38×10^{-8} molec^{-1} cm^2 s^{-1}, and 3.30×10^9 M^{-1} s^{-1}, respectively. The fractions of remaining PA in the gas phase, on the surface, and in the bulk aqueous phase are tracked. Initial partitioning of PA between the surface/air and surface/water is at equilibrium (see SI.VIII for detailed calculation), indicating that >99% of PA remains on the surface of a 5 μm droplet, while ~90% remains on the surface of a 100 μm droplet.

By matching the mass flux through the interface with accommodation coefficients and relating the gas phase to the aqueous phase via Henry's law constants,[49,65] one can, in a simplified model, exclude the effect of the interfacial reaction. To distinguish between the two models, we call the former M1 and the latter M2. To minimize the effect of interfacial
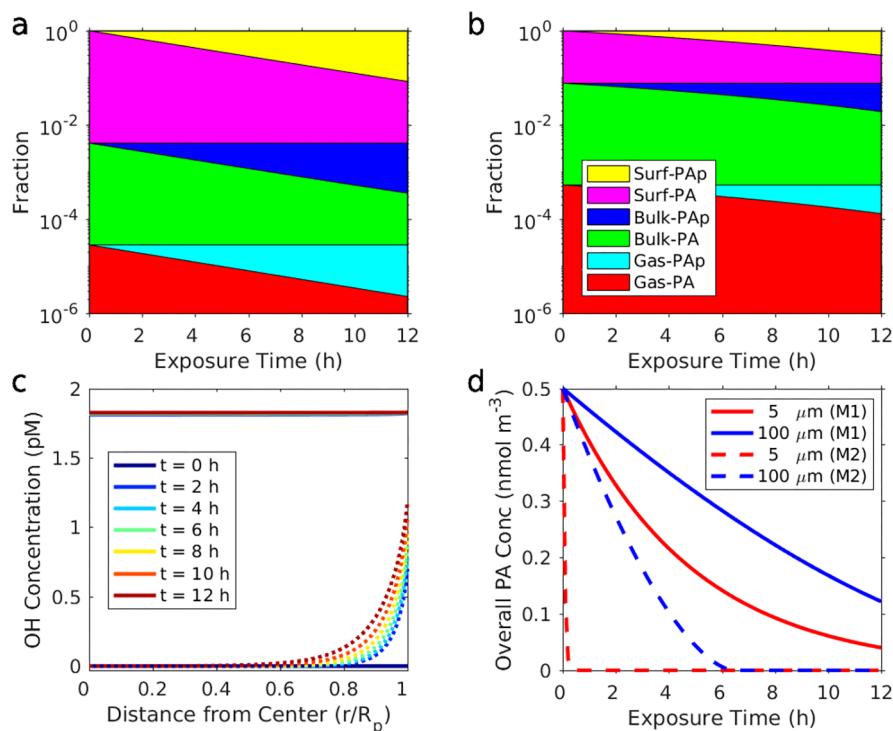
Figure 7. Simulated multiphase OH oxidation of PA in droplets of 5 μm (a) and 100 μm (b), with an overall PA concentration of 0.5 nmol m^{-3} under typical ambient conditions (gas-phase OH concentration ~10^6 molecules cm^{-3}). (a,b) Fraction of the overall quantities of PA and PA products that resides on the surface, in the bulk aqueous phase, and in the gas phase. (c) Predicted bulk aqueous-phase distribution of OH at different OH exposure times by M1 (solid lines: 5 μm droplets, dashed lines: 100 μm droplets). (d) Temporal profiles of overall PA as exposed to OH.

transport in M2, we adopt the accommodation coefficients as unity for PA, PA products, and OH. The effective Henry's law constant is $H = \frac{K_{sg}}{K_{sb}} = 1.95 \times 10^7$ M atm^{-1} for PA and PA products, consistent with that reported in Lignell et al.,[22] and 39 M atm^{-1} for OH.[37] As opposed to M1, partition of PA between gas phase and aqueous phase at equilibrium[59] in M2 is independent of droplet size ($F_{aq} = \frac{Hw_L}{1 + Hw_L} > 99\%$), and diffusion of OH inside the droplet is found to be the rate-limiting step of the multiphase oxidation.

For both models, an overall simulation time is taken as 12 h, corresponding to an equivalent OH exposure as used in the FIDI experiments. Shrinkage or growth of the droplets is not considered during the 12 h simulation, given that water vapor is at equilibrium in the cloud.

Figure 7a,b present the predicted fractions of different PA fates in the systems in droplets of 5 and 100 μm, respectively. Since the surface properties of PA and PA products are identical in M1, the constant fraction of the sum of PA and PA products within any phase during the simulation indicates that the partitioning of PA and PA products between the gas phase, the surface, and the bulk aqueous phase remains at equilibrium. This quasi-equilibrium partitioning can be attributed to the fact that the reaction rates are sufficiently slow (because of the relatively low OH concentration) such that mass transport between the gas phase, the surface, and the bulk aqueous phase is no longer a rate-limiting step. The consumption of PA in the 5 μm system occurs exclusively at the air−water interface, while ~10% is contributed by the aqueous-phase OH oxidation in the 100 μm system. Both panels a and b of Figure 7 suggest that gas-phase oxidation of PA is unimportant in the cloud and

fog system, which also applies to M2, i.e., without accounting for interfacial effects, aqueous phase oxidation predominates.

The simulated bulk aqueous-phase OH distributions (Figure 7c) suggest that the smaller the droplet, the more uniform the bulk. For larger droplets, the reaction is constrained to the subsurface region, which is characterized by the OH reactive-diffusive length (eq 1), since less PA resides on the surface leaving the bulk aqueous-phase with relatively stronger OH reactivity ($k_b^{OH + PA} C_b^{PA}$). The OH uptake coefficient by 5 μm droplet surface is ~1 order of magnitude smaller than that by 100 μm droplet surface (Figure S10b). However, given the much larger surface area concentration in the 5 μm droplet system, under the same OH exposure, the overall PA concentration is predicted to decay ~90%, higher than ~75% in the 100 μm droplet system (Figure 7d). By comparison, if the interfacial interaction is not considered (M2), the model predictions suggest that PA is depleted in ~30 min in the 5 μm system and ~6 h in the 100 μm system. The longer lifetime of PA in the larger droplet system reflects the fact that in the absence of the interfacial resistance (i.e., interfacial reaction and accommodation), the rate-limiting step is bulk aqueous-phase diffusion of OH.

CONCLUSIONS

Interfacial effects of surfactants have been recognized to lower the surface tension and facilitate cloud droplet formation.[66,67] The present case study highlights the significance of air−water interfacial partitioning and reaction of surface-active species (e.g., PA). For the cloud and fog system with characteristically higher air−water surface area concentration, the sink of the surface-active species can be expected to occur predominantly on the surface, so that the surface reaction rate is the rate-

limiting step in the multiphase OH oxidation. The quasi-equilibrium partitioning state during the oxidation suggests that in the absence of a source of surface-active species (either from outside of the air parcel or from oxidation of precursors), multiphase OH oxidation can be simplified as occurring in three individual regions (gas phase, surface, and bulk aqueous phase), for which, the explicit dynamic multiphase model developed here applies. For species that are less surface-active (e.g., glyoxal),[59,68,69] the effect of air–water interfacial processes may not be as significant as those for surface-active species. Since the simulation treats the gas-phase OH as the sole source, given the high solubility of H_2O_2 (Henry's law constant = 8.70×10^4 M atm^{-1} at 298 K),[70] potential photolysis of dissolved H_2O_2 can serve as a large source of aqueous-phase OH[71] and the fate of surface-active species may change. Moreover, photosensitized chemistry has been proved to play a critical role on the radical–radical reaction at the air–water interface.[72–74] Additional studies are needed to clarify the competitive OH oxidations of surface-active species among gas phase, surface, and bulk aqueous phase under different conditions.

ASSOCIATED CONTENT

S Supporting Information

The Supporting Information is available free of charge on the ACS Publications website at DOI: 10.1021/acs.jpca.8b05353.

The Supporting Information contains eight sections: that is, I. Model Description, II. Surface Coverage of PA at Surface-Bulk Equilibrium, III. Air-Surface-Water Equilibrium Constants, IV. Evaporation of PA from Droplet, V. Identification of PA + OH Products, VI. SDS + OH Fitting, VII. PA + OH and SDS + OH Fitting, and VIII. Droplet Simulation (PDF)

AUTHOR INFORMATION

Corresponding Author

*E-mail: seinfeld@caltech.edu. Phone: +1 626 395 4635. Fax: +1 626 568 8743.

ORCID

Yuanlong Huang: 0000-0002-6726-8904
Christopher M. Kenseth: 0000-0003-3188-2336
Ran Zhao: 0000-0002-1096-7632
Chen Wang: 0000-0001-9565-8777
John H. Seinfeld: 0000-0003-1344-4068

Present Address

⊥R.Z.: Department of Chemistry, University of Alberta, Edmonton, AB, Canada T6G2G2

Author Contributions

∥Y.H., K.M.B.: These authors contributed equally to this work

Notes

The authors declare no competing financial interest.

ACKNOWLEDGMENTS

REFERENCES

(1) George, I. J.; Abbatt, J. P. D. Heterogeneous Oxidation of Atmospheric Aerosol Particles by Gas-Phase Radicals. *Nat. Chem.* **2010**, 2, 713.

(2) Houle, F. A.; Wiegel, A. A.; Wilson, K. R. Changes in Reactivity as Chemistry Becomes Confined to an Interface. The Case of Free Radical Oxidation of $C_{30}H_{62}$ Alkane by OH. *J. Phys. Chem. Lett.* **2018**, 9, 1053−1057.

(3) Zhong, J.; Kumar, M.; Francisco, J. S.; Zeng, X. C. Insight into Chemistry on Cloud/Aerosol Water Surfaces. *Acc. Chem. Res.* **2018**, 51, 1229−1237.

(4) Wren, S. N.; Gordon, B. P.; Valley, N. A.; McWilliams, L. E.; Richmond, G. L. Hydration, Orientation, and Conformation of Methylglyoxal at the Air-Water Interface. *J. Phys. Chem. A* **2015**, 119, 6391−6403.

(5) Heath, A. A.; Valsaraj, K. T. Effects of Temperature, Oxygen Level, Ionic Strength, and pH on the Reaction of Benzene with Hydroxyl Radicals at the Air-Water Interface in Comparison to the Bulk Aqueous Phase. *J. Phys. Chem. A* **2015**, 119, 8527−8536.

(6) Hua, W.; Verreault, D.; Allen, H. C. Relative Order of Sulfuric Acid, Bisulfate, Hydronium, and Cations at the Air-Water Interface. *J. Am. Chem. Soc.* **2015**, 137, 13920−13926.

(7) Martins-Costa, M. T. C.; García-Prieto, F. F.; Ruiz-López, M. F. Reactivity of Aldehydes at the Air-Water Interface. Insights from Molecular Dynamics Simulations and ab initio Calculations. *Org. Biomol. Chem.* **2015**, 13, 1673−1679.

(8) Enami, S.; Colussi, A. J. Efficient Scavenging of Criegee Intermediates on Water by Surface-Active *cis*-pinonic Acid. *Phys. Chem. Chem. Phys.* **2017**, 19, 17044−17051.

(9) Jones, S. H.; King, M. D.; Ward, A. D.; Rennie, A. R.; Jones, A. C.; Arnold, T. Are Organic Films from Atmospheric Aerosol and Sea Water Inert to Oxidation by Ozone at the Air-Water Interface? *Atmos. Environ.* **2017**, 161, 274−287.

(10) Wellen, B. A.; Lach, E. A.; Allen, H. C. Surface pK_a of Octanoic, Nonanoic, and Decanoic Fatty Acids at the Air-Water Interface: Applications to Atmospheric Aerosol Chemistry. *Phys. Chem. Chem. Phys.* **2017**, 19, 26551−26558.

(11) Kumar, M.; Li, H.; Zhang, X.; Zeng, X. C.; Francisco, J. S. Nitric Acid-Amine Chemistry in the Gas Phase and at the Air-Water Interface. *J. Am. Chem. Soc.* **2018**, 140, 6456.

(12) Pillar, E. A.; Guzman, M. I. Oxidation of Substituted Catechols at the Air-Water Interface: Production of Carboxylic Acids, Quinones, and Polyphenols. *Environ. Sci. Technol.* **2017**, 51, 4951−4959.

(13) King, M. D.; Rennie, A. R.; Thompson, K. C.; Fisher, F. N.; Dong, C. C.; Thomas, R. K.; Pfrang, C.; Hughes, A. V. Oxidation of Oleic Acid at the Air-Water Interface and Its Potential Effects on Cloud Critical Supersaturations. *Phys. Chem. Chem. Phys.* **2009**, 11, 7699−7707.

(14) Xiao, P.; Wang, Q.; Fang, W.-H.; Cui, G. Quantum Chemical Investigation on Photochemical Reactions of Nonanoic Acids at Air-Water Interface. *J. Phys. Chem. A* **2017**, 121, 4253−4262.

(15) Sebastiani, F.; Campbell, R. A.; Rastogi, K.; Pfrang, C. Nighttime Oxidation of Surfactants at the Air-Water Interface: Effects of Chain Length, Head Group and Saturation. *Atmos. Chem. Phys.* **2018**, 18, 3249−3268.

(16) Guenther, A. B.; Jiang, X.; Heald, C. L.; Sakulyanontvittaya, T.; Duhl, T.; Emmons, L. K.; Wang, X. The Model of Emissions of Gases and Aerosols from Nature version 2.1 (MEGAN2.1): An Extended and Updated Framework for Modeling Biogenic Emissions. *Geosci. Model Dev.* **2012**, 5, 1471−1492.

(17) Müller, L.; Reinnig, M.-C.; Naumann, K. H.; Saathoff, H.; Mentel, T. F.; Donahue, N. M.; Hoffmann, T. Formation of 3-Methyl-1,2,3-Butanetricarboxylic Acid via Gas Phase Oxidation of Pinonic Acid - A Mass Spectrometric Study of SOA Aging. *Atmos. Chem. Phys.* **2012**, 12, 1483−1496.

(18) Witkowski, B.; Gierczak, T. *cis*-Pinonic Acid Oxidation by Hydroxyl Radicals in the Aqueous Phase under Acidic and Basic Conditions: Kinetics and Mechanism. *Environ. Sci. Technol.* **2017**, 51, 9765−9773.

(19) Lee, A. K. Y.; Herckes, P.; Leaitch, W. R.; Macdonald, A. M.; Abbatt, J. P. D. Aqueous OH Oxidation of Ambient Organic Aerosol and Cloud Water Organics: Formation of Highly Oxidized Products. *Geophys. Res. Lett.* **2011**, *38*, L11805.

(20) Aljawhary, D.; Zhao, R.; Lee, A. K. Y.; Wang, C.; Abbatt, J. P. D. Kinetics, Mechanism, and Secondary Organic Aerosol Yield of Aqueous Phase Photo-Oxidation of α-Pinene Oxidation Products. *J. Phys. Chem. A* **2016**, *120*, 1395−1407.

(21) Bilde, M.; Pandis, S. N. Evaporation Rates and Vapor Pressures of Individual Aerosol Species Formed in the Atmospheric Oxidation of α- and β-Pinene. *Environ. Sci. Technol.* **2001**, *35*, 3344−3349.

(22) Lignell, H.; Epstein, S. A.; Marvin, M. R.; Shemesh, D.; Gerber, B.; Nizkorodov, S. Experimental and Theoretical Study of Aqueous cis-Pinonic Acid Photolysis. *J. Phys. Chem. A* **2013**, *117*, 12930−12945.

(23) Li, X.; Hede, T.; Tu, Y.; Leck, C.; Ågren, H. Surface-Active cis-Pinonic Acid in Atmospheric Droplets: A Molecular Dynamics Study. *J. Phys. Chem. Lett.* **2010**, *1*, 769−773.

(24) Enami, S.; Sakamoto, Y. OH-Radical Oxidation of Surface-Active cis-Pinonic Acid at the Air-Water Interface. *J. Phys. Chem. A* **2016**, *120*, 3578−3587.

(25) Lai, C.; Liu, Y.; Ma, J.; Ma, Q.; Chu, B.; He, H. Heterogeneous Kinetics of cis-Pinonic Acid with Hydroxyl Radical under Different Environmental Conditions. *J. Phys. Chem. A* **2015**, *119*, 6583−6593.

(26) Grimm, R. L.; Beauchamp, J. L. Field-Induced Droplet Ionization Mass Spectrometry. *J. Phys. Chem. B* **2003**, *107*, 14161−14163.

(27) Grimm, R. L.; Beauchamp, J. L. Dynamics of Field-Induced Droplet Ionization: Time-Resolved Studies of Distortion, Jetting, and Progeny Formation from Charged and Neutral Methanol Droplets Exposed to Strong Electric Fields. *J. Phys. Chem. B* **2005**, *109*, 8244−8250.

(28) Grimm, R. L.; Hodyss, R.; Beauchamp, J. L. Probing Interfacial Chemistry of Single Droplets with Field-Induced Droplet Ionization Mass Spectrometry: Physical Adsorption of Polycyclic Aromatic Hydrocarbons and Ozonolysis of Oleic Acid and Related Compounds. *Anal. Chem.* **2006**, *78*, 3800−3806.

(29) Thomas, D. A.; Coggon, M. M.; Lignell, H.; Schilling, K. A.; Zhang, X.; Schwantes, R. H.; Flagan, R. C.; Seinfeld, J. H.; Beauchamp, J. L. Real-Time Studies of Iron Oxalate-Mediated Oxidation of Glycolaldehyde as a Model for Photochemical Aging of Aqueous Tropospheric Aerosols. *Environ. Sci. Technol.* **2016**, *50*, 12241−12249.

(30) Zhang, X.; Barraza, K. M.; Upton, K. T.; Beauchamp, J. L. Time Resolved Study of Hydroxyl Radical Oxidation of Oleic Acid at the Air-Water Interface. *Chem. Phys. Lett.* **2017**, *683*, 76−82.

(31) Kim, H. I.; Kim, H.; Shin, Y. S.; Beegle, L. W.; Goddard, W. A.; Heath, J. R.; Kanik, I.; Beauchamp, J. L. Time Resolved Studies of Interfacial Reactions of Ozone with Pulmonary Phospholipid Surfactants Using Field Induced Droplet Ionization Mass Spectrometry. *J. Phys. Chem. B* **2010**, *114*, 9496−9503.

(32) Kim, H. I.; Kim, H.; Shin, Y. S.; Beegle, L. W.; Jang, S. S.; Neidholdt, E. L.; Goddard, W. A.; Heath, J. R.; Kanik, I.; Beauchamp, J. L. Interfacial Reactions of Ozone with Surfactant Protein B in a Model Lung Surfactant System. *J. Am. Chem. Soc.* **2010**, *132*, 2254−2263.

(33) Zhang, X.; Barraza, K. M.; Beauchamp, J. L. Cholesterol Provides Nonsacrificial Protection of Membrane Lipids from Chemical Damage at Air-Water Interface. *Proc. Natl. Acad. Sci. U.S.A.* **2018**, *115*, 3255.

(34) Barraza, K. M. The Study of the Stepwise Hydroxyl Radical-Mediated Oxidation of Alkyl Surfactants at the Air-Water Interface. Ph.D. Thesis, California Institute of Technology, 2018.

(35) Pöschl, U.; Rudich, Y.; Ammann, M. Kinetic Model Framework for Aerosol and Cloud Surface Chemistry and Gas-Particle Interactions - Part 1: General Equations, Parameters, and Terminology. *Atmos. Chem. Phys.* **2007**, *7*, 5989−6023.

(36) Socorro, J.; Lakey, P. S. J.; Han, L.; Berkemeier, T.; Lammel, G.; Zetzsch, C.; Pöschl, U.; Shiraiwa, M. Heterogeneous OH Oxidation, Shielding Effects, and Implications for the Atmospheric Fate of Terbuthylazine and Other Pesticides. *Environ. Sci. Technol.* **2017**, *51*, 13749−13754.

(37) Vácha, R.; Slavíček, P.; Mucha, M.; Finlayson-Pitts, B. J.; Jungwirth, P. Adsorption of Atmospherically Relevant Gases at the Air/Water Interface: Free Energy Profiles of Aqueous Solvation of N_2, O_2, O_3, OH, H_2O, HO_2, and H_2O_2. *J. Phys. Chem. A* **2004**, *108*, 11573−11579.

(38) Svishchev, I. M.; Plugatyr, A. Y. Hydroxyl Radical in Aqueous Solution: Computer Simulation. *J. Phys. Chem. B* **2005**, *109*, 4123−4128.

(39) Goss, K.-U. Predicting Adsorption of Organic Chemicals at the Air-Water Interface. *J. Phys. Chem. A* **2009**, *113*, 12256−12259.

(40) Wang, C.; Goss, K.-U.; Lei, Y. D.; Abbatt, J. P. D.; Wania, F. Calculating Equilibrium Phase Distribution during the Formation of Secondary Organic Aerosol Using COSMOtherm. *Environ. Sci. Technol.* **2015**, *49*, 8585−8594.

(41) Vereecken, L.; Peeters, J. Enhanced H-Atom Abstraction from Pinonaldehyde, Pinonic Acid, Pinic Acid, and Related Compounds: Theoretical Study of C-H Bond Strengths. *Phys. Chem. Chem. Phys.* **2002**, *4*, 467−472.

(42) Atkinson, R.; Arey, J. Atmospheric Degradation of Volatile Organic Compounds. *Chem. Rev.* **2003**, *103*, 4605−4638.

(43) Orlando, J. J.; Tyndall, G. S. Laboratory Studies of Organic Peroxy Radical Chemistry: An Overview with Emphasis on Recent Issues of Atmospheric Significance. *Chem. Soc. Rev.* **2012**, *41*, 6294−6317.

(44) von Sonntag, C.; Schuchmann, H.-P. The Elucidation of Peroxyl Radical Reactions in Aqueous Solution with the Help of Radiation-Chemical Methods. *Angew. Chem., Int. Ed. Engl.* **1991**, *30*, 1229−1253.

(45) Ervens, B.; Volkamer, R. Glyoxal Processing by Aerosol Multiphase Chemistry: Towards a Kinetic Modeling Framework of Secondary Organic Aerosol Formation in Aqueous Particles. *Atmos. Chem. Phys.* **2010**, *10*, 8219−8244.

(46) California Air Resources Board. Air Quality and Meteorological Information System. https://www.arb.ca.gov/aqmis2/aqdselect.php.

(47) Praske, E.; Otkjær, R. V.; Crounse, J. D.; Hethcox, J. C.; Stoltz, B. M.; Kjaergaard, H. G.; Wennberg, P. O. Atmospheric Autoxidation is Increasingly Important in Urban and Suburban North America. *Proc. Natl. Acad. Sci. U. S. A.* **2018**, *115*, 64.

(48) Carslaw, N. A New Detailed Chemical Model for Indoor Air Pollution. *Atmos. Environ.* **2007**, *41*, 1164−1179.

(49) Seinfeld, J. H.; Pandis, S. N. *Atmospheric Chemistry and Physics: From Air Pollution to Climate Change*, 3rd ed.; John Wiley & Sons, Inc., 2016.

(50) Yasmeen, F.; Vermeylen, R.; Szmigielski, R.; Iinuma, Y.; Böge, O.; Herrmann, H.; Maenhaut, W.; Claeys, M. Terpenylic Acid and Related Compounds: Precursors for Dimers in Secondary Organic Aerosol from the Ozonolysis of α- and β-Pinene. *Atmos. Chem. Phys.* **2010**, *10*, 9383−9392.

(51) Demarque, D. P.; Crotti, A. E. M.; Vessecchi, R.; Lopes, J. L. C.; Lopes, N. P. Fragmentation Reactions Using Electrospray Ionization Mass Spectrometry: An Important Tool for the Structural Elucidation and Characterization of Synthetic and Natural Products. *Nat. Prod. Rep.* **2016**, *33*, 432−455.

(52) Russell, G. A. Deuterium-Isotope Effects in the Autoxidation of Aralkyl Hydrocarbons. Mechanism of the Interaction of Peroxy Radicals. *J. Am. Chem. Soc.* **1957**, *79*, 3871−3877.

(53) Howell, H.; Fisher, G. S. The Dissociation Constants of Some of the Terpene Acids. *J. Am. Chem. Soc.* **1958**, *80*, 6316−6319.

(54) Ervens, B.; Gligorovski, S.; Herrmann, H. Temperature-Dependent Rate Constants for Hydroxyl Radical reactions with Organic Compounds in Aqueous Solutions. *Phys. Chem. Chem. Phys.* **2003**, *5*, 1811−1824.

(55) Lee, M.-T.; Orlando, F.; Artiglia, L.; Chen, S.; Ammann, M. Chemical Composition and Properties of the Liquid-Vapor Interface of Aqueous C1 to C4 Monofunctional Acid and Alcohol Solutions. *J. Phys. Chem. A* **2016**, *120*, 9749−9758.

(56) Tan, A.; Ziegler, A.; Steinbauer, B.; Seelig, J. Thermodynamics of Sodium Dodecyl Sulfate Partitioning into Lipid Membranes. *Biophys. J.* **2002**, *83*, 1547−1556.

(57) Blando, J. D.; Turpin, B. J. Secondary Organic Aerosol Formation in Cloud and Fog Droplets: a Literature Evaluation of Plausibility. *Atmos. Environ.* **2000**, *34*, 1623−1632.

(58) Lim, Y. B.; Tan, Y.; Perri, M. J.; Seitzinger, S. P.; Turpin, B. J. Aqueous Chemistry and Its Role in Secondary Organic Aerosol (SOA) Formation. *Atmos. Chem. Phys.* **2010**, *10*, 10521−10539.

(59) Ervens, B.; Turpin, B. J.; Weber, R. J. Secondary Organic Aerosol Formation in Cloud Droplets and Aqueous Particles (aqSOA): A Review of Laboratory, Field and Model Studies. *Atmos. Chem. Phys.* **2011**, *11*, 11069−11102.

(60) Lim, H.-J.; Carlton, A. G.; Turpin, B. J. Isoprene Forms Secondary Organic Aerosol through Cloud Processing: Model Simulations. *Environ. Sci. Technol.* **2005**, *39*, 4441−4446.

(61) McNeill, V. F.; Woo, J. L.; Kim, D. D.; Schwier, A. N.; Wannell, N. J.; Sumner, A. J.; Barakat, J. M. Aqueous-Phase Secondary Organic Aerosol and Organosulfate Formation in Atmospheric Aerosols: A Modeling Study. *Environ. Sci. Technol.* **2012**, *46*, 8075−8081.

(62) Kavouras, I. G.; Mihalopoulos, N.; Stephanou, E. G. Secondary Organic Aerosol Formation vs Primary Organic Aerosol Emission: In Situ Evidence for the Chemical Coupling between Monoterpene Acidic Photooxidation Products and New Particle Formation over Forests. *Environ. Sci. Technol.* **1999**, *33*, 1028−1037.

(63) Vestenius, M.; Hellén, H.; Levula, J.; Kuronen, P.; Helminen, K. J.; Nieminen, T.; Kulmala, M.; Hakola, H. Acidic Reaction Products of Monoterpenes and Sesquiterpenes in Atmospheric Fine Particles in a Boreal Forest. *Atmos. Chem. Phys.* **2014**, *14*, 7883−7893.

(64) Bréon, F.-M.; Tanré, D.; Generoso, S. Aerosol Effect on Cloud Droplet Size Monitored from Satellite. *Science* **2002**, *295*, 834−838.

(65) Mai, H.; Shiraiwa, M.; Flagan, R. C.; Seinfeld, J. H. Under What Conditions Can Equilibrium Gas-Particle Partitioning Be Expected to Hold in the Atmosphere? *Environ. Sci. Technol.* **2015**, *49*, 11485−11491.

(66) Nozière, B. Don't Forget the Surface. *Science* **2016**, *351*, 1396−1397.

(67) Ruehl, C. R.; Davies, J. F.; Wilson, K. R. An Interfacial Mechanism for Cloud Droplet Formation on Organic Aerosols. *Science* **2016**, *351*, 1447−1450.

(68) Tan, Y.; Perri, M. J.; Seitzinger, S. P.; Turpin, B. J. Effects of Precursor Concentration and Acidic Sulfate in Aqueous Glyoxal-OH Radical Oxidation and Implications for Secondary Organic Aerosol. *Environ. Sci. Technol.* **2009**, *43*, 8105−8112.

(69) Galloway, M. M.; Loza, C. L.; Chhabra, P. S.; Chan, A. W. H.; Yee, L. D.; Seinfeld, J. H.; Keutsch, F. N. Analysis of Photochemical and Dark Glyoxal Uptake: Implications for SOA Formation. *Geophys. Res. Lett.* **2011**, *38*, L17811.

(70) Burkholder, J. B.; Sander, S. P.; Abbatt, J. P. D.; Barker, J. R.; Huie, R. E.; Kolb, C. E.; Kurylo, M. J.; Orkin, V. L.; Wilmouth, D. M.; Wine, P. H. *Chemical Kinetics and Photochemical Data for Use in Atmospheric Studies, Evaluation No. 18*; JPL Publication 15-10; Jet Propulsion Laboratory: Pasadena, 2015.

(71) Kameel, F. R.; Hoffmann, M. R.; Colussi, A. J. OH Radical-Initiated Chemistry of Isoprene in Aqueous Media. Atmospheric Implications. *J. Phys. Chem. A* **2013**, *117*, 5117−5123.

(72) Tinel, L.; Rossignol, S.; Bianco, A.; Passananti, M.; Perrier, S.; Wang, X.; Brigante, M.; Donaldson, D. J.; George, C. Mechanistic Insights on the Photosensitized Chemistry of a Fatty Acid at the Air/Water Interface. *Environ. Sci. Technol.* **2016**, *50*, 11041−11048.

(73) Bernard, F.; Ciuraru, R.; Boréave, A.; George, C. Photo-sensitized Formation of Secondary Organic Aerosols above the Air/Water Interface. *Environ. Sci. Technol.* **2016**, *50*, 8678−8686.

(74) Rossignol, S.; Tinel, L.; Bianco, A.; Passananti, M.; Brigante, M.; Donaldson, D. J.; George, C. Atmospheric Photochemistry at a Fatty Acid-Coated Air-Water Interface. *Science* **2016**, *353*, 699−702.

(75) Ivanov, A. V.; Trakhtenberg, S.; Bertram, A. K.; Gershenzon, Y. M.; Molina, M. J. OH HO$_2$, and Ozone Gaseous Diffusion Coefficients. *J. Phys. Chem. A* **2007**, *111*, 1632−1637.

A p p e n d i x   E

CHARACTERIZATION OF AEROSOL HYGROSCOPICITY OVER THE NORTHEAST PACIFIC OCEAN: IMPACTS ON PREDICTION OF CCN AND STRATOCUMULUS CLOUD DROPLET NUMBER CONCENTRATIONS

Schulze, B. C.; Charan, S. M.; Kenseth, C. M.; Kong, W.; Bates, K. H.; Williams, W.; Metcalf, A. R.; Jonsson, H. H.; Woods, R.; Sorooshian, A.; Flagan, R. C.; Seinfeld, J. H. Characterization of Aerosol Hygroscopicity Over the Northeast Pacific Ocean: Impacts on Prediction of CCN and Stratocumulus Cloud Droplet Number Concentrations. *Earth Space Sci.* **2020**, *7*, e2020EA001098. DOI: 10.1029/2020EA001098.

Earth and Space Science

Key Points:
- Aerosol hygroscopicity exhibited substantial temporal variability in the MBL
- Errors in predicted MBL CCN concentrations produced by assuming a constant aerosol size distribution or hygroscopicity are discussed
- Sensitivity of simulated CDNC to hygroscopicity is maximized in marine clouds with either very weak or relatively strong updraft velocities

Supporting Information:
- Supporting Information S1

Characterization of Aerosol Hygroscopicity Over the Northeast Pacific Ocean: Impacts on Prediction of CCN and Stratocumulus Cloud Droplet Number Concentrations

B. C. Schulze[1] , S. M. Charan[2] , C. M. Kenseth[2] , W. Kong[2] , K. H. Bates[3] , W. Williams[4], A. R. Metcalf[4] , H. H. Jonsson[5], R. Woods[5], A. Sorooshian[6,7] , R. C. Flagan[8,2] , and J. H. Seinfeld[8,2]

[1]Department of Environmental Science and Engineering, California Institute of Technology, Pasadena, CA, USA, [2]Division of Chemistry and Chemical Engineering, California Institute of Technology, Pasadena, CA, USA, [3]Center for the Environment, Harvard University, Cambridge, MA, USA, [4]Department of Environmental Engineering and Earth Sciences, Clemson University, Anderson, SC, USA, [5]Naval Postgraduate School, Monterey, CA, USA, [6]Department of Chemical and Environmental Engineering, University of Arizona, Tucson, AZ, USA, [7]Department of Hydrology and Atmospheric Sciences, University of Arizona, Tucson, AZ, USA, [8]Division of Engineering and Applied Science, California Institute of Technology, Pasadena, CA, USA

Abstract During the Marine Aerosol Cloud and Wildfire Study (MACAWS) in June and July of 2018, aerosol composition and cloud condensation nuclei (CCN) properties were measured over the N.E. Pacific to characterize the influence of aerosol hygroscopicity on predictions of ambient CCN and stratocumulus cloud droplet number concentrations (CDNC). Three vertical regions were characterized, corresponding to the marine boundary layer (MBL), an above-cloud organic aerosol layer (AC-OAL), and the free troposphere (FT) above the AC-OAL. The aerosol hygroscopicity parameter (κ) was calculated from CCN measurements (κ_{CCN}) and bulk aerosol mass spectrometer (AMS) measurements (κ_{AMS}). Within the MBL, measured hygroscopicities varied between values typical of both continental environments (~0.2) and remote marine locations (~0.7). For most flights, CCN closure was achieved within 20% in the MBL. For five of the seven flights, assuming a constant aerosol size distribution produced similar or better CCN closure than assuming a constant "marine" hygroscopicity ($\kappa = 0.72$). An aerosol-cloud parcel model was used to characterize the sensitivity of predicted stratocumulus CDNC to aerosol hygroscopicity, size distribution properties, and updraft velocity. Average CDNC sensitivity to accumulation mode aerosol hygroscopicity is 39% as large as the sensitivity to the geometric median diameter in this environment. Simulations suggest CDNC sensitivity to hygroscopicity is largest in marine stratocumulus with low updraft velocities (<0.2 m s^{-1}), where accumulation mode particles are most relevant to CDNC, and in marine stratocumulus or cumulus with large updraft velocities (>0.6 m s^{-1}), where hygroscopic properties of the Aitken mode dominate hygroscopicity sensitivity.

1. Introduction

Marine stratocumulus (MSc) clouds, commonly observed off the Western coasts of North America, South America, Africa, and Australia, cover nearly one fifth of the Earth's surface and exert a large impact on its radiative balance (Wood, 2012). These cloud decks are particularly relevant to global climate due to their high albedo contrast with the underlying ocean and relatively low altitude, resulting in stronger shortwave reflectance than longwave absorption (Brenguier et al., 2000; Randall et al., 1984; Wood, 2012). Previous estimates suggest that a ~12% increase in the albedo of these clouds would produce a negative radiative forcing equivalent in magnitude to that of doubling atmospheric CO_2 concentrations (Latham et al., 2008; Stevens & Brenguier, 2009). Remote sensing, parcel modeling, and large eddy simulation (LES) studies have all established that MSc exhibit substantial albedo susceptibility to variations in cloud droplet number concentrations (CDNC) (Berner et al., 2015; Chen et al., 2011; Oreopoulos & Platnick, 2008; Platnick & Twomey, 1994; Sanchez et al., 2016). Understanding the sensitivity of MSc CDNC to aerosols acting as

cloud condensation nuclei (CCN) is therefore a critical aspect of reducing uncertainty in climate change predictions (Seinfeld et al., 2016).

The CDNC and albedo of MSc are substantially influenced by the abundance of below-cloud CCN. A recent satellite analysis suggested that variability in below-cloud CCN concentration may be responsible for ~45% of the variability in the radiative effect of marine boundary layer clouds (Rosenfeld et al., 2019). This influence results from the fact that increased CCN abundance enhances cloud reflectivity at constant liquid water path (Twomey, 1977) and has the potential to reduce MSc precipitation rates, increasing cloud lifetime (Ackerman et al., 1993; Albrecht, 1989; Goren & Rosenfeld, 2012; Rosenfeld, 2006). As a result, a major component of the uncertainty in the estimated indirect aerosol forcing has been attributed to the prediction of below-cloud CCN concentrations (Rosenfeld et al., 2014; Sotiropoulou et al., 2007). While the aerosol size distribution is generally thought to be the most important determinant of CCN activity (e.g., Dusek et al., 2006; Ervens et al., 2007; McFiggans et al., 2006; Reutter et al., 2009), particle composition has also been shown to exert a substantial influence (Jimenez et al., 2009; Liu & Wang, 2010; Mei et al., 2013; Quinn et al., 2008; Sanchez et al., 2016).

The propensity of a given aerosol particle to act as a CCN can be described using Köhler theory (Köhler, 1936; Seinfeld et al., 2016), provided sufficient information is known regarding particle size and solute properties (e.g., molecular weight, solubility, density, and activity). A novel framework, κ-Köhler theory, condenses these solute characteristics into a single parameter κ (the aerosol hygroscopicity) that can be easily incorporated into large-scale models (Petters & Kreidenweis, 2007). Substantial effort has, therefore, been devoted to quantifying κ values in a multitude of environments (Ervens et al., 2010; Gunthe et al., 2009; Pringle et al., 2010; Rose et al., 2010; Thalman et al., 2017). While κ values characteristic of inorganic aerosol components are relatively well-established, atmospheric organic aerosol is composed of numerous, highly diverse organic compounds, complicating representation of organic hygroscopicity using a single parameter (Kanakidou et al., 2005). Experimental studies have characterized κ values of secondary organic aerosol (SOA) (e.g., Asa-Awuku et al., 2010; Duplissy et al., 2008, 2011; Frosch et al., 2013; Lambe et al., 2011; Massoli et al., 2010; Zhao et al., 2015), and field studies have characterized the typical range of organic κ values (κ_{org}) observed in the atmosphere (Chang et al., 2010; Gunthe et al., 2009; Levin et al., 2014; Mei et al., 2013; Thalman et al., 2017; Wang et al., 2008). Generally, ambient κ_{org} values are found to be 0.1–0.2 for aged aerosol and primary marine organics and ~0 for freshly emitted combustion aerosol (e.g., soot) (Kreidenweis & Asa-Awuku, 2014). A linear relationship has been noted between observed κ_{org} values and organic aerosol oxygen-to-carbon (O:C) ratios in both the laboratory and the field (Chang et al., 2010; Lambe et al., 2011; Mei et al., 2013; Wang et al., 2019).

Ambient particle hygroscopicity data have been combined with aerosol size distribution measurements in CCN closure studies to assess the extent to which Köhler theory can be used to predict ambient CCN concentrations (e.g., Almeida et al., 2014; Asa-Awuku et al., 2011; Cubison et al., 2008; Medina et al., 2007; McFiggans et al., 2006; Moore et al., 2012; Ren et al., 2018; VanReken et al., 2003). Analyzing the accuracy of predicted CCN concentrations can provide insight into the influence of specific aerosol characteristics on CCN activity (Bougiatioti et al., 2011; Cubison et al., 2008; Medina et al., 2007; VanReken et al., 2003; Wang et al., 2010). For instance, size-resolved compositional (i.e., hygroscopicity) data are often required to accurately reproduce observed CCN concentrations in locations dominated by organic aerosol (Bhattu & Tripathi, 2015; Medina et al., 2007; Ren et al., 2018), while aerosol mixing state has been shown to strongly impact total CCN concentrations in urban environments (Cubison et al., 2008; Ervens et al., 2010; Quinn et al., 2008). By analyzing data from five ambient measurement campaigns, Ervens et al. (2010) found that for aerosol measured farther than a few tens of kilometers from the emission source, CCN activity could be predicted within a factor of two independent of either aerosol mixing state (i.e., internal or external) or organic solubility (i.e., insoluble or slightly soluble). Wang et al. (2010) further demonstrated that CCN concentrations can often be reproduced within 20% assuming internal mixing of aerosol components if the overall κ of the aerosol population is >0.1. The direct impact of variability in aerosol hygroscopicity on CCN concentrations is often assessed by assuming an invariant chemical composition, represented as a fixed κ, in CCN closure analyses. Field campaigns in continental environments ranging from polluted megacities to the pristine tropical rainforest have shown that CCN concentrations could be reproduced within 20% and 50%, respectively, assuming a constant $\kappa = 0.3$ (Gunthe et al., 2009; Rose et al., 2010), a value representative of average continental conditions (Andreae & Rosenfeld, 2008; Pringle et al., 2010). However, in coastal regions, MBL aerosol can result from a mixture of

distinct marine and continental emissions (e.g., Coggon et al., 2014; Mardi et al., 2018; Modini et al., 2015; Sorooshian et al., 2009), which complicates aerosol representation using regional or global models. CCN closure analysis can provide insight into the uncertainties in CCN concentrations that may result from inaccurate model representation of aerosol composition in these environments.

Due to the importance of the persistent stratocumulus cloud decks over the N.E. Pacific to global climate, aerosol characteristics in this region have received considerable attention. However, the diverse range of particle sources, including shipping exhaust (Coggon et al., 2012; Murphy et al., 2009; Prabhakar et al., 2014; Wonaschütz et al., 2013), primary and secondary natural marine emissions (Modini et al., 2015; Prabhakar et al., 2014; Sorooshian et al., 2009), anthropogenic and biogenic continental emissions (Coggon et al., 2014; Hegg et al., 2010; Moore et al., 2012), wildfire plumes (Brioude et al., 2009; Mardi et al., 2018), and aged aerosol from the Asian continent (Roberts et al., 2006, 2010), combined with strong temporal and spatial variability due to variable meteorological conditions, has hindered determination of general characteristics of the marine atmosphere in this location. This complexity is reflected in the diversity of hygroscopicity measurements previously reported in the marine boundary layer (MBL) and free troposphere (FT). For instance, average κ values reported from MBL measurements have varied from ~0.2–0.3 (Moore et al., 2012; Roberts et al., 2010) to ~0.5–0.7 (Royalty et al., 2017; Yakobi-Hancock et al., 2014). Measurements in the FT, while sparse, have been even more variable (κ ~0.05–1.0) (Roberts et al., 2006, 2010). While these measurements could largely be reconciled assuming various mixtures of continental (0.27 $\pm$ 0.2) and marine (0.72 $\pm$ 0.2) aerosol, determining the major emissions sources and meteorological patterns dictating these changes is important for improving model representation of the region (Pringle et al., 2010). CCN-based measurements of aerosol hygroscopicity and the resulting information about small particle composition can be especially useful in this regard, as knowledge of small particle composition can provide substantial insight into particle sources.

While hygroscopicity and mixing state characterization are important components of understanding the CCN activity of ambient aerosol, the dynamic processes controlling supersaturation, droplet nucleation, and droplet growth within clouds lead to nonlinear relationships between aerosol properties and CDNC. As a result, aerosol-cloud parcel modeling is instrumental to fully understand the role of aerosol hygroscopicity and mixing state on CDNC. Reutter et al. (2009) used such a model to distinguish three regimes of aerosol activation, defined as the aerosol-limited, updraft-limited, and transitional regimes, based on the ratio of updraft velocity to aerosol number concentration at the cloud base. The dependence of CDNC on aerosol hygroscopicity, while limited relative to other parameters such as particle number concentration and updraft velocity, was found to vary substantially between regimes. Additional modeling revealed that CDNC sensitivity to aerosol hygroscopicity is highly dependent on the below-cloud aerosol size distribution, with sensitivity increasing substantially with smaller median radii (Ward et al., 2010). Sanchez et al. (2016) concluded that modeled stratocumulus albedo is insensitive to the assumed hygroscopicity of the organic aerosol fraction; however, the sensitivity of CDNC to bulk hygroscopicity has yet to be fully evaluated in this environment.

The present study uses measurements of aerosol composition and CCN activity collected during the Marine Aerosol Cloud and Wildfire Study (MACAWS), combined with an aerosol-cloud parcel model, to gain insight into near-coastal aerosol hygroscopicity and its influence on prediction of CCN and MSc CDNC. Hygroscopicity measurements are combined with airmass backward trajectories and meteorological parameters to attribute observed particle characteristics to distinct sources when possible. CCN closure analyses are performed to investigate the impact of compositional and mixing state assumptions on CCN predictions. Finally, aerosol-cloud parcel model simulations constrained with MSc microphysical measurements are used to directly investigate the sensitivity of stratocumulus CDNC to aerosol hygroscopicity, mixing state, and size distribution properties.

2. Methodology

2.1. MACAWS Field Mission

The 2018 Marine Aerosol Cloud and Wildfire Study (MACAWS) consisted of 16 research flights operated out of the Center for Interdisciplinary Remotely-Piloted Aircraft Studies (CIRPAS) in Marina, California, during June and July. Measurements were performed on-board the CIRPAS Navy Twin Otter aircraft

(a) (b)
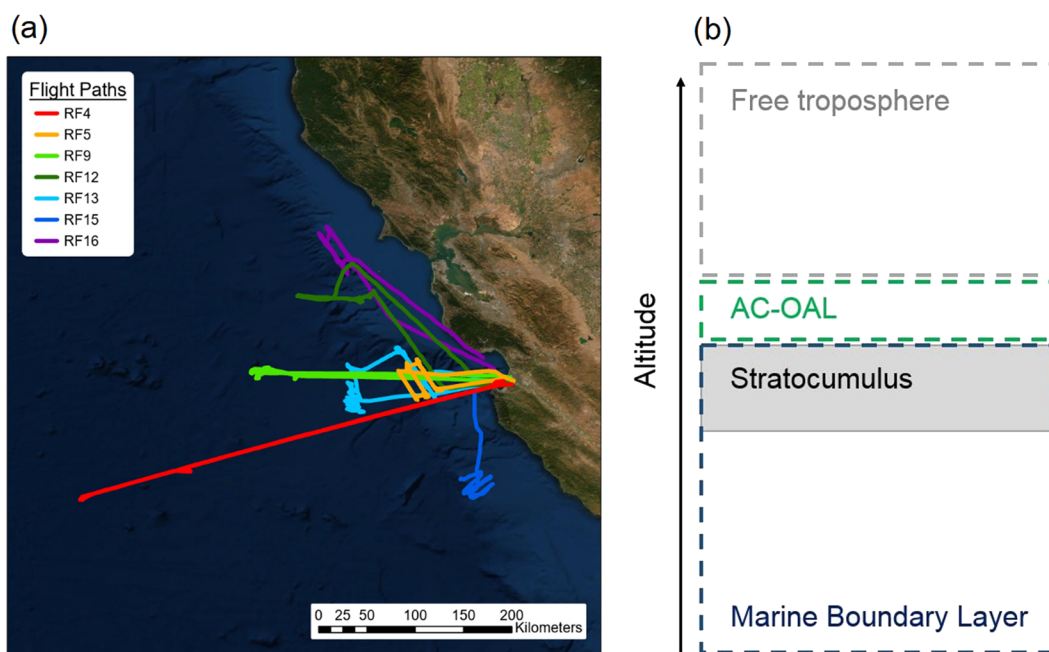
Figure 1. (a) Trajectories of the seven MACAWS research flights analyzed in this study. (b) Relative vertical locations of the marine boundary layer, the above-cloud organic-aerosol layer (AC-OAL), and the free troposphere.

(Coggon et al., 2012, 2014; Russell et al., 2013; Sorooshian et al., 2019; Wang et al., 2016). The scientific objectives of individual flights included characterization of marine aerosols and clouds, sampling of shipping vessel exhaust plumes, and investigation of nearby wildfire emissions. The present study focuses on seven research flights primarily aimed at characterization of the relationship between marine aerosol and the overlying stratocumulus cloud deck. Paths of these seven flights are depicted in Figure 1. Flight strategies typically involved a series of level legs at varying altitudes within the MBL and overlying FT. Slant or spiral soundings were generally performed before and after a series of level legs.

2.2. Twin Otter Instrumentation

The navigational and meteorological instrumentation utilized by the Twin Otter aircraft is described in detail by Sorooshian et al. (2018). Ambient aerosol was sampled using a forward-facing sub-isokinetic inlet (Hegg et al., 2005). Aerosol and cloud droplet number concentrations were characterized using a variety of instruments, including multiple condensation particle counters (CPC, TSI 3010, $D_p > 10$ nm; ultrafine CPC, TSI UFCPC, $D_p > 3$ nm), a passive cavity aerosol spectrometer probe (PCASP, $D_p \sim 0.11$–3.4 μm), and forward scattering spectrometer probe (FSSP, Particle Measuring Systems [PMS], $D_p \sim 1.6$–45 μm). Cloud liquid water content was measured using a PVM-100A probe (Gerber et al., 1994), and a threshold value of 0.02 g m^{-3} was used to distinguish in-cloud sampling (Dadashazar et al., 2018; MacDonald et al., 2018).

Cloud condensation nuclei (CCN) number concentrations were measured at four supersaturations (SS) (0.1%, 0.3%, 0.43%, and 0.57%) using a Droplet Measurement Technologies (DMT) dual-column streamwise thermal-gradient cloud condensation nuclei counter (CCNC) (Lance et al., 2006; Roberts & Nenes, 2005). The CCNC operates by applying a linear temperature gradient to a cylindrical sampling tube with continuously wetted walls. As the thermal diffusivity of water vapor exceeds the diffusivity of air, supersaturated conditions are produced along the sampling column centerline. For this study, activated droplets grown to sizes larger than 0.75-μm diameter were counted and sized by an optical particle counter. The sheath and sample flows of each column were maintained at 0.45 and 0.05 L min^{-1}, respectively. Instrument pressure was maintained at 750 mb using a flow orifice and active pressure control system at the instrument inlet. Each column of the CCNC was calibrated using ammonium sulfate particles following standard methods as described in Rose et al. (2008). Calibrations were performed before and after the campaign, and observed

deviations in applied SS for a given temperature gradient imply uncertainties of ~6%, similar to the 5% value typical of field campaigns, as reported by Rose et al. (2008).

Aerosol size distributions and number concentrations for D_p between ~15 and 800 nm were measured with a custom-built scanning mobility particle sizer (SMPS) consisting of a differential mobility analyzer (DMA, TSI 3081) coupled to a condensation particle counter (TSI 3010). The DMA is operated in a closed-system configuration with a recirculating sheath and excess flow of 2.67 L min^{-1} and an aerosol flow of 0.515 L min^{-1}. The column voltage was scanned from 15 to 9,850 V over a ~2-min interval.

Aerosol chemical composition was measured using a high-resolution time-of-flight aerosol mass spectrometer (HR-ToF-AMS, Aerodyne Research Inc., hereafter referred to AMS) (DeCarlo et al., 2006). Incoming air enters the AMS through a 100-μm critical orifice, after which an aerodynamic lens produces a particle beam that is accelerated under high vacuum. The particle beam is flash-vaporized on a resistively heated surface (600°C), and the resulting gases are ionized by electron impaction (70 eV). Individual ion identity is determined using a high-resolution time-of-flight mass spectrometer. Due to the limited amount of aerosol mass present over the MBL, data were collected in high-sensitivity V-mode. The ionization efficiency (IE) of the AMS was calibrated using dry, 350-nm ammonium nitrate particles before each flight. Data were averaged over 1-min intervals, and all data were analyzed using standard AMS software (SQUIRREL v1.57 and PIKA v1.16l) within Igor Pro 6.37. The collection efficiency (CE) was determined using the composition-dependent calculator within the SQUIRREL and PIKA software packages (Middlebrook et al., 2012). Elemental H:C and O:C ratios were calculated using the "Improved-Ambient" elemental analysis method for AMS mass spectra (Canagaratna et al., 2015). Positive matrix factorization (PMF) analysis (Paatero & Tapper, 1994) was performed on the high-resolution AMS mass spectra in order to distinguish major classes and transformation processes of measured OA. Three factors were extracted, two of which factors correspond to OA subtypes characteristic of the MBL and above-cloud organic aerosol layer (AC-OAL), respectively, and resemble low-volatility oxygenated organic aerosol (LV-OOA). The third factor, which was rarely observed, is likely a result of primary anthropogenic emissions and resembles hydrocarbon-like organic aerosol (HOA). Further discussion of PMF data preparation and factor interpretation is included in the supporting information.

2.3. Determination of Aerosol Hygroscopicity

Aerosol hygroscopicity was calculated using two distinct methods based on measurements with the CCNC and AMS, respectively. Assuming a particle population is internally mixed, the critical activation diameter ($D_{p,c}$) (the diameter at which all larger particles will activate into cloud droplets) produced by a given SS can be determined by integrating the particle size distribution until the total CN concentration is equivalent to the measured CCN concentration:

$$N_{CCN} = \int_{D_{p,c}}^{\infty} n_{CN} dD_p \qquad (1)$$

Knowledge of the critical diameter can then be used to calculate a single parameter representation of aerosol hygroscopicity from Köhler theory (Petters & Kreidenweis, 2007):

$$s = \frac{D_{wet}^3 - D_{p,c}^3}{D_{wet}^3 - D_{p,c}^3(1 - \kappa_{CCN})} \exp\left(\frac{4\sigma M_w}{RT\rho_w D_{wet}}\right) \qquad (2)$$

where s is the equilibrium supersaturation, $D_{p,c}$ is the critical activation diameter, D_{wet} is the droplet diameter, R is the universal gas constant, T is the absolute temperature, ρ_w is the molar density of water, M_w is the molecular weight of water, and σ is the surface tension of the droplet at the point of activation. Following Rose et al. (2010), κ was determined by applying the observed activation diameter and varying both D_{wet} and κ until s is equivalent to the applied supersaturation of the CCNC and the maximum of a Köhler curve of CCN activation. The droplet surface tension is assumed equal to that of water for comparison with other studies (Collins et al., 2013; Petters & Kreidenweis, 2007; Roberts et al., 2010; Yakobi-Hancock et al., 2014). Hygroscopicity values calculated using this method are referred to as "CCN-derived." Since the likelihood of particle activation at a given SS tends to be a stronger function

of size than composition (Dusek et al., 2006), κ_{CCN} values correspond to particles with diameters near the calculated critical diameter.

A Monte Carlo approach was used to estimate the uncertainty in CCN-derived kappa values (Wang et al., 2019). A detailed description is provided in the supporting information. For a given measurement of the aerosol size distribution and CCN number concentration, the distribution of possible κ_{CCN} values calculated by varying these input parameters (i.e., CCN number concentration and size distribution) within their respective uncertainties is lognormally distributed. As a result, uncertainties attributed to κ_{CCN} are not symmetric about the geometric mean values. In general, we estimate 1σ uncertainties of +55%/−40% for κ_{CCN} calculated at SS = 0.3%, ~+75%/−45% at SS = 0.43%, and +100%/−50% to values calculated at SS = 0.57%. Due to the low CCN number concentrations observed at SS = 0.1% (<100 cm^{-3}) and possibility of counting unactivated particles (expected to only be a few per cm^{-3}), κ_{CCN} at SS = 0.1% are not reported, as small absolute deviations in particle number concentration measured by the CCNC and DMA due to differential inlet losses could strongly influence the resulting κ_{CCN} estimates.

Hygroscopicity estimates can also be made using component volume fractions measured by the HR-ToF-AMS using the following equation (Petters & Kreidenweis, 2007):

$$\kappa_{AMS} = \sum_{i}^{N} \epsilon_i \kappa_i \tag{3}$$

where ϵ_i and κ_i represent the volume fraction and hygroscopicity of the ith NR-PM$_1$ component, respectively. While this calculation cannot capture the contribution of refractory components (sea salt, mineral dust, etc.), further analysis suggests their contribution is minor, as discussed in the supporting information. Organic aerosol density was assumed to be 1.4 g cm^{-3} for volume fraction calculations given the remote nature of the environments sampled and the oxidized character of the measured organic aerosol (e.g., O:C ratios of MBL and AC-OAL PMF factors were 0.91 and 0.76, respectively) (Hallquist et al., 2009; Roberts et al., 2010). The hygroscopicity of individual inorganic components is calculated using

$$\kappa_i = \left(\frac{M_w}{\rho_w}\right)\left(\frac{\rho_i}{M_i}\right)v_i \tag{4}$$

where M_w and ρ_w are the molar mass and density of water, respectively, and M_i, ρ_i, and v_i are the molar mass, density, and van't Hoff factor of the inorganic component. Inorganic aerosol was dominated by sulfate and ammonium. The relative abundances of ammonium sulfate, ammonium bisulfate, and sulfuric acid were calculated using the molar ratio of ammonium to sulfate (Asa-Awuku et al., 2011; Nenes et al., 1998). Ammonium sulfate and bisulfate were assigned van't Hoff factors of 2.5, while sulfuric acid was assigned $\kappa = 0.9$ to align with previous measurements (Petters & Kreidenweis, 2007). Modifying the van't Hoff factors of ammonium sulfate and ammonium bisulfate and assumed κ of sulfuric acid within reasonable limits had a negligible influence on the presented results. Chloride measured by the AMS was assumed to represent sodium chloride and was assigned a hygroscopicity of 1.28 (Petters & Kreidenweis, 2007). AMS-measured nitrate aerosol was assumed to be ammonium nitrate with a hygroscopicity of 0.67 (Petters & Kreidenweis, 2007). The hygroscopicity of the organic component (κ_{org}) was assumed to be either 0 (non-hygroscopic), 0.1 (slightly-hygroscopic), or a function OA composition using a parameterization based on bulk O:C ratios developed in the literature (Lambe et al., 2011). Comparisons of κ_{CCN} and κ_{AMS} values, analysis of PMF factor composition, and evaluation of CCN-closure calculations are used to evaluate these different κ_{org} estimates.

An uncertainty analysis similar to that described for κ_{CCN} values was performed for κ_{AMS} values and is described in detail in the supporting information. For median conditions in the MBL and FT, the relative uncertainty in κ_{AMS} is estimated to be ~10–20%, due primarily to uncertainty in the estimated hygroscopicity of the organic component (κ_{org}). In the AC-OAL, the dominant contribution of organic aerosol increases the relative uncertainty to ~50%; however, due to the low absolute κ_{AMS} values observed in the AC-OAL, the absolute uncertainty is only ~0.1 or less.
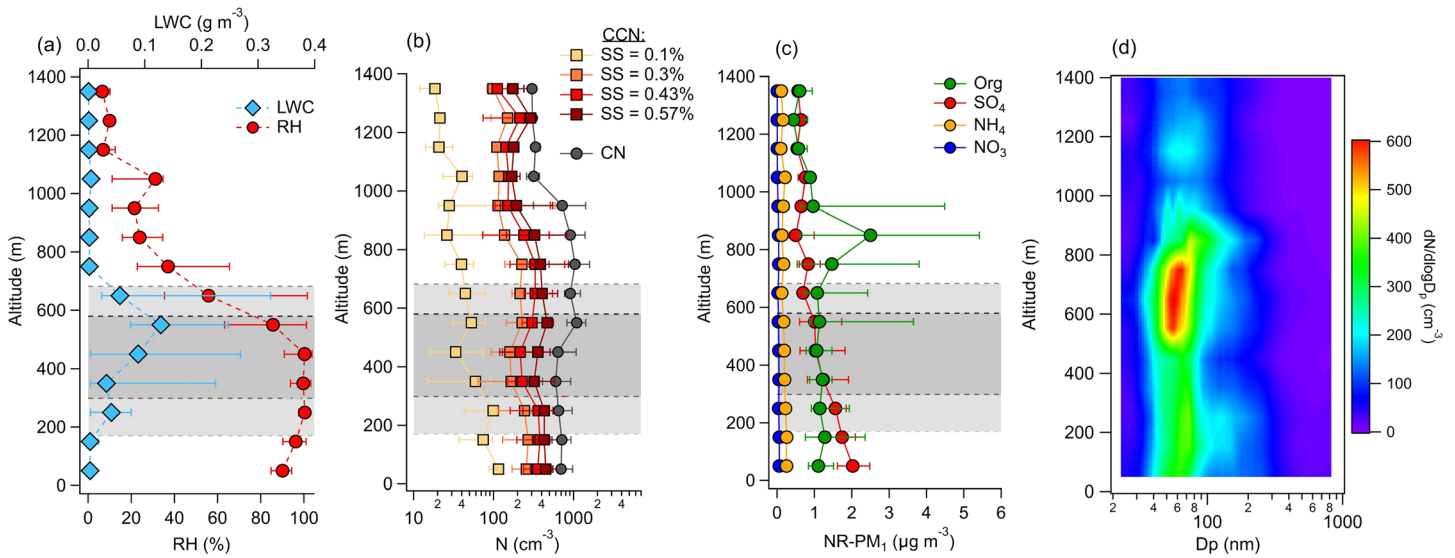
Figure 2. Vertical profiles of (a) RH and LWC, (b) CCN and CN concentrations, and (c) non-refractory (NR) PM$_1$ component mass loadings for the seven RFs in Figure 1. Markers represent median values, while horizontal bars span the interquartile range. (d) Vertical contour plot of median size distributions measured during the seven RFs. The dark grey region in panels a–c represents the average stratocumulus cloud depth (avg. cloud top height ≈ 570 m; avg. cloud bottom height ≈ 300 m). The lighter grey region represents the standard deviation of cloud top and bottom heights (e.g., avg. cloud top + cloud top height S.D. ≈ 680 m).

2.4. Aerosol-Cloud Parcel Model

The aerosol-cloud parcel model used in this study employs a user-specified updraft velocity to induce adiabatic cooling of an air parcel, leading to water vapor supersaturation. The predicted parcel supersaturation at each time step is determined by the relative rates of production through adiabatic cooling and loss through condensation of water vapor onto activated cloud droplets (Pruppacher & Klett, 1997; Seinfeld et al., 2016). In the present study, meteorological parameters such as ambient pressure, temperature, and lapse rate are obtained from MACAWS aircraft measurements and are specified before model execution. The below-cloud dry size distribution is assumed to contain Aitken and accumulation modes, the characteristics of which (i.e., number concentration, geometric mean diameter, hygroscopicity) are set by the user. Particles within each mode can be specified as either internally or externally mixed. Each compositional class, 1 per size mode if internally mixed or 2 per size mode if externally mixed, contains 300 lognormally spaced bins ranging from 1 nm to 3 μm. Droplet activation is assumed to occur when the ambient supersaturation of the parcel exceeds the critical supersaturation of the particles in a given size bin, as determined from κ-Kohler theory (Petters & Kreidenweis, 2007). Following activation, the growth of individual cloud droplet bins due to water vapor diffusion is explicitly represented. Additional physical processes such as droplet coagulation, coalescence, and deposition are not included, as previous parcel model studies have demonstrated that these processes have little influence on model predictions for typical marine stratocumulus conditions (Sanchez et al., 2016). Model execution proceeds until a user-specified liquid water content (0.4 g m^{-3} in this study) has been reached. Activated particle size bins larger than 1 μm are considered cloud droplets; however, using an alternative size threshold of 2 μm or 0.75 μm has a negligible influence on the results.

2.5. Air Mass Backward Trajectories

Air mass backward trajectories (120 hr) were calculated in the MBL for each flight using the NOAA HYSPLIT v4.2 model with the global data assimilation system (GDAS) 1° × 1° meteorological data set (Draxler & Hess, 1997, 1998; Stein et al., 2015). The higher spatial resolution EDAS 40 km × 40 km meteorological data set was not used due to its limited spatial range over the Pacific Ocean. The ending altitude of each trajectory was the approximate midpoint of the MBL during each flight.

Table 1
Median Aerosol Number (N) and Cloud Condensation Nuclei (CCN) Concentrations Measured in the Marine Boundary Layer (MBL), Above-Cloud Organic Aerosol Layer (AC-OAL), and Free Troposphere (FT)

Location	N (cm^{-3})	CCN: 0.1% (cm^{-3})	CCN: 0.3% (cm^{-3})	CCN: 0.43% (cm^{-3})	CCN: 0.57% (cm^{-3})
MBL	754 (509–978)	75 (33–106)	194 (146–285)	302 (187–410)	410 (229–522)
AC-OAL	1,662 (1,303–1,959)	58 (41–84)	363 (260–537)	574 (403–876)	781 (539–1,051)
FT	333 (296–555)	21 (14–35)	115 (89–145)	144 (102–194)	162 (118–240)

Note. Values in parentheses represent the interquartile range. CCN concentrations are provided as a function of the instrument supersaturation (%).

3. Results and Discussion

3.1. Aerosol Characteristics Over the N.E. Pacific

Results from the seven flights analyzed in this study are summarized in Figure 2 and Tables 1–3. In the subsequent analyses, "all flights" refers to these seven. Typical flight patterns included sampling within the MBL, FT, and, when present, the above-cloud organic aerosol layer (AC-OAL). The AC-OAL is operationally defined as the narrow altitude band (generally <200 m) directly above the marine stratocumulus cloud decks where OA mass loadings were relatively large (>1.5 μg m^{-3}) and a distinct AC-OAL PMF factor contributed >80% of total OA mass (Figure S6). This region occupies a similar location as the commonly referenced entrainment interface layer (EIL) above cloud decks (Dadashazar et al., 2018; Wood, 2012), but is defined by the aerosol characteristics described above rather than by turbulence and buoyancy characteristics, as is common for the EIL (Carman et al., 2012). Median aerosol properties are reported in Tables 1–3 for each of these three regions, while Figure 2 displays vertical profiles of aerosol and meteorological properties.

Distinct differences in particle properties were observed within each vertical region. Median aerosol number concentrations observed in the MBL (754 cm^{-3}) exceeded those in the FT (333 cm^{-3}), as expected. Observed particle concentrations were maximized within the AC-OAL (1,662 cm^{-3}), where intense actinic fluxes and elevated concentrations of the hydroxyl radical may drive new particle formation (Dadashazar et al., 2018; Mauldin et al., 1999). For all measured SS > 0.1%, observed CCN concentrations were also largest within the AC-OAL, rather than the MBL or FT, underscoring the importance of understanding the hygroscopicity of above-cloud CCN-active particles (Coggon et al., 2014; Sorooshian, Lu, et al., 2007; Sorooshian et al., 2007; Wang et al., 2008).

Observed aerosol composition in the MBL was relatively evenly divided between organic aerosol (OA) (43%) and sulfate (SO$_4$) (48%), with a minor contribution from ammonium (NH$_4$) (~10%) and negligible nitrate (NO$_3$) (≤1%). Prabhakar et al. (2014) have demonstrated that nitrate is preferentially distributed in super-micron particles in this marine environment, in agreement with the minor contribution observed with the AMS in this study. Using the "clean" versus "perturbed" threshold introduced by Coggon et al. (2012) for this region (where "clean" is defined by aerosol mass concentrations <1 μg m^{-3}), average MBL conditions were "perturbed" by shipping vessel emissions or other anthropogenic sources such as continental outflow. A distinct, highly oxidized MBL PMF factor was extracted from the data set (Figure S6). The oxidized nature of the MBL factor (O:C = 0.91) precludes the use of marker ions to distinguish individual sources; however, potential sources include shipping and biogenic emissions, as well as oxidized continental outflow aerosol (Coggon et al., 2012; Hegg et al., 2010; Sorooshian et al., 2009). In the AC-OAL, observed aerosol composition was dominated by organics (80%), as has been previously reported (Coggon et al., 2014;

Table 2
Median Mass Loadings of Total Non-Refractory PM1 (NR-PM$_1$), and Organic (Org.), Sulfate (SO$_4$), Ammonium (NH$_4$), and Nitrate (NO$_3$) Aerosol Components in the Marine Boundary Layer (MBL), Above-Cloud Organic Aerosol Layer (AC-OAL), and Free Troposphere (FT)

Location	NR-PM$_1$ (μg m^{-3})	Org. (μg m^{-3})	SO$_4$ (μg m^{-3})	NH$_4$ (μg m^{-3})	NO$_3$ (μg m^{-3})
MBL	2.8 (2.3–2.5)	1.1 (0.8–1.4)	1.5 (0.9–2.0)	0.2 (0.2–0.3)	0.0 (0.0–0.1)
AC-OAL	5.5 (4.5–7.5)	4.4 (3.2–6.1)	0.7 (0.6–1.1)	0.2 (0.2–0.3)	0.1 (0.0–0.1)
FT	1.5 (1.2–2.1)	0.7 (0.5–1.0)	0.6 (0.4–0.7)	0.1 (0.1–0.2)	0.0 (0.0–0.0)

Note. Values in parentheses represent the interquartile range.

Table 3

Median Values of the AMS-Derived (κ_{AMS}) and CCN-Derived (κ_{CCN}) Hygroscopicity Factor Measured in the Marine Boundary Layer (MBL), Above-Cloud Organic Aerosol Layer (AC-OAL), and Free Troposphere (FT)

Location	κ_{AMS}	κ_{CCN}: 0.3%	κ_{CCN}: 0.43%	κ_{CCN}: 0.57%
MBL	0.45 (0.35–0.52)	0.39 (0.20–0.61)	0.35 (0.24–0.50)	0.40 (0.27–0.54)
AC-OAL	0.19 (0.17–0.25)	0.13 (0.08–0.20)	0.19 (0.14–0.25)	0.17 (0.12–0.27)
FT	0.37 (0.30–0.43)	0.32 (0.18–0.65)	0.50 (0.29–0.88)	0.37 (0.21–0.72)

Note. Values in parentheses represent the interquartile range. κ_{CCN} are provided as a function of the instrument supersaturation (%).

Hersey et al., 2009; Sorooshian et al., 2007; Sorooshian, Ng, et al., 2007; Wang et al., 2008). A second, distinct factor displayed large mass loadings (up to 8 μg m^{-3}) within the AC-OAL (Figure S6) (O:C = 0.76), and the mass ratio of the AC-OAL to the MBL PMF factor is used as a tracer of AC-OAL entrainment into the MBL, as discussed in section 3.3.2. Possible aerosol production mechanisms in the AC-OAL include oxidation and transport of biogenic volatile organic compounds emitted by forested regions in the northwest United States, cloud droplet evaporation, and oxidation of sparingly soluble organics vented through the stratocumulus layer (Coggon et al., 2014; Heald et al., 2005; Sorooshian, Lu, et al., 2007). While large eddy simulations (LES) have demonstrated that the altitude of the top of the stratocumulus cloud deck can undergo diurnal variations of 10–100 m, providing a potential mechanism for AC-OAL aerosol production through droplet evaporation (Chen et al., 2011; Sorooshian, Lu, et al., 2007), the substantially larger mass fraction of organic aerosol in the AC-OAL than the MBL suggests that particle production is primarily a result of continental biogenic sources (Coggon et al., 2014). Observed aerosol mass loadings in the FT were the lowest sampled (1.5 μg m^{-3}) but agree well with previous aircraft measurements by Wang et al. (2008) off the coast of Pt. Reyes, CA, at a similar time of year (June–July).

3.2. Overview of Observed Aerosol Hygroscopicity

Figure 3 displays median aerosol number size distributions, κ_{AMS}, and κ_{CCN} values observed within the MBL, AC-OAL, and FT during each flight. For these comparisons, κ_{AMS} values are calculated assuming $\kappa_{org} = 0.1$, as is typical for non-urban regions (Mei et al., 2013; Moore et al., 2011, 2012). However, we note that using the parameterization developed by Lambe et al. (2011), the calculated κ_{org} values for the MBL and AC-OAL PMF factors are 0.19 and 0.17, respectively, due to their highly oxidized nature (Figure S6), suggesting the true κ_{org} values for large particles may be greater than 0.1.

Within the MBL, observed hygroscopicity values appear to cluster into three relatively distinct groups that span the range of values previously observed in this environment (Roberts et al., 2010; Royalty et al., 2017; Yakobi-Hancock et al., 2014). The strong temporal variation observed in both particle number size distributions and hygroscopicities underscores the complexity involved in accurately modeling CCN in coastal environments influenced by continental and marine sources. This is further demonstrated in Table 4, which depicts estimated organic and inorganic volume fractions of Aitken mode particles derived from MBL κ_{CCN} values. Assuming inorganic aerosol is entirely ammonium sulfate for these calculations, estimated organic fractions vary from effectively zero, as median κ_{CCN} during RF13 are larger than that of ammonium sulfate ($\kappa = 0.61$) to as high as 84%. The low hygroscopicities and subsequently large estimated organic fractions observed during flights RF9 and RF15 are uncharacteristic of remote marine environments and imply a continental influence on particle characteristics. κ_{AMS} values calculated during these flights are ~50–100% larger than κ_{CCN} values, implying addition of particle mass during growth that is more hygroscopic than the Aitken mode particles. While the difference between κ_{AMS} and κ_{CCN} values during these flights are nearly within the uncertainty range of the κ_{CCN} calculation, these observations align with those in many continental locations, where addition of inorganic mass to organic-rich Aitken mode particles growth is thought to lead to a positive relationship between particle hygroscopicity and size (Ervens et al., 2010; Kawana et al., 2016; Levin et al., 2014; Moore et al., 2012; Rose et al., 2011). On the other hand, κ_{AMS} and κ_{CCN} are quite similar during the other five flights, with relative deviations on the order of ~25% or less, which is well within the uncertainty of the κ_{CCN} measurements. A compilation of data reported by Royalty et al. (2017) suggests that minor variation of particle hygroscopicity with size is a common feature of remote marine aerosol, which generally exhibits elevated Aitken mode hygroscopicity. Four individual flights (RF4, RF5, RF13, and RF15) provide
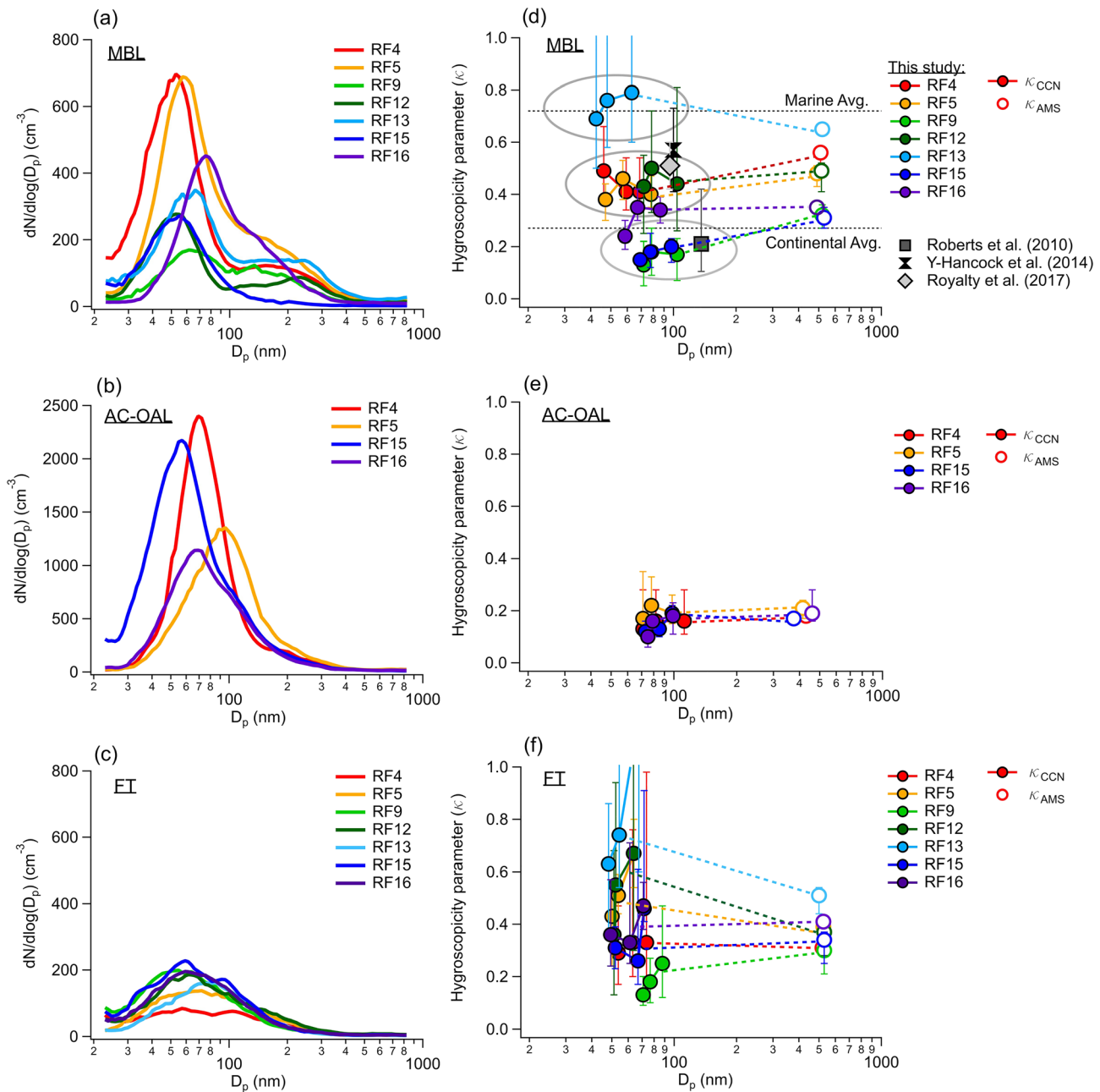
Figure 3. Median aerosol size distributions (a–c) and hygroscopicities (κ_{CCN} and κ_{AMS}) (d–f) measured in the marine boundary layer (MBL), above-cloud organic aerosol layer (AC-OAL), and free troposphere (FT), during the seven RFs. κ_{AMS} values are calculated assuming $\kappa_{org} = 0.1$ and are plotted at the median of the cumulative aerosol volume distribution. Vertical bars represent the interquartile range of hygroscopicity measurements. Previously observed values in the MBL are included for reference in (d), as are typical values for continental and marine environments from Pringle et al. (2010).

specific insight into the combined roles of aerosol sources and meteorological processes in determining aerosol hygroscopicity in the MBL, and these are discussed in further detail in section 3.3.2.

Within the AC-OAL, observed aerosol hygroscopicity is remarkably similar from flight-to-flight, and little difference is observed between κ_{CCN} and κ_{AMS} values. The combination of reduced hygroscopicity (i.e., κ ~0.2) and little variation with particle size suggests that within the AC-OAL, Aitken mode particles are organic-rich and grow through condensation of additional organic vapors, rather than addition of inorganic mass. Even under the assumption that the organic species in Aitken mode AC-OAL particles are entirely

Table 4

Calculated Aitken Mode Organic (f_{org}) and Inorganic (f_{inorg}) Volume Fractions Based on Median κ_{CCN} Values Derived From CCN Measurements at SS = 0.43% for MBL Measurements During Each Flight

Flight	κ_{CCN} − SS = 0.43%	Inorg. = $(NH_4)_2SO_4$		Inorg. = H_2SO_4	
		f_{org}	f_{inorg}	f_{org}	f_{inorg}
RF4	0.41	0.39	0.61	0.61	0.39
RF5	0.46	0.29	0.71	0.55	0.45
RF9	0.18	0.84	0.16	0.90	0.10
RF12	0.50	0.22	0.78	0.50	0.50
RF13	0.76	~	~	0.18	0.82
RF15	0.18	0.84	0.16	0.90	0.10
RF16	0.28	0.65	0.35	0.78	0.22

Note. Values of f_{org} and f_{inorg} are calculated assuming the inorganic aerosol component is either ammonium sulfate ($(NH_4)_2SO_4$) or sulfuric acid (H_2SO_4). Note that the hygroscopicity measured during RF13 cannot be reproduced assuming the inorganic component is entirely $(NH_4)_2SO_4$.

insoluble, total particle volume must be at least 66% organic to produce a hygroscopicity of 0.2 (assuming ammonium sulfate as the inorganic component). Chamber studies of monoterpene aerosol often observe κ_{org} of ~0.1–0.15 for Aitken mode particles (Alfarra et al., 2013; Zhao et al., 2015), which increases the estimated organic volume fraction to 80–89%. While the peak in the AC-OAL size distribution varies considerably between flights, the presence of a dominant Aitken mode in three out of four observations suggests particle formation may have occurred recently.

Coggon et al. (2014) first demonstrated that expansive dry air masses originating over the northwestern United States loft biogenic organic aerosol over the MBL and act as the main particle source to the AC-OAL. Our measurements support this conclusion; however, an additional contribution from organic gases vented through the stratocumulus layer cannot be ruled out. Comparing AC-OAL and MBL Aitken mode hygroscopicity suggests cloud droplet evaporation is at most a minor particle source to the AC-OAL, as during three of the four flights in which the AC-OAL was sampled, average MBL Aitken mode particles were substantially more hygroscopic than those in the AC-OAL (κ_{MBL} ~0.4; κ_{AC-OAL} ~0.2). As the most hygroscopic particles in an air mass are likely to activate into cloud droplets, and as addition of inorganic mass is common during cloud processing in marine environments (Faloona, 2009; Seinfeld et al., 2016), it is unlikely that residual aerosol formed from evaporated cloud droplets would be less hygroscopic than the MBL aerosol population. Observations during RF15, discussed further in section 3.3.2, suggest entrainment during precipitation events can lead to a major AC-OAL signature in the MBL, directly demonstrating the importance of understanding the source of these particles.

Due to the low aerosol number concentrations in the FT, observed κ_{CCN} values vary widely between flights and exhibit large variability within individual flights. As a result, we hesitate to draw definitive conclusions based on these data. Other than RF13, average κ_{AMS} values from each flight are near or below 0.4, implying a substantial organic contribution to free tropospheric aerosol. In the absence of continental influence, observation of aerosols of such low hygroscopicity is unexpected, given that particle formation in the upper FT over tropical oceans is driven primarily by sulfuric acid nucleation and growth (Clarke, 1993; Clarke et al., 1998, 1999, 2013). Long range transport of organic aerosol layers from the Asian continent have been noted previously (Roberts et al., 2006, 2010), but estimates of aerosol hygroscopicity in such layers have varied dramatically. For instance, during the CIFEX experiments (Roberts et al., 2006), average κ attributed to aged aerosol layers were only ~0.04, whereas our measurements suggest a more moderate value of ~0.4, while observations by Roberts et al. (2010) indicated a value of 0.93 was more appropriate. While the substantial difference in particle concentrations in the MBL and FT observed during this campaign suggests FT aerosol plays a minor role in dictating MBL CCN activity on average, in remote marine environments, entrainment from the FT is the dominant source of MBL particles (Clarke, 1993; Clarke et al., 1996, 1998, 2013; Raes, 1995), and as such further research into the variability of FT aerosol composition is warranted.

3.3. Observation of Distinct Influences on MBL Particle Characteristics

Observations shown in Figure 3 indicate highly variable flight-averaged hygroscopicities in the MBL, suggesting that temporal variations in regional meteorology and/or particle source strengths can strongly influence CCN characteristics in this environment. Further analysis suggests that in four of the seven flights discussed in this study, specific meteorological patterns and emissions sources influencing particle characteristics can be identified. We discuss these observations to provide insight into the level of physicochemical detail (both in terms of emissions and atmospheric dynamics) required for atmospheric models to simulate MBL CCN concentrations with high fidelity.

3.3.1. Shipping Emissions

Aerosol properties measured during RF4 and RF5 suggest a prominent influence of regional shipping emissions on particle characteristics and hygroscopicity in this environment. During these flights, the dominance of an Aitken mode near ~50–60 nm with much larger concentrations than in the FT suggests relatively

(a)

(b)
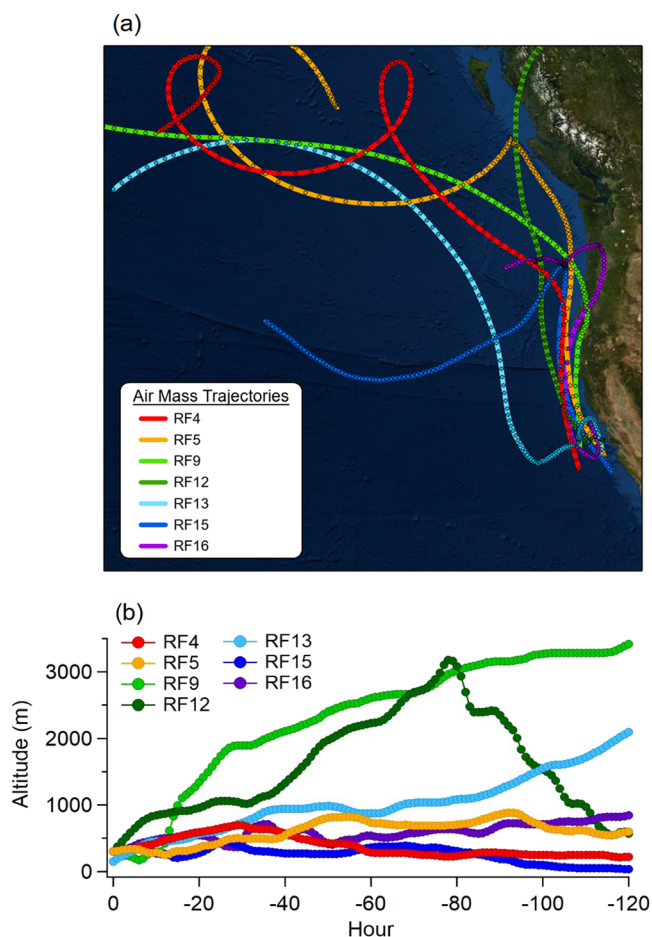
Figure 4. (a) 120-hr air mass backward trajectories calculated using the HYSPLIT model (Stein et al., 2015) from the approximate midpoint of each flight path at an altitude representative of the marine boundary layer. For six of the seven flights, the starting altitude was 300 m, while the starting altitude for the RF13 trajectory was 150 m due to the shallow height of the boundary layer. (b) Air mass altitude during the 120-hr transit to the measurement site.

recent formation from an MBL-based particle source. While such size distributions could hypothetically result from continental outflow (Moore et al., 2012), air mass backward trajectories remained over the ocean and near or within the MBL (<1,000 m) for the previous 5 days (Figure 4). Furthermore, trajectories transited primarily within the major shipping corridor along the coast, as observed for flights "perturbed" by shipping vessel emissions by Coggon et al. (2012), rather than recently arriving from the remote ocean (e.g., RF13). Downward mixing of AC-OAL particles is also ruled out as an Aitken mode particle source during these flights due to the distinctly different hygroscopicities observed in the MBL and AC-OAL (Figure 3). Finally, average wind speeds within the MBL were ~12 m s^{-1} and ~9 m s^{-1} during RF4 and RF5, respectively. Modini et al. (2015) previously noted that primary sea spray emissions produced particle concentrations of only 12 cm^{-3} during periods with similar windspeeds (12 m s^{-1}) in the same marine environment (equivalent to ~2% of particle number concentrations in the MBL during RF4 and RF5).

Shipping emissions have been previously noted as major contributors to aerosol and cloud properties in the N.E. Pacific environment (Cappa et al., 2014; Coggon et al., 2012; Lack et al., 2011; Murphy et al., 2009). Coggon et al. (2012) demonstrated that 70% of cloud residual particles measured in the California shipping lanes were impacted by nearby shipping emissions. Available compositional data further suggest that shipping emissions could be expected to produce Aitken mode hygroscopicities observed during RF4 and RF5. For instance, Lack et al. (2011) observed an effective κ value of 0.68–0.73 from exhaust produced by a
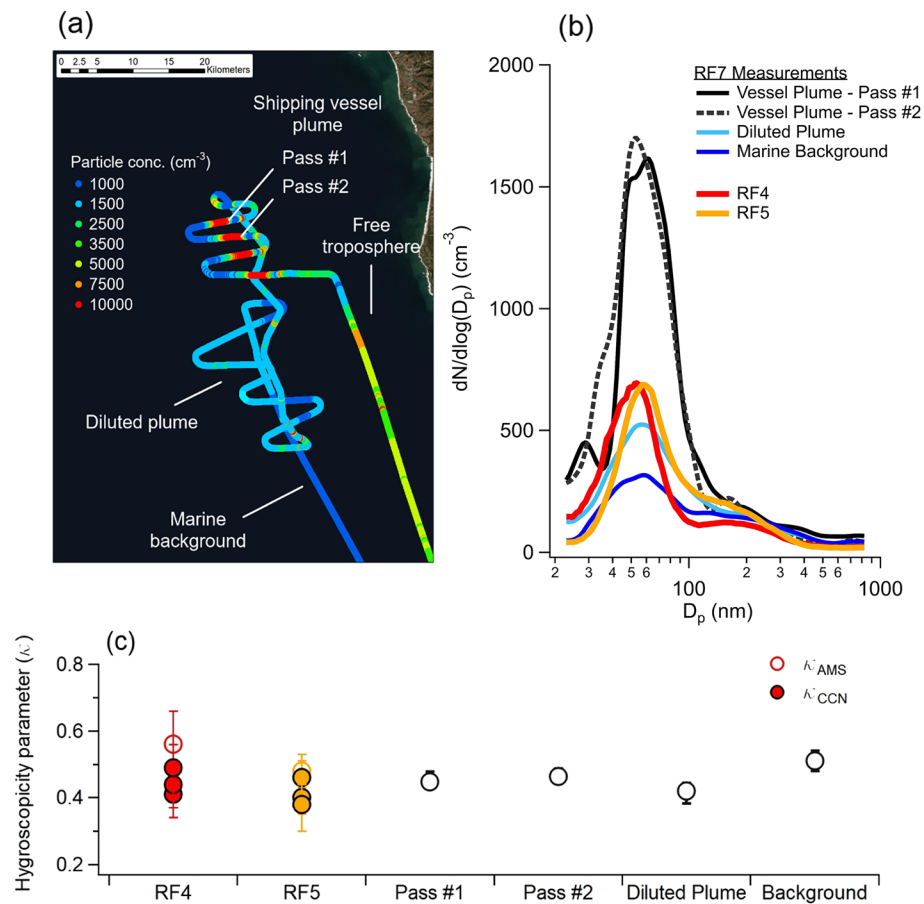
Figure 5. (a) Map of the Twin Otter trajectory during repeated sampling of the exhaust plume from a 330-m shipping vessel during RF7. Points are colored by the particle concentration measured by the CPC, and individual segments of the flight path are labeled. (b) Aerosol size distributions measured during the labeled segments in (a) compared to median distributions measured during RF4 and RF5. (c) Comparison of κ values derived from CCN and AMS measurements in RF4 and RF5 with those derived from AMS measurements during the flight segments shown in (a).

large (96,500 ton) container vessel, while the smaller Research Vessel Atlantis sampled during the same study produced a value of ~0.2. Hygroscopic growth factor measurements of shipping exhaust emitted by another large (90,000 ton) container vessel by Murphy et al. (2009) suggest an effective $\kappa = 0.1–0.5$.

Direct measurements of a large container vessel exhaust plume during RF7 provide further support for the attribution of aerosol characteristics to shipping emissions in RF4 and RF5. As shown in Figure 5, the strong Aitken mode peak in the size distribution measured directly within the plume aligns well with those measured in RF4 and RF5, while the total magnitude of the flight-median size distributions agree well with those measured in the diluted plume more than 20 km downwind. As the plume was relatively narrow directly behind the ship, κ_{CCN} values are not available, but κ_{AMS} measurements agree well with those in RF4 and RF5 (Figure 5c). However, given the variability in the measured κ values of particulate shipping exhaust just discussed, this agreement cannot be viewed as definitive. Ultimately, while the insights provided by the size distributions, backward trajectories, and κ_{AMS} values would not be definitive on their own, taken together they support a shipping emission signature on aerosol characteristics during these flights. This influence highlights the importance of accurate physicochemical representation of shipping vessel emissions within the California coastal zone. As an example, the implementation of recent regulations on the sulfur content of shipping fuel within coastal waters of the United States (up to 200 miles off the coast) should increase the organic:inorganic ratio of particulate shipping emissions in major shipping lanes over time (Cappa et al., 2014; Lack et al., 2011). Assuming, as a strictly upper limit estimate, that all Aitken mode particles observed during RF4 and RF5 are derived from shipping vessel emissions,
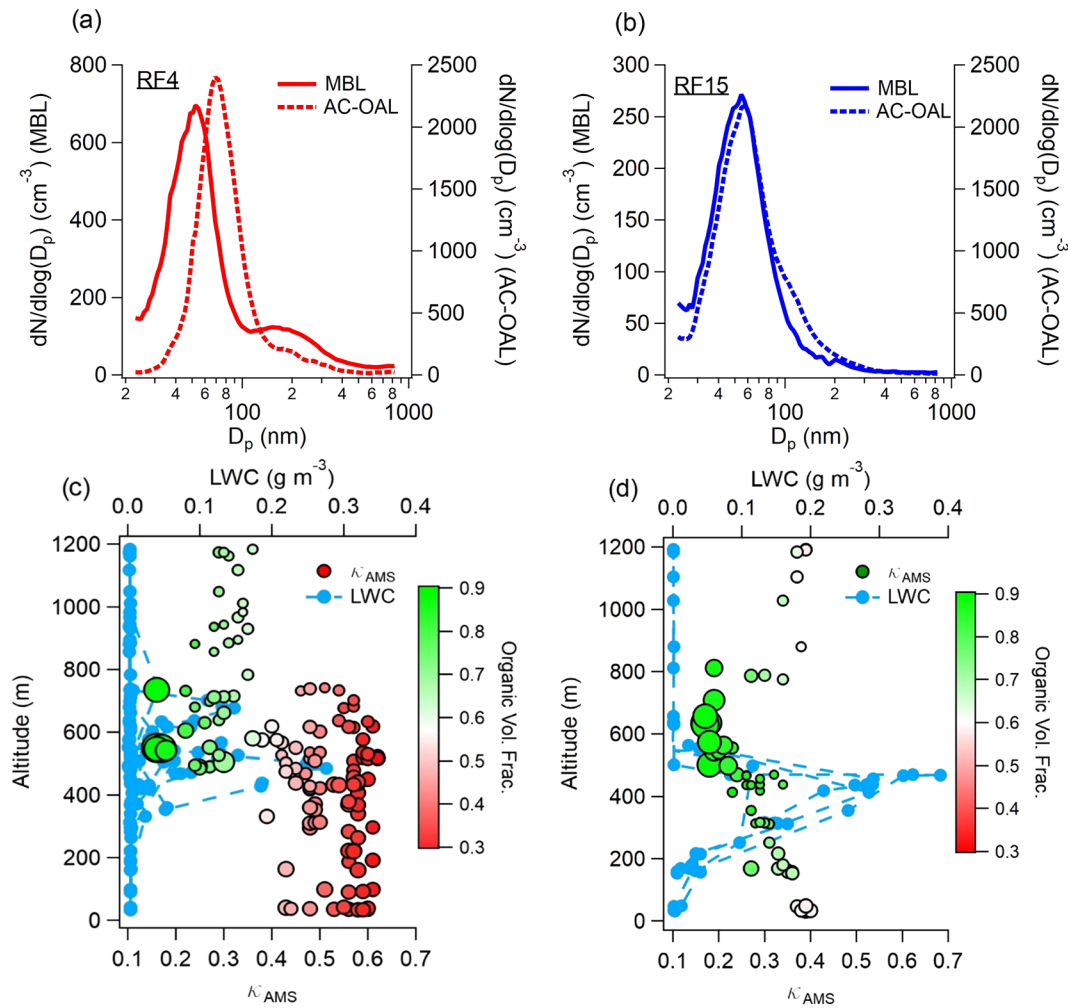
Figure 6. (Top) Median aerosol size distributions measured in the marine boundary layer (MBL) and above-cloud organic aerosol layer (AC-OAL) during RF4 (a) and RF15 (b). (Bottom) Vertical profile of AMS-derived hygroscopicity (κ_{AMS}) and liquid water content (LWC) during each flight. Values of κ_{AMS} are colored by the organic volume fraction measured by the AMS to aid interpretation of the figure.

changing the assumed hygroscopicity of these emissions from the value observed during ambient measurements in this study (~0.4–0.5) to a value of 0.1 (purely organic, partially hygroscopic), would change the CCN concentration at SS = 0.3% by 15–36%.

3.3.2. Entrainment From the AC-OAL

The observation of a single, dominant Aitken mode with reduced hygroscopicity during RF15 suggests an influence of the AC-OAL on MBL particle properties. According to Figure 4, the air mass sampled during RF15 had not recently transited over the continent or within the FT, which has previously shown to occasionally contain distinct layers of reduced hygroscopicity aerosol (Roberts et al., 2006, 2010). Clear evidence of entrainment from the AC-OAL is provided in Figure 6, which contrasts size distributions and κ_{AMS} values observed during RF15 and RF4, another flight with a prominent Aitken particle mode and relatively similar backward trajectory. During RF15, the MBL and AC-OAL size distributions are remarkably similar, exhibiting peak diameters at ~55 nm and lacking a larger accumulation mode. Liquid water contents measured within the MBL during RF15 demonstrate a fully developed stratocumulus layer encompassing roughly half of the MBL. κ_{AMS} values vary linearly with altitude from ~0.4 near the ocean surface to ~0.15–0.2 at the top of the cloud layer, aligning with the hypothesis of downward mixing of AC-OAL particles into the MBL. These observations are in stark contrast to those from RF4, where the Aitken mode diameter of the MBL and AC-OAL aerosol differ by ~20–25 nm, and importantly, the Aitken mode diameter in the MBL is smaller
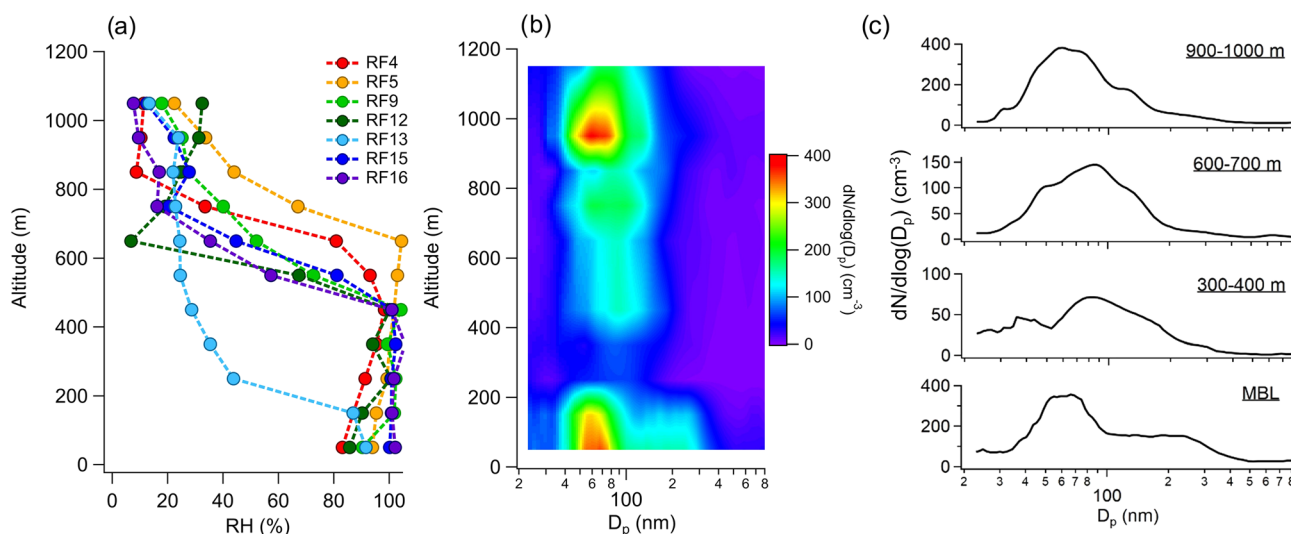
Figure 7. (a) Measured relative humidity vertical profile during each flight, demonstrating the reduced marine boundary layer (MBL) height during RF13. (b) Vertical profile of aerosol number size distributions during RF13. (c) Individual aerosol size distributions at different altitudes during RF13.

than the AC-OAL, suggesting a distinct particle source in each location. Finally, as the AC-OAL and MBL PMF factors are clearly distinguished in each flight where the AC-OAL layer was observed, the AC-OAL: MBL PMF factor mass ratio acts as a tracer for entrainment mixing. During RF15, the median AC-OAL: MBL PMF factor mass ratio was 0.81 in the MBL, in contrast to a value of 0.36 measured during RF4 and a median value of 0.42 in all flights other than RF15 where the AC-OAL was observed. The information obtained from the aerosol size distribution (no accumulation mode) and hygroscopicity (similar to the AC-OAL) in the MBL suggests that the distinct AC-OAL signature may result from entrainment following precipitation scavenging of the preexisting MBL aerosol. As typical AC-OAL particle concentrations are ~5 times as large as those in the overlying FT, failure to simulate this layer will result in underprediction of MBL particle concentrations during such distinct precipitation/entrainment events.

3.3.3. Transport From the Remote Pacific Ocean

Hygroscopicity measurements made during RF13 are notably larger than those from the other six flights, indicating a lack of organic aerosol across the particle size distribution. As expected, backward trajectories calculated within the MBL during this flight indicate recent arrival from the remote Pacific Ocean, rather than extended transport through the major shipping lanes along the coast. The boundary layer was substantially compressed (<300 m) and cloud-free during the flight, suggesting ongoing subsidence of free tropospheric air masses (Figure 7a). As new particle formation through sulfuric acid nucleation is known to be a notable source of CCN throughout the marine boundary layer (Clarke, 1993; Clarke et al., 1998, 2013), downwelling and entrainment of such nucleated particles is a possible explanation for the elevated Aitken mode hygroscopicities observed. While low number concentrations in the FT make κ_{CCN} estimates less reliable, the values observed in RF13 are relatively similar to those in the MBL, supporting entrainment. While aerosol size distribution measurements in the FT suggest such entrainment was not responsible for increases in Aitken mode particles locally, as concentrations directly above the MBL are substantially lower than those in the MBL, the elevated aerosol concentrations at ~1,000 m suggest entrainment may have produced MBL Aitken mode particles during transport (Figure 7b). Furthermore, the vertical profile of the aerosol size distribution in the FT is consistent with past observations of growth of nucleation-produced Aitken mode particles during large-scale subsidence (Clarke et al., 1999).

Due to the compressed height of the MBL during RF13, the potential contribution of primary sea spray aerosol to MBL particle characteristics is also enhanced. However, using the size distribution fitting technique established by Modini et al. (2015), the calculated concentration of primary sea spray aerosol is only 18 cm^{-3} or ~4% of the average MBL particle concentration during the flight, suggesting sea spray provides at most a minor contribution.
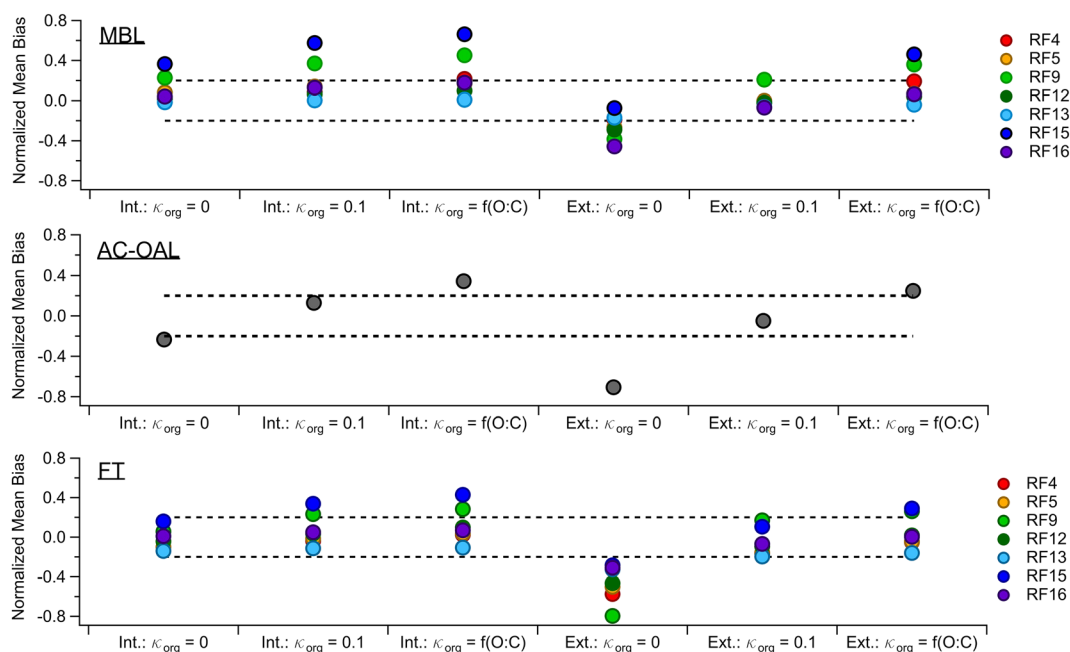
Figure 8. Normalized mean bias resulting from CCN closure analysis performed on data from each flight. A value of 0.2 is equivalent to an average overprediction of 20%. Int. indicates aerosol were assumed internally mixed, while Ext. indicates organic and inorganic aerosol were assumed to be externally mixed. κ_{org} represents the assumed hygroscopicity of the organic aerosol component, and f(O:C) indicates κ_{org} was calculated based on the bulk aerosol O:C ratio using the parameterization derived by Lambe et al. (2011).

3.4. CCN Closure Analysis

Figure 8 shows CCN closure results for the three sampled environments using six different assumptions regarding aerosol composition and mixing state. Three cases assume internally mixed aerosol components with composition determined by AMS measurements. These cases are differentiated by their assumptions regarding organic aerosol hygroscopicity, with κ_{org} increasing from 0 (first case), to 0.1 (second case), and finally to values predicted from time-varying measured OA O:C ratios according to the relationship developed by Lambe et al. (2011) (third case). The final three cases are similar to the internally mixed cases in their treatment of κ_{org}; however, the organic and inorganic aerosol components are assumed to be externally mixed. Bulk aerosol mass loadings were too low to obtain robust estimates of size-resolved composition, precluding more detailed treatment of composition in CCN closure calculations. Closure was assessed in terms of the normalized mean bias ($NMB = \sum (CCN_{pred,i} - CCN_{meas,i})/ \sum CCN_{meas}$), similarly to Asa-Awuku et al. (2011), which provides a representation of the average CCN prediction error observed for each flight. Data for the MBL and FT are shown for individual flights, while data from the AC-OAL are aggregated from all flights where the layer was observed, as fewer size distributions were obtained from the AC-OAL during each flight (and the AC-OAL was not observed at all during three flights).

For the majority of analyzed flights (five out of seven), closure is obtained within 20% using AMS-measured bulk composition and an assumption of either insoluble ($\kappa_{org} = 0$) or slightly hygroscopic organics ($\kappa_{org} = 0.1$). While the assumption of insoluble organics disagrees with observed O:C ratios (e.g., the O:C ratio of the MBL PMF factor is 0.85), CCN closure studies often find this assumption is ideal when assuming internal mixing (Chang et al., 2007; Lance et al., 2009; Moore et al., 2011; Wang et al., 2008). The lack of strong dependence on κ_{org} suggests that in non-urban areas, regional models may be able to assign a single value to organic aerosol rather than attempt to dynamically model changes in organic aerosol hygroscopicity with aging (Wang et al., 2008). This is further highlighted by the fact that closure results assuming a constant κ_{org} value (0.1) are generally more accurate than those produced by parameterizing κ_{org} based on the observed O:C ratio (Lambe et al., 2011). As larger aerosols are more likely to have undergone cloud-processing, parameterizing organic hygroscopicity based on bulk measurements of the organic O:C ratio, which is biased by the largest particles, may also overpredict the oxidation state of particles near the

critical diameter of CCN activation. Without size-resolved compositional data, it is difficult to definitively conclude whether the overprediction observed when κ_{org} is parameterized based on the organic O:C ratio is due to such variability with size or is the result of a different relationship between O:C and κ_{org} for organic aerosols in this environment. However, other published parameterizations between O:C and κ_{org} in the literature either agree well with the Lambe parameterization (Chang et al., 2010; Massoli et al., 2010; Thalman et al., 2017) or predict more hygroscopic particles at the same O:C ratio (and as a result would lead to further overprediction if implemented in the CCN closure analysis) (Mei et al., 2013). The overprediction in CCN observed here when incorporating the Lambe parameterization therefore suggests that small particles near the critical activation diameter are less hygroscopic than larger particles that dominate the mass size distribution and thereby dictate AMS-measured composition.

Overall, generally good closure is expected in a semi-remote environment such as the California coastal zone, as previous studies have noted that closure is likely to be achieved within 20% when the bulk aerosol κ exceeds 0.1 (Wang et al., 2010). Furthermore, it is expected that aerosol in this coastal environment can be modeled as internally mixed, regardless of its true mixing state, due to the substantial contribution of inorganic constituents and distance from emission sources (Ervens et al., 2010; Fierce et al., 2016; Moore et al., 2012). Fierce et al. (2016) have demonstrated that in semi-remote environments (i.e., non-urban locations), initially externally mixed aerosol becomes internally mixed on a time scale of about 1 day, while the conversion is even faster (on the order of hours) in urban environments, in agreement with the results of Wang et al. (2010). Notable underpredictions (i.e., >20%) of CCN concentrations are produced when assuming externally mixed aerosol with insoluble organics, in agreement with the aged nature of the aerosol in this environment, which should lead to both oxidized organic aerosol and an appreciable amount of internal mixing.

CCN are strongly overpredicted in the MBL during RF9 (37%) and RF15 (57%) when assuming an internal mixture with hygroscopic organics. Aerosol composition during these flights was dominated by organic species in the MBL (59% and 58% of AMS-derived aerosol mass, respectively), indicative of a continental influence on aerosol properties. AMS-derived hygroscopicities are substantially larger than those derived from CCN measurements (Figure 3), suggesting that size-dependent composition may lead to the observed overprediction of CCN concentrations when using bulk AMS measurements of aerosol composition. Comparison of CCN closure results when assuming internal versus external mixing suggests that organic and inorganic components are externally mixed, implying either distinct particle sources or a lack of significant aging prior to measurement. In the case of RF15, this external mixing aligns with the hypothesis of downward mixing from the organic-rich AC-OAL. Figure S7 depicts the CCN closure normalized mean bias resulting from an assumption of internally mixed aerosols with hygroscopic organics as a function of the CCN-derived hygroscopicity. In general, CCN closure error increases rapidly as κ_{CCN} decreases past ~0.25, suggesting that detailed mixing state and/or size resolved compositional information is critical for accurate CCN prediction in this coastal environment during periods of intense organic aerosol intrusion into the MBL. As the aerosol hygroscopicity calculation used in this study relies on an assumption of internal mixing of organic and inorganic aerosol components, it is difficult to determine whether CCN closure error when assuming internal mixing during this flights is a result of externally mixed organic and inorganic aerosol or a result of variable composition with size. Ultimately, as these atypical organic aerosol-dominated marine conditions are the least likely to be accurately reproduced by regional models, further investigation of their frequency, particle characteristics, and resulting impact on cloud properties is warranted.

The analysis presented in Figure 8 implies that for typical conditions in the MBL (5 out of 7 flights in this study), mixing state and organic hygroscopicity have relatively little influence on CCN number concentrations. Additional closure analyses were performed assuming a constant κ equivalent to values attributed to average continental ($\kappa = 0.27$) and marine ($\kappa = 0.72$) environments (Pringle et al., 2010) (Figure 9). These results highlight the fact that assuming coastal aerosols have a strictly marine character leads to substantial errors in CCN prediction (>20% for 8 out of 9 flights) even if size distribution parameters are well characterized. Furthermore, for five out of the seven analyzed flights (RF4, RF5, RF9, RF13, RF16), assuming a constant marine κ (0.72) results in CCN prediction error similar to or larger than the error produced by assuming a constant aerosol size distribution derived from the median value measured in the MBL during this study. This underscores the importance of capturing organic contributions to coastal MBL aerosol, whether due to continental outflow, downwelling from the AC-OAL, shipping emissions, or marine biota.
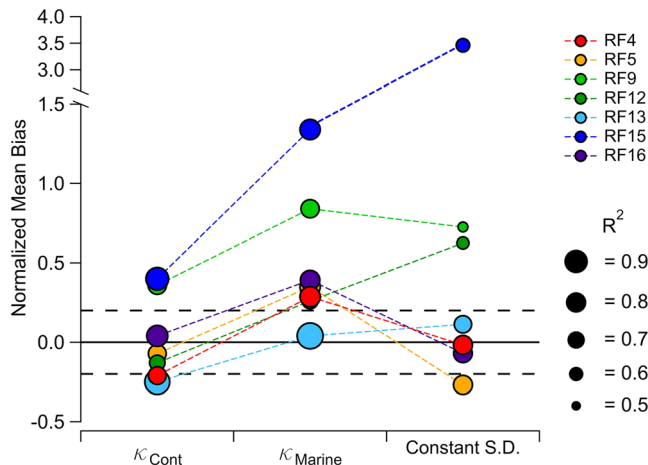
Figure 9. Normalized mean bias resulting from additional CCN closure analyses performed on data from each flight. κ_{Cont} and κ_{Marine} refer to analyses assuming a constant κ equivalent to values representative of continental (0.27) and marine (0.72) environments (Pringle et al., 2010). The Constant S.D. case assumes a constant aerosol number size distribution equivalent to the median value observed in the MBL during the campaign. Blacked dashed lines indicate closure error of $\pm 20\%$. Marker size corresponds to the R^2 value computed from a linear fit of observed and predicted CCN from each flight. Note the split in the y-axis.

3.5. Sensitivity of Stratocumulus CDNC to Below-Cloud Aerosol Hygroscopicity

In order to directly investigate the sensitivity of N.E. Pacific stratocumulus CDNC to below-cloud aerosol properties, droplet activation was simulated using an aerosol-cloud parcel model constrained with detailed below-cloud aerosol measurements obtained from three cloud sampling passes performed during the campaign. While a number of previous cloud parcel modeling studies have assumed unimodal size distributions (Chen et al., 2016; Reutter et al., 2009 ; Ward et al., 2010), observed aerosol size distributions over the N.E. Pacific were frequently bimodal (Figure 3). As many current aerosol modules incorporated within global atmospheric chemistry models involve multiple aerosol size modes (Liu & Wang, 2010; Pringle et al., 2010; Rothenberg et al., 2018), we carried out parcel model runs to analyze CDNC sensitivity to properties of the Aitken and accumulation modes separately. Sensitivities were calculated following McFiggans et al. (2006), where $S(X_i) = \delta ln N_{CDNC}/\delta ln X_i$ and X_i is the parameter under investigation. Standard linear regressions of $ln N_{CDNC}$ versus $ln X_i$ were used to determine $S(X_i)$ values, as is convention (Reutter et al., 2009; Sánchez-Gácita et al., 2017; Ward et al., 2010). Measured aerosol and meteorological properties utilized as model constraints are summarized in Table 5. Sensitivity to hygroscopicity was computed across the range of $\kappa = 0.2$–0.6. Initial results confirmed that for observed MSc updraft velocities ($w = 0.15$–0.3 m s^{-1}), below-cloud particle number concentrations (~500–800 cm^{-3}), and typical hygroscopicities ($\kappa \sim 0.2$–0.4), properties of the Aitken mode have a minor impact on stratocumulus properties ($S(X_i) < 0.05$), as minimum simulated activation diameters exceed 100 nm. Therefore, Figure 10 depicts the sensitivity of stratocumulus CDNC to properties of the accumulation mode and the simulated updraft velocity.

The average sensitivity of CDNC to aerosol hygroscopicity (0.19), while smaller than the sensitivity to size distribution parameters, is 39% as large as the sensitivity to the geometric mean diameter of the accumulation mode. This agrees with the consensus that particle size distribution properties have a larger influence on CCN concentration than particle composition (Dusek et al., 2006; McFiggans et al., 2006; Reutter et al., 2009), but also suggests accurate hygroscopicity reproduction should be included in future model improvement efforts. Observed below-cloud particle number concentrations and updraft velocities suggest that CCN activation occurs in the transitional regime according to the designations defined by Reutter et al. (2009), and simulated sensitivity to hygroscopicity agrees well with those previously reported for the transition regime (0.17–0.2) (Reutter et al., 2009; Ward et al., 2010).

Aging processes during transport likely lead to internally rather than externally mixed aerosol in the MBL. The simulated error in predicted CDNC when assuming fully externally mixed components is only 7.6–8.7% for the three modeled cases. This aligns with the observation of similarly accurate CCN closure results for the MBL when assuming internally or externally mixed components and a κ_{org} of 0.1 or larger. As the volume fraction of inorganic aerosol in the accumulation mode is likely to increase with increasing distance from the coast, this predicted mixing-state-related error may be an upper bound for marine conditions in general.

Previous aerosol-cloud parcel modeling studies have demonstrated that the sensitivity of predicted CDNC to aerosol hygroscopicity tends to decrease as bulk hygroscopicity increases, especially for the aerosol-limited and transitional aerosol activation regimes (Reutter et al., 2009; Sánchez-Gácita et al., 2017). If this is the case, accurate hygroscopicity characterization in marine regions subject to organic

Table 5

Below-Cloud Aerosol and Meteorological Data Used as Aerosol-Cloud-Parcel Model Constraints for Calculation of CDNC Sensitivities Depicted in Figure 10

Parameter	RF5-1	RF5-2	RF16
$N_{CN, \text{Aitken}}$ (cm^{-3})	296	301	128
$D_{pg, \text{Aitken}}$ (nm)	55	57	70
σ_{Aitken}	1.27	1.27	1.24
κ_{Aitken}	0.36	0.42	0.21
$N_{CN, \text{Accum.}}$ (cm^{-3})	492	465	406
$D_{pg, \text{Accum.}}$ (nm)	104	109	124
$\sigma_{\text{Accum.}}$	2.21	2.20	1.96
$\kappa_{\text{Accum.}}$	0.37	0.34	0.28
w (m s^{-1})	0.22	0.26	0.25
w/N_{CN} (m s^{-1} cm^{-3})	2.8×10^{-4}	3.4×10^{-4}	4.7×10^{-4}
Activation Regime	Trans.	Trans.	Trans.

Note. "Activation Regime" refers to the classifications of cloud droplet formation environments developed by Reutter et al. (2009). "Trans." = transitional.
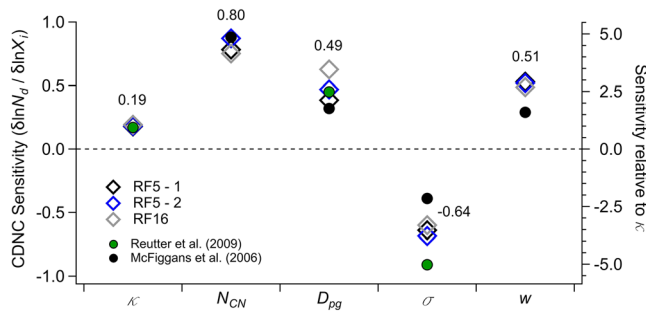
Figure 10. Sensitivity of calculated CDNC to accumulation mode aerosol hygroscopicity (κ), below-cloud aerosol particle number concentration (N_{CN}), accumulation mode geometric mean diameter (D_{pg}), accumulation mode standard deviation (σ), and updraft velocity (w). Data obtained during three cloud sampling passes were used as model constraints and are listed in Table 5. Numbers near each group of symbols represent average values from simulations in this study. Green symbols correspond to values reported by Reutter et al. (2009) for the transitional activation regime, while those in black correspond to values reported by McFiggans et al. (2006).

aerosol inputs, which contain aerosol with lower-than-average κ values, may be more important for global CDNC prediction accuracy than accurate hygroscopicity characterization in remote regions subject to aerosol sources with different, but elevated, hygroscopicities (e.g., ammonium sulfate [$\kappa = 0.61$] vs. sodium chloride [$\kappa = 1.28$]). To investigate this possibility, we calculated local CDNC sensitivity to aerosol hygroscopicity for four hypothetical marine aerosol size distributions. Rather than performing a linear regression on data obtained from a broad range of hygroscopicities, as was done for the data shown in Figure 10, local sensitivities refer to calculations performed on incremental variations in κ (e.g., $\kappa = 0.1$ vs. 0.2). Figure 11 displays the size distributions used as well as the sensitivity results. In order to span the likely range of size distributions observed in marine environments, the "Coastal" distribution is similar to median distributions observed during RF4 and RF5. A "Remote" distribution was generated using reported size distribution parameters from measurements over the remote subtropical N. Pacific by Ueda et al. (2016). Two additional size distributions were produced by interpolating between the "Coastal" and "Remote" distributions.

Total particle concentrations in the simulations varied between 300 and 800 cm^{-3} depending on the size distribution used. Five different updraft velocities were simulated ($w = 0.1–0.5$ m s^{-1}), corresponding to the range typically observed within MSc over the Pacific (Zheng et al., 2016).

A few notable trends are evident in the results shown in Figure 11. As has been previously reported, CDNC sensitivity to aerosol hygroscopicity tends to decrease as hygroscopicity increases. However, even at low hygroscopicities, calculated sensitivities never exceed 0.3, suggesting that at a maximum, a 50% error in marine aerosol hygroscopicity should lead to an error of only 15% in predicted CDNC. Sensitivity slightly increases as the assumed particle concentration increases, and therefore, hygroscopicity is slightly less important in remote marine environments than in more polluted, coastal locations, as expected. In typical remote marine conditions ($\kappa \approx 0.6$) for instance, a 50% error in hygroscopicity is associated with only a ~2.5–7.5% error in predicted CDNC, while in coastal environments ($\kappa \approx 0.35$) the error is estimated to be ~7.5–15%.
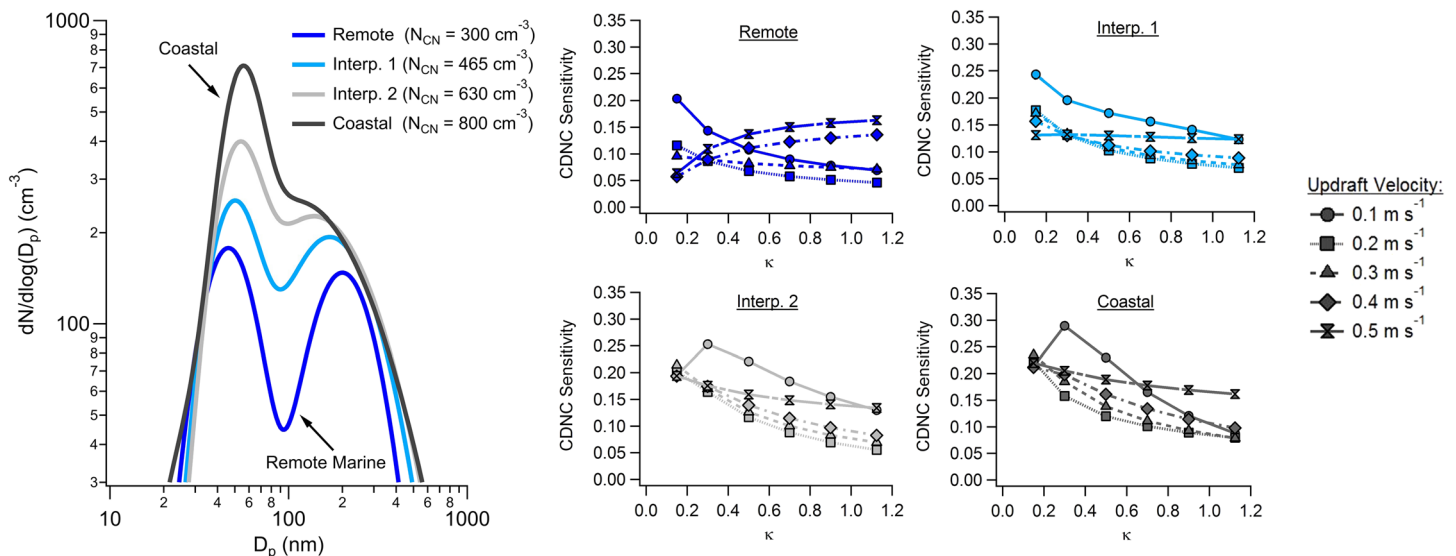
Figure 11. (Left) Aerosol number size distributions used as aerosol-cloud-parcel model inputs and (right) local CDNC sensitivities to aerosol hygroscopicity calculated using five updraft velocities. N_{CN} refers to the aerosol number concentration represented by each aerosol size distribution.
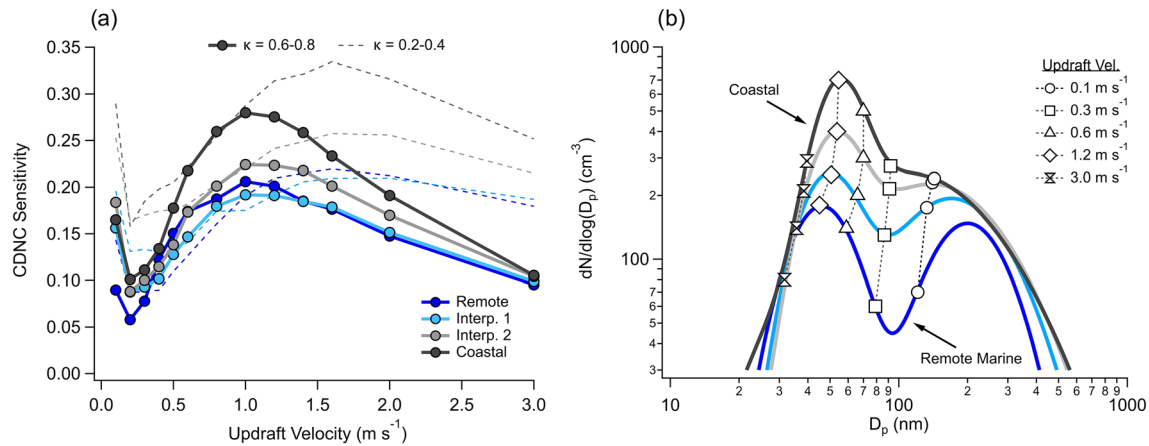
Figure 12. (a) Simulated local CDNC sensitivity to aerosol hygroscopicity in the range $\kappa = 0.6$–0.8 and $\kappa = 0.2$–0.4 as a function of updraft velocity. (b) Critical diameters (markers) calculated at the maximum supersaturation predicted by the aerosol-cloud-parcel model for five different updraft velocities assuming $\kappa = 0.6$.

When simulating certain combinations of updraft velocity and aerosol size distribution, the sensitivity of predicted CDNC to aerosol hygroscopicity does not decrease monotonically as hygroscopicity increases. Furthermore, at a given hygroscopicity value shown in Figure 11, CDNC sensitivity is a non-monotonic function of updraft velocity. Here, we demonstrate that these phenomena are a result of activation of the distinct Aitken aerosol mode. Variation in CDNC sensitivity to hygroscopicity with increasing updraft velocity is shown in Figure 12 for $\kappa = 0.6$–0.8. Local CDNC sensitivity to hygroscopicity initially decreases with increasing updraft velocity before increasing again at updraft velocities >0.2–0.3 m s^{-1}. This trend is consistent regardless of κ range analyzed; however, the shape of the curve becomes "stretched" horizontally as κ values decrease (Figure 12). Using a unimodal size distribution, Reutter et al. (2009) demonstrated that moving from the transitional to the aerosol-limited regime caused CDNC sensitivity to hygroscopicity to decline for all $\kappa > 0.05$. For the four marine size distributions simulated in this study, increasing the updraft velocity from 0.1 to 1.0 m s^{-1} shifts activation from the transitional regime to the aerosol-limited regime, implying CDNC sensitivity to hygroscopicity should subsequently decline. Our observation of the opposite phenomenon is due to the fact that at low ($w = 0.1$ m s^{-1}) and high ($w = 1$–1.5 m s^{-1}) updraft velocities, critical diameters produced within the rising air parcel occur near the peak of the accumulation and Aitken aerosol modes, respectively (Figure 12b). As the size distribution is peaked at these locations, subtle changes in aerosol hygroscopicity that induce small changes in the critical diameter result in a relatively large change in computed CDNC—hence elevated sensitivity to hygroscopicity. In contrast, for moderate ($w \sim 0.2$–0.3 m s^{-1}) updraft velocities, minimum critical diameters occur between the peaks of the Aitken and accumulation modes, and for very strong updraft velocities ($w > 1.5$–2 m s^{-1}) minimum critical diameters occur at sizes smaller than the peak of the Aitken mode, leading to lowered sensitivity (Figure 12b). This implies that in aerosol-limited environments with bimodal aerosol size distributions, the sensitivity of CDNC to hygroscopicity cannot necessarily be assumed to be negligible based solely on the ratio of the updraft velocity to particle number concentration. Ultimately, our results suggest that the sensitivity of marine CDNC to hygroscopicity is maximized in weak updraft conditions occurring in MSc ($w < 0.2$ m s^{-1}), where hygroscopicity of the accumulation, rather than the Aitken, mode is most relevant to accurate CDNC prediction, and in relatively strong updraft conditions ($0.5 < w < 2$ m s^{-1}) in either MSc or marine cumulus (Clarke et al., 1996), where Aitken mode hygroscopicity has a larger influence on CDNC than that of the accumulation mode.

4. Summary and Conclusions

Measurements of aerosol properties obtained over the N.E. Pacific Ocean during the MACAWS campaign in June and July 2018 were combined with results from an aerosol-cloud-parcel model to gain insight into aerosol hygroscopicity and its influence on CCN and MSc CDNC prediction in this environment. Three characteristic vertical regions were characterized, corresponding to the MBL, FT, and AC-OAL. Within the MBL,

flight-averaged hygroscopicities varied from values typical of continental environments ($\kappa = 0.27$), to those representative of remote marine locations ($\kappa = 0.72$) (Pringle et al., 2010). Distinct influences on MBL particle characteristics, including shipping emissions, entrainment from the AC-OAL, and transport from the remote Pacific, were identified through analysis of hygroscopicity data. In the AC-OAL, observed hygroscopicity suggests a dominant contribution of organic aerosol in both the Aitken and accumulation mode size ranges.

For the majority of flights, measured CCN concentrations could be reproduced within 20% using measurements of the aerosol size distribution, bulk hygroscopicity, and an assumption of either internally or externally mixed organic and inorganic components, in agreement with past results in non-urban locations (e.g., Ervens et al., 2010). Notably, for five of the seven flights, MBL CCN were better predicted when assuming a constant aerosol number size distribution derived from the median value measured in the MBL than when assuming a constant κ typical of remote marine locations (0.72).

Results from an aerosol-cloud-parcel model confirm that the sensitivity ($S(Xi) = \delta lnN_{CDNC}/\delta lnX_i$) of predicted CDNC to accumulation mode aerosol hygroscopicity (0.19) is substantially smaller than sensitivity to size distribution parameters, such as the accumulation mode geometric diameter (0.49) and standard deviation (-0.64). Simulations using a variety of possible MBL aerosol size distributions and hygroscopicities suggest that a 50% error in predicted hygroscopicity should rarely produce a CDNC error greater than 15%. However, model results further suggest that CDNC sensitivity to hygroscopicity does not monotonically decrease with increasing updraft velocity. Rather, sensitivity appears to decrease or remain constant with increasing updraft velocities from low to moderate values (e.g., 0.1–0.3 m s^{-1}) and then increase as updraft velocities increase further (>0.4 m s^{-1}) due to activation of the distinct Aitken mode of the aerosol size distribution. This phenomenon is observed despite the fact that at large updraft velocities (>0.4–0.5 m s^{-1}), marine conditions generally occupy the aerosol-limited regime of cloud droplet activation. Ultimately, CDNC sensitivity to hygroscopicity is predicted to be maximized in weak updraft conditions occurring in MSc (<0.2 m s^{-1}) and in strong updraft conditions (>0.5 m s^{-1}) expected to occur in either MSc or marine cumulus.

Data Availability Statement

Airborne field data used in this work can be accessed on the Figshare database (Sorooshian et al., 2017: https://doi.org/10.6084/m9.figshare.5099983.v10).

References

Ackerman, A. S., Toon, O. B., & Hobbs, P. V. (1993). Dissipation of marine stratiform clouds and collapse of the marine boundary layer due to the depletion of cloud condensation nuclei by clouds. *Science*, *262*(5131), 226–229. https://doi.org/10.1126/science.262.5131.226

Albrecht, B. A. (1989). Aerosols, cloud microphysics, and fractional cloudiness. *Science*, *245*(4923), 1227–1230. https://doi.org/10.1126/science.245.4923.1227

Alfarra, M. R., Good, N., Wyche, K. P., Hamilton, J. F., Monks, P. S., Lewis, A. C., & McFiggans, G. (2013). Water uptake is independent of the inferred composition of secondary aerosols derived from multiple biogenic VOCs. *Atmospheric Chemistry and Physics*, *13*(23), 11,769–11,789. https://doi.org/10.5194/acp-13-11769-2013

Almeida, G. P., Brito, J., Morales, C. A., Andrade, M. F., & Artaxo, P. (2014). Measured and modelled cloud condensation nuclei (CCN) concentration in São Paulo, Brazil: The importance of aerosol size-resolved chemical composition on CCN concentration prediction. *Atmospheric Chemistry and Physics*, *14*(14), 7559–7572. https://doi.org/10.5194/acp-14-7559-2014

Andreae, M. O., & Rosenfeld, D. (2008). Aerosol–cloud–precipitation interactions. Part 1. The nature and sources of cloud-active aerosols. *Earth-Science Reviews*, *89*(1), 13–41. https://doi.org/10.1016/j.earscirev.2008.03.001

Asa-Awuku, A., Moore, R. H., Nenes, A., Bahreini, R., Holloway, J. S., Brock, C. A., et al. (2011). Airborne cloud condensation nuclei measurements during the 2006 Texas Air Quality Study. *Journal of Geophysical Research*, *116*, D11201. https://doi.org/10.1029/2010JD014874

Asa-Awuku, A., Nenes, A., Gao, S., Flagan, R. C., & Seinfeld, J. H. (2010). Water-soluble SOA from alkene ozonolysis: Composition and droplet activation kinetics inferences from analysis of CCN activity. *Atmospheric Chemistry and Physics*, *10*(4), 1585–1597. https://doi.org/10.5194/acp-10-1585-2010

Berner, A. H., Bretherton, C. S., & Wood, R. (2015). Large eddy simulation of ship tracks in the collapsed marine boundary layer: A case study from the Monterey area ship track experiment. *Atmospheric Chemistry and Physics*, *15*(10), 5851–5871. https://doi.org/10.5194/acp-15-5851-2015

Bhattu, D., & Tripathi, S. N. (2015). CCN closure study: Effects of aerosol chemical composition and mixing state. *Journal of Geophysical Research: Atmospheres*, *120*, 766–783. https://doi.org/10.1002/2014JD021978

Bougiatioti, A., Nenes, A., Fountoukis, C., Kalivitis, N., Pandis, S. N., & Mihalopoulos, N. (2011). Size-resolved CCN distributions and activation kinetics of aged continental and marine aerosol. *Atmospheric Chemistry and Physics*, *11*(16), 8791–8808. https://doi.org/10.5194/acp-11-8791-2011

Brenguier, J.-L., Pawlowska, H., Schüller, L., Preusker, R., Fischer, J., & Fouquart, Y. (2000). Radiative properties of boundary layer clouds: Droplet effective radius versus number concentration. *Journal of the Atmospheric Sciences*, *57*(6), 803–821. https://doi.org/10.1175/1520-0469(2000)057%3C0803:RPOBLC%3E2.0.CO;2

Brioude, J., Cooper, O. R., Feingold, G., Trainer, M., Freitas, S. R., Kowal, D., et al. (2009). Effect of biomass burning on marine stratocumulus clouds off the California coast. *Atmospheric Chemistry and Physics*, *9*(22), 8841–8856. https://doi.org/10.5194/acp-9-8841-2009

Canagaratna, M. R., Jimenez, J. L., Kroll, J. H., Chen, Q., Kessler, S. H., Massoli, P., et al. (2015). Elemental ratio measurements of organic compounds using aerosol mass spectrometry: Characterization, improved calibration, and implications. *Atmospheric Chemistry and Physics*, *15*(1), 253–272. https://doi.org/10.5194/acp-15-253-2015

Cappa, C. D., Williams, E. J., Lack, D. A., Buffaloe, G. M., Coffman, D., Hayden, K. L., et al. (2014). A case study into the measurement of ship emissions from plume intercepts of the NOAA ship Miller Freeman. *Atmospheric Chemistry and Physics*, *14*(3), 1337–1352. https://doi.org/10.5194/acp-14-1337-2014

Carman, J. K., Rossiter, D. L., Khelif, D., Jonsson, H. H., Faloona, I. C., & Chuang, P. Y. (2012). Observational constraints on entrainment and the entrainment interface layer in stratocumulus. *Atmospheric Chemistry and Physics*, *12*(22), 11,135–11,152. https://doi.org/10.5194/acp-12-11135-2012

Chang, R. Y.-W., Liu, P. S. K., Leaitch, W. R., & Abbatt, J. P. D. (2007). Comparison between measured and predicted CCN concentrations at Egbert, Ontario: Focus on the organic aerosol fraction at a semi-rural site. *Atmospheric Environment*, *41*(37), 8172–8182. https://doi.org/10.1016/j.atmosenv.2007.06.039

Chang, R. Y.-W., Slowik, J. G., Shantz, N. C., Vlasenko, A., Liggio, J., Sjostedt, S. J., et al. (2010). The hygroscopicity parameter (κ) of ambient organic aerosol at a field site subject to biogenic and anthropogenic influences: Relationship to degree of aerosol oxidation. *Atmospheric Chemistry and Physics*, *10*(11), 5047–5064. https://doi.org/10.5194/acp-10-5047-2010

Chen, J., Liu, Y., Zhang, M., & Peng, Y. (2016). New understanding and quantification of the regime dependence of aerosol-cloud inter-action for studying aerosol cloud indirect effects. *Geophysical Research Letters*, *43*, 1780–1787. https://doi.org/10.1002/2016GL067683

Chen, Y.-C., Xue, L., Lebo, Z. J., Wang, H., Rasmussen, R. M., & Seinfeld, J. H. (2011). A comprehensive numerical study of aerosol-cloud-precipitation interactions in marine stratocumulus. *Atmospheric Chemistry and Physics*, *11*(18), 9749–9769. https://doi.org/10.5194/acp-11-9749-2011

Clarke, A. D. (1993). Atmospheric nuclei in the Pacific midtroposphere: Their nature, concentration, and evolution. *Journal of Geophysical Research*, *98*(D11), 20,633–20,647. https://doi.org/10.1029/93JD00797

Clarke, A. D., Eisele, F., Kapustin, V. N., Moore, K., Tanner, D., Mauldin, L., et al. (1999). Nucleation in the equatorial free troposphere: Favorable environments during PEM-Tropics. *Journal of Geophysical Research*, *104*(D5), 5735–5744. https://doi.org/10.1029/98JD02303

Clarke, A. D., Freitag, S., Simpson, R. M. C., Hudson, J. G., Howell, S. G., Brekhovskikh, V. L., et al. (2013). Free troposphere as a major source of CCN for the equatorial pacific boundary layer: Long-range transport and teleconnections. *Atmospheric Chemistry and Physics*, *13*(15), 7511–7529. https://doi.org/10.5194/acp-13-7511-2013

Clarke, A. D., Li, Z., & Litchy, M. (1996). Aerosol dynamics in the equatorial Pacific marine boundary layer: Microphysics, diurnal cycles and entrainment. *Geophysical Research Letters*, *23*(7), 733–736. https://doi.org/10.1029/96GL00778

Clarke, A. D., Varner, J. L., Eisele, F., Mauldin, R. L., Tanner, D., & Litchy, M. (1998). Particle production in the remote marine atmosphere: Cloud outflow and subsidence during ACE 1. *Journal of Geophysical Research*, *103*(D13), 16,397–16,409. https://doi.org/10.1029/97JD02987

Coggon, M. M., Sorooshian, A., Wang, Z., Craven, J. S., Metcalf, A. R., Lin, J. J., et al. (2014). Observations of continental biogenic impacts on marine aerosol and clouds off the coast of California. *Journal of Geophysical Research: Atmospheres*, *119*, 6724–6748. https://doi.org/10.1002/2013JD021228

Coggon, M. M., Sorooshian, A., Wang, Z., Metcalf, A. R., Frossard, A. A., Lin, J. J., et al. (2012). Ship impacts on the marine atmosphere: Insights into the contribution of shipping emissions to the properties of marine aerosol and clouds. *Atmospheric Chemistry and Physics*, *12*(18), 8439–8458. https://doi.org/10.5194/acp-12-8439-2012

Collins, D. B., Ault, A. P., Moffet, R. C., Ruppel, M. J., Cuadra-Rodriguez, L. A., Guasco, T. L., et al. (2013). Impact of marine biogeo-chemistry on the chemical mixing state and cloud forming ability of nascent sea spray aerosol. *Journal of Geophysical Research: Atmospheres*, *118*, 8553–8565. https://doi.org/10.1002/jgrd.50598

Cubison, M. J., Ervens, B., Feingold, G., Docherty, K. S., Ulbrich, I. M., Shields, L., et al. (2008). The influence of chemical composition and mixing state of Los Angeles urban aerosol on CCN number and cloud properties. *Atmospheric Chemistry and Physics*, *8*(18), 5649–5667. https://doi.org/10.5194/acp-8-5649-2008

Dadashazar, H., Braun, R. A., Crosbie, E., Chuang, P. Y., Woods, R. K., Jonsson, H. H., & Sorooshian, A. (2018). Aerosol characteristics in the entrainment interface layer in relation to the marine boundary layer and free troposphere. *Atmospheric Chemistry and Physics*, *18*(3), 1495–1506. https://doi.org/10.5194/acp-18-1495-2018

DeCarlo, P. F., Kimmel, J. R., Trimborn, A., Northway, M. J., Jayne, J. T., Aiken, A. C., et al. (2006). Field-deployable, high-resolution, time-of-flight aerosol mass spectrometer. *Analytical Chemistry*, *78*(24), 8281–8289. https://doi.org/10.1021/ac061249n

Draxler, R. R., & Hess, G. D. (1997). Description of the HYSPLIT_4 modeling system. *NOAA. Tech. Memo. ERL ARL-224* (pp. 1–24). Silver Spring: NOAA Air Resources Laboratory.

Draxler, R. R., & Hess, G. D. (1998). An overview of the HYSPLIT_4 modelling system for trajectories, dispersion, and deposition. *Australian Meteorological Magazine*, *47*, 295–308.

Duplissy, J., DeCarlo, P. F., Dommen, J., Alfarra, M. R., Metzger, A., Barmpadimos, I., et al. (2011). Relating hygroscopicity and composition of organic aerosol particulate matter. *Atmospheric Chemistry and Physics*, *11*(3), 1155–1165. https://doi.org/10.5194/acp-11-1155-2011

Duplissy, J., Gysel, M., Alfarra, M. R., Dommen, J., Metzger, A., Prevot, A. S. H., et al. (2008). Cloud forming potential of secondary organic aerosol under near atmospheric conditions. *Geophysical Research Letters*, *35*, L03818. https://doi.org/10.1029/2007GL031075

Dusek, U., Frank, G. P., Hildebrandt, L., Curtius, J., Schneider, J., Walter, S., et al. (2006). Size matters more than chemistry for cloud-nucleating ability of aerosol particles. *Science*, *312*(5778), 1375–1378. https://doi.org/10.1126/science.1125261

Ervens, B., Cubison, M., Andrews, E., Feingold, G., Ogren, J. A., Jimenez, J. L., et al. (2007). Prediction of cloud condensation nucleus number concentration using measurements of aerosol size distributions and composition and light scattering enhancement due to humidity. *Journal of Geophysical Research*, *112*, D10S32. https://doi.org/10.1029/2006JD007426

Ervens, B., Cubison, M. J., Andrews, E., Feingold, G., Ogren, J. A., Jimenez, J. L., et al. (2010). CCN predictions using simplified assumptions of organic aerosol composition and mixing state: A synthesis from six different locations. *Atmospheric Chemistry and Physics*, *10*(10), 4795–4807. https://doi.org/10.5194/acp-10-4795-2010

Faloona, I. (2009). Sulfur processing in the marine atmospheric boundary layer: A review and critical assessment of modeling uncertainties. *Atmospheric Environment*, *43*(18), 2841–2854. https://doi.org/10.1016/j.atmosenv.2009.02.043

Fierce, L., Riemer, N., & Bond, T. C. (2016). Toward reduced representation of mixing state for simulating aerosol effects on climate. *Bulletin of the American Meteorological Society*, *98*(5), 971–980. https://doi.org/10.1175/BAMS-D-16-0028.1

Frosch, M., Bilde, M., Nenes, A., Praplan, A. P., Jurányi, Z., Dommen, J., et al. (2013). CCN activity and volatility of β-caryophyllene secondary organic aerosol. *Atmospheric Chemistry and Physics*, *13*(4), 2283–2297. https://doi.org/10.5194/acp-13-2283-2013

Gerber, H., Arends, B. G., & Ackerman, A. S. (1994). New microphysics sensor for aircraft use. *Atmospheric Research*, *31*(4), 235–252. https://doi.org/10.1016/0169-8095(94)90001-9

Goren, T., & Rosenfeld, D. (2012). Satellite observations of ship emission induced transitions from broken to closed cell marine stratocumulus over large areas. *Journal of Geophysical Research*, *117*, D17206. https://doi.org/10.1029/2012JD017981

Gunthe, S. S., King, S. M., Rose, D., Chen, Q., Roldin, P., Farmer, D. K., et al. (2009). Cloud condensation nuclei in pristine tropical rainforest air of Amazonia: Size-resolved measurements and modeling of atmospheric aerosol composition and CCN activity. *Atmospheric Chemistry and Physics*, *9*(19), 7551–7575. https://doi.org/10.5194/acp-9-7551-2009

Hallquist, M., Wenger, J. C., Baltensperger, U., Rudich, Y., Simpson, D., Claeys, M., et al. (2009). The formation, properties and impact of secondary organic aerosol: Current and emerging issues. *Atmospheric Chemistry and Physics*, *9*(14), 5155–5236. https://doi.org/10.5194/acp-9-5155-2009

Heald, C. L., Jacob, D. J., Park, R. J., Russell, L. M., Huebert, B. J., Seinfeld, J. H., et al. (2005). A large organic aerosol source in the free troposphere missing from current models. *Geophysical Research Letters*, *32*, L18809. https://doi.org/10.1029/2005GL023831

Hegg, D. A., Covert, D. S., Jonsson, H., & Covert, P. A. (2005). Determination of the transmission efficiency of an aircraft aerosol inlet. *Aerosol Science and Technology*, *39*(10), 966–971. https://doi.org/10.1080/02786820500377814

Hegg, D. A., Covert, D. S., Jonsson, H. H., & Woods, R. K. (2010). The contribution of anthropogenic aerosols to aerosol light-scattering and CCN activity in the California coastal zone. *Atmospheric Chemistry and Physics*, *10*(15), 7341–7351. https://doi.org/10.5194/acp-10-7341-2010

Hersey, S. P., Sorooshian, A., Murphy, S. M., Flagan, R. C., & Seinfeld, J. H. (2009). Aerosol hygroscopicity in the marine atmosphere: A closure study using high-time-resolution, multiple-RH DASH-SP and size-resolved C-ToF-AMS data. *Atmospheric Chemistry and Physics*, *9*(7), 2543–2554. https://doi.org/10.5194/acp-9-2543-2009

Jimenez, J. L., Canagaratna, M. R., Donahue, N. M., Prevot, A. S. H., Zhang, Q., Kroll, J. H., et al. (2009). Evolution of organic aerosols in the atmosphere. *Science*, *326*(5959), 1525–1529. https://doi.org/10.1126/science.1180353

Kanakidou, M., Seinfeld, J. H., Pandis, S. N., Barnes, I., Dentener, F. J., Facchini, M. C., et al. (2005). Organic aerosol and global climate modelling: A review. *Atmospheric Chemistry and Physics*, *5*(4), 1053–1123. https://doi.org/10.5194/acp-5-1053-2005

Kawana, K., Nakayama, T., & Mochida, M. (2016). Hygroscopicity and CCN activity of atmospheric aerosol particles and their relation to organics: Characteristics of urban aerosols in Nagoya, Japan. *Journal of Geophysical Research: Atmospheres*, *121*, 4100–4121. https://doi.org/10.1002/2015JD023213

Köhler, H. (1936). The nucleus in and the growth of hygroscopic droplets. *Transactions of the Faraday Society*, *32*(0), 1152–1161. https://doi.org/10.1039/TF9363201152

Kreidenweis, S. M., & Asa-Awuku, A. (2014). 5.13—Aerosol Hygroscopicity: Particle water content and its role in atmospheric processes. In H. D. Holland, & K. K. Turekian (Eds.), *Treatise on geochemistry* (Second ed.pp. 331–361). Oxford: Elsevier. https://doi.org/10.1016/B978-0-08-095975-7.00418-6

Lack, D. A., Cappa, C. D., Langridge, J., Bahreini, R., Buffaloe, G., Brock, C., et al. (2011). Impact of fuel quality regulation and speed reductions on shipping emissions: Implications for climate and air quality. *Environmental Science & Technology*, *45*(20), 9052–9060. https://doi.org/10.1021/es2013424

Lambe, A. T., Onasch, T. B., Massoli, P., Croasdale, D. R., Wright, J. P., Ahern, A. T., et al. (2011). Laboratory studies of the chemical composition and cloud condensation nuclei (CCN) activity of secondary organic aerosol (SOA) and oxidized primary organic aerosol (OPOA). *Atmospheric Chemistry and Physics*, *11*(17), 8913–8928. https://doi.org/10.5194/acp-11-8913-2011

Lance, S., Nenes, A., Mazzoleni, C., Dubey, M. K., Gates, H., Varutbangkul, V., et al. (2009). Cloud condensation nuclei activity, closure, and droplet growth kinetics of Houston aerosol during the Gulf of Mexico Atmospheric Composition and Climate Study (GoMACCS). *Journal of Geophysical Research*, *114*, D00F15. https://doi.org/10.1029/2008JD011699

Lance, S., Nenes, A., Medina, J., & Smith, J. N. (2006). Mapping the operation of the DMT continuous flow CCN counter. *Aerosol Science and Technology*, *40*(4), 242–254. https://doi.org/10.1080/02786820500543290

Latham, J., Rasch, P., Chen, C.-C., Kettles, L., Gadian, A., Gettelman, A., et al. (2008). Global temperature stabilization via controlled albedo enhancement of low-level maritime clouds. *Philosophical Transactions of the Royal Society A: Mathematical, Physical and Engineering Sciences*, *366*(1882), 3969–3987. https://doi.org/10.1098/rsta.2008.0137

Levin, E. J. T., Prenni, A. J., Palm, B. B., Day, D. A., Campuzano-Jost, P., Winkler, P. M., et al. (2014). Size-resolved aerosol composition and its link to hygroscopicity at a forested site in Colorado. *Atmospheric Chemistry and Physics*, *14*(5), 2657–2667. https://doi.org/10.5194/acp-14-2657-2014

Liu, X., & Wang, J. (2010). How important is organic aerosol hygroscopicity to aerosol indirect forcing? *Environmental Research Letters*, *5*(4), 044010. https://doi.org/10.1088/1748-9326/5/4/044010

MacDonald, A. B., Dadashazar, H., Chuang, P. Y., Crosbie, E., Wang, H., Wang, Z., et al. (2018). Characteristic vertical profiles of cloud water composition in marine stratocumulus clouds and relationships with precipitation. *Journal of Geophysical Research: Atmospheres*, *123*, 3704–3723. https://doi.org/10.1002/2017JD027900

Mardi, A. H., Dadashazar, H., MacDonald, A. B., Braun, R. A., Crosbie, E., Xian, P., et al. (2018). Biomass burning plumes in the vicinity of the California coast: Airborne characterization of physicochemical properties, heating rates, and spatiotemporal features. *Journal of Geophysical Research: Atmospheres*, *123*, 13,560–13,582. https://doi.org/10.1029/2018JD029134

Massoli, P., Lambe, A. T., Ahern, A. T., Williams, L. R., Ehn, M., Mikkilä, J., et al. (2010). Relationship between aerosol oxidation level and hygroscopic properties of laboratory generated secondary organic aerosol (SOA) particles. *Geophysical Research Letters*, *37*, L24801. https://doi.org/10.1029/2010GL045258

Mauldin, R. L., Tanner, D. J., Heath, J. A., Huebert, B. J., & Eisele, F. L. (1999). Observations of H2SO4 and MSA during PEM-Tropics-A. *Journal of Geophysical Research*, *104*(D5), 5801–5816. https://doi.org/10.1029/98JD02612

McFiggans, G., Artaxo, P., Baltensperger, U., Coe, H., Facchini, M. C., Feingold, G., et al. (2006). The effect of physical and chemical aerosol properties on warm cloud droplet activation. *Atmospheric Chemistry and Physics*, *6*(9), 2593–2649. https://doi.org/10.5194/acp-6-2593-2006

Medina, J., Nenes, A., Sotiropoulou, R.-E. P., Cottrell, L. D., Ziemba, L. D., Beckman, P. J., & Griffin, R. J. (2007). Cloud condensation nuclei closure during the International Consortium for Atmospheric Research on Transport and Transformation 2004 campaign: Effects of size-resolved composition. *Journal of Geophysical Research*, *112*, D10S31. https://doi.org/10.1029/2006JD007588

Mei, F., Setyan, A., Zhang, Q., & Wang, J. (2013). CCN activity of organic aerosols observed downwind of urban emissions during CARES. *Atmospheric Chemistry and Physics*, *13*(24), 12,155–12,169. https://doi.org/10.5194/acp-13-12155-2013

Middlebrook, A. M., Bahreini, R., Jimenez, J. L., & Canagaratna, M. R. (2012). Evaluation of composition-dependent collection efficiencies for the aerodyne aerosol mass spectrometer using field data. *Aerosol Science and Technology*, *46*(3), 258–271. https://doi.org/10.1080/02786826.2011.620041

Modini, R. L., Frossard, A. A., Ahlm, L., Russell, L. M., Corrigan, C. E., Roberts, G. C., et al. (2015). Primary marine aerosol-cloud interactions off the coast of California. *Journal of Geophysical Research: Atmospheres*, *120*, 4282–4303. https://doi.org/10.1002/2014JD022963

Moore, R. H., Bahreini, R., Brock, C. A., Froyd, K. D., Cozic, J., Holloway, J. S., et al. (2011). Hygroscopicity and composition of Alaskan Arctic CCN during April 2008. *Atmospheric Chemistry and Physics*, *11*(22), 11,807–11,825. https://doi.org/10.5194/acp-11-11807-2011

Moore, R. H., Cerully, K., Bahreini, R., Brock, C. A., Middlebrook, A. M., & Nenes, A. (2012). Hygroscopicity and composition of California CCN during summer 2010. *Journal of Geophysical Research*, *117*, D00V12. https://doi.org/10.1029/2011JD017352

Murphy, S. M., Agrawal, H., Sorooshian, A., Padró, L. T., Gates, H., Hersey, S., et al. (2009). Comprehensive simultaneous shipboard and airborne characterization of exhaust from a modern container ship at sea. *Environmental Science & Technology*, *43*(13), 4626–4640. https://doi.org/10.1021/es802413j

Nenes, A., Pandis, S. N., & Pilinis, C. (1998). ISORROPIA: A new thermodynamic equilibrium model for multiphase multicomponent inorganic aerosols. *Aquatic Geochemistry*, *4*(1), 123–152. https://doi.org/10.1023/A:1009604003981

Oreopoulos, L., & Platnick, S. (2008). Radiative susceptibility of cloudy atmospheres to droplet number perturbations: 2. Global analysis from MODIS. *Journal of Geophysical Research*, *113*, D14S21. https://doi.org/10.1029/2007JD009655

Paatero, P., & Tapper, U. (1994). Positive matrix factorization: a non-negative factor model with optimal utilization of error estimates of data values. *Environmetrics*, *5*(2), 111–126. https://doi.org/10.1002/env.3170050203

Petters, M. D., & Kreidenweis, S. M. (2007). A single parameter representation of hygroscopic growth and cloud condensation nucleus activity. *Atmospheric Chemistry and Physics*, *7*(8), 1961–1971. https://doi.org/10.5194/acp-7-1961-2007

Platnick, S., & Twomey, S. (1994). Determining the susceptibility of cloud albedo to changes in droplet concentration with the advanced very high resolution radiometer. *Journal of Applied Meteorology*, *33*(3), 334–347. https://doi.org/10.1175/1520-0450(1994)033%3C0334:DTSOCA%3E2.0.CO;2

Prabhakar, G., Ervens, B., Wang, Z., Maudlin, L. C., Coggon, M. M., Jonsson, H. H., et al. (2014). Sources of nitrate in stratocumulus cloud water: Airborne measurements during the 2011 E-PEACE and 2013 NiCE studies. *Atmospheric Environment*, *97*, 166–173. https://doi.org/10.1016/j.atmosenv.2014.08.019

Pringle, K. J., Tost, H., Pozzer, A., Pöschl, U., & Lelieveld, J. (2010). Global distribution of the effective aerosol hygroscopicity parameter for CCN activation. *Atmospheric Chemistry and Physics*, *10*(12), 5241–5255. https://doi.org/10.5194/acp-10-5241-2010

Pruppacher, H. R., & Klett, J. D. (1997). *Microphysics of clouds and precipitation*. Dordrecht, The Netherlands: Kluwer.

Quinn, P. K., Bates, T. S., Coffman, D. J., & Covert, D. S. (2008). Influence of particle size and chemistry on the cloud nucleating properties of aerosols. *Atmospheric Chemistry and Physics*, *8*(4), 1029–1042. https://doi.org/10.5194/acp-8-1029-2008

Raes, F. (1995). Entrainment of free tropospheric aerosols as a regulating mechanism for cloud condensation nuclei in the remote marine boundary layer. *Journal of Geophysical Research*, *100*(D2), 2893–2903. https://doi.org/10.1029/94JD02832

Randall, D. A., Coakley, J. A., Fairall, C. W., Kropfli, R. A., & Lenschow, D. H. (1984). Outlook for research on subtropical marine stratiform clouds. *Bulletin of the American Meteorological Society*, *65*(12), 1290–1301. https://doi.org/10.1175/1520-0477(1984)065%3C1290:OFROSM%3E2.0.CO;2

Ren, J., Zhang, F., Wang, Y., Collins, D., Fan, X., Jin, X., et al. (2018). Using different assumptions of aerosol mixing state and chemical composition to predict CCN concentrations based on field measurements in urban Beijing. *Atmospheric Chemistry and Physics*, *18*(9), 6907–6921. https://doi.org/10.5194/acp-18-6907-2018

Reutter, P., Su, H., Trentmann, J., Simmel, M., Rose, D., Gunthe, S. S., et al. (2009). Aerosol- and updraft-limited regimes of cloud droplet formation: Influence of particle number, size and hygroscopicity on the activation of cloud condensation nuclei (CCN). *Atmospheric Chemistry and Physics*, *9*(18), 7067–7080. https://doi.org/10.5194/acp-9-7067-2009

Roberts, G., Mauger, G., Hadley, O., & Ramanathan, V. (2006). North American and Asian aerosols over the eastern Pacific Ocean and their role in regulating cloud condensation nuclei. *Journal of Geophysical Research*, *111*, D13205. https://doi.org/10.1029/2005JD006661

Roberts, G. C., Day, D. A., Russell, L. M., Dunlea, E. J., Jimenez, J. L., Tomlinson, J. M., et al. (2010). Characterization of particle cloud droplet activity and composition in the free troposphere and the boundary layer during INTEX-B. *Atmospheric Chemistry and Physics*, *10*(14), 6627–6644. https://doi.org/10.5194/acp-10-6627-2010

Roberts, G. C., & Nenes, A. (2005). A continuous-flow streamwise thermal-gradient CCN chamber for atmospheric measurements. *Aerosol Science and Technology*, *39*(3), 206–221. https://doi.org/10.1080/027868290913988

Rose, D., Gunthe, S. S., Mikhailov, E., Frank, G. P., Dusek, U., Andreae, M. O., & Pöschl, U. (2008). Calibration and measurement uncertainties of a continuous-flow cloud condensation nuclei counter (DMT-CCNC): CCN activation of ammonium sulfate and sodium chloride aerosol particles in theory and experiment. *Atmospheric Chemistry and Physics*, *8*(5), 1153–1179. https://doi.org/10.5194/acp-8-1153-2008

Rose, D., Gunthe, S. S., Su, H., Garland, R. M., Yang, H., Berghof, M., et al. (2011). Cloud condensation nuclei in polluted air and biomass burning smoke near the mega-city Guangzhou, China—Part 2: Size-resolved aerosol chemical composition, diurnal cycles, and externally mixed weakly CCN-active soot particles. *Atmospheric Chemistry and Physics*, *11*(6), 2817–2836. https://doi.org/10.5194/acp-11-2817-2011

Rose, D., Nowak, A., Achtert, P., Wiedensohler, A., Hu, M., Shao, M., et al. (2010). Cloud condensation nuclei in polluted air and biomass burning smoke near the mega-city Guangzhou, China—Part 1: Size-resolved measurements and implications for the modeling of aerosol particle hygroscopicity and CCN activity. *Atmospheric Chemistry and Physics*, *10*(7), 3365–3383. https://doi.org/10.5194/acp-10-3365-2010

Rosenfeld, D. (2006). Aerosol-cloud interactions control of earth radiation and latent heat release budgets. *Space Science Reviews*, *125*(1-4), 149–157. https://doi.org/10.1007/s11214-006-9053-6

Rosenfeld, D., Andreae, M. O., Asmi, A., Chin, M., de Leeuw, G., Donovan, D. P., et al. (2014). Global observations of aerosol-cloud-precipitation-climate interactions. *Reviews of Geophysics*, *52*, 750–808. https://doi.org/10.1002/2013RG000441

Rosenfeld, D., Zhu, Y., Wang, M., Zheng, Y., Goren, T., & Yu, S. (2019). Aerosol-driven droplet concentrations dominate coverage and water of oceanic low-level clouds. *Science*, *363*, eaav0566. https://doi.org/10.1126/science.aav0566

Rothenberg, D., Avramov, A., & Wang, C. (2018). On the representation of aerosol activation and its influence on model-derived estimates of the aerosol indirect effect. *Atmospheric Chemistry and Physics*, *18*(11), 7961–7983. https://doi.org/10.5194/acp-18-7961-2018

Royalty, T. M., Phillips, B. N., Dawson, K. W., Reed, R., Meskhidze, N., & Petters, M. D. (2017). Aerosol properties observed in the subtropical North Pacific boundary layer. *Journal of Geophysical Research: Atmospheres*, *122*, 9990–10,012. https://doi.org/10.1002/2017JD026897

Russell, L. M., Sorooshian, A., Seinfeld, J. H., Albrecht, B. A., Nenes, A., Ahlm, L., et al. (2013). Eastern Pacific emitted aerosol cloud experiment. *Bulletin of the American Meteorological Society*, *94*(5), 709–729. https://doi.org/10.1175/BAMS-D-12-00015.1

Sanchez, K. J., Russell, L. M., Modini, R. L., Frossard, A. A., Ahlm, L., Corrigan, C. E., et al. (2016). Meteorological and aerosol effects on marine cloud microphysical properties. *Journal of Geophysical Research: Atmospheres*, *121*, 4142–4161. https://doi.org/10.1002/2015JD024595

Sánchez-Gácita, M., Longo, K. M., Freire, J. L. M., Freitas, S. R., & Martin, S. T. (2017). Impact of mixing state and hygroscopicity on CCN activity of biomass burning aerosol in Amazonia. *Atmospheric Chemistry and Physics*, *17*(3), 2373–2392. https://doi.org/10.5194/acp-17-2373-2017

Seinfeld, J. H., Bretherton, C., Carslaw, K. S., Coe, H., DeMott, P. J., Dunlea, E. J., et al. (2016). Improving our fundamental understanding of the role of aerosol−cloud interactions in the climate system. *PNAS*, *113*(21), 5781–5790. https://doi.org/10.1073/pnas.1514043113

Sorooshian, A., Anderson, B., Bauer, S. E., Braun, R. A., Cairns, B., Crosbie, E., et al. (2019). Aerosol-cloud-meteorology interaction airborne field investigations: Using lessons learned from the US West Coast in the design of ACTIVATE off the US East Coast. *Bulletin of the American Meteorological Society*, *100*(8), 1511–1528. https://doi.org/10.1175/BAMS-D-18-0100.1

Sorooshian, A., Lu, M.-L., Brechtel, F. J., Jonsson, H., Feingold, G., Flagan, R. C., & Seinfeld, J. H. (2007). On the source of organic acid aerosol layers above clouds. *Environmental Science & Technology*, *41*(13), 4647–4654. https://doi.org/10.1021/es0630442

Sorooshian, A., MacDonald, A. B., Dadashazar, H., Bates, K. H., Coggon, M. M., Craven, J. S., et al. (2017). A multi-year data set on aerosol-cloud-precipitation-meteorology interactions for marine stratocumulus clouds. *Figshare Dataset*. https://doi.org/10.6084/m9.figshare.5099983.v10

Sorooshian, A., MacDonald, A. B., Dadashazar, H., Bates, K. H., Coggon, M. M., Craven, J. S., et al. (2018). A multi-year data set on aerosol-cloud-precipitation-meteorology interactions for marine stratocumulus clouds. *Scientific Data*, *5*, 180026. https://doi.org/10.1038/sdata.2018.26

Sorooshian, A., Ng, N. L., Chan, A. W. H., Feingold, G., Flagan, R. C., & Seinfeld, J. H. (2007). Particulate organic acids and overall water-soluble aerosol composition measurements from the 2006 Gulf of Mexico Atmospheric Composition and Climate Study (GoMACCS). *Journal of Geophysical Research*, *112*, D13201. https://doi.org/10.1029/2007JD008537

Sorooshian, A., Padró, L. T., Nenes, A., Feingold, G., McComiskey, A., Hersey, S. P., et al. (2009). On the link between ocean biota emissions, aerosol, and maritime clouds: Airborne, ground, and satellite measurements off the coast of California. *Global Biogeochemical Cycles*, *23*, GB4007. https://doi.org/10.1029/2009GB003464

Sotiropoulou, R.-E. P., Nenes, A., Adams, P. J., & Seinfeld, J. H. (2007). Cloud condensation nuclei prediction error from application of Köhler theory: Importance for the aerosol indirect effect. *Journal of Geophysical Research*, *112*, D12202. https://doi.org/10.1029/2006JD007834

Stein, A. F., Draxler, R. R., Rolph, G. D., Stunder, B. J. B., Cohen, M. D., & Ngan, F. (2015). NOAA's HYSPLIT atmospheric transport and dispersion modeling system. *Bulletin of the American Meteorological Society*, *96*(12), 2059–2077. https://doi.org/10.1175/BAMS-D-14-00110.1

Stevens, B., & Brenguier, J.-L. (2009). *Cloud-controlling factors: Low clouds*. Cambridge, MA: The MIT Press. Retrieved from https://mitpress.universitypressscholarship.com/view/, https://doi.org/10.7551/mitpress/9780262012874.001.0001/upso-9780262012874-chapter-8

Thalman, R., de Sá, S. S., Palm, B. B., Barbosa, H. M. J., Pöhlker, M. L., Alexander, M. L., et al. (2017). CCN activity and organic hygroscopicity of aerosols downwind of an urban region in central Amazonia: Seasonal and diel variations and impact of anthropogenic emissions. *Atmospheric Chemistry and Physics*, *17*(19), 11,779–11,801. https://doi.org/10.5194/acp-17-11779-2017

Twomey, S. (1977). The influence of pollution on the shortwave albedo of clouds. *Journal of the Atmospheric Sciences*, *34*(7), 1149–1152. https://doi.org/10.1175/1520-0469(1977)034%3C1149:TIOPOT%3E2.0.CO;2

Ueda, S., Miura, K., Kawata, R., Furutani, H., Uematsu, M., Omori, Y., & Tanimoto, H. (2016). Number–size distribution of aerosol particles and new particle formation events in tropical and subtropical Pacific Oceans. *Atmospheric Environment*, *142*, 324–339. https://doi.org/10.1016/j.atmosenv.2016.07.055

VanReken, T. M., Rissman, T. A., Roberts, G. C., Varutbangkul, V., Jonsson, H. H., Flagan, R. C., & Seinfeld, J. H. (2003). Toward aerosol/cloud condensation nuclei (CCN) closure during CRYSTAL-FACE. *Journal of Geophysical Research*, *108*(D20), 4633. https://doi.org/10.1029/2003JD003582

Wang, J., Cubison, M. J., Aiken, A. C., Jimenez, J. L., & Collins, D. R. (2010). The importance of aerosol mixing state and size-resolved composition on CCN concentration and the variation of the importance with atmospheric aging of aerosols. *Atmospheric Chemistry and Physics*, *10*(15), 7267–7283. https://doi.org/10.5194/acp-10-7267-2010

Wang, J., Lee, Y.-N., Daum, P. H., Jayne, J., & Alexander, M. L. (2008). Effects of aerosol organics on cloud condensation nucleus (CCN) concentration and first indirect aerosol effect. *Atmospheric Chemistry and Physics*, *8*(21), 6325–6339. https://doi.org/10.5194/acp-8-6325-2008

Wang, J., Shilling, J. E., Liu, J., Zelenyuk, A., Bell, D. M., Petters, M. D., et al. (2019). Cloud droplet activation of secondary organic aerosol is mainly controlled by molecular weight, not water solubility. *Atmospheric Chemistry and Physics*, *19*(2), 941–954. https://doi.org/10.5194/acp-19-941-2019

Wang, Z., Ramirez, M. M., Dadashazar, H., MacDonald, A. B., Crosbie, E., Bates, K. H., et al. (2016). Contrasting cloud composition between coupled and decoupled marine boundary layer clouds. *Journal of Geophysical Research: Atmospheres*, *121*, 11,679–11,691. https://doi.org/10.1002/2016JD025695

Ward, D. S., Eidhammer, T., Cotton, W. R., & Kreidenweis, S. M. (2010). The role of the particle size distribution in assessing aerosol composition effects on simulated droplet activation. *Atmospheric Chemistry and Physics*, *10*(12), 5435–5447. https://doi.org/10.5194/acp-10-5435-2010

Wonaschütz, A., Coggon, M., Sorooshian, A., Modini, R., Frossard, A. A., Ahlm, L., et al. (2013). Hygroscopic properties of smoke-generated organic aerosol particles emitted in the marine atmosphere. *Atmospheric Chemistry and Physics*, *13*(19), 9819–9835. https://doi.org/10.5194/acp-13-9819-2013

Wood, R. (2012). Stratocumulus clouds. *Monthly Weather Review*, *140*(8), 2373–2423. https://doi.org/10.1175/MWR-D-11-00121.1

Yakobi-Hancock, J. D., Ladino, L. A., Bertram, A. K., Huffman, J. A., Jones, K., Leaitch, W. R., et al. (2014). CCN activity of size-selected aerosol at a Pacific coastal location. *Atmospheric Chemistry and Physics*, *14*(22), 12,307–12,317. https://doi.org/10.5194/acp-14-12307-2014

Zhao, D. F., Buchholz, A., Kortner, B., Schlag, P., Rubach, F., Kiendler-Scharr, A., et al. (2015). Size-dependent hygroscopicity parameter (κ) and chemical composition of secondary organic cloud condensation nuclei. *Geophysical Research Letters*, *42*, 10,920–10,928. https://doi.org/10.1002/2015GL066497

Zheng, Y., Rosenfeld, D., & Li, Z. (2016). Quantifying cloud base updraft speeds of marine stratocumulus from cloud top radiative cooling. *Geophysical Research Letters*, *43*, 11,407–11,413. https://doi.org/10.1002/2016GL071185

References From the Supporting Information

Aiken, A. C., DeCarlo, P. F., Kroll, J. H., Worsnop, D. R., Huffman, J. A., Docherty, K. S., et al. (2008). O/C and OM/OC ratios of primary, secondary, and ambient organic aerosols with high-resolution time-of-flight aerosol mass spectrometry. *Environmental Science &Technology*, *42*(12), 4478–4485. https://doi.org/10.1021/es703009q

Bahreini, R., Ervens, B., Middlebrook, A. M., Warneke, C., de Gouw, J. A., DeCarlo, P. F., et al. (2009). Organic aerosol formation in urban and industrial plumes near Houston and Dallas, Texas. *Journal of Geophysical Research*, *114*, D00F16. https://doi.org/10.1029/2008JD011493

Frossard, A. A., Russell, L. M., Burrows, S. M., Elliott, S. M., Bates, T. S., & Quinn, P. K. (2014). Sources and composition of submicron organic mass in marine aerosol particles. *Journal of Geophysical Research: Atmospheres*, *119*, 12,977–13,003. https://doi.org/10.1002/2014JD021913

Hegg, D. A., Covert, D. S., & Jonsson, H. H. (2008). Measurements of size-resolved hygroscopicity in the California coastal zone. *Atmospheric Chemistry and Physics*, *8*(23), 7193–7203. https://doi.org/10.5194/acp-8-7193-2008

Hildebrandt, L., Kostenidou, E., Lanz, V. A., Prevot, A. S. H., Baltensperger, U., Mihalopoulos, N., et al. (2011). Sources and atmospheric processing of organic aerosol in the Mediterranean: Insights from aerosol mass spectrometer factor analysis. *Atmospheric Chemistry and Physics*, *11*(23), 12,499–12,1515. https://doi.org/10.5194/acp-11-12499-2011

Huang, S., Wu, Z., Poulain, L., van Pinxteren, M., Merkel, M., Assmann, D., et al. (2018). Source apportionment of the organic aerosol over the Atlantic Ocean from 53°N to 53°S: Significant contributions from marine emissions and long-range transport. *Atmospheric Chemistry and Physics*, *18*(24), 18,043–18,062. https://doi.org/10.5194/acp-18-18043-2018

Jimenez, J. L., Jayne, J. T., Shi, Q., Kolb, C. E., Worsnop, D. R., Yourshaw, I., et al. (2003). Ambient aerosol sampling using the aerodyne aerosol mass spectrometer. *Journal of Geophysical Research*, *108*(D7), 8425. https://doi.org/10.1029/2001JD001213

Ng, N. L., Canagaratna, M. R., Zhang, Q., Jimenez, J. L., Tian, J., Ulbrich, I. M., et al. (2010). Organic aerosol components observed in northern hemispheric datasets from aerosol mass spectrometry. *Atmospheric Chemistry and Physics*, *10*(10), 4625–4641. https://doi.org/10.5194/acp-10-4625-2010

Ovadnevaite, J., Zuend, A., Laaksonen, A., Sanchez, K. J., Roberts, G., Ceburnis, D., et al. (2017). Surface tension prevails over solute effect in organic-influenced cloud droplet activation. *Nature*, *546*(7660), 637–641. https://doi.org/10.1038/nature22806

Schmale, J., Schneider, J., Nemitz, E., Tang, Y. S., Dragosits, U., Blackall, T. D., et al. (2013). Sub-Antarctic marine aerosol: Dominant contributions from biogenic sources. *Atmospheric Chemistry and Physics*, *13*(17), 8669–8694. https://doi.org/10.5194/acp-13-8669-2013

Suda, S. R., Petters, M. D., Yeh, G. K., Strollo, C., Matsunaga, A., Faulhaber, A., et al. (2014). Influence of functional groups on organic aerosol cloud condensation nucleus activity. *Environmental Science & Technology*, *48*(17), 10,182–10,190. https://doi.org/10.1021/es502147y

Ulbrich, I. M., Canagaratna, M. R., Zhang, Q., Worsnop, D. R., & Jimenez, J. L. (2009). Interpretation of organic components from positive matrix factorization of aerosol mass spectrometric data. *Atmospheric Chemistry and Physics*, *9*(9), 2891–2918. https://doi.org/10.5194/acp-9-2891-2009

A p p e n d i x   F

PHOTOPOLARIMETRIC SENSITIVITY TO BLACK CARBON CONTENT OF WILDFIRE SMOKE: RESULTS FROM THE 2016 IMPACT-PM FIELD CAMPAIGN

Key Points:
- Polarimetric observations are shown to be sensitive to the amount of black carbon in a wildfire smoke plume
- Radiative closure was achieved between multiangle polarimetric remote sensing and in situ airborne measurements in the smoke plume
- We demonstrated the ability of polarimetric data to constrain the black carbon mass fraction assuming external mixing of chemical components

Photopolarimetric Sensitivity to Black Carbon Content of Wildfire Smoke: Results From the 2016 ImPACT-PM Field Campaign

O. V. Kalashnikova[1] [ID], M. J. Garay[1] [ID], K. H. Bates[2,3] [ID], C. M. Kenseth[2] [ID], W. Kong[2] [ID], C. D. Cappa[4] [ID], A. I. Lyapustin[5] [ID], H. H. Jonsson[6], F. C. Seidel[1] [ID], F. Xu[1] [ID], D. J. Diner[1] [ID], and J. H. Seinfeld[2] [ID]

[1] Jet Propulsion Laboratory, California Institute of Technology, Pasadena, CA, USA, [2] Department of Chemical Engineering, California Institute of Technology, Pasadena, CA, USA, [3] Now at Harvard University Center for the Environment, Cambridge, MA, USA, [4] Department of Civil and Environmental Engineering, University of California, Davis, CA, USA, [5] NASA Goddard Flight Space Center, Greenbelt, MD, USA, [6] CIRPAS, Naval Postgraduate School, Monterey, CA, USA

Abstract Detailed characterization of the aerosol content of wildfire smoke plumes is typically performed through in situ aircraft observations, which have limited temporal and spatial coverage. Extending such observations to regional or global scales requires new remote sensing approaches, such as retrievals that make use of spectropolarimetric, multiangle imaging. In this work measurements made during the Imaging Polarimetric Assessment and Characterization of Tropospheric Particulate Matter (ImPACT-PM) field campaign in a smoke plume near the town of Lebec in Southern California by the Navy Center for Interdisciplinary Remotely Piloted Aircraft Studies Twin Otter aircraft on 8 July 2016 are used in conjunction with near-coincident measurements from the Airborne Multiangle SpectroPolarimetric Imager (AirMSPI) on the National Aeronautics and Space Administration ER-2 high-altitude research aircraft to assess the sensitivity of spectropolarimetric measurements to the black carbon content of the plume. Tracking visible features in the smoke through the sequence of AirMSPI observations allowed the height of the plume to be estimated through geometric techniques. Then, by constraining the fractional amounts of the aerosol constituents with the in situ data, radiative closure was obtained through simulations performed with a polarimetric radiative transfer code, demonstrating the ability to constrain the black carbon mass fraction to approximately 5%, given the uncertainties in the AirMSPI measurements and the assumption of external mixing of aerosol components. The AirMSPI retrieval, made using a limited set of observations from the 470 nm polarimetric spectral band alone, was also generally consistent with operational retrievals of aerosol optical depth and surface reflectance made by the Multi-Angle Implementation of Atmospheric Correction algorithm at 1 km resolution.

Plain Language Summary The sensitivity of polarimetric remote sensing imagery to the black carbon content of wildfire smoke was demonstrated using the results of a NASA field campaign that took place over central California in July 2016. The chemical contents of the smoke plume were measured by an aircraft flying inside the smoke. This information was used to build a model of the smoke that was then used to estimate what would be observed by the remote sensing instrument. Good agreement was achieved in terms of the total amount of aerosol, the brightness of the underlying surface, and the fraction of black carbon in the plume.

1. Introduction

The extent of land burned by both wildfires and prescribed burning and the length of the fire season in the United States have increased dramatically in recent years, as shown in Figure 1. Based on data from the National Interagency Fire Center, the annual increase in the area burned in the United States is about 800 km^2/year. Dennison et al. (2014) reported similar trends for large wildfires in western states. Together, wildfires and prescribed burning, so-called "landscape fires," are estimated to produce about one third of the total airborne particulate matter (PM) in the United States (Park et al., 2007; Watson, 2002); and, in the western states,
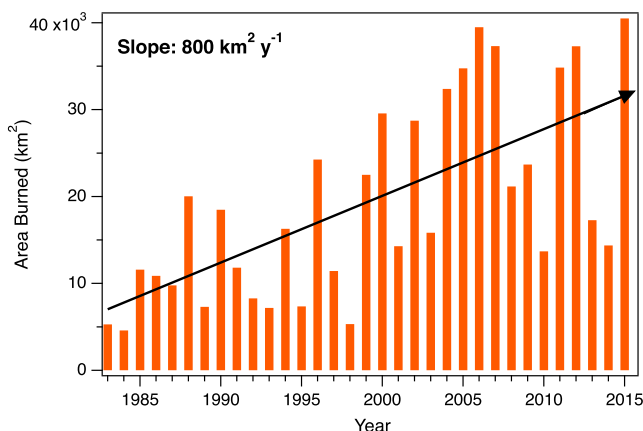
Figure 1. Area burned in the United States from 1983 to 2015 based on data from the National Interagency Fire Center. The trend line calculated using a nonparametric Theil-Sen estimator shows an annual increase in burned area of 800 km^2 per year following the approach of Dennison et al. (2014), who found similar trends for large wildfires in the western United States.

fires can contribute up to nearly 40% of the total PM emissions annually, and they dominate the overall PM emissions in months with greatest fire activity (Urbanski et al., 2011). Because population growth continues to enlarge the wildland-urban interface (Hammer et al., 2009), the potential for adverse health impacts associated with fire-emitted particulate components is increasing as well. In order for health professionals and decision makers to respond to the growing threat of fire emissions, increased understanding of landscape fire processes, smoke emissions, and downwind transport are essential.

While in situ and ground-based measurements can be used effectively at small scales to constrain smoke properties, larger-scale smoke plume characterization is more difficult. Although satellite remote sensing is useful for overall context, the temporal and spatial resolutions of satellite instruments are typically too coarse for detailed, process-oriented studies. Ideally, a quantitative chain of verification could be established linking detailed laboratory and airborne in situ measurements to satellite observations of smoke plumes from landscape fires. This, however, requires an intermediate stage of medium-scale, remote sensing observations made at resolutions on the order of tens of meters spatially and minutes temporally. State-of-the-art airborne

Table 1
NASA ER-2 and Navy CIRPAS Twin Otter Instruments and Products

Platform	Instrument	Science Product	Accuracy at High S/N ($\pm 1\sigma$)
NASA ER-2	Airborne Multiangle Spectro Polarimetric Imager (AirMSPI)	Spectropolarimetric intensities (10 m spatial resolution, eight wavelengths in 355–935 nm spectral range, three polarimetric bands)	3.0% absolute intensity, <0.5% degree of linear polarization
Navy CIRPAS Twin Otter	Aerodyne Aerosol Mass Spectrometer (AMS)	Submicrometer nonrefractory bulk aerosol chemical composition	17–19%
	Single Particle Soot Photometer (SP2)	Size-resolved aerosol BC mass	30%
	Scanning Mobility Particle Sizer (SMPS)	Aerosol particle size, 15 nm to 1μm	See Note
	Particle Soot Absorption Photometer (PSAP)	Absorption at 467, 530, and 660 nm	<20%
	Three-wavelength Integrating Nephelometer (TSINeph)	Wet and dry scattering at 450, 550, and 700 nm	2–10% for submicron mode

Note. The measurement accuracy values are taken from Diner et al. (2013) and Ryerson et al. (2013) for the AirMSPI and the CIRPAS instruments, respectively. Uncertainty of fine mode aerosol number is $\pm(9\% + 14/cm^3)$, surface area is $+(17\% + 0.2\ mm^2/cm^3)$, $-(8\% + 0.2\ mm^2/cm^3)$, and volume is $+(26\% + 0.03\ mm^3/cm^3)$, $-(12\% + 0.03\ mm^3/cm^3)$. NASA = National Aeronautics and Space Administration; CIRPAS = Center for Interdisciplinary Remotely-Piloted Aircraft Studies.

remote sensing instruments, such as imaging polarimeters, could potentially contribute to such efforts by generating high-resolution aerosol property information over smoke-affected areas.

In this paper, we first briefly describe the Imaging Polarimetric Assessment and Characterization of Tropospheric Particulate Matter (ImPACT-PM) field campaign and discuss the suite of instruments on the two participating aircraft—the Naval Postgraduate School Center for Interdisciplinary Remotely-Piloted Aircraft Studies (CIRPAS) Twin Otter, and the National Aeronautics and Space Administration (NASA) ER-2 high-altitude research aircraft. The central observations of interest from the perspective of studying landscape fires took place on 8 July 2016 in the vicinity of Lebec, CA, where a wildfire was simultaneously observed by the two coordinated aircraft. We describe the in situ observations of this event and discuss the leading uncertainties in optically modeling the aerosols within the smoke plume. The in situ PM size and composition are provided by an Aerodyne Aerosol Mass Spectrometer (AMS), a Scanning Mobility Particle Sizer (SMPS), a Single Particle Soot Photometer (SP2), a Particle Soot Absorption Photometer (PSAP), and a nephelometer (see Table 1). The Airborne Multiangle SpectroPolarimetric Imager (AirMSPI) instrument (Diner et al., 2013) on the NASA ER-2 aircraft provides the key remotely sensed data, which is first used to derive the height of the smoke plume using a geometric approach. Then, a radiometric closure study is performed to assess the ability of a polarimetric radiative transfer model of the plume, constrained by the in situ observations, to match a limited set of AirMSPI measurements. This leads to an evaluation of the sensitivity of remotely sensed, multiangular, polarimetric observations to the amount of black carbon in a wildfire smoke plume. Finally, we discuss the results of this exercise, describe the significance for remote sensing retrievals, and mention potential next steps.

2. The ImPACT-PM Field Campaign

The ImPACT-PM field campaign was carried out in California's San Joaquin Valley (SJV) from 5 to 8 July 2016. The joint Jet Propulsion Laboratory (JPL) and California Institute of Technology (Caltech) study, supported by NASA, was conducted to evaluate the ability of multiangle, spectropolarimetric remote sensing to retrieve information on the distributions of atmospheric particle types, with emphasis on carbon-containing compounds—black carbon (BC) and organic carbon (OC). The main goal of the campaign was to advance the science needed to support air quality management policy with state-of-the-art remote sensing observations, which is one of the primary objectives of the planned Multi-Angle Imager for Aerosol (MAIA) satellite investigation, currently in development under the third NASA Earth Venture Instrument (EVI-3) Program. The SJV was chosen because it has among the highest PM concentrations in the United States, including BC from vehicular and industrial combustion, organic (brown) carbon emitted by motor vehicles and biomass burning, and inorganic aerosols (sulfates, nitrates, and ammonium; Young et al., 2016). AirMSPI observations from on board the NASA ER-2 research aircraft were collected in coordination with the suite of science instruments on the lower flying Navy CIRPAS Twin Otter aircraft (see Table 1).

Although selected targets included ground-based measurement sites operated by the U.S. Environmental Protection Agency (EPA) and the California Air Resources Board (CARB) in Fresno, Modesto, Visalia, and Bakersfield, the prime target of opportunity for the ImPACT-PM field campaign was a local wildfire, the Fort Fire, that occurred on 8 July 2016 near the town of Lebec, CA (see Figure 2). This event provided a unique opportunity to evaluate the sensitivity of remotely sensed, multiangular, polarimetric observations to the amount of black carbon in a wildfire smoke plume by combining information from in situ measurements made by the CIRPAS Twin Otter with AirMSPI remote sensing data to establish radiative closure through radiative transfer simulations.

2.1. Remote Sensing Instrumentation

The AirMSPI instrument (Diner et al., 2013) has been flying aboard the NASA ER-2 since October 2010 and has participated in a number of field campaigns in the United States and internationally. AirMSPI is an eight-band (355, 380, 445, 470, 555, 660, 865, and 935 nm) pushbroom camera system, measuring polarization (Stokes Q and U) in the 470, 660, and 865 nm bands, mounted on a gimbal to acquire multiangular observations over a $\pm 67°$ along-track range. The imaged area typically covers about 10 km × 11 km with 10-m pixel resolution from the 20-km altitude of the ER-2 aircraft. AirMSPI has been demonstrated to have a high sensitivity to aerosol optical properties with ∼0.015 uncertainties in aerosol optical depth (AOD) and 0.03 in single-scattering albedo (SSA) as compared with ground-based validation data sets over both ocean (Xu et al., 2016) and land (Xu et al., 2017) targets. Intercomparison of AirMSPI aerosol property retrievals from observations collected during recent field campaigns with collocated ground-based measurements from the Aerosol Robotic Net-

(a)   (b)   (c)
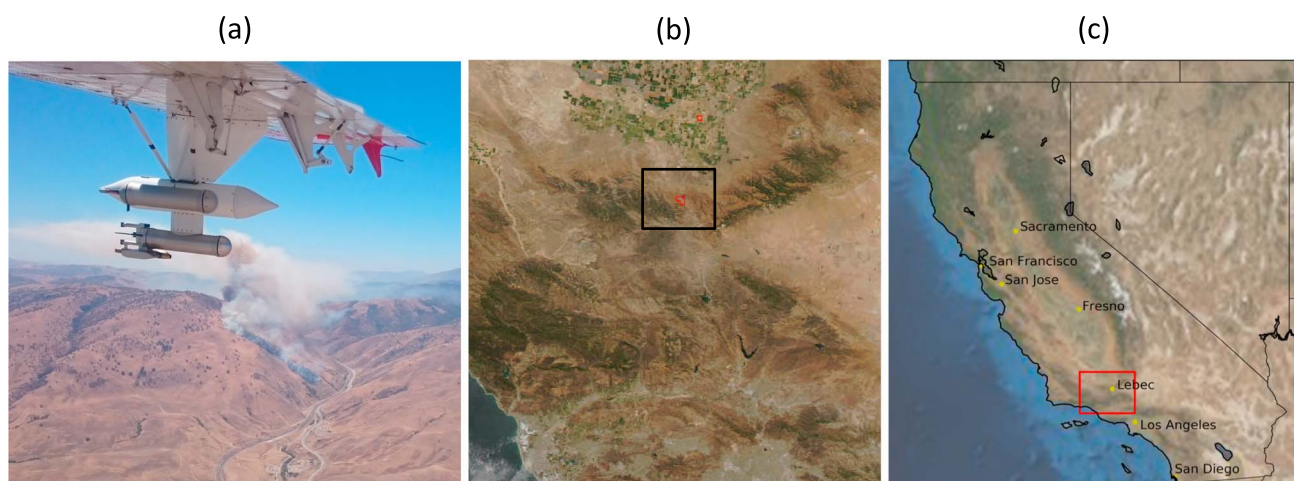
Figure 2. (a) Fort Fire near Lebec, CA photographed from the Center for Interdisciplinary Remotely-Piloted Aircraft Studies Twin Otter aircraft on 8 July 2016 at around 12:03 PDT (19:03 UTC); (b) MODerate resolution Imaging Spectroradiometer (MODIS) red-green-blue 250 m resolution image with MODIS thermal anomaly pixels (red boxes) indicating the fire near Lebec from MODIS-Aqua around 14:10 PDT (21:10 UTC granule; Image credit National Aeronautics and Space Administration/Goddard Space Flight Center, Rapid Response); (c) overview map showing the location of Lebec, CA (red rectangle).

work (AERONET; Holben et al., 1998) yielded AOD regressions with an R^2 of 0.95, a slope of 0.97, and an intercept of ~0.01, which reflect the high quality of aerosol retrievals based on AirMSPI data. While SSA and refractive index validations show relatively larger differences between AirMSPI and AERONET retrievals, the differences are generally within their respective uncertainties (Xu et al., 2017).

2.2. In Situ Instrumentation

In situ measurements of aerosol particle size, composition, and optical properties were made aboard the Navy CIRPAS Twin Otter aircraft, using an SMPS, AMS, SP2, PSAP, and nephelometer (Table 1). The SMPS, consisting of a differential mobility analyzer (DMA; TSI model 3081) coupled to a condensation particle counter (CPC; TSI model 3010), measured particle size distributions between ~15- and 1,000-nm diameter every 90 s. The SMPS was calibrated before the campaign using polystyrene latex spheres. The High-Resolution Time-of-Flight AMS (HR-ToF-AMS; Aerodyne Research, Inc.) quantified submicrometer, nonrefractory aerosol chemical composition and provided chemical speciation of sulfate, nitrate, ammonium, chloride, and organic components with a frequency of 0.1 Hz. The HR-ToF-AMS, described in more detail by DeCarlo et al. (2006), uses an aerodynamic lens to focus submicrometer aerosol onto a resistively heated surface (~600°C), where the particles undergo vaporization and electron impact ionization (70 eV), and the resulting ions are measured in a time-of-flight mass analyzer. On the aircraft, the sample flow rate into the AMS was maintained at ~1.4 cm^3/s using a pressure-controlled inlet. Spectra were analyzed using the SQUIRREL (v. 1.56D), and PIKA (v. 1.15D) modules for IGOR Pro (v. 6.36, WaveMetrics, Inc.), and were corrected for gas-phase interferences (Aiken et al., 2008; Allan et al., 2004) and composition-dependent collection efficiencies (Middlebrook et al., 2012). Detection limits for each chemical component were calculated as 3 times the standard deviations measured on filter samples before each flight, and the instrumental ionization efficiency was calibrated using atomized ammonium nitrate particles after each flight.

Particle total scattering was measured using a three-wavelength nephelometer (Radiance Research) with a correction for angular truncation applied; here only the measurements at 550 nm are used. Particle absorption was measured using a three-wavelength particle soot absorption photometer (PSAP; Radiance Research). The PSAP absorption data were corrected for filter loading and scattering artifacts as in Virkkula (2010). The single particle soot photometer (SP2; Droplet Measurement Technologies, Inc.) measured refractory BC mass concentrations and BC-specific size distributions (Schwarz et al., 2008). The SP2 was calibrated before each flight using dried, size-selected fullerene soot particles, and the size-dependent counting efficiency was determined by comparison with the particle concentration measured by a condensation particle counter. The BC detection efficiency fell off precipitously below 67 nm volume equivalent diameter, and thus, only data for particles larger than that size are included in the analysis. The mass contained in particles smaller than this threshold was estimated by fitting a log-normal distribution to the observed mass-weighted distribution. For the Fort Fire plume observations described below, the amount of undetected BC mass was

(a)   (b)
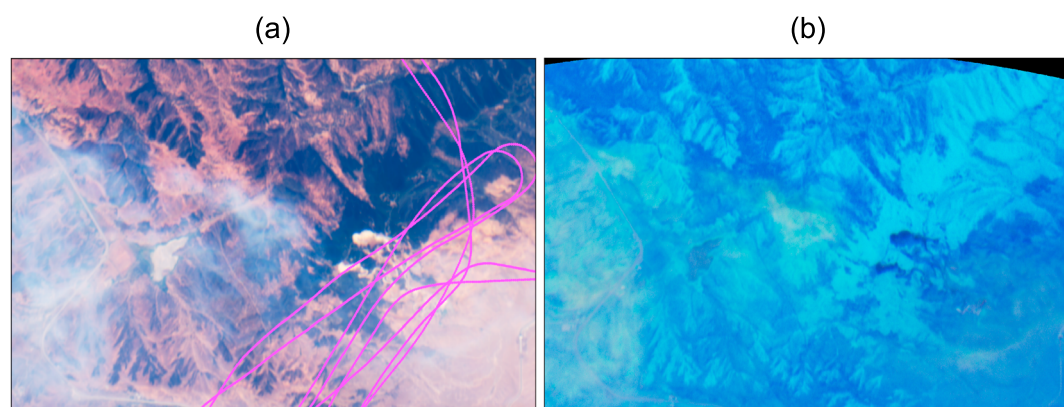
Figure 3. (a) Airborne Multiangle SpectroPolarimetric Imager (AirMSPI) true-color image of the Fort Fire from the 60° aftward view, covering an area of about 17.4 km east-west and 11.6 km north-south—a total of 202 km². The smoke appears as bluish-white, in contrast to the browns and greens of the surface. The Center for Interdisciplinary Remotely-Piloted Aircraft Studies Twin Otter flight tracks in the area are shown in magenta. (b) AirMSPI color composite image of the Fort Fire showing degree of linear polarization (DoLP), which depicts the smoke as greenish yellow over the bluish surface in these spectral bands.

estimated in this manner to be ~13%. Similarly, log-normal fits to the number-weighted BC size distributions were performed to estimate the number-weighted size distribution from 10 to 500 nm for use in Mie theory calculations.

2.3. Fort Fire Observations

A signature event of the ImPACT-PM campaign was the Fort Fire, a wildfire that began around 11:15 Pacific daylight time (PDT; 18:15 UTC, universal time coordinated) on 8 July 2016 in the vicinity of Lebec, CA, on the Tejon Ranch property near Interstate-5. The fire eventually burned 2.24 km² of primarily grass and scrub before it was extinguished the next day. The ER-2 and the Twin Otter coordinated to overfly the fire around 13:30 PDT (20:30 UTC). AirMSPI imaged smoke from the wildfire for about 7 min, centered at 13:19:46 PDT (20:19:46 UTC). Instruments on the Twin Otter sampled the smoke plume from 13:15 to 13:50 PDT (20:15 to 20:50 UTC), while the aircraft was circling in the downwind smoke layer to the east of the fire itself. Figure 2a shows a photograph of the smoke plume looking to the west taken at 12:03 PDT (19:03 UTC) from the Twin Otter more than an hour before the coordination with the ER-2. While flying in the smoke plume the Twin Otter altitude varied between 1,445 and 1,678 m above mean sea level (MSL), but the aircraft did not fly above the smoke layer. The Fort Fire was detected as a temperature anomaly by the MODerate resolution Imaging Spectroradiometer (MODIS) instrument on the NASA Aqua Earth Observing System (EOS) satellite that imaged the area around 14:10 PDT (21:10 UTC; Figure 2b).

Figure 3a shows the region imaged by the 60° aftward AirMSPI view in true-color intensity with the Twin Otter flight tracks overlaid in magenta. Figure 3b shows the same view in degree of linear polarization (DoLP). The color of the smoke in the polarization image shows that the particles in the smoke plume polarize the light differently than the light scattered from the underlying surface. Figure 4 shows aerosol mass concentrations retrieved from the AMS (green) and SP2 (black). The AMS measures mainly inorganic particles such as nitrate, sulfate, ammonium, and chloride, and organic compounds, while the SP2 measures BC concentrations. Figure 4 also shows the particle size distributions derived from the SMPS at two locations: Bakersfield (blue) acquired at 11:46 PDT (18:46 UTC), and Lebec (brown) acquired at 13:19 PDT (20:19 UTC). Particles measured downwind of the Fort Fire have larger concentrations and larger mean diameters than those measured in relatively polluted conditions near Bakersfield, where, in the summertime, secondary organic aerosols are dominant (Liu et al., 2012) and which also has much less BC.

The mass-weighted BC size distribution measured by the SP2 instrument within the Fort Fire plume can be approximated as log-normal with a median volume-equivalent diameter of 149 nm. Note that this is somewhat smaller than the size of the aerosol reported by the SMPS shown in the inset in Figure 4. This size is also somewhat smaller than that reported for most other biomass burning-impacted measurements, which typically have median volume-equivalent diameters closer to 200 nm (Kondo et al., 2011; Sahu et al., 2012; Schwarz et al., 2008; Taylor et al., 2014). The observed BC mass median diameter does, however, compare
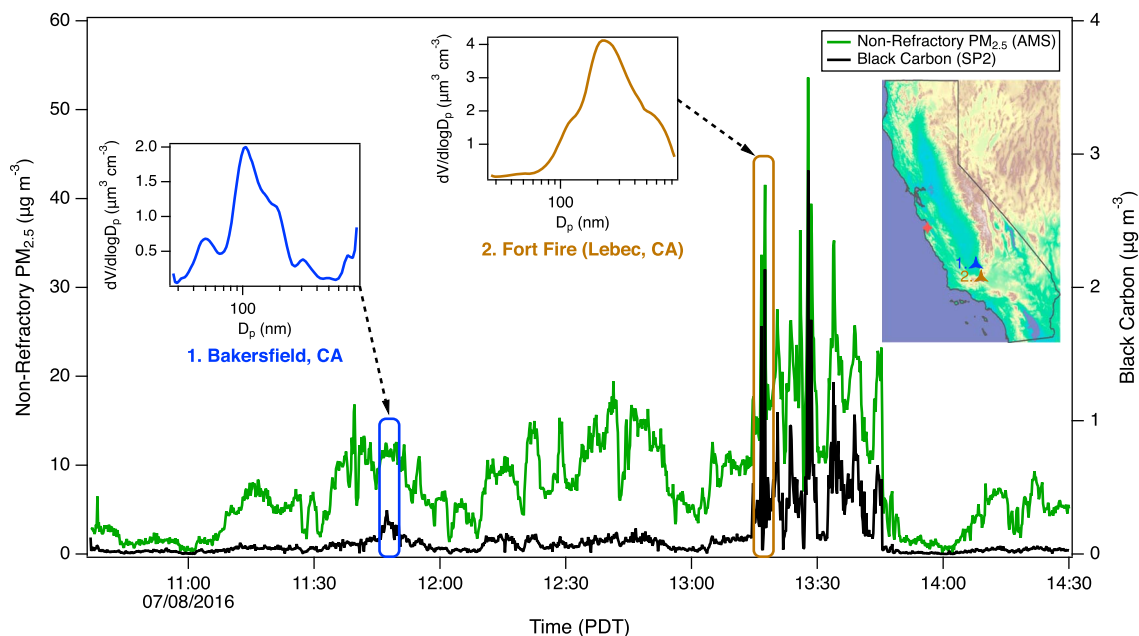
Figure 4. Total Aerosol Mass Spectrometer-measured aerosol mass concentration (green) and the SP2-derived black carbon mass concentration (black) during the 8 July 2016 flight over the San Joaquin Valley and Ventura County. Note the increased mass concentration during the 13:20–13:50 Pacific daylight time (PDT; 20:20–20:50 UTC, universal time coordinated) flight line over the smoke. Inset plots show the aerosol size distribution measured by Scanning Mobility Particle Sizer at the time of the Airborne Multiangle SpectroPolarimetric Imager (AirMSPI) overpass over Bakersfield, CA, at 11:47 PDT (18:47 UTC) and aerosol size distributions measured during the AirMSPI/Twin Otter coordination over the Fort Fire near Lebec, CA, at 13:30 PDT (20:30 UTC).

favorably to preliminary measurements for fresh BC from laboratory biomass combustion of a wide variety of different fuel types (average = 159 ± 20 nm; C. D. Cappa, initial FIREX data analysis).

In order to better characterize the vertical distribution of the smoke, we looked at hourly, ground-based observations of particulate matter with aerodynamic diameter less than 2.5 μm ($PM_{2.5}$) at the Lebec CARB site reported by the beta attenuation monitor (BAM). These data indicate that smoke from the Fort Fire extended to the ground during the time of the AirMSPI overpass. In the hourly BAM data, shown in Figure 5, the $PM_{2.5}$ concentration spiked to 45 μg/m^3 at local noon (19:00 UTC) from a background level as low as 4 μg/m^3 reported 1 hr earlier at 11:00 PDT (18:00 UTC). Near the time of the airborne observations, at 13:00 PDT (20:00 UTC), the BAM reported a value of 60 μg/m^3. After this peak, there was a gradual decrease in $PM_{2.5}$ over the next few hours to a background level of 5 μg/m^3 at 19:00 PDT (02:00 UTC the next day). By way of comparison, the total aerosol mass concentration measured in the plume from the combined AMS and SP2 observations varied between 40 and 60 μg/m^3, in good agreement with the maximum value reported by the BAM. The correspondence between the mass concentrations measured by the aircraft in the plume and the BAM on the ground indicates that the smoke was fairly well mixed down to ground level, consistent with the behavior of the plume shown in the photograph in Figure 2a.

Ground-based Sun-photometer measurements were not available in the vicinity of the Fort Fire to provide a reference for the total column aerosol optical loading described in terms of the AOD. The 3-km resolution Collection 6 (C6) MODIS Dark Target AOD product did not yield any useful data in this case, most likely due to the complex terrain (see Figure 6). However, remote sensing retrievals using MODIS data and the 1-km Multi-Angle Implementation of Atmospheric Correction (MAIAC) algorithm yielded an AOD of about 0.22 with a spatial standard deviation of ±0.03 at 470 nm in the vicinity of the downwind smoke sampled by the Twin Otter. The surface reflectance at this wavelength in the same area has a mean of 0.09, with a spatial standard deviation of ±0.02. MAIAC is an advanced aerosol retrieval algorithm that uses time series analysis and a combination of pixel- and image-based processing to improve accuracy of cloud detection, aerosol retrievals, and atmospheric correction, and it works well over desert and complex terrain yielding high-resolution retrievals of aerosol and surface properties (Lyapustin et al., 2011). In particular, MAIAC provides suites of gridded 1-km atmosphere and surface products, including the following: cloud masking, column water vapor, AOD, aerosol type (background, biomass burning, or dust), surface spectral bidirectional reflectance factors (BRFs), sur-
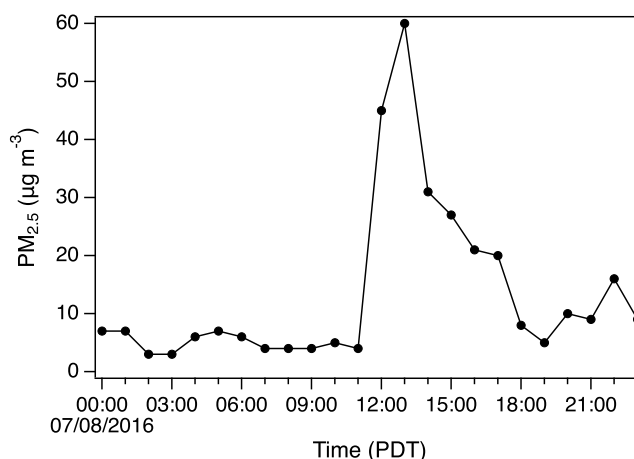
Figure 5. $PM_{2.5}$ measured through the day of 8 July 2016 by the California Air Resources Board beta attenuation monitor station near Lebec, CA (34.84155°N, −118.86058°E, 1,069 m elevation). The effects of the Fort Fire on the ambient air quality can be seen in the peak concentration observed at 13:00 Pacific daylight time (PDT; 20:00 UTC, universal time coordinated).

face reflectance, and Ross-Thick Li-Sparse (RTLS) bidirectional reflectance distribution function (BRDF) model parameters in seven MODIS land bands. Figure 6 shows the AirMSPI red-green-blue (RGB) image of the smoke from the Fort Fire along with the MAIAC AOD and surface reflectance at 470 nm, the wavelength used in our polarimetric sensitivity studies, described below, subsetted to the AirMSPI imaged area. The C6 MODIS 3-km Dark Target AOD retrievals are shown for reference. The MAIAC surface reflectance is derived from an 8-day time series and is, therefore, not expected to be affected by the smoke. The ~50 min time difference between the AirMSPI observation of the smoke plume and the MODIS overpass means that it is unlikely that the smoke and the reported AODs would be exactly coincident, but the overall agreement between AirMSPI image of the smoke and the locations of high AOD reported by MAIAC appears to be very good. Near-coincident meteorological observations made just off the lower right corner of the map at the Sandberg weather station (KSDB, 34.7436°N, −118.7242°E, 1,375 m elevation) at 13:48 PTD (20:48 UTC) show a temperature of 29°C, a relative humidity (RH) of 24%, and winds out of the south at 6.2 m/s, gusting to 9.3 m/s, with consistent wind speeds and directions for the previous 3 hr. This suggests that the spatial pattern of the smoke would likely be more or less consistent during this time frame.

3. Methodology and Optical Modeling

Atmospheric aerosols, which are complex, heterogeneous mixtures of liquids and solids, can undergo aging processes that change their physicochemical and optical properties leading to complex internal mixtures of components. As a first step in characterizing the aerosol in the smoke plume downwind from the Fort Fire, we employ the AMS and SP2 measured aerosol species fractions to determine the relative contribution of different components to the overall spectropolarimetric signal that would be observed by AirMSPI. To simplify the polarimetric radiative transfer calculations, we assume that all particles are externally mixed; that is, each individual particle consists of only a single component, such as sulfate, organics, or BC. The idealized assumption of aerosol external mixing is expected to lead to biases in the calculated bulk aerosol optical properties, especially for BC-containing particles. For example, depending on the local RH and the amount of BC, the SSA values of an externally mixed aerosol could be 2% to 5% higher than those for an internally mixed aerosol with a BC core and a sulfate-nitrate-ammonium (SNA) or OC shell (Drury et al., 2010; Wang & Martin, 2007). These uncertainties are well within the expected error tolerance of our optical modeling and radiative transfer approaches, and the assumption of external mixing is commonly used in satellite remote sensing retrievals due to the computational expense of correctly evaluating coated, internally mixed particles.

The RH measured by the CIRPAS Twin Otter meteorological sensors in the smoke plume was, on average, 30%, and did not exceed 35%, in good agreement with the 24% RH reported at the nearby weather station. Particle water uptake tends to be small for RH < 35% (Hess et al., 1998); therefore, the optical properties of the aerosol components were assumed to correspond to dry particle conditions. To derive the in situ, chemically speciated, submicrometer particulate mass concentrations in the plume shown in Figure 7a, the AMS
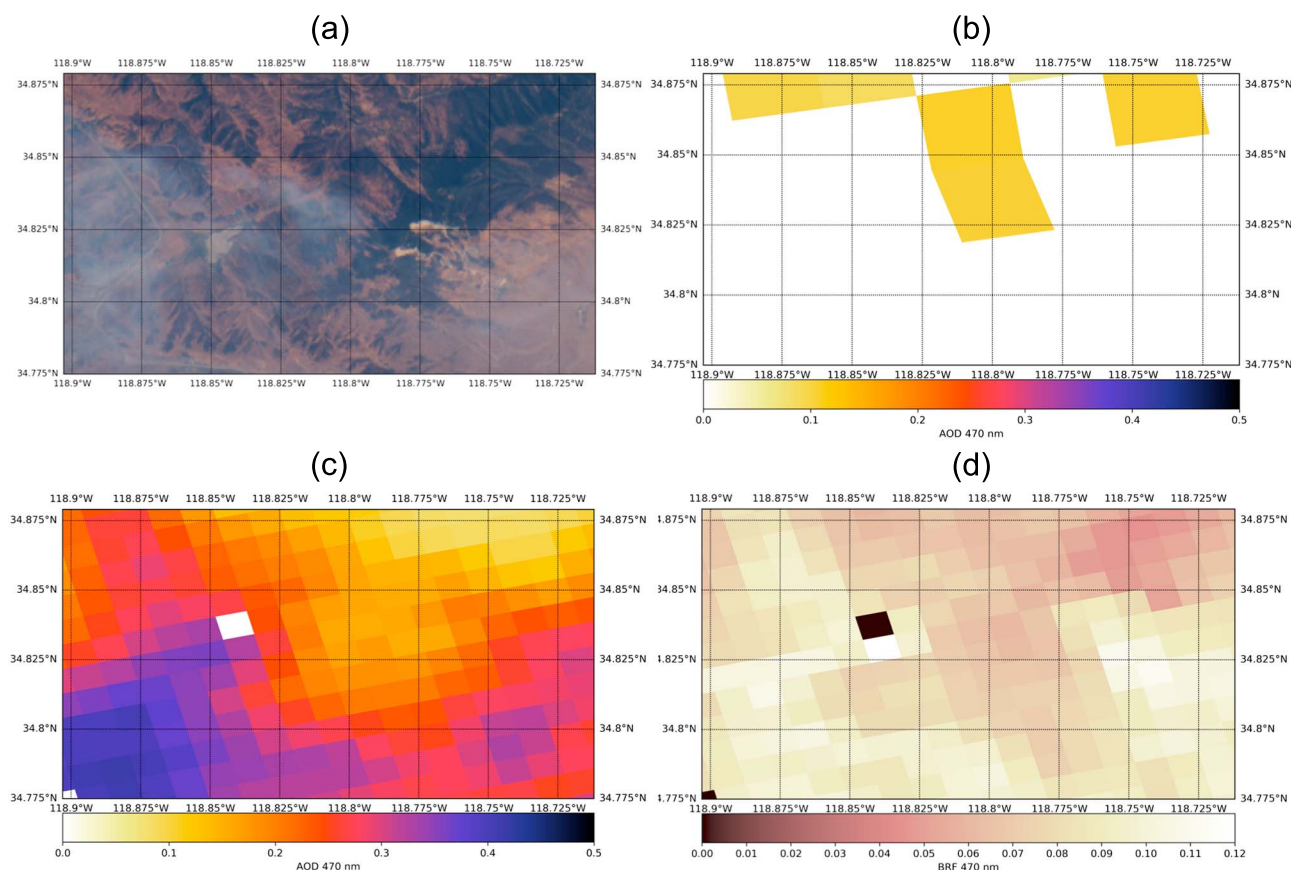
Figure 6. (a) Airborne Multiangle SpectroPolarimetric Imager (AirMSPI) red-green-blue image of the Fort Fire smoke plume area at 13:22 PDT (20:22 UTC) on 8 July 2016; (b) MODerate resolution Imaging Spectroradiometer (MODIS) C6 Dark Target 3-km aerosol optical depth (AOD) at 470 nm from 14:10 PDT (21:10 UTC) matched to AirMSPI-imaged area; (c) Multi-Angle Implementation of Atmospheric Correction (MAIAC) MODIS Aqua 1-km resolution aerosol optical depth at 470 nm; (d) Lower right panel: MAIAC 1-km surface reflectance at 470 nm. BRF = bidirectional reflectance factor.

and SP2 data were averaged over the period during which the SP2 indicated the presence of large amounts of BC — 13:15:33 to 13:46:11 PDT (20:15:33 to 20:46:11 UTC) — excluding samples taken while the plane was turning around outside the plume. During this time, the particles were primarily composed of organics (73.1% $\pm$ 0.9%), followed by sulfate and nitrate in approximately equal abundance (9.0% $\pm$ 1.3% and 7.4% $\pm$ 0.4%, respectively), then BC (5.0% $\pm$ 0.9%), ammonium (3.5% $\pm$ 0.5%), and chloride (2.0% $\pm$ 0.6%). The ranges correspond to 1 standard deviation of the values measured within the plume. The ion balance suggests that the particles were somewhat acidic.

The SP2-derived average BC mass within the plume seems relatively small for wildfire smoke, only 5%. Laboratory observations of fire-derived particles show that the BC fraction can vary over a wide range, depending on the fuel type and burning conditions, which are interrelated (McMeeking et al., 2009, 2014). A 5% BC mass fraction is consistent with visual observations of the smoke plume during the encounter. As seen in Figure 2a, the smoke appears primarily white or light brown instead of black, suggesting little light absorption and, therefore, a small BC content. The fuel type for the Fort Fire was predominantly dry grass and scrub, which might also imply less BC emission in a smoldering phase (Chow et al., 2010). However, OC/BC fractions show a high degree of variability, both between and within different fuel types and species (Jolleys et al., 2014), making the amount of BC difficult to evaluate based on the fuel type alone. Other field observations within major wildfire plumes in California yielded similarly small BC mass fractions (sometimes as low as 2–3%), although again dependent on burning conditions (Kondo et al., 2011).

In order to use the aerosol components determined from the in situ AMS and SP2 observations in radiative transfer calculations, measured mass fractions were converted to volume fractions based on their assumed bulk densities. While the inorganic species (sulfate, nitrate, ammonium, and chloride) should technically be apportioned to their constituent salts and scaled by those densities (ammonium sulfate = 1.78 g/cm^3,
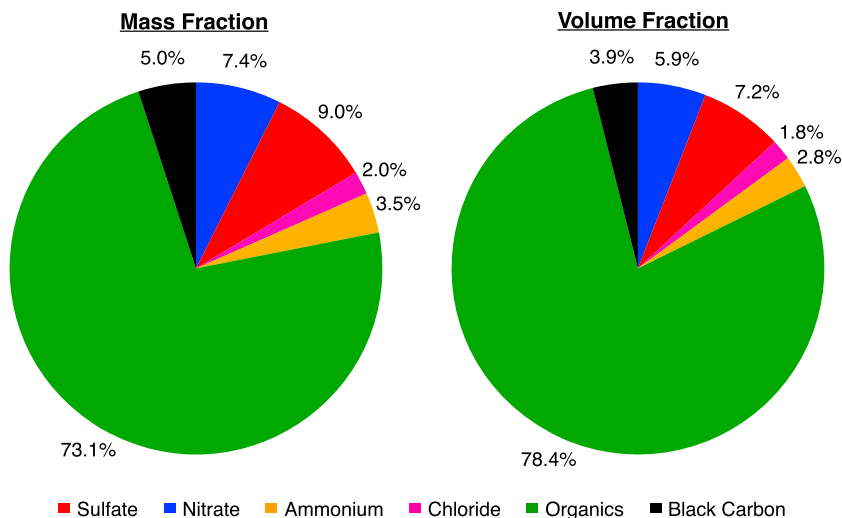
Figure 7. (left) In situ chemically speciated submicrometer particulate mass fractions in the smoke plume from the Center for Interdisciplinary Remotely-Piloted Aircraft Studies Twin Otter, obtained assuming that the total aerosol mass concentration is given by the sum of SP2 measured mass concentration of BC and AMS-derived mass concentrations of sulfate, nitrate, ammonium, chloride, and organics; (right) Volume fractions of submicrometer aerosol components derived from AMS and SP2 measured mass and assumed bulk densities.

ammonium nitrate = 1.72 g/cm^3, ammonium chloride = 1.52 g/cm^3), the SNA component was assigned a density of 1.75 g cm^{-3}, and chloride was assigned a density of 1.52 g cm^{-3} (Salcedo et al., 2006). The density of the organic component depends on the specific composition and usually lies between 1.0 and 1.4 g/cm^3. AMS O/C and H/C ratios were used to estimate the density of the organic components following the approach of Kuwata et al. (2012). Based on those data points within the plume used to derive the mass fractions shown in Figure 7a, the O/C ratio was determined to be 0.555 and the H/C ratio was found to be 1.6, yielding a density of 1.3 g/cm^3 for the organics, the value adopted here. There is continuing discussion in the literature concerning the density of BC particles (Bond et al., 2013). Following Park et al. (2004), a value of 1.8 g/cm^3 was adopted. Derived particle volume fractions are shown in Figure 7b.

Refractive indices for the different aerosol components are also needed for radiative transfer calculations. The refractive indices for sulfate and OC were taken from the Optical Properties of Aerosols and Clouds (OPAC) database used in the Global Aerosol Data Set (GADS) (Hess et al., 1998; Koepke et al., 1997), and currently used in the Goddard Earth Observing System (GEOS)-Chem model (Martin et al., 2003). Following the GEOS-Chem implementation (Martin et al., 2003), the refractive indices of nitrate, ammonium, and chloride were taken to be identical to those of sulfate. Refractive indices of BC, which continue to be a subject of attention in the literature (Stier et al., 2007), were varied in the range suggested by Hess et al. (1998) and Bond and Bergstrom (2006), as described in greater detail below.

The number-weighted log-normal size distribution parameters measured by the in situ instruments at the time of the AirMSPI overpass were used with the appropriate refractive indices in Mie calculations assuming spherical particles (Mishchenko et al., 1999). While flaming fires are known to produce long-chain aggregates of particles, the assumption of particle sphericity for smoldering-dominated fires and transported smoke is typically adequate (Reid et al., 2005). For example, Chakrabarty et al. (2014) examined a large number of scanning electron microscope (SEM) filters taken from a range of different wildfires and found that large particle aggregates were only common for samples taken near the source of flaming fires and nearly completely absent in samples taken from organic carbon-dominated smoldering fires.

Particle size distributions for the different individual components were based on SMPS and SP2 measurements through log-normal fits to the data:

$$n(r) = \frac{N}{(2\pi)^{\frac{1}{2}} r \cdot \ln \sigma} \cdot \exp \left[\frac{-(\ln r - \ln r_c)^2}{2(\ln \sigma)^2} \right], \tag{1}$$

where n is the number of particles, N is a scaling factor, r is the particle radius, r_c is the characteristic (median) radius, and σ is the width of the distribution. The number-weighted, log-normal fit to the SP2 measurements

Table 2

Aerosol Size Distribution Parameters for Number-Weighted, Log-Normal Size Distributions Derived from SP2 and SMPS Observations in the Smoke

	OC	BC	SNA
Median diameter (μm)	0.10–0.15 (0.11)	0.05–0.08 (0.08)	0.10–0.15 (0.11)
Width of the size distribution (σ)	1.45–1.65 (1.6)	1.1–2.1 (1.6)	1.45–1.65 (1.6)

Note. Values in parentheses correspond to those used in the Mie calculations. SP2 = Single Particle Soot Photometer; SMPS = Scanning Mobility Particle Sizer; OC = organic carbon; BC = black carbon; SNA = sulfate-nitrate-ammonium.

in the smoke plume implies a BC median diameter in the range from 50 to 80 nm, and width of the log-normal distribution of 1.1 to 2.1. The size distribution parameters are listed in Table 2 and the parameters adopted for the Mie calculations are shown in parentheses. Particle refractive indices interpolated to AirMSPI midvisible and NIR wavelengths are summarized in Table 3, which contains the values from Hess et al. (1998) as well as from Bond and Bergstrom (2006), the latter of which assumes the same spectral dependence as those from Hess et al. (1998).

We recognize that OC absorption at short visible wavelengths is affected by the presence of brown carbon (BrC) released by the combustion of organic matter, resulting in a larger value of the imaginary part of the refractive index at short visible wavelengths. This may limit the applicability of the Hess et al. (1998) refractive indices for the OC component in fire emissions. However, measurements show that the imaginary part of the refractive index in smoke is relatively constant for wavelengths longer than 440 nm (Mok et al., 2016), which yields relatively small deviations from the BC-predicted spectral slope of SSA at midvisible and near-infrared wavelengths (Liu et al., 2014). Since the radiative transfer calculations are performed for the shortest polarized wavelength of AirMSPI, 470 nm, we argue that the presence of BrC in the smoke plume will likely only have a minimal impact on our results.

Knowing the aerosol refractive indices and the size distribution for each species, *j*, the aerosol phase matrix, $P_j(\Theta)$, extinction coefficient, $K_{ext,j}$, scattering coefficient, $K_{sca,j}$, and SSA, ϖ_j were computed using Mie theory (Mishchenko et al., 1999). Field measurements show that smoke aerosols are typically spherical, to a good approximation, at some distance from the source, as is the case for the AirMSPI and CIRPAS Twin Otter observations of the Fort Fire plume (Martins et al., 1998; Reid et al., 2005). Figure 8 shows elements of the scattering phase matrix for SNA, OC, and BC calculated using the OPAC refractive indices for the three polarized AirMSPI wavelengths—470 nm (blue), 660 nm (red), and 865 nm (magenta). The P11 element of the phase matrix describes the effect of single scattering on intensity, while the P12 element describes the linear polarizing effect of single scattering on unpolarized incident radiation. The ratio of the these two represents the DoLP induced by single scattering. In all cases, for these relatively small particles, the maximum DoLP is almost 100% near a scattering angle of 90°, similar to Rayleigh scattering. The vertical lines indicate the AirMSPI viewing geometry for the Fort Fire case. As this example shows, the AirMSPI observations cover a wide range of scattering angles from 110° to 170°. Importantly, AirMSPI observes the backscattering portion of the phase matrix where significant differences exist among the scattering by different aerosol types. This illustrates how AirMSPI spectropolarimetric observations can be used to characterize atmospheric aerosols.

Table 3

Refractive Indices for Organic Carbon (OC), Black Carbon (BC), and Sulfate-Nitrate-Ammonia (SNA) Interpolated to AirMSPI Wavelengths

	OC		BC				SNA	
λ (nm)	n_r	n_i	n_r (Hess)	n_i (Hess)	n_r (Bond)	n_i (Bond)	n_r	n_i
470	1.530	5×10^{-3}	1.750	0.4530	1.850	0.7230	1.432	1×10^{-9}
555	1.530	5×10^{-3}	1.750	0.4395	1.850	0.7095	1.430	1×10^{-9}
660	1.530	5×10^{-3}	1.750	0.4340	1.850	0.7040	1.429	1×10^{-9}
865	1.520	5×10^{-3}	1.750	0.4333	1.850	0.7031	1.425	1×10^{-9}
935	1.520	5×10^{-3}	1.753	0.4367	1.853	0.7067	1.422	1×10^{-9}

Note. Values for OC and SNA from Hess et al. (1998). BC values from Hess et al. (1998) and Bond and Bergstrom (2006).
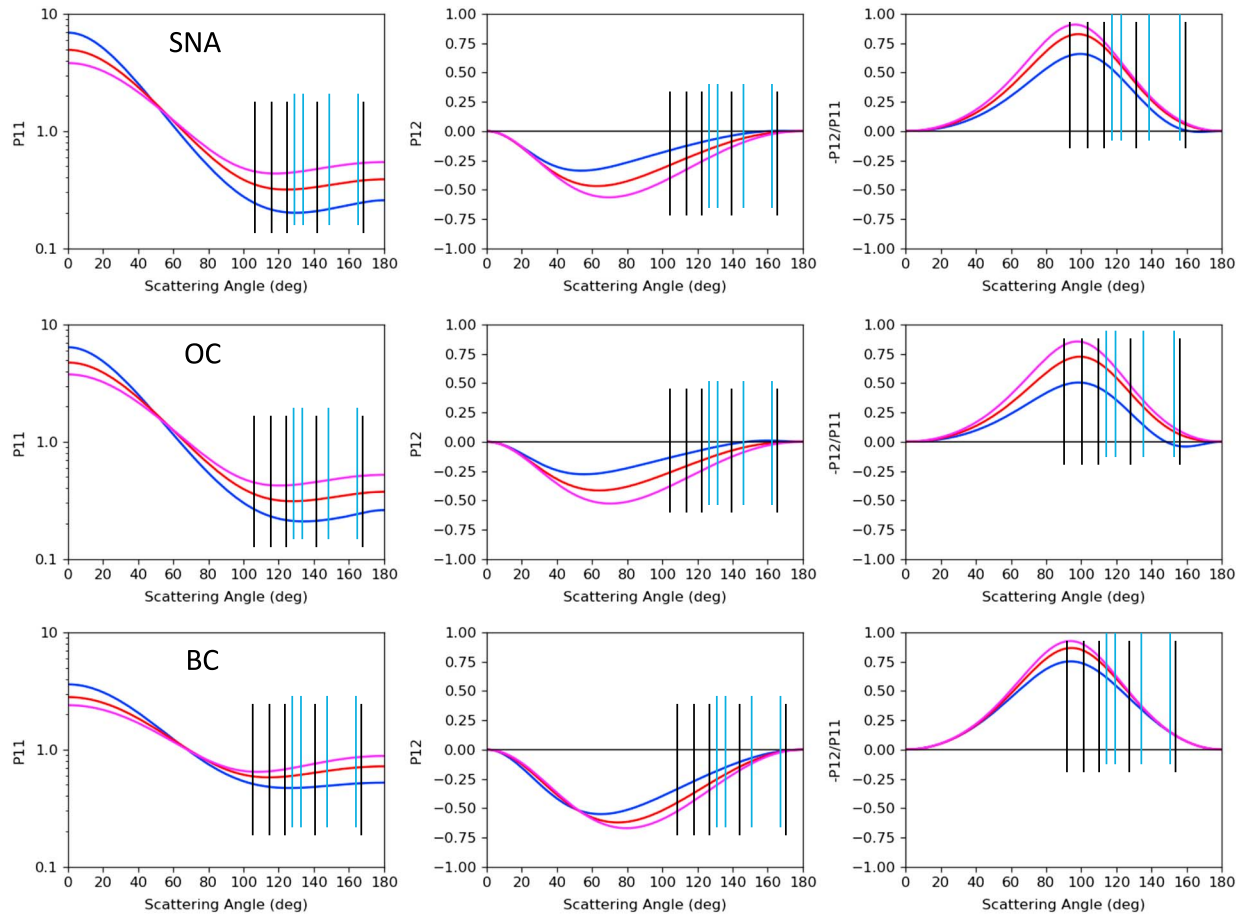
Figure 8. Phase matrix elements from Mie modeling at 470 nm (blue), 660 nm (red), and 865 nm (magenta) for Sulfate-Nitrate Ammonium (SNA) (top row); Organic Carbon (OC) (middle row); and Black Carbon (BC) (bottom row). Columns correspond to the elements P11 (left), P12 (middle), and the ratio of P12 to P11 (right). The Airborne Multiangle SpectroPolarimetric Imager viewing geometry for the Fort Fire case is overplotted with vertical black lines corresponding to forward viewing angles and vertical light blue lines corresponding to aftward viewing angles.

Using the single-scattering results for SNA, OC, and BC, the optical properties for the aerosol mixtures, which were assumed to be dry and externally mixed, were calculated as follows (Hess et al., 1998):

$$K_{ext}(\lambda) = \sum_j K_{ext,j}(\lambda) \tag{2}$$

$$K_{scat}(\lambda) = \sum_j K_{scat,j}(\lambda) \tag{3}$$

$$\varpi(\lambda) = \frac{K_{scat}(\lambda)}{K_{ext}(\lambda)} \tag{4}$$

$$P(\Theta, \lambda) = \frac{\sum_j K_{scat,j}(\lambda) \times P_j(\Theta, \lambda)}{K_{scat}(\lambda)} \tag{5}$$

for j corresponding to SNA, OC, and BC.

Figure 9a shows the spectral SSA of the resulting mixtures calculated using this approach for different BC mass concentrations, with the mass concentrations of the other components fixed to those reported by the AMS (i.e., ammonium = 0.77 µg/m³; sulfate = 1.98 µg/m³, nitrate = 1.61 µg/m³, chloride = 0.43 µg/m³, OC = 16.02 µg/m³). The 1.1 µg/m³ corresponds to 5% of the total mass fraction, which the SP2 assigns to BC. BC mass fractions were varied in the range from 5% to 20% to cover the range of smoke SSAs found in a variety of AERONET observations (Sayer et al., 2014). The resulting SSA spectral slopes demonstrate the expected
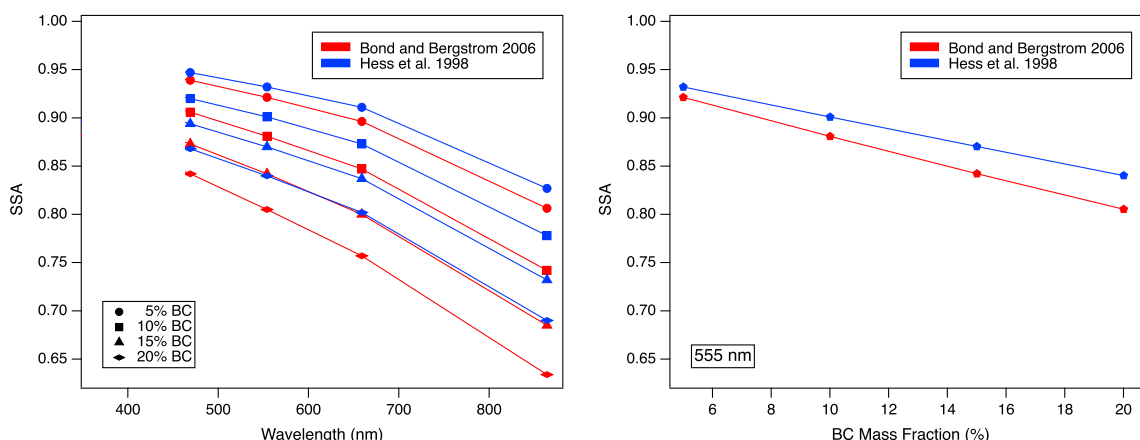
Figure 9. SSA calculated using Mie theory with prescribed optical properties for smoke aerosol based on Aerosol Mass Spectrometer-derived mass fractions assuming external mixing of components. (left) Single-scattering albedo (SSA) spectral dependence assuming black carbon (BC) mass concentrations from 5% to 20%; (right) SSA at 555 nm assuming BC mass concentrations from 5% to 20% and refractive indices for BC from Hess et al. (1998) and Bond and Bergstrom (2006).

behavior of BC-containing aerosols with near-spectrally invariant refractive indices, showing increasing absorption at longer wavelengths. Figure 9b compares the SSA at 555 nm as a function of BC mass fraction calculated with the different refractive indices for BC suggested by Hess et al. (1998) and Bond and Bergstrom (2006). The calculations are performed for the 555 nm AirMSPI wavelength in order to facilitate comparisons with the SSA values derived from the SP2 and the PSAP absorption measurements matched to the nephelometer scattering observations in the Fort Fire plume to evaluate the validity of the external mixing assumption and the representativeness of the selected range of BC mass concentrations.

Figure 10 shows the in-plume SSA at 550 nm derived from 10-s averaged (lightly shaded) and 1-min averaged (dark shaded) absorption data from the SP2 in gray and from the ratio of the PSAP absorption to the nephelometer scattering data in green. Short periods when the nephelometer scattering was less than 10 M/m were not included in the analysis to account for times when the Twin Otter was flying outside the plume. The absorption coefficient, b_{abs} (with units of M/m), from the SP2 was estimated from the directly measured BC mass concentration while the Twin Otter was within the plume as $b_{abs} = 7.5 \times [BC]$, where 7.5 is the mass absorption coefficient (MAC, m^2/g) for "pure" BC at 550 nm (Bond & Bergstrom, 2006). Typically, this MAC value is considered a lower bound for atmospheric BC since the presence of nonabsorbing coatings on BC can enhance the absorption and thus increase the apparent MAC (Fuller et al., 1999).

The plume-averaged b_{abs} from the SP2 was 3.3 (± 2.7) M/m, while that estimated from the PSAP and nephelometer was 8.3 (± 6.1) M/m. These values correspond to a plume-averaged SSA of 0.94 ± 0.01 (1σ) from the SP2 and 0.88 ± 0.04 (1σ) from the PSAP and nephelometer. However, the relatively large uncertainties reported here, which correspond to 1 standard deviation of the values determined while the Twin Otter was in the plume, show that there was substantial spatial variability in the absorption. The larger absorption and lower SSA derived from the PSAP and nephelometer data could also be a result of a bias due to the relatively large observed concentration of organic aerosol (OA) in the smoke plume, as organics are not fully accounted for in the filter loading correction. Biases as large as two or three have been observed previously when the OA/BC ratio was large (Cappa et al., 2008; Lack et al., 2008). Alternatively, the bias could be attributed to uncertainty in the MAC for BC (estimated at ± 1.2 m^2/g, not accounting for any potential enhancements) or in the SP2 BC mass concentration measurement itself. Finally, some of the difference between the SP2 and PSAP/nephelometer results might be due to absorption by non-BC species, specifically BrC. The PSAP absorption measurement includes contributions from non-BC species, while the SP2 estimate does not. For biomass combustion-derived particles, the contribution of BrC to total absorption depends on the fuel type, burning conditions, and wavelength, with larger BrC contributions at shorter wavelengths, but almost negligible differences at midvisible wavelengths (Kirchstetter et al., 2004; McMeeking et al., 2014; Pokhrel et al., 2017; Saleh et al., 2014; Zhang et al., 2016). Given that the SP2-derived SSA does not include potential contributions of BrC to the total absorption, it is possible that the SP2 estimate of absorption might be biased low; however, it is not likely to result in a difference of a factor of 2.5 in the absorption coefficient; 3.3 M/m for the SP2 compared to 8.3 M/m for the PSAP and nephelometer. This difference justifies testing BC concentrations ranging
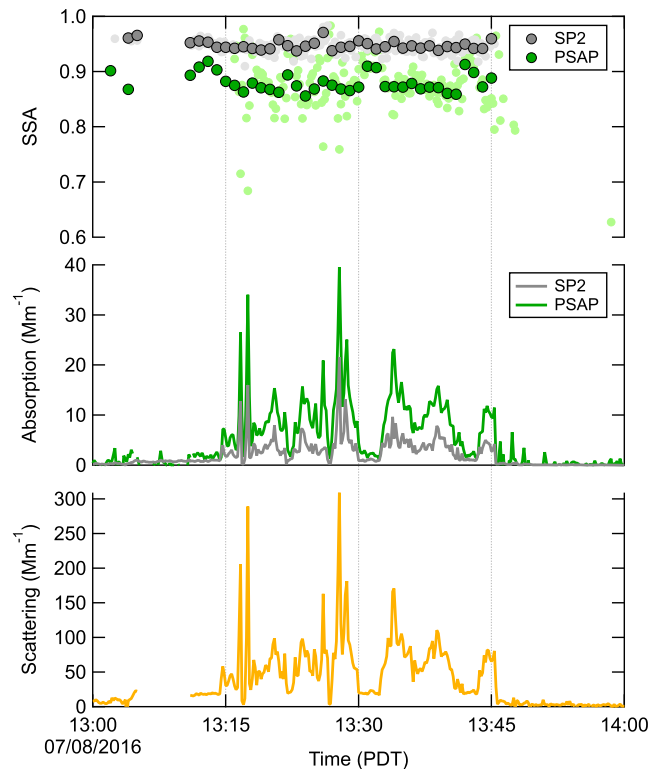
Figure 10. (top) Single-scattering albedo (SSA) at 550 nm in the Fort Fire smoke plume derived from Single Particle Soot Photometer (SP2) and Particle Soot Absorption Photometer (PSAP)/nephelometer observations. Light shading indicates 10-s averages in the plume, while dark shading corresponds to 1-min averages. The average SSA in the plume from the SP2 is 0.94 ± 0.01 (1σ), compared to 0.88 ± 0.04 (1σ) derived from the PSAP/nephelometer. (middle) Estimated absorption coefficient at 550 nm from the SP2 (gray) and the PSAP (green). (bottom) Extinction coefficient at 550 nm derived from the nephelometer.

from 5% to 20%, which changes the SSA of the aerosol mixtures by 0.06. Laboratory measurements of SSA values for smoke produced from biomass combustion demonstrate that the SSA for fresh, fire-derived particles can be highly variable, depending importantly on the fuel type (Chakrabarty et al., 2010; Griffin & Critchfield, 1972) and combustion conditions (Liu et al., 2014).

4. AirMSPI Observations and Closure Study

Closure studies, which are made possible by simultaneous remote sensing and in situ sampling, are helpful for evaluating spectropolarimetric sensitivities to BC fraction and deriving error estimates (Dubovik et al., 2011; Xu et al., 2016). In the case of the Fort Fire, we use radiative closure to attempt to resolve the differences in the BC content and SSA reported by the SP2 and the PSAP/nephelometer data. Recall that the average SSA at 550 nm in the smoke plume derived from the SP2 measurements was 0.94 ± 0.01 (1σ), compared to 0.88 ± 0.04 (1σ) derived from the PSAP/nephelometer measurements. Scattering models were constructed for smoke aerosols with differing fractions of BC ranging from 5% to 20%, corresponding to the observed range of SSAs, based on the in situ measurements of the composition from the AMS and SP2 (Figure 7) and the size distribution from the SMPS (Figure 4, inset). After addressing the issue of the apparent plume motion through the sequence of AirMSPI observations that can be used to derive the height of the plume, the remaining unknowns are the total column AOD for the smoke and the surface reflectance, which we take to be Lambertian, for simplicity. Closure, then, involves finding the AOD-surface albedo-SSA combination that yields the best agreement with the AirMSPI observations using full vector (polarimetric) radiative transfer modeling.

The height of the smoke plume causes its apparent location to shift from one view to the next through the sequence of AirMSPI observations due to parallax. This shift can be used to estimate the plume height geometrically following the method employed by the Multi-angle Imaging SpectroRadiometer (MISR) INteractive eXplorer (MINX) tool (Nelson et al., 2013). Well-defined features at the top of the plume observed at 470 nm
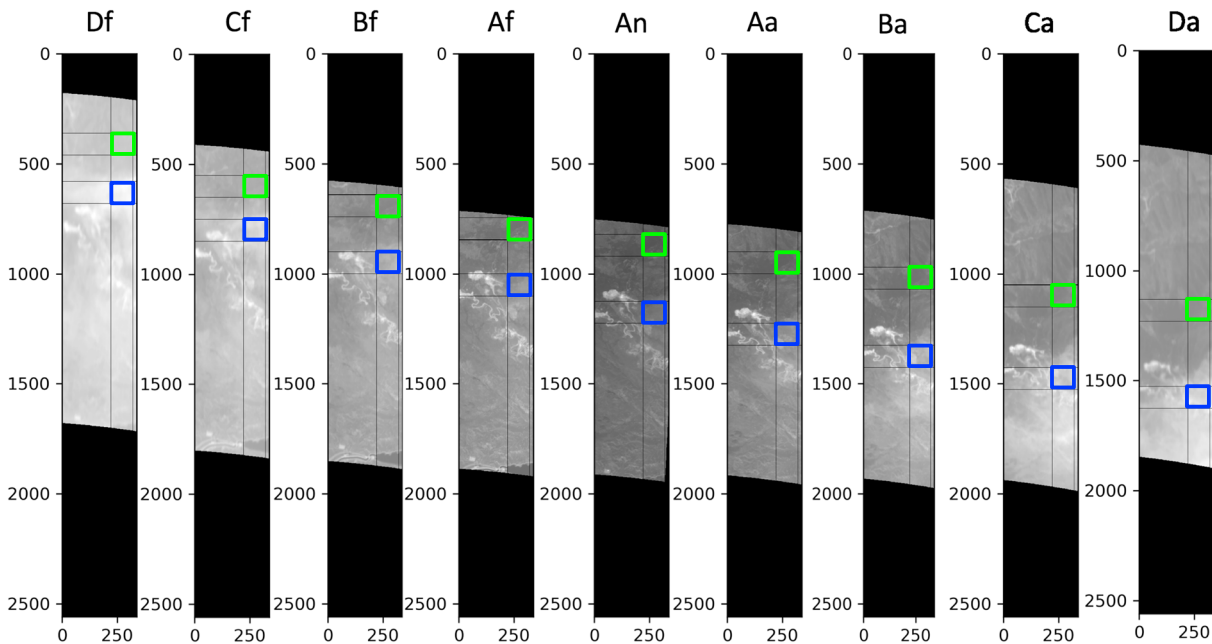
Figure 11. Airborne Multiangle SpectroPolarimetric Imager (AirMSPI) views of the Fort Fire smoke plume at 470 nm. Thin strips corresponding to the full length of the AirMSPI images with a width of approximately 3 km were selected to highlight the plume in the region where the Center for Interdisciplinary Remotely-Piloted Aircraft Studies Twin Otter was operating. The blue box shows the location of a 1 km^2 patch in the smoke plume tracked through the nine images. The Multi-angle Imaging SpectroRadiometer convention for the views is adopted here for convenience with Df = 68.4°, Cf = 61.2°, Bf = 50.2°, Af = 32.1°, An = 9.0°, Aa = 28.3°, Ba = 47.3°, Ca = 60.0°, and Da = 65.6°.

are tracked manually through multiple AirMSPI views as shown in Figure 11. A single band is selected because the spectral bands are offset in the direction of the flight motion (along-track) in the AirMSPI detector (Diner et al., 2013). Since AirMSPI is a pushbroom sensor, this offset leads to a shift in the location of features from band to band that is typically handled by the L1B2 processing, which coregisters the individual bands to "pixels" on the surface. The 470 nm band was selected because this is the shortest polarimetric wavelength in AirMSPI, smoke features are easier to identify due to the somewhat larger AOD, and the surface reflectance is expected to be fairly low. For example, the Advanced Spaceborne Thermal Emission Reflection Radiometer (ASTER) instrument on the Terra satellite has a spectral library (v2.0) that gives a reflectance of grass at 470 nm of 4.2% and of brown, gravelly, sandy loam of about 10% (Baldridge et al., 2009).

Two 1-km × 1-km boxes were manually "tracked" through the AirMSPI image sequence shown in Figure 11. The blue box corresponds to a feature at the top of the smoke plume. The green box is a "patch" of the same size corresponding to the surface in the clear air outside the plume. For convenience, the convention used by MISR is adopted here, with the triplet of angles closest to (and including) nadir being designated "A," the next most oblique pair of views designated "B," and so on (Diner et al., 1998). The spatial separation between the patches changes from view to view due to the height-induced parallax of the features associated with the smoke plume. The length of the strips in the image represents the full image swath of the AirMSPI L1B2 data in the along-track direction (in this case from south to north), which is common to all nine views. Taking only the shift in the along-track direction relative to the An (near-nadir) view a mean height of 2, 700 ± 200 m is obtained for the smoke plume. The uncertainty reflects the standard deviation of the estimates of the stereo pairs (each individual view forms a pair with the An view). The height estimate also does not take into account motion of the plume due to the wind or higher-order details of the viewing geometry (Nelson et al., 2013). By way of comparison, the CIRPAS Twin Otter never flew high enough to be above the smoke. The maximum reported flight altitude of 1,800 m above mean sea level (ASL) is consistent with being inside a smoke plume with a top height of 2,700 m. For the subsequent radiative transfer calculations and AirMSPI data comparisons, we use the mean geometry from the selected 1-km × 1-km smoke patch (see Table 4).

Figure 12 shows the AirMSPI observations for the "Smoke" and "Clear" patches in the previous figure. Instead of working with the "raw" AirMSPI radiances, we convert them to bidirectional reflectance factors (BRFs) or
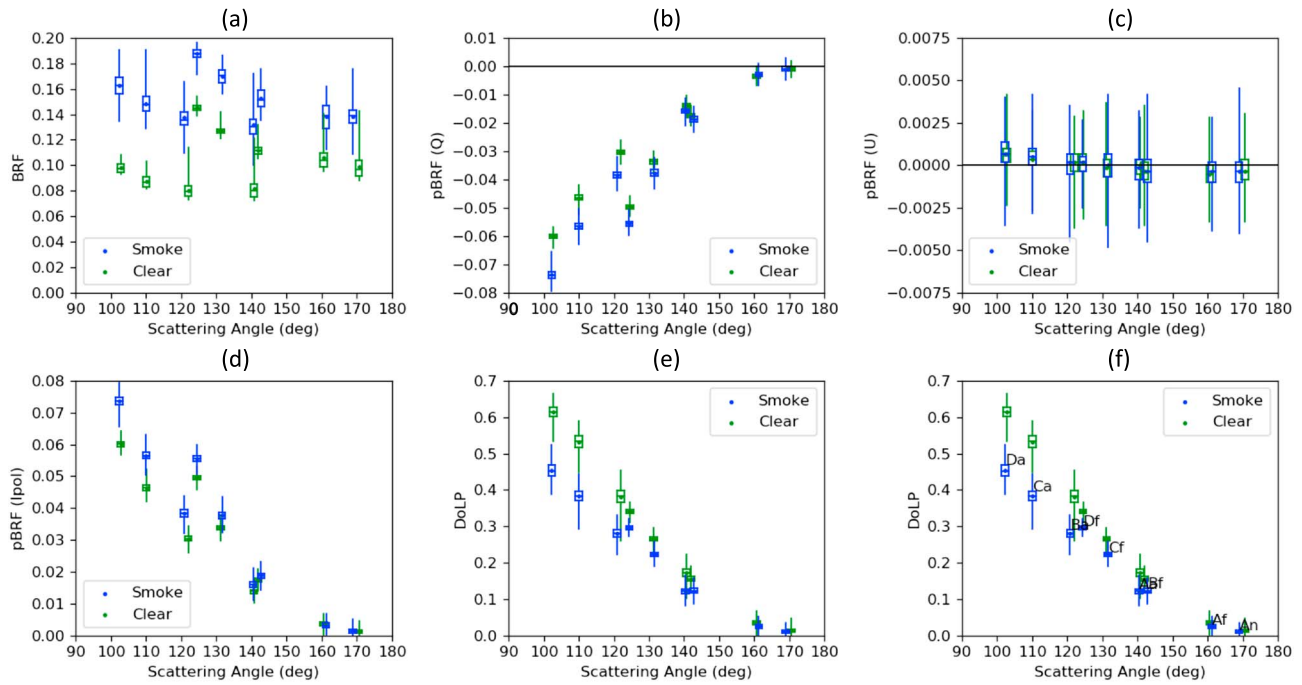
Figure 12. Airborne Multiangle SpectroPolarimetric Imager (AirMSPI) observations of the smoke and clear patches as a function of scattering angle. The box plots represent the variability of the AirMSPI 10 m^2 observations within the 1-km × 1-km patches. (a) BRF; (b) pBRF for Stokes Q; (c) pBRF for Stokes U; (d) Ipol; (e) DoLP; (f) DoLP with AirMSPI cameras labeled following the Multi-angle Imaging SpectroRadiometer convention.

polarized bidirectional reflectance factors (pBRFs), as appropriate. The BRF is given by the following relation:

$$\text{BRF} = \frac{\pi I}{\mu_0 E_0}, \tag{6}$$

where I is the radiance observed by the instrument, μ_0 is the cosine of the solar zenith angle, and E_0 is the extraterrestrial solar spectral irradiance for the AirMSPI band (in this case 470 nm). By analogy, the pBRF for the Q component of the Stokes vector (representing the excess of horizontally over vertically polarized light), is given by

$$\text{pBRF} = \frac{\pi Q}{\mu_0 E_0}. \tag{7}$$

Figure 12a shows box plots of the BRF observed by AirMSPI at 470 nm in the smoke plume and the nearby clear patch. The mean value is represented by a dot, the median value by a horizontal line, the interquartile range (25% to 75%) by the box, and the extremes by the whiskers. The results are presented as a function of the scattering angle, Θ, which is given by the equation

$$\cos \Theta = -\mu\mu_0 + \nu\nu_0 \cos \Delta\phi, \tag{8}$$

where μ is the cosine of the view angle, ν is the sine of the view angle, ν_0 is the sine of the solar zenith angle, and $\Delta\phi$ is the relative azimuth angle. Note that AirMSPI does not sample the scattering angles sequentially by view (see Figure 12f). Not surprisingly, the BRF of the smoke plume is larger than the BRF in the clear patch because, as shown in Figure 11, the smoke appears brighter in the AirMSPI images in all views.

Figure 12b shows box plots of pBRF for Stokes Q. In an absolute sense, the smoke appears more polarized than the clear region, especially at scattering angles near 100°. The total Rayleigh optical depth at 470 nm for an altitude of 1,000 m, which is the mean elevation of the area around Lebec, CA, is 0.1637 (Bodhaine et al., 1999). Therefore, both the clear and smoke patches have a significant Rayleigh contribution to the polarization, which reaches a maximum at a scattering angle of 90°. In the scattering plane observations reported by AirMSPI, the pBRF for the Stokes U component (excess of 45° over 135° polarized light) is typically near zero, as shown in Figure 12c (Schutgens et al., 2004).

Table 4
AirMSPI Viewing Geometry for Smoke Patch Used in Radiative Transfer Calculations

View number	View name	Solar zenith angle (deg)	Solar azimuth angle (deg)	View zenith angle (deg)	View azimuth angle (deg)	Scattering angle (deg)
1	Df	13.76	26.35	68.38	185.09	124.38
2	Cf	13.76	26.35	61.19	186.46	131.63
3	Bf	13.76	26.35	50.19	189.02	142.78
4	Af	13.76	26.35	32.07	195.87	161.28
5	An	13.76	26.35	9.00	259.97	168.94
6	Aa	13.76	26.35	28.32	344.89	140.45
7	Ba	13.76	26.35	47.33	353.38	120.83
8	Ca	13.76	26.35	57.98	356.02	110.01
9	Da	13.76	26.35	65.60	357.54	102.30

Note. AirMSPI = Airborne Multiangle SpectroPolarimetric Imager.

The linearly polarized intensity, Ipol, combines the contributions of the Stokes Q and U components such that

$$\text{Ipol} = \sqrt{Q^2 + U^2}. \tag{9}$$

In this case, the box plots of the Ipol values in Figure 12d essentially represent the absolute values of Q because U is near zero.

Finally, the degree of linear polarization, DoLP, is simply the ratio of the linearly polarized intensity, Ipol, to the intensity, I. The box plots of DoLP shown in Figures 12e and 12f indicate that the degree of linear polarization is somewhat larger for the clear region compared to the smoke region. Initially, this seems counterintuitive as the smoke particles are clearly more polarizing, as shown in Figures 12b and 12d (Q and Ipol, respectively). However, the smoke itself is brighter, which increases the denominator in the calculation of DoLP, reducing the overall value. Figure 12f includes labels for the different AirMSPI views as a function of scattering angle on the plot of DoLP values. The three most oblique aftward views (Da, Ca, Ba) correspond to the smallest scattering angles. The most oblique forward view, Df, has a scattering angle similar to the Ba view. The An and Af views are near a scattering angle of 180° and show very little polarization.

Given the AirMSPI intensity and polarimetric observations shown in Figure 12, we next assess the sensitivity of these observations to the choice of the BC fraction in the smoke aerosol mixture. This is done through full multiple scattering radiative transfer calculations for atmospheres containing a uniformly mixed smoke layer from the surface (taken to be 1 km above sea level) to an altitude of 2.7 km above sea level, which is the height derived for the top of the plume from the AirMSPI observations, with different fractions of BC. All other parameters are fixed based on the in situ observations, with the exception of the AOD and the surface albedo. The successive orders of scatter (SOS) radiative transfer model developed for a coupled atmosphere-ocean system (Zhai et al., 2009, 2010) was used for the calculations, similar to what was done in Kalashnikova et al. (2013). The AOD at 470 nm was varied in the range from 0.17 to 0.51 in increments of 0.01. The surface albedo was assumed to be Lambertian, for simplicity, and was varied in the range from 0.0650 to 0.0975 in increments of 0.0025. Four aerosol mixtures were tested, which correspond to BC fractions of 5%, 10%, 15%, and 20%. The BC refractive indices were taken from Bond and Bergstrom (2006). The viewing geometry used in the radiative transfer calculations is summarized in Table 4.

The sum of the z scores, also called standard scores, was used to assess the agreement between the AirMSPI observations in the smoke plume and the output of the SOS model, similar to what was done in Kalashnikova et al. (2011). A single z score, z_i, for a parameter, f, is calculated as the absolute difference between the observation and the modeled result, normalized by the uncertainty in the observation, σ_i:

$$z_i = \frac{\left| f_{\text{modeled}} - f_{\text{observed}} \right|}{\sigma_i}. \tag{10}$$

As described in greater detail in Kalashnikova et al. (2011), the z scores depend on which observations are used in the comparison, which, in turn, affects the value of σ. The standard deviation of the intensity, σ_I, is directly related to the uncertainty in the radiometric calibration, δ_I, through the relation
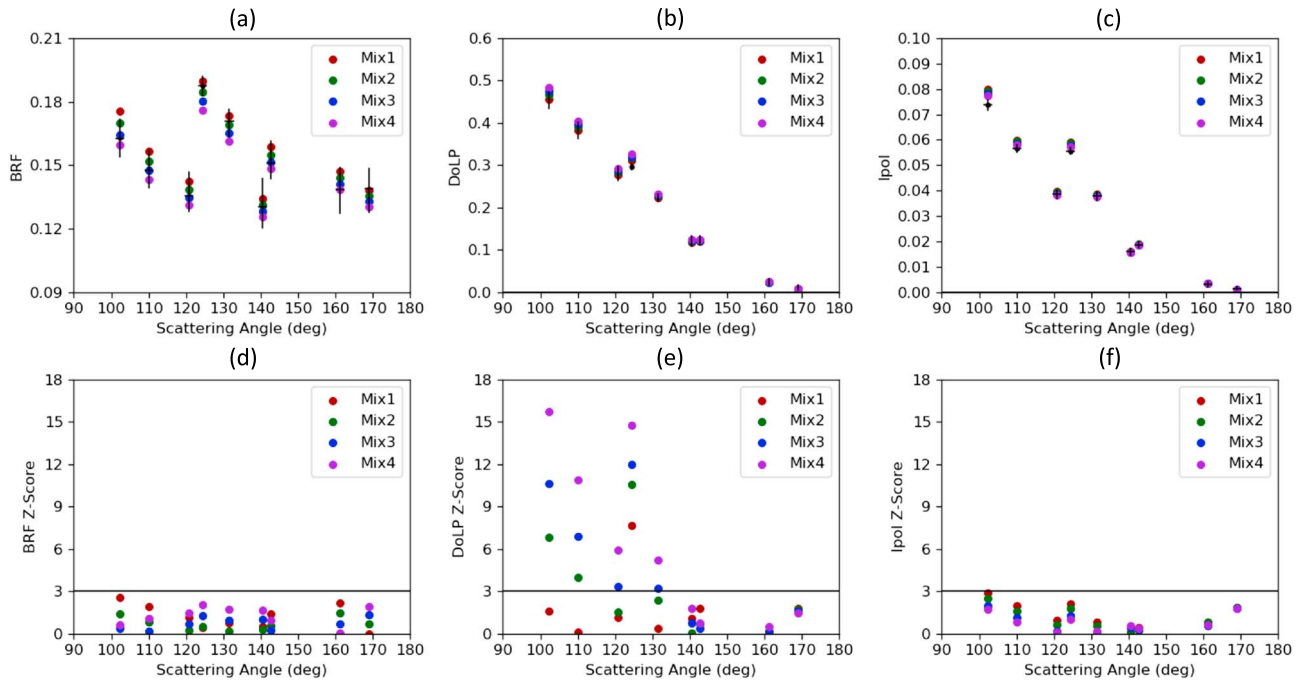
Figure 13. Comparison of Airborne Multiangle SpectroPolarimetric Imager (AirMSPI) observations and successive orders of scatter model results for the best fitting aerosol optical depth and surface albedo at 470 nm. (top row) The box plots represent the variability of the AirMSPI 10 m² observations within the 1-km × 1-km smoke patch. The different colors represent the aerosol mixtures containing different fractions of black carbon (5%, 10%, 15%, and 20%). (a) BRF; (b) DoLP; (c) pBRF (Ipol). (bottom row) Sum of z scores for each mixture at each scattering angle. The horizontal line shows a distinguishability threshold of 3. (d) BRF; (e) DoLP; (f) pBRF (Ipol).

$$\sigma_I = \delta_I I, \tag{11}$$

We take δ_I for AirMSPI to be approximately 3% at 470 nm, based on vicarious calibration results from previous field campaigns and experience with the MISR instrument on NASA's Terra EOS satellite (Bruegge et al., 2002) (Table 1). It is important to note that the uncertainty in I, and therefore BRF, depends on the magnitude of I itself. The uncertainty in DoLP, σ_{DoLP}, for AirMSPI has been determined to be less than the requirement of 0.005 (given in Table 1), and we take $\sigma_{DoLP} = 0.002$ as a typical value based on laboratory comparisons with a polarimetric state generator (Diner et al., 2013). For DoLP the uncertainty is absolute and so does not depend on the magnitude of the DoLP observations. Polarized intensity, Ipol, can be derived from DoLP and I and is, therefore, not an independent quantity. This means that the uncertainty in Ipol, σ_{Ipol}, can be determined using the standard approach for the propagation of errors, as discussed in Kalashnikova et al. (2011). The result is

$$\sigma_{Ipol} = \sqrt{\left(I \cdot \sigma_{DoLP}\right)^2 + \left(Ipol \cdot \delta_I\right)^2}. \tag{12}$$

This equation shows that the uncertainty in Ipol depends on the uncertainty in both the DoLP and the intensity. In fact, the uncertainty in the intensity, δ_I, dominates the uncertainty in Ipol for AirMSPI due to the significant difference in the magnitude of δ_I compared to σ_{DoLP} (3% versus 0.2%, respectively). This is to be expected because polarized intensity is actually another measure of intensity, and thus, the uncertainty in Ipol should depend on the radiometric calibration of the instrument.

The sum of the z scores for each parameter, BRF, DoLP, and pBRF (Ipol) was examined independently to choose the best solution in the parameter space of AOD, surface albedo, and mixture. A z score greater than a specific threshold was taken to represent an unacceptable solution. The minimum threshold that provided a solution in all three parameters, therefore, provided the final result, which was an AOD at 470 nm of 0.33 ± 0.01, a surface albedo at 470 nm of 0.0725 ± 0.0015, and a mixture containing a BC content of 5%. The other mixtures with larger fractions of BC did not provide agreement with the AirMSPI observations within the same z score threshold for any combination of AODs or surface albedos. Recall that the MAIAC retrieval from MODIS-Aqua reported an AOD at 470 nm of 0.22 ± 0.03 and a surface reflectance of 0.09 ± 0.02, where the range represents

the spatial standard deviation. As discussed above, the time difference between the AirMSPI and MODIS-Aqua observations was ~50 min, so exact agreement in the AOD would not necessarily be expected. Moreover, the AirMSPI observations were for a patch selected in a dense portion of the plume, which would likely correspond to a larger AOD. The MAIAC surface retrieval is based on an 8-day average and would be less likely to be affected by the presence of smoke. The AirMSPI and MAIAC surface retrievals are in very good agreement, and the BC content is also in good agreement with the SP2 results.

A comparison of the AirMSPI observations and the solutions for the four different BC mixture options is shown in Figure 13. Figures 13a–13c compare the BRF, DoLP, and pBRF (Ipol) results, respectively. The AirMSPI observations are plotted in box plot format, while the SOS results are shown as different-colored dots ranging from Mix1 (5% BC, dark red) to Mix4 (20% BC, purple). Visually, the agreement between the observations and the models is extremely good in all cases. Figures 13d–13f show the z scores calculated for each of these comparisons. The horizontal line indicates a z score of 3, which was taken in Kalashnikova et al. (2011) to represent the threshold for distinguishability. The actual acceptance threshold for the AirMSPI solution in this case was 2.5, which is slightly lower than the original threshold. The z scores for BRF (Figure 13d) show that the mixtures all agree with the AirMSPI observations and are not distinguishable using this metric alone. Similarly, the z scores for pBRF (Ipol) (Figure 13f) also show agreement with the AirMSPI observations and even less distinguishability. This is due to the relatively large value of the uncertainty in the AirMSPI observations of intensity, which affects both these metrics in nearly the same way. The uncertainty in AirMSPI observations of DoLP is an order of magnitude smaller, and thus, Figure 13e shows that Mix1 agrees with the AirMSPI observations for all viewing angles, while the other mixtures do not. As mentioned previously, Mix1, with 5% BC, is the only one of the four options that provides agreement with the AirMSPI observations for any choice of AOD and surface albedo within the z score threshold.

5. Conclusions

The results in the previous section show how multiangle, spectropolarimetric remote sensing can be used to evaluate the relative contribution of BC particles to the overall aerosol mass in a wildfire smoke plume. This was accomplished through a detailed closure experiment that required extensive use of in situ data provided by the instruments on the CIRPAS Twin Otter aircraft as well as a number of simplifying assumptions. The in situ information was used to constrain the aerosol size distribution and the fractional distribution of components, with the exception of BC, which was allowed to vary in a narrow range from 5% to 20%, consistent with the data from the SP2 and PSAP/nephelometer. The height of the plume was determined by manually tracking a "patch" in the smoke through the sequence of AirMSPI views made from the NASA ER-2 aircraft. The free parameters in the forward radiative transfer model were, therefore, the BC fraction, the AOD, and the surface albedo. The results of a set of radiative transfer runs were compared with the AirMPSI observations in a single polarimetric spectral band (470 nm) taking into account the instrument uncertainties. With these constraints, an AOD of 0.33 ± 0.01, a Lambertian surface albedo of 0.0725 ± 0.0015, and a mixture containing a BC content of 5% were found. Mixtures with larger fractions of BC (10%, 15%, and 20%) did not yield any valid solutions for any combination of AOD or surface albedo. The AOD result is somewhat larger than the MAIAC retrieval from MODIS-Aqua obtained from observations made ~50 min later, but changes in the location and optical depth of the plume limit the utility of such a direct comparison. The surface reflectance, on the other hand, is in very good agreement with the MAIAC retrievals based on an 8-day average of MODIS observations. The BC content is also in good agreement with the SP2 results, which suggests that the BC content and SSA derived from the SP2 data are more trustworthy than the SSA derived from the PSAP/nephelometer data in this case.

The polarimetric sensitivity to BC with an absolute uncertainty of 5% in BC mass fraction for an AOD of 0.33 at 470 nm corresponds to an SSA uncertainty of 0.04 for the refractive indices given by Bond and Bergstrom (2006) and 0.03 for the refractive indices of Hess et al. (1998) (see Figure 9b). This agrees well with known polarimetric sensitivities to SSA over the land (Waquet et al., 2009; Xu et al., 2017). Waquet et al. (2009) demonstrated that an AOD greater than 0.2 at midvisible wavelengths is required to achieve good polarimetric retrieval sensitivity to SSA. The conditions in the Fort Fire case were very close to this limit, and better polarimetric sensitivity to BC may be expected at higher aerosol loadings. The observation viewing geometry could also be a limiting factor, as polarimetric sensitivity depends on instrument viewing conditions (Waquet et al., 2009; Xu et al., 2016). However, the question of retrieval sensitivity was not directly addressed in this study. Further work is needed to better characterize the information contained in the intensity, polarimetric, and multiangle observations.

In terms of the simplifying assumptions, perhaps the one with the greatest influence on the results is the assumption of aerosol external mixing. It is well known that aerosols from wildfires become rapidly coated as they age, which can dramatically change their optical properties (Reid et al., 2005). In addition to acquiring coatings, smoke aerosols can also be highly nonspherical (Chakrabarty et al., 2014), requiring specialized single-scattering techniques beyond the simple Mie calculations used here. While proper treatment of these effects is an active area of research (e.g., Schuster et al., 2016), in this initial study we assume that the magnitude of these effects is small relative to other uncertainties. Additional types of in situ measurements not performed as part of the ImPACT-PM field campaign, such as scanning electron microscopy, would also be required to test more sophisticated approaches.

With 10 m spatial resolution, AirMSPI observations serve as an important bridge between detailed in situ characterization of aerosol plumes and retrievals from future satellite instruments. This work describes an initial step in the direction of satellite characterization of aerosol plume content. Additional coordinated flights and in situ data are needed to more fully evaluate the capability of spectropolarimetric multiangle imaging observations to characterize the aerosol content of atmospheric plumes.

References

Aiken, A. C., DeCarlo, P. F., Kroll, J. H., Worsnop, D. R., Huffman, J. A., Docherty, K. S., et al. (2008). O/C and OM/OC ratios of primary, secondary, and ambient organic aerosols with high-resolution time-of-flight aerosol mass spectrometry. *Environmental Science and Technology*, *42*, 4478–4485. https://doi.org/10.1021/es703009q

Allan, J. D., Deli, A. E., Coe, H., Bower, K. N., Alfarra, M. R., Jimenez, J. L., et al. (2004). A generalised method for the extraction of chemically resolved mass spectra from Aerodyne aerosol mass spectrometer data. *Journal of Aerosol Science*, *35*, 909–922. https://doi.org/10.1016/j.jaerosci.2004.02.007

Baldridge, A. M., Hook, S. J., Grove, C. I., & Rivera, G. (2009). The ASTER spectral library version 2.0. *Remote Sensing of Environment*, *113*, 711–715. https://doi.org/10.1016/j.rse.2008.11.007

Bodhaine, B. A., Wood, N. B., Dutton, E. G., & Slusser, J. R. (1999). On Rayleigh optical depth calculations. *Journal of Atmospheric and Oceanic Technology*, *16*, 1854–1861.

Bond, T. C., & Bergstrom, R. W. (2006). Light absorption by carbonaceous particles: An investigative review. *Aerosol Science and Technology*, *40*(1), 27–67. https://doi.org/10.1080/02786820500421521

Bond, T. C., Doherty, S. J., Fahey, D. W., Forster, P. M., Berntsen, T., DeAngelo, B. J., et al. (2013). Bounding the role of black carbon in the climate system: A scientific assessment. *Journal of Geophysical Research: Atmospheres*, *118*, 5380–5552. https://doi.org/10.1002/jgrd.50171

Bruegge, C. J., Chrien, N. L., Ando, R. R., Diner, D. J., Abdou, W. A., Helmlinger, M. C., et al. (2002). Early validation of the Multi-angle Imaging SpectroRadiometer (MISR) radiometric scale. *IEEE Transactions on Geoscience and Remote Sensing*, *40*(7), 1477–1492. https://doi.org/10.1109/TGRS.2002.801583

Cappa, C. D., Lack, D. A., Burkholder, J. B., & Ravishankara, A. R. (2008). Bias in filter-based aerosol light absorption measurements due to organic aerosol loading: Evidence from laboratory measurements. *Aerosol Science and Technology*, *42*(12), 1022–1032. https://doi.org/10.1080/02786820802389285

Chakrabarty, R. K., Beres, N. D., Moosmuller, H., China, S., Mazzoleni, C., Dubey, M. K., et al. (2014). Soot superaggregates from flaming wildfires and their direct radiative forcing. *Scientific Reports*, *4*, 5508 EP–07. https://doi.org/10.1038/srep05508

Chakrabarty, R. K., Moosmüller, H., Chen, L.-W. A., Lewis, K., Arnott, W. P., Mazzoleni, C., et al. (2010). Brown carbon in tar balls from smoldering biomass combustion. *Atmospheric Chemistry and Physics*, *10*(13), 6363–6370. https://doi.org/10.5194/acp-10-6363-2010

Chow, J. C., Watson, J. G., Lowenthal, D. H., Chen, L.-W. A., & Motallebi, N. (2010). Black and organic carbon emission inventories: Review and application to California. *Journal of the Air & Waste Management Association*, *60*(4), 497–507. https://doi.org/10.3155/1047-3289.60.4.497

DeCarlo, P. F., Kimmel, J. R., Trimborn, A., Northway, M. J., Jayne, J. T., Aiken, A. C., et al. (2006). Field-deployable, high-resolution, time-of-flight aerosol mass spectrometer. *Analytical Chemistry*, *78*(24), 8281–8289. https://doi.org/10.1021/ac061249n

Dennison, P. E., Brewer, S. C., Arnold, J. D., & Moritz, M. A. (2014). Large wildfire trends in the western United States, 1984–2011. *Geophysical Research Letters*, *41*, 2928–2933. https://doi.org/10.1002/2014GL059576

Diner, D. J., Beckert, J. C., Reilly, T. H., Bruegge, C. J., Conel, J. E., Kahn, R. A., et al. (1998). Multi-angle imaging spectroradiometer (MISR) instrument description and experiment overview. *IEEE Transactions on Geoscience and Remote Sensing*, *36*(4), 1072–1087. https://doi.org/10.1109/36.700992

Diner, D. J., Xu, F., Garay, M. J., Martonchik, J. V., Rheingans, B. E., Geier, S., et al. (2013). The Airborne Multiangle SpectroPolarimetric Imager (AirMSPI): A new tool for aerosol and cloud remote sensing. *Atmospheric Measurement Techniques*, *6*(8), 2007–2025. https://doi.org/10.5194/amt-6-2007-2013

Drury, E., Jacob, D. J., Spurr, R. J. D., Wang, J., Shinozuka, Y., Anderson, B. E., et al. (2010). Synthesis of satellite (MODIS), aircraft (ICARTT), and surface (IMPROVE, EPA-AQS, AERONET) aerosol observations over eastern North America to improve MODIS aerosol retrievals and constrain surface aerosol concentrations and sources. *Journal of Geophysical Research*, *115*, D14204. https://doi.org/10.1029/2009JD012629

Dubovik, O., Herman, M., Holdak, A., Lapyonok, T., Tanré, D., Deuzé, J. L., et al. (2011). Statistically optimized inversion algorithm for enhanced retrieval of aerosol properties from spectral multi-angle polarimetric satellite observations. *Atmospheric Measurement Techniques*, *4*(5), 975–1018. https://doi.org/10.5194/amt-4-975-2011

Fuller, K. A., Malm, W. C., & Kreidenweis, S. M. (1999). Effects of mixing on extinction by carbonaceous particles. *Journal of Geophysical Research*, *104*(D13), 15,941–15,954. https://doi.org/10.1029/1998JD100069

Griffin, J. R., & Critchfield, W. B. (1972). The distribution of forest trees in California. In *Pacific Southwest Forest and Range Experiment Station, Forest Service, U.S. Department of Agriculture* (60 pp.).

Hammer, R. B., Stewart, S. I., & Radeloff, V. C. (2009). Demographic trends, the wildland-urban interface, and wildfire management. *Society and Natural Resources*, *22*, 777–782.

Hess, M. P., Koepke, P., & Schult, I. (1998). Optical properties of aerosols and clouds: The software package OPAC. *Bulletin of the American Meteorological Society*, *79*, 831–844.

Holben, B. N., Eck, T. F., Slutsker, I., Tanré, D., Buis, J. P., Setzer, A., et al. (1998). Aeronet—A federated instrument network and data archive for aerosol characterization. *Remote Sensing of Environment*, *66*, 1–16.

Jolleys, M. D., Coe, H., McFiggans, G., McMeeking, G. R., Lee, T., Kreidenweis, S. M., et al. (2014). Organic aerosol emission ratios from the laboratory combustion of biomass fuels. *Journal of Geophysical Research: Atmospheres*, *119*, 12,850–12,871. https://doi.org/10.1002/2014JD021589

Kalashnikova, O. V., Garay, M. J., Davis, A. B., Diner, D. J., & Martonchik, J. V. (2011). Sensitivity of multi-angle photo-polarimetry to vertical layering and mixing of absorbing aerosols: Quantifying measurement uncertainties. *Journal of Quantitative Spectroscopy and Radiative Transfer*, *112*(13), 2149–2163. https://doi.org/10.1016/j.jqsrt.2011.05.010

Kalashnikova, O. V., Garay, M. J., Martonchik, J. V., & Diner, D. J. (2013). MISR Dark Water aerosol retrievals: Operational algorithm sensitivity to particle non-sphericity. *Atmospheric Measurement Techniques*, *6*(8), 2131–2154. https://doi.org/10.5194/amt-6-2131-2013

Kirchstetter, T. W., Novakov, T., & Hobbs, P. V. (2004). Evidence that the spectral dependence of light absorption by aerosols is affected by organic carbon. *Journal of Geophysical Research*, *109*, D21208. https://doi.org/10.1029/2004JD004999

Koepke, P., Hess, M., Schult, I., & Shettle, E. P. (1997). Global aerosol data set (Report N 243). Max-Plank-Institut für Meteorologie, 44.

Kondo, Y., Matsui, H., Moteki, N., Sahu, L., Takegawa, N., Kajino, M., et al. (2011). Emissions of black carbon, organic, and inorganic aerosols from biomass burning in North America and Asia in 2008. *Journal of Geophysical Research*, *116*, D08204. https://doi.org/10.1029/2010JD015152

Kuwata, M., Zorn, S. R., & Martin, S. T. (2012). Using elemental ratios to predict the density of organic material composed of carbon, hydrogen, and oxygen. *Environmental Science & Technology*, *46*(2), 787–794. https://doi.org/10.1021/es202525q

Lack, D. A., Cappa, C. D., Covert, D. S., Baynard, T., Massoli, P., Sierau, B., et al. (2008). Bias in filter-based aerosol light absorption measurements due to organic aerosol loading: Evidence from ambient measurements. *Aerosol Science and Technology*, *42*(12), 1033–1041. https://doi.org/10.1080/02786820802389277

Liu, S., Aiken, A. C., Arata, C., Dubey, M. K., Stockwell, C. E., Yokelson, R. J., et al. (2014). Aerosol single scattering albedo dependence on biomass combustion efficiency: Laboratory and field studies. *Geophysical Research Letters*, *41*, 742–748. https://doi.org/10.1002/2013GL058392

Liu, S., Ahlm, L., Day, D. A., Russell, L. M., Zhao, Y., Gentner, D. R., et al. (2012). Secondary organic aerosol formation from fossil fuel sources contribute majority of summertime organic mass at Bakersfield. *Journal of Geophysical Research*, *117*, D00V26. https://doi.org/10.1029/2012JD018170

Lyapustin, A., Wang, Y., Laszlo, I., Kahn, R., Korkin, S., Remer, L., et al. (2011). Multiangle implementation of atmospheric correction (MAIAC): 2. Aerosol algorithm. *Journal of Geophysical Research*, *116*, D03211. https://doi.org/10.1029/2010JD014986

Martins, J. V., Hobbs, P. V., Weiss, R. E., & Artaxo, P. (1998). Sphericity and morphology of smoke particles from biomass burning in Brazil. *Journal of Geophysical Research*, *103*(D24), 32,051–32,057. https://doi.org/10.1029/98JD01153

Martin, R. V., Jacob, D. J., Yantosca, R. M., Chin, M., & Ginoux, P. (2003). Global and regional decreases in tropospheric oxidants from photochemical effects of aerosols. *Journal of Geophysical Research*, *108*(D3), 4097. https://doi.org/10.1029/2002JD002622

McMeeking, G. R., Fortner, E., Onasch, T. B., Taylor, J. W., Flynn, M., Coe, H., & Kreidenweis, S. M. (2014). Impacts of nonrefractory material on light absorption by aerosols emitted from biomass burning. *Journal of Geophysical Research: Atmospheres*, *119*, 12,272–12,286. https://doi.org/10.1002/2014JD021750

McMeeking, G. R., Kreidenweis, S. M., Baker, S., Carrico, C. M., Chow, J. C., Collett, J. L., et al. (2009). Emissions of trace gases and aerosols during the open combustion of biomass in the laboratory. *Journal of Geophysical Research*, *114*, D19210. https://doi.org/10.1029/2009JD011836

Middlebrook, A. M., Bahreini, R., Jimenez, J. L., & Canagaratna, M. R. (2012). Evaluation of composition-dependent collection efficiencies for the Aerodyne aerosol mass spectrometer using field data. *Aerosol Science and Technology*, *46*(3), 258–271. https://doi.org/10.1080/02786826.2011.620041

Mishchenko, M. I., Dlugach, J. M., Yanovitskij, E. G., & Zakharova, N. T. (1999). Bidirectional reflectance of flat, optically thick particulate layers: An efficient radiative transfer solution and applications to snow and soil surfaces. *Journal of Quantitative Spectroscopy and Radiative Transfer*, *63*(2), 409–432. https://doi.org/10.1016/S0022-4073(99)00028-X

Mok, J., Krotkov, N. A., Arola, A., Torres, O., Jethva, H., Andrade, M., et al. (2016). Impacts of brown carbon from biomass burning on surface UV and ozone photochemistry in the Amazon Basin. *Scientific Reports (Nature Publisher Group)*, *6*, 36940.

Nelson, D. L., Garay, M. J., Kahn, R. A., & Dunst, B. A. (2013). Stereoscopic height and wind retrievals for aerosol plumes with the MISR INteractive eXplorer (MINX). *Remote Sensing*, *5*(9), 4593–4628. https://doi.org/10.3390/rs5094593

Park, K., Kittelson, D. B., Zachariah, M. R., & McMurry, P. H. (2004). Measurement of inherent material density of nanoparticle agglomerates. *Journal of Nanoparticle Research*, *6*(2), 267–272. https://doi.org/10.1023/B:NANO.0000034657.71309.e6

Park, R. J., Jacob, D. J., & Logan, J. A. (2007). Fire and biofuel contributions to annual mean aerosol mass concentrations in the United States. *Atmospheric Environment*, *41*(35), 7389–7400. https://doi.org/10.1016/j.atmosenv.2007.05.061

Pokhrel, R. P., Beamesderfer, E. R., Wagner, N. L., Langridge, J. M., Lack, D. A., Jayarathne, T., et al. (2017). Relative importance of black carbon, brown carbon, and absorption enhancement from clear coatings in biomass burning emissions. *Atmospheric Chemistry and Physics*, *17*(8), 5063–5078. https://doi.org/10.5194/acp-17-5063-2017

Reid, J. S., Eck, T. F., Christopher, S. A., Koppmann, R., Dubovik, O., Eleuterio, D. P., et al. (2005). A review of biomass burning emissions Part III: Intensive optical properties of biomass burning particles. *Atmospheric Chemistry and Physics*, *5*(3), 827–849. https://doi.org/10.5194/acp-5-827-2005

Ryerson, T. B., Andrews, A. E., Angevine, W. M., Bates, T. S., Brock, C. A., Cairns, B., et al. (2013). The 2010 California research at the nexus of air quality and climate change (CalNex) field study. *Journal of Geophysical Research: Atmospheres*, *118*, 5830–5866. https://doi.org/10.1002/jgrd.50331

Sahu, L. K., Kondo, Y., Moteki, N., Takegawa, N., Zhao, Y., Cubison, M. J., et al. (2012). Emission characteristics of black carbon in anthropogenic and biomass burning plumes over California during ARCTAS-CARB 2008. *Journal of Geophysical Research*, *117*, D16302. https://doi.org/10.1029/2011JD017401

Salcedo, D., Onasch, T. B., Dzepina, K., Canagaratna, M. R., Zhang, Q., Huffman, J. A., et al. (2006). Characterization of ambient aerosols in Mexico City during the MCMA-2003 campaign with aerosol mass spectrometry: Results from the CENICA Supersite. *Atmospheric Chemistry and Physics*, *6*(4), 925–946. https://doi.org/10.5194/acp-6-925-2006

Saleh, R., Robinson, E. S., Tkacik, D. S., Ahern, A. T., Liu, S., Aiken, A. C., et al. (2014). Brownness of organics in aerosols from biomass burning linked to their black carbon content. *Nature Geoscience*, *7*(9), 647–650. https://doi.org/10.1038/ngeo2220

Sayer, A. M., Hsu, N. C., Eck, T. F., Smirnov, A., & Holben, B. N. (2014). AERONET-based models of smoke-dominated aerosol near source regions and transported over oceans, and implications for satellite retrievals of aerosol optical depth. *Atmospheric Chemistry and Physics*, *14*(20), 11,493–11,523. https://doi.org/10.5194/acp-14-11493-2014

Schuster, G. L., Dubovik, O., Arola, A., Eck, T. F., & Holben, B. N. (2016). Remote sensing of soot carbon — Part 2: Understanding the absorption ångström exponent. *Atmospheric Chemistry and Physics*, *16*(3), 1587–1602. https://doi.org/10.5194/acp-16-1587-2016

Schutgens, N. A. J., Tilstra, L. G., Stammes, P., & Bréon, F.-M. (2004). On the relationship between Stokes parameters Q and U of atmospheric ultraviolet/visible/near-infrared radiation. *Journal of Geophysical Research*, *109*, D09205. https://doi.org/10.1029/2003JD004081

Schwarz, J. P., Gao, R. S., Spackman, J. R., Watts, L. A., Thomson, D. S., Fahey, D. W., et al. (2008). Measurement of the mixing state, mass, and optical size of individual black carbon particles in urban and biomass burning emissions. *Geophysical Research Letters*, *35*, L13810. https://doi.org/10.1029/2008GL033968

Stier, P., Seinfeld, J. H., Kinne, S., & Boucher, O. (2007). Aerosol absorption and radiative forcing. *Atmospheric Chemistry and Physics*, *7*(19), 5237–5261. https://doi.org/10.5194/acp-7-5237-2007

Taylor, J. W., Allan, J. D., Allen, G., Coe, H., Williams, P. I., Flynn, M. J., et al. (2014). Size-dependent wet removal of black carbon in Canadian biomass burning plumes. *Atmospheric Chemistry and Physics*, *14*(24), 13,755–13,771. https://doi.org/10.5194/acp-14-13755-2014

Urbanski, S. P., Hao, W. M., & Nordgren, B. (2011). The wildland fire emission inventory: Western United States emission estimates and an evaluation of uncertainty. *Atmospheric Chemistry and Physics*, *11*(24), 12,973–13,000. https://doi.org/10.5194/acp-11-12973-2011

Virkkula, A. (2010). Correction of the calibration of the 3-wavelength particle soot absorption photometer (3λ PSAP). *Aerosol Science and Technology*, *44*(8), 706–712. https://doi.org/10.1080/02786826.2010.482110

Wang, J., & Martin, S. T. (2007). Satellite characterization of urban aerosols: Importance of including hygroscopicity and mixing state in the retrieval algorithms. *Journal of Geophysical Research*, *112*, D17203. https://doi.org/10.1029/2006JD008078

Waquet, F., Cairns, B., Knobelspiesse, K., Chowdhary, J., Travis, L. D., Schmid, B., & Mishchenko, M. I. (2009). Polarimetric remote sensing of aerosols over land. *Journal of Geophysical Research*, *114*, D01206. https://doi.org/10.1029/2008JD010619

Watson, J. G. (2002). Visibility: Science and regulation. *Journal of the Air and Waste Management Association*, *52*(6), 628–713. https://doi.org/10.1080/10473289.2002.10470813

Xu, F., Dubovik, O., Zhai, P.-W., Diner, D. J., Kalashnikova, O. V., Seidel, F. C., et al. (2016). Joint retrieval of aerosol and water-leaving radiance from multispectral, multiangular and polarimetric measurements over ocean. *Atmospheric Measurement Techniques*, *9*(7), 2877–2907. https://doi.org/10.5194/amt-9-2877-2016

Xu, F., van Harten, G., Diner, D. J., Kalashnikova, O. V., Seidel, F. C., Bruegge, C. J., & Dubovik, O. (2017). Coupled retrieval of aerosol properties and land surface reflection using the Airborne Multiangle SpectroPolarimetric Imager. *Journal of Geophysical Research: Atmospheres*, *122*, 7004–7026. https://doi.org/10.1002/2017JD026776

Young, D. E., Kim, H., Parworth, C., Zhou, S., Zhang, X., Cappa, C. D., et al. (2016). Influences of emission sources and meteorology on aerosol chemistry in a polluted urban environment: Results from DISCOVER-AQ California. *Atmospheric Chemistry and Physics*, *16*(8), 5427–5451. https://doi.org/10.5194/acp-16-5427-2016

Zhai, P.-W., Hu, Y., Chowdhary, J., Trepte, C. R., Lucker, P. L., & Josset, D. (2010). A vector radiative transfer model for coupled atmosphere and ocean systems with a rough interface. *Journal of Quantitative Spectroscopy and Radiative Transfer*, *111*, 1025–1040. https://doi.org/10.1016/j.jqsrt.2009.12.005

Zhai, P. W., Hu, Y., Trepte, C. R., & Lucker, P. L. (2009). A vector radiative transfer model for coupled atmosphere and ocean systems based on successive order of scatter method. *Optics Express*, *17*, 2057–2079.

Zhang, X., Kim, H., Parworth, C. L., Young, D. E., Zhang, Q., Metcalf, A. R., & Cappa, C. D. (2016). Optical properties of wintertime aerosols from residential wood burning in Fresno, CA: Results from DISCOVER-AQ 2013. *Environmental Science & Technology*, *50*(4), 1681–1690. https://doi.org/10.1021/acs.est.5b04134

A p p e n d i x G

OBSERVATIONS OF VOLATILE ORGANIC COMPOUNDS IN THE LOS ANGELES BASIN DURING COVID-19

Van Rooy, P.; Tasnia, A.; Barletta, B.; Buenconsejo, R.; Crounse, J. D.; Kenseth, C. M.; Meinardi, S.; Murphy, S.; Parker, H.; Schulze, B.; Seinfeld, J. H.; Wennberg, P. O.; Blake, D. R.; Barsanti, K. C. Observations of Volatile Organic Compounds in the Los Angeles Basin during COVID-19. *ACS Earth Space Chem.* **2021**, *5* (11), 3045–3055. DOI: 10.1021/acsearthspacechem.1c00248.

Observations of Volatile Organic Compounds in the Los Angeles Basin during COVID-19

Paul Van Rooy, Afsara Tasnia, Barbara Barletta, Reina Buenconsejo, John D. Crounse, Christopher M. Kenseth, Simone Meinardi, Sara Murphy, Harrison Parker, Benjamin Schulze, John H. Seinfeld, Paul O. Wennberg, Donald R. Blake, and Kelley C. Barsanti*

Read Online

ACCESS | Metrics & More | Article Recommendations | Supporting Information

ABSTRACT: Volatile organic compounds (VOCs) were measured in the Los Angeles (LA) Basin from mid-April to mid-July 2020 during the COVID-19 pandemic, as a part of the Los Angeles Air Quality Campaign (LAAQC). VOCs were quantified in over 450 samples using one- and two-dimensional gas chromatography with different detectors; mixing ratios were determined for 150 compounds associated with on- and off-road mobile, volatile chemical product, and biogenic sources. During the sampling period, traffic counts increased from ∼55% to ∼80% of pre-COVID levels. While the average afternoon combustion-derived VOCs and carbon monoxide (CO) mixing ratios did not change significantly between April−May and June−July, there was a shift in the distribution to higher mixing ratios in June−July, particularly for VOCs associated with gasoline evaporation. Compared to observations made in the last major air quality campaign in the LA Basin (CalNex-2010), emission ratios for 40 compounds relative to acetylene (VOC/acetylene) have remained similar, while emission ratios relative to CO (VOC/CO) have dropped to ∼60% of their 2010 values. This divergence in trends suggests that whereas mobile sources are still the dominant source of the combustion-derived VOCs measured in the LA Basin, there has been a shift in the mobile source sectors, with a growing contribution from sources that have lower CO/acetylene emission ratios, including off-road equipment and vehicles. In addition to the observed shift in source sector contributions, estimated OH exposure was 70−120% higher than in 2010.

KEYWORDS: VOCs, urban air quality, COVID-19, mobile source emissions, off-road emissions, VCPs
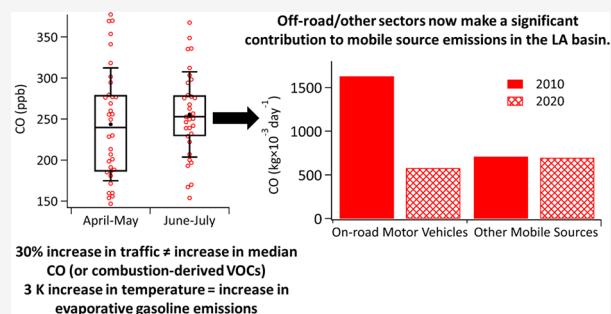
1. HISTORICAL CONTEXT FOR THE 2020 OBSERVATIONS

During the 1950s, the Los Angeles (LA) Basin became infamous for its severely poor air quality. Since then, bans on open burning, regulation of emissions from electric power generation, and most notably, regulation of vehicle emissions and fuels have led to dramatic improvements in air quality.[1] Warneke et al.[2] showed that between 1960 and 2010, carbon monoxide (CO) and volatile organic compounds (VOCs) decreased substantially: a factor of ∼100 between 1960 and 2010, at a rate of ∼7.5% per year.[2] An exception to this decrease was short-chain alkanes (ethane and propane) associated with loss of processed natural gas and emissions from oil and gas production. In separate analyses of VOCs measured in the LA Basin during the 2010 California Research at the Nexus of Air Quality and Climate Change (CalNex-2010) campaign, Parrish et al.[1] and Warneke et al.[2] concluded that even though significant reductions in on-road vehicle emissions had been achieved, emissions from gasoline vehicles remained the dominant source of VOCs.

Early modeling studies of secondary organic aerosol (SOA) formation during CalNex-2010 demonstrated that oxidation of VOCs alone was insufficient (15−53%) to explain the observed SOA mass.[3] Various parametrizations were tested to consider the contribution of lower volatility emissions, including intermediate VOCs (IVOCs). Depending on the model variant, biogenic sources were predicted to account for 3−7% of observed SOA, diesel 16−27%, nonfossil (likely cooking) 19−35%, and gasoline 36−81%. More recent modeling studies of SOA formation during CalNex-2010 focused on the overall contribution of mobile source IVOCs and VOCs using updated emissions profiles for those sources, and the potential contribution of IVOCs from other sources.[4]

Lu et al.[4] reported that IVOCs from mobile sources increased the predicted peak SOA mass by 70%, but the increase did not represent observed ambient IVOCs or SOA mass, suggesting IVOCs are an important, but inadequately represented, source of SOA. An additional 12% of nonmobile gaseous organic emissions was required to match observed IVOCs (mobile IVOCs = 2.76×10^4 kg day^{-1}, nonmobile IVOCs = 3.07×10^4 kg day^{-1}), while an additional 14.8% of nonmobile gaseous organic emissions (nonmobile IVOCs = 6.85×10^4 kg day^{-1}) was required to match observed SOA. Lu et al.[4] noted that the additional amounts were likely unrealistic, and thus better constraints on sources and processes were still needed.

McDonald et al.[5] highlighted the importance of non-combustion source emissions in the LA Basin for atmospheric composition and chemistry more broadly. The addition of volatile chemical product (VCP) emissions was found to improve agreement between measured and predicted VOCs during CalNex-2010; particularly acetone, ethanol, and 1-propanol. Using chemical production statistics and indoor and outdoor measurements, they estimated that VCPs could contribute ~53% of VOC emissions, ~55% of VOC reactivity, and ~61% of SOA formation in the LA Basin in 2010. They also estimated that combustion source emissions contributed ~32% of the VOC emissions, ~37% of the VOC reactivity, and ~37% of the SOA formation.

Historical trends suggest that atmospheric composition and chemistry have changed since 2010. In the context of trace and greenhouse gas emissions, between 2010 and 2020 new vehicle emissions regulations have been implemented in California,[6] fuel economy standards have been updated,[6] and the on-road vehicle fleet has shifted toward hybrid and electric vehicles.[7] The influence of these changes on VOC and CO levels has not been quantified. Further, levels of nitrogen oxides (NO_x) have dropped within the LA Basin by an average of 49% (Figure S1), including in Pasadena, CA;[8] the effects of the last ten years of NO_x emissions reductions and changing OH levels on the VOC chemistry in the LA Basin are also poorly quantified.

2. THE LOS ANGELES AIR QUALITY CAMPAIGN (LAAQC)

LAAQC was organized to document atmospheric composition and diagnose the underlying emissions and photochemistry during the unprecedented shift in human activity associated with the COVID-19 pandemic and shelter-in-place restrictions. Over 450 samples were collected from April to July 2020 at a ground site in Pasadena, CA. The samples were analyzed for VOCs using one-dimensional gas chromatography (GC) with multiple detectors (including flame ionization (FID), electron capture (ECD), and mass spectrometry (MSD)) and two-dimensional gas chromatography with time-of-flight mass spectrometry (GC/GC-TOF-MS). Changes in mobile source patterns were well documented during LAAQC.[9−12] Using traffic counts obtained from Caltrans as one metric, travel across the LA Basin during LAAQC began at only ~55% of pre-COVID levels and increased approximately linearly to ~80% by the end of the campaign.[13] Other changes in human activity associated with urban emissions (e.g., ordering takeout, using personal care and cleaning products, using motorized landscaping equipment, etc.) are still being quantified.[14−18] The data collected during LAAQC were analyzed to (1) identify changes in VOC concentration and composition in the LA Basin during the COVID-19 pandemic associated with changes in human activity; and (2) quantify changes in VOC concentration and composition in the LA Basin since 2010 to better understand current composition and chemistry in this urban atmosphere. Changes in VOC sources during LAAQC, as well as changes in VOC sources and OH levels since 2010, are discussed.

3. EXPERIMENTAL METHODS

3.1. LAAQC Sampling. LAAQC was conducted from April 17 to July 19, 2020 in the midst of the COVID-19 pandemic; a state of emergency was issued on March 4, 2020 and shelter-in-place restrictions were issued on March 19, 2020. Air samples were collected from atop the Ronald and Maxine Linde Laboratory for Global Environmental Science on the Caltech campus in Pasadena, CA using canisters and adsorbent cartridges and analyzed for VOCs using GC with FID, ECD, and MSD (canisters) and GC/GC-TOF-MS (cartridges). Continuous measurements of trace gases, including CO, were collected using the Caltech air quality system (CITAQS).[13] Meteorological data, including temperature, wind speed, and wind direction, were collected at the Caltech Total Carbon Column Observing Network (TCCON) weather station.[19] Wind data were also obtained from the NOAA integrated surface database (ISD) accessed through Visual Crossing[20] to facilitate comparison with 2010. Afternoon wind speed was, on average, 3 m/s and wind direction was primarily from the west and southwest; nighttime wind speed was typically below the detection limit (<1.5 m/s) and wind direction was primarily from the east and northeast. Wind speeds and directions were relatively consistent throughout the measurement campaign (Figures S2−S3). Comparisons between 2020 and 2010 wind speeds and directions are shown in Figure S4 and calculated weekly back trajectories for LAAQC are shown in Figure S5.

3.2. UCI Canisters. A total of 314 whole air samples (WAS) were collected into evacuated 2-L electropolished stainless steel canisters using an automated 32-canister sampler (Atmospheric Technology Model 8001) capable of pressurizing the individual canisters to 20 psi. WAS canisters were collected three times per day between April 17 and July 19, 2020 at 05:30−06:30 PDT (hereafter referred to as "nighttime samples"), 09:00−10:00 PDT (hereafter referred to as "morning samples"), and 14:00−15:00 PDT (hereafter referred to as "afternoon samples").

Samples were analyzed at the University of California, Irvine (UCI) using a multi-column, multi-detector (FID, ECD, and MSD) GC system. A detailed description of the analytical techniques, including the use of standards and detection limits, precision, and accuracy for each reported compound can be found in Simpson et al.[21] Briefly, samples were cryogenically preconcentrated, vaporized, and split into five streams directed to a multi-column, multi-detector (FID, ECD, and MSD) GC system (Hewlett-Packard 6890 GC units). The various column and detector combinations allowed the identification and quantification of 92 VOCs across different classes of compounds, including hydrocarbons (C_2−C_{10}), alkyl nitrates (C_2−C_5), halogenated compounds, and sulfur compounds. The hydrocarbons and alkyl nitrates were analyzed using GC-FID, halogenated compounds using GC-ECD, and sulfur and all other compounds using GC-MSD.[21]

3.3. UCR Cartridges. A total of 154 dual sorbent bed (100 mg Tenax TA 35/60 and 200 mg Carbograph 1 TD 60/80 in series) cartridge samples were collected at a flow rate of ~250 ccm, at the same location as the canister samples. Cartridges were collected twice daily, 7 days per week, between April 17

and June 21, 2020; between June 24 and July 19, 2020 samples were collected twice daily on Wednesdays, Thursdays, Saturdays, and Sundays. The first sample was collected from 05:30−06:30 PDT (nighttime samples) and the second was collected from 14:00−15:00 PDT (afternoon samples). A glass fiber filter coated in sodium thiosulfate was mounted directly upstream of the cartridge to capture particles, and remove ozone (O_3) to prevent oxidation of compounds captured on the cartridge.[22,23] Samples were stored in a freezer on the Caltech campus before being transported to the University of California, Riverside (UCR) for analysis. Loading and travel blanks were also collected to correct for background contamination. Cartridges were analyzed at UCR using a Turbomatrix 650 automated thermal desorption (ATD) system (PerkinElmer, Waltham, MA) coupled to a Pegasus 4D GC/GC-TOF-MS (LECO Corp., St. Joseph MI). Details of the VOC analysis can be found in Hatch et al.,[24] in which the same approach was applied to speciation of VOCs emitted from biomass burning; errors in VOC mixing ratios were estimated to be ±30%. Data were analyzed using proprietary software from LECO (ChromaTOF) as well as in-house algorithms. A total of 58 compounds were identified and quantified across different compound classes including alkenes, higher alkanes (C_9−C_{14}), aromatics, aldehydes, ketones, terpenes, and halogenated compounds.

Nine compounds (octane, nonane, decane, 2-methylpentane, 2,3-dimethylpentane, o-xylene, m+p-xylene, toluene, and ethylbenzene) quantified by both UCR and UCI in 130 paired samples, for a total of 1170 paired VOC measurements. The agreement was within ±50% for 84% of the paired VOC measurements and within ±25% for 58% of the paired measurements (Figure S6). Figure 1 shows the overall
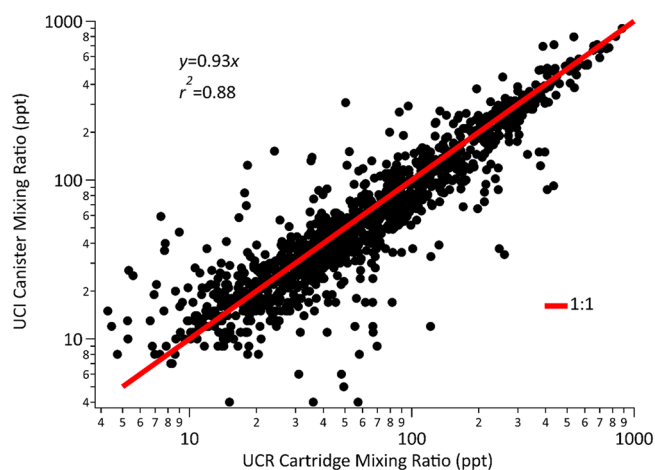
Figure 1. Mixing ratios of compounds (decane, octane, nonane, 2-methylpentane, 2,3-dimethylpentane, ethylbenzene, o-xylene, m+p-xylene, and toluene) quantified by both UCR and UCI.

correlation between the two data sets; the slope was 0.93 with an r^2-value of 0.88. This agreement is within the uncertainty of the UCR GC/GC-TOF-MS data, and is in the range reported by Hatch et al.[23] for biomass burning emissions (UCI vs UCR slope = 0.76 and r^2 = 0.82 across all samples, slope = 0.90 and r^2 = 0.95 when peat data were removed). Comparisons of individual compounds are shown in Figures S7−S15. For all overlapping compounds, the UCI WAS data were used in subsequent analysis due to the greater

number of samples and higher precision and accuracy of the analytical methods.

3.4. Emission Ratio Calculations. Emission ratios (ERs), as defined by Warneke et al.,[25] were calculated for measured VOCs relative to CO and relative to acetylene (ethyne). ERs were calculated using the approach of de Gouw et al.[26] to account for reactive losses of VOCs with OH (OH-corrected ERs), the details of which are presented in Sections S3 and S4. First, the background CO level was calculated based on the average CO intercept of linear fits with m+p-xylene, 1,3,5-trimethylbenzene, and 1,2,4-trimethylbenzene (Figure S24). A value of 90 ± 15 ppb was calculated using the LAAQC-2020 data, which represents an ∼14−22% decrease from background CO levels of ∼105 ppb[3] and ∼115 ppb[26] reported for CalNex-2010. Next, the ratio of VOC to excess CO above background (VOC/ΔCO) was calculated for each VOC and plotted against the corresponding OH exposure (Figure S18). The OH-corrected ER to ΔCO, when OH exposure is zero, was then defined as the y-intercept. The error associated with OH-corrected ERs was calculated using the high and low values for background CO (105 and 75 ppb).

For OH-corrected ER to Δacetylene, the background acetylene was calculated as described in Section S4; the OH-corrected ER to Δacetylene was then defined as the y-intercept of the ratio of VOC to excess acetylene above background (VOC/Δacetylene) plotted against the corresponding OH exposure. ERs were also calculated using linear regression (see Section S4) from the nighttime data only (ER_{night}) for comparison with Borbon et al.[27] To account for reactive losses of VOCs with O_3 in the nighttime samples, O_3-corrected ERs_{night} were calculated analogously to OH-corrected ERs (see Section S4) based on de Gouw et al.[26] The OH-corrected ERs to ΔCO and ERs_{night} to CO and acetylene are summarized in Table 1, along with the ERs reported by Borbon et al.[27] and de Gouw et al.[26] OH-corrected ERs to acetylene and O_3-corrected ERs_{night} to ΔCO and Δacetylene are reported in Table S1. Following de Gouw et al.,[26] OH-corrected ERs and O_3-corrected ERs_{night} are relative to background-corrected CO (ΔCO) and to background-corrected acetylene (Δacetylene). Following Borbon et al.,[27] ERs_{night} are relative to total CO and to acetylene (not background corrected). Since constant values for background CO and acetylene were used in the ER calculations (see Section S3), ERs_{night} would not change if background corrections were applied.

3.5. OH Exposure Calculations. OH exposure ([OH]Δt) is a measure of atmospheric aging and represents the photochemical loss of reactive VOCs. In the derivation of OH-corrected ERs, OH exposure was estimated based on de Gouw et al.[26] using the ratio of benzene/1,2,4-trimethylbenzene (Figure S19) as an indicator of photochemical aging. The change in OH exposure relative to the past decade was also estimated based on Warneke et al.[29] Warneke et al.[29] used the ratio of weekday to weekend ERs to quantify the increase in OH exposure on weekends due to decreased NO_x. Here, the ratio of 2010 ER to 2020 ER was used to quantify the change in OH exposure between 2010 and 2020.

With daytime winds predominantly from the southwest, back trajectory analysis during CalNex-2010 showed air masses being transported from LA to Pasadena with approximate photochemical ages of up to 0.5 days.[3] Similar daytime wind direction and speeds were observed in 2020 (Figure S5). To account for photochemical loses, the relationship between

Table 1. 2020 and 2010 Emission Ratios (ERs) to CO and Acetylene

compound	OH-corrected ER (ppt [ppb ΔCO]$^{-1}$)		ER$_{night}$ (ppt [ppb CO]$^{-1}$)		ER$_{night}$ (ppt [ppt acetylene]$^{-1}$)		r^2 w/ CO	r^2 w/ acetylene
	2020	2010[a]	2020	2010[b]	2020	2010[c]	2020	2020
ethane	60.09 ± 8.02	16.5	58.34	18.4	18.22	4.16	0.76	0.72
ethene	6.80 ± 0.90	11.2	4.99	10.35	1.61	1.80	0.79	0.81
acetylene[d]	2.91 ± 0.44	6.4	2.96	5.87	–	–	0.90	–
1,2-propadiene	0.09 ± 0.01	–	0.07	–	0.02	–	0.79	0.73
propyne	0.10 ± 0.01	–	0.10	–	0.03	–	0.70	0.66
propane[d]	14.5 ± 3.33	–	14.45	11.2	4.71	2.05	0.74	0.80
propene	1.57 ± 0.22	4.1	1.07	3.74	0.34	–	0.77	0.76
i-butane[d]	2.67 ± 0.61	3.18	2.80	3.08	0.92	0.55	0.70	0.77
n-butane[d]	4.17 ± 0.96	4.94	4.44	4.42	1.47	0.78	0.70	0.75
1-butene	0.32 ± 0.04	0.39	0.17	0.34	0.06	0.05	0.67	0.67
i-butene	0.58 ± 0.08	0.9	0.27	–	0.08	–	0.35	0.33
trans-2-butene	0.06 ± 0.01	0.32	0.05	0.1	0.02	0.02	0.40	0.36
cis-2-butene	0.06 ± 0.01	0.28	0.04	0.09	0.01	0.02	0.42	0.37
i-pentane	4.62 ± 0.66	8.7	5.03	8.69	1.58	1.81	0.86	0.83
n-pentane	2.29 ± 0.31	3.4	2.42	3.26	0.76	0.65	0.83	0.81
1,3-butadiene	0.18 ± 0.02	0.4	0.10	0.35	0.03	0.06	0.55	0.56
1-pentene	0.14 ± 0.02	–	0.10	–	0.03	–	0.74	0.72
trans-2-pentene	0.06 ± 0.01	–	0.07	–	0.02	0.09	0.39	0.33
cis-2-pentene	0.03 ± 0.00	–	0.04	–	0.01	–	0.35	0.36
3-methyl-1-butene	0.05 ± 0.01	0.068	0.04	–	0.01	–	0.64	0.63
2-methyl-1-butene	0.12 ± 0.02	–	0.10	–	0.03	–	0.44	0.48
2-methyl-2-butene	0.07 ± 0.01	–	0.07	–	0.02	–	0.36	0.33
n-hexane	0.96 ± 0.12	1.39	1.10	1.13	0.34	0.21	0.48	0.44
n-heptane	0.45 ± 0.06	0.83	0.39	–	0.13	–	0.76	0.78
n-octane	0.22 ± 0.03	0.355	0.16	–	0.05	–	0.81	0.83
n-nonane	0.22 ± 0.03	0.326	0.16	0.22	0.05	0.04	0.73	0.74
n-decane	0.19 ± 0.03	0.3	0.10	0.18	0.03	0.04	0.56	0.64
2,2-dimethylbutane	0.14 ± 0.02	–	0.15	–	0.05	–	0.73	0.67
2,3-dimethylbutane	0.46 ± 0.06	–	0.45	–	0.14	–	0.88	0.83
2-methylpentane	1.17 ± 0.12	1.43	1.18	–	0.37	–	0.87	0.83
3-methylpentane	0.74 ± 0.02	1.39	0.78	–	0.24	–	0.78	0.74
2-methylhexane	0.45 ± 0.06	0.58	0.44	–	0.14	–	0.87	0.83
3-methylhexane	0.48 ± 0.07	0.58	0.47	–	0.15	–	0.87	0.84
2-methylheptane	0.17 ± 0.03	–	0.14	–	0.05	–	0.86	0.85
3-methylheptane	0.14 ± 0.02	–	0.12	–	0.04	–	0.89	0.87
2,4-dimethylpentane	0.37 ± 0.05	–	0.38	–	0.12	–	0.90	0.86
2,3-dimethylpentane	0.65 ± 0.09	–	0.64	–	0.20	–	0.89	0.85
2,2,4-trimethylpentane	1.01 ± 0.14	–	1.05	–	0.33	–	0.93	0.87
2,3,4-trimethylpentane	0.32 ± 0.04	–	0.33	–	0.10	–	0.94	0.89
cyclopentane	0.27 ± 0.04	–	0.24	–	0.08	–	0.77	0.75
methylcyclopentane	0.84 ± 0.04	1.34	0.81	–	0.25	–	0.76	0.72
cyclohexane	0.43 ± 0.06	0.53	0.35	–	0.11	–	0.79	0.81
methylcyclohexane	0.34 ± 0.05	0.43	0.29	–	0.09	–	0.79	0.83
benzene[d]	0.64 ± 0.17	1.26	0.76	1.3	0.24	0.23	0.82	0.83
toluene	2.84 ± 0.38	3.4	2.56	3.18	0.83	0.61	0.82	0.84
ethylbenzene	0.35 ± 0.05	0.61	0.33	0.57	0.10	0.10	0.91	0.89
m- and p-xylene	1.37 ± 0.18	2.07	1.29	1.79	0.41	0.34	0.90	0.89
o-xylene	0.50 ± 0.07	0.77	0.44	0.67	0.14	0.12	0.91	0.89
styrene	0.15 ± 0.02	0.36	0.07	0.22	0.03	0.04	0.32	0.38
i-propylbenzene	0.03 ± 0.00	0.0305	0.02	0.03	0.01	0.01	0.56	0.52
n-propylbenzene	0.08 ± 0.01	0.103	0.06	0.11	0.02	0.02	0.79	0.78
3-ethyltoluene	0.33 ± 0.05	0.44	0.25	–	0.08	–	0.88	0.88
4-ethyltoluene	0.15 ± 0.02	0.44	0.11	–	0.04	–	0.79	0.77
2-ethyltoluene	0.11 ± 0.02	0.123	0.07	0.12	0.02	0.02	0.74	0.76
1,3,5-trimethylbenzene	0.14 ± 0.02	0.39	0.10	0.31	0.03	0.06	0.77	0.80
1,2,4-trimethylbenzene	0.45 ± 0.06	0.79	0.31	0.62	0.10	0.12	0.79	0.80

[a]de Gouw et al.[26] [b]Borbon et al.[27] [c]Calculated using CalNex ground site data.[28] [d]Relatively unreactive compounds ($k_{OH} < 5 \times 10^{-12}$ cm^3 molecule^{-1} s^{-1}) were background corrected (see Section S3); correction values were 110, 294, 49, 79, and 60 ppt for acetylene, propane, i-butane, n-butane, and benzene, respectively.

ER_{day} and ER_{night} was approximated by a first-order loss equation (eq 1):

$$ER_{day} \cong ER_{night} \times e^{k_{OH}[OH]\Delta t} \qquad (1)$$

where ER_{day} was calculated using linear regression from the daytime data only and $k_{OH} = -k_{VOC} + k_{CO}$. Then, to estimate the change in weekday OH exposure relative to 2010, the ratio of 2010 weekday ERs to 2020 weekday ERs was calculated (eq 2):

$$\frac{ER_{day(2010)} \times ER_{night(2020)}}{ER_{day(2020)} \times ER_{night(2010)}}$$

$$\cong \frac{e^{k_{OH}([OH]t)_{2010}}}{e^{k_{OH}([OH]t)_{2020}}}$$

$$= e^{-k_{OH}(([OH]\Delta t)_{2020} - ([OH]\Delta t)_{2010})} \qquad (2)$$

This ratio was plotted against the rate constant (k) with OH for a subset of compounds; a fit was applied to the data, giving the change in weekday OH exposure between 2010 and 2020. The same method was applied to calculate the change in weekend OH exposure.

4. RESULTS AND DISCUSSION

4.1. Compounds, Sources, and Trends during LAAQC.

In Table S2, the average nighttime, morning, and afternoon mixing ratios are summarized for the 92 compounds identified and quantified using multi-column and multi-detector GC and 58 compounds using GC/GC-TOF-MS. Common sources for each compound are summarized in Table S3. Combustion source emissions include on- and off-road gasoline and diesel exhaust. In addition, there are evaporative fuel emissions from these sources which include contributions from light-duty cars and trucks ("passenger" vehicles), heavy-duty trucks, ocean-going vessels, recreational boats, construction equipment, farm equipment, and landscaping equipment. Nonmobile source emissions include VCPs and industrial cooking, with specific contributions from pesticides, coatings, inks, adhesives, cleaning agents and solvents, and personal care products.

While the broad changes in human activity during COVID-19 are still being examined, the change in travel demand in the LA Basin was striking. Between the beginning and end of the campaign, traffic counts increased by approximately 30%; the increase in average April−May traffic to average June−July traffic was approximately 10%.[13] Despite the increase in traffic, the average afternoon concentrations of CO and VOCs did not significantly increase; June−July mixing ratios were within one standard deviation of the April−May values (Figure 2). However, Figure 3 illustrates that the afternoon 25th percentile (Q1) mixing ratio, calculated for 54 compounds, increased substantially for some compounds. The Q1 mixing ratio of CO increased 23%, and acetylene increased 47%. CO, long-lived in the atmosphere, is a tracer of combustion sources; acetylene, also long-lived in the atmosphere, is emitted from gasoline exhaust and used to separate distinct sources of CO such as traffic and biomass burning.[30] Both CO and acetylene are useful tracers for on- and off-road mobile sources.

For the combined data set, April−July, acetylene was found to have the highest afternoon correlation with CO ($r^2 = 0.91$); the strength of relationship, defined by the r^2-value, indicates they were both primarily emitted from gasoline exhaust. Figure 3 illustrates that compounds with the greatest increase in
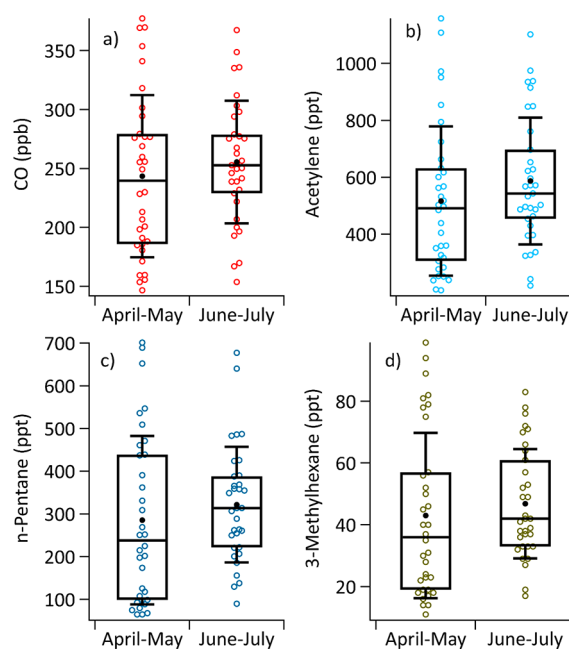
Figure 2. Box and whisker plots of (a) CO, (b) acetylene, (c) *n*-pentane, and (d) 3-methylhexane measured in April−May and June−July. The shaded circles indicate the afternoon mixing ratios of individual samples. The black dot indicates the mean mixing ratio. The whiskers represent one standard deviation from the mean. The black line represents the median, and the 25th and 75th percentiles are represented by the edges of the black box.

afternoon Q1 mixing ratios also have the strongest correlation with CO. VOCs with Q1 mixing ratios that increased >60% between April−May and June−July had an average r^2 with CO of 0.72, while VOCs with Q1 mixing ratios that increased or decreased <40% had an average r^2 with CO of only 0.35. This is consistent with combustion source emissions increasing between April−May and June−July while source emissions of the other measured VOCs were not increasing.

A majority of the VOCs with Q1 mixing ratios that increased >60% are emitted from both gasoline exhaust and gasoline evaporation.[5] The afternoon Q1 mixing ratio of *n*-pentane, a major component of gasoline vapor, increased by 119%, and 3-methylhexane, a component of both gasoline exhaust and vapor,[5] increased by 86%. While many of the compounds overlap between the two sources, the relative contributions of VOCs vary between gasoline exhaust and gasoline vapor emissions. For example, *n*-pentane makes up 8.7% of gasoline vapor and only 1.9% of gasoline exhaust.[5] VOC speciation profiles for gasoline exhaust and vapor were reported in McDonald et al.[5] To determine the extent to which the increase in Q1 mixing ratios for compounds emitted from mobile sources could be attributed to an increase in exhaust or evaporation, the percent increase in Q1 VOC mixing ratio was plotted against the corresponding ratio of gasoline vapor weight % to gasoline exhaust weight % in Figure 4 (e.g., for *n*-pentane, the vapor to exhaust ratio would be 8.7:1.9). Figure 4 illustrates that compounds with higher vapor to exhaust ratios had greater increases in afternoon Q1 mixing ratios, suggesting that evaporative emissions increased more than exhaust emissions between April−May and June−July. VOCs with a vapor to exhaust ratio of >1 increased, on average, 83%. The Q1 mixing ratio of isoprene, a biogenic VOC that exhibited strong positive correlation with temperature ($r^2 = 0.89$),
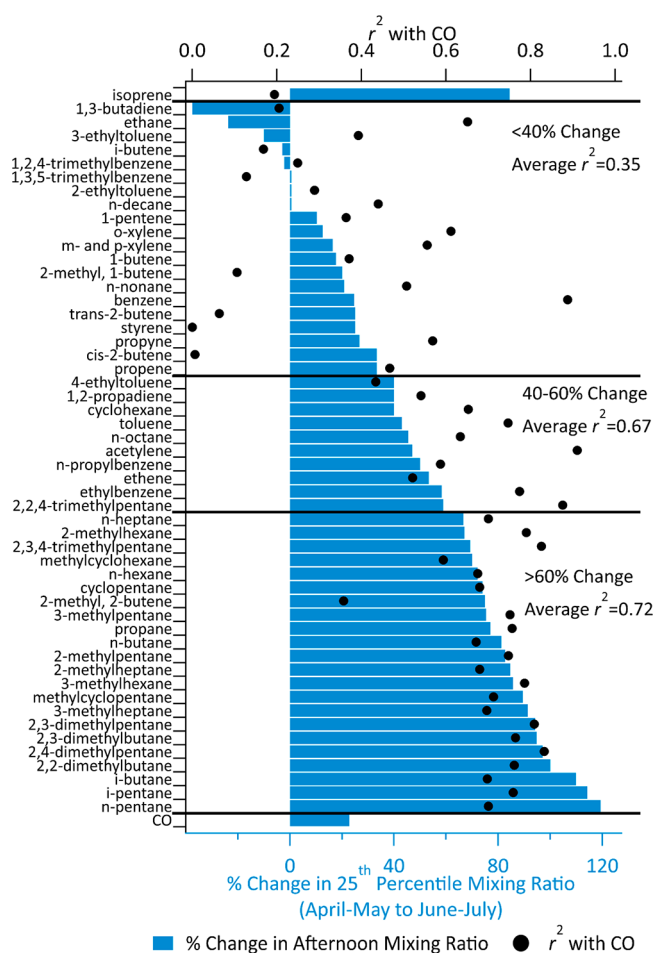
Figure 3. Percent change in the afternoon 25th percentile mixing ratio (Q1) from April−May to June−July for CO and a subset of VOCs (blue bars, bottom axis), plotted with the campaign r^2-value between the VOC and CO (black dots, top axis).
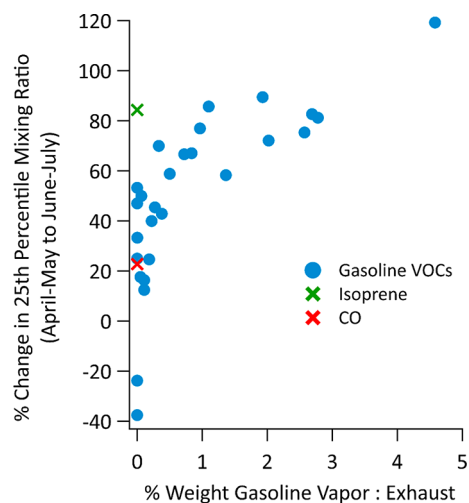
Figure 4. Percent change in the 25th percentile (Q1) mixing ratio from April−May to June−July plotted against the ratio of VOC weight (%) in gasoline vapor to VOC weight (%) in gasoline exhaust. VOCs are represented by blue dots, isoprene is represented by the green ×, and CO is represented by the red ×.

increased 84%. The Q1 temperature increased from 295.7 K in April−May to 298.6 K in June−July. These observations

suggest that the increase in afternoon Q1 mixing ratios between April−May and June−July was largely due to an increase in temperature, and thus an increased contribution of measured VOCs from evaporative emissions.

In addition to VOCs associated with anthropogenic sources, a number of VOCs associated with biogenic sources were quantified during LAAQC, particularly terpenes. Terpenes are also emitted from anthropogenic sources; for example, fragrances have been reported to contribute significantly to terpene levels, especially limonene, in urban areas.[31] However, there was no clear evidence of a distinct contribution of anthropogenic sources to the terpenes quantified during LAAQC. Biogenic terpene emissions exhibit a light and temperature response and thus trend strongly with temperature.[32] During LAAQC, afternoon mixing ratios of α-pinene, camphene, and eucalyptol increased with temperature (Figure S23). However, β-pinene, β-myrcene, and limonene exhibited weaker temperature dependence, suggesting the primary driver of these terpenes changed during the campaign. In Figure 5 it
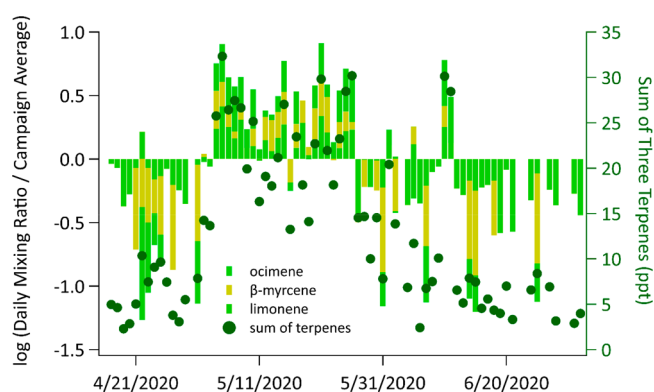
Figure 5. Log of daily afternoon mixing ratio normalized to campaign average afternoon mixing ratio for three terpenes (ocimene, β-myrcene, and limonene). Bars for the three compounds correspond to the left axis; values above zero indicate the daily summed concentration for the three compounds is greater than the campaign average summed concentration. The right axis corresponds to the total concentration for the three terpenes (green dots).

can be seen that the ocimene, β-myrcene, and limonene mixing ratios were elevated during the month of May. This trend is likely a result of higher emission rates from citrus trees during flowering.[33]

4.2. Changes in OH Exposure Since 2010. In 2010, Warneke et al.[29] reported that OH exposure ([OH]Δt) was 65−75% higher on weekends than on weekdays in Southern California due to a 35−50% decrease in NO_x levels on weekends. The lower NO_x levels on weekends have been attributed to reduced truck traffic.[34−37] Nussbaumer and Cohen[38] reported that NO_x levels in the LA Basin decreased up to ~80% between 1994 and 2019, and remained lower on weekends compared to weekdays. On the basis of data obtained from a California Air Resources Board monitoring site located in Pasadena,[8] NO_x levels averaged over the April−July sampling period were an average of 50% lower than in 2020 than 2010; NO_x levels in 2020 were an average of 45% higher on weekdays compared to weekends (Table S4). The calculated OH exposures were used to probe the effect of changes in atmospheric composition, particularly NO_x levels, on OH exposure between 2010 and 2020.

Figure 6 illustrates the ratio of the 2010 ER to the 2020 ER for a subset of VOCs, plotted against their k_{OH}, measured on
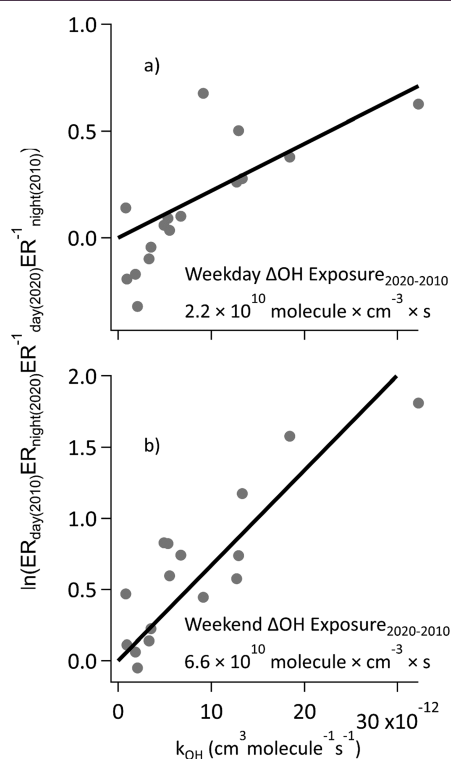
Figure 6. Increase in OH exposure between 2010 and 2020: (a) weekdays and (b) weekends. Each point represents a single VOC that was measured in both years; 2010 ER values were reported by Warneke et al.[29]

weekdays and weekends. Applying a linear fit to the data yielded an increase in weekday and weekend peak (afternoon) OH exposure by ~2.2 × 10^{10} molecules cm⁻³ s and ~6.6 × 10^{10} molecules cm⁻³ s, respectively, since 2010. The average peak OH exposure in 2010 was reported to be ~3 × 10^{10} molecules cm⁻³ s;[29] the weekly average change in OH exposure between 2010 and 2020 was calculated to be ~3.5 × 10^{10} molecules cm⁻³ s. Using the 2010 average peak OH exposure and calculated increase in weekly average change in peak exposure, the average peak OH exposure in 2020 was calculated to be ~6.5 × 10^{10} molecules cm⁻³ s. In comparison, using the ratio of benzene to 1,2,4-trimethylbenzene to estimate OH exposure (Section S4) resulted in an average peak OH exposure of 5.2 × 10^{10} molecules cm⁻³ s. Based on the similar wind speeds and directions (Figure S4), it can be assumed that transport time has remained relatively constant between 2010 and 2020, and thus the average peak OH concentration can be estimated using the ratio of average peak OH exposure in 2020 to 2010; by that approach, OH concentration has increased by a factor of 2, from ~4 × 10^{6} molecules cm⁻³ in 2010 to ~8 × 10^{6} molecules cm⁻³ in 2020.

The extent to which the OH concentrations are wholly representative of recent non-COVID periods, depends in part on whether the yet unknown trends in human activities and emissions significantly affected OH reactivity during the LAAQC sampling period. To evaluate whether the 2020 VOC mixing ratios were anomalously low during the sampling period, the average mixing ratios of three combustion-derived compounds (CO, acetylene, and i-pentane) and total non-

methane hydrocarbons (NMHCs) measured during LAAQC-2020 were compared with average mixing ratios measured over the LA Basin during the NASA Student Airborne Research Program (SARP) between 2015 and 2019. It is expected that the mixing ratios of the shorter-lived compounds would be lower in the samples collected aloft than those collected at the Pasadena ground site. For all three individual compounds (Figures S25−S27) and total NMHCs (Figure S28), the median LAAQC values fall within the upper quartile of the SARP values. This suggests that the decreasing trends in OH are not an anomaly and more generally are expected based on trends in NO_x and supports the use of the LAAQC-2020 data for comparisons with CalNex-2010.

4.3. Changes in VOCs, Sources, and Emission Ratios Since 2010. Coincident reductions in CO and VOCs over the decades prior to 2010 resulted in roughly constant ERs relative to CO and to acetylene.[2] The reductions resulted from improved vehicle emission control technologies and more stringent emissions standards. Anomalies from the observed trends, however, suggest the impact of other emissions sources. For example, several smaller alkanes (C2−C5), abundant in both processed and raw natural gas and associated gas (natural gas that was produced by oil wells),[39,40] did not follow the ~7.5% decrease per year over that time period. Peischl et al.[39] reported that nearly all ethane emissions measured in the LA Basin in 2010 could be attributed to such sources, as well as significant fractions of propane (~90%) and n-butane (~75%). Evaporated gasoline was identified as the primary source of n-pentane (~33%) and i-pentane (~50%) emissions; the remainder of n- and i-pentane was attributed to other mobile sources and natural gas.[39] As the on-road mobile source emissions of small alkanes decreased, other sources became more important and their ERs relative to CO increased.

Using the California Emissions Projection Analysis Model (CEPAM),[41] the California Air Resources Board (CARB) projected a reduction in emissions from on-road sources between 2010 and 2020, due to retirement of old vehicles and updates in regulations to on-road motor vehicles. Those regulations were assumed to result in negligible changes in the VOC composition of emissions, as supported by speciation profiles and associated documentation.[42,43] Figure 7 illustrates the estimated change in VOC and CO emissions from on-road motor vehicles, dominated by light-duty passenger vehicles and light-duty trucks, as reported in the CEPAM, and other mobile sources, dominated by off-road equipment. In 2010, on-road motor vehicles were projected to be the dominant contributor to mobile source CO (70%) and VOCs (65%) in the South Coast Air Basin. In 2020, other/off-road combustion and evaporative sources were projected to be the dominant contributor to mobile source CO (55%), and an equal contributor to VOC (50%) emissions. Thus, total VOCs from off-road sources were projected to drop 30% between 2010 and 2020, while total CO was projected to drop only 2%. In 2010, the most abundant off-road source of CO was riding mowers, which was projected to increase from 4.6 × 10^{4} kg day⁻¹ to 5.3 × 10^{4} kg day⁻¹ between 2010 and 2020. The most abundant off-road source of VOCs was gasoline evaporation from lawn mowers, which was projected to decrease from 7.8 × 10^{3} kg day⁻¹ to 4.3 × 10^{3} kg day⁻¹ between 2010 and 2020. The projected shift from on-road to other/off-road sectors as the dominant emitters of mobile source VOCs and CO likely changed measured VOCs levels and calculated ERs for
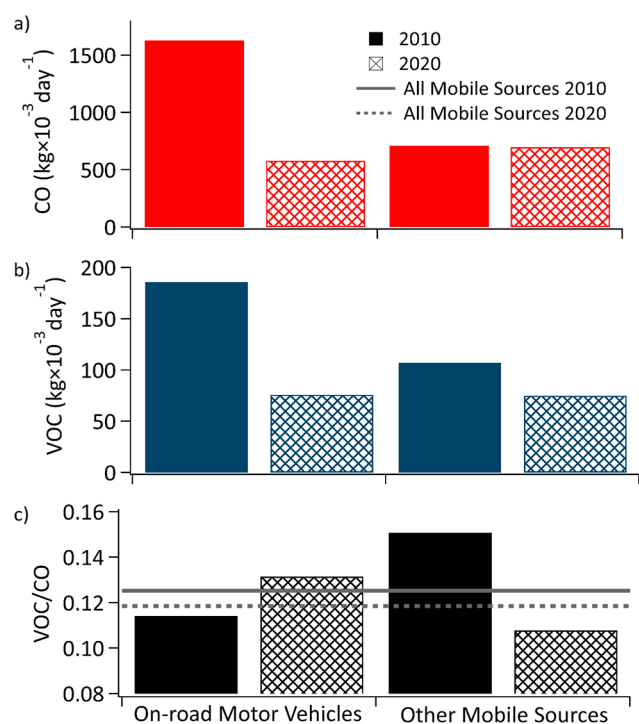
Figure 7. Projected emissions of (a) CO, (b) VOCs, and (c) the ratio of VOCs to CO from on-road motor vehicles and other/off-road mobile sources in the LA Basin. The solid line in (c) represents the 2010 VOC to CO ratio for all mobile sources (on-road motor vehicles + other mobile sources); the dotted line represents the 2020 VOC to CO ratio for all mobile sources. Projected emission values were obtained using the California Emissions Projection Analysis Model.[41]

Figure 8. Percent change in VOC mixing ratios from 2010 to 2020 for CO (red line) and 30 VOCs, including acetylene (blue line). Average 2010 mixing ratios were calculated during the same times of day as samples collected during LAAQC using data in the CalNex-2010 database.[28]

Figure 9. Relationship between 2010 and 2020 VOC ERs relative to acetylene (top) and CO (bottom). The solid burgundy line represents a slope of 1; the dashed gray line represents a slope of 0.6. Shading indicates ±25% from the line. 2010 VOC/CO emission ratios values were reported in Borbon et al.[27] 2010 VOC/acetylene emission ratios were calculated using CalNex-2010 VOC data.[28]

compounds that have been historically emitted primarily by on-road mobile sources.

As illustrated in Figure 8, CO has dropped approximately 25% since 2010 while acetylene has dropped approximately 60%. Most VOCs followed acetylene, dropping ∼60% since 2010. As noted previously, the correlation between CO and acetylene was strong in 2020, suggesting the dominant source of CO remains gasoline exhaust. ERs$_{night}$ relative to acetylene remained constant between 2010 and 2020 (Figure 9, top), while ERs$_{night}$ relative to CO and OH-corrected ERs to ΔCO dropped to ∼60% of the 2010 values reported by Borbon et al.[27] and de Gouw et al.[26] (Figure 9, bottom). The divergence of CO and VOCs indicates a change in combustion source sectors, and is supported by the projected shift from on-road motor vehicles to other mobile/off-road sectors as equal or dominant contributors to mobile source CO and VOCs.

In Table S5, VOCs are classified as combustion, unknown, and noncombustion based on the 2010 vs 2020 ERs plotted in Figure 9. VOCs with ERs$_{night}$ to acetylene within 25% of the 1:1 line and with ERs$_{night}$ to CO and OH-corrected ERs to ΔCO within 25% of the 0.6:1 line were classified as combustion dominant (18 of 40 compounds). The majority of VOCs with ERs$_{night}$ to acetylene that fell within 25% of the 1:1 line, also had ERs$_{night}$ and OH-corrected ERs that fell within 25% of the 0.6:1 line; these VOCs likely were primarily from gasoline combustion. VOCs with ERs outside the 25% threshold were classified as noncombustion (15 of 40), and include small alkanes, butenes, and toluene. Small alkanes like ethane, propane, and butane are known to be emitted from natural gas and petroleum extraction.[39,40] The smaller change

in butenes (average ∼30%), may be due to the growing relative importance of biogenic butene sources.[44,45] Toluene was identified in Seltzer et al.[46] to be the fourth most abundant VOC emitted by VCPs, with a predicted emission rate of 0.37 kg person^{-1} year^{-1}. VOCs were classified as unknown (7 of 40) if only one or two of the three ERs (with acetylene, CO, or ΔCO) fell within the 25% threshold. The calculated OH-reactivity for VOCs classified as unknown was 0.06 s^{-1}; the calculated OH-reactivity for combustion and noncombustion VOCs was roughly equal, 0.37 s^{-1} and 0.36 s^{-1}, respectively.

5. CONCLUSIONS

As a part of the LAAQC, 150 VOCs were measured in the LA Basin during shelter-in-place restrictions associated with the COVID-19 pandemic (April 2020 to July 2020). Compounds that were identified (alkanes, alkenes, aldehydes, ketones, aromatics, etc.) are emitted from a variety of mobile, nonmobile, and biogenic sources. While traffic counts increased markedly during the measurement period, no significant change was observed in the mean VOC concentrations of combustion source emissions. Evaluation of the increases from April−May to June−July in Q1 mixing ratios of CO and acetylene (23% and 47%), as well as VOCs present in gasoline exhaust and evaporative emissions, suggest that the increase in traffic resulted in a relatively minor impact on gasoline exhaust emissions compared to gasoline vapor emissions.

A comparison of CO and VOC levels and ERs calculated from data collected during the CalNex-2010 campaign provided insight into the changing source contributions in the LA Basin, as well as changes in chemical composition and atmospheric reactivity. ERs relative to CO and ΔCO dropped to approximately 60% of their 2010 values, while ERs relative to acetylene remained constant. This suggests that sources with higher CO to acetylene ratios are becoming more important. Relative to 2010, the OH concentration increased 2-fold to approximately ∼8 × 10^6 molecules cm^{-3}. OH reactivity was calculated for VOCs with ERs relative to acetylene that remained constant since 2010 (combustion VOCs) and for VOCs with ERs that did not remain constant (noncombustion VOCs); VOCs attributed to combustion vs noncombustion had roughly equal OH reactivity.

■ ASSOCIATED CONTENT

ⓈⒾ Supporting Information

The Supporting Information is available free of charge at https://pubs.acs.org/doi/10.1021/acsearthspace-chem.1c00248.

> Tables S1−S5: Emission ratios, average VOC mixing ratios, possible VOC sources, 2010 and 2020 NO$_x$ data, and a list VOCs sorted by combustion vs non-combustion sources (XLSX)
>
> Chemical and meteorological data, UCI vs UCR VOC mixing ratio comparisons, background CO and VOC calculations, emission ratio calculations, temperature dependence of terpene emissions, and trends in VOC mixing ratios (PDF)

■ AUTHOR INFORMATION

Corresponding Author

Kelley C. Barsanti − *Bourns College of Engineering, Center for Environmental Research and Technology, Riverside,* *California 92507, United States; Department of Chemical and Environmental Engineering, University of California, Riverside, California 92507, United States;* ⓞ orcid.org/ 0000-0002-6065-8643; Email: kbarsanti@engr.ucr.edu

Authors

Paul Van Rooy − *Bourns College of Engineering, Center for Environmental Research and Technology, Riverside, California 92507, United States;* ⓞ orcid.org/0000-0003-1193-0994

Afsara Tasnia − *Bourns College of Engineering, Center for Environmental Research and Technology, Riverside, California 92507, United States; Department of Chemical and Environmental Engineering, University of California, Riverside, California 92507, United States*

Barbara Barletta − *Department of Chemistry, University of California, Irvine, California 92697, United States*

Reina Buenconsejo − *Division of Chemistry and Chemical Engineering, California Institute of Technology, Pasadena, California 91125, United States*

John D. Crounse − *Division of Chemistry and Chemical Engineering and Division of Engineering and Applied Science, California Institute of Technology, Pasadena, California 91125, United States;* ⓞ orcid.org/0000-0001-5443-729X

Christopher M. Kenseth − *Division of Chemistry and Chemical Engineering, California Institute of Technology, Pasadena, California 91125, United States;* ⓞ orcid.org/ 0000-0003-3188-2336

Simone Meinardi − *Department of Chemistry, University of California, Irvine, California 92697, United States*

Sara Murphy − *Division of Geological and Planetary Sciences, California Institute of Technology, Pasadena, California 91125, United States*

Harrison Parker − *Division of Geological and Planetary Sciences, California Institute of Technology, Pasadena, California 91125, United States*

Benjamin Schulze − *Division of Geological and Planetary Sciences, California Institute of Technology, Pasadena, California 91125, United States*

John H. Seinfeld − *Division of Geological and Planetary Sciences and Division of Engineering and Applied Science, California Institute of Technology, Pasadena, California 91125, United States;* ⓞ orcid.org/0000-0003-1344-4068

Paul O. Wennberg − *Division of Geological and Planetary Sciences and Division of Engineering and Applied Science, California Institute of Technology, Pasadena, California 91125, United States;* ⓞ orcid.org/0000-0002-6126-3854

Donald R. Blake − *Department of Chemistry, University of California, Irvine, California 92697, United States*

Complete contact information is available at:
https://pubs.acs.org/10.1021/acsearthspacechem.1c00248

Author Contributions

The study was conceived by KCB, JHS, DRB, and POW. All authors contributed to data collection, analysis, and/or interpretation. The manuscript was written largely by PVR and KCB, with contributions from AT, BB, JDC, HP, PS, and POW. The manuscript was edited through contributions of all authors. All authors have given approval to the final version of the manuscript.

■ REFERENCES

(1) Parrish, D. D.; Xu, J.; Croes, B.; Shao, M. Air Quality Improvement in Los Angeles—Perspectives for Developing Cities. *Front. Environ. Sci. Eng.* **2016**, *10* (5), 11.

(2) Warneke, C.; de Gouw, J. A.; Holloway, J. S.; Peischl, J.; Ryerson, T. B.; Atlas, E.; Blake, D.; Trainer, M.; Parrish, D. D. Multiyear Trends in Volatile Organic Compounds in Los Angeles, California: Five Decades of Decreasing Emissions. *J. Geophys. Res. Atmospheres* **2012**, DOI: 10.1029/2012JD017899.

(3) Hayes, P. L.; Ortega, A. M.; Cubison, M. J.; Froyd, K. D.; Zhao, Y.; Cliff, S. S.; Hu, W. W.; Toohey, D. W.; Flynn, J. H.; Lefer, B. L.; Grossberg, N.; Alvarez, S.; Rappenglück, B.; Taylor, J. W.; Allan, J. D.; Holloway, J. S.; Gilman, J. B.; Kuster, W. C.; de Gouw, J. A.; Massoli, P.; Zhang, X.; Liu, J.; Weber, R. J.; Corrigan, A. L.; Russell, L. M.; Isaacman, G.; Worton, D. R.; Kreisberg, N. M.; Goldstein, A. H.; Thalman, R.; Waxman, E. M.; Volkamer, R.; Lin, Y. H.; Surratt, J. D.; Kleindienst, T. E.; Offenberg, J. H.; Dusanter, S.; Griffith, S.; Stevens, P. S.; Brioude, J.; Angevine, W. M.; Jimenez, J. L. Organic Aerosol Composition and Sources in Pasadena, California, during the 2010 CalNex Campaign. *J. Geophys. Res. Atmospheres* **2013**, *118* (16), 9233–9257.

(4) Lu, Q.; Murphy, B. N.; Qin, M.; Adams, P. J.; Zhao, Y.; Pye, H. O. T.; Efstathiou, C.; Allen, C.; Robinson, A. L. Simulation of Organic Aerosol Formation during the CalNex Study: Updated Mobile Emissions and Secondary Organic Aerosol Parameterization for Intermediate-Volatility Organic Compounds. *Atmos. Chem. Phys.* **2020**, *20* (7), 4313–4332.

(5) McDonald, B. C.; de Gouw, J. A.; Gilman, J. B.; Jathar, S. H.; Akherati, A.; Cappa, C. D.; Jimenez, J. L.; Lee-Taylor, J.; Hayes, P. L.; McKeen, S. A.; Cui, Y. Y.; Kim, S.-W.; Gentner, D. R.; Isaacman-VanWertz, G.; Goldstein, A. H.; Harley, R. A.; Frost, G. J.; Roberts, J. M.; Ryerson, T. B.; Trainer, M. Volatile Chemical Products Emerging as Largest Petrochemical Source of Urban Organic Emissions. *Science* **2018**, *359* (6377), 760–764.

(6) CFR. CFR. 49 CFR § 531.5 Fuel economy standards. https://ecfr.io/Title-49/Section-531.5 (accessed June 15, 2021).

(7) Alternative Fuels Data Center: Maps and Data. https://afdc.energy.gov/data/ (accessed June 15, 2021).

(8) Air Quality Data (PST) Query Tool. https://www.arb.ca.gov/aqmis2/aqdselect.php (accessed July 9, 2021).

(9) Gensheimer, J.; Turner, A. J.; Shekhar, A.; Wenzel, A.; Keutsch, F. N.; Chen, J. What Are the Different Measures of Mobility Telling Us About Surface Transportation CO2 Emissions During the COVID-19 Pandemic? *J. Geophys. Res.: Atmos.* **2021**, *126* (11), No. e2021JD034664.

(10) Turner, A. J.; Kim, J.; Fitzmaurice, H.; Newman, C.; Worthington, K.; Chan, K.; Wooldridge, P. J.; Köehler, P.; Frankenberg, C.; Cohen, R. C. Observed Impacts of COVID-19 on Urban CO2 Emissions. *Geophys. Res. Lett.* **2020**, *47* (22), No. e2020GL090037.

(11) Yang, J.; Wen, Y.; Wang, Y.; Zhang, S.; Pinto, J. P.; Pennington, E. A.; Wang, Z.; Wu, Y.; Sander, S. P.; Jiang, J. H.; Hao, J.; Yung, Y. L.; Seinfeld, J. H. From COVID-19 to Future Electrification: Assessing Traffic Impacts on Air Quality by a Machine-Learning Model. *Proc. Natl. Acad. Sci. U. S. A.* **2021**, *118* (26), e2102705118.

(12) Liu, J.; Lipsitt, J.; Jerrett, M.; Zhu, Y. Decreases in Near-Road NO and NO2 Concentrations during the COVID-19 Pandemic in California. *Environ. Sci. Technol. Lett.* **2021**, *8* (2), 161–167.

(13) Parker, H. A.; Hasheminassab, S.; Crounse, J. D.; Roehl, C. M.; Wennberg, P. O. Impacts of Traffic Reductions Associated With COVID-19 on Southern California Air Quality. *Geophys. Res. Lett.* **2020**, *47* (23), No. e2020GL090164.

(14) Eldeirawi, K.; Huntington-Moskos, L.; Nyenhuis, S. M.; Polivka, B. Increased Disinfectant Use among Adults with Asthma in the Era of COVID-19. *J. Allergy Clin. Immunol. Pract.* **2021**, *9* (3), 1378–1380.

(15) Koksoy Vayisoglu, S.; Oncu, E. The Use of Cleaning Products and Its Relationship with the Increasing Health Risks during the Covid-19 Pandemic. *Int. J. Clin. Pract.* **2021**, *75*, No. e14534.

(16) Antonioni, M. The Impact of COVID-19 on the Cosmetic and Personal Care Sectors: Trade Data & Analysis. https://blog.marketresearch.com/the-impact-of-covid-19-on-the-cosmetic-and-personal-care-sectors-trade-data-and-analysis (accessed June 16, 2021).

(17) Corley, J.; Okely, J. A.; Taylor, A. M.; Page, D.; Welstead, M.; Skarabela, B.; Redmond, P.; Cox, S. R.; Russ, T. C. Home Garden Use during COVID-19: Associations with Physical and Mental Wellbeing in Older Adults. *J. Environ. Psychol.* **2021**, *73*, 101545.

(18) Unnikrishnan, A.; Figliozzi, M. A. A Study of the Impact of COVID-19 on Home Delivery Purchases and Expenditures, 2020. https://archives.pdx.edu/ds/psu/33410.

(19) TCCON Weather. http://tccon-weather.caltech.edu/ (accessed June 16, 2021).

(20) Weather Data & Weather API. Visual Crossing. https://www.visualcrossing.com/ (accessed September 19, 2021).

(21) Simpson, I. J.; Blake, N. J.; Barletta, B.; Diskin, G. S.; Fuelberg, H. E.; Gorham, K.; Huey, L. G.; Meinardi, S.; Rowland, F. S.; Vay, S. A.; Weinheimer, A. J.; Yang, M.; Blake, D. R. Characterization of Trace Gases Measured over Alberta Oil Sands Mining Operations: 76 Speciated C_2–C_{10} Volatile Organic Compounds (VOCs), CO_2, CH_4, CO, NO, NO_2, NO_y, O_3 and SO_2. *Atmos. Chem. Phys.* **2010**, *10* (23), 11931–11954.

(22) Helmig, D. Ozone Removal Techniques in the Sampling of Atmospheric Volatile Organic Trace Gases. *Atmos. Environ.* **1997**, *31* (21), 3635–3651.

(23) Hatch, L. E.; Yokelson, R. J.; Stockwell, C. E.; Veres, P. R.; Simpson, I. J.; Blake, D. R.; Orlando, J. J.; Barsanti, K. C. Multi-Instrument Comparison and Compilation of Non-Methane Organic Gas Emissions from Biomass Burning and Implications for Smoke-Derived Secondary Organic Aerosol Precursors. *Atmos. Chem. Phys.* **2017**, *17* (2), 1471–1489.

(24) Hatch, L. E.; Jen, C. N.; Kreisberg, N. M.; Selimovic, V.; Yokelson, R. J.; Stamatis, C.; York, R. A.; Foster, D.; Stephens, S. L.; Goldstein, A. H.; Barsanti, K. C. Highly Speciated Measurements of Terpenoids Emitted from Laboratory and Mixed-Conifer Forest Prescribed Fires. *Environ. Sci. Technol.* **2019**, *53* (16), 9418–9428.

(25) Warneke, C.; McKeen, S. A.; de Gouw, J. A.; Goldan, P. D.; Kuster, W. C.; Holloway, J. S.; Williams, E. J.; Lerner, B. M.; Parrish, D. D.; Trainer, M.; Fehsenfeld, F. C.; Kato, S.; Atlas, E. L.; Baker, A.; Blake, D. R. Determination of Urban Volatile Organic Compound Emission Ratios and Comparison with an Emissions Database. *J. Geophys. Res. Atmospheres* **2007**, DOI: 10.1029/2006JD007930.

(26) de Gouw, J. A.; Gilman, J. B.; Kim, S.-W.; Lerner, B. M.; Isaacman-VanWertz, G.; McDonald, B. C.; Warneke, C.; Kuster, W. C.; Lefer, B. L.; Griffith, S. M.; Dusanter, S.; Stevens, P. S.; Stutz, J. Chemistry of Volatile Organic Compounds in the Los Angeles Basin: Nighttime Removal of Alkenes and Determination of Emission Ratios. *J. Geophys. Res. Atmospheres* **2017**, *122* (21), 11843–11861.

(27) Borbon, A.; Gilman, J. B.; Kuster, W. C.; Grand, N.; Chevaillier, S.; Colomb, A.; Dolgorouky, C.; Gros, V.; Lopez, M.; Sarda-Esteve, R.; Holloway, J.; Stutz, J.; Petetin, H.; McKeen, S.; Beekmann, M.; Warneke, C.; Parrish, D. D.; de Gouw, J. A. Emission Ratios of Anthropogenic Volatile Organic Compounds in Northern Mid-Latitude Megacities: Observations versus Emission Inventories in Los Angeles and Paris. *J. Geophys. Res. Atmospheres* **2013**, *118* (4), 2041−2057.

(28) US Department of Commerce. N. CalNex 2010 LA Ground Site Data Download. https://csl.noaa.gov/groups/csl7/measurements/2010calnex/Ground/DataDownload/index.php?page=/groups/csl7/measurements/2010calnex/Ground/DataDownload/ (accessed June 15, 2021).

(29) Warneke, C.; de Gouw, J. A.; Edwards, P. M.; Holloway, J. S.; Gilman, J. B.; Kuster, W. C.; Graus, M.; Atlas, E.; Blake, D.; Gentner, D. R.; Goldstein, A. H.; Harley, R. A.; Alvarez, S.; Rappenglueck, B.; Trainer, M.; Parrish, D. D. Photochemical Aging of Volatile Organic Compounds in the Los Angeles Basin: Weekday-Weekend Effect. *J. Geophys. Res. Atmospheres* **2013**, *118* (10), 5018−5028.

(30) Crounse, J. D.; DeCarlo, P. F.; Blake, D. R.; Emmons, L. K.; Campos, T. L.; Apel, E. C.; Clarke, A. D.; Weinheimer, A. J.; McCabe, D. C.; Yokelson, R. J.; Jimenez, J. L.; Wennberg, P. O. Biomass Burning and Urban Air Pollution over the Central Mexican Plateau. *Atmos. Chem. Phys.* **2009**, *9* (14), 4929−4944.

(31) Gkatzelis, G. I.; Coggon, M. M.; McDonald, B. C.; Peischl, J.; Aikin, K. C.; Gilman, J. B.; Trainer, M.; Warneke, C. Identifying Volatile Chemical Product Tracer Compounds in U.S. Cities. *Environ. Sci. Technol.* **2021**, *55* (1), 188−199.

(32) Guenther, A. B.; Jiang, X.; Heald, C. L.; Sakulyanontvittaya, T.; Duhl, T.; Emmons, L. K.; Wang, X. The Model of Emissions of Gases and Aerosols from Nature Version 2.1 (MEGAN2.1): An Extended and Updated Framework for Modeling Biogenic Emissions. *Geosci. Model Dev.* **2012**, *5* (6), 1471−1492.

(33) Baghi, R.; Helmig, D.; Guenther, A.; Duhl, T.; Daly, R. Contribution of Flowering Trees to Urban Atmospheric Biogenic Volatile Organic Compound Emissions. *Biogeosciences* **2012**, *9* (10), 3777−3785.

(34) Kim, S.-W.; McDonald, B. C.; Baidar, S.; Brown, S. S.; Dube, B.; Ferrare, R. A.; Frost, G. J.; Harley, R. A.; Holloway, J. S.; Lee, H.-J.; McKeen, S. A.; Neuman, J. A.; Nowak, J. B.; Oetjen, H.; Ortega, I.; Pollack, I. B.; Roberts, J. M.; Ryerson, T. B.; Scarino, A. J.; Senff, C. J.; Thalman, R.; Trainer, M.; Volkamer, R.; Wagner, N.; Washenfelder, R. A.; Waxman, E.; Young, C. J. Modeling the Weekly Cycle of NOx and CO Emissions and Their Impacts on O3 in the Los Angeles-South Coast Air Basin during the CalNex 2010 Field Campaign. *J. Geophys. Res. Atmospheres* **2016**, *121* (3), 1340−1360.

(35) Qin, Y.; Tonnesen, G. S.; Wang, Z. Weekend/Weekday Differences of Ozone, NOx, Co, VOCs, PM10 and the Light Scatter during Ozone Season in Southern California. *Atmos. Environ.* **2004**, *38* (19), 3069−3087.

(36) Pollack, I. B.; Ryerson, T. B.; Trainer, M.; Parrish, D. D.; Andrews, A. E.; Atlas, E. L.; Blake, D. R.; Brown, S. S.; Commane, R.; Daube, B. C.; de Gouw, J. A.; Dube, W. P.; Flynn, J.; Frost, G. J.; Gilman, J. B.; Grossberg, N.; Holloway, J. S.; Kofler, J.; Kort, E. A.; Kuster, W. C.; Lang, P. M.; Lefer, B.; Lueb, R. A.; Neuman, J. A.; Nowak, J. B.; Novelli, P. C.; Peischl, J.; Perring, A. E.; Roberts, J. M.; Santoni, G.; Schwarz, J. P.; Spackman, J. R.; Wagner, N. L.; Warneke, C.; Washenfelder, R. A.; Wofsy, S. C.; Xiang, B. Airborne and Ground-Based Observations of a Weekend Effect in Ozone, Precursors, and Oxidation Products in the California South Coast Air Basin. *J. Geophys. Res. Atmospheres* **2012**, DOI: 10.1029/2011JD016772.

(37) Yarwood, G.; Stoeckenius, T. E.; Heiken, J. G.; Dunker, A. M. Modeling Weekday/Weekend Ozone Differences in the Los Angeles Region for 1997. *J. Air Waste Manage. Assoc.* **2003**, *53* (7), 864−875.

(38) Nussbaumer, C. M.; Cohen, R. C. The Role of Temperature and NOx in Ozone Trends in the Los Angeles Basin. *Environ. Sci. Technol.* **2020**, *54* (24), 15652−15659.

(39) Peischl, J.; Ryerson, T. B.; Brioude, J.; Aikin, K. C.; Andrews, A. E.; Atlas, E.; Blake, D.; Daube, B. C.; de Gouw, J. A.; Dlugokencky, E.; Frost, G. J.; Gentner, D. R.; Gilman, J. B.; Goldstein, A. H.; Harley, R. A.; Holloway, J. S.; Kofler, J.; Kuster, W. C.; Lang, P. M.; Novelli, P. C.; Santoni, G. W.; Trainer, M.; Wofsy, S. C.; Parrish, D. D. Quantifying Sources of Methane Using Light Alkanes in the Los Angeles Basin, California. *J. Geophys. Res. Atmospheres* **2013**, *118* (10), 4974−4990.

(40) Rossabi, S.; Helmig, D. Changes in Atmospheric Butanes and Pentanes and Their Isomeric Ratios in the Continental United States. *J. Geophys. Res.: Atmos.* **2018**, *123* (7), 3772−3790.

(41) CEPAM: 2016 SIP − Standard Emission Tool. https://www.arb.ca.gov/app/emsinv/fcemssumcat2016.php (accessed June 22, 2021).

(42) Speciation Profiles Used in CARB Modeling. California Air Resources Board. https://ww2.arb.ca.gov/speciation-profiles-used-carb-modeling (accessed September 19, 2021).

(43) MSEI - Modeling Tools − EMFAC Software and Technical Support Documentation. California Air Resources Board. https://ww2.arb.ca.gov/our-work/programs/mobile-source-emissions-inventory/msei-modeling-tools-emfac-software-and (accessed September 19, 2021).

(44) Rhew, R. C.; Deventer, M. J.; Turnipseed, A. A.; Warneke, C.; Ortega, J.; Shen, S.; Martinez, L.; Koss, A.; Lerner, B. M.; Gilman, J. B.; Smith, J. N.; Guenther, A. B.; de Gouw, J. A. Ethene, Propene, Butene and Isoprene Emissions from a Ponderosa Pine Forest Measured by Relaxed Eddy Accumulation. *Atmos. Chem. Phys.* **2017**, *17* (21), 13417−13438.

(45) Tripathi, N.; Sahu, L. K.; Singh, A.; Yadav, R.; Patel, A.; Patel, K.; Meenu, P. Elevated Levels of Biogenic Nonmethane Hydrocarbons in the Marine Boundary Layer of the Arabian Sea During the Intermonsoon. *J. Geophys. Res.: Atmos.* **2020**, *125* (22), No. e2020JD032869.

(46) Seltzer, K. M.; Pennington, E.; Rao, V.; Murphy, B. N.; Strum, M.; Isaacs, K. K.; Pye, H. O. T. Reactive Organic Carbon Emissions from Volatile Chemical Products. *Atmos. Chem. Phys.* **2021**, *21* (6), 5079−5100.

A p p e n d i x   H

UNIFIED THEORY OF VAPOR-WALL MASS TRANSPORT IN TEFLON-WALLED ENVIRONMENTAL CHAMBERS

Huang, Y.; Zhao, R.; Charan, S. M.; Kenseth, C. M.; Zhang, X.; Seinfeld, J. H. Unified Theory of Vapor-Wall Mass Transport in Teflon-Walled Environmental Chambers. *Environ. Sci. Technol.* **2018**, *52* (4), 2134–2142. DOI: 10.1021/acs.est.7b05575.

Unified Theory of Vapor−Wall Mass Transport in Teflon-Walled Environmental Chambers

Yuanlong Huang,[†] Ran Zhao,[‡] Sophia M. Charan,[‡] Christopher M. Kenseth,[‡] Xuan Zhang,[¶] and John H. Seinfeld*,[‡,§]

[†]Division of Geological and Planetary Sciences, California Institute of Technology, Pasadena, California 91125, United States
[‡]Division of Chemistry and Chemical Engineering, California Institute of Technology, Pasadena, California 91125, United States
[¶]National Center for Atmospheric Research, Boulder, Colorado 80301, United States
[§]Division of Engineering and Applied Science, California Institute of Technology, Pasadena, California 91125, United States

S *Supporting Information*

ABSTRACT: Secondary organic aerosol (SOA) formation is studied in laboratory chambers, in which volatile organic compounds (VOCs) are oxidized to produce low-volatility compounds that condense into the aerosol phase. It has been established that such oxidized low-volatility compounds can partition into the chamber walls, which traditionally consist of Teflon film. Several studies exist in which the rates of uptake of individual vapor compounds to the chamber walls have been measured, but a unified theory capable of describing the range of experimental measurements has been lacking. Here, a two-layer model of observed short and long vapor−wall interaction time scales in Teflon-walled environmental chambers is presented and shown to be consistent with experimental data on the rate of wall deposition of more than 90 compounds. Semiempirical relationships between key parameters in the model and vapor molecular properties are derived, which can be used to predict the fate of gas-phase vapor in the chamber under dry conditions.
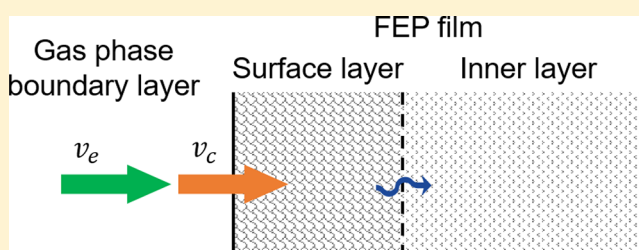
INTRODUCTION

The environmental chamber is a principal laboratory system used to study the formation, properties, and evolution of secondary organic aerosol (SOA).[1] The typical material from which chambers are constructed is Teflon film (fluorinated ethylene propylene, FEP). The process of SOA formation involves oxidation of a volatile organic compound (VOC) to generate low-volatility gas-phase products that subsequently condense into the aerosol phase. It has been established that these oxidized products may also partition into the Teflon chamber walls.[2−16] Such vapor−wall loss reduces the potential yield of SOA and must be accounted for in analysis of experiments. Current treatments of vapor−wall deposition in chambers consider the FEP film as an infinite medium into which vapor molecules dissolve.

The extent of partitioning of oxidized organic species typical of SOA into Teflon film has been studied experimentally by introducing species individually into a chamber and measuring their rate of decay from wall uptake. The uptake has been characterized by the time scale required to approach vapor−wall equilibrium (τ_w). Previous studies indicate that τ_w can be competitive with the time scales of other processes occurring in the chamber, such as the rate of VOC oxidation and the time scale associated with vapor−particle partitioning.[4,14] The time scale τ_w is governed by gas-phase diffusion through the boundary layer adjacent to the chamber wall, followed by uptake into the wall itself. Two major studies of vapor−wall uptake of individual

organic species typical of VOC oxidation products have reported significantly different time scales for vapor uptake, namely $\tau_w \sim$ 10 min[12] and $\tau_w \sim$ 10 h.[10] Possible reasons for the observed discrepancy in vapor−wall uptake rates include differences in the particular chemical systems studied or in the experimental protocol itself. The goal of the present work is to formulate and evaluate experimentally a unified theory of vapor−wall mass transport and uptake in Teflon-walled environmental chambers.

TWO-LAYER KINETIC SORPTION MODEL

We introduce a two-layer kinetic sorption model (Figure 1A), inspired by that proposed by Crank,[17] to explain the stress-dependent diffusion of vapor molecules into polymer film. In the two-layer model, after traversing a gas-phase boundary layer, vapor molecules enter a sharp, swollen outer layer in the Teflon that is thought to be stress-free, in which equilibrium with the gas phase is established relatively rapidly. It is estimated that a pseudosteady state profile in the gas-phase boundary layer is achieved on a time scale of order 10 s (Supporting Information, SI. I). Vapor molecules absorbed into the outer polymer layer (denoted the "Surface layer" in Figure 1A) then slowly diffuse into the interior of the polymer film (the "Inner layer" in Figure
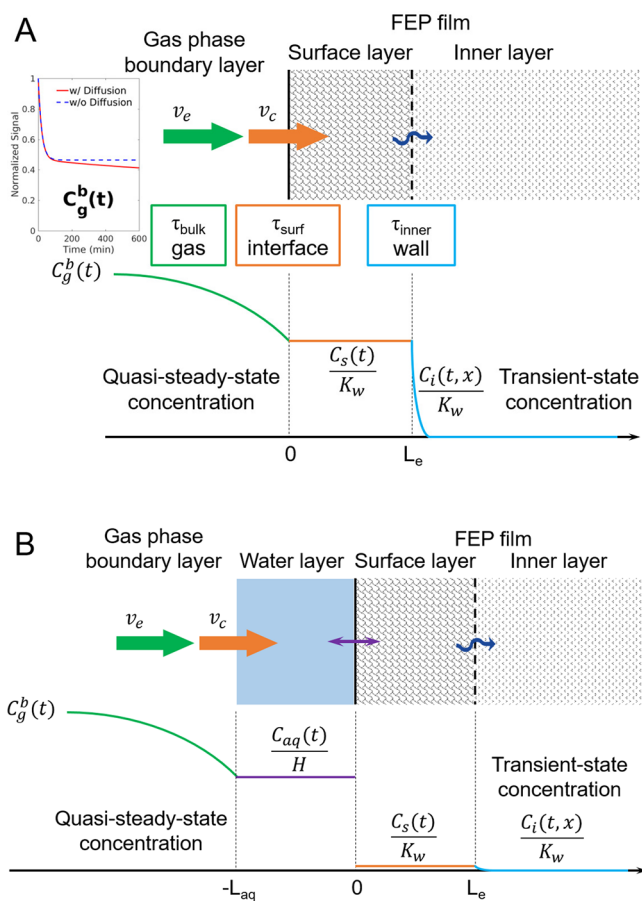
Figure 1. Two-layer (dry) and three-layer (moist) models of vapor uptake at the surface of Teflon film in a laboratory chamber. (A) Two-layer kinetic sorption model. v_e and v_c are gas-phase boundary layer and interfacial mass transport coefficients, respectively. $C_g^b(t)$ is the bulk gas-phase concentration, $C_s(t)$ is the concentration (assumed to rapidly achieve uniformity) within the Surface Layer, and C_i is the transient concentration in the Inner Layer. The vapor−Teflon wall equilibrium constant, K_w, plays a role similar to that of a Henry's law dissolution constant. Time scales, τ_{bulk}, τ_{surf}, and τ_{inner}, corresponding to each layer are indicated. (B) Vapor uptake process in the presence of a thin aqueous film on the Teflon wall. Assumption of $H \gg K_w$, where H is the corresponding Henry's Law constant, is made. $C_{aq}(t)$ denotes the concentration of dissolved vapor in the aqueous film. L_e and L_{aq} represent the surface layer and aqueous film thicknesses, respectively.

1A) by breaking interchain bonds, impeded by the stress exerted by the polymer network.

Surface Layer. The Teflon FEP film is treated as a solution into which the molecules dissolve. Matsunaga and Ziemann[3] proposed that vapor-wall partitioning equilibrium can be represented by an effective organic mass concentration of the wall itself, C_w, by analogy to the effective aerosol mass concentration used in describing vapor-particle uptake.[18] Here, we introduce C_w and C_w', respectively, to distinguish between the compound-independent and -dependent equivalent mass concentration of the Teflon wall. These quantities are related by $C_w' = \frac{C_w}{\gamma^\infty}$, where γ^∞ is the activity coefficient of the solute vapor dissolved in an infinitely dilute solution of Teflon film. The compound-dependent C_w' reflects, therefore, the effect of the compound's activity in Teflon film. The process of partitioning into C_w corresponds to the surface layer absorption.

It is advantageous to define an effective thickness of the surface layer, L_e'. L_e' is related to C_w' by $L_e' = \frac{V}{A} \frac{C_w'}{\rho_w}$, where V and A are the volume and surface area of the chamber, respectively, and the density of FEP film[19] is $\rho_w = 2150 \text{ kg m}^{-3}$. Note that this effective thickness L_e' is related to the physical thickness of the surface layer L_e by $L_e' = \frac{L_e}{\gamma^\infty}$. Measurements of C_w suggest that L_e is of order 1 nm,[3,9,12] corresponding to a sharp air−polymer interface. This behavior is similar to that of a typical vapor−liquid interface, wherein the density increases sharply from the bulk vapor to the bulk liquid over a distance of order 1 nm (10−20 nominal molecular diameters).[20] For water molecules, this distance is ~3.3−8.4 Å.[21] For Teflon film, in determining C_w', Matsunaga and Ziemann[3] assumed an effective molecular weight of Teflon film of 200 g mol^{-1}; we adopt this assumption here, for which the effective Teflon molecular diameter is 0.54 nm. We tentatively take $L_e = 5$ nm, corresponding to a value of $C_w = 32.2 \text{ mg m}^{-3}$ (assuming $\gamma^\infty = 1$ and $\frac{A}{V} = 3 \text{ m}^{-1}$), consistent with the suggestions by Krechmer et al.[12] and Yeh and Ziemann.[9] The molecular diffusivity in the swollen and stress-free surface layer, that is of order $10^{-13} \text{ m}^2 \text{ s}^{-1}$,[22] establishes a time scale of ~1 ms to achieve concentration uniformity within the surface layer.

A key parameter in the kinetic sorption model is the vapor−wall equilibrium constant, K_w, similar to a Henry's law constant. The dimensionless $K_w = \frac{\rho_w}{\gamma^\infty c*} \frac{MW_{voc}}{MW_w}$, where MW_{voc} and MW_w are the mean molecular weights of the VOC vapor and FEP film, respectively, and $c*$ is the saturation mass concentration of the vapor. Typically, the activity coefficient of a compound in Teflon film, γ^∞, is the only unknown parameter in the expression for K_w. Limited information exists to constrain the value of γ^∞, and the activity coefficient γ^∞ is often assumed to be unity.[3,9,12] Within the consistent model framework developed here, γ^∞ is defined as the ratio of the physical thickness of the surface layer, L_e, to the effective thickness, L_e'; that is, $\gamma^\infty = \frac{L_e}{L_e'}$. If $\gamma^\infty = 1$, the FEP film behaves as an ideal solution. If $\gamma^\infty > 1$, the vapor molecules prefer to remain in the gas phase; if $\gamma^\infty < 1$, vice versa. The values of γ^∞ for a wide variety of compounds calculated from the literature[3,5,9,12] as a function of $c*$ estimated by EVAPORATION[23,24] as shown in Figure S2-A and Table 1 indicate that $\gamma^\infty > 1$. The inverse linear relationship between γ^∞ and $c*$ suggests that the FEP polymer is not generally hospitable for VOCs. This behavior, however, does not conflict with the presence of low volatility compounds in the Teflon film, since the vapor−wall equilibrium constant depends more strongly on $c*$ than γ^∞, such that compounds with lower $c*$ will haver higher K_w values (see Table 1 for dependence of γ^∞ on $c*$). Furthermore, the equilibrium fraction of the solute remaining in the gas phase, F_g, (Figure S2−B) is consistent with the observation that less volatile compounds tend to reside preferentially in the wall.

Inner Layer. The magnitude of the inner layer (Figure 1) effective diffusivity, $\mathcal{D}_{eff}$, is key to determining the temporal behavior of the bulk gas-phase concentration, $C_g^b(t)$, in a sufficiently long-duration experiment (~10 h). $\mathcal{D}_{eff}$ is considered to be influenced by the existence of FEP film in a glassy state, a coexistence of liquid and solid states, the latter of which comprises immobile microvoids.[25] Dual sorption theory[26] asserts that whereas free molecules can diffuse through the liquid layer, deeper diffusion must satisfy the Langmuir adsorption isotherm on the inner surface of local microvoids.[26] As a result, the molecular diffusivity in polymer is lower than that in pure liquid

Table 1. Parameters Representing Vapor−Wall Deposition in the Chambers[a]

	parameter	expression
k_1	forward rate (s^{-1})	$\left(\frac{A}{V}\right)v_l$
k_{-1}	backward rate (s^{-1})	$\frac{10^9}{L_e K_w}v_l$ or $\left(\frac{A}{V}\right)v_l\frac{\gamma^\infty c^*}{10^3 C_w}\frac{MW_w}{MW_{voc}}$
k_2	first-order loss rate (s^{-1})	Figure 5 or from measurement[b]
L_e	surface layer thickness (nm)	5
K_w	dimensionless equilibrium constant	$\frac{10^9 \rho_w}{\gamma^\infty c^*}\frac{MW_{voc}}{MW_w}$
C_w	equivalent wall concentration (mg m^{-3})	$10.8\left(\frac{A}{V}\right)$
γ^∞	activity coefficient in FEP	$10^{3.299}(c^*)^{-0.6407}$ (Figure S2-A)
v_l	wall deposition velocity (m s^{-1})	$\left(\frac{\pi}{2}\frac{1}{\sqrt{k_e \mathcal{D}_g}} + \frac{4}{\alpha_w \omega}\right)^{-1}$
α_w	wall accommodation coefficient	$10^{-2.744}(c^*)^{-0.6566}$ (Figure S3)
$\mathcal{D}_{eff}$	effective diffusivity in FEP film (m^2 s^{-1})	$10^{-17.05}(\theta-110.9)^{-1.695}(c^*)^{0.1831}$
ρ_w	Teflon FEP density[19] (kg m^{-3})	2150
c^*	vapor saturation concentration (μg m^{-3})	species dependent (ref 23)
k_e	eddy diffusivity coefficient[12] (s^{-1})	$0.004 + 10^{-2.25}(V)^{0.74}$
V	chamber volume (m^3)	chamber dependent
A	chamber surface area (m^2)	chamber dependent
$\mathcal{D}_g$	diffusivity in gas phase (m^2 s^{-1})	5×10^{-6}
ω	mean molecular velocity (m s^{-1})	$\sqrt{\frac{8RT}{\pi MW_{voc}}}$
R	gas constant (kg m^2 s^{-2} K^{-1} mol^{-1})	8.314
MW_w	average molecular weight of FEP[3] (g mol^{-1})	200
MW_{voc}	vapor molecular weight (g mol^{-1})	species dependent
θ	molecular volume (cm^3 mol^{-1})	species dependent (Figure 3)

[a]The parameters listed here correspond to the dynamic system $X \underset{k_{-1}}{\overset{k_1}{\rightleftharpoons}} Y \overset{k_2}{\rightarrow} Z$, where X is the species of interest. Detailed discussion of the incorporation of this model framework into chamber models can be found in SI. VII. [b]It is recommended to fit the measured signal decay of species X to the analytical equation in SI. VI to obtain k_2, or simply use the asymptotic relationship $k_w^X = \frac{K_{eq}}{1 + K_{eq}}k_2$, where k_w^X is the "apparent" first-order decay rate constant of species X, and $K_{eq} = \frac{k_1}{k_{-1}}$. In general, the use of the asymptote will not lead to a significant difference if the measurement lasts several hours.

$(10^{-13} - 10^{-9}$ m^2 s^{-1}).[27] The overall $\mathcal{D}_{eff}$ of molecules absorbed in the Teflon inner layer is of order 10^{-22} to 10^{-17} m^2 s^{-1}, well within the range of semisolid diffusivities.[28] By fitting time-dependent Teflon uptake rates of a variety of species, one can estimate the $\mathcal{D}_{eff}$ values.

Governing Equations Describing Uptake of Vapor Molecules in the Two-Layer Model. The mass transport coefficients across the gas-phase boundary layer and through the vapor-Teflon interface (Figure 1) can be written as $v_e = \frac{2}{\pi}\sqrt{k_e \mathcal{D}_g}$ and $v_c = \frac{\alpha_w \omega}{4}$, respectively, where k_e is the eddy diffusivity coefficient for mixing in the chamber, $\mathcal{D}_g$ is the vapor molecular diffusivity in air, α_w is the vapor−wall accommodation coefficient (see discussion in SI. II), and ω is the vapor molecular mean speed. From mass transfer resistance theory, the overall mass

transport coefficient across the gas-phase boundary layer and the air-Teflon interface is $v_l = \left(\frac{1}{v_e} + \frac{1}{v_c}\right)^{-1}$. For quasi-steady state gas-phase boundary layer diffusion (see discussion in SI. I), the bulk gas-phase mass flux J_b (μg s^{-1}) to the Teflon surface is

$$J_b = Av_l\left(C_g^b(t) - \frac{C_s(t)}{K_w}\right) \tag{1}$$

where C_g^b is the gas-phase concentration in the bulk chamber and C_s is the concentration of vapor dissolved in the wall surface layer. The mass balance for C_g^b involving vapor-wall mass transfer and gas-phase chemical reactions is

$$\frac{dC_g^b(t)}{dt} = -\left(\frac{A}{V}\right)v_l\left(C_g^b(t) - \frac{C_s(t)}{K_w}\right) + \sum^i R_i \tag{2}$$

where $\sum^i R_i$ represents the net generation or consumption of the species by chemical reaction.

Within the Teflon surface layer, the diffusive flux, J_d (μg s^{-1}), at the surface layer−inner layer boundary is

$$J_d = -A\mathcal{D}_{eff}\frac{\partial C_i(x, t)}{\partial x}\bigg|_{x=L_e} \tag{3}$$

where C_i is the concentration of vapor molecules in the wall inner layer. Time-dependent mass conservation for C_s is given by

$$\frac{dC_s(t)}{dt} = \frac{v_l}{L_e}\left(C_g^b(t) - \frac{C_s(t)}{K_w}\right) + \frac{\mathcal{D}_{eff}}{L_e}\frac{\partial C_i(x, t)}{\partial x}\bigg|_{x=L_e} \tag{4}$$

Diffusion of the dissolved solute in the inner Teflon layer obeys

$$\frac{\partial C_i(x, t)}{\partial t} = \mathcal{D}_{eff}\frac{\partial^2 C_i(x, t)}{\partial x^2} \tag{5}$$

Associated initial and boundary conditions are

$$C_g^b(0) = C_{g0}^b; \quad C_s(0) = C_{s0}; \quad C_i(x, 0) = 0;$$
$$C_i(0, t) = C_s(t); \quad C_i(\infty, t) = 0 \tag{6}$$

C_{g0}^b and C_{s0} are appropriate initial concentrations. For example, $C_{s0} = 0$ corresponds to a pristine chamber condition, while $C_{g0}^b = \frac{C_{s0}}{K_w}$ applies if the bulk gas-phase and surface layer concentrations are at equilibrium at the beginning of an experiment. The boundary condition as $x \rightarrow \infty$ expresses the consequence of the slow diffusion in the inner layer relative to the overall extent of the layer itself. If $\mathcal{D}_{eff}$ is sufficiently small such that penetration into the inner layer is negligible over an experiment, the mass conservation equations reduce to a single-layer sorption model, in which the corresponding vapor−wall equilibrium time scale (τ_{vwe}) is

$$\tau_{vwe} = \left(\frac{A}{V}\right)^{-1}\left(1 + \frac{V}{K_w L_e A}\right)^{-1}v_l^{-1} \tag{7}$$

Table 1 summarizes the key parameters that represent vapor−wall deposition in chamber experiment simulations.

Aqueous Film Model. Under sufficiently high relative humidity conditions (RH > 90%), it is assumed that an aqueous film of thickness L_{aq} exists on the chamber wall (Figure 1B). Since the diffusivity of vapor molecules in water $\mathcal{D}_{aq}$ is $\sim 1 \times 10^{-9}$

m^2 s^{-1},[29] the estimated time scale $\left(\frac{L_{aq}^2}{\mathcal{D}_{aq}}\right)$ for the dissolved vapor concentration to reach uniformity in this thin layer of water is sufficiently small (e.g., ~10^{-1} s if L_{aq} = 10 μm) such that the rate-limiting step for uptake is either gas-phase boundary layer diffusion or interfacial accommodation at the air—water interface.

Since oxidized VOCs tend to be polar molecules, γ^∞ in aqueous solution should be smaller than that in a Teflon polymer solution, such that partitioning in the aqueous phase is preferred over the polymer phase. Thus, in this case, a reasonable assumption is that vapor partitioning does not proceed beyond the thin water film on the Teflon surface.

For this single-layer model, eq 7 can be directly applied to the aqueous film uptake, replacing K_w and L_e with the Henry's law constant H and L_{aq}, respectively. As described in SI. II, on the basis of measured time scale and equilibrium constants, it is possible to estimate the accommodation coefficient of the water surface.

■ EXPERIMENTAL STUDY OF VAPOR—WALL UPTAKE

To study vapor—wall interaction, we either (i) generated the compounds in situ by VOC oxidation in the chamber,[10,12,30−34] or (ii) injected the compounds of interest (purchased or synthesized) into the chamber.[2,3,9,28,35−38] The two-layer kinetic model is applied to two laboratory data sets from the Caltech Environmental Chamber (24 m^3, $\frac{A}{V} \sim 2$ m^{-1}) on the dynamics of vapor—wall deposition of individual compounds: (i) Zhang et al.[10] corresponding to in situ generation and (ii) deposition measurements of alcohols (1-hexanol 98%, 1-heptanol 98%, 1-octanol ≥ 99%, 1-nonanol 98%, 1-decanol ≥ 99%, 1-undecanol ≥ 97.5%, and 1-dodecanol 98%), aromatics (toluene 99.8%, m-xylene ≥ 99%, o-xylene 98%, and 1,3,5-trimethylbenzene 98%), alkanes (n-dodecane ≥ 99%, n-tridecane ≥ 99%, n-tetradecane ≥ 99%, n-octylcyclohexane 98%), and biogenics (isoprene 99%, methacrolein 95%, methyl vinyl ketone 99%, and α-pinene ≥ 99%) (all purchased through Sigma-Aldrich) by direct injection.

In the experiments conducted by Zhang et al.,[10] in situ oxidation of α-pinene, n-dodecane, toluene, and isoprene were carried out under high- and low-NO$_x$ conditions, with oxidation periods varying from 1 to 7 h. A customized CF$_3$O$^-$−CIMS[39] (chemical ionization mass spectrometry) was used to monitor the vapor-wall decay rates. Refer to Zhang et al.[10] for more experimental details. In the direct injection experiments, a bulb containing 10 to 50 μL of pure or mixed liquid VOCs was maintained at 65 °C (as well as the 50 cm stainless injection line, 3/8 in. OD) to ensure complete injection at a flow rate of 5 L min^{-1} of clean air (~100 ppb in the chamber, several orders of magnitude lower than the saturation vapor pressure). Before each injection, the chamber has been flushed with clean air at a flow rate of 370 L min^{-1} for 24 h at 45 °C. The injection period varied from minutes (biogenics) to hours (alcohols). After the injection period, 5 pulse injections of clean air were used to actively mix the chamber without significantly altering its volume. The chamber is considered to be well mixed ~5 min after this operation, which is especially relevant for compounds with short injection periods. A series of RH-dependent studies were carried out in the chamber under 8% ± 5%, 50% ± 5%, and 80% ± 5% RH at 20 °C.

Over ~18 h in the dark, a gas chromatograph with flame ionization detector (GC/FID, Agilent 6890N) was used to monitor the temporal concentration changes at a continuous sampling flow rate of 0.29 L min^{-1} through a perfluoroalkoxy (PFA) Teflon tube (1/4 in. o.d., 3/16 in. i.d., and 2.0 m length). Pagonis et al.[40] note that the use of a PFA Teflon tube induces a response time lag for "sticky" compounds; the continuous flow through the sampling tube and lower sampling time resolution (~10 min) act to smooth this effect. A HP-5 column (30 m × 0.32 mm i.d. × 0.25 μm film thickness) was used for alcohols, aromatics, alkanes, and α-pinene, and a HP-PLOT Q column (15 m × 0.53 mm i.d. × 40 μm film thickness) was used for isoprene, methacrolein (MACR), and methyl vinyl ketone (MVK). For mixtures, the GC temperature ramping procedure was adjusted to obtain full peak resolution. It is challenging to clearly define the start time for GC measurements of compound dark decay. We ignore the first 3 to 5 data points of the GC measurements, which is ~1 h after injection, on the assumption that the vapor concentrations in the gas phase and the surface layer have reached equilibrium.

Additionally, studies of in situ 20 s-pulse generated compounds[12] from isoprene oxidation under 8% ± 5%, 50% ± 5%, and > 90% RH were carried out. When RH was greater than 90%, an aqueous film was introduced to the surface of Teflon film by injecting water vapor into the chamber at 30 °C until the RH reached ~80% and cooling to 20 °C to facilitate a uniform water film condensation on the wall, as evidenced visually by the blurry appearance of the chamber. Isoprene (~200 ppb), ~1.2 ppm of NO (Airgas, 500 ppm ±1%), and ~1.2 ppm of CH$_3$ONO (synthesized following Taylor et al.[41]) were injected to the chamber, respectively. UV lights were turned on for 20 s (j_{NO_2} = 0.0044 s^{-1}), and no nucleation was observed after lights off. Oxidation products were monitored with a custom-modified I$^-$-CIMS[42] with a 2 L min^{-1} sampling rate through $^1/_4$ in. PFA tube. A permeation tube with pure liquid CH$_3$I (Sigma-Aldrich, 99%) was used for reagent ion generation in I$^-$-CIMS, where vapor molecules X are detected as the cluster (X·I$^-$).

In the two-layer kinetic model simulation, the values of k_e and $\mathcal{D}_g$ used are 0.075 s^{-1} and 5 × 10^{-6} m^2 s^{-1}, respectively, for all compounds.[6] The accommodation coefficient α_w is calculated by a fitted empirical equation based on literature data (Table 1 and Figure S3, see SI. II for details). Activity coefficients for the compounds studied in Zhang et al.[10] are predicted by the equation in Table 1 and Figure S2-A. Since the oxidation period in Zhang et al.[10] varied from 1 to 7 h, it is reasonable to assume that an equilibrium state between the bulk chamber and the surface layer had been reached; that is, $C_g^b = \frac{C_s}{K_w}$, when lights are off. This assumption excludes the oxidation period from the fitting process. We will address subsequently the effect of the oxidation period on the temporal profile of bulk concentration.

■ RESULTS AND DISCUSSION

Effect of Oxidation Period on Vapor—Wall Partitioning. To study vapor—wall interaction, the species of interest is introduced to the chamber by either direct injection or in situ generation. During injection, the more volatile compounds generally require less time to inject but achieve wall partitioning more slowly (e.g., n-alkanes[3]), whereas less volatile compounds require a longer injection time, during which the bulk chamber and the wall may have already reached equilibrium when injection is completed. Even though the injection period can be shortened by heating the bulb and the injection line,[3,9] for passively mixed chambers the chamber mixing time scale may be the limiting factor to obtain a well-mixed concentration in the chamber. This mixing issue is avoided with in situ generation of

oxidation products. Ideally, the VOC oxidation period is short, so as to approximate as closely as possible a pulse input of oxidation products.[12] This is important, as the anticipated equilibration time between generation in the chamber and absorption by the surface layer of Teflon is of order 10^3 s.[12] However, generation of detectable concentration of products usually requires a relatively long oxidation time (OH concentration is typically $\sim 10^6$ molecules cm^{-3}), during which period equilibrium between the bulk chamber and the surface layer is likely to be achieved.

An idealized kinetic model is useful to describe the interplay between in situ oxidation and the approach to vapor–wall equilibrium. Let us assume that the VOC oxidation can be represented by the first-order reaction $G \xrightarrow{k_0} X$, where G is the VOC precursor, X is the oxidation product (i.e., the bulk concentration $C_g^b(t)$ in eq 2), and k_0 is an effective first-order rate constant. Since diffusion in the inner layer of the Teflon film is sufficiently slow, it is reasonable to ignore the inner layer uptake of the vapors during the oxidation period, that is, the second term in eq 4. By multiplying a scaling factor $\frac{A}{V}L_e$ to $C_s(t)$ in eq 4, the system can be represented kinetically by $G \xrightarrow{k_0} X \underset{k_{-1}}{\overset{k_1}{\rightleftharpoons}} Y$, where $Y = \frac{A}{V}L_e C_s(t)$, $k_1 = \frac{A}{V}v_1$, and $k_{-1} = \frac{1}{L_e K_w}v_1$. The equilibrium constant for this system is $K_{eq} = \frac{k_1}{k_{-1}} = K_w\frac{A}{V}L_e$. By this representation, vapor–wall partitioning during the VOC oxidation period is mathematically analogous to a classical equilibrium reaction system.

The departure from vapor–wall equilibrium at the end of the reaction period is defined by the normalized deviation $\epsilon = \frac{Y_e - Y_0}{Y_e} = \frac{X_0 - X_e}{X_e K_{eq}}$, where X_0 and Y_0 are the concentrations of X and Y at the end of the oxidation period, and X_e and Y_e are the concentrations at equilibrium. Thus, a value of $\epsilon = 0$ indicates that equilibrium has already been reached at the end of the oxidation period, whereas a value of ϵ close to 1 suggests that from the measured concentration change of X one can derive the characteristic time scale and equilibrium constant for vapor–wall deposition. Note that it is necessary only to focus on species X since that is the compound being measured. An analytical solution for the time-dependent dynamics of this kinetic system is given in SI. III.

For the compounds examined in this study and by Zhang et al.,[10] the oxidation period τ_{ox} varies from ~ 10 s to ~ 7 h. Assuming that 5% of the precursor G is consumed at the end of the oxidation period, the reaction rate constant k_0 follows the relationship $\tau_{ox}k_0 = 0.05$. The forward rate constant k_1 is determined by the mixing time scale in the chamber (k_e), as well as the surface accommodation coefficient (α_w). Using $k_e = 0.075$ s^{-1}, $\mathcal{D}_g = 5 \times 10^{-6}$ m^2 s^{-1}, and $\alpha_w = 10^{-5}$ (discussion in SI. II suggests that most of the compounds studied here are located in the gas-phase boundary layer diffusion regime, where the critical $\alpha_w \sim 10^{-6}$, for simplicity, a fixed value of 10^{-5} for α_w is assumed here), a value of $k_1 = 4.02 \times 10^{-4}$ s^{-1} is obtained, which is of the same order of magnitude as the values reported in the wall deposition study by Krechmer et al.[12] A contour plot (Figure 2) of ϵ as a function of vapor–wall equilibrium constant, $K_w\frac{A}{V}L_e$, and oxidation period, τ_{ox}, indicates that the majority ($\sim 75\%$) of the compounds studied in Zhang et al.[10] had already reached vapor–wall equilibrium at the end of the relatively lengthy oxidation period. In such a case, it is reasonable to estimate the
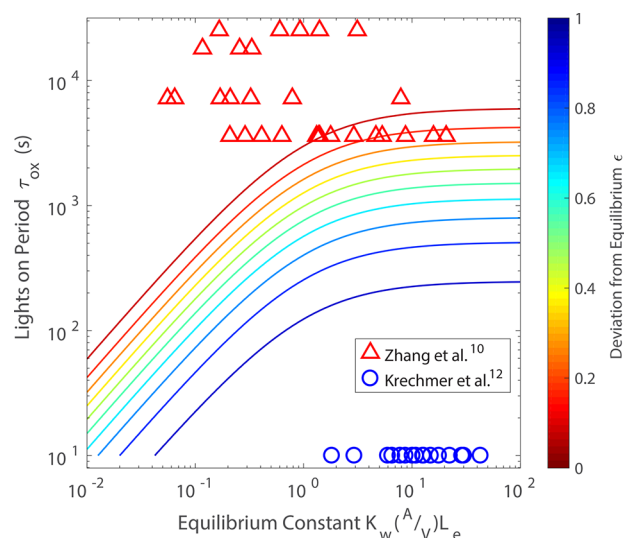

Figure 2. Deviation from equilibrium state at the end of oxidation period τ_{ox} as a function of equilibrium constant $K_W(A/V)L_e$ and oxidation period τ_{ox} for the system represented by $G \xrightarrow{k_0} X \underset{k_{-1}}{\overset{k_1}{\rightleftharpoons}} Y$, where $k_0 = 0.05/\tau_{ox}$ (s^{-1}, assume 5% of G is consumed at the end of oxidation period τ_{ox}), $k_1 = (A/V)v_1$ (s^{-1}), $k_{-1} = (1/L_e K_w)v_1$ (s^{-1}), A/V is the surface area to volume ratio of the chamber (m^{-1}), v_1 is the vapor-to-wall mass transport coefficient (m s^{-1}), L_e is the surface layer thickness (m), and K_w is the dissolution equilibrium constant of vapor molecule in the Teflon film. The equilibrium constant $K_{eq} = \frac{k_1}{k_{-1}} = K_w\frac{A}{V}L_e$.

diffusivity in the inner layer by assuming equilibrium between the bulk chamber and the surface layer. The small value of the wall accommodation coefficient reported by Zhang et al.[10] likely represents a combination of surface accommodation and inner layer diffusion. Figure 2 shows explicitly the effect of the length of the oxidation period on the surface-layer equilibrium process, since inner-layer diffusion will dominate the dynamics of the vapor sink in a long-duration oxidation experiment.

Diffusion in Teflon Polymer. The inferred diffusivities $\mathcal{D}_{eff}$ of species dissolved in Teflon film obtained by fitting data to the two-layer model as a function of the molecular saturation concentration c^* are shown in Figure 3A. $\mathcal{D}_{eff}$ values are in the range of 10^{-22} to 10^{-17} m^2 s^{-1}, which is of the order 10^6 smaller than those of small organic molecules in polymer film,[22,27,43] a result that is consistent with the higher energy barrier for larger molecules.[17,43] A transition state between solid and liquid diffusivities of this order of magnitude is well within the range of those in semisolid organic aerosol particles.[27]

With the assumption that the molecular diffusivity in the FEP film can be expressed as a function of molecular volume, we apply a semiempirical equation to correlate the diffusivity as a function of vapor molecular volume (θ in cm^3 mol^{-1})[44] and vapor saturation concentration (c^* in μg m^{-3}). c^* is used as the parameter that incorporates the contribution from different functional groups, and as noted earlier, is estimated by the empirical routine EVAPORATION.[23,24] The diffusivities obtained from the semiempirical eq (Table 1) are shown in Figure 3B. 95% of the predicted diffusivities lie within an order of magnitude of those inferred $\mathcal{D}_{eff}$. The high order of negative molecular volume dependence is consistent with the expectation that the larger the molecule, the smaller the diffusivity. The critical volume in the semiempirical eq (110.9 cm^3 mol^{-1}) can be viewed as a characteristic "hole" in the film; thus, small molecules
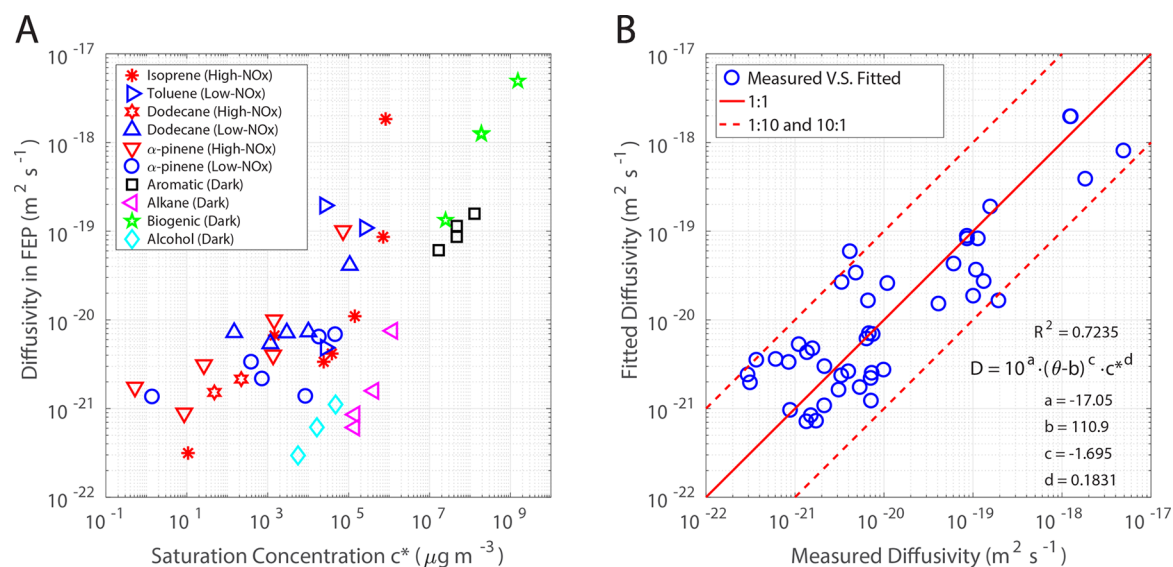
Figure 3. (A) Diffusivity in FEP film inferred from measurements by Zhang et al.[10] using CIMS and from this study using GC/FID as a function of saturation concentration ($c*$) predicted by EVAPORATION.[23,24] (B) Comparison between measured and fitted diffusivity ($\mathcal{D}_{eff}$ in m² s⁻¹) in Teflon film. The molecular volume (θ in cm³ mol⁻¹) and saturation vapor concentration ($c*$ in μg m⁻³) dependent fitting equation in panel B is used. Molecular volume is estimated by summing the characteristic atomic volumes ($\theta = C \times 16.35 + H \times 8.71 + O \times 12.43 + N \times 14.39$ cm³ mol⁻¹, where C, H, O, and N represent the number of carbon, hydrogen, oxygen, and nitrogen atoms in the compound).[44] Note: this equation applies only for molecules with a volume exceeding 110.9 cm³ mol⁻¹.
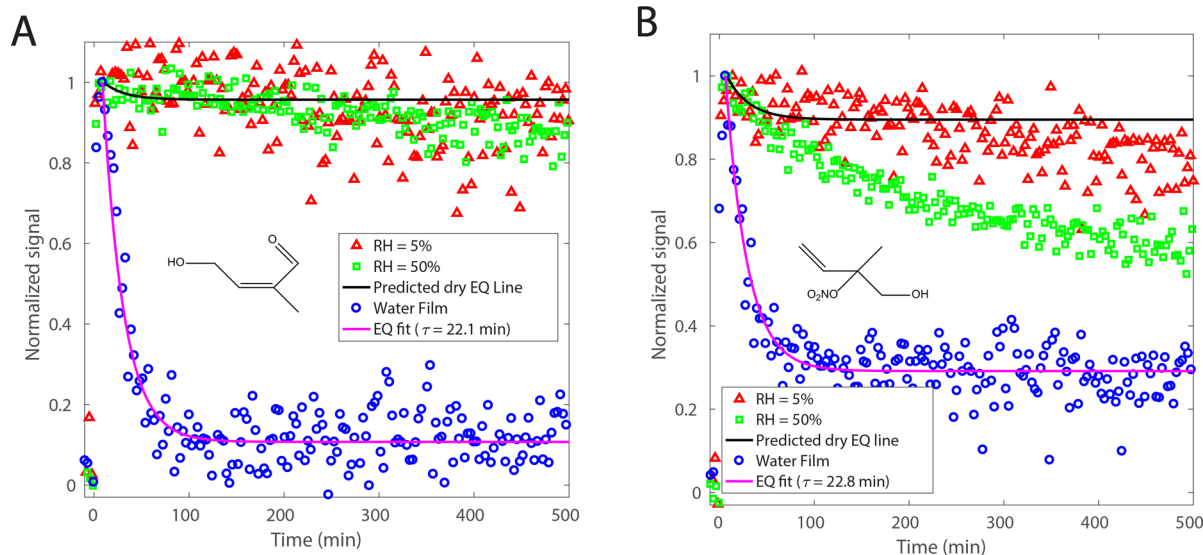
Figure 4. Signal decay after 20 s of in situ generation of isoprene oxidation products: (A) $C_5H_8O_2$ and (B) $C_5H_9O_4N$ at RH = 5%, 50%, and >90% (with aqueous film). Because of the signal decay caused by the "memory effect" arising from the sampling tube and instrument inlet,[40] the peaks show up ~5 min after lights off.

only have to overcome the cross-links between polymer chains. The fitted value of the critical volume is found to exceed those of most of the molecules studied previously;[22,43] thus the semiempirical relation given in Figure 3B cannot be used for molecules smaller than the critical volume. The diffusivity is found to be mildly dependent on vapor saturation concentration, reflecting the effect of the presence of functional groups (or molecular shape) on molecular diffusivity.

Diffusivities of vapor molecules in fresh and aged Teflon chambers have also been investigated. Though the absorption properties of the surface layer were reported to be unchanged in either fresh or aged Teflon chambers,[3] by fitting experimental data in the Caltech chamber,[10] we found that the inner layer

diffusivity increased with use of chambers, consistent with the observations by Loza et al.[2] Such behavior could be attributed to alteration of interchain bonds, such that subsequent diffusion is characterized by internal stress relaxation.[17,43] See the discussion in SI.IV for additional details.

Humidity Effect. For polymer film chambers, permeation of ubiquitous ambient water vapor through the film is possible given the small molecular volume and high diffusivity ($\sim 10^{-12}$ m² s⁻¹) of water in such polymer films.[45] The dissolution of water molecules in the Teflon film can exert an impact on the behavior of organic molecules therein. For hydrophilic compounds, the water could facilitate the absorption of the vapors into the film, while for hydrophobic compounds, it could exert a retarding

effect. In the high humidity case, in which an aqueous film is hypothesized to be present on the Teflon surface (panel B of Figure 1), it is evident that hydrophilic compounds would dissolve in the aqueous film.

The limited studies of RH-dependent vapor−wall interaction in chambers that exist report that the vapor−wall loss rate increases at higher RH (>50%).[2,35,37,38] It is notable that the compounds that have been studied in this regard are either reactive with water (e.g., IEPOX[35,37]) or highly water-soluble (e.g., HCOOH, H_2O_2,[38] and glyoxal[2]). These observations are consistent with the existence of water molecules in the Teflon film facilitating the absorption of hydrophilic compounds. We used two experimental strategies to investigate the role of RH in vapor−wall interaction.
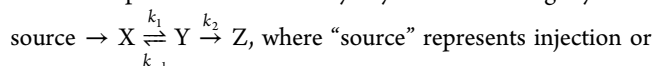
In the first class of experiments, we injected into the chamber at different RH levels several groups of compounds (alcohols, alkanes, aromatics, and biogenics) that are not highly water-soluble and have relatively large molecular volume. A GC/FID was used to monitor the long-term dark decay of these compounds. The inferred diffusivities of the alcohols, alkanes, aromatics, and biogenics in Teflon are shown in Figure S5, indicating that most of the diffusivities decrease as RH increases. It is expected that at high RH, more water molecules dissolve in the Teflon film, such that intrusion of hydrophobic compounds is hindered.

Second, we carried out the same experimental protocol as that of Krechmer et al.[12] based on an in situ pulse generation of oxidation products (OH concentration is ∼10^8 molecules cm^{-3}). The temporal profiles of two isoprene oxidation products ($C_5H_8O_2$ and $C_5H_9O_4N$) are shown in Figure 4. Under dry conditions (RH ∼ 5%), $C_5H_8O_2$ and $C_5H_9O_4N$ exhibit essentially the same diffusivities as those observed by Zhang et al.[10] However, at RH ∼ 50%, the two compounds behave differently; a faster decay rate is observed for $C_5H_9O_4N$, which is likely attributable to hydrolysis of the compound containing a −ONO_2 group.[46] When a water film is introduced intentionally (RH > 90%), the signals of both compounds decrease rapidly after the lights are off at almost the same rates, reaching a constant level for the next 8 h. By fitting the data at RH > 90% in Figure 4 to the aqueous film model (Figure 1B), a characteristic time scale is found to be ∼22 min for each compound, considerably faster than that due to inner layer diffusion under dry conditions. This value is in the range of vapor−wall equilibrium time scales (τ_w) reported by Krechmer et al.[12] and Matsunaga and Ziemann.[3] With an estimated chamber eddy diffusivity of 0.075 s^{-1},[6] the calculated accommodation coefficients of $C_5H_8O_2$ and $C_5H_9O_4N$ at the water surface are 3.06×10^{-5} and 1.32×10^{-5}, respectively, consistent with gas-phase boundary layer mass transport being the rate-limiting step in the fast equilibrium sorption process.

The water film serves as a substantial reservoir given that both compounds are water active (soluble or reactive). By comparison, the inferred equilibrium constants, K_{eq}, for both compounds in the aqueous film exceed those in the dry Teflon film by factors of 186 and 21, suggesting that the majority of the vapor molecules remain within the aqueous layer. The results of this aqueous film experiment are consistent with the conclusion that in SOA formation experiments under high RH conditions, the presence of a condensed water film on the wall will exacerbate vapor−wall loss of hydrophilic oxidation products.

Mechanistic Representation of Vapor−Wall Deposition. After the introduction of vapors into the chamber (either by injection or in situ generation), loss due to wall uptake is generally reported as first order. The experimental results reported here show that, in addition to the establishment of rapid equilibrium between the bulk gas phase and the surface layer of the chamber wall ($\tau_{surf} \sim 10^3$ s), inner layer diffusion as well as chemical reactions (e.g., hydrolysis) can lead to a continuous decay of the gas-phase vapors in the bulk chamber. This process can be represented kinetically by the following system: source → $X \underset{k_{-1}}{\overset{k_1}{\rightleftharpoons}} Y \overset{k_2}{\rightarrow} Z$, where "source" represents injection or in situ oxidation. Species X and Y represent the same compound in different phases, and species Z is the same compound in the third phase (e.g., the inner layer in this case). Correspondingly, k_2 represents either the first-order chemical reaction rate constant or the mass transfer coefficient. The forward and backward rate constants k_1 and k_{-1} govern the approach to phase equilibrium of X and Y.

When injection or in situ oxidation has ceased, the above dynamic system can be represented simply as $X \underset{k_{-1}}{\overset{k_1}{\rightleftharpoons}} Y \overset{k_2}{\rightarrow} Z$. If species X and Y have reached equilibrium, and if $k_2 \ll k_1 + k_{-1}$, a slow decay follows a rapid equilibrium. The time-dependent analytical solution of this kinetic system is presented in SI. VI. The apparent first-order decay rate constant, k_w^X, of species X exhibits the long-time asymptote $\frac{K_{eq}}{1+K_{eq}}k_2$, where $K_{eq} = \frac{k_1}{k_{-1}}$ as defined above.

The net loss rate constant k_2 is a function of diffusivity $\mathcal{D}_{eff}$. To obtain a relationship between k_2 and $\mathcal{D}_{eff}$, an empirical equation can be fitted as shown in Figure 5, where k_2 and $\mathcal{D}_{eff}$ both emerge from fitting experimental data from the equilibrium reaction model and the two-layer diffusion model. For comparison, k_2 values derived from reported apparent first-order loss rates, k_w, by the asymptotic relationship, $k_w = \frac{K_{eq}}{1+K_{eq}}k_2$, and the inferred diffusivities are shown in Figure 5. Many of these reported data
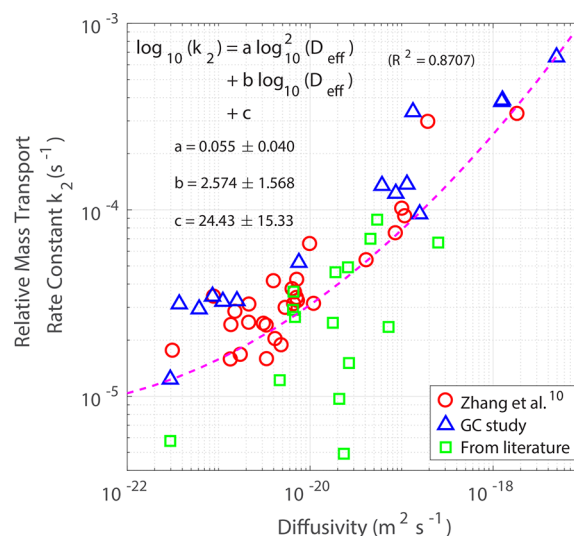
Figure 5. Empirical relationship between compound molecular diffusivity $\mathcal{D}_{eff}$ (m^2 s^{-1}) and relative inner layer mass transport rate constant k_2 (s^{-1}). k_2 is derived by fitting the analytical solution in SI.V to the experimental data, whereas data points from the literature[2,28,30−33,35,36] are calculated by the asymptotic relationship between k_w (reported data) and k_2. Diffusivity is predicted by the equation in Figure 3.

points lie within the uncertainty of the empirical relationship. The small reported k_2 values may be the result of different chamber conditions,[30,32,35] or the use of the asymptote, since some of the data are from the observation within 2 h (as indicated in SI. VI, in the short time period, the apparent k_w is small). Note that this empirical relationship does not account for the presence of heterogeneous reactions, which may change the value of k_2.

Atmospheric Implications. Teflon-walled laboratory chambers serve as the predominant system for the study of atmospheric SOA formation. Clear evidence exists for the deposition of VOC oxidation products on polymeric Teflon chamber walls. Such deposition removes products that would otherwise condense onto particles as SOA. Since the presence of wall deposition of vapors leads to an underestimate of the atmospheric SOA-forming potential of the parent VOC, data that have been influenced by such wall deposition will lead to an underprediction of SOA formation when extrapolated to the atmosphere.

The wall deposition process involves transport of vapor molecules from the core of the chamber to a boundary layer on the wall of the chamber, through which vapors are transported to the wall surface by a combination of molecular diffusion and macroscopic mixing. Vapor molecules diffuse into the Teflon polymer matrix by a process akin to that of uptake into a condensed phase. Observed rates of molecular uptake into Teflon polymer are found to be consistent with a model of the Teflon film consisting of two layers: (1) a thin surface layer into which vapor molecules penetrate first through the gas-phase boundary layer and second across the interface, over a time scale of order 10^3 s; and (2) a deeper layer of effectively semi-infinite extent into which the absorbed vapor molecules diffuse from the surface layer. The uptake rates by Teflon-walled chamber of over 90 individual organic vapor species are found to depend upon their molecular saturation vapor concentration (c^*) and molecular size (θ).

Semiempirical equations have been formulated to describe the absorptive properties (γ^∞ and α_w) of the surface layer and the diffusivity in the inner layer of FEP film. Additional studies are needed to characterize the temperature effect on the vapor uptake process. Water molecules dissolved in the Teflon film provide extra sinks on the wall for hydrophilic compounds. Under sufficiently high RH conditions, where a thin film of condensed water is present on the Teflon surface, the wall becomes an increasingly competitive reservoir for hydrophilic compounds. The challenge is to design VOC oxidation chamber experiments under different RH levels so as to minimize vapor transport to the chamber walls. To better constrain the measured vapor−wall loss rate (e.g., the "apparent" first-order rate constant k_w), recommended parameters and guidelines are given in Table 1, which can facilitate a comprehensive consideration of the sinks of gas-phase species in a typical SOA formation experiment.

ASSOCIATED CONTENT

Supporting Information

This material is available free of charge via the Internet at http://pubs.acs.org/. The Supporting Information is available free of charge on the ACS Publications website at DOI: 10.1021/acs.est.7b05575.

> Discussion of the time scale of gas-phase boundary layer transport; parametrization of the activity and accommodation coefficients in the surface layer absorption; additional calculations; diffusivities in fresh and aged

Teflon chambers; humidity effect on Teflon inner layer diffusivity; application of the two-layer framework in chamber simulations (PDF)

AUTHOR INFORMATION

Corresponding Author
*Phone: +1 626 395 4635; fax: +1 626 568 8743; e-mail: seinfeld@caltech.edu.

ORCID
Ran Zhao: 0000-0002-1096-7632
Christopher M. Kenseth: 0000-0003-3188-2336
Xuan Zhang: 0000-0003-1548-8021
John H. Seinfeld: 0000-0003-1344-4068

Notes
The authors declare no competing financial interest.

REFERENCES

(1) Schwantes, R. H.; McVay, R. C.; Zhang, X.; Coggon, M. M.; Lignell, H.; Flagan, R. C.; Wennberg, P. O.; Seinfeld, J. H. *Advances in Atmospheric Chemistry*; World Scientific, 2017; Chapter 1 Science of the Environmental Chamber, pp 1−93.

(2) Loza, C. L.; Chan, A. W. H.; Galloway, M. M.; Keutsch, F. N.; Flagan, R. C.; Seinfeld, J. H. Characterization of vapor wall loss in laboratory chambers. *Environ. Sci. Technol.* **2010**, *44*, 5074−5078.

(3) Matsunaga, A.; Ziemann, P. J. Gas-wall partitioning of organic compounds in a Teflon film chamber and potential effects on reaction product and aerosol yield measurements. *Aerosol Sci. Technol.* **2010**, *44*, 881−892.

(4) McVay, R. C.; Cappa, C. D.; Seinfeld, J. H. Vapor-wall deposition in chambers: Theoretical considerations. *Environ. Sci. Technol.* **2014**, *48*, 10251−10258.

(5) Yeh, G. K.; Ziemann, P. J. Alkyl nitrate formation from the reactions of C8-C14 n-alkanes with OH radicals in the presence of NOx: Measured yields with essential corrections for gas-wall partitioning. *J. Phys. Chem. A* **2014**, *118*, 8147−8157.

(6) Zhang, X.; Cappa, C. D.; Jathar, S. H.; McVay, R. C.; Ensberg, J. J.; Kleeman, M. J.; Seinfeld, J. H. Influence of vapor wall loss in laboratory chambers on yields of secondary organic aerosol. *Proc. Natl. Acad. Sci. U. S. A.* **2014**, *111*, 5802−5807.

(7) Bian, Q.; May, A. A.; Kreidenweis, S. M.; Pierce, J. R. Investigation of particle and vapor wall-loss effects on controlled wood-smoke smog-chamber experiments. *Atmos. Chem. Phys.* **2015**, *15*, 11027−11045.

(8) Krechmer, J. E.; et al. Formation of low volatility organic compounds and secondary organic aerosol from isoprene hydroxyhydroperoxide low-NO oxidation. *Environ. Sci. Technol.* **2015**, *49*, 10330−10339.

(9) Yeh, G. K.; Ziemann, P. J. Gas-wall partitioning of oxygenated organic compounds: Measurements, structure-activity relationships, and correlation with gas chromatographic retention factor. *Aerosol Sci. Technol.* **2015**, *49*, 727−738.

(10) Zhang, X.; Schwantes, R. H.; McVay, R. C.; Lignell, H.; Coggon, M. M.; Flagan, R. C.; Seinfeld, J. H. Vapor wall deposition in Teflon chambers. *Atmos. Chem. Phys.* **2015**, *15*, 4197−4214.

(11) Cappa, C. D.; Jathar, S. H.; Kleeman, M. J.; Docherty, K. S.; Jimenez, J. L.; Seinfeld, J. H.; Wexler, A. S. Simulating secondary organic aerosol in a regional air quality model using the statistical oxidation model - Part 2: Assessing the influence of vapor wall losses. *Atmos. Chem. Phys.* **2016**, *16*, 3041−3059.

(12) Krechmer, J. E.; Pagonis, D.; Ziemann, P. J.; Jimenez, J. L. Quantification of gas-wall partitioning in Teflon environmental chambers using rapid bursts of low-volatility oxidized species generated in situ. *Environ. Sci. Technol.* **2016**, *50*, 5757−5765.

(13) La, Y. S.; Camredon, M.; Ziemann, P. J.; Valorso, R.; Matsunaga, A.; Lannuque, V.; Lee-Taylor, J.; Hodzic, A.; Madronich, S.; Aumont, B. Impact of chamber wall loss of gaseous organic compounds on secondary organic aerosol formation: explicit modeling of SOA formation from alkane and alkene oxidation. *Atmos. Chem. Phys.* **2016**, *16*, 1417−1431.

(14) Nah, T.; McVay, R. C.; Zhang, X.; Boyd, C. M.; Seinfeld, J. H.; Ng, N. L. Influence of seed aerosol surface area and oxidation rate on vapor wall deposition and SOA mass yields: a case study with α-pinene ozonolysis. *Atmos. Chem. Phys.* **2016**, *16*, 9361−9379.

(15) Trump, E. R.; Epstein, S. A.; Riipinen, I.; Donahue, N. M. Wall effects in smog chamber experiments: A model study. *Aerosol Sci. Technol.* **2016**, *50*, 1180−1200.

(16) Ye, P.; Ding, X.; Hakala, J.; Hofbauer, V.; Robinson, E. S.; Donahue, N. M. Vapor wall loss of semi-volatile organic compounds in a Teflon chamber. *Aerosol Sci. Technol.* **2016**, *50*, 822−834.

(17) Crank, J. A theoretical investigation of the influence of molecular relaxation and internal stress on diffusion in polymers. *J. Polym. Sci.* **1953**, *11*, 151−168.

(18) Seinfeld, J. H.; Pankow, J. F. Organic atmospheric particulate material. *Annu. Rev. Phys. Chem.* **2003**, *54*, 121−140.

(19) PTFE, FEP, and PFA Specifications. Boedeker, 2014; http://www.boedeker.com/feppfa_p.htm.

(20) Frezzotti, A. Boundary conditions at the vapor-liquid interface. *Phys. Fluids* **2011**, *23*, 030609.

(21) Davidovits, P.; Jayne, J. T.; Duan, S. X.; Worsnop, D. R.; Zahniser, M. S.; Kolb, C. E. Uptake of gas molecules by liquids: a model. *J. Phys. Chem.* **1991**, *95*, 6337−6340.

(22) Tokarev, A.; Friess, K.; Machkova, J.; Sipek, M.; Yampolskii, Y. Sorption and diffusion of organic vapors in amorphous Teflon AF2400. *J. Polym. Sci., Part B: Polym. Phys.* **2006**, *44*, 832−844.

(23) Vapour pressure of Pure Liquid Organic Compounds. Tropo, 2014; http://tropo.aeronomie.be/models/evaporation_run.htm.

(24) Compernolle, S.; Ceulemans, K.; Müller, J.-F. EVAPORATION: a new vapour pressure estimation method for organic molecules including non-additivity and intramolecular interactions. *Atmos. Chem. Phys.* **2011**, *11*, 9431−9450.

(25) Frisch, H. L. Sorption and transport in glassy polymers - a review. *Polym. Eng. Sci.* **1980**, *20*, 2−13.

(26) Vieth, W.; Howell, J.; Hsieh, J. Dual sorption theory. *J. Membr. Sci.* **1976**, *1*, 177−220.

(27) Shiraiwa, M.; Ammann, M.; Koop, T.; Pöschl, U. Gas uptake and chemical aging of semisolid organic aerosol particles. *Proc. Natl. Acad. Sci. U. S. A.* **2011**, *108*, 11003−11008.

(28) Shiraiwa, M.; Yee, L. D.; Schilling, K. A.; Loza, C. L.; Craven, J. S.; Zuend, A.; Ziemann, P. J.; Seinfeld, J. H. Size distribution dynamics reveal particle-phase chemistry in organic aerosol formation. *Proc. Natl. Acad. Sci. U. S. A.* **2013**, *110*, 11746−11750.

(29) Schwarzenbach, R. P.; Gschwend, P. M.; Imboden, D. M. *Environmental Organic Chemistry*, 2nd ed.; John Wiley & Sons, Inc.: Hoboken, NJ, 2005.

(30) Praske, E.; Crounse, J. D.; Bates, K. H.; Kurtén, T.; Kjaergaard, H. G.; Wennberg, P. O. Atmospheric fate of methyl vinyl ketone: Peroxy radical reactions with NO and HO2. *J. Phys. Chem. A* **2015**, *119*, 4562−4572.

(31) Schwantes, R. H.; Teng, A. P.; Nguyen, T. B.; Coggon, M. M.; Crounse, J. D.; St. Clair, J. M.; Zhang, X.; Schilling, K. A.; Seinfeld, J. H.; Wennberg, P. O. Isoprene NO₃ oxidation products from the RO₂ + HO₂ pathway. *J. Phys. Chem. A* **2015**, *119*, 10158−10171.

(32) St. Clair, J. M.; Rivera-Rios, J. C.; Crounse, J. D.; Knap, H. C.; Bates, K. H.; Teng, A. P.; Jørgensen, S.; Kjaergaard, H. G.; Keutsch, F. N.; Wennberg, P. O. Kinetics and products of the reaction of the first-generation isoprene hydroxy hydroperoxide (ISOPOOH) with OH. *J. Phys. Chem. A* **2016**, *120*, 1441−1451.

(33) Schwantes, R. H.; Schilling, K. A.; McVay, R. C.; Lignell, H.; Coggon, M. M.; Zhang, X.; Wennberg, P. O.; Seinfeld, J. H. Formation of highly oxygenated low-volatility products from cresol oxidation. *Atmos. Chem. Phys.* **2017**, *17*, 3453−3474.

(34) Teng, A. P.; Crounse, J. D.; Wennberg, P. O. Isoprene peroxy radical dynamics. *J. Am. Chem. Soc.* **2017**, *139*, 5367−5377.

(35) Bates, K. H.; Crounse, J. D.; St. Clair, J. M.; Bennett, N. B.; Nguyen, T. B.; Seinfeld, J. H.; Stoltz, B. M.; Wennberg, P. O. Gas phase production and loss of isoprene epoxydiols. *J. Phys. Chem. A* **2014**, *118*, 1237−1246.

(36) Loza, C. L.; Craven, J. S.; Yee, L. D.; Coggon, M. M.; Schwantes, R. H.; Shiraiwa, M.; Zhang, X.; Schilling, K. A.; Ng, N. L.; Canagaratna, M. R.; Ziemann, P. J.; Flagan, R. C.; Seinfeld, J. H. Secondary organic aerosol yields of 12-carbon alkanes. *Atmos. Chem. Phys.* **2014**, *14*, 1423−1439.

(37) Nguyen, T. B.; Coggon, M. M.; Bates, K. H.; Zhang, X.; Schwantes, R. H.; Schilling, K. A.; Loza, C. L.; Flagan, R. C.; Wennberg, P. O.; Seinfeld, J. H. Organic aerosol formation from the reactive uptake of isoprene epoxydiols (IEPOX) onto non-acidified inorganic seeds. *Atmos. Chem. Phys.* **2014**, *14*, 3497−3510.

(38) Nguyen, T. B.; et al. Atmospheric fates of Criegee intermediates in the ozonolysis of isoprene. *Phys. Chem. Chem. Phys.* **2016**, *18*, 10241−10254.

(39) Crounse, J. D.; McKinney, K. A.; Kwan, A. J.; Wennberg, P. O. Measurement of gas-phase hydroperoxides by chemical ionization mass spectrometry. *Anal. Chem.* **2006**, *78*, 6726−6732.

(40) Pagonis, D.; Krechmer, J. E.; de Gouw, J.; Jimenez, J. L.; Ziemann, P. J. Effects of gas−wall partitioning in Teflon tubing and instrumentation on time-resolved measurements of gas-phase organic compounds. *Atmos. Meas. Tech.* **2017**, *10*, 4687−4696.

(41) Taylor, W. D.; Allston, T. D.; Moscato, M. J.; Fazekas, G. B.; Kozlowski, R.; Takacs, G. A. Atmospheric photodissociation lifetimes for nitromethane, methyl nitrite, and methyl nitrate. *Int. J. Chem. Kinet.* **1980**, *12*, 231−240.

(42) Lee, B. H.; Lopez-Hilfiker, F. D.; Mohr, C.; Kurtén, T.; Worsnop, D. R.; Thornton, J. A. An Iodide-adduct high-resolution time-of-flight chemical-ionization mass spectrometer: Application to atmospheric inorganic and organic compounds. *Environ. Sci. Technol.* **2014**, *48*, 6309−6317.

(43) Bagley, E.; Long, F. A. Two-stage sorption and desorption of organic vapors in cellulose acetate[1,2]. *J. Am. Chem. Soc.* **1955**, *77*, 2172−2178.

(44) Abraham, M. H.; McGowan, J. C. The use of characteristic volumes to measure cavity terms in reversed phase liquid chromatography. *Chromatographia* **1987**, *23*, 243−246.

(45) Linossier, I.; Gaillard, F.; Romand, M.; Feller, J. F. Measuring water diffusion in polymer films on the substrate by internal reflection fourier transform infrared spectroscopy. *J. Appl. Polym. Sci.* **1997**, *66*, 2465−2473.

(46) Bean, J. K.; Hildebrandt Ruiz, L. Gas-particle partitioning and hydrolysis of organic nitrates formed from the oxidation of α-pinene in environmental chamber experiments. *Atmos. Chem. Phys.* **2016**, *16*, 2175−2184.

EFFICACY OF A PORTABLE, MODERATE-RESOLUTION, FAST-SCANNING DIFFERENTIAL MOBILITY ANALYZER FOR AMBIENT AEROSOL SIZE DISTRIBUTION MEASUREMENTS

Amanatidis, S.; Huang, Y.; Pushpawela, B.; Schulze, B. C.; Kenseth, C. M.; Ward, R. X.; Seinfeld, J. H.; Hering, S. V.; Flagan, R. C. Efficacy of a Portable, Moderate-Resolution, Fast-Scanning Differential Mobility Analyzer for Ambient Aerosol Size Distribution Measurements. *Atmos. Meas. Tech.* **2021**, *14* (6), 4507–4516. DOI: 10.5194/amt-14-4507-2021.

Atmospheric
Measurement
Techniques

Efficacy of a portable, moderate-resolution, fast-scanning differential mobility analyzer for ambient aerosol size distribution measurements

Stavros Amanatidis[1,2]**, Yuanlong Huang**[3]**, Buddhi Pushpawela**[1]**, Benjamin C. Schulze**[3]**, Christopher M. Kenseth**[1]**, Ryan X. Ward**[3]**, John H. Seinfeld**[1,3]**, Susanne V. Hering**[2]**, and Richard C. Flagan**[1,3]

[1]Division of Chemistry and Chemical Engineering, California Institute of Technology, Pasadena, CA 91125, USA
[2]Aerosol Dynamics Inc., Berkeley, CA 94710, USA
[3]Department of Environmental Science and Engineering, California Institute of Technology, Pasadena, CA 91125, USA

Correspondence: Richard C. Flagan (flagan@caltech.edu)

Abstract. Ambient aerosol size distributions obtained with a compact scanning mobility analyzer, the "Spider" differential mobility analyzer (DMA), are compared to those obtained with a conventional mobility analyzer, with specific attention to the effect of mobility resolution on the measured size distribution parameters. The Spider is a 12 cm diameter radial differential mobility analyzer that spans the 10–500 nm size range with 30 s mobility scans. It achieves its compact size by operating at a nominal mobility resolution $R = 3$ (sheath flow $= 0.9$ L min^{-1}; aerosol flow $= 0.3$ L min^{-1}) in place of the higher ratio of sheath flow to aerosol flow commonly used. The question addressed here is whether the lower resolution is sufficient to capture key characteristics of ambient aerosol size distributions. The Spider, operated at $R = 3$ with 30 s up- and downscans, was co-located with a TSI 3081 long-column mobility analyzer, operated at $R = 10$ with a 360 s sampling duty cycle. Ambient aerosol data were collected over 26 consecutive days of continuous operation, in Pasadena, CA. Over the 17–500 nm size range, the two instruments exhibit excellent correlation in the total particle number concentrations and geometric mean diameters, with regression slopes of 1.13 and 1.00, respectively. Our results suggest that particle sizing at a lower resolution than typically employed may be sufficient to obtain key properties of ambient size distributions, at least for these two moments of the size distribution. Moreover, it enables better counting statistics, as the wider transfer function for a given aerosol flow rate results in a higher counting rate.

1 Introduction

Mobility measurements of atmospheric aerosols in the 10–500 nm size range are important to atmospheric aerosol characterization (McMurry, 2000). Measurements aloft are especially important to understand aerosols in remote regions (Creamean et al., 2021; Herenz et al., 2018) and for mapping three-dimensional profiles (Mamali et al., 2018; Ortega et al., 2019; Zheng et al., 2021). Traditional mobility analyzers that span this size range are large and not suitable for most unmanned aerial vehicle (UAV) or tethered balloon payloads, which increasingly serve as platforms for aerosol characterization aloft. Moreover, aircraft measurements also require a fast scan time resolution to enable a good spatial resolution, as time is proportional to distance traveled in a moving platform.

To that end, Amanatidis et al. (2020) developed the "Spider DMA", a compact, lightweight, and fast differential mobility analyzer (DMA). The instrument was designed for 10–500 nm sizing, with an aerosol flow rate of 0.3 L min^{-1} to provide adequate counting statistics on ambient aerosol over the time window appropriate for moving platforms. Its compact size was achieved in part through reduction of mobility resolution. Instead of the typical ratio of sheath-to-aerosol flows of 10, the Spider DMA employs a flow ratio of 3. For given sample flow rate, the most commonly used flow rate ratio of 10 requires a larger sheath flow, which in turn requires a larger mobility analyzer to reach the same maximum particle size.

While high size resolution is important for specific applications, such as in laboratory calibrations that employ a DMA as a calibration aerosol source, it may not be critical for ambient size distribution measurements, wherein the particle distribution spans a much wider size range than the transfer function of the DMA. Lower DMA resolution has also been successfully employed for reconstructing aerosol dynamics process rates in chamber experiments (Ozon et al., 2021). In addition to the smaller physical size of the instrument, operating at lower resolution increases the particle count rate owing to the wider DMA mobility window, thereby reducing measurement uncertainty. This can be an important factor for low-concentration measurements. Moreover, the resulting lower sheath flow requirements enable the usage of more compact and less power-demanding pumps, which further facilitates the overall portability of the instrument.

The question explored in this paper is whether the moderate-resolution mobility sizing of the Spider DMA is sufficient to capture the important characteristics of atmospheric aerosol size distributions. We begin with the derivation of the Spider DMA transfer function through a combination of finite-element simulations and laboratory calibrations. We then present a field validation by comparison of ambient aerosol data from the new instrument with that obtained from a traditional long-column cylindrical DMA (LDMA) operated at a nominal resolution of $R = 10$ during nearly 1 month of continuous operation of the two co-located instruments.

2   Methods

2.1   Spider DMA

The prototype Spider DMA sizing system consists of the Spider DMA (Amanatidis et al., 2020) and the "MAGIC" (Moderated Aerosol Growth with Internal water Cycling) particle counter (Hering et al., 2014, 2019). The Spider is a compact mobility analyzer designed for applications requiring high portability and time resolution. It features a radial flow geometry and a sample inlet system that distributes the flow azimuthally through curved (spider-like) flow channels. The instrument was designed to operate at $0.3\,\text{L}\,\text{min}^{-1}$ sample and $0.6\text{–}1.2\,\text{L}\,\text{min}^{-1}$ sheath flow rates, offering size classification in the 10–500 nm size range. Owing to its small classification volume, the mean gas residence time in the classifier is on the order of $\sim 1\,\text{s}$, making it possible to complete its voltage scan in times well below 60 s without significant smearing of its transfer function.

The MAGIC particle counter is a laminar-flow water-based condensation particle counter (CPC). It employs a particle growth tube chamber with three stages (cool, warm, and cool), in which ultrafine particles grow by heterogeneous water vapor condensation to $> 1\,\mu\text{m}$ and are subsequently counted by an optical detector. The final stage of the MAGIC CPC growth tube (moderator) recovers excess water vapor,

enabling long-term operation without the need of a reservoir or water refilling. The instrument operates at a sample flow rate of $0.3\,\text{L}\,\text{min}^{-1}$ and has a 50 % detection cut point of $\sim 6\,\text{nm}$.

2.2   Transfer function determination by finite-element modeling

Amanatidis et al. (2020) evaluated the Spider DMA transfer function in static mode based on the Stolzenburg (1988) transfer function model and its derivation for radial flow classifiers (Zhang et al., 1995; Zhang and Flagan, 1996). Here, we evaluate its transfer function in "scanning" mobility mode, wherein the electric field is varied continuously in an exponential voltage ramp (Wang and Flagan, 1990). The scanning transfer function was evaluated with 2D finite-element COMSOL Multiphysics simulations of flows, quasi-steady-state electric field, and particle trajectories. Simulations were performed for $0.9\,\text{L}\,\text{min}^{-1}$ sheath and $0.3\,\text{L}\,\text{min}^{-1}$ aerosol flow rates, scanning voltage in the range 5–5000 V, and 30 s exponential ramps for both up- and downscans. Particles were modeled with the "mathematical particle tracing" module, in which particle mass was assumed to be negligible since the electric field varies slowly, on a timescale that is long compared to the aerodynamic relaxation time of the particles being measured. Particle trajectories were calculated by assigning particle velocity vector components equal to the steady-state fluid field solution, combined with the axial velocity acquired from interaction with the time-varying electrostatic field. Moreover, a Gaussian random walk was employed in each time step of the solver to simulate particle Brownian motion, with a standard deviation proportional to particle diffusivity, i.e., $d\sigma = \sqrt{2D dt}$. Monodisperse particles were injected in regular intervals over the scan, varying from 0.025 s for large particles to 0.003 s for those in the diffusing size range to capture in sufficient detail the Brownian motion along the particle trajectories. Modeling was repeated for 10 discrete particle sizes, spanning the dynamic range of the classifier. Details on the Spider DMA geometry employed in the modeling, as well as an example with particle trajectories over the Spider voltage scan, are included in the Supplement (Figs. S1 and S2).

2.3   Experimental

The two sizing instruments, the Spider DMA and the LDMA system, were operated in parallel, sampling ambient air from a roof top at the Caltech campus in Pasadena, CA. Measurements were made between 16 May–11 June 2020 and were done as part of a study of the impacts of the COVID-19 pandemic shutdown on air quality. The experimental setup used is shown in Fig. 1. Ambient aerosol samples passed through a soft X-ray charge conditioner and were subsequently split between the two mobility sizing systems, thereby ensuring that the charge status of the aerosols seen by the two instru-
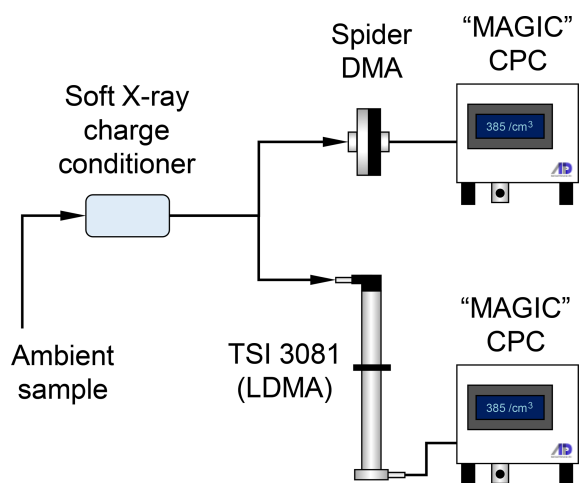
Figure 1. Schematic of the experimental setup used to evaluate the Spider DMA. The prototype instrument was operated at 0.9 L min^{-1} sheath and 0.3 L min^{-1} aerosol flow rates, with a scanning voltage program consisting of a 30 s upscan followed by a 30 s downscan. A TSI 3081 long-column DMA, operated at 3.0 L min^{-1} sheath and 0.3 L min^{-1} aerosol flows, with 240 s upscans, was used for comparison. Both sizing systems used an ADI "MAGIC" CPC as the particle detector.

ments was identical. The charge conditioner is a prototype device that was developed recently at Caltech. It is based upon a Hamamatsu soft X-ray source that directly ionizes the air around the incoming aerosol flow. Both DMA systems were operated in scanning mode. Both used a MAGIC water-based CPC as the detector. The size pre-cut stage in the inlet of both CPCs was removed to avoid additional smearing of the transfer functions.

The Spider DMA was operated at 0.9 L min^{-1} sheath and 0.3 L min^{-1} aerosol flow rates. A piezoelectric blower (Murata, MZB1001T02) was enclosed into a sealed housing to serve as a recirculating pump for the Spider sheath flow. The pump assembly weighs $\sim$ 60 g. Operating at a frequency of 24–27 kHz, this pump produces only very small pressure fluctuations that are effectively damped by the capacitance of the downstream filter. With feedback control, the pump attains a steady flow up to $\sim$ 1 L min^{-1} within about 1 s, making it well suited to operating in an environment in which the pressure varies slowly, as in UAV applications. The Spider DMA scanning program included a 30 s upscan followed by a 30 s downscan, during which the electrode voltage was exponentially varied between 5–5000 V. The voltage was held steady for an additional 2 s at each end of the voltage ramp to allow for incoming particles to transmit through the classifier. Particle counts over the scan were recorded with a 5 Hz rate.

The LDMA system was based on a TSI 3081 long-column DMA operated at 3.0 L min^{-1} sheath and 0.3 L min^{-1} aerosol flow rates, offering classification in the 17–989 nm size range. The scans consisted of an exponentially increas-

ing (upscan) voltage ramp between 25–9875 V with a 240 s duration. As with the Spider DMA, the LDMA voltage was held constant at the beginning and end of the ramp. Owing to its longer mean flow residence time, the LDMA voltage hold periods were set at 40 s, bringing its overall duty cycle to 360 s. Particle counts for the LDMA system were recorded with a 2 Hz sampling rate. Data acquisition and instrument control (flows, high voltage) was performed with custom LabVIEW software for both systems.

2.4 DMA scanning conditions

Comparison of the scanning voltage conditions between the two DMAs requires accounting for differences in geometry, flow rates, and voltage scanning rates. The appropriate non-dimensional quantity that describes the DMA scanning rate is given by $\theta_s = \frac{\tau_{HV}}{t_g}$, the ratio of the exponential voltage ramp time constant, τ_{HV}, to the classifier mean gas residence time, t_g. At large θ_s values, typically $\theta_s > 10$, the rate at which the scanning voltage varies as particles transmit through the classifier is slow, and the transfer function approximates the "static" DMA transfer function. At small θ_s values, the scanning voltage changes quickly relative to the particle residence time, smearing the transfer function, which becomes pronounced as θ_s approaches unity (Russell et al., 1995; Collins et al., 2004). For the Spider DMA operating conditions, $\tau_{HV} = 4.34$ s and $t_g = 1.30$ s, resulting in $\theta_s = 3.35$. For the LDMA, $\tau_{HV} = 40.14$ s and $t_g = 7.52$ s, resulting in $\theta_s = 5.34$. Here, even though τ_{HV} of the LDMA is about 10 times larger (i.e., slower) than that of the Spider, its dimensionless scanning rate (θ_s) is only about 1.6 times smaller owing to its much longer flow residence time. In absolute terms, the scanning rate employed in both DMAs is moderate.

2.5 Data inversion and analysis

Particle size distributions were obtained by inverting the raw particle counts recorded over each voltage scan. Raw counts were smoothed prior to the inversion to minimize inversion artifacts. Locally weighted scatterplot smoothing (LOWESS) regression (Cleveland, 1979) was employed for the Spider DMA data with a 10 % smoothing window (i.e., 15 data points). The LDMA raw counts were smoothed by applying a moving average filter with a span of 5 data points. The smoothed data were then inverted by regularized non-negative least-squares minimization. Tikhonov regularization was used for both systems, with $\lambda = 0.140$ and $\lambda = 0.015$ regularization parameters for the Spider DMA and LDMA data, respectively. Those values were found to provide stable solutions without over-constraining the inversion results.

The inversion kernel for the Spider DMA system was based on the scanning transfer function of the Spider DMA obtained by finite-element modeling. In order to generate a

dense kernel required for the inversion, the modeled transfer function data were fitted to Gaussian distributions, whose parameters were subsequently fitted to analytical expressions that allowed generation of transfer functions at any instant (i.e., time bin) over the voltage scan. The Spider transfer functions were subsequently convoluted with a continuous stirred-tank reactor (CSTR) model (Russell et al., 1995; Collins et al., 2002; Mai et al., 2018) to take into account the time response of the MAGIC CPC. A 0.35 s time constant was used for the CSTR model in the Spider DMA system (Hering et al., 2017). The resulting transfer function was combined with a size-dependent transmission efficiency model described by Amanatidis et al. (2020) to take into account particle losses occurring at the Spider inlet, as those are not evaluated in the 2D finite-element modeling. Raw counts were shifted to earlier time bins to account for the 1.50 s plumbing time delay between the Spider outlet and the MAGIC CPC detector. Because the simulation enabled a strictly monodisperse "calibration" aerosol, the ratio of the number exiting the DMA during a particular counting time interval to the upstream particle number is the instrument transfer function. The kernel for the LDMA system was based on the scanning transfer function model derived recently by Huang et al. (2020). A CSTR model with a characteristic time of 0.35 s and a plumbing delay time of 0.95 s were used to incorporate the response of the MAGIC CPC used in the LDMA system.

The Wiedensohler (1988) fit to the Hoppel and Frick (1986) numerical evaluation of the Fuchs (1963) charge distribution has been used in the data inversion. Note that, since both instruments took samples from the same soft X-ray charge conditioner, any deviations from the assumed charge distribution will not affect the comparison between the two instruments.

3 Results

3.1 Spider scanning transfer function

Figure 2 shows the scanning transfer function of the Spider DMA evaluated by finite-element modeling. Results are plotted as a function of time in the scan for upscan and downscan voltage ramps. Each peak represents the ratio of particle number at the outlet to the inlet for a specific input particle size. Finite-element modeling data, shown with symbols, have been fitted to Gaussian distributions, shown with solid lines, which provide a close approximation to both upscan and downscan modeling data. As will be shown next, the Gaussian fits are subsequently employed to generate the transfer function at any time instance over the scan.

Comparison between upscan and downscan peaks reveals a distinct difference; downscan peaks have a higher maximum number ratio. Moreover, they are somewhat narrower than the upscan peaks. It should be noted that the transmis-
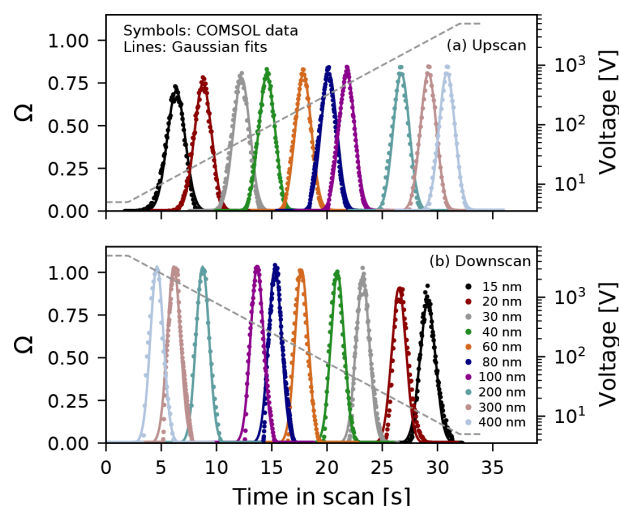
Figure 2. Finite-element modeling of the Spider DMA scanning transfer function for **(a)** upscan and **(b)** downscan exponential voltage ramps with 30 s duration and $0.9\,\mathrm{L\,min^{-1}}$ sheath and $0.3\,\mathrm{L\,min^{-1}}$ aerosol flow rates. Symbols correspond to finite-element modeling data (ratio of particle number at the outlet to the inlet), solid lines show Gaussian distributions fitted to the modeling data, and dashed lines indicate the scanning voltage program (values shown on right y axis).

sion efficiency through the classification zone of a DMA is proportional to the area under the peak, rather than its maximum value. Hence, particle transmission over downscans is not necessarily higher than that over upscans. Here, the area of the Gaussian curves used to fit the transfer function modeling data was on average ∼3.5 % larger for downscans than upscans. This difference is likely due to the slightly asymmetrical shape of the downscan transfer function, which can be observed at the onset (i.e., lower left side) of each peak in Fig. 2b where the fitted curves are somewhat wider than the modeling data. A closer comparison between upscan and downscan fitting parameters is provided in the Supplement (Fig. S3). Diffusional broadening of the transfer function becomes important in the low-voltage region of each ramp, increasing the transfer function width as voltage decreases, though the broadening is less than would be seen with a higher-resolution DMA (Flagan, 1999).

The differences in the transfer function between upscans and downscans is the result of the scanning voltage operating mode and particle interaction with the boundary flow layers near the DMA electrode walls. Owing to the laminar flow profile, particles near the electrode walls acquire lower velocities than those in the middle of the electrode gap. Over downscans, a fraction of the incoming particles interacts with the boundary layer adjacent to the wall that houses the exit slit of the classifier. As voltage drops below a certain threshold, those particles reach the exit of the classifier, albeit with a time delay relative to particles of the same mobility whose trajectories did not interact with the boundary layer.

This results in a particle exit time reallocation, which alters the shape of the downscan transfer function as the voltage drop becomes more rapid. This condition is inhibited over upscans, since the respective boundary layer is formed on the wall opposite to the exit flow and is exhausted through the excess flow.

Collins et al. (2004) and Mamakos et al. (2008) demonstrated the impact of scanning voltage on the transfer function of the cylindrical DMA. Over downscans, the transfer function deviates from the symmetric triangular or Gaussian shape and becomes skewed. The effect becomes larger for fast scans and is significant when the effective scan rate $\theta_s < 2$. This is also true for the Spider DMA, as shown in Fig. 2b; however the shape distortion is relatively small given the moderate Spider scan rate ($\theta_s = 3.4$). Moreover, in contrast to the cylindrical DMA, the boundary layers in the radial DMA are symmetric, which reduces the downscan distortion compared to its cylindrical counterpart. Over upscans, the width of the scanning transfer function broadens but retains its symmetric shape. For this reason, downscan data are often discarded in scanning DMA data analyses, as the more irregular shape of the transfer function is more difficult to parameterize. However, this strategy comes with a penalty in sampling time resolution, owing to the "dead" time associated with the discarded downscan that is required after each upscan. The dead time required depends on the classifier mean gas residence time (typically $> 2\text{–}3 \times t_g$) and the capacitance of the DMA high-voltage supply. As the Spider DMA scanning transfer function can be described with good fidelity for both upscans and downscans, both are included in the data analysis to maximize its time resolution.

Figure 3 shows the integrated transfer function of the Spider DMA system for the same operating conditions as those used in the experiments. The voltage program, shown in Fig. 3a, consists of a 2 s hold time at 5 V, followed by a 30 s upscan up to 5000 V, a 2 s hold time at 5000 V, and a 30 s downscan to 5 V. The classified particle size follows roughly the exponential increase and decrease of the voltage over the scan. The peaks shown in Fig. 3b consist of the Gaussian approximation of the Spider transfer function shown in Fig. 2, combined with the size and time response of the MAGIC CPC, and the size-dependent transmission efficiency in the Spider inlet (Amanatidis et al., 2020).

3.2 Data inversion example

Figure 4 demonstrates an inversion example for representative Spider DMA data. Particle raw counts recorded at each time bin over the upscan and downscan are shown in Fig. 4a. Smooth curves are fitted to the raw count data to minimize artifacts in the inversion process. The resulting size distributions, employing an inversion kernel based on the scanning transfer function in Fig. 3b, are shown in Fig. 4b. Up- and downscan distributions are almost identical in both shape and magnitude. The mean of the two distributions, as shown
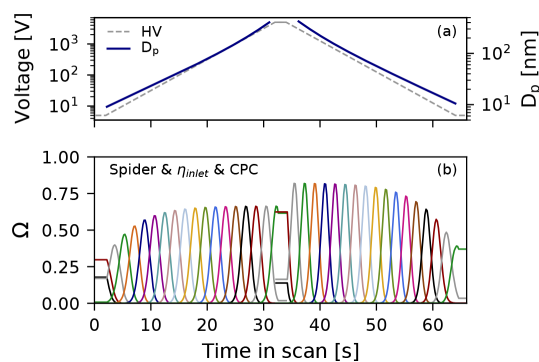
Figure 3. (a) Scanning voltage and classified particle size over the Spider DMA scan. (b) Transfer function of the integrated Spider DMA–MAGIC CPC system (ratio of particle number at the outlet to the inlet), consisting of the Spider DMA scanning transfer function combined with its inlet transmission efficiency and the MAGIC CPC response.
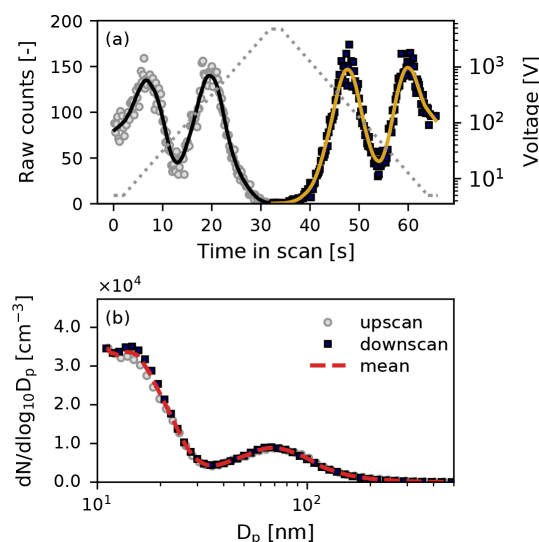
Figure 4. Example of Spider DMA data inversion. (a) Raw counts per time bin (symbols) recorded over the voltage ramp (up- and downscan). Solid lines indicate LOWESS smoothing to the raw counts. (b) Resulting size distributions after data inversion. The dashed line shows the mean of the up- and downscan distributions.

here, is used as the output of each scan. Overall, considering all measurement data collected in this work, upscan raw count data inversion yielded distributions with consistent but slightly higher (3.7 % ± 2.3 %) total particle number than downscans.

3.3 Instrument comparison

Figure 5 demonstrates the effect of sizing resolution on the counting rate of the downstream particle detector. As both the Spider DMA and the LDMA operated at the same aerosol flow rate, one would expect a higher counting rate for the
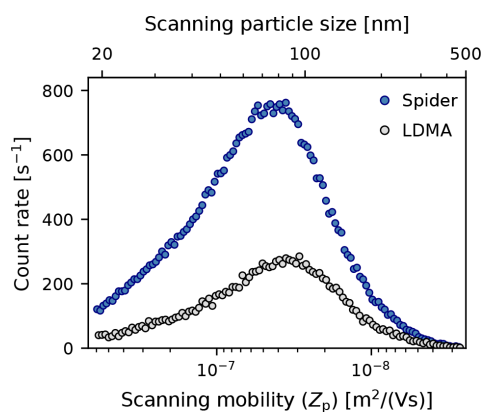
**Figure 5.** Sizing resolution effect on the particle count rate of the Spider DMA ($R = 3$) and LDMA ($R = 10$) systems. Data shown are the average of raw particle count rates during upscans over a period of 18 min (corresponding to 3 LDMA upscans and 17 Spider upscans) measured in the morning of 1 June 2020. Both systems operated at $0.3\,\mathrm{L\,min^{-1}}$ aerosol flow rate.

Spider DMA system owing to its wider transfer function. Indeed, as shown in Fig. 5, this was the case. The data presented here are the average of particle count rates during upscans over a period of 18 min (corresponding to 3 LDMA upscans and 17 Spider upscans). This example was selected as a representative comparison case since the resulting particle count distribution is centered near the middle of the overlapping mobility range. The integral of the counting rate with respect to scanning mobility for each instrument (i.e., area below the data points in Fig. 5) was larger by a factor of 3.325 in the Spider measurement than the LDMA; this is almost exactly the same as the inverse of the sizing resolution ratio (i.e., 10/3) of the two DMAs. In fact, this ratio was rather consistent (within $\pm 10\,\%$) despite the size distribution variation over the course of the day, corroborating that, for given aerosol flow rate, lower DMA resolution results in higher counting rates and thus enables better counting statistics.

Figure 6 illustrates an excerpt of the Spider and LDMA size distribution measurements over a time period of 3 d. The two instruments report similar diurnal variation in the particle size distribution, in both size and number concentration. Increased particle concentrations were recorded in the early afternoon of each day, a regular occurrence as particles from morning traffic are transported by the sea breeze from Los Angeles to Pasadena, where the measurements took place. Concentrations begin to drop later in the afternoon and through the evening, from about $15\,000\,\mathrm{cm^{-3}}$ to below $5000\,\mathrm{cm^{-3}}$. The geometric mean diameter (GMD) of the size distribution ranged between about 30–60 nm and was smaller over the high-number-concentration events recorded in the early afternoon.
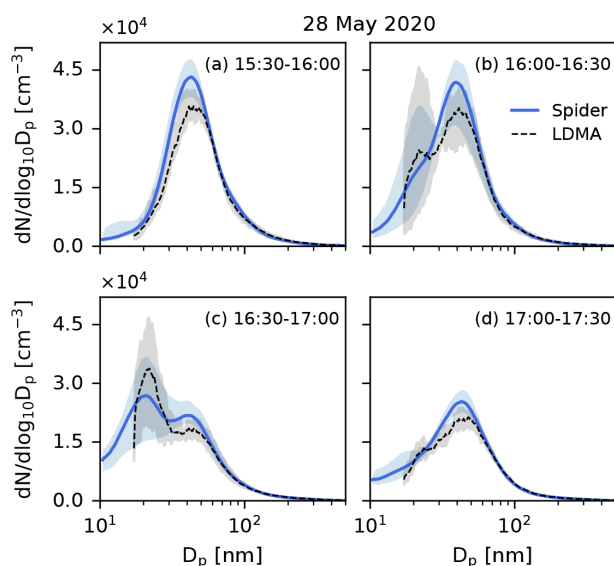
Figure 7 shows the evolution of the size distribution over a period of 2 h in the afternoon of 28 May 2020 (indicated with
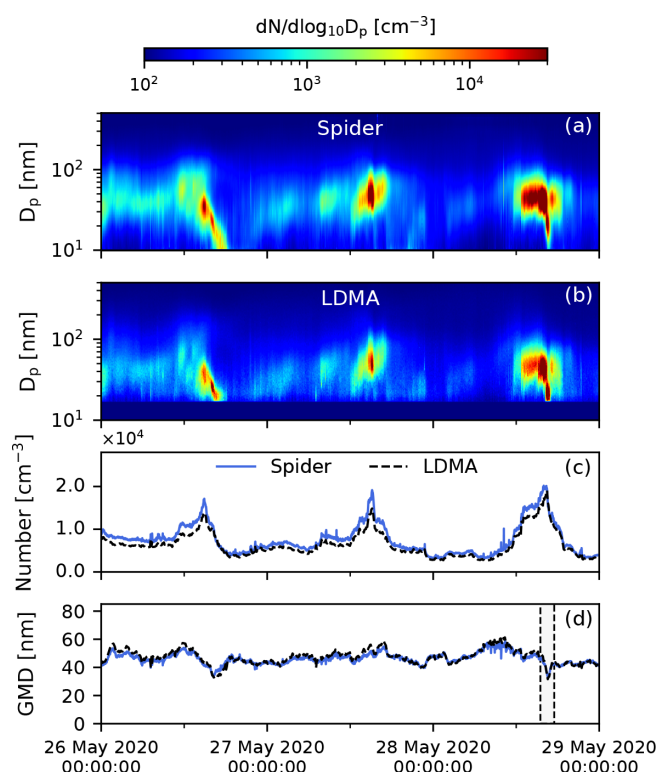
Figure 6. Evolution of the particle size distribution over a period of 3 d measured by **(a)** the Spider DMA and **(b)** the LDMA system. Corresponding total particle number and geometric mean diameter, calculated over the 17–500 nm size range, are shown in panels **(c)** and **(d)**, respectively. Solid blue color in panel **(b)** (size range < 17 nm) was used for no available data in the LDMA system. The dashed box in panel **(d)** indicates the time period shown in Fig. 7.

a dashed box in Fig. 6d), measured with the Spider and the LDMA system. Since the measurement duty cycle of the two instruments was different (66 s for the Spider vs. 360 s for the LDMA), we employed 30 min averaging of the recorded size distributions. This corresponds to 5 scans for the LDMA and about 27 up- and downscans for the Spider. The shaded areas of the averaged distributions represent the variation over the averaging period. Starting from a mono-modal distribution with a peak at ~ 45 nm (panel a), the size distribution transitioned to a bi-modal one over a period of 60 min (panels b, c) before transitioning back to a mono-modal distribution (panel d). As indicated by the shaded areas, there was high variation in the aerosol concentration during this transition event. Overall, the measurement of the two instruments was in good agreement in terms of both sizing and concentration, suggesting that the lower sizing resolution in the Spider DMA was adequate in capturing the details of the size distribution. An animation video with side-by-side comparison of 30 min averaged distributions for the entire testing period is included in the video supplement (Amanatidis et al., 2021a).

Figure 8 compares the total number and geometric mean diameter measured by the two instruments over the entire

Figure 7. Evolution of the size distribution in the afternoon of 28 May 2020, as measured by the Spider and LDMA systems. Lines represent the mean of size distributions measured over a period of 30 min. Shaded areas demonstrate the variation of the size distribution over the averaging period, indicating maximum and minimum values.

testing period. Each data point corresponds to a 1 h average of the size distribution measured by each instrument, calculated over the 17–500 nm size range where the two systems overlap. Overall, the comparison includes 550 h of measurement data. In order to identify outliers in the data, we employed the "RANSAC" (random sample consensus) algorithm (Fischler and Bolles, 1981). In this, random samples of the data are selected, analyzed, and classified as inliers and outliers through an iterative routine. The outliers identified are shown in Fig. 8 with open square symbols.

Next, a linear regression model (no intercept) was fitted to the data (excluding outliers) to evaluate the correlation between the two instruments. Since both instruments include measurement errors, we employed orthogonal distance regression (Boggs et al., 1987), where errors on both the dependent and independent variable are taken into account in the least-squares minimization. The resulting regression lines exhibit slopes of $\alpha = 1.13$ and $\alpha = 1.00$ for number concentration and GMD, respectively, suggesting an overall excellent agreement between the instruments. Moreover, Pearson correlation coefficients of $\rho = 0.98$ and $\rho = 0.93$ indicate a strong correlation for both metrics of the size distribution.

3.4 Operational observations

The prototype Spider DMA used in this study incorporated an electrostatic-dissipative plastic that failed after several months of continuous operation, causing arcing within the instrument at the highest voltages. The Spider DMA has been
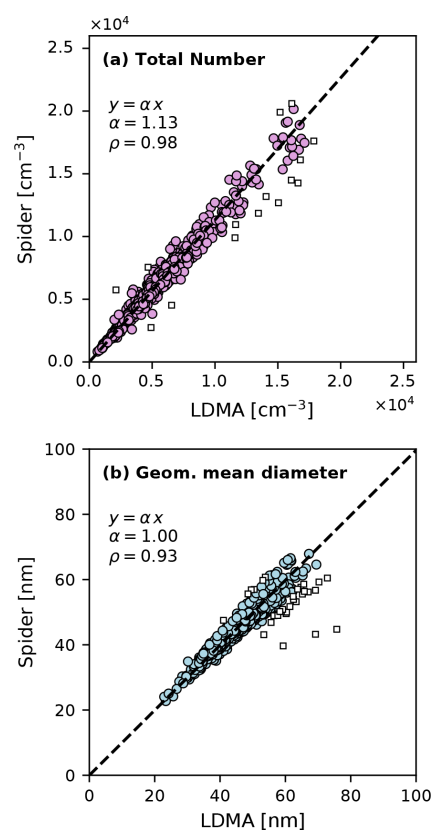
Figure 8. Comparison of **(a)** total particle number and **(b)** geometric mean diameter measured by the Spider and LDMA systems over a period of 26 d of continuous testing. Each point represents 1 h averaged data, calculated over the 17–500 nm size range where the two instruments overlap. Square symbols show outliers excluded from the regression analysis. Dashed lines represent a linear regression model (no intercept) fitted to the data. ρ values denote the Pearson correlation coefficient between the measurement data of the two instruments.

redesigned to eliminate this material and is currently being tested. This new Spider DMA has relatively minor changes to the classification region of the prototype presented here and employs the same moderate-resolution approach to maintain a compact size.

4 Summary and conclusions

We evaluated the performance of the Spider DMA, a highly portable particle sizer, in measuring ambient size distributions against a co-located particle sizer based on a TSI 3081 long-column differential mobility analyzer (LDMA). Comparison measurements were performed at the Caltech campus in Pasadena, CA, over a period of 26 d, between 16 May–11 June 2020, as part of a field campaign examining the effects of the COVID-19 shutdown on air quality. The Spider DMA system was operated at a lower nominal sizing resolution ($0.9 \, \text{L min}^{-1}$ sheath and $0.3 \, \text{L min}^{-1}$ aerosol flow rates,

$R = 3$) than the LDMA ($3.0\,\text{L min}^{-1}$ sheath and $0.3\,\text{L min}^{-1}$ aerosol flow rates, $R = 10$) and at a higher time resolution ($30\,\text{s}$ vs. $240\,\text{s}$ scans).

The transfer function of the Spider DMA was obtained by finite-element modeling at the conditions employed in the experiment, which included both up- and downscan exponential voltage ramps with $30\,\text{s}$ duration. Owing to the Spider radial flow geometry and short gas flow residence time, distortion of the downscan transfer function shape is minimal at the scan rates employed, enabling usage of both upscan and downscan data, thereby increasing time resolution. Modeling data were fitted to Gaussian distributions and were combined with the experimentally determined transmission efficiency of the Spider DMA and the MAGIC particle counter response function to generate the inversion kernel of the combined system. Data inversion of the LDMA system was based on the semi-analytical model of the LDMA scanning transfer function derived by Huang et al. (2020).

Regression analysis of $550\,\text{h}$ of measurement data showed an overall excellent correlation between the two instruments, with slopes of $\alpha = 1.13$ and $\alpha = 1.00$ and Pearson correlation coefficients of $\rho = 0.98$ and $\rho = 0.93$ in the reported particle number and geometric mean diameter, respectively. The present results suggest that two key characteristics of ambient size distributions, geometric mean diameter and number concentration, are sufficiently captured when operating the DMA at lower resolution than is typically employed. Moreover, use of lower resolution, where appropriate, has several distinct advantages. For the same aerosol flow rate and range in particle mobilities, reducing the nominal resolution reduces the required sheath flow and hence reduces the physical size of the DMA. In turn, this reduction in physical size at the same aerosol flow rate reduces the residence time within the classification region, enabling faster scans. Additionally, for the same aerosol flow, the wider mobility window increases the particle count rate, thereby improving measurement statistics. While some applications may require higher resolution, this study demonstrates the efficacy of lower-resolution measurements for ambient aerosol characterization and illustrates the commensurate advantages of faster measurements in a smaller package.

Code availability. The code used for data analysis in this work can be made available upon request from the authors.

Data availability. The Spider DMA and LDMA measurement data can be accessed from the Caltech data repository: https://doi.org/10.22002/D1.1998 (Amanatidis et al., 2021b)

Video supplement. This video supplement shows the evolution of the ambient aerosol size distribution in Pasadena, CA between 16 May–11 June 2020, as measured by the Spider DMA

and LDMA systems (https://doi.org/10.22002/D1.1896, Amanatidis et al., 2021a).

Supplement. The supplement related to this article is available online at: https://doi.org/10.5194/amt-14-4507-2021-supplement.

Author contributions. SA performed the finite-element modeling for the Spider DMA instrument, analyzed its measurement data, generated the figures, and wrote the manuscript text. YH analyzed the LDMA instrument data and prepared the experimental setup. BP, BCS, CMK, and RXW collected the measurement data and provided technical maintenance to the instruments. JHS reviewed and provided editorial feedback on the manuscript. SVH and RCF planned the experiments and contributed to interpretation of the results and editing of the manuscript.

Competing interests. Richard C. Flagan and Stavros Amanatidis are inventors of the "Spider" DMA technology patent (US10775290B2), which is licensed to Susanne V. Hering's company. The rest of the authors declare that they have no conflict of interest.

Disclaimer. Neither the United States Government nor any agency thereof, nor any of their employees, makes any warranty, express or implied, or assumes any legal liability or responsibility for the accuracy, completeness, or usefulness of any information, apparatus, product, or process disclosed, or represents that its use would not infringe privately owned rights. Reference herein to any specific commercial product, process, or service by trade name, trademark, manufacturer, or otherwise does not necessarily constitute or imply its endorsement, recommendation, or favoring by the United States Government or any agency thereof. The views and opinions of authors expressed herein do not necessarily state or reflect those of the United States Government or any agency thereof.

Review statement. This paper was edited by Francis Pope and reviewed by three anonymous referees.

References

Amanatidis, S., Kim, C., Spielman, S. R., Lewis, G. S., Hering, S. V., and Flagan, R. C.: The Spider DMA: A miniature radial differential mobility analyzer, Aerosol Sci. Tech., 54, 75–189, https://doi.org/10.1080/02786826.2019.1626974, 2020.

Amanatidis, S., Huang, Y., Pushpawela, B., Schulze, B. C., Kenseth, C. M., Ward, R. X., Seinfeld, J. H., Hering, S. V., and Flagan, R. C.: Efficacy of a portable, moderate-resolution, fast-scanning DMA for ambient aerosol size distribution measurements (Version 1.0), CaltechDATA, https://doi.org/10.22002/D1.1896, 2021a.

Amanatidis, S., Huang, Y., Pushpawela, B., Schulze, B. C., Kenseth, C. M., Ward, R. X., Seinfeld, J. H., Hering, S. V., and Flagan, R. C.: Size distribution measurement datasets of the "Spider DMA" and "LDMA" particle sizers, collected in Pasadena, CA between 16 May–11 June 2020. (Version 1.0), CaltechDATA [data set], https://doi.org/10.22002/D1.1998, 2021b.

Boggs, P. T., Byrd, R. H., and Schnabel, R. B.: A Stable and Efficient Algorithm for Nonlinear Orthogonal Distance Regression, SIAM J. Sci. Stat. Comp., 8, 1052–1078, https://doi.org/10.1137/0908085, 1987.

Cleveland, W. S.: Robust Locally Weighted Regression and Smoothing Scatterplots, J. Am. Stat. Assoc., 74, 829–836, https://doi.org/10.1080/01621459.1979.10481038, 1979.

Collins, D. R., Flagan, R. C., and Seinfeld, J. H.: Improved inversion of scanning DMA data, Aerosol Sci. Tech., 36, 1–9, https://doi.org/10.1080/027868202753339032, 2002.

Collins, D. R., Cocker, D. R., Flagan, R. C., and Seinfeld, J. H.: The scanning DMA transfer function, Aerosol Sci. Tech., 38, 833–850, https://doi.org/10.1080/027868290503082, 2004.

Creamean, J. M., de Boer, G., Telg, H., Mei, F., Dexheimer, D., Shupe, M. D., Solomon, A., and McComiskey, A.: Assessing the vertical structure of Arctic aerosols using balloon-borne measurements, Atmos. Chem. Phys., 21, 1737–1757, https://doi.org/10.5194/acp-21-1737-2021, 2021.

Fischler, M. A. and Bolles, R. C.: Random sample consensus, Commun. ACM, 24, 381–395, https://doi.org/10.1145/358669.358692, 1981.

Flagan, R. C.: On Differential Mobility Analyzer Resolution, Aerosol Sci. Tech., 30, 556–570, https://doi.org/10.1080/027868299304417, 1999.

Fuchs, N. A.: On the stationary charge distribution on aerosol particles in a bipolar ionic atmosphere, Geofisica Pura e Applicata, 56, 185–193, https://doi.org/10.1007/BF01993343, 1963.

Herenz, P., Wex, H., Henning, S., Kristensen, T. B., Rubach, F., Roth, A., Borrmann, S., Bozem, H., Schulz, H., and Stratmann, F.: Measurements of aerosol and CCN properties in the Mackenzie River delta (Canadian Arctic) during spring–summer transition in May 2014, Atmos. Chem. Phys., 18, 4477–4496, https://doi.org/10.5194/acp-18-4477-2018, 2018.

Hering, S. V., Spielman, S. R., and Lewis, G. S.: Moderated, Water-Based, Condensational Particle Growth in a Laminar Flow, Aerosol Sci. Tech., 48, 401–408, https://doi.org/10.1080/02786826.2014.881460, 2014.

Hering, S. V., Lewis, G. S., Spielman, S. R., Eiguren-Fernandez, A., Kreisberg, N. M., Kuang, C., and Attoui, M.: Detection near 1-nm with a laminar-flow, water-based condensation particle counter, Aerosol Sci. Tech., 51, 354–362, https://doi.org/10.1080/02786826.2016.1262531, 2017.

Hering, S. V., Lewis, G. S., Spielman, S. R., and Eiguren-Fernandez, A.: A MAGIC concept for self-sustained, water-based, ultrafine particle counting, Aerosol Sci. Tech., 53, 63–72, https://doi.org/10.1080/02786826.2018.1538549, 2019.

Hoppel, W. A. and Frick, G. M.: Ion–aerosol attachment coefficients and the steady-state charge distribution on aerosols in a bipolar ion environment, Aerosol Sci. Tech., 5, 1–21, https://doi.org/10.1080/02786828608959073, 1986.

Huang, Y., Seinfeld, J. H., and Flagan, R. C.: Diffusional Transfer Function for the Scanning Electrical Mobility Spectrometer (SEMS), Aerosol Sci. Tech., 6826, 1–24, https://doi.org/10.1080/02786826.2020.1760199, 2020.

Mai, H., Kong, W., Seinfeld, J. H., and Flagan, R. C.: Scanning DMA Data Analysis II. Integrated DMA-CPC Instrument Response and Data Inversion, Aerosol Sci. Tech., 52, 1–35, https://doi.org/10.1080/02786826.2018.1528006, 2018.

Mamakos, A., Ntziachristos, L., and Samaras, Z.: Differential mobility analyser transfer functions in scanning mode, J. Aerosol Sci., 39, 227–243, https://doi.org/10.1016/j.jaerosci.2007.11.005, 2008.

Mamali, D., Marinou, E., Sciare, J., Pikridas, M., Kokkalis, P., Kottas, M., Binietoglou, I., Tsekeri, A., Keleshis, C., Engelmann, R., Baars, H., Ansmann, A., Amiridis, V., Russchenberg, H., and Biskos, G.: Vertical profiles of aerosol mass concentration derived by unmanned airborne in situ and remote sensing instruments during dust events, Atmos. Meas. Tech., 11, 2897–2910, https://doi.org/10.5194/amt-11-2897-2018, 2018.

McMurry, P. H.: A review of atmospheric aerosol measurements, Atmos. Environ., 34, 1959–1999, https://doi.org/10.1016/S1352-2310(99)00455-0, 2000.

Ortega, J., Snider, J. R., Smith, J. N., and Reeves, J. M.: Comparison of aerosol measurement systems during the 2016 airborne ARISTO campaign, Aerosol Sci. Tech., 53, 871–885, https://doi.org/10.1080/02786826.2019.1610554, 2019.

Ozon, M., Stolzenburg, D., Dada, L., Seppänen, A., and Lehtinen, K. E. J.: Aerosol formation and growth rates from chamber experiments using Kalman smoothing, Atmos. Chem. Phys. Discuss. [preprint], https://doi.org/10.5194/acp-2021-99, in review, 2021.

Russell, L. M., Flagan, R. C., and Seinfeld, J. H.: Asymmetric instrument response resulting from mixing effects in accelerated DMA-CPC measurements, Aerosol Sci. Tech., 23, 491–509, https://doi.org/10.1080/02786829508965332, 1995.

Stolzenburg, M. R.: An ultrafine aerosol size distribution measuring system, Doctoral dissertation, Department of Mechanical Engineering, University of Minnesota, Minneapolis, MN, USA, 1988.

Wang, S. C. and Flagan, R. C.: Scanning electrical mobility spectrometer, Aerosol Sci. Tech., 13, 230–240, https://doi.org/10.1080/02786829008959441, 1990.

Wiedensohler, A.: An approximation of the bipolar charge distribution for particles in the submicron size range, J. Aerosol Sci., 19, 387–389, https://doi.org/10.1016/0021-8502(88)90278-9, 1988.

Zhang, S.-H. and Flagan, R. C.: Resolution of the radial differential mobility analyzer for ultrafine particles, J. Aerosol Sci., 27, 1179–1200, https://doi.org/10.1016/0021-8502(96)00036-5, 1996.

Zhang, S.-H., Akutsu, Y., Russell, L. M., Flagan, R. C., and Seinfeld, J. H.: Radial Differential Mo-

bility Analyzer, Aerosol Sci. Tech., 23, 357–372, https://doi.org/10.1080/02786829508965320, 1995.

Zheng, G., Wang, Y., Wood, R., Jensen, M. P., Kuang, C., McCoy, I. L., Matthews, A., Mei, F., Tomlinson, J. M., Shilling, J. E., Zawadowicz, M. A., Crosbie, E., Moore, R., Ziemba, L., Andreae, M. O., and Wang, J.: New particle formation in the remote marine boundary layer, Nat. Commun., 12, 527, https://doi.org/10.1038/s41467-020-20773-1, 2021.

ABOUT THE AUTHOR

Christopher M. Kenseth was born in Berlin, Vermont, on August 28, 1992. Growing up in Montpelier, the capital of the Green Mountain State, with his parents, Marian and Evan, and older brother, Peter, he developed a deep appreciation for the natural world and lifelong passion for the outdoors, especially skiing and baseball. Inspired by the instruction of his high school chemistry teacher, Ms. Toni Ceckler, Chris came to regard chemistry as a compelling framework through which to view and understand the world. In 2011, he matriculated to the University of Vermont (UVM) as a Green and Gold Scholar to pursue a BS in chemistry.

At UVM, Chris spent three years conducting research in atmospheric aerosol chemistry with Prof. Giuseppe Petrucci, speciating emissions of green leaf volatiles from cut grass, quantifying their aerosol formation potential, and characterizing a novel soft-ionization aerosol mass spectrometer for on-line, molecular-level analysis. The time that he spent as a member of the Petrucci Lab was the most rewarding and invaluable aspect of his undergraduate career.

After graduating from UVM *summa cum laude* as a Goldwater Scholar and member of Phi Beta Kappa, Chris came to the California Institute of Technology (Caltech) in 2015 to pursue a PhD in atmospheric chemistry. Jointly advised by Profs. John Seinfeld, Paul Wennberg, and Brian Stoltz, he applied advanced mass spectrometric, chromatographic, and synthetic techniques to characterize the molecular composition, and in turn elucidate the formation and aging mechanisms, of secondary organic aerosol (SOA) derived from the atmospheric oxidation of α-pinene and β-pinene. In 2021, he received the Herbert Newby McCoy Award, which "recognizes the most outstanding achievements in research by a Chemistry and Chemical Engineering graduate student." This July, Chris will begin an NSF Atmospheric and Geospace Sciences Postdoctoral Research Fellowship in the Department of Atmospheric Sciences at the University of Washington with Prof. Joel Thornton, where he will combine organic synthesis, laboratory experiments, atmospheric modeling, and field measurements to study the chemistry of monoterpene organic nitrates.